10th ICCSM

10th International Congress of Croatian Society of Mechanics

Organised by
Croatian Society of Mechanics

Under the Auspices of
Croatian Academy of Sciences and Arts

Co-organizer
Central European Association for Computational Mechanics

Proceedings

of the 10th International Congress of Croatian Society of Mechanics

Editors:
Ivica Skozrit
Jurica Sorić
Zdenko Tonković

CSM
CROATIAN SOCIETY OF MECHANICS
ZAGREB - OSIJEK - RIJEKA - SL. BROD - SPLIT

Pula, Croatia, September 28 – 30, 2022

Published by
Croatian Society of Mechanics

Head Office
Croatian Society of Mechanics
Ivana Lučića 5, 10000 Zagreb, Croatia
www.csm.hr

Design:
Ivica Skozit

Printed in
Eurotisak

Issues: 220 copies

ISSN 2623-6133

General Chairs

Zdenko TONKOVIĆ, University of Zagreb
Jurica SORIĆ, University of Zagreb

Organising Committee

Ivica SKOZRIT, University of Zagreb, President
Marko ČANAĐIJA, University of Rijeka
Darko DAMJANOVIĆ, University of Slavonski Brod
Antonia JAGULJNJAK-LAZAREVIĆ, University of Zagreb
Gordan JELENIĆ, University of Rijeka
Dražan KOZAK, University of Slavonski Brod
Hrvoje KOZMAR, University of Zagreb
Ivica KOŽAR, University of Rijeka
Ivan KRAUS, University of Osijek
Lovre KRSTULOVIĆ-OPARA, University of Split
Pavao MAROVIĆ, University of Split
Mladen MEŠTROVIĆ, University of Zagreb
Davorin PENAVA, University of Osijek
Ivica SMOJVER, University of Zagreb

International Scientific Committee

Giulio ALFANO, Brunel University London, UK
Ferri M.H. ALIABADI, Imperial College, London, UK
Oliver ALLIX, Ecole Normale Supérieure de Cachan, France
Satya N. ATLURI, Texas Tech University, USA
Ferdinando AURICCHIO, University of Pavia, Italy
Klaus-Juergen BATHE, Massachusetts Institute of Technology, USA
Ivano BENEDETTI, University of Palermo, Italy
Peter BETCH, Karlsruhe Institute of Technology, Germany
Manfred BISCHOFF, Universitaet Stuttgart, Germany
Bert BLOCKEN, Eindhoven University of Technology, Netherlands
Claudio BORRI, University of Florence, Italy
Boštjan BRANK, University of Ljubljana, Slovenia
Rene DE BORST, University of Sheffield, UK
Laura DE LORENZIS, ETH Zuerich, Switzerland
Josef EBERHARDSTEINER, Vienna Technical University, Austria
Anaxagoras ELENAS, Democritus University of Thrace, Greece
Ugo GALVANETTO, University of Padua, Italy
Marc G.D. GEERS, Eindhoven University of Technology, Netherland
Antonio J. GIL, Swansea University, UK
Srečko GLODEŽ, University of Maribor, Slovenia
Friedrich GRUTTMANN, TU Darmstadt, Germany
Nenad GUBELJAK, University of Maribor, Slovenia
Gerhard A. HOLZAPFEL, Graz University of Technology, Austria
Adnan IBRAHIMBEGOVIĆ, Universite de technologie Compiegne, France
Mikhail ITSKOV, RWTH Aachen, Germany
Alojz IVANKOVIĆ, University College Dublin, UK
Michael KALISKE, TU Dresden, Germany
Ahsan KAREEM, University of Notre Dame, USA
Gabriel KATUL, Duke University, USA

Sven KLINKEL,	RWTH Aachen, Germany
Carsten KOENKE,	Bauhaus-University Weimar, Germany
Jože KORELC,	University of Ljubljana, Slovenia
Meinhard KUNA,	TU Bergakademie Freiberg, Germany
Wing Kam LIU,	Northwestern University, USA
Stefan LOEHNERT,	TU Dresden, Germany
Herbert A. MANG,	Vienna Technical University, Austria
Hermann G. MATTHIES,	TU Braunschweig, Germany
Hiroshi OKADA,	Tokyo University of Science, Japan
Joško OŽBOLT,	Universitaet Stuttgart, Germany
Anna PANDOLFI,	Politecnico di Milano, Italy
Manolis PAPADRAKAKIS,	National Technical University Athens, Greece
Henryk PETRYK,	Polish Academy of Sciences, Poland
Yuri PETRYNA,	TU Berlin, Germany
Bernhard PICHLER,	Vienna University of Technology, Austria
Demosthenes POLYZOS,	University of Patras, Greece
Franz G. RAMMERSTORFER,	Vienna Technical University, Austria
Zoran REN,	University of Maribor, Slovenia
Stefanie REESE,	RWTH Aachen, Germany
Bernhard SCHREFLER,	University of Padua, Italy
Joerg SCHROEDER,	Universitaet Duisburg-Essen, Germany
Sebastian SKATULLA,	University of Cape Town, South Africa
Jan SLADEK,	Slovak Academy of Sciences, Slovakia
Božidar ŠARLER,	University of Ljubljana, Slovenia
Matej VESELNJAK,	University of Maribor, Slovenia
Rade VIGNJEVIĆ,	Brunel University London, UK
Jens WACKERFUSS,	University Kassel, Germany
Werner WAGNER,	Karlsruhe Institute of Technology, Germany
Peter WRIGGERS,	Leibniz University of Hannover, Germany

Congress secretariat

Tourist agency PerfectMeetings.hr,
URKA d.o.o., Cernička 21, 10000 Zagreb

SPONSORS:

Golden sponsors

AVL AST d.o.o. CROATIA, Strojarska 22, HR-10020 Zagreb, Croatia

ECON ENGINEERING KFT., Kondorosi út 3., 4th floor, H-116 Budapest, Hungary

Silver sponsor

KONČAR – Electrical Industry, Fallerovo šetalište 22, 10000 Zagreb, Croatia

Bronze sponsors

CVH – CENTER FOR VEHICLES OF CROATIA, Capraška 6, HR-10000 Zagreb, Croatia

KONČAR – Distribution and Special Transformers Inc., Josipa Mokrovića 8, 10090 Zagreb, Croatia

TOPOMATIKA three-dimensional scanning, optical measuring systems and computer processing d.o.o., Industrijska ulica 3, Novaki, HR-10431 Sveta Nedelja, Croatia

Sponsor

KONČAR – Steel Structures Inc., Fallerovo šetalište 22, HR-10000, Zagreb, Croatia

Preface

The Croatian Society of Mechanics is an association with the objective of promoting education, research and application in the field of fluid and solid mechanics. Within the framework of this Society, scientific gatherings have been organised in order to make an environment for the exchange of new ideas and achievements in mechanical sciences. The most prominent scientific events are the international congresses of the Croatian Society of Mechanics. The nine previous congresses took place in Pula in 1994, Supetar in 1997, Cavtat in 2000, Bizovac in 2003, Seget in 2006, Dubrovnik in 2009, Zadar in 2012, Opatija in 2015 and in Split 2018. It has always been the intention to hold the conference in an attractive environment. Therefore, the place of the 10th International Congress of the Croatian Society of Mechanics (10th ICCSM) is Pula, the city of the Istrian peninsula, and one of the Croatia's most popular tourist destination. After nine very successful ICCSM conferences we are returning to the same venue, where the conferences started. The Congress has been organised under the auspices of the Croatian Academy of Sciences and Arts and the co-organizer is Central European Association for Computational Mechanics, CACM.

The scientific programme of the 10th ICCSM consists of 4 plenary lectures and 136 regular lectures divided into 29 sessions in which there are 4 organized sessions. In the plenary lectures, prominent researches have addressed the state-of-the-art advances in the mechanical sciences. In other contributions, the scientists from all over the world have provided an international forum for the presentation and discussion of recent advances in various fields of theoretical and applied mechanics. Special attention is directed to the development of modern numerical formulations. This scientific gathering is also an opportunity for valuable interactions between junior and senior researchers that may result in new ideas as well as new in prospective research directions.

This proceedings contains the extended abstracts of the three plenary contributions and the extended abstracts of all 136 regular presentations. All contributions are printed from camera-ready copies submitted by the authors. Therefore, the editors do not assume liability for possible errors or inconsistencies. The extended abstracts are also published in Book of abstracts.

We gratefully acknowledge the valuable contribution of the plenary speakers who gladly accepted our invitations, and all the authors of the contributed papers. Furthermore, we express our gratitude to the members of the Scientific Committee who promoted our Congress worldwide as well as to the colleagues who chair the Congress sessions. Many thanks go to our sponsors, especially the golden sponsors AVL AST d.o.o. CROATIA, Zagreb and ECON ENGINEERING KFT., Budapest, Hungary, the silver sponsor KONČAR – Electrical Industry, Zagreb, the bronze sponsors CVH – CENTER FOR VEHICLES OF CROATIA, Zagreb, KONČAR – Distribution and Special Transformers Inc., Zagreb and TOPOMATIKA three-dimensional scanning, optical measuring systems and computer processing d.o.o., Sveta Nedelja, Croatia as well as the sponsor KONČAR – Steel Structures Inc., Zagreb. Without their valuable financial support we were not able to organize this scientific gathering successfully.

Special thanks go to Tina Pintar our administrative secretary, who contributed to the success of the Congress. Finally, we would like to thank everyone who helped in any way in organising this scientific event.

Ivica Skozrit,
Jurica Sorić,
Zdenko Tonković

TABLE OF CONTENTS

Plenary Lectures

Organized Sessions

Cellular structures *by L. Krstulović-Opara, M. Vesenjak and Z. Ren*

Contributed lectures

10th ICCSM, Pula, 2022

Plenary Lectures

EUCLID: Efficient Unsupervised Constitutive Law Identification and Discovery

Moritz Flaschel[*], Siddhant Kumar[+], Laura De Lorenzis[*]

[*]*Department of Mechanical and Process Engineering, ETH Zürich, 8092 Zürich, Switzerland*
E-mails: {mflaschel,ldelorenzis}@ethz.ch

[+]*Department of Materials Science and Engineering, Delft University of Technology, 2628 CD Delft, The Netherlands*
E-mail: sid.kumar@tudelft.nl

Keywords: material modeling, unsupervised learning, inverse problems, sparse regression

1. Introduction

Computational simulations provide a powerful tool for predicting the behavior of solid bodies under external loading. However, their predictive ability highly depends on the correct choice and calibration of the material model, a ubiquitous problem in solid mechanics. Traditional material models with an a priori-chosen mathematical form require trial-and-error procedures to update the choice of this form until the model succeeds to accurately describe the material behavior observed in experiments. Machine-learning based material models provide a promising alternative, but training such models generally relies on large amounts of stress-strain data pairs, that are not realistically available from experiments. In this light, we propose EUCLID (Efficient Unsupervised Constitutive Law Identification and Discovery); a method for automatically discovering material models and their probability distributions. The two main features of this method are: i. the mathematical form of the material model is not chosen a priori, but automatically selected from a large ansatz space, ii. the method solely relies on experimentally measurable data, i.e. full-field displacements and net reaction forces.

2. EUCLID

The objective of EUCLID is to discover interpretable material models from a large catalogue of candidate models, which is constructed through a general parametric ansatz that depends on a large set of material parameters $\boldsymbol{\theta}$. To compensate for the lack of labeled data, EUCLID employs physics knowledge, i.e., given the full-field displacements and net reaction forces, the residuals of the weak linear momentum balance are minimized together with a sparsity promoting regularization term

$$\boldsymbol{\theta}^{\mathrm{opt}} = \mathrm{argmin} \sum_i \left\| \boldsymbol{f}_i^{\mathrm{int}}(\boldsymbol{\theta}) \right\|_2^2 + \lambda_r \sum_j \left\| R_j^{\mathrm{int}}(\boldsymbol{\theta}) - R_j \right\|_2^2 + \lambda_p \|\boldsymbol{\theta}\|_p^p, \tag{1}$$

where $\boldsymbol{f}_i^{\mathrm{int}}$ are the internal forces in the bulk material, R_j^{int} are the integrated internal forces at the boundary, R_j are the measured reaction forces, λ_r and λ_p are weighting coefficients, and $\|\boldsymbol{\theta}\|_p^p$ is the (quasi) L_p-norm for $0 < p \leq 1$, which promotes sparse material parameter vectors and hence mathematically concise and physically interpretable material models.

EUCLID has been successfully demonstrated for the discovery of hyperelastic [1] and elasto-plastic [2] material models. In these two cases, large catalogues are constructed respectively for the strain energy density function or for plastic yield surfaces with hardening laws, and the minimization problem in Equation (1) is solved. Figure 1 shows exemplary results of true and discovered yield functions for different noise levels σ and different benchmark models, as well as yield surface plots of the true and discovered Tresca model after isotropic and kinematic hardening. It is observed that EUCLID discovers in many cases the correct mathematical form of the yield function and accurately identifies the shape of the yield surface.

	Benchmarks	Yield Function (f)
VM	Truth	$\sqrt{3/2}r - 0.2400$
	$\sigma = 0$	$\sqrt{3/2}r - 0.2400$
	$\sigma = 10^{-4}$	$\sqrt{3/2}r - 0.2402$
	$\sigma = 3 \cdot 10^{-4}$	$\sqrt{3/2}r - 0.2440$
F1	Truth	$\sqrt{3/2}r - (0.2200 + 0.0200\cos(3\alpha))$
	$\sigma = 0$	$\sqrt{3/2}r - (0.2200 + 0.0200\cos(3\alpha))$
	$\sigma = 10^{-4}$	$\sqrt{3/2}r - (0.2187 + 0.0220\cos(3\alpha))$
	$\sigma = 3 \cdot 10^{-4}$	$\sqrt{3/2}r - (0.2223 + 0.0252\cos(3\alpha))$
TR	Truth	$\max(\lvert\sigma_1 - \sigma_2\rvert, \lvert\sigma_2 - \sigma_3\rvert, \lvert\sigma_3 - \sigma_1\rvert) - 0.2400$
	$\sigma = 0$	$\sqrt{3/2}r - (0.2139 - 0.0012\cos(3\alpha) + 0.0169\cos(6\alpha) + 0.0013\cos(9\alpha) + 0.0046\cos(12\alpha))$
	$\sigma = 10^{-4}$	$\sqrt{3/2}r - (0.2143 - 0.0024\cos(3\alpha) + 0.0158\cos(6\alpha) + 0.0012\cos(9\alpha) + 0.0049\cos(12\alpha))$
	$\sigma = 3 \cdot 10^{-4}$	$\sqrt{3/2}r - (0.2188 + 0.0114\cos(6\alpha) + 0.0056\cos(12\alpha))$

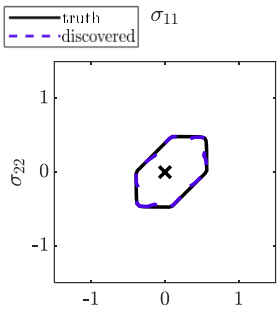

Figure 1. True and discovered yield functions for different benchmark models [2]

3. Bayesian-EUCLID

In our most recent work [3], the problem of material model discovery is considered from a Bayesian perspective. Through Markov Chain Monte Carlo sampling, Bayesian-EUCLID deduces a posterior probability distribution for the unknown material parameters $\boldsymbol{\theta}$, which is a joint distribution of the model likelihood and a sparsity promoting spike-and-slab prior. In this way, parsimonious and interpretable material models can be discovered with quantifiable uncertainties. An example considering the hyperelastic Isihara model is shown in Figure 2, where it is seen that the method assigns high probabilities to true parameters and suppresses the activity of false parameters. Further, the strain energy density functions of the true and discovered models along different deformation paths are in good agreement and narrow confidence intervals are observed.

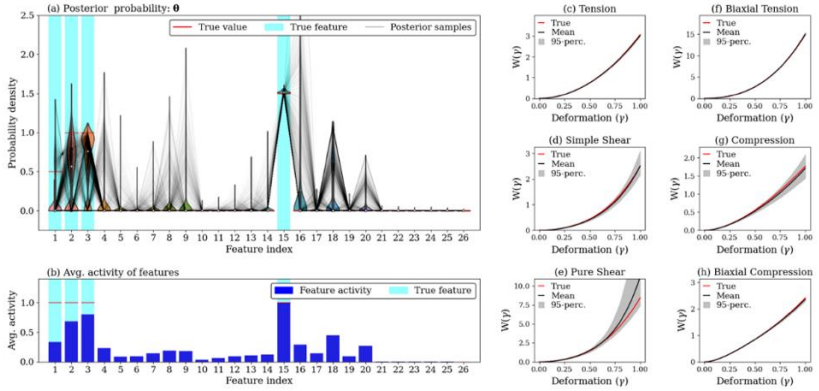

Figure 2. Posterior distribution (a) and activity (b) of the material parameters, and strain energy density of the true and discovered models along the different deformation paths (c-h) [3]

References

[1] M. Flaschel, S. Kumar, and L. De Lorenzis, "Unsupervised discovery of interpretable hyperelastic constitutive laws," *Comput. Methods Appl. Mech. Eng.*, vol. 381, p. 113852, Aug. 2021, doi: 10.1016/j.cma.2021.113852.

[2] M. Flaschel, S. Kumar, and L. De Lorenzis, "Discovering plasticity models without stress data," *ArXiv220204916 Cs*, Feb. 2022, Accessed: Mar. 17, 2022. [Online]. Available: http://arxiv.org/abs/2202.04916. In press on npj Computational Materials.

[3] A. Joshi *et al.*, "Bayesian-EUCLID: discovering hyperelastic material laws with uncertainties," *ArXiv220307422 Cs*, Mar. 2022, Accessed: Mar. 17, 2022. [Online]. Available: http://arxiv.org/abs/2203.07422

Extreme mechanics: the tungsten plasma-facing shields in the future fusion reactors

Marc Geers[*], Varun Shah[#], Mathieu Oude Vrielink[*], Yu Li[+],
Hans van Dommelen[*], Thomas Morgan[+], Johan Hoefnagels[*]

[*]*Eindhoven University of Technology*
Department of Mechanical Engineering, The Netherlands

[+]*Dutch Institute for fundamental energy research*
DIFFER, Eindhoven, The Netherlands

[#]*Computational Mechanical and Materials Engineering*
University of Groningen, The Netherlands

Keywords: Energy, Fusion reactor, Tungsten, Multiscale, Extreme mechanics

1. Introduction

The growing demand for green and clean energy is one of the major challenges for our society in the coming decades and century. Nuclear fusion is one of the most attractive and unlimited sources of energy that would be able to solve this problem. However, a nuclear fusion reactor puts unprecedented requirements on materials to sustain the harsh operation conditions in the tokamak that magnetically confines the plasma.

2. Problem statement

One of the critical components is the divertor, which extracts heat and serves as an exhaust. The divertor is typically composed of tungsten monoblocks, consisting of a tungsten tile that is bonded to a water-cooled copper alloy heat sink.

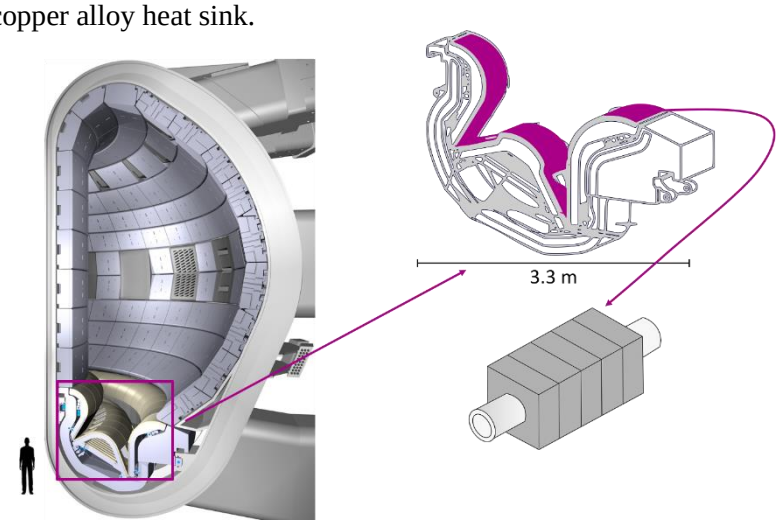

Figure 1. Cross-section of a fusion reactor, with the divertor components highlighted

As a plasma-facing material, tungsten is subjected to high thermal and particle loads (neutrons and ions). The high thermal loads do not only induce large thermal gradients, but they also entail microstructural evolution. The particle loads result in the generation of point defects (vacancies, self-interstitials) and clustered lattice defects (e.g. nano-pores). The ingression of helium leads to interactions with these defects, affecting the overall properties and performance of the tungsten material. Understanding the mechanical performance, damage and (loss of) ductility of tungsten under these harsh conditions is only possible through an integrated multi-scale modelling approach.

3. Multiscale model for tungsten in fusion conditions

This contribution presents a multi-scale model for the complex mechanical and physical behaviour of tungsten in fusion conditions. The key ingredients of this multiscale approach are:

- Neutron-induced displacement cascade damage in tungsten, using a cluster dynamics model [1,2]
- Multiscale model for the Helium implantation from the plasma, leading to bubble formation and complex interactions with the irradiation induced defects [6]
- Thermal loads and excursions, entailing microstructural recrystallization with evolving defects, for which a numerical approach to predict the monoblocks' recrystallization during cyclic heat load exposure is presented [1,3,9]
- The brittle-to-ductile transition: a crystal plasticity model with a novel cleavage criterion to capture the sharp transition from a brittle response to a more ductile behaviour in high-purity tungsten [5,7,8,10].
- A two-scale fracture probability analysis investigating the unstable growth of pre-existing cracks for different loading scenarios of a tungsten monoblock [11].

The presented work is complemented by advanced experiments, exploiting the extreme conditions generated by the linear plasma generator Magnum- PSI [4].

4. Conclusions

The proposed multi-scale approach bridges length scales ranging from the level of lattice point defects (in the form of vacancies and interstitials) to the polycrystalline microstructure and to the scale of a tungsten monoblock. The developed models provide adequate qualitative insights in the complex brittle-to-ductile fracture behaviour of tungsten.

References

[1] A. Mannheim, J.A.W. van Dommelen, M.G.D. Geers, Modelling recrystallization and grain growth of tungsten induced by neutron displacement defects, *Mechanics of Materials* 123, pp. 43-58, 2018

[2] A. Mannheim, J.A.W. van Dommelen, M.G.D. Geers, Long-term microstructural evolution of tungsten under heat and neutron loads, *Computational Materials Science* 170, article 109146, 2019

[3] V. Shah, …, J.A.W. van Dommelen, M.G.D. Geers, Experimental investigation of the microstructural changes of tungsten monoblocks exposed to pulsed high heat loads, *Nuclear materials and Energy* 22, article 100716, 2020

[4] Y. Li, T.W. Morgan, …, M.G.D. Geers, Fracture behavior of tungsten-based composites exposed to steady-state/transient hydrogen plasma, *Nuclear Fusion 60*(4), article 046029, 2020

[5] M.A. Oude Vrielink, J.A.W. van Dommelen and M.G.D. Geers. Numerical investigation of the brittle-to-ductile transition temperature of rolled high- purity tungsten, *Mechanics of Materials*, 145:103394, 2020

[6] V. Shah, J.A.W. van Dommelen, M.G.D. Geers, Spatially dependent kinetics of helium in tungsten under fusion conditions, *Journal of Nuclear Materials* 535, article 152104, 2020

[7] V. Shah, J.A.W. van Dommelen, …, M.G.D. Geers, Brittle-ductile transition temperature of recrystallized tungsten following exposure to fusion relevant cyclic high heat load, *Journal of Nuclear Materials* 541, article 152416, 2020

[8] M.A. Oude Vrielink, J.A.W. van Dommelen and M.G.D. Geers. Computational analysis of the evolution of the brittle-to-ductile transition of tungsten under fusion conditions. *Modelling and Simulation in Materials Science and Engineering*, 29(1):015005, 2020.

[9] V. Shah, J.A.W. van Dommelen, S.E.S. Heijkoop, M.A. Oude Vrielink, M.G.D. Geers, A numerical model for the recrystallization kinetics of tungsten monoblocks under cyclic heat loads, *Fusion Engineering Design* 173, article 112827, 2021.

[10] M.A. Oude Vrielink, V. Shah, J.A.W. van Dommelen, M.G.D. Geers, Modelling the brittle-to-ductile transition of high-purity tungsten under neutron irradiation, *Journal of Nuclear Materials* 554, article 153068, 2021

[11] M.A. Oude Vrielink, J.A.W. van Dommelen, M.G.D. Geers, Multi-scale fracture probability analysis of tungsten monoblocks under fusion conditions, *Nuclear Materials and Energy* 28, article 101032, 2021

Magnetic microstructures – modeling and FE discretization schemes

Jörg Schröder*, Maximilian Reichel+

*Institute of Mechanics, University of Duisburg-Essen, Universitätsstr. 14, 45141 Essen, Germany
E-mails: {j.schroeder, maximilian.reichel}@uni-due.de

Keywords: Micromagnetic Simulations, Landau-Lifshitz-Gilbert, Finite Elements, Microstructure

1. Introduction

Current challenges such as the "Energiewende" and novel cooling systems are creating a steadily increasing demand for high-performance magnets. To meet this demand, new powerful magnets must be developed. Besides a particularly high power density, these magnets must also satisfy high requirements in terms of environmental compatibility as well as geopolitical factors. Here, micromagnetic simulations can be a very powerful tool to predict promising magnetic composites.

2. Magneto-elastic micromagnetic framework

The considered boundary value problem can be described by the magnetic Gauss law div $\boldsymbol{B} = 0$ and the balance of linear momentum div $\boldsymbol{\sigma} = \boldsymbol{0}$, where $\boldsymbol{B}$ represents the magnetic induction and $\boldsymbol{\sigma}$ the mechanical stress. The induction can be stated as $\boldsymbol{B} = \mu_0(\boldsymbol{H} + \boldsymbol{M})$, with the vacuum permeability μ_0, the magnetic field $\boldsymbol{H}$ and the magnetization $\boldsymbol{M}$. The latter can be split into $\boldsymbol{M} = M_s\boldsymbol{m}$, where M_s denotes the magnetization saturation and $\boldsymbol{m}$ the magnetic unit director. The magnetic field is derived form a magnetic scalar potential $\boldsymbol{H} = -\nabla\varphi$, while the mechanical stress is given by the linear relation $\boldsymbol{\sigma} = \mathbb{C} : \boldsymbol{\varepsilon}$, with the material tangent $\mathbb{C}$ and the linear strains $\boldsymbol{\varepsilon} = \frac{1}{2}(\nabla^{\mathrm{T}}\boldsymbol{u} + \boldsymbol{\nabla u})$. Inside the magnetic solid, several different energy contributions are in competition with each other. The here considered energies include a magnetostatic contribution $\mathcal{H}^{\mathrm{mag}}$, a magnetic exchange contribution $\mathcal{H}^{\mathrm{exc}}$, a contribution to the magneto crystalline anisotropy $\mathcal{H}^{\mathrm{ani}}$ and an elastic contribution $\mathcal{H}^{\mathrm{ela}}$. Hence, the total magnetic energy functional can be stated as

$$\mathcal{H}(\boldsymbol{\varepsilon}, \boldsymbol{H}, \boldsymbol{m}, \nabla\boldsymbol{m}) = \mathcal{H}^{\mathrm{mag}}(\boldsymbol{H}, \boldsymbol{m}) + \mathcal{H}^{\mathrm{exc}}(\nabla\boldsymbol{m}) + \mathcal{H}^{\mathrm{ani}}(\boldsymbol{m}) + \mathcal{H}^{\mathrm{ela}}(\boldsymbol{\varepsilon}, \boldsymbol{m}). \tag{1}$$

Both the magnetic induction and the mechanical stress can be derived via constitutive relations from the energy functional as $\boldsymbol{B} = -\partial\mathcal{H}/\partial\boldsymbol{H}$ and $\boldsymbol{\sigma} = \partial\mathcal{H}/\partial\boldsymbol{\varepsilon}$. To predict the evolution of the magnetization vectors, the Landau-Lifshitz-Gilbert (LLG) equation is introduced at this point as

$$\dot{\boldsymbol{m}} = -\gamma_0\mu_0\,\boldsymbol{m} \times \boldsymbol{H}^{\boldsymbol{eff}} + \alpha\,\boldsymbol{m} \times \dot{\boldsymbol{m}}, \tag{2}$$

where the $\boldsymbol{H}^{\mathbf{eff}} = \frac{-1}{\mu_0 \mathrm{Ms}}\delta\mathcal{H}/\delta\boldsymbol{m}$ is the effective field and γ_0 the gyromagnetic ratio and α the Gilbert damping parameter. The LLG equation requires the fulfillment of the unit constraint $||\boldsymbol{m}||=1$, that is considered here by adding a penalty term $\mathcal{H}^{\mathrm{pen}}(\boldsymbol{m})=\kappa(||\boldsymbol{m}|| - 1)^2$ to the total energy, where κ denotes the penalty parameter. An overview of magnitude preserving strategies is given in [1].

3. Numerical examples

By combining ferromagnetic and non-ferromagnetic materials, improved values in the coercive field strength can be achieved. The aim is to decouple the grains from the surrounding grains by using the non-ferromagnetic material as a boundary layer [2]. Hence, a polycrystalline microstructure is considered here, which is a composition of 7 $Nd_2Fe_{14}B$ hexagonal grains of 65nm diameter. The grains are separated from each other by an Nd-rich intergranular phase, which is assumed to be 3nm and 8nm thick in the following example. Thinner interphases, in contrast to thicker ones, allow for

significantly more exchange between the grains. The influence of the exchange coupling or decoupling of the grains, by the interphase layer, on the magnetization reversal and thus on the resulting coercivity is investigated here. The magneto crystalline anisotropy (K), the saturation magnetization (M_s), and the exchange interactions (A_{exc}) within the 3nm interphase are chosen in analogy to [2], to be 0 J/m^3, 0.64 MA/m and 4 pJ/m, while the 8nm interphase is considered to behave purely paramagnetic. The magnetic and the mechanical material parameters are taken from [2] and [3]. The hysteresis loops were calculated by minimizing the total energy. Therefore, an external magnetic field with a step size of $\mu_0 H_2$=0.01T was cycled between -10T and 10T. For faster convergency of the quasi-static states, a Gilbert damping parameter α = 1 was applied. The stray field effects were considered by a free space matrix surrounding the grains.

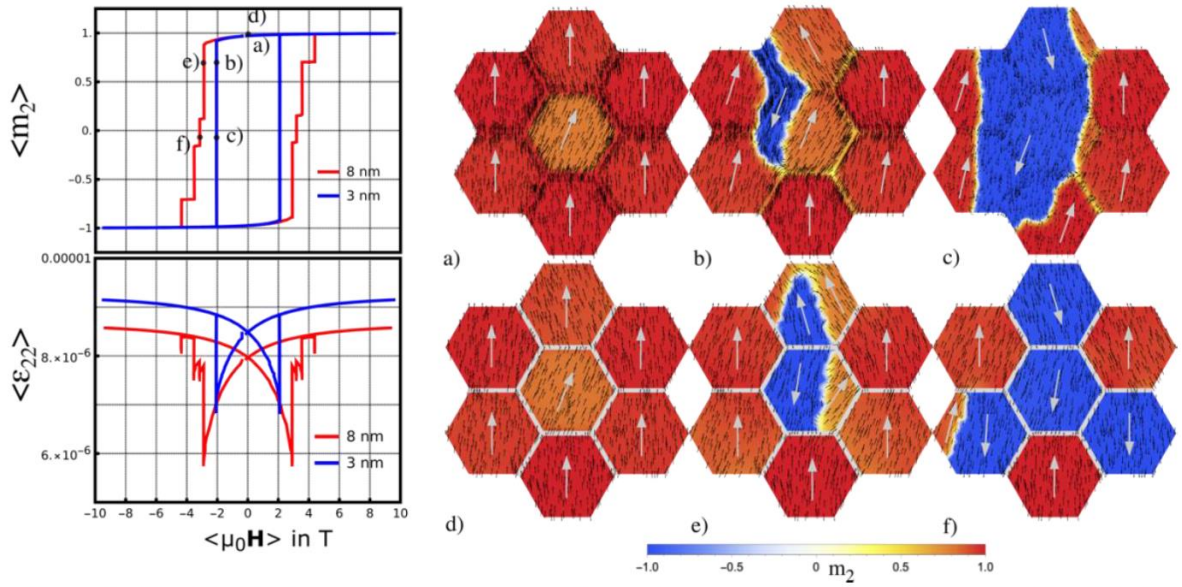

Figure 1. The effective hysteresis loops $< m_2 - H_2 >$ and $< \varepsilon_{22} - H_2 >$ are given on the left with the corresponding switching states shown in a)-f).

4. Conclusions

In this contribution, the influence of exchange coupled and decoupled grains on magnetization reversal was investigated. Exchange coupled systems have significantly lower coercivity than decoupled systems. Once the reversal starts, it propagates cascade-like through the structure. In a decoupled system, the grains switch independently. A jumping over of the reversal to neighboring grains is mainly prevented by the interphase layer.

Acknowledgement We gratefully acknowledge the financial support of the German Research Foundation (DFG) in the framework of the CRC/TRR 270, project A07 "Scale-bridging of magneto-mechanical mesostructures of additive manufactured and severe plastically deformed materials", project number 405553726.

References

[1] Yi, M., Xu, B.-X., A constraint-free phase field model for ferromagnetic domain evolution. *Proceedings of the Royal Society A: Mathematical, Physical and Engineering Science*, 470, 20140517, 2014.

[2] Soderžnick, M., Sepheri-Amin, H.,Sasaki, T.T., Ohkubo, T., Takada, Y., Sato, T., Kaneko, Y., Kato, A., Schrefl, T., Hono, K., Magnetization reversal of exchange-coupled and exchange-decouipled Nd-Fe-B magnets observed by magneto-optical Kerr effect microscopy. Acta Materialia, 135, 68-76, 2017.

[3] Sridhar, A., Keip, M.-A., Miehe, C., Homogenization in micro-magneto-mechanics. Computational Mechanics, 58, 151-169, 2016.

10th ICCSM, Pula, 2022

Organized Session:

Cellular structures by L. Krstulović-Opara, M. Vesenjak and Z. Ren

Experimental Determination of Shear Modulus of Polyurethane Foam Using Two Test Procedures

Antonio Bakran*, Paulina Krolo*, Lazar Lukačević*

*Faculty of Civil Engineering University of Rijeka
E-mails: {abakran, paulina.krolo,llukacevic}@gradri.uniri.hr

Keywords: polyurethane foam, sandwich core materials, shear properties, ISO 1922

1. Introduction

Polyurethane (PU) foams are widely used as core materials for sandwich structures as insulating systems, in construction, marine application, etc. An important part of the sandwich structure is the core, which usually carries shear loads. Choosing a reliable test method and knowing the exact shear properties of the core used in structural design is useful for engineering practice. The shear properties of the core can be determined by several test methods described in ASTM C273 [1] and ISO 1922 [2] standards. Determination of shear properties of PVC foam according to ASTM C273 standard and using DIC technology is described in [3].

This paper aims to present the ISO 1922 standard test method used to determine the PU foam core shear modulus using two procedures of measuring the displacements, in a standard known as Procedure A and B. While Procedure A is only recommended for obtaining shear strength, Procedure B is recommended for obtaining shear modulus using extensometers. The aim of this paper is to determine the influence of the accuracy of displacement measurement obtained by Procedure A and B on the shear modulus of PU foam.

2. Experimental research

The laboratory tests were performed on PU foam with a nominal density of 45 kg/m^3. A total of five specimens with dimensions of 250×50×25 mm were cut out of the sandwich panel core. The apparent density was measured for each specimen according to ISO 845 [4] standard, and the average value for five specimens is equal to 39.5 kg/m^3.

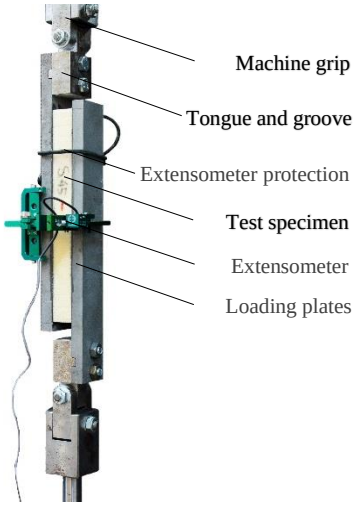

Figure 1. Test set-up for the shear test with an extensometer

According to ISO 1922 standard, the test specimen consists of a sandwich core material and metal loading plates attached to the tensile metal fittings (Figure 1). PU foam prisms are glued to the loading plates using a two-component epoxy adhesive Araldite 2014-2. The specimen is fitted into testing machine loading grips that transfer the shear force to the core material.

Test specimens are marked as S45-1, where the first mark defines the type of test (S-shear), the second mark defines the nominal density of PU foam, and the last mark defines the number of specimens.

The tests were performed on the universal tension-compression Zwick/Roell Z600 testing machine using a load cell of capacity 50 kN. Mechanical grips with a capacity of 10 kN were used. Prior to testing, specimens were conditioned for 6 hours at a room temperature of 22 °C with a relative humidity of 42,7%. The shear in the specimen is applied using displacement control of moving crosshead, with a test speed of 1 mm/min.

According to Procedure A, displacement was recorded on the test machine, while Procedure B demands the usage of an external extensometer that measure the relative displacement between loading plates.

2. Results

The typical force-displacement curves obtained by the shear tests of specimens with a nominal density of 45 kg/m^3 are plotted in Figure 2a. The curve represents the results for procedure A. The shear modulus was calculated using the expression according to ISO 1922 standard, in such a way that the thickness of the specimen is multiplied by the slope of the linear portion of the force-displacement diagram and divided with a shear cross-section of the specimen. The average value of the shear modulus for five specimens according to Procedure A is equal to 2.47 MPa, while the shear modulus according to Procedure B is equal to 3.30 MPa (Figure 2b).

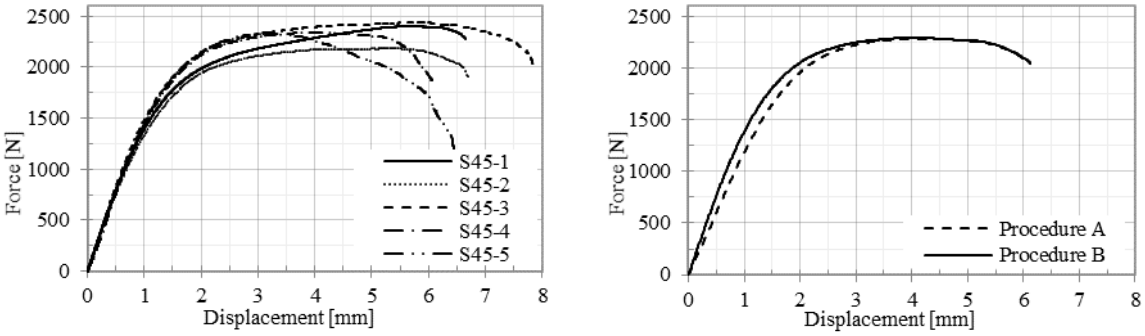

(a) (b)

Figure 2. (a) Force-displacement curves for Procedure A, and (b) Comparison between Procedure A and Procedure B for average values of forces and displacements

6. Conclusions

This paper was focused on determining the shear modulus of PU foam according to a Standard ISO 1922 where two different procedures displacement measurement were used. Despite the fact that it is recommended to use Procedure B to determine the shear modulus, it can also be obtained by Procedure A. The advantage of Procedure A is that it is not necessary to use additional measuring devices on specimens. However, for PU foams of lower densities, it is evident that measuring the displacement using Procedure A gives a significant difference in the shear modulus. The study showed that the difference between average values of the shear modulus obtained by Procedure A and B is equal to 22.9%.

Acknowledgements

The research presented in this work was done within the scientific project “Investigation of the behaviour of composite panel components with integrated steel core” (ZIP-UNIRI-1500-2-20) and IRI 2 industrial project “Prefabricated buildings of almost zero energy produced in an industrial way” (KK.01.2.1.02.0046).

References

[1] ISO 1922:2018; Rigid Cellular Plastics–Determination of Shear Properties. ISO: Geneva, Switzerland, 2018.

[2] ASTM C273/C273M-16; Standard Test Method for Shear Properties of Sandwich Core materials. ASTM International: West Conshohocken, PA, USA, 2016.

[3] Bolf, D.; Zamarin, A.; Krolo, P.; Hadjina, M. Experimental Evaluation of Shear Properties of Lightweight PVC Core for Marine Application Using Digital Image Correlation System. J. Mar. Sci. Eng. 2022, 10, 280. https://doi.org/10.3390/jmse10020280

[4] ISO 845:2006; Cellular plastics and rubbers – Determination of apparent density. ISO: Geneva, Switzerland, 2006.

Advanced numerical methodology for impact damage modelling in laminated CFRP structures

Darko Ivančević*, Luka Stanić*

*Faculty of Mechanical Engineering and Naval Architecture, I. Lučića 5, 10000 Zagreb
E-mails: {darko.ivancevic, luka.stanic}@fsb.hr

Keywords: composite materials, failure criteria, strain rate effects, impact damage, VUMAT subroutine

1. Introduction

Due to the high specific stiffness and strength and other significant advantages, composite materials are increasingly used as materials for main load-bearing structures. A representative example of their application are the structural elements of various vehicles, aeroplanes, helicopters and cars, where Carbon Fibre Reinforced Composites (CFRP) are most often used. Due to the anisotropic properties of fibre reinforced composites and the heterogeneity of the material at the microstructural level, their failure modes are very complex and often difficult to predict. Damage of composite materials is a complex phenomenon that involves many, sometimes interactive, failure mechanisms at the microlevel and inelastic response of the material. This phenomenon becomes even more complicated in impact loading conditions due to the strain rate dependence of epoxy matrices. Consequently, a numerical strain rate dependent damage prediction methodology is implemented in this work to simulate impact damage in CFRP structures at a wide range of impact velocities.

2. Numerical model and results

Numerous approaches to modelling strain rate effects in composites have been proposed and evaluated, including nonlinear visco-plastic models, damage mechanics and macro-level failure criteria. These approaches are most often applied in the analysis of composite structures and are primarily used for quasi-static load conditions. The available failure criteria and design guidelines are still not completely reliable, especially in cases of certain biaxial and triaxial stress states and dynamic loading conditions. One of the reasons for the unreliability of theories is the lack of adequate, complete and reliable experimental data that would provide all the required model parameters. However, advanced numerical models at various levels are increasingly used to simulate the impact loading of composite structures in engineering problems. Established failure criteria, e.g. Puck [1] or LaRC [2] criteria, that showed good results for static and quasi-static cases, are modified for application in dynamic loading conditions by including the conclusions of the strain rate effects in unidirectional composite materials.

The influence of strain rate effects is introduced into the existing failure criteria in dynamic loading conditions using scaling functions. Typically, the strengths or moduli of elasticity are scaled by logarithmic functions such as in eq. (1), after [3],

$$k(\dot{\gamma}_{xy}) = K_0 + K_1 \log_{10} \dot{\gamma}_{xy} + K_2 (\log_{10} \dot{\gamma}_{xy})^2. \tag{1}$$

The drawback of such functions is that their application requires calibration of parameters using experimental data that is available for a limited number of CFRP materials, with IM7/8552 as the most widely studied example. To remedy this obstacle, a significant advantage of the approach to defining the scaling function in [3] is that all effects on strengths, moduli of elasticity and the failure surface are modelled using the same function with parameters calibrated according to the strain rate dependence of the composite ply in-plane shear strength.

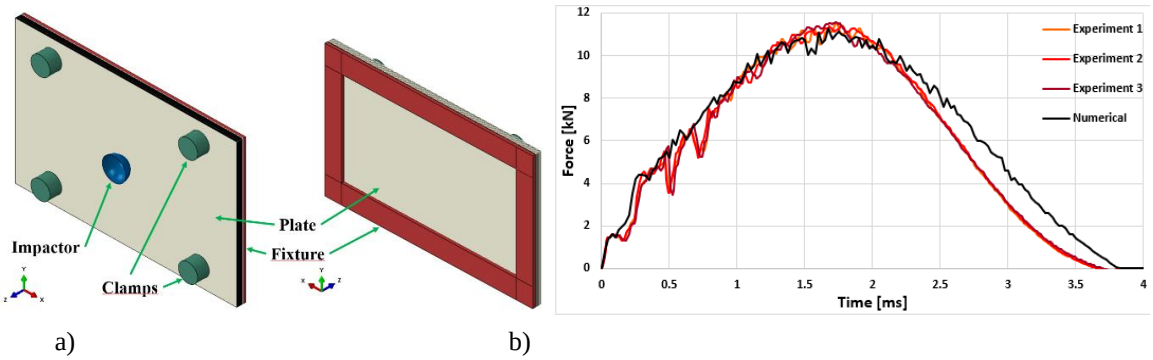

a) b)

Figure 1.a) Numerical model of low velocity impact (LVI), b) Comparison between experimental and numerical results of LVI at 30 J impact energy

The damage model applied in this work is based on the failure theory introduced in [3] and the mesh-objective progressive damage modelling approach after [4]. The damage model is defined using three independent damage variables - one variable for tensile and compressive damage in the fibre direction and one variable for matrix damage. Since the applied failure criterion is based on Puck's theory, damage propagation was also modelled in the fracture plane coordinate system using Bazant's crack band model to alleviate the size effects in the strain-softening regime [5]. The developed model was built into the Abaqus/Explicit software package using VUMAT subroutine and validated using experimental studies of various impact cases. Figure 1.a) shows the numerical model of the drop weight tower impact test, used for low velocity impact simulation, where the laminated plate was discretized using solid finite elements. Excellent agreement between experimental [6] and numerical results of LVI at 30 J impact energy is shown in Figure 1.b).

3. Conclusions

The analysed low-velocity impact case results in strain rates that considerably affect the behaviour of the CFRP material. As shown in this work, the inclusion of the strain rate effects into the damage model significantly increases the accuracy of the numerical results in the impact damage prediction.

Acknowledgements

The research is fully funded by the Croatian Science Foundation (HRZZ) within the project "COmputational modelliNg of COmposite stRuctures impact DamagE" (CONCORDE), grant number UIP-HRZZ-2020-02-9317.

References

[1] Puck, A., Schurmann, H., Failure analysis of FRP laminates by means of physically based phenomenological models, *Composite Science and Technology*, 58, 1045-1067, 1998.

[2] Pinho, S.T., Davila, C.G., Camanho, P.P., Iannucci, L., Robinson, P., Failure models and criteria for FRP under in-plane or three-dimensional stress states including shear nonlinearity, tech. rep. NASA/TM-2005-213530 (Nasa Langley Research Center, Hampton, 2005).

[3] Raimondo, L., Iannucci, L., Robinson, P., Curtis, P.T., Modelling of strain rate effects on matrix dominated elastic and failure properties of unidirectional fibre-reinforced polymer-matrix composites. *Composite Science and Technology*, 72, 819-827, 2012.

[4] Raimondo, L., Iannucci, L., Robinson, P., Curtis, P.T., A progressive failure model for mesh-size-independent FE analysis of composite laminates subject to low-velocity impact damage. *Composite Science and Technology*, 72, 624-632, 2012.

[5] Bazant, Z.P., Oh, B.H., Crack band theory for fracture of concrete, *Materials and structures*, 16, 155-177, 1983.

[6] Giannaros, E., Kotzakolios, A., Sotiriadis, G., Kostopoulos, V., A multi-stage material model calibration procedure for enhancing numerical solution fidelity in the case of impact loading of composites. *Journal of composite materials*, 55(1), 39-56, 2021.

Impact testing of novel axisymmetric auxetic cellular metamaterial with graded structure

Anja Mauko[1], Nejc Novak[1], Miran Ulbin[1], Lovre Krstulović-Opara[2], Matej Vesenjak[1], Zoran Ren[1]

[1]*University of Maribor, Faculty of Mechanical Engineering, Slovenia*
E-mails: {anja.mauko,nejc.novak, miran.ulbin, matej.vesenjak, zoran.ren}@um.si

[2]*Faculty of Electrical Engineering, Mechanical Engineering and Naval Architecture, University of Split, Split, Croatia*
E-mails: {lovre.krstulovic-opara}@ fesb.hr

Keywords: axisymmetric auxetic cellular metamaterials, graded structures, DIHB testing apparatus, impact loading, digital image correlation, mechanical properties

1. Introduction

Auxetic cellular metamaterials exhibit advanced material properties, such as high stiffness to mass ratio, increased energy absorption capacity and vibration damping. Orthogonal chiral auxetic metamaterials were studied in previous research [1]–[3] where their strain rate dependency was observed. Most cylindrically designed auxetic structures have been developed by mapping two-dimensional auxetic geometry to the outer surface [4], [5]. An innovative axisymmetric auxetic metamaterial was developed and patented by the Laboratory for Advanced Engineering Simulations and Experimentation (ACE-X) at the Faculty of Mechanical Engineering, University of Maribor [6]. This study reports on the impact response of the novel axisymmetric auxetic metamaterial with graded structure at different loading-rates to determine its strain fields, the Poisson's ratio, and the strain rate sensitivity.

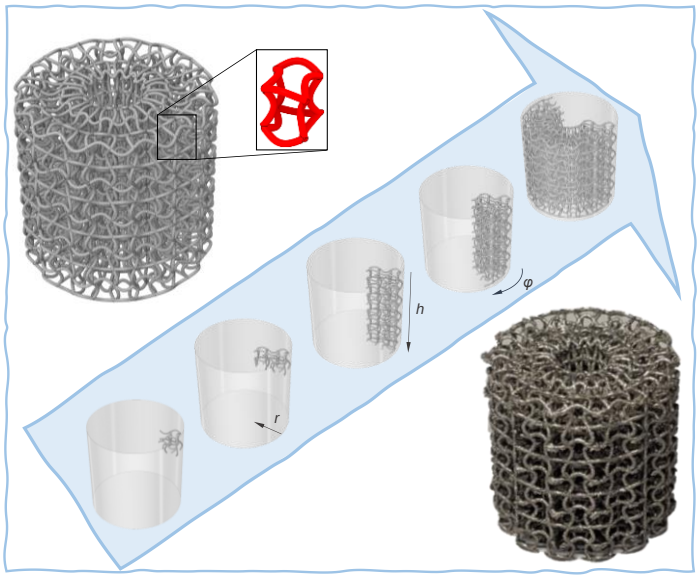

Figure 1. Axisymmetric cellular metamaterial and the geometry design process

2. Materials and testing methods

2.1. Axisymmetric auxetic specimens with graded structure

The three-dimensional geometry of the novel structure corresponds to the 10th eigenmode of the regular cubic unit cell. The cellular struts in the structure are sinusoidal curves of concave or convex curvature. The three-dimensional four-chiral unit cells are spatially distributed in the radial and axial directions (Figure 1). Radially graded structure was achived by scaling the length and amplitude of the vertical struts. From produced CAD models, axisymmetric samples of average dimensions of Ø21 mm × 21 mm were manufactured using the advanced powder fusion method (PBF) with basic material 316L stainless steel.

2.2 Quasi-static and dynamic testing

The basic mechanical parameters were determined by conducting quasi-static compression experiments using the INSTRON 8801 at loading velocity 0.1 mm/s (strain rate 0.005 s^{-1}). To evaluate the strain rate dependency of the studied structures, the second set of tests was conducted by increasing the loading velocity to 284 mm/s. Higher strain-rate experimental tests were conducted on the direct impact Hopkinson bar (DIHB) apparatus at two impact velocities: 10 m/s and 21 m/s (strain rate 1050 s^{-1}). All tests were recorded with high-resolution camera Photron Fastcam SA-Z at image resolution 640 × 280 px with frequency 70,000 fps. The digital image correlation (DIC) was employed to determine Poisson's ratio and strain fields. Engineering stress values were calculated from experimental measurements using strain gauges.

3. Results and conclusions

Full-filed strain analysis using DIC showed the formation and propagation of deformation fronts. Deformation fronts are the main indicators of the different loading rates, such as quasi-static, transitional, and shock loading rates. The quasi-static deformation regime was observed at loading velocities 0,1 mm/s, 284 mm/s and 10 m/s, while the transitional dynamic deformation regime was observed at impact velocity 21 m/s. Evident material strain rate hardening was observed at an increasing strain rate. The Poisson's ratio gradually increased during the deformation process. The strain rate increase enhanced the auxetic effect. The retrieved engineering stress-strain data showed smooth, gradual compressive deformation behaviour in all tests. With a graded internal chiral structure of axisymmetric cellular metamaterials, a constant plateau stress without oscillations was achieved.

References

[1] N. Novak, L. Starčevič, M. Vesenjak, and Z. Ren, Blast response study of the sandwich composite panels with 3D chiral auxetic core, *Compos. Struct.*, vol. 210, pp. 167–178, Feb. 2019, doi: 10.1016/J.COMPSTRUCT.2018.11.050.

[2] A. Mauko *et al.*, Dynamic Deformation Behaviour of Chiral Auxetic Lattices at Low and High Strain-Rates, *Metals (Basel).*, vol. 11, no. 1, p. 52, Dec. 2020, doi: 10.3390/met11010052.

[3] N. Novak, K. Hokamoto, M. Vesenjak, and Z. Ren, Mechanical behaviour of auxetic cellular structures built from inverted tetrapods at high strain rates, *Int. J. Impact Eng.*, vol. 122, no. March, pp. 83–90, 2018, doi: 10.1016/j.ijimpeng.2018.08.001.

[4] W. Wu *et al.*, Mechanical properties of hierarchical anti-tetrachiral metastructures, *Extrem. Mech. Lett.*, vol. 16, pp. 18–32, Oct. 2017, doi: 10.1016/J.EML.2017.08.004.

[5] C. Luo, C. Z. Han, X. Y. Zhang, X. G. Zhang, X. Ren, and Y. M. Xie, Design, manufacturing and applications of auxetic tubular structures: A review, *Thin-Walled Struct.*, vol. 163, p. 107682, Jun. 2021, doi: 10.1016/j.tws.2021.107682.

[6] Z. R. M. Vesenjak, N. Novak, Axisymmetric chiral auxetic structure, EP21197296.3 patent pending, 2021.

The computational design and experimental mechanical validation of hybrid Triply Periodical Minimal Surface (TPMS) cellular structures

Nejc Novak*, Oraib Al-Ketan+, Lovre Krstulović-Opara°, Matej Vesenjak*, Zoran Ren*

* *Faculty of Mechanical Engineering, University of Maribor, Smetanova ul. 17, 2000 Maribor, Slovenia*
E-mails: {n.novak, matej.vesenjak, zoran.ren}@um.si

+ *Core Technology Platforms Operations, New York University Abu Dhabi, PO Box 129188, Saadiyat Island, Abu Dhabi, United Arab Emirates*
E-mail: oga2@nyu.edu

°*Faculty of Electrical Engineering, Mechanical Engineering and Naval Architecture, University of Split, Split, Croatia*
E-mail: lovre.krstulovic-opara@fesb.hr

Keywords: cellular structure, triply periodical minimal surface, TPMS, experimental testing, computational modelling, mechanical behaviour

1. Introduction

Uniform lattices composed of one type of lattice structure repeated periodically have been extensively investigated in literature for their mechanical and physical properties. Their promising properties, which include a desirable combination of high strength, stiffness and toughness, suggest that hybrid structures made of two or more lattice (unit cell) types can exhibit even more advantageous and desired properties. Recent advances in additive manufacturing enable the fabrication of very complex cellular geometries like Triply Periodical Minimal Surface (TPMS) cellular structures [1].
This work aims to (1) investigate the mechanical properties of multi-morphology (hybrid) lattices with spatially variable unit cell types designed based on implicit functions, and (2) utilise and validate shell-based finite element computational models to decrease the computational costs. The new computational models can be used to design and evaluate other implicit function-based lattices and their mechanical performance (e.g., improved crashworthiness, increased energy absorption capacity).

2. Methods and materials

The uniform and hybrid (longitudinal and radial) TPMS lattices were designed and generated using the software MSLattice [2] with 4 different relative densities (ranging from 11% to 22 %). The generated lattices shown in Figure 1 were fabricated from stainless steel using the powder bed fusion system EOS M280. Uniaxial compression tests following the standard ISO 13314:2011 were performed by using a servo-hydraulic INSTRON 8801 testing machine with a position-controlled cross-head rate of 0.1 mm/s (quasi-static) and 284 mm/s (dynamic).

The computational models of TPMS samples were generated using MSLattice. The generated mid-surface lattice geometries were discretised with shell finite elements by using the PrePoMax software [3]. The boundary conditions and elasto-plastic material model were defined using the LS-PrePost software. The LS-DYNA finite element software was used for all computer simulations presented in this study.

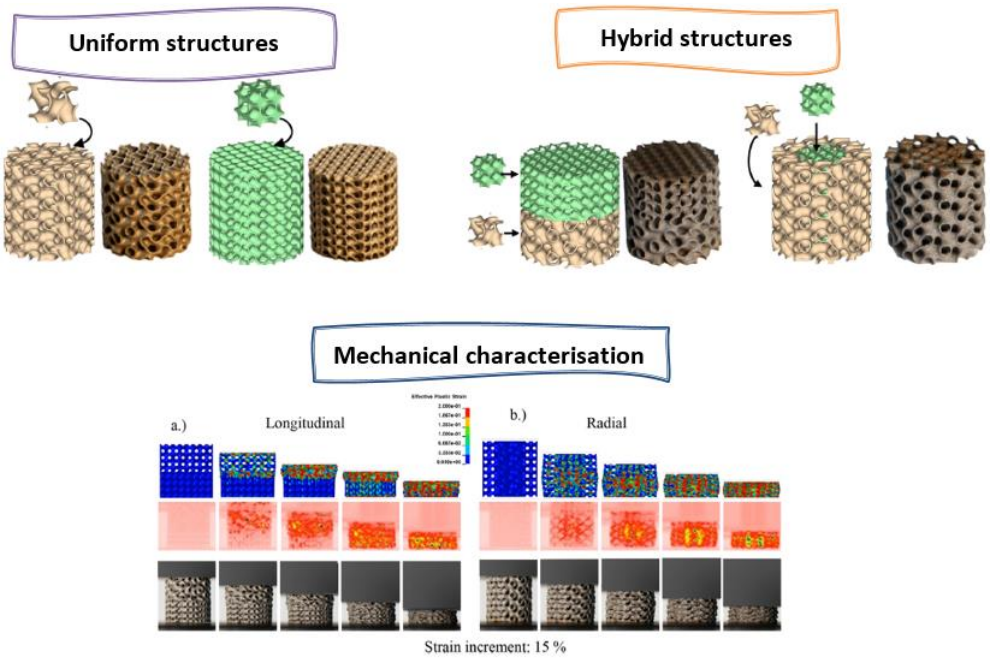

Figure 1. Geometry and deformation behaviour of uniform and hybrid TPMS structures

3. Results and conclusions

After validating the computational models for four different fundamental TPMS lattices (diamond, gyroid, IWP and primitive), the mechanical behaviour of hybrid TPMS lattices was analysed. The compressive experimental tests in this study were performed at the same conditions as for the uniform lattices [4]. The validation study showed that the computational models can predict the correct deformation behaviour. The computed mechanical responses (stress-strain relationships) are also comparable to experimental results. The plateau stress and specific energy absorption differ up to 24 % and 12 %, respectively, for analysed high relative densities. The main reason for the discrepancy is the generation of computational models based on the shell finite elements (FE). This could be alleviated by using the volume FE instead of shell FE, which would result in significantly increased computational times and divergence issues at large deformations. The use of both shell and volume FE leads to delayed densification of the computational model. This study shows that the shell FEs are appropriate for computational simulations of TPMS lattices up to the densification.

Longitudinal and radial hybrid TPMS lattices consisting of diamond and gyroid lattices were then developed, fabricated and evaluated using both experiments and computational simulations. Longitudinal hybrid lattices exhibit an inclined plateau region with hardening behaviour due to consecutive deformation and densification of the less stiff Gyroid lattice. A layer-wise collapse is followed by more controlled deformation and densification of stiffer Diamond lattice. The plateau stress in radial hybrid lattices is much more uniform and constant due to the concurrent deformation of radially spaced lattices.

References

[1] O. Al-Ketan, R. Rowshan, and R. K. R. Abu Al-Rub, “Topology-mechanical property relationship of 3D printed strut, skeletal, and sheet based periodic metallic cellular materials,” *Addit. Manuf.*, vol. 19, pp. 167–183, 2018.

[2] O. Al-Ketan and R. K. Abu Al-Rub, “MSLattice: A free software for generating uniform and graded lattices based on triply periodic minimal surfaces,” *Mater. Des. Process. Commun.*, vol. 3, no. 6, pp. 1–10, Dec. 2021.

[3] M. Borovinšek, “PrePoMax.” [Online]. Available: https://prepomax.fs.um.si/.

[4] N. Novak *et al.*, “Quasi-static and dynamic compressive behaviour of sheet TPMS cellular,” *Compos. Struct.*, vol. 266, p. 113801, 2021.

Challenges in characterizing cellular materials in direct impact tests

Yunus Emre Yılmaz*, Zoran Ren*

*University of Maribor, Faculty of Mechanical Engineering, Slovenia
E-mails: {y.yilmaz,zoran.ren}@um.si

Keywords: cellular materials, high-strain-rate, impact test, specific-energy-absorption

1. Introduction

Cellular materials attract engineers and scientists by their exclusive mechanical and thermal properties [1]. Their long plateau behaviour makes the cellular materials perfect candidates for energy absorption applications. Therefore, the determination of the mechanical properties of these materials is of great importance. Quasi-static experiments are widely used to determine the mechanical properties of cellular materials. However, at high strain rates, the behaviour of cellular materials changes depending on the geometry of the cellular material [2], the sensitivity of the base material to strain rates [3], the microinertia effect [3], the internal gas effect [3], and the shock wave effect. For this reason, characterization of cellular materials should be performed at the strain rate of the anticipated application.

Characterization of cellular materials at high strain rates is currently the subject of study. The requirements for high strains, the establishment and observation of dynamic equilibrium are the main challenges and prerequisites for adequate characterization of cellular materials. This article reviews the current state-of-the-art characterization of cellular materials in direct impact tests.

2. Challenges in the characterization of cellular materials at high strain rates

Since cellular materials are used in shock absorption applications, it is essential to determine how much energy they absorb during their deformation. For this reason, it is necessary to determine the stress-strain behaviour of the specimen until it is densified during testing. However, materials with high specific energy absorption may not be deformed sufficiently due to the limited input energy of the test setup.

The Direct impact Hopkinson bar (DIHB) is an experimental setup for studying the dynamic response of cellular materials. The striker is accelerated in the accelerating barrel with pressurized gas and directly impacts the sample. The kinetic energy of the striker is transferred directly to the specimen. The configuration of the test setup is shown in Figure 1.

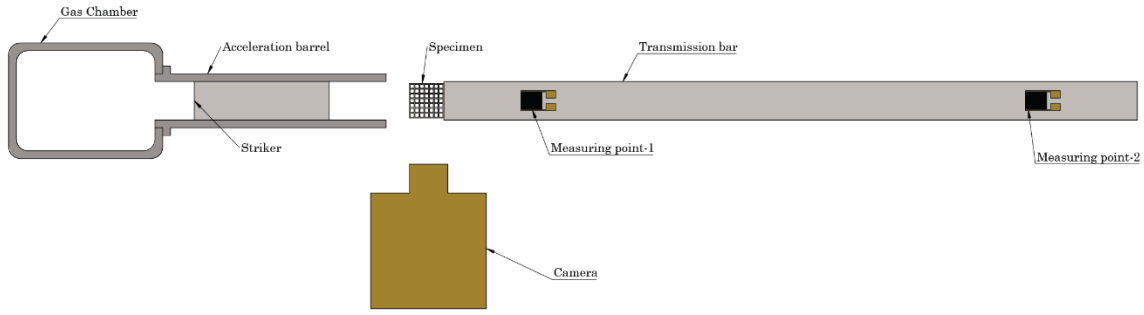

Figure 1. Direct impact Hopkinson bar (DIHB) configuration

The striker's kinetic energy depends on the pressure of the accelerating gas, the length of the barrel, and the friction in the system. The kinetic energy transferred to the sample should be greater than the specific energy absorption (SEA) of the sample multiplied by the sample volume to deform the sample to its densification. Consequently, some high specific energy absorption materials cannot be deformed sufficiently due to the limited kinetic energy that is reachable by testing apparatus configuration. This

problem can be solved by reducing the volume of the material, which is possible only to a certain extent, depending on the manufacturing capabilities. The kinetic energy can also be increased to a certain degree by increasing the length of the accelerating barrel and the accelerating gas pressure.

In the DIHB test setup, the deformation of the specimen by the direct striker and the passage of the striker through the accelerating barrel with close tolerances make it difficult to attach a measuring device (e.g., a strain gauge) to the striker. Consequently, the dynamic equilibrium cannot be observed and verified. It should be noted that the observation of the dynamic equilibrium is necessary to determine the strain range and time interval with valid obtained stress-strain relationship.

Recently, an Open Hopkinson pressure bar (OHPB) test setup was developed by Govender and Curry [4] that allows strain gauges to be used on both sides of the specimen, thus observing the stress state on both sides of the specimen. The specimen is deformed directly by the kinetic energy of the striker, but this setup requires additional bearings to support the striker outside of the acceleration barrel.

The use of high-speed cameras in conjunction with the digital image correlation technique has great potential to accurately measure the surface deformation, the Poisson's ratio, and the strain rate sensitivity of cellular materials at high deformation rates. Such a setup enables the use of advanced and more accurate analysis methods for high-speed experiments. One of such methods is the non-parametric approach. Othman et al. presented this method for determining the stress-strain field in non-homogeneous materials [5]. The specimen is divided into finite slices in the direction of loading. Using Newton's law of motion, the internal stresses formed in the slices are correlated with each other, considering the inertia effect. This method uses a force measurement at the specimen boundary and a displacement measurement performed with a digital image correlation technique as input. It allows the identification of the strain-stress relationship at any slice of the specimen.

3. Conclusions

This paper provides insight into the principles of the direct impact test, its limitations, and possible solutions for these limitations. Sufficient striker kinetic energy is needed to deform cellular materials in the direct impact setup fully. The non-parametric approach is a promising method to overcome the missing data problem caused by the inability to attach a measuring device to the striker in direct impact tests.

References

[1] Novak, N., Vesenjak, M. and Ren, Z., "Auxetic Cellular Materials - a Review", Strojniški vestnik – Journal of Mechanical Engineering, 62(9), pp.485–493,2016.

[2] Shinde, R.B. and Mali, K.D., "An Overview on Impact Behaviour and Energy Absorption of Collapsible Metallic and Non-Metallic Energy Absorbers used in Automotive Applications.", *IOP Conference Series: Materials Science and Engineering*, 346, p.012054, 2018.

[3] Vesenjak, M., Veyhl, C. and Fiedler, T., "Analysis of anisotropy and strain rate sensitivity of open-cell metal foam.", Materials Science and Engineering: A, 541, pp.105–109, 2012.

[4] Govender, R.A. and Curry, R.J., "The "Open" Hopkinson Pressure Bar: Towards Addressing Force Equilibrium in Specimens with Non-uniform Deformation.", Journal of Dynamic Behavior of Materials, 2(1), pp.43–49, 2015.

[5] Othman, R., Aloui, S. and Poitou, A., "Identification of non-homogeneous stress fields in dynamic experiments with a non-parametric method.", Polymer Testing, 29(5), pp.616–623, 2010.

Mechanical characterization of a woven GFRP composite subjected to simple shear loading

Andrija Zaplatić*, Zvonimir Tomičević*, Juro Bilobrk, Petar Kosec, François Hild+

*University of Zagreb, Faculty of Mechanical Engineering and Naval Architecture, Ivana Lučića 5, 10000 Zagreb, Croatia
E-mails: {andrija.zaplatic,zvonimir.tomicevic}@fsb.hr

+Université Paris-Saclay, Centrale Supélec, ENS Paris-Saclay, CNRS, LMPS - Laboratoire de Mécanique Paris-Saclay, 91190 Gif-sur-Yvette, France
E-mail: Francois.Hild@ens-paris-saclay.fr

Keywords: Arcan fixture, butterfly sample, digital image correlation, woven composite

1. Introduction

Fiber reinforced polymers (FRPs) have seen an increase of their application across many industrial areas due to their outstanding mechanical properties and the possibility to adapt with predefined fiber architectures. However, it is challenging to describe their complex mechanical behavior caused by their heterogeneous microstructures. For that purpose, comprehensive experimental investigations are required to determine in detail the FRPs response. Full-filed measurement techniques, such as Digital Image Correlation (DIC) and X-ray computed tomography (XCT) 0 are often used to meet these challenges. Moreover, the characterization of the orthotropic behavior of fibrous materials calls for experimental investigations under different loading regimes.

In the present study, comprehensive mechanical characterization of a glass fiber woven fabric (WF) subjected to simple shear loading is presented. The Modified Arcan Fixture (MAF) 0 was used to prescribe simple cyclic shear loading on a butterfly sample geometry. In order to reveal the complex material behavior, 2D and stereoDIC techniques were simultaneously employed. Furthermore, X-ray micro-computed tomography scans were acquired after each loading cycle to assess damage mechanisms in the bulk of the investigated WF sample.

2. Experimental protocol and results

An *ex-situ* simple shear test was carried out with the MAF on a butterfly sample made of a woven glass fiber fabric infused with a vinylester resin. During mechanical loading, the two surfaces of the butterfly specimen were monitored with single and stereo camera systems. To mitigate the influence of out of plane motions on the measured displacement fields, the single camera was equipped with a telecentric lens. Moreover, after each loading cycle, a CT scan was acquired in the unloaded state to assess the damage state in the bulk.

From the measured displacement fields, the mean strain levels were calculated in the shear zone (*i.e.*, between the two V notches). In **Figure 1** the shear stress vs. principal strain curves obtained via 2D and stereoDIC are presented. The results obtained from the two measurement sources show a good agreement until the onset of macroscopic damage. After each loading cycle, the slope of the linear part of the global material response significantly decreased, thereby indicating the degradation of the sample integrity and stiffness reduction. As damage grew in the analyzed region of interest (ROI), the difference between the mean strain levels became more pronounced.

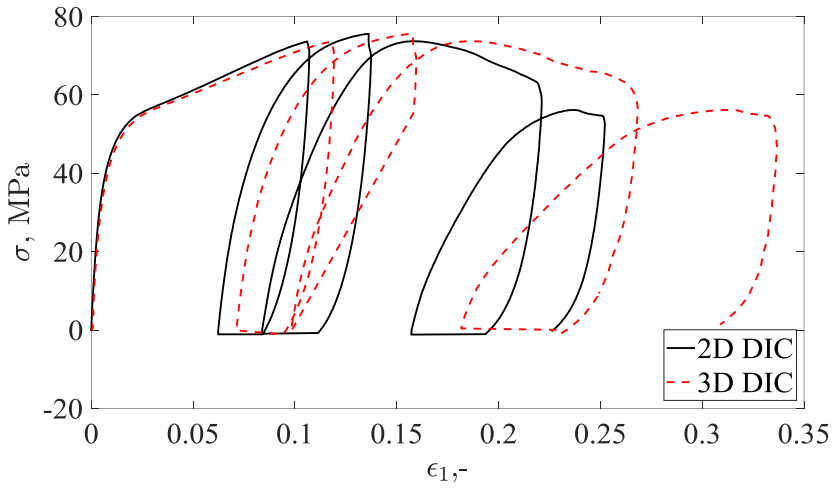

Figure 1. Comparison of the material response obtained from 2D and stereoDIC measurements

Severe damage was observed between the V notches of the butterfly sample from the CT scans captured in the reference configuration (**Figure 2** (a)) and after each loading cycle (**Figure 2** (b)). From the 3D images, different damage mechanisms were detected (*e.g.*, fiber breakage, fiber pullout and matrix cracking).

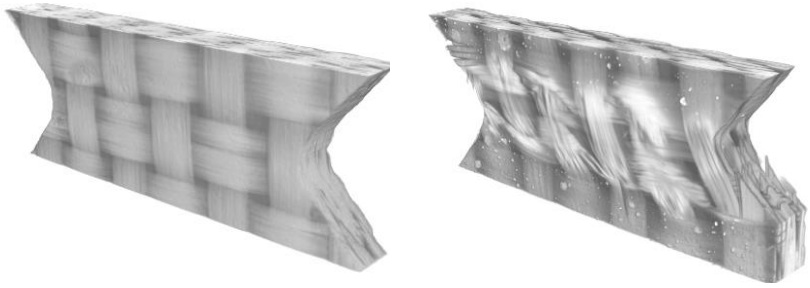

a) **b)**

Figure 2. CT scans of the ROI acquired (a) prior to and (b) after the prescribed mechanical load

3. Conclusion

The comparison of the mean strain levels obtained with 2D and stereoDIC showed a negligible influence of out-of-plane displacements in the reported experiment. DIC results and image analysis of the CT scans proved that damage initiated around the V notches in zones with dominant tensile stresses. Moreover, volumetric images revealed a heterogeneous distribution of the constituents induced by the manufacturing process. This feature resulted in asymmetric rigidity of the observed sample surfaces, which was noted from the comparison of the measured strain levels.

Acknowledgements

This work was performed within the FULLINSPECT project supported by the Croatian Science Foundation (UIP-2019-04-5460 Grant). The authors would also like to thank and acknowledge *NeoDens d.o.o.* for their availability and provided resources.

References

[1] Vrgoč A., Tomičević, Z., Smaniotto, B., Hild, F., Application of different imaging techniques for the characterization of damage in fiber reinforced polymer, *Composites Part A: Applied Science and Manufacturing*, 150, 106576, 2021.

[2] Zaplatić, A., Tomičević, Z., Čakmak, D., Hild, F., Improvement of the Arcan setup for the investigation of thin sheet behavior under shear loading, *Experimental Mechanics*, 63, 313-332, 2022.

10th ICCSM, Pula, 2022

Organized Session:

Natural Hazards and Resilience of Masonry Structures by M. Meštrović, S. Markušić, L. Abrahamczyk and D. Penava

Holographic/virtual experiments for higher education in structural engineering

Lars Abrahamczyk[*], Mahsa Mirboland[*], Christian Koch[*], Davorin Penava[+], Rüdiger Höffer[°], Roberta Apostolska[†], Nuno Lopes[#], Uwe Kähler[#]

[*]*Bauhaus-Universität Weimar, Faculty of Civil Engineering, Marienstr. 7A, 99423 Weimar, Germany*
E-mails: {lars.abrahamczyk,mahsa.mirboland,c.koch}@uni-weimar.de

[+]*Josip Juraj Strossmayer University of Osijek, Faculty of Civil Engineering and Architecture Osijek, Ulica Vladimira Preloga 3, 31000 Osijek, Croatia*
E-mail: davorin.penava@gmail.com

[°]*Ruhr Univeristy Bochum, Faculty of Civil and Environmental Engineering Sciences, D-44780 Bochum, Germany*
E-mail: ruediger.hoeffer@rub.de

[†]*Ss. Cyril and Methodius University in Skopje, Institute of Earthquake Engineering and Engineering Seismology,, Todor Aleksandrov 165, 1000 Skopje, Republic of North Macedonia*
E-mail: beti@iziis.ukim.edu.mk

[#]*Universidade de Aveiro, P-3810-193 Aveiro, Portugal*
E-mail: {ukaehler,nlopes}@ua.pt

Keywords: virtual experiments, structural engineering, Virtual, augmented, and mixed reality

1. Introduction

The sudden change in teaching from the physical attendance in classrooms to the online format because of the Covid-19 pandemic has shown that decentralized digital teaching is in general possible. However, a lack of clear frameworks and evaluation concepts pose challenges to rapid practical implementations of digital teaching. Particularly, the most challenging aspect of digitalization in higher education studies consists in coupling it with laboratory experiments and tests [1]. As a vital part of curricula in civil engineering studies, laboratory experiments are often devised for better understanding of theoretical knowledge and for evaluation purposes. Thus, laboratory experiments must be included in digitalization efforts [2]. Hereby, technology-enhanced learning environments offer several benefits, namely in terms of interoperability of course materials, re-usability and continuous modification, as well as decentralized learning experiences. Virtual, augmented, and mixed reality (VARM) applications are foreseen as tools providing capacities for remote-access experiments and virtual laboratories; thus, they aim to broaden digital teaching possibilities in civil engineering courses. Several implementations of VARM applications are reported and shown to be effective tools for interactive and immersive trainings in various educational fields [4, 5].

Participation in experiments will allow students to apply their theoretical knowledge and competences in solving complex practical tasks, and thus, it supports an overall understanding of the teaching material by building a "mental model". A mental model stands at the end of each learning process and implies understanding of the learned knowledge in its overall context [3]. In this context, virtual reality provides a possibility for students to participate virtually in experiments that have been carried out at another institute, without compromising realistic settings and the content-correctness of the experiment.

Competences are described as cognitive abilities and skills available to individuals or learnable by them to solve certain problems [6]. The creation of competence requires not only pure knowledge, but also an understanding of what has been learned [7]. For the human brain, pictorial information is easier to process than textual information, and using cognitive image processing the path to the mental

model can be shortened [8]. Based on these findings, virtual reality scenarios offer the possibility of contributing to a more efficient formation of a mental model due to their pictorial nature.

This paper presents first project results in the development of the concept of holographic / virtual representation of advanced experiments. Based on the description of the characteristics of a "remote-access / virtual perceptible" experiment (metamodel) different approaches are discussed with respect to visual representation (2D vs. 3D; picture vs. movie), pedagogical purpose, and expected learning outcomes. Two case studies will be presented to highlight the potential and the variety and provide a guide for the implementation of different items (additional added informative elements).

2. Project PARFORCE

Bauhaus-University Weimar (BUW), Ruhr University Bochum (RUB), University Aveiro (UA), University Osijek (UNIOS), and Ss. Cyril and Methodius University in Skopje, Institute of Earthquake Engineering and Engineering Seismology (IZIIS) constitute a strategic partnership (SP) with the PARFORCE project within the framework of Erasmus+. The SP aims at developing a joint platform for digital/virtual laboratory experiments to support European civil engineering higher education, and thus, making an essential contribution to understanding of teaching materials by the students. The main objective of the project consists in achieving availability of various laboratory experiments, which are not part of standard education at each university, but are carried out at specialized institutes. The experiments planned in this project are: boundary layer wind tunnel experiments at RUB, non-destructive and destructive experiments on shaking table at IZIIS, and fire resistance tests at UA.

Within the scope of the project, the concept of immersive 3D representations for detailed and realistic real-time visualization in Virtual Reality will be applied for the provision of laboratory tests in the context of higher education in civil engineering. Hereby, the project partners will benefit from recent developments, e.g. DigiLab4U, AuCity 2 and 3reCapSL projects, as well as already existing platforms for virtual laboratories like openMINTlabs.

References

[1] Höhner, N., Rodewald, J., Mints, M. O., Kammerlohr, V. (2019): The next step of digital laboratories: Connecting real and virtual world. Proceedings of The 17th International Conference on Virtual-Reality Continuum and its Applications in Industry, Article No.: 57, pp. 1–2.

[2] Feisel, L.D., Rosa, A.J. (2005): The role of the laboratory in undergraduate engineering education. Journal of Engineering Education, 94(1), pp. 121-130.

[3] Krischler, J., Vogt, A., Albus, P., Koch, C. (2021): Design principles affecting motivational and cognitive requirements for VR learning environments in engineering education. Proceedings of the 18th International Conference on Computing in Civil and Building Engineering. ICCCBE 2020. Lecture Notes in Civil Engineering, vol 98. Springer, Cham.

[4] Gerup, J., Soerensen, C. B. & Dieckmann, P. (2020): Augmented reality and mixed reality for healthcare education beyond surgery: an integrative review, International Journal of Medical Education 11, 1–18.

[5] Bartik, J., Ruff, H. A., Calhoun, G. L., Behymer, K. J., Goodman, T. J. & Frost, E. (2019): Virtual, augmented and mixed reality. applications and case studies, in 'Lecture Notes in Computer Science'.

[6] Weinert, F.E. (2014): Leistungsmessungen in Schulen. 3., aktualisierte Auflage, Beltz Verlag, Weinheim.

[7] Lersch, R., Schreder, G. (2013): Grundlagen Kompetenzorientierten Unterrichtens: Von den Bildungs-standards zum Schulcurriculum. Verlag Barbara Budrich, Opladen.

[8] Schnotz, W., Bannert, M. (1999): Einflüsse der Visualisierungsform auf die Konstruktion mentaler Modelle beim Text- und Bildverstehen. Experimental Psychology (3), pp. 217–236.

[9] Tasliarmut, F., Mirboland, M., Abrahamczyk, L., Koch, C. (2022): A mixed reality application for holographic structural analysis experiments. Proceedings of the European Conference on Computing in Construction. Rhodes, Greece (accepted).

Quantification of irregularity in unreinforced masonry façades with respect to the reliability of equivalent frame method.

Lars Abrahamczyk*, Aanis Uzair*, Daniel Agudelo+

*Chair of Advanced Structures, Bauhaus-Universität Weimar, Marienstraße 7A, 99423 Weimar
E-mails: {lars.abrahamczyk, aanis.uzair}@uni-weimar.de

+Student Assistant, Bauhaus-Universität Weimar, Marienstraße 7A, 99423 Weimar
E-mail: daniel.andres.agudelo.gomez@uni-weimar.de

Keywords: Unreinforced Masonry Walls, Irregularity Index, Equivalent Frame Method, Nonlinear Analysis.

1. Introduction

The in-plane nonlinear analysis of Unreinforced Masonry Structures (URM) is usually performed with the Equivalent Frame Method (EFM) as a simplified macro-modeling technique [1]. However, several aspects such as the discretization choice of the equivalent pier height and irregular layout of openings in a façade have non-negligible influence on the force and displacement capacity [2]. The uncertainity in results is supported by many previous benchmark studies [3-5] and blind prediction experiments [6]. Despite extensive research on the reliability of EFM, up till date, there is no unified criterion for the discretization and non-linear analysis of URM façades with irregular opening layouts. Furthermore, since the irregularity of openings in a façade inversly affects the reliability of EFM [7], the idea of quantifying irregularity to establish a threshold at which the application of the EFM is no longer recommended, results very appealing.
Parisi et al. in 2012 explored the way of estimating irregularity with a simple method based on the geometry and configuration of openings [8]. Moreover, other authors such as Berti et al. (2016) [9], Siano et al. (2017) [10], Kouri (2020) [11], proposed formulations for the calculation of irregularity by considering aspects like slenderness of the piers, geometrical center of the opening's location and the percentage of opening area. These existing methods focus on the presence of individual irregularities without the consideration of a combined irregularity index. Consequently, this study evaluates the existing methods and proposes a methodology to assess a URM façade by using combined irregularity index as a maximum threshold for precise application of EFM.

2. Methodology

With the intent of improving the existing calculation of irregularity index, realistic facades are evaluated with the above-mentioned methods and the difference in results are compared with the aim of proposing a scale in which a low index value represents low irregularity and vice versa. Preliminary calculation shows that some specific opening layouts leads to unrealistic values of the irregularity index. Therefore, the proposed methodology is carried out in two steps. In the first step, façades which do not comply with the minimum criteria of the EFM theory are diregarded. These requirements cover the amount of total opening area, the minimum distances from the piers to the free edges or in between the piers, the integrity and redundancy of the frame, etc. Many of these requirements are studied by different researchers [12-15] but are not clearly specified in the structural design codes. The second step involves the calculation of a combined irregularity index, starting from Parisi et al. theory and using statistical analysis of the modeled façades to determine generalized weighting factors for the combination of different types of irregularities. Moreover, the floor-location of irregularity is assessed and considered in the global irregularity index. The outcome of the methodology is a recommended

threshold of irregularity index for the application of EFM with an expected lower difference of the structural response in comparison to more refined methods of analysis.

3. Conclusions

The irregular opening layout in a URM façade contributes to the reduced accuracy of EFM in predicting correct structural response. A methodology to calculate the combined irregularity index acting as a maximum acceptable threshold for the application of EFM is presented. The accuracy of EFM is determined by comparing the error in maximum base shear and drift capacity with more refined modeling techniques. The error in results of EFM and refined methods of analysis is presented in terms of the mean error with a 95% confidence interval. The threshold of irregularity index for the application of EFM is determined for an acceptable level of error.

References

[1] Morandini, C., Malomo, D., & Penna, A. (2022). Equivalent frame discretisation for URM façades with irregular opening layouts. *Bulletin of Earthquake Engineering*, 1-30.

[2] Cattari, S., Calderoni, B., Caliò, I., Camata, G., de Miranda, S., Magenes, G., Milani, G. & Saetta, A. (2021). Nonlinear modeling of the seismic response of masonry structures: Critical review and open issues towards engineering practice. *Bulletin of Earthquake Engineering*, 1-59.

[3] Manzini, C. F., Ottonelli, D., Degli Abbati, S., Marano, C., & Cordasco, E. A. (2021). Modelling the seismic response of a 2-storey URM benchmark case study: comparison among different equivalent frame models. *Bulletin of Earthquake Engineering*, 1-40.

[4] Aşıkoğlu, A., Vasconcelos, G., Lourenço, P. B., & Pantò, B. (2020). Pushover analysis of unreinforced irregular masonry buildings: Lessons from different modeling approaches. *Engineering Structures*, 218, 110830.

[5] Cannizzaro, F., Castellazzi, G., Grillanda, N., Pantò, B., & Petracca, M. (2021). Modelling the nonlinear static response of a 2-storey URM benchmark case study: comparison among different modelling strategies using two-and three-dimensional elements. *Bulletin of Earthquake Engineering*, 1-30.

[6] Parisse, F., Cattari, S., Marques, R., Lourenco, P. B., Magenes, G., Beyer, K., ... & Sousamli, M. (2021, June). Benchmarking the seismic assessment of unreinforced masonry buildings from a blind prediction test. In *Structures* (Vol. 31, pp. 982-1005). Elsevier.

[7] Malomo, D., Morandini, C., Penna, A., & DeJong, M. J. (2019, September). Assessing the reliability of the Equivalent-Frame idealisation of URM façades with irregular opening layouts by comparison with the discrete micro-models. In *Proceedings of SECED 2019 conference*. Greenwich, London.

[8] Parisi, F., & Augenti, N. (2013). Seismic capacity of irregular unreinforced masonry walls with openings. *Earthquake Engineering & Structural Dynamics*, 42(1), 101-121.

[9] Berti, M., Salvatori, L., Orlando, M., & Spinelli, P. (2017). Unreinforced masonry walls with irregular opening layouts: reliability of equivalent-frame modelling for seismic vulnerability assessment. *Bulletin of earthquake engineering*, *15*(3), 1213-1239.

[10] Siano, R., Sepe, V., Camata, G., Spacone, E., Roca, P., & Pelà, L. (2017). Analysis of the performance in the linear field of equivalent-frame models for regular and irregular masonry walls. *Engineering Structures*, 145, 190-210.

[11] El Kouri, A. (2020). Influence of Geometrical irregularities on the in-plane behaviour of a masonry wall façade in macro-element based and analytical mechanism based analyses.

[12] Liu, Z., & Crewe, A. (2020). Effects of size and position of openings on in-plane capacity of unreinforced masonry walls. *Bulletin of Earthquake Engineering, 18*(10), 4783-4812.

[13] Camilletti, D. (2019). *Equivalent Frame modelling of URM buildings: numerical validation and rules* (Doctoral dissertation, PhD thesis, University of Genova, Genova (Italy)).

[14] Cattari, S., Camilletti, D., D'Altri, A. M., & Lagomarsino, S. (2021). On the use of continuum Finite Element and Equivalent Frame models for the seismic assessment of masonry walls. *Journal of Building Engineering*, *43*, 102519.

[15] Aşıkoğlu, A., Vasconcelos, G., & Lourenço, P. B. (2021). Overview on the nonlinear static procedures and performance-based approach on modern unreinforced masonry buildings with structural irregularity. *Buildings*, *11*(4), 147.

Environmental risk assessment and mitigation on cultural heritage assets in Central Asia

Lars Abrahamczyk[1], Kemmar Webber[1], Fulvio Rinaudo[2], Davorin Penava[3], Saidislom Usmanov[4], Gulnora Anvarova[5], Mukhsin Hidirov[6], Jafar Niyazov[7], Shuhrat Usmonov[8]

[1]*Bauhaus-Universität Weimar, Faculty of Civil Engineering, Marienstr. 7A, 99423 Weimar, Germany*
E-mail: {lars.abrahamczyk, kemmar.theodore.webber}@uni-weimar.de

[2]*Politecnico Di Torino – DAD, Viale P.A. Mattioli 39, 10125 Torino, Italy*
E-mail: fulvio.rinaudo@polito.it

[3]*Josip Juraj Strossmayer University of Osijek, Faculty of Civil Engineering and Architecture Osijek, Ulica Vladimira Preloga 3, 31000 Osijek, Croatia*
E-mail: davorin.penava@gmail.com

[4]*Turin Polytechnic University in Tashkent, 17, Kichik Khalka yuli, Tashkent 100095, Uzbekistan*
E-mail: saidislomkhon.usmanov@polito.uz

[5]*Tajik Technical University, acad. Rajabov's ave. 10, 734042 Dushanbe, Tajikistan*
E-mail: anvarovagb@gmail.com

[6]*Samarkand State Architectural and Civil Engineering Institute, 140147 Samarkand, Uzbekistan*
E-mail: mhihdirov@gmail.com

[7]*Institute of Water Problems, Hydropower and Ecology, Academy of Sciences, Republic of Tajikistan*
E-Mail: niyazovjafar@mail.ru

[8]*Khujand Polytechnic Institute of Tajik Technical University, I. Somoni ave, 226, 735700 Khijand, Tajikistan.*
E-Mail: usmonov.shuhrat@gmail.com

Keywords: Cultural Heritage, Central Asia, Capacity Building, Higher Education

1. Introduction

Uzbekistan owns more than 7.500 Cultural Heritage (CH) assets. Due to the impact of environmental and anthropogenic factors, 29 CH sites have been lost and 26 are in phase of destruction. The government has made considerable efforts to comply with its obligations under the UNESCO 1972 Convention. Currently, Uzbekistan has a number of concepts for preservation architectural heritage. However, these concepts have many disadvantages, since they are not based on the results of current international practices. In Uzbekistan, the threats of physical loss of CH sites are associated with natural and anthropogenic wear processes caused by: adverse climatic conditions and structural instability of buildings; humidity and natural disasters; geological and hydrological motions and earthquakes; inappropriate intervention on buildings; fires, vandalism and other aggressive actions. One of the main lacks is the almost complete absence of a full documentation of each CH asset and an appropriate monitoring of their real conditions.

Main strategies of CH conservation were pointed out in Decree of the Cabinet of Ministers of the Republic of Uzbekistan on "Preservation and Utilization of Culture Heritage

Properties" (N: 265 in March 30, 2019) https://lex.uz/ru/docs/4274003 and law of republic of Tajikistan on "Protection and Utilization of historical and cultural heritages" (N:377 in May 17, 2017). http://base.spinform.ru/show_doc.fwx?rgn=97674 According to these documents, one of the main strategies are: strengthening the capacity of young teachers to develop conservation and restoration projects by using advanced technologies considering internationally accepted concepts of conservation, prepare an electronic and cadastral document to all cultural heritages by using modern techniques, systematic monitoring of urban transformation in traditional urban fabrics of world heritage cities, assessing the condition of cultural heritage monuments which is not in heritage list of government, establishing the conservation and restoration schools.

The paper will present the findings of the partner's investigations as well as the concept and objectives for the development of a Master Course in Cultural Heritage Conservation in Central Asia with focus on environmental risk assessment and mitigation on structures and natural places, documentation and monitoring strategies of structures and landscapes, restoration and conservation strategies and others.

2. Project ERAMCA

The ERAMCA project (https://www.eramca.com/) aims to integrate the knowledge of environmental and civil engineers in an interdisciplinary process aimed at providing practical solutions to complex problems related to the evaluation and reduction of environmental risk on cultural heritage in compliance with international policies related to conservation and restoration promoted by UNESCO and from international charters on restoration [1]. The wider ERAMCA objective is the Building Capacity in Environmental risk assessment and mitigation on Cultural Heritage Assets in Central Asia by designing and developing an innovative educational platform based on new interdisciplinary courses, e-learning methods and digital tools to promote an effective conservation strategy of Cultural Heritage assets at different interest level.

The ERAMCA project aims to consider the environmental action on CH assets: climatic changes, hydrogeological phenomena, seismic phenomena and pollution. The correct interpretation of those phenomena could help the simulation of the effects of the foreseen environmental actions and therefore give significant information about the possible diseases on CH assets (buildings, historical centers, urban and natural landscapes, etc.). The correct knowledge of these interactions between CH assets and Environment could help a correct design of reduction actions and a preventive design of possible intervention in case of catastrophic events. CH in Central Asia is prone to those problematics therefore ERAMCA would like to give to the involved Countries (Uzbekistan and Tajikistan) effective solutions by acting and enhancing local potentialities represented by young generations of teachers and students and by inviting local stakeholders (mainly public authorities and agencies) to give specific objectives to be reached.

ERAMCA join three European universities where update research and teaching activities are developed on environmental risk assessment and reduction on CH assets by using an interdisciplinary approach.

References

[1] ERASMUS+ KA2– Cooperation for innovation and the exchange of good practices – Capacity Building in the field of Higher Education. Application Form. Call for Proposals 2019 - EAC/A03/2018. Environmental Risk Assessment and Mitigation on Cultural Heritage assets in Central Asia / ERAMCA. Detailed description of the project.

Study of simultaneous inter-storey drift IP and OoP loads on reinforced concrete frames with and without masonry infill walls and openings by a variating angle

Filip Anić*, Davorin Penava*, Vasilis Sarhosis+, Lars Abrahamczyk°

*Josip Juraj Strossmayer University of Osijek, Faculty of Civil Engineering and Architecture Osijek
E-mails: {filip.anic, davorin.penava}@gfos.hr

+University of Leeds, Faculty of Engineering and Physical Sciences, School of Civil Engineering
E-mail: v.sarhosis@leeds.ac.uk

° Bauhaus-Universität Weimar, Faculty of Civil Engineering
E-mail: lars.abrahamczyk@uni-weimar.de

Keywords: simultaneous loads, out-of-plane, in-plane, varied angle

1. Introduction

Most research regarding the out-of-plane (OoP) loads on frames with infill walls is done by inertial loads that pressurize the infill wall [1]. The OoP, inter-storey drift forces are scarcely investigated. Therefore, the authors of this paper invested research efforts to test RC frames with and without infill walls and openings loaded by the inter-storey drift forces. After the experiments were conducted and along with the previous in-plane (IP) ones, computational 3D micromodels were assembled and calibrated [2]. Using those calibrated models, simultaneous IP and OoP inter-storey drift loads were incorporated into them, which is the topic of this paper.

2. Typing area

The calibrated models were loaded by vertical, *i.e.*, gravity (N), IP (V_{IP}) and OoP (V_{OoP}) inter-storey drift loads (Fig. 1). The vertical load of 365 kN's was introduced to the model in 5 steps. After which, the column supports and simultaneous IP and OoP loads were active. Monotonous force control protocol, *i.e.* pushover method, was used. The IP load was kept at a constant 5 kN's per step, while the OoP ones were varied. It resulted in the resultant load (Eq. 1) and its angle to differentiate (Eq. 2). The angle goes from pure IP (0°) to OoP (90°) load, covering the combined loads in between. The angles were refined from 15° to 5° in between 75° – 90° to cover the abrupt decline in the resistance.

$$V_{R,\alpha}=\sqrt{V_{R,IP,\alpha}+V_{R,OoP,\alpha}} \tag{1}$$

$$\alpha=\tan\left(\frac{V_{R,IP}}{V_{R,OoP}}\right)\rightarrow \alpha\in\{0,15,30,45,60,75,80,85,90\}° \tag{2}$$

The simulations were carried out on 6 models: Bare frame (BF); Fully infilled frame (FI); Frame with centric door opening (CD); Frame with centric window opening (CW); Frame with eccentric door opening (ED); Frame with eccentric window opening (EW).

The models with eccentric openings (ED, EW) were loaded by the IP forces from both sides seperatley (left or right), as it plays a significant role in the IP resistance.

The results are presented in Figure 2, where the models with openings are plotted against BF and FI ones. The plot was placed inside a polar coordinate system, with angle (α), resultant force (V_R), and the ratio of the resultant force of the given model and the BF ones ($V_{R,\alpha}/ V_{R,BF,IP}$).

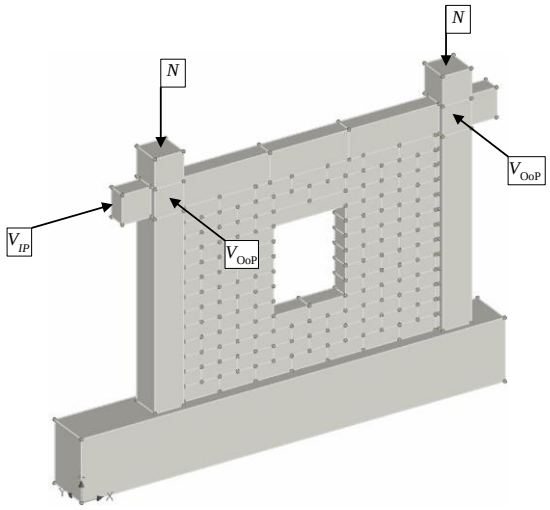

Figure 1. Micordel's load setup

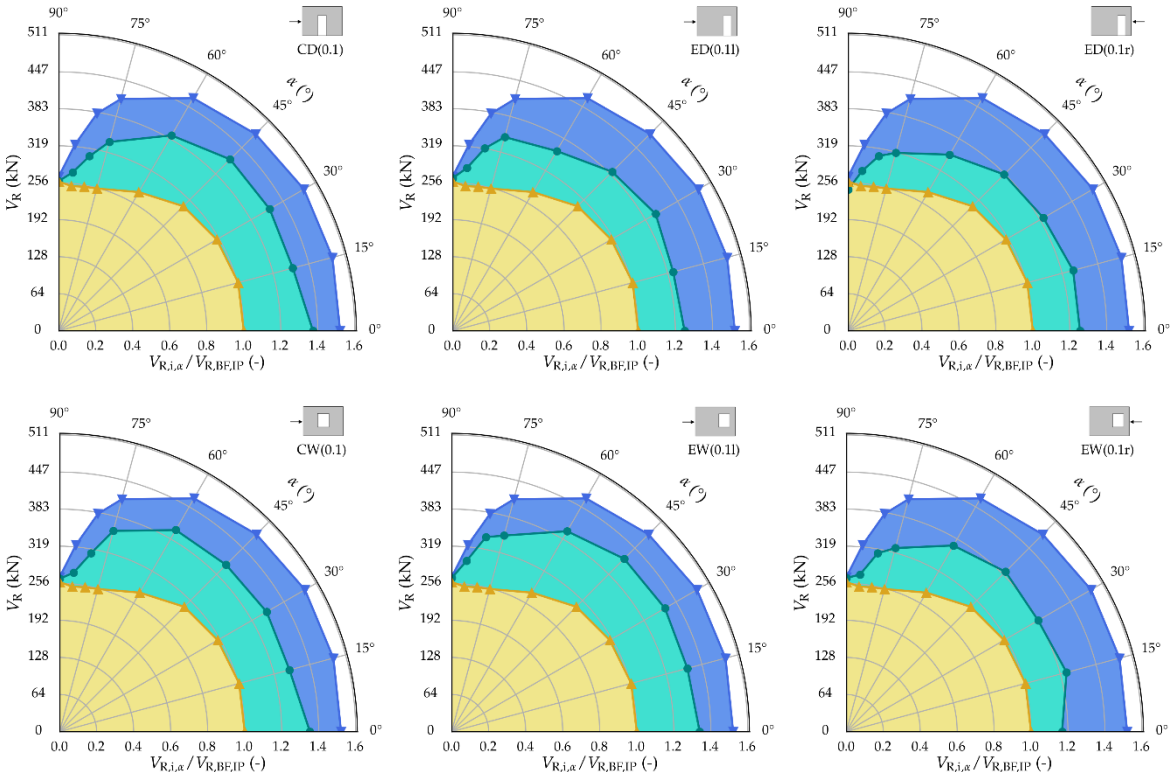

Figure 2. Results from the simultaneous load

4. Conclusions

The results have shown a correlation between the micromodels resistance and the angle α, infill wall, and openings up to 90°. At which it all disseminates. The resistance is greatest with pure IP load, after which it declines up to the lowest point of pure OoP load. The sharpest decline was noted after 60°, due to dominant OoP forces that unload the IP struts and bypass the positive effects of the wall-frame interactions.

References

[1] F. Anić, D. Penava, L. Abrahamczyk, V. Sarhosis, A review of experimental and analytical studies on the out-of-plane behaviour of masonry infilled frames, *Bull. Earthq. Eng.* 18 (2020) 2191–2246.

[2] F. Anić, D. Penava, V. Sarhosis, L. Abrahamczyk, Development and Calibration of a 3D Micromodel for Evaluation of Masonry Infilled RC Frame Structural Vulnerability to Earthquakes, *Geosciences*. 11 (2021) 468.

Kinematic analysis of out-of-plane wall failure using visual programming

Marija Demšić*, Maja Baničeк*, Petra Gidak*, Damir Lazarević*

* *University of Zagreb, Faculty of Civil Engineering*
E-mails: {mdemsic, mbanicek, pgidak, damir}@grad.hr

Keywords: masonry structures, local mechanisms, activation coefficient, visual programming

1. Introduction

The mechanism of out-of-plane wall failure is one of the most critical for masonry buildings, as it can lead to the loss of the global box-like behavior of the structure. This type of failure depends largely on the quality of connections with orthogonal walls and floors, the axial load applied, and the existing retrofit measures (tie rods, ring beams, etc.). This form of failure is usually analyzed using submodels consisting of macroelements. A common approach to modelling these mechanisms is an *a priori* defined geometry based on engineer judgement, analysis of crack patterns, and connections with other load-bearing elements. Kinematic analysis is applied to determine the activation coefficient (or a capacity) and the acceleration value that cause the element to overturn. Very often, complex geometry is a fundamental problem for kinematic analysis of local mechanisms. However, if a three-dimensional model of the geometry is available, the kinematic analysis of the element can easily be performed especially if the analysis is parametrized.

2. Procedure for kinematic analysis of the model

The procedure of kinematic analysis of out-of-plane wall failure [1] begins with the definition of macroelements and the assumption of the type of mechanism (Figure 1). For all vertical forces that have an inertial effect, a horizontally equivalent static load is assumed. For a given mechanism type, the displacement of control node is assigned and horizontal and vertical displacement schemes are obtained. The calculation of the activation factor of the mechanism is determined using the equation of virtual work:

$$\alpha_0 \left(\sum_{i=1}^{n} P_i \, \delta_{x,i} + \sum_{j=n+1}^{n+m} P_j \, \delta_{x,j} \right) - \sum_{i=1}^{n} P_i \, \delta_{y,i} - \sum_{h=1}^{o} F_h \, \delta_h = L_{fi} \qquad (1)$$

Where P_i are the gravity forces directly transmitted to the element, and P_j are the forces that do not act directly on the element but whose mass generates horizontal inertial forces on the mechanism due to seismic actions, F_h are general external forces acting on the element that do not generate inertial forces (e.g. vault thrust, friction), and L_{fi} is the virtual work of the internal forces (e.g. tie rods). The values of virtual displacements δ for each force are determined based on the displacement scheme.

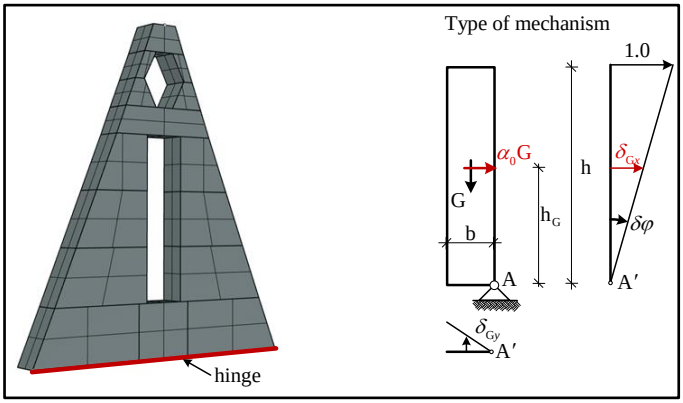

Figure 1. Geometry of the element and assumed type of the mechanism

To determine the corresponding acceleration that induces overturning, it is necessary to determine the effective modal mass M^* and the corresponding mass participation factor e^* of the mechanism:

$$M^* = \frac{\left(\sum_{i=1}^{n+m} P_i \, \delta_{Px,i}\right)^2}{g \sum_{i=1}^{n+m} P_i \, \delta_{Px,i}^2} \; ; \quad e^* = \frac{g \, M^*}{\sum_{i=1}^{n+m} P_i} \tag{2}$$

The corresponding spectral acceleration a_0^* of the equivalent system, which activates the mechanism, is determined by the expression:

$$a_0^* = \frac{\alpha_0 g}{e^* \, \mathrm{F_C}} \tag{3}$$

3. Visual programming using Grasshopper3D

Visual programming with *Grasshopper3D* [2], an add-in for *Rhino3D* [3], has made it possible to develop a code that parametrically links control node displacement with the position of the line hinge to create the virtual displacements scheme and calculate the activation coefficient based on upper bound limit analysis (Figure 2). Most of the programs used in practice to calculate the out-of-plane failure of walls are based on a predefined basic geometry of the walls and are usually calculated using spreadsheet software programs. Some programs for structural analysis, such as *3muri* [4], have modules for the calculation of local mechanisms, but there are certain limitations in terms of the specific position of the line hinges and the geometry of the elements, which is greatly simplified by the definition of equivalent frames of the structure. A great advantage of the program code created using *Grasshopper3D* is the possibility of assigning an arbitrarily complex geometry and the ability to choose the any position for the line hinge.

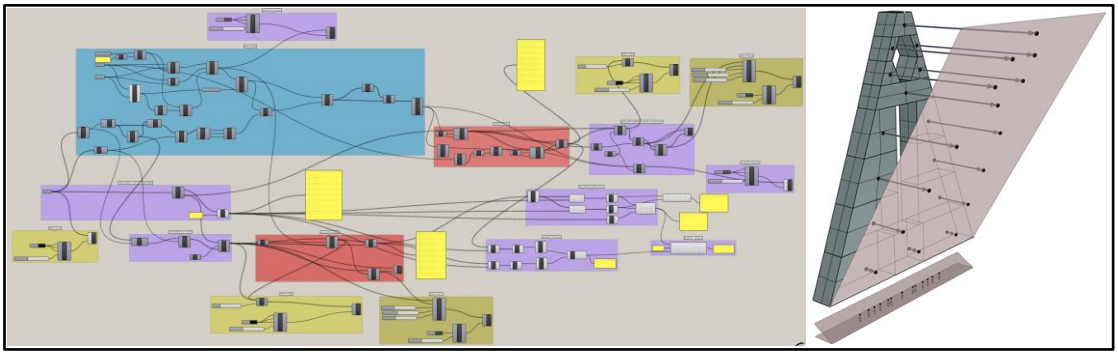

Figure 2. Grasshopper program code and virtual displacement scheme for the element

Acknowledgmentsw

We gratefully acknowledge financial support from the Croatian Science Foundation (grant number UIP-2020-02-1128).

References

[1] Demšić, M., Uroš, M., Šavor Novak, M., Atalić, J., Baniček, M.: D. Načela i metode proračuna - D.2. Otkazivanje zidova izvan ravnine. In: I. Uroš, M., Todorić, II. M., Crnogorac, M., III. Atalić, J., IV. Šavor Novak, M., V. Lakušić, S., eds. (ur.), *POTRESNO INŽENJERSTVO - Obnova zidanih zgrada*, 193-206, Građevinski fakultet Sveučilišta u Zagrebu, Zagreb, 2021. (in Croatian)

[2] *Grasshopper user manual*: https://www.rhino3d.com/learn/?keyword=kind:%20grasshopper, accessed on: 1.4.2022.

[3] *Rhinoceros manual*: http://docs.mcneel.com/rhino/6/usersguide/en-us/index.htm, accessed on: 1.4.2022.

[4] *3muri user manual*, Version 12.5.0, S.T.A. DATA, http://www.3muri.com/documenti/brochure/en/3Muri12.2.1_ENG.pdf, 256-272 accessed on: 1.4.2022.

Adaptation of Abaqus output data for application in seismic analysis of buildings

Romano Jevtić Rundek*, Ante Pilipović*, Mario Uroš*, Marija Demšić*

*Faculty of civil engineering in Zagreb; Fra Andrije Kačića-Miošića 26, 10 000 Zagreb
E-mails: {romano.jevtic.rundek; ante.pilipovic; mario.uros; marija.demsic} @grad.unizg.hr

Keywords: Abaqus, Phyton, Seismic analysis, Masonry

1. Introduction

Abaqus is a quality engineering simulation software that offers FEM, DEM, MEM and other simulation methods to the user. In seismic analysis of structures, it is a valuable tool for performing time-history analyses because it provides complex simulation of material behaviour under dynamic excitation, geometric nonlinearities, and has a very efficient solver. While Abaqus is powerful and can perform a wide range of general-purpose engineering simulations, it also comes at a cost of inefficient workflows for some specific tasks required in the analysis of buildings. In calculating the response of masonry walls and buildings to seismic action using Abaqus time-history analysis, the main problem is the interpretation of the results, as a large number of elements need to provide output data for each time step. That is a large number of walls, consisting of a large number of 3D elements. It is impractical to do this in the native Abaqus GUI.

To analyse the seismic response of a building, the analysis results for each wall need to be compared with the predefined limit states for each time step of the analysis. Two groups of analysis results are used: the internal forces acting on the top and bottom of the wall and the in-plane wall drift. Both datasets can easily be extracted directly from Abaqus through native GUI, however only for one wall and one frame at a time. To analyse the building properly, the forces and drifts of each wall need to be extracted for every step of time-history analysis, which is impractical. This is streamlined using Python scripts, which can go through all time steps, extract the necessary datasets, and even perform a check of wall stability. It needs to be said, the current scripts are made for a model consisting of 3D finite elements, and the purpose of the scripts is extracting the forces and displacements from the model in a timely and clear manner.

Abaqus includes a Python interface. It is easy to log or translate user activity in the GUI into Python commands, and it is also easy to run scripts through the GUI. This allows the user to quickly learn and use Abaqus specific commands.

2. Structure of the scripts and workflow

In the Python code itself, a combination of native Abaqus commands and standard Python commands is used to extract data from Abaqus. In the scripts provided, element cross sections in the model are identified, their time-history outputs requested [1] and extracted into Excel or another common data manipulation software (Mathematica, MatLab etc.). It is necessary to define which outputs are required, this is done through defining SETs. Elements contained in a SET define which points/planes on the model need to be tracked, while the name of the set defines the way the values will be processed, and which values will be requested in the history output (force or displacement or both). This workflow is shown in Fig 1. The provided scripts are also suitable for parametric studies and can be further expanded.

2.1. Benchmarks:

These scripts will be used to perform benchmarks on several walls in Abaqus, calibrate material properties and mesh size. The calibrated values are then used to calculate the response of a full-scale building consisting of these walls, which have now been calibrated to empirical data (Fig 2). The wall in Fig 2 is a 150/100/60 cm stone wall, described by Kržan et al. [2], the church tower in Fig 2 is a Stone tower described by Pojatina et al.[3]. Calibration is tested on the wall, and result export scripts are tested on the tower model.

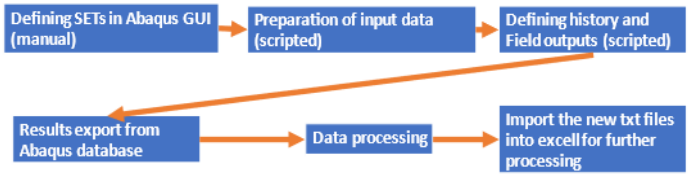

Figure 3: Workflow diagram

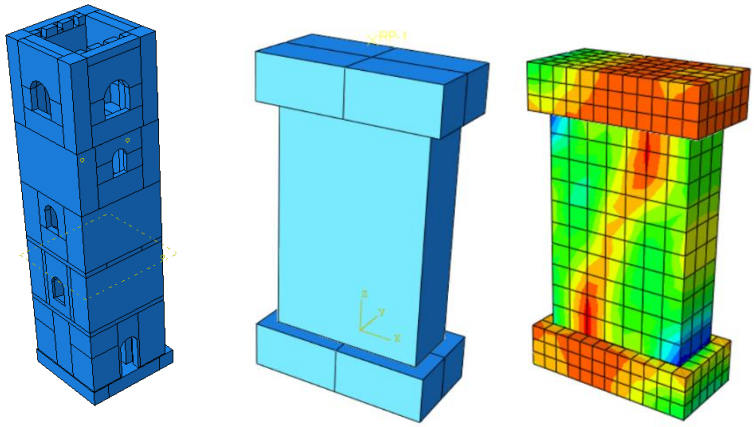

Figure 4: Benchmark of a wall, and a building model

3. Conclusion:

Abaqus provides nonlinear time-history analysis that is superior to most software packages available today, especially in civil engineering. Detailed input data is required to create a quality model, but much better results can be obtained. In this paper inefficiency in data interpretation was addressed, when analyzing a seismic time-history(TH) analysis of a building modeled in 3D finite elements. Obtaining the results and compiling them for interpretation is done through Python scripts. This improves the workflow of performing a time history seismic analysis by a few orders of magnitude compared to stock Abaqus GUI, depending on building size. In their current form, the scripts allow a quick export of data, in a form that allows easy interpretation. In their future form, they could allow somewhat automatic construction of fragility curves for buildings. When such an improvement on the scripts is performed, it will introduce new challenges of checking the result validity, for an example, checking automatically if there is some critical crack forming, or a local collapse mechanism etc… In conclusion, for the purpose of seismic analysis, Abaqus is capable of producing models of greater quality, but simultaneously requires more detailed input data and scripts for result extraction and interpretation.

Acknowledgments

This script is being developed as a part of the 2BESAFE project, we gratefully acknowledge financial support from the Croatian Science Foundation (grant number UIP-2020-02-1128)

Literature:

[1] Abaqus manual

[2] Kržan, M., Gostič, S., Cattari, S., & Bosiljkov, V. (2015). Acquiring reference parameters of masonry for the structural performance analysis of historical buildings. *Bulletin of earthquake engineering*, 13(1), 203-236.

[3] Pojatina, J., Horvat, T., Uroš, M., Baniček, M., Pristup konstrukcijskoj obnovi crkve sv. Mihaela u Gračanima. In: Lakušić, Stjepan, ed., *Zbornik sažetaka predavanja,* pages 43-43. Dani Hrvatske komore inženjera građevinsratva Opatija, 17. – 19. 6. 2021., Zagreb, 2021.

The effect of confinement of openings on shear resistance of RC frame with URM infill wall structure components

Davorin Penava[1], Lars Abrahamczyk[2], Shashikant Shambhu Sharma[2], Liborio Cavaleri[3], Amin Mohebkhah[4], Vasilis Sarhosis[5]

[1] *Josip Juraj Strossmayer University of Osijek, Faculty of Civil Engineering and Architecture Osijek,3 Vladimir Prelog Str., 31000 Osijek, Croatia, e-mail: davorin.penava@gfos.hr*

[2] *Bauhaus-Universität Weimar, Faculty of Civil Engineering, Institute of Structural Engineering, Chair of Advanced Structures, Marienstr. 13D, 99423 Weimar, Germany, e-mail: {lars.abrahamczyk,; shashikant.shambhu.sharma}@uni-weimar.de*

[3] *Università degli Studi di Palermo, Dipartimento di Ingegneria, Viale delle Scienze, Edificio 8, 90133 Palermo, Italy, e-mail: liborio.cavaleri@unipa.it*

[4] *Malayer University, Faculty of Civil Engineering and Architecture, Malayer, Iran, e-mail: amoheb@malayeru.ac.ir*

[5] *University of Leeds, School of Civil Engineering, LS2 9JT, Leeds, UK, e-mail: v.sarhosis@leeds.ac.uk*

Keywords: opening, confinement, RC frame, URM infill wall, shear resistance

1. Introduction

The resistance to horizontal shear (seismic) forces of RC frames with URM infill walls, with door or window openings of various sizes and positions within the wall, is markedly enhanced by construction of vertical RC confining elements along opening vertical edges, as compared to unconfined ones [1, 2].

2. Tests on RC frames with URM infill walls

The ten model structures of one story-one bay RC frames with URM infill walls were constructed at a scale of 1:2.5 and tested in the laboratory under cyclic force-controlled loading [1, 2]. They were designed as medium ductility (DCM) moment-resisting RC frames in compliance with EN 1992-1-1:2004 and EN 1998-1:2004. The URM infill walls were constructed from clay blocks and masonry mortar in compliance with the seismic design requirements for structural masonry as given in EN1996-1-1:2005 and EN 1998-1:2004. The model structures were divided in three groups as shown in Table 1.

Table 1. Groups of tested model structures of RC frames with URM infill walls w.r.t. opening size (A_o/A_i*100=15 %), type and position ($e_o=h_i/5+l_o/2$ or $e_o=l_i/2$)

Group 1	Group 2	Group 3
RC frame with URM infill wall with: - centric door opening - centric window opening - centric door opening - eccentric window opening without confinement.	RC frame with URM infill wall with: - centric door opening - centric window opening - centric door opening - eccentric window opening with confinement.	Reference specimens: - RC frame without URM infill wall - RC frame with URM infill wall without opening

2. Computational micromodel calibration and parametric analysis

The computational micromodel of the RC frame with URM infill wall model (test) structure was built in ATENA 2D Eng software and calibrated against the tests, as described in [3].

After establishing the correlation with the tests within the 10 % of the model accuracy, the parametric (pushover displacement controlled) analysis was performed. The analysis covered the variation of door and window openings in size in range 10 % (EN1996-1-1:2005 as the lower boundary) < A_o/A_i*100 < 30 % ([3,4] as the upper boundary) and position i.e. either $e_o=h_i/5+l_o/2$ or $e_o=l_i/2$.

In Figure 1 shown is the ratio of opening area A_o w.r.t. infill wall area A_i, against the maximum shear resistance of the RC frame with URM infill wall structure component i.e. $V_{R,if,\{f,i,c\}}$ (where "if" designates infilled frame, "f" frame,, "i" infill wall and "c" confinement) w.r.t. maximum shear resistance of the RC frame without URM infill wall i.e. $V_{R,f,max}$.

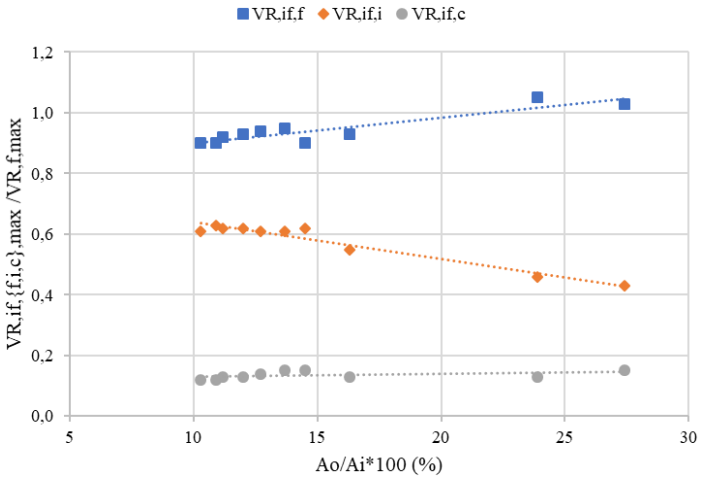

Figure 1. The shear (seismic) resistance of RC frame, URM infill wall and RC confining element components in case of eccentric door opening (right-to-left loading)

4. Conclusions

With respect to the RC frame, URM infill wall and vertical RC confining element component contribution to shear (seismic) resistance of the structure, it can be concluded that the presence of confinement of opening, under various opening size (A_o/A_i), type and position ($e_o=h_i/5+l_o/2$ or $e_o=l_i/2$) cases, improved the performance of the structure, as compared to the their unconfined counterparts.In case of the RC frames with URM infill wall with unconfined openings, the shear demand for the RC frame, i.e. $V_{R,if,f,max}/V_{R,f,max}$ ratio, was higher than the designed value i.e. $V_{R,f,max}$, in compliance with EN 1992-1-1:2004 and EN 1998-1:2004 provisions).

References

[1] Penava, D., Influence of openings on seismic response of reinforced concrete frames with masonry infill wall. Ph. D. Thesis, Josip Juraj Strossmayer University of Osijek, Osijek, Croatia, 2012.

[2] Sigmund, V., Penava, D., Influence of Openings, With and Without Confinement, on Cyclic Response of Infilled R-C Frames — An Experimental Study. *Journal of earthquake engineering*, 18, 113-146, 2014.

[3] Penava, D., Sarhosis, V., Kožar, I., Guljaš, I., Contribution of RC columns and masonry wall to the shear resistance of masonry infilled RC frames containing different in size window and door openings. *Engineering structures*, 172, 105-130, 2018.

[4] Shambhu Sharma, S. *Assessment of in-plane behavior of URM infill walls with openings and confining elements*. M. Sc. Thesis, Bauhaus-Universität Weimar, Faculty of Civil Engineering, Chair of Advanced Structures, Weimar, Germany, 2021.

Episcopal seminary building and classical gymnasium (Jesuit college) in Dubrovnik construction 1662-1765 in terms of contemporary earthquake resistant design supported by measurements

Davorin Penava[*], Ante Vrban[+], Jakov Uglešić[*], Davor Stanko[*], Snježana Markušić[*]

[*] *Josip Juraj Strossmayer University of Osijek, Faculty of Civil Engineering and Architecture Osijek,3 Vladimir Prelog Str., 31000 Osijek, Croatia, e-mail: davorin.penava@gfos.hr*
[+] *Architect Ante Vrban, Trg J. J. Strossmayera 11, 10000 Zagreb, Croatia, e-mail: architectantevrban@gmail.com*
[*] *University of Zagreb, Faculty of Science, Department of Geophysics, Horvatovac ul. 95, 10000, Zagreb, Croatia, e-mail: {jakov.stanislav.uglesic, davor.stanko, markusic}@gfz.hr*

Keywords: Jesuit college, Dubrovnik, construction, earthquake resistant design, measurements

1. Introduction

The construction of Jesuit college (UNESCO cultural heritage site) begun in 1662, as is known, on an elevated position next to the southern ramparts, according to the project of Serafin Fabrini (see Fig. 1a). The college, just like the Jesuit church, was transformed after the earthquake thanks to the new spatial circumstances into a building whose construction development took more than century (1765) tried by various architects (see Fig. 1b) [1].

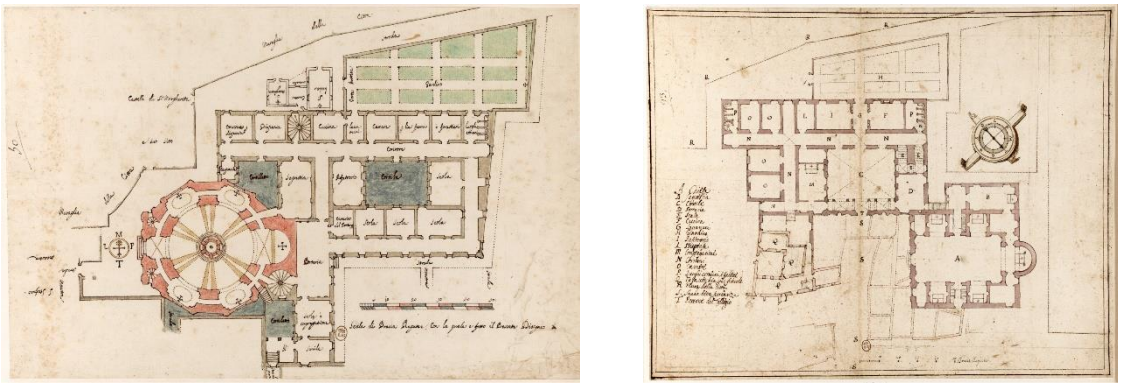

(a) (b)

Figure 1. Jesuit college architectural drawings by (a) Serafino Fabrini in 1659 and (b) Henri Lalojau in 1699, from National Library in Paris [1]

The construction was hindered by the 1667 Great Dubrovnik Earthquake. Consequently, the original building design was subjected to modifications (as observed in Fig. 1a and 1b). after 1979 Monte Negro earthquake the building suffered from structural damage [2]. The building is consisting of three main parts i.e. east, west and south wing (see Fig. 2).

2. Seismological and seismotectonic aspects

Dubrovnik region is seismically and tectonically very active. By its seismic and tectonic potential, it is also the most striking area in Croatia with estimated maximum possible magnitude of 7.5. Historic data note about ten earthquakes in the region with intensity of VIII or more ºMCS out of which the most significant one is the 1667 earthquake of X °MCS [3].

2. Structural characteristics

In cpl. with the EN1998-1:2004 [4] the Jesuit college is an unreinf. irregular masonry building (vulner. class B in cpl. with EMS). The wall texture is consisted of variable in size natural stone

(dominantly) or brick masonry units alternately laid out (fully grouted) in lime mortar. Considering the lime mortar's ($f_m \leq 2.5$ MPa i.e. $< f_{m,min} = 5$ MPa) and masonry unit's comp. strength ($5.0 \leq f_b \leq 35.0$ MPa i.e. $f_{b,min} = 5.0$ MPa [4]) the wall comp. strength is possibly ranging from 2.0 to 4.0 MPa [5] (with elast. modulus ranging from 1715 to 3210 MPa). The thickness of the walls is $t_{ef} > t_{ef,min} = 350$ mm. The floor structure consists mainly of masonry cross-vaults, arches or wooden joists.

Figure 2. Jesuit college: (a) view on the location within the Old City (b) east wing, (c) south wing

3. Measurement of ambient vibration

The ambient vibration measurement within the building was performed two-way i.e. up to 20 min long in the 2nd story and attic (at five diff. locations per story), and 3-day long in the 2nd story (at one location), respectively. The North-South (NS) i.e. longer direction of the building's south wing (see Fig. 2b) and East-West (EW) response components were simultaneously measured. In average, the first period value of about T = 0.25 sec (EW) and 0.11 sec (NS).

4. Conclusions

The investigation aimed at determining the seismic risk and vulnerability of UNESCO's cultural heritage site Jesuit college, positioned within the Old City of Dubrovnik, was performed, and its initial findings reported.

Acknowledgments

This work has been supported in part by Croatian Science Foundation under the projects HRZZ IP-2016-06-1854 and HRZZ IP-2020- 02-3531.

References

[1] Horvat Levaj K, Haničar Buljan I, Vareško G. The building of the Episcopal Seminary and Classical Gymnasium Jesuit College in Dubrovnik. Conservation study with guidelines for restoration (in Croatian: Zgrada biskupskog sjemeništa i klasične gimnazije (Isusovački kolegij) u Dubrovniku. Konzervatorska studija sa smjernicama za obnovu). Zagreb: Institute of art history; 2022.

[2] Knežević S. The Restoration of Dubrovnik 1979 - 1989 (in Croatian: Obnova Dubrovnika 1979 - 1989). Dubrovnik: Institute for the Restoration of Dubrovnik; 1989.

[3] Markušić, S., Ivančić, I. & Sović, I. The 1667 Dubrovnik earthquake–some new insights. Stud Geophys Geod 61, 587–600 (2017). https://doi.org/10.1007/s11200-016-1065-4

[4] CEN EN 1998-1 (2004). Eurocode 8: Design of Structures for Earthquake Resistance—Part 1: General Rules, Seismic Actions and Rules for Buildings (EN 1998-1:2004); European Committee for Standardization (CEN): Brussels, Belgium, 2004.

[5] CEN EN 1996-1-1 (2005). Eurocode 6: Design of Masonry Structures—Part 1-1: General Rules for Reinforced and Unreinforced Masonry Structures (EN 1996-1-1:2005); EC6; European Committee for Standardization (CEN): Brussels, Belgium, 2005.

Model-driven design of seismic upgrade interventions in heritage structures

Linda Scussolini*, Gaetano Miraglia*, Erica Lenticchia*, Rosario Ceravolo*

*Department of Structural, Geotechnical and Building Engineering – DISEG, Polytechnic of Turin, Corso Duca degli Abruzzi 24, Turin, 10129, Italy
E-mails: {linda.scussolini, gaetano.miraglia, erica.lenticchia, rosario.ceravolo}@polito.it

Keywords: Model-Driven Approaches, Seismic Engineering, Heritage Architectures, Masonry Structures, Digital Twin.

1. Introduction

Historical architectural structures represent an intrinsic vulnerability of the built heritage [1]. This is mainly due to their conception. They were designed to resist actions whose entity and shape were not completely clear at the construction time. For example, historic masonry structures are mostly designed to withstand vertical actions. However, in recent years it has emerged that hazardous natural events are more and more frequent, this probably also due to increasing environmental instability [2]. Among the different phenomena that can threaten historic masonry structures, the seismic action represents one of the important one, since it generates horizontal forces and consequent internal stresses for which the masonry structures were not meant for. To help this, Structural Health Monitoring (SHM) [3], and in particular seismic monitoring [4] plays a fundamental role, thanks to which the parameters of a structural system is monitored over time to define the health state of the system [5]. These parameters can then be used to inform virtual models of the monitored structure, generating numerical tools capable of replicating the behavior of the real system in a more truthful way [6–8]. These models, also known as digital twin [9], can thus be used to carry out virtual experiments. In the present study, virtual experiments were carried out on a numerical model of an existing system [10] (i.e., the baroque masonry church of *S. Caterina in Casale Monferrato*) in order to define the best solution for a seismic upgrade intervention to be carried out on the lantern of the church.

2. The case study of Santa Caterina

The Church of Santa Maria delle Grazie, also known as Church of Santa Caterina, located in Casale Monferrato (see Fig. 1), is one of the most important examples of baroque religious architecture of that territory. The oval dome, the lantern, and the façade are indeed just some elements that make the church a significant case study. The church presented some signs of damage due to previous seismic events and of deterioration mainly due to percolation and infiltration phenomena. Therefore, a vast test campaign was carried out during September 2010. The setups of the tests were designed exploiting a preliminary Finite Element (FE) model. The structural identification was carried out in the time-domain exploiting an algorithm of the Stochastic Subspace Identification (SSI) family. Exploiting the results obtained from the identification process, a vibration-based model updating has been conducted. For additional information, one can refer to [10].

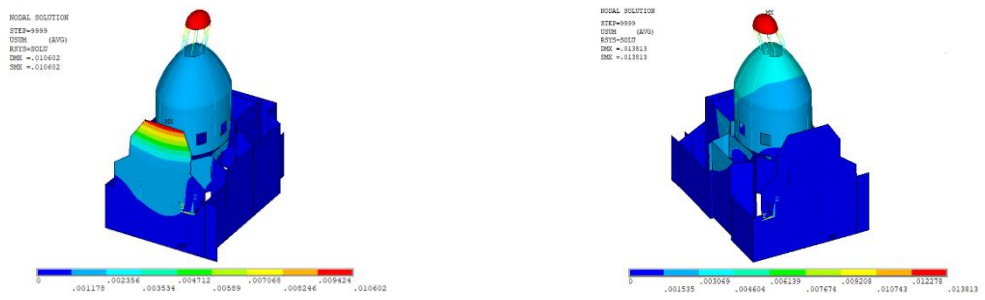

(a) (b)

Figure 1. Maximum displacements of response spectrum analysis in the updated model: (a) x-direction; (b) y-direction.

The vibrations modes resulting from a modal analysis on the calibrated model allowed to understand the most vulnerable elements of the church: indeed, the first vibration mode, at a frequency of 2.94 Hz, mainly involves the lantern, the second one, at 3.53 Hz, involves the facade, and the third one, at 4.29 Hz, mainly involves the drum-dome

system. Consequently, a multi-modal analysis with response spectrum confirmed the vulnerability of the lantern and of the façade. Indeed, applying the spectrum in the x-direction, the maximum displacement of 1.06 cm occurs at the top of the façade, but also the lantern results to be affected (Fig.1a). For what concerns the y-direction, the maximum displacement of 1.40 cm occurs at the highest point of the lantern, while the façade seems not to be affected (Fig. 1b).

3. Upgrade interventions on the lantern

The hypothesis of vulnerability of the lantern was also supported by the verifications concerning the small columns of the lantern and the façade, for which the safety factor is lower than 1. Since the lantern is the element presenting the lowest safety factor, it has a priority of intervention. The high vulnerability of the lantern can be attributed to the thickness of the columns and to the mass of the above small dome, as observable in Fig. 2a. The structural intervention on the lantern had as main objective the stiffening of the masonry small columns, to limit the deformations, mostly horizontal, that could take place during an earthquake. As reported in Fig. 2b, 16 L-shaped profiles in structural steel were installed on the small columns. Moreover, three U-shaped profiles in INOX AISI 304 steel were inserted on the lintel and on the base of each opening of the windows. The whole set of profiles were then linked to the two lateral uprights through screws. To integrate each frame with the remaining ones, three plates of dimension 25x10 mm were placed at three different heights, anchored to the masonry small columns through screws and chemical anchor.

(a) (b)

Figure 2. Model of the lantern of S. Caterina: (a) before intervention; (b) after intervention.

4. Conclusions

Model-driven approaches represent an efficient tool to design structural interventions. These approaches are especially essential when intervening on historic structures, for which destructive in situ experiments must be reduced to a minimum. Furthermore, a global collapse experimentation of the structure would not be possible and therefore the use of virtual models of the system is required. In this context, it is clear how the use of predictive calibrated models can make a difference on the choice of a seismic upgrade and therefore on the future shape and conception of the structural system. This paper remarked these concepts, showing a successful application of a model-driven approach for designing a seismic upgrade intervention.

References

[1] Worthing, D.; Bond, S. *Managing built heritage: The role of cultural significance*; John Wiley \& Sons, 2008;

[2] Sanchez, G.; Rolland, Y.; Corsini, M.; Braucher, R.; Bourlès, D.; Arnold, M.; Auma\^\itre, G. Relationships between tectonics, slope instability and climate change: cosmic ray exposure dating of active faults, landslides and glacial surfaces in the SW Alps. *Geomorphology* **2010**, *117*, 1–13.

[3] Farrar, C.R.; Worden, K. An introduction to structural health monitoring. *Philos. Trans. R. Soc. A Math. Phys. Eng. Sci.* **2007**, *365*, 303–315.

[4] Dolce, M.; Nicoletti, M.; De Sortis, A.; Marchesini, S.; Spina, D.; Talanas, F. Osservatorio sismico delle strutture: the Italian structural seismic monitoring network. *Bull. Earthq. Eng.* **2017**, *15*, 621–641.

[5] Pecorelli, M.L.; Ceravolo, R.; Epicoco, R. An Automatic Modal Identification Procedure for the Permanent Dynamic Monitoring of the Sanctuary of Vicoforte. *Int. J. Archit. Herit.* **2018**, doi:10.1080/15583058.2018.1554725.

[6] Ceravolo, R.; De Lucia, G.; Miraglia, G.; Pecorelli, M.L. Thermoelastic finite element model updating with application to monumental buildings. *Comput. Civ. Infrastruct. Eng.* **2020**, *35*, 628–642.

[7] Venanzi, I.; Kita, A.; Cavalagli, N.; Ierimonti, L.; Ubertini, F. Earthquake-induced damage localization in an historic masonry tower through long-term dynamic monitoring and FE model calibration. *Bull. Earthq. Eng.* **2020**, *18*, 2247–2274.

[8] Civera, M.; Fragonara, L.Z.; Surace, C. A computer vision-based approach for non-contact modal analysis and finite element model updating. In Proceedings of the European Workshop on Structural Health Monitoring; 2020; pp. 481–493.

[9] Semeraro, C.; Lezoche, M.; Panetto, H.; Dassisti, M. Digital twin paradigm: A systematic literature review. *Comput. Ind.* **2021**, *130*, 103469.

[10] Ceravolo, R.; Pistone, G.; Fragonara, L.Z.; Massetto, S.; Abbiati, G. Vibration-based monitoring and diagnosis of cultural heritage: a methodological discussion in three examples. *Int. J. Archit. Herit.* **2016**, *10*, 375–395.

On the selection of distinct element method for numerical analysis of Zagreb Cathedral

Elizabeta Šamec*, Petra Gidak*, Antonia Jaguljnjak Lazarević+, , Jakov Oreb*

*Faculty of Civil Engineering University of Zagreb
E-mails: {elizabeta.samec, petra.gidak, jakov.oreb}@grad.unizg.hr

+Faculty of Mining, Geology and Petroleum Engineering University of Zagreb
E-mail: antonia.jaguljnjak-lazarevic@rgn.unizg.hr

Keywords: distinct element method, masonry, historical structures

1. Introduction

Zagreb Cathedral, the largest Croatian sacral building and one of the most valuable monuments of Croatian cultural heritage, was severely damaged by the 5.4 magnitude earthquake on March 22, 2020. Seismic hazard is especially emphasized due to the proximity (just over 15 km) of two active faults, the North Medvednica Boundary and the Kašina Fault. The Cathedral had been already hit by a hard earthquake of Richer magnitude 6.1 in 1880. Moreover, it suffered fire, wars, and a centennial environmental impact, so it has been fixed, repaired, upgraded, and retrofitted many times. It was restored in the neo-Gothic style (by H. Bolle) with ribbed vaults and arches supported by slender columns, but the spatial connection between the load-bearing elements is poorly executed and the structural system for horizontal loads has not been significantly improved. The two 108-meter towers erected next to the church during the restoration caused a strong asymmetry of mass and stiffness, resulting in a significant torsional response confirmed by damage after the 2020 earthquake, and following li measurement.

The material of the structure of the Zagreb Cathedral is and will always be discontinuous (with cracks and joints). As soon as one looks at the structure, different types of stone can be seen. Numerous old and new damages to load-bearing and non-load bearing (especially decorative) elements are noticeable - the stone is cracked and deteriorated in many places. In addition to material discontinuities, and given the past events, there are undoubtedly hidden cracks within structural components that reduce the load-bearing capacity. Post-earthquake inspection indicates a very distinct nature of the material (porous stone structure) and load-bearing Cathedral elements (stepped cracks in the walls, broken joints), which confirm and emphasize the previously stated assumptions. Globally it is a significantly discontinuous medium without any reinforcement. Based on these findings it is justified to conclude that the material model as a continuum (FEM) cannot, in this case, approximate the on-field state.

2. Problem formulation using distinct element method

The distinct element method has shown good results in simulating large displacements or collapse of masonry structures, as it can better approximate failure along head and bed joints (relatively strong elements versus weak mortar) compared to methods based on a continuum. The numerical model consists of deformable blocks and their contacts. The blocks are discretized by tetrahedra based on the finite difference method, and their behavior is nonlinear with the possibility of hardening and softening. The connection between the discretized blocks is defined by a series of nonlinear springs (Fig. 1a). Each spring is connected by a node to a contact plane. Contact point has a participating area needed to define the spring's behavior law, which depends on the relative displacement of its ends. With a spring perpendicular to the contact plane, the relationship between normal stress and normal relative displacement between contacts can be defined, and with a spring lying in the plane, the relationship between shear stress and relative shear displacement. (Fig. 1b). With the model based on

elements and springs connected and discretized blocks can deform and move (slip, separate, break, rotate, fall) practically without restrictions.

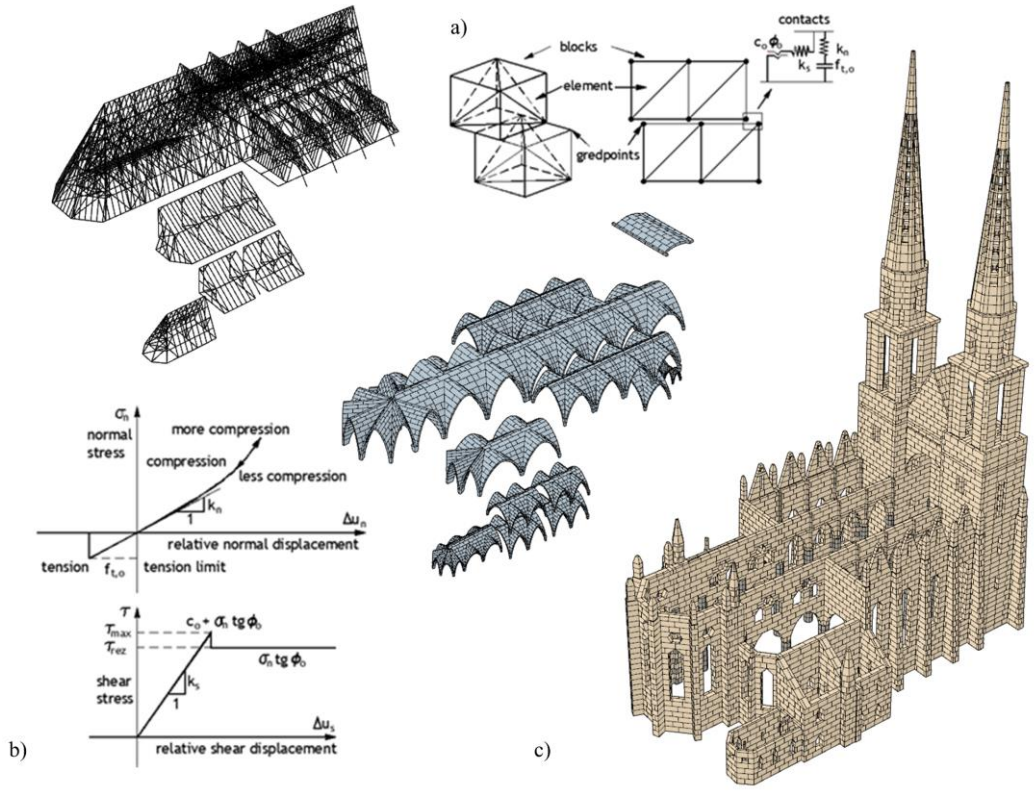

Figure 1. a) basic elements of the DEM model, b) behavior laws of springs on contact, c) numerical model of the Cathedral (distinct elements of walls and vaults, and beam elements for the wooden roof)

The software 3DEC [1] is used for the structural analysis of the Cathedral. Due to the complicated geometry, considerable effort was invested in the generation of the numerical model. A cloud of more than three billion points was used as the basis for creating a volume and then a block-based numerical model (Fig. 1c). Parametric modeling was used to partially automate the process. The brick-like arrangement of the blocks is used to model walls and vaults, and their nonlinear responses. Since the method is mesh-dependent, the size, shape, and connections of the blocks were adjusted so that their response curves match those from literature and experiments.

3. Conclusions

The choice, essentially a good engineering assessment of the computational parameters, is extremely important. The numerical model must be consistent with what we are modeling - a very complex structure of extremely heterogeneous properties. Thus, neither a simple nor too complex model is needed, but good enough to gain insight into the global behavior of the structure.

References

[1] 3DEC™ Version 7.0, Distinct – Element Modelling of Jointed and Blocky Material in 3D, [accessed 12/01/2022], URL: https://www.itascacg.com/software/3DEC

The effect of a skew angle on spatial behavior of masonry arch bridges on spreading supports: A computational study

Domagoj Trajber[1], Davorin Penava[1], Ivica Guljaš[1]

[1] *Josip Juraj Strossmayer University of Osijek, Faculty of Civil Engineering and Architecture Osijek,3 Vladimir Prelog Str., 31000, Croatia, e-mail: {dtrajber, dpenava, iguljas}@gfos.hr*

[2] *University of Leeds, School of Civil Engineering, LS2 9JT, Leeds, UK, e-mail: v.sarhosis@leeds.ac.uk*

Keywords: skew angle, masonry arch bridge, spatial behaviour, spreading supports, computational study

1. Introduction

The construction types and typologies of existing brick masonry arch bridges in Croatia, are comprised from single-span (67 %) or multi-span (33 %) bridges with circular (25 %) or segmental arch (28 %), in accordance with [1]. The damage of the bridge described as "spatial deformation", caused by e.g. supports spreading, was noticeable in 30 % of the observed cases. The structural form and the skew angle of the bridge arch (vault) affect its spatial behavior as reported by [2-4]. The spatial behavior of masonry arch bridges under spreading supports w. r. t. different skew angles was investigated and the key parameters governing their response were identified.

2. Description of the micromodel

The effect of a skew angle on spatial behavior of masonry arch bridges on spreading supports (assigned as prescribed displacement) was investigated via 3D computational micromodels built in computer program ATENA Science [5]. The brick masonry (segmental) arch bridges were modelled as vaults, with a square span of 3 m, and rise of 0.75 m (1:4 span to height ratio). The skew angle was varied from 0° to 45° by the increments of 5°.

3. Spatial behavior and analysis

Fig. 1 shows the sequence of the hinge opening w. r. t. horizontal displacement (spreading supports).

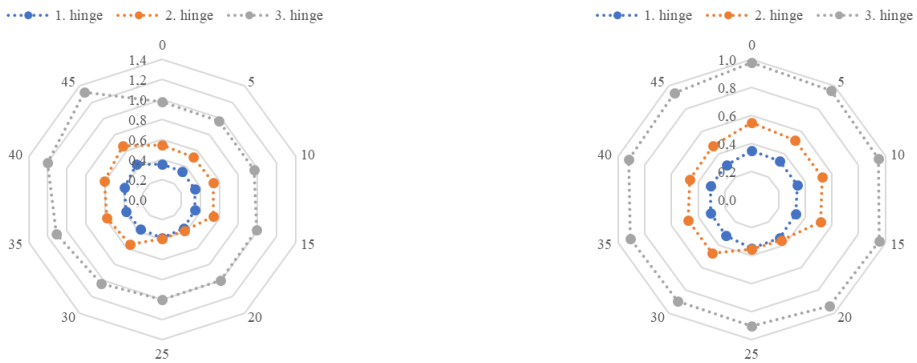

Figure 1. Masonry arch bridge horizontal support displacement vs. square span ratio (left) and skewed span ratio at hinge opening (‰) w. r. t. skew angle (°)

Fig. 2. provides an insight into the deformed shape of the bridge for the reference's cases with 0° and 45° skew angle, respectively.

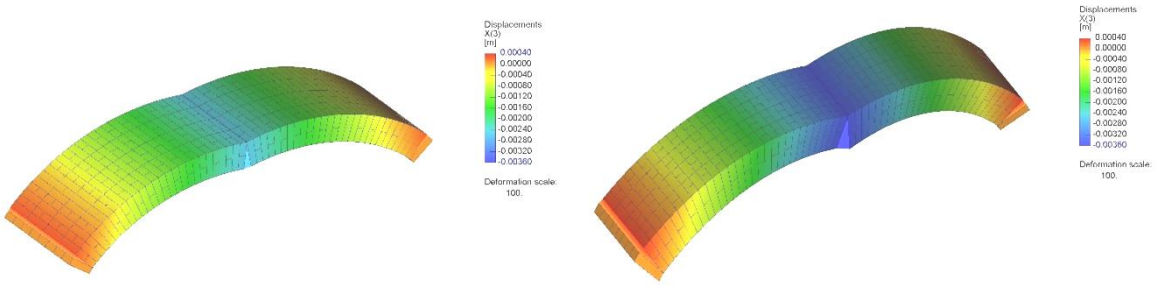

a) b)

Figure 2. Masonry arch (vault) deformed shape (×100) side (up) and spatial (down) view including vertical displacements after 3rd hinge opening: a) at 0° skew angle; b) at 45° skew angle

The hinge opening sequence was the same for all bridges by the location of their appearance i.e. the first hinge opened above the loaded support, the second above the opposite support, and the third at the crown of the arch (vault). The support spreading i.e. horizontal displacement at which the individual hinges occurred, as observed in Fig. 1., has different values e.g. at third hinge for 0° and 45° skew angle the displacements were $d_h/s = 0{,}98$ ‰ and $d_h/s = 1{,}32$ ‰, respectively.

The twisting effect was observed in all skewed bridge cases, and was increasing with the increase of the skew angle.

4. Conclusions

The spatial behavior of the single-span brick masonry arch bridge (1:4 span to height ratio) of segmental arch (vault) form under spreading supports w. r. t. skew angle was assessed computationally. The bridge selection was based on the bridge construction type and typology study in Croatia, as the most representative bridge among total of 178 existing bridges.

It was observed by the bridge spatial behavior computational simulations that the skew angle didn't affect the location and the order of the hinge opening, however it affected the support spreading displacement value at which they occur.

In addition, the spatial behavior of the skewed bridges was accompanied with the twisting appearance.

References

[1] Trajber, Domagoj; Penava, Davorin; Sarhosis, Vasilis; Abrahamczyk, Lars. Construction types and typologies of existing masonry arch bridges in Croatia // Young Scientist 2021 (YS21) 13th-15th October 2021, High Tatras, Slovakia / Mésároš, Peter ; Jothiprakash, Vinayakam ; Kotrasová, Kamila ; Zeleňáková, Martina (ur.). Štrbské Pleso, High Tatras, Slovačka, 2021. 1209, 11 doi:10.1088/1757-899X/1209/1/012063

[2] Hodgson, J.A., The behaviour of skewed masonry arch bridges, Dissertation, University of Salford, Department of Civil Engineering, 1996.

[3] Sarhosis, V., Oliveira, D.V., Lemos, J.V., Lourenco, P.B., The effect of skew angle on the mechanical behaviour of masonry arches. *Mechanics Research Communications*, 61, 53-59, 2014.

[4] Choo, B.S., Gong, N.G., Effect of skew on the strength of masonry arch bridges. Proceedings of 1st International Conference on arch bridges, Bolton, United Kingdom, 1995.

[5] Červenka V., Jendele, L., Červenka, J., ATENA Program Documentation – Part 1, Theory. Červenka Consulting s.r.o., Prag, 2020.

10th ICCSM, Pula, 2022

Organized Session:

Risk assessment and resilience estimation of civil engineering structures and systems by Ž. Nikolić, M. Hadzima-Nyarko and E. Benvenuti

The project "Earthquake risk assessment of the City of Zagreb": the development of the building database

Alen Kadić*, Maja Lončar Jamičić*, Josip Atalić*, Marta Šavor Novak*, Mario Uroš*, Maja Baničeк*

*University of Zagreb, Faculty of Civil Engineering
E-mails: {alen.kadic, maja.loncar.jamicic, josip.atalic, marta.savor.novak, mario.uros, maja.banicek}@grad.unizg.hr

Keywords: hazard, exposure, building stock, GIS-database, risk reduction

1. Introduction

According to the results of the official National Risk Assessments of the Republic of Croatia, the earthquake risk is pointed out as unacceptable for the country [1]. During the work on the assessment, many deficiencies in the input data were identified, especially, the lack of data on the buildings stock [2]. The project "Earthquake risk assessment of the City of Zagreb" was initiated as a pilot-study for the Republic of Croatia, and it will tackle the identified deficiencies and determine the earthquake risk of Zagreb using state-of-the-art methodology.

2. Earthquake risk assessment of the City of Zagreb: the project description

The City of Zagreb, along with a few other authorities, is the leader of civil protection development on the regional and local level of the Republic of Croatia. A great example of this is the implementation of the project „Multisensory aerial capturing of the Republic of Croatia for disaster risk reduction evaluation" with the State Geodetic Administration as the coordinator, and the City of Zagreb as one of the partners, co-financed by the European Regional Development Fund. The project is divided into multiple parts. One part is the "Earthquake risk assessment of the City of Zagreb" project, that started in April 2021 and will last for three years (36 months). It will be carried out by the Faculty of Civil Engineering, University of Zagreb as the main contractor. The main objective of this project is to determine the earthquake risk for structures and people. In addition to quantifying the risk, it is necessary to ensure vital data for preparation of the civil protection system in the phase of post-earthquake response, as well as preparation of measures for a rapid response in the phase of early recovery of the earthquake affected area and the necessary decision making. The main activities of the project include: the definition of the methodology for earthquake risk assessment, the definition of seismic hazard; gathering and analysis of data on structures and creation of a database on buildings and population (which is the focus of this paper), and finally the assessment of earthquake risk for the City of Zagreb. The earthquake risk for the City of Zagreb is going to be estimated for characteristic geographic sectors, as well as for all the categories of buildings by purpose. It will be based on the input data for the three main risk elements: seismic hazard, exposure and vulnerability of buildings, and expressed in terms of damaged/collapsed buildings, financial losses and affected people.

A significant part of the project is related to the collection of data on buildings, necessary for the development of the building stock database. In cooperation with the company GDi d.o.o., the City of Zagreb developed a basic layer in the GIS environment for data collection of more than 325,000 objects (Figure 1). There are 35 mandatory attributes (by the contract) that need to be collected for buildings, but by the development of the methodology that number is continuously growing (more than 100 attributes). The definition of the attributes in the exposure model is primarily based on the latest GEM building taxonomy [3], but is adapted to the local building stock. Buildings can then be classified into different building classes according to a number of structural attributes, and the appropriate vulnerability models can be applied to these classes.

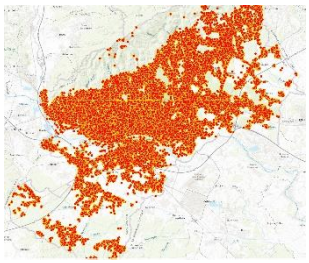

Figure 1. GIS Layer for collecting data (325.000 buildings)

Data collection includes the building-by-building field surveys, documentation from various sources, and in the later phases, the LIDAR recording which will be made in scope of the project. In the initial phases, the data from the damage and usability assessments after the Zagreb 2020 Earthquake, comprising more than 23,000 inspections, is being implemented into the newly developed database [4].

Two ArcGIS Survey123 forms for the collection of the buildings attributes have been created and are being used, one is for the citizens and the other for a field team of civil engineers engaged in a project. The entry form for citizens is simplified - it covers the main attributes necessary for describing the buildings seismic performance, and it can be easily completed by owners or building managers by attaching the documents (e.g. design documentations, drawings, etc.) or filling out the questionnaire. The entry form for field teams is more comprehensive and includes all attributes defined in the proposed methodology.

The final result will be comprehensive building and population database. Based on the collected input data, a basis for the earthquake risk assessment will be established, earthquake risk assessment for the City of Zagreb will be conducted, and the data will be made available to all relevant institutions.

Even though a significant part of the planned activities has been carried out, there are still two years left for the project. During the remaining time, the implementation of the methodology will be completed, but also the collection and processing of all required data and finally the calculation of the earthquake risk. After the end of the project, new opportunities will open up, firstly for the second phase of the project in the City of Zagreb, but also for the implementation of similar projects on the territory of the entire Republic of Croatia.

3. Conclusions

This paper briefly presents an ongoing earthquake risk assessment project for the City of Zagreb. It is important to highlight that the project is a pilot study for Croatia. This is a very important step forward, because reliable earthquake risk assessments are the first step towards disaster risk reduction strategies and preventive actions. Unfortunately, the 2020 earthquakes have shown that Croatia is in urgent need of them.

References

[1] Atalić, J., Šavor Novak, M., Uroš, M., *Updated risk assessment of natural disasters in Republic of Croatia – seismic risk assessment* (in Croatian). Faculty of Civil Engineering in collaboration with Ministry of Construction and Physical Planning and National Protection and Rescue Directorate, Croatia, 2018

[2] Atalić, J., Šavor Novak, M., Uroš, M., Seismic risk for Croatia: overview of research activities and present assessments with guidelines for the future. *GRAĐEVINAR*, 71 (10), 923-947, 2019.

[3] Silva, V., Yepes-Estrada, C., Dabbeek, J., Martins, L., Brzev, S., *GED4ALL: Global exposure database for multi-hazard risk analysis —Multi-hazard exposure taxonomy*. GEM technical report 2018-01. Pavia: GEM Foundation, 2018.

[4] CCEE: GIS-based building usability database. Croatian Centre for Earthquake Engineering, Faculty of Civil Engineering, University of Zagreb (in Croatian; accessed March 2, 2022).

An Overview of the Design Guidelines for Blast Loaded Columns

Sanja Lukić, Hrvoje Draganić, Marijana Hadzima-Nyarko, Goran Gazić

Faculty of Civil Engineering and Architecture Osijek, Vladimira Preloga 3, 31000 Osijek
E-mails: {slukic, draganic, mhadzima, ggazic}@gfos.hr

Keywords: blast load, RC column, design, reinforcement

1. Introduction

In recent decades, we have witnessed an increasing number of terrorist attacks. Explosive devices make over 50 % of all attacks [1]. Due to a heavy occupancy in multi-story buildings and the concentration of traffic on bridges, these constructions are becoming desirable targets. Special attention is necessary when designing the primary load-bearing components to lower the probability of progressive collapse [2]. The most vulnerable primary elements in buildings and bridges are columns because their loss of load-bearing capacity affects the stability of the entire structure. In the past, column design did not account for large lateral loads, so it is necessary to consider the given guidelines and instructions for reinforced concrete columns exposed to blast loads [3].

2. Guidelines

Eurocode does not provide recommendations for designing the elements to the influence of blast load. American standards, mainly ASCE/SEI 59-11 [4], provide specific guidelines for RC member design. Five main variables play a significant role in the action of the blast load. Four relate to the column itself: location and type of transverse reinforcement, volumetric reinforcement ratio, and the cross-section, while the last guideline refers to how to increase the charge distance from the column, i.e. standoff distance. Table 1 provides guidelines for the design and detailing depending on the bridge category. The given categories A (gravity load), B (seismic load), and C (blast load) depend on the scaled distance (Z) [3]. The higher scaled distance requires fewer requirements for design details due to lower blast load.

Table 1. Design category concerning scaled distance (*Z*) [3]

Design category	Scaled distance (Z)	Category description
A	$Z > 1.2 \frac{\mathrm{m}}{\mathrm{kg}^{1/3}}$	Bridges that are designed without additional requirements; do not take into account the action of the blast load.
B	$1.2 \frac{\mathrm{m}}{\mathrm{kg}^{1/3}} \geq Z > 0.6 \frac{\mathrm{m}}{\mathrm{kg}^{1/3}}$	Seismic-designed bridges.
C	$Z \leq 0.6 \frac{\mathrm{m}}{\mathrm{kg}^{1/3}}$	Try to avoid this category by increasing the distance between the explosion and the target.

2.1. Location of longitudinal splices

The splice location of the longitudinal reinforcement should be avoided, especially under blast load. If the connection is unavoidable, it should be at a very small or zero bending moment.

2.2. Type of transverse reinforcement

Increasing the amount of transverse reinforcement increases the column ductility and the bearing capacity. The recommendation is to use continuous spiral reinforcement because it retains the protective layer of the column in the area where the shear occurs. Also, better anchoring improves the characteristics of discrete hoops. Figure 5 shows spiral hoop and anchoring depending on the design category.

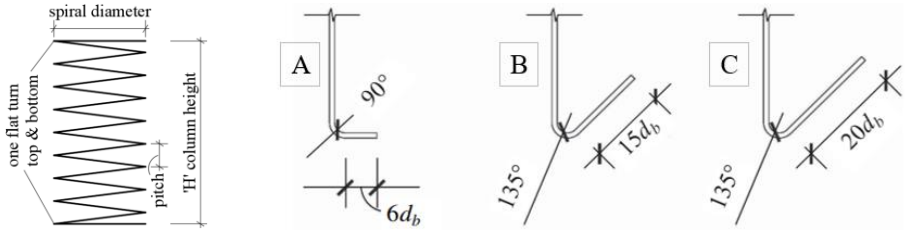

Figure 5. Spiral hoop and discrete hook anchorage for design categories: gravity, seismic and blast

2.3. Volumetric reinforcement ratio

The volumetric reinforcement ratio depends on the cross-section (circular or rectangular) and the column design category. The transverse reinforcement spacing affects load-bearing capacity at small-scaled distances while, at large-scaled distances, the contribution of spacing is negligible.

Table 2. Expressions for the required volumetric reinforcement ratio in a circular column [3]

Load type	Circular
Gravity-loaded columns	$\rho_s \geq 0{,}45(\frac{A_g}{A_c} - 1) \cdot \frac{f_c'}{f_y}$
Seismic loaded columns	$\rho_s \geq 0{,}12 \cdot \frac{f_c'}{f_y}$
Blast loaded columns	$\rho_s \geq 0{,}18 \cdot \frac{f_c'}{f_y}$

2.4. Cross-sectional shape and standoff distance

Experimental research indicates that even a minimal increase of the column cross-section area can result in a significant reduction of the blast-induced damage [3]. A square column is more resistant to shear than a circular column of similar dimensions but is influenced by higher impulses under blast load [5]. The standoff distance is the main parameter to consider in blast load mitigation. Increasing the standoff distance by only a few centimeters significantly increases the probability of element survival, especially when considering near field charges [3].

3. Conclusions

Seismically-designed columns show better behavior under blast load than gravity-loaded columns. When designing new structures, it is essential to consider the distance, quantity, and type of transverse reinforcement. Protection of existing columns is possible by strengthening or preventing vehicles from approaching the column using barriers and obstacles.

Acknowledgments

This paper has been supported in part by Croatian Science Foundation (HRZZ) under the project UIP-2017-05-7041 “Blast Load Capacity of Highway Bridge Columns”, and support for this research is gratefully acknowledged.

References

[1] START. National consortium for the study of terrorism and responses to terrorism. Global terrorism database [Data file 2017.]. 2017.
[2] FEMA. *Reference Manual to Mitigate Potential Terrorist Attacks Against Buildings*. FEMA-426/BIPS-06/; 2011.
[3] Board TR, National Academies of Sciences E, Medicine. *Blast-Resistant Highway Bridges: Design and Detailing Guidelines*. Washington, DC: The National Academies Press; 2010.
[4] ASCE. *Blast protection of buildings*. ASCE-59-11. Reston, VA, USA2011.
[5] Lukić S, Draganić H. Blast load analysis of overpass columns with various cross-sections. IOP Conference Series: *Materials Science and Engineering*. 2020;867:012028. https://doi.org/10.1088/1757-899x/867/1/012028

Assessment of seismic vulnerability of existing masonry buildings in urban area

Željana Nikolić[*], *Elena Benvenuti*[+], *Luka Runjić*[++], *Vedrana Kozulić*[*], *Nives Ostojić Škomrlj*[*]

[*]*Faculty of Civil Engineering, Architecture and Geodesy, University of Split, Matice hrvatske 15, Split, Croatia*
E-mails: {zeljana.nikolic, vedrana.kozulic, nives.ostojic}@gradst.hr

[+] *Engineering Department, University of Ferrara, 44121 Ferrara, Italy; bnvlne@unife.it*
E-mails: elena.benvenuti@unife.it

[++] *Projektni Biro Runjić, 21000 Split, Croatia; lrunjic.ured@gmail.com*
E-mail: lrunjic.ured@gmail.com

Keywords: seismic vulnerability assessment; hybrid procedure; vulnerability index method; pushover method; masonry buildings

1. Introduction

The assessment of seismic vulnerability of masonry buildings in an existing urban area is a demanding task, especially in old cities which have been gradually growing and expanding over the course of centuries. Different approaches like empirical, analytical or hybrid, can be used for the evaluation of structural vulnerability. This study uses hybrid empirical-analytical procedure which combines seismic vulnerability indexes with critical peak ground accelerations computed through a non-linear pushover analysis. The proposed approach is based on detail evaluation of the seismic performance of characteristic buildings in the observed urban area by pushover analysis. Peak ground accelerations for different limit states are linking with the vulnerability index of the buildings for the chosen sample. Established relations are used to estimate peak ground accelerations, damage index and seismic risk index for other buildings in the urban area, based on their vulnerability indexes. The methodology has demonstrated at the Croatian settlement Kaštel Kambelovac.

2. Case study

The case study Kaštel Kambelovac is a small Mediterranean urban settlement placed along the Croatian coast. It consists of a historical core constituted by stone masonry, erected between the 15th and the 19th century, and the periphery outside of the historical core which includes mix of the buildings made of stone, concrete or brick blocks built in 20th and 21st century. In particular, five main categories of buildings have been recognized: before 1948, 1949 – 1964, 1964 – 1982, 1982 to 2005 and modern buildings erected from 2005 onwards. All these buildings exhibit different seismic performance depending on the period of construction and applied technical regulation [1,2].

3. Seismic vulnerability assessment procedure

The vulnerability index method is used to calculate the vulnerability index for the building based on the calculation of 11 geometrical, structural and non-structural vulnerability parameters of the buildings [1, 2]. Seismic behavior and the capacity of the building for three limit state (LS) conditions [3] are evaluated by static non-linear (pushover) method [4]. Eighteen buildings in the settlement (10 in historical core and 8 outside of the core) were modelled using 3MURI software [5]. The buildings have been chosen considering different material and structural characteristics as well as the period of construction. The results for 18 analyzed buildings are used to establish the vulnerability index – peak ground acceleration (PGA) relation for DL, SD and NC limit states at the entire test site. Figure 1 shows the relationships between the vulnerability index and the critical peak ground accelerations associated with the DL, SD and NC limit states. The trend lines I_v–PGA_{DL}, I_v–PGA_{SD} and I_v–PGA_{NC}

for three limit states expressed by exponential functions have been established. They are used to approximate the yield, significant damage and collapse PGA for the entire test site.

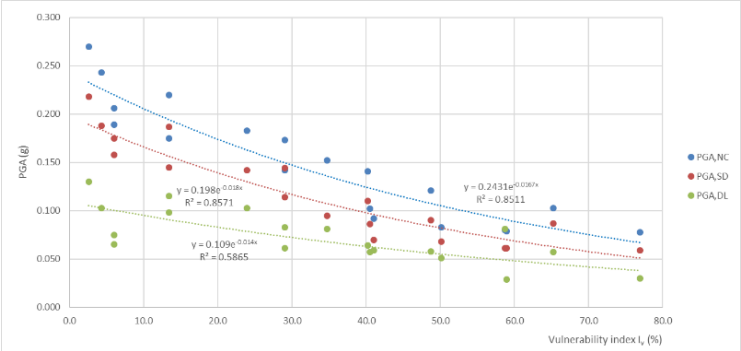

Figure 1. Relations I_{v11}–PGA_{DL}, I_{v11}–PGA_{SD} and I_{v11}–PGA_{NC}

The values of yield and collapse accelerations are the basis for deriving vulnerability curves and detection of the damage index for the given intensity of the earthquake. Three seismic scenarios corresponding to return periods 95, 225 and 475 years and demand PGA of 0.11g, 0.17g and 0.22g, respectively, have been chosen, and damage indexes have been calculated for the buildings at the whole test site. The seismic risk index $\alpha_{PGA,C}$ is defined as the ratio of the PGA_C associated to the capacity of the structure and the demand ground acceleration PGA_D. The values $\alpha_{PGA,C}>1$ refer to safe structures, while the values $\alpha_{PGA,C}<1$ refer to non-safe structures. The seismic risk index for the collapse (NC limit state) of the buildings for three return periods are calculated for the settlement.

4. Conclusions

A comprehensive hybrid approach to large-scale seismic vulnerability and risk assessment of existing urban areas is presented in this study. The approach combines the advantages of the vulnerability index method in assessing the vulnerability of a large number of buildings with the pushover method, that allows to determine the capacity curves and detect the specific limit states of the buildings. The present procedure has resulted in seismic vulnerability indexes, damage indexes, critical accelerations for different limit states and seismic risk indexes for the case study Kaštel Kambelovac.

Funding: This research was funded by: (1) the EUROPEAN UNION, Programme Interreg Italy-Croatia, Project "Preventing, managing and overcoming natural-hazards risks to mitigate economic and social impact"—PMO-GATE ID 10046122; (2) the CROATIAN GOVERNMENT and the EUROPEAN UNION through the European Regional Development Fund—the Competitiveness and Cohesion Operational Programme (Project KK.01.1.1.02.0027).

References

[1] Nikolić, Ž., Runjić, L., Ostojić Škomrlj, N., Benvenuti, E. Seismic vulnerability assessment of historical masonry buildings in Croatian coastal area. *Applied Sciences*, 11(13), 5997, 2021.

[2] Nikolić, Ž., Benvenuti, E., Runjić, L., Seismic risk assessment of urban areas by a hybrid empirical-analytical procedure based on peak ground acceleration. Submitted to *Applied Sciences*, 2022.

[3] HRN EN 1998-3 Eurocode 8: Design of structures for earthquake resistance—Part 3: Assessment and retrofiting of buildings; Croatian Standards Institute: Zagreb, Croatia, 2011.

[4] 3MURI Software, Professional version; S.T.A. DATA: Torino, 2019.

[5] Fajfar, P., Eeri, M. A nonlinear analysis method for performance based seismic design. *Earthquake Spectra*, 16, 573–592, 2000.

Seismic risk assessment of a traditional rammed earth structure from Eastern Croatia

Ana Perić*, Ivan Kraus*, Marijana Hadzima-Nyarko*

*Faculty of Civil Engineering and Architecture Osijek, Josip Juraj Strossmayer University of Osijek
E-mails: {aperic,ikraus,mhadzima}@gfos.hr

Keywords: rammed earth structure, numerical model, seismic behavior, incremental dynamic analysis, fragility curves

1. Introduction

Traditional houses in Eastern Croatia were usually built using local earthen material [1, 2]. However, earthen architecture faded away when artificial stone (e.g. fired brick and concrete) replaced traditional building techniques (e.g. rammed earth and adobe). Today, earthen architecture in Slavonia and Baranja is in deteriorating state since there has been minimal concern for reparation and preservation. With no guidelines or standards for building and preserving earthen structures in Croatia, it is easy to presume that a part of Croatian cultural heritage will soon disappear. Moreover, poor seismic performance of earthen structures poses one of the biggest obstacles in finding proper ways of preserving existing and building new earthen architecture.

It is fair to assume that from the middle of the 19th century to today, earthen buildings encountered strong ground motions, but their seismic performance and possible fracture mechanisms are still unknown. Therefore, this paper deals with seismic risk assessment determined on a numerical model of a rammed earth structure. Only few papers worldwide have delt with seismic behavior of rammed earth structures [3-10]. Authors worldwide have mostly focused on seismic performance of rammed earth walls with means of experimental testing and numerical analyses. Merely two papers [8, 10] have described rammed earth house model tested on a shaking table. However, to our knowledge, no previous research has been conducted that produced fragility curves of rammed earth structures.

2. Methodology, numerical model and analysis

The method used to determine fragility curves of an observed rammed earth structure in this paper is Incremental Dynamic Analysis (IDA). Vamvatsikos and Cornell [11] proposed the algorithm for analysis in 2002 and according to them, the basis of IDA is scaling. Essentially, structures are subjected to a suite of several ground motions, each scaled to multiple levels of intensity, all resulting in the IDA curve. However, IDA on a micromodel would take enormous amount of time and computational effort making it unreasonable to conduct. For that purpose, Dolšek [12] proposed a simplified method for seismic risk assessment of buildings based on aleatory and epistemic uncertainty. The method combines micromodel pushover analysis with IDA of an SDOF model. Moreover, it is important to note that simplification regarding IDA conducted on the SDOF model rather than the model of the house was necessary for rammed earth structure. Namely, IDA can be performed on frame structures. Nevertheless, to our knowledge, rammed earth structures should not be modelled as frame structures but as solid structures. For that reason, in this paper the method proposed by Dolšek [12] was used. First, pushover analysis on micromodel of rammed earth house was conducted using ANSYS software. Then, particular parts of N2 method [13, 14] were used. Namely, capacity curve obtained from the pushover analysis was used to determine parameters needed to define the SDOF model, as described according to the N2 method. Lastly, IDA was conducted on the SDOF model, using SeismoStruct software, to determine fragility curves. It is important to note that in this paper, analysis was conducted on deterministic model to test only seismic performance of a rammed earth structure. Material properties were assumed with their average values, based on literature review [15] since material properties of rammed earth architecture from Eastern Croatia are yet to be determined. Furthermore, ground motion records for ground type C [16] with peak acceleration lower than 0,1 g were used.

3. Concluding remarks

Fragility curves determined within this analysis indicate that single story rammed earth structures built on ground type C, using material with average material properties, would be severely damaged by earthquakes with peak acceleration lower than 0,1 g. However, this is the first seismic risk assessment of rammed earth structures from Croatia, thus more research with different ground motion records and different ground types is mandatory. However, with this paper, determining fragility curves of rammed earth structure using method conventionally used for steel or concrete structures was proven possible.

Acknowledgements

This research was supported by Croatian Science Foundation under the project UIP-2020-02-7363 Rammed earth for modelling and standardization in seismically active areas - RE-forMS.

References

[1] Lončar-Vicković, S., Stober, D., *Tradicijska kuća Slavonije i Baranje*. Ministarstvo turizma Republike Hrvatske, Sveučilište Josipa Jurja Strossmayera u Osijeku, Građevinski fakultet Osijek, Osijek, 2011.

[2] Živković, Z., *Hrvatsko tradicijsko graditeljstvo*, Minstarstvo culture, Uprava za zaštitu kulturne baštine, Zagreb, 2013

[3] Arslan, M.E., Emiroğlu, M., Yalama, A., Structural behavior of rammed earth walls under lateral cyclic loading: A comparative experimental study, *Construction and Building Materials*, 133:433–42, 2017.

[4] Bui, Q.-B., Morel, J.-C., Hans. S., Meunier, N., Compression behaviour of non-industrial materials in civil engineering by three scale experiments: The case of rammed earth, *Materials and Structures/Materiaux et Constructions*, 42(8):1101–16, 2009.

[5] El-Nabouch, R., Bui, Q.-B., Plé, O., Perrotin, P., Assessing the in-plane seismic performance of rammed earth walls by using horizontal loading tests, *Engineering Structures* 145:153–61, 2017.

[6] Miccoli, L., Drougkas, A., Müller, U., In-plane behaviour of rammed earth under cyclic loading: Experimental testing and finite element modelling, *Engineering Structures*, 125:144–52, 2016.

[7] Shrestha, K.C., Aoki, T., Miyamoto, M., Wangmo, P., Pema, 2020. In-plane shear resistance between the rammed earth blocks with simple interventions: Experimentation and finite element study, *Buildings*, 10(3), 2020.

[8] Wang, Y., Wang, M., Liu, K., Pan, W., Yang, X., Shaking table tests on seismic retrofitting of rammed-earth structures, *Bulletin of Earthquake Engineering*, 15(3):1037–55, 2017.

[9] Wangmo, P., Shrestha, K.C., Miyamoto, M., Aoki, T., Assessment of out-of-plane behavior of rammed earth walls by pull-down tests, *International Journal of Architectural Heritage*, 00(00):1–15, 2018.

[10] Zhou, T., Liu, B., Experimental study on the shaking table tests of a modern inner-reinforced rammed earth structure, *Construction and Building Materials*, 203:567–78, 2019.

[11] Vamvatsikos, D., Cornell, C.A., Incremental dynamic analysis, *Earthquake Engineering and Structural Dynamics*, 31(3):491–514, 2002.

[12] Dolšek, M. Simplified method for seismic risk assessment of buildings with consideration of aleatory and epistemic uncertainty, *Structure and Infrastructure Engineering*, 8(10):939–53, 2012.

[13] Fajfar, P., Fischinger, M., N2-a method for non-linear seismic analysis of regular buildings, Ninth World Conference on Earthquake Engineering, Tokyo-Kyoto, pp. 111-116, 1988.

[14] Fajfar, P., Gašperšić, P., The N2 method for seismic damage analysis of RC buildings, *Earthquake Engineering and Structural Dynamics*, 25, pp. 31-46, 1996.

[15] Perić, A., Kraus, I., Kaluđer, J., Kraus, L., Experimental campaigns on mechanical properties and seismic performance of unstabilized rammed earth—A literature review, *Buildings*, 11(8), 2021.

[16] Čaušević, M., *Dinamika konstrukcija - potresno inženjerstvo, aerodinamika, konstrukcijske euronorme*, 2. dopunjeno izdanje. Golden marketing - Tehnička knjiga, Zagreb, 2014

10th ICCSM, Pula, 2022

Organized Session:

Special session in honor of Professor Jurica Sorić on Advanced Numerical Methods in Structural Analysis: Recent Developments and Future Challenges, organized by Central European Association for Computational Mechanics (CEACM), A. Ibrahimbegović, B. Pichler and Z. Tonković

Mechanical properties of carbon nanotubes: molecular dynamics simulations and machine learning predictions

Marko Čanađija*

*Faculty of Engineering, University of Rijeka, Vukovarska 58, 51000 Rijeka, Croatia
E-mail: {marko.canadija}@riteh.hr

Keywords: single walled carbon nanotubes, molecular dynamics, deep learning

1. Introduction

For almost three decades, carbon nanotubes have been among the most studied objects in nanotechnology. This is due to their exceptional mechanical and electrical properties. In most cases, molecular dynamics is the main tool used in research, while experimental approaches are still rather rare.

As an alternative approach a lot of research is aiming to develop analytical structural models, rods and beams in particular, to approximate carbon nanotube behavior. Such analytical models differ from classical macroscopic models. The central problem is the existence of nonlocal potentials leading to nonlocal force fields at the nanoscopic level. Due to this behavior, the neighborhood contributes to the stress state in a point. Closer points have a stronger influence and this influence decreases when the distance between the points is increased. The most important parameter describing this behavior is the so-called nonlocal parameter. Unfortunately, the exact value of the nonlocal parameter is still unknown, although a large number of analytical models have now been developed.

There have been a number of attempts to determine the value of the nonlocal parameter by molecular dynamics simulations. The issue is far from simple to solve. The choice of potentials governing the interactions between carbon atoms, the thermal vibrations of the atoms, and other problems have a significant effect on the results. In the present research, an attempt is made to gain a deeper insight into the mechanical behavior of single-walled carbon nanotubes (SWCNTs) by performing a comprehensive set of molecular dynamics simulations, followed by the development of a deep neural network. First, the deep neural network should be a reliable tool for predicting mechanical properties. The Young's modulus, Poisson's ratio, elongation at fracture and ultimate tensile strength were analyzed. Second, the comprehensive set of molecular dynamics simulations should also give an indication of the non-local behavior of SWCNT.

2. Molecular dynamics simulations of SWCNT

The starting point is the choice of the potential describing the interactions between carbon atoms. In the present case, the modified AIREBO potential is chosen. Among the classical potentials (i.e., those not developed using density functional theory supported by machine learning), this potential is considered to most realistically capture the behavior at break and to have the fewest drawbacks.

Using the modified AIREBO potential, 818 different configurations of carbon nanotubes were generated. To reduce the influence of thermal vibrations each configuration was run 3 times and the results were averaged. The theoretical SWCNT diameters ranged from 0.36 nm to 3.916 nm, taking into account all possible chiralities defined as (n,m) within this diameter range. In all cases, the length-to-diameter ratio was about 5. One end of the SWCNT was prevented from moving, while a constant velocity was imposed at the other end. The velocity was calculated for each carbon nanotube to achieve a strain rate of 0.001 1/ps in all cases. More details on the modeling technique can be found in [1, 2].

Fig. 1 shows a single stress-strain curve to illustrate the results obtained. While the elongation at break and ultimate tensile strength can be readily determined, the Young's modulus and Poisson's ratio are somewhat more involved.

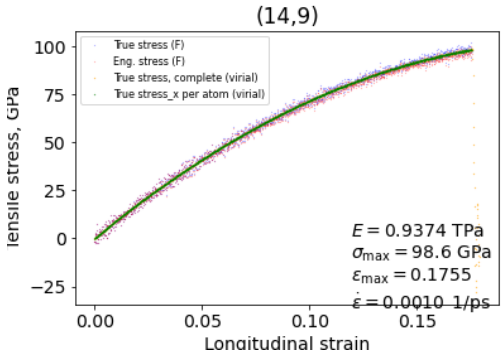

Figure 1. Uniaxial tensile tests of a (14,9) SWCNT

The average Young's modulus, Poisson's ratio, ultimate tensile strength and elongation at break were 947.45 GPa, 0.207, 94.86 GPa and 0.021, respectively.

3. Deep neural network

The obtained values of mechanical properties were used as a dataset for a deep learned neural network (DNN). The developed DNN has two roles. First, to remove or reduce the influence of thermal fluctuations, as clearly visible in Fig. 1. Second, to provide a reliable model for predicting the mechanical properties of SWCNT. For this purpose, a neural network with sequential architecture was chosen. The dense layers had 128-64-64-32-32-32-32-32-8-8-4 neurons. ReLU activation functions were used in all layers except the first and last layers. Data were normalized and mean square error (MSE) was used as the loss function.

The simulations lasted an average of 1247 epochs. The dataset was divided into training, validation, and test sets in a 70:15:15 ratio. The final MSE losses were 0.00277/0.00323/0.00484 for each set. Detailed results can be found in [1]. WThe nonlocal effect, i.e., the manifestation of the size effects, cannot be clearly established. At first, this may be visible for SWCNTs with smaller diameter, but one should bear in mind that the calculation of mechanical properties involves an approximation of the cross-section by a circular ring. This is not true, especially for smaller diameters where the cross section more or less resembles a polygon of thickness t and not a ring. Such an assumption can easily be misinterpreted as a nonlocal effect. Therefore, the nonlocal effect is very weak in SWCNT. DNN successfully manages to average the thermal fluctuations of the carbon atoms. The classical approach in this case would be to repeat the simulations as many times as possible and average the obtained results. This leads to significant computational costs. DNN has proven to be a viable alternative to this approach and significantly reduces these costs.

4. Conclusions

The present study provided a comprehensive set of MD simulations of SWCNT, and the mechanical properties were calculated. Based on these results, a dataset was created and used as input to DNN that can successfully approximate the mechanical properties of SWCNT.

Acknowledgments

This work has been fully supported by Croatian Science Foundation under the project IP-2019-04-4703. This support is gratefully acknowledged.

References

[1] Čanađija, M. Deep learning framework for carbon nanotubes: Mechanical properties and modeling strategies. *Carbon*, vol. 184, 2021, p. 891-901.

[2] Košmerl, V., Štajduhar, I., Čanađija, M. Predicting stress-strain behavior of carbon nanotubes using neural networks, *submitted*, 2022.

Finite element formulations for layered composite shells

Friedrich Gruttmann

Chair of Solid Mechanics, Technical University of Darmstadt, Germany
E-mail: gruttmann@mechanik.tu-darmstadt.de

Keywords: Layered plates and shells, coupled global local boundary value problems, four-node shell element, standard nodal degrees of freedom, fast computation of the load deflection behaviour

1. Introduction

Shell elements which account for the layer sequence of a laminated structure are able to accurately predict the deformation behaviour of the reference surface, a sufficiently refined mesh presupposed. For elasticity this holds also for the shape of the in–plane stresses, if the shell is not too thick. In contrast to that only averaged transverse shear strains through the thickness are obtained within the Reissner-Mindlin theory. As a consequence only the average of the transverse shear stresses is accurate. Neither the shape of the stresses is correct nor the boundary conditions at the outer surfaces are fulfilled. In a standard version the thickness normal stresses are neglected. In several papers the equilibrium equations are exploited within a post–processing procedure to obtain the interlaminar stresses. The essential restriction of the approach is the fact that these stresses are not embedded in the variational formulation and an immediate extension to geometrical and physical nonlinearity is not possible.

Higher order plate and shell formulations and layerwise approaches represent a wide class of advanced models. These theories are associated with global layerwise degrees of freedom which makes the general handling complicated for practical problems, e.g. when structures with intersections occur [1]. The use of brick elements or so-called solid shell elements represents a computationally expensive approach. For a sufficient accurate evaluation of the interlaminar stresses each layer must be discretized with several elements (≈4 - 10) in thickness direction. Especially for nonlinear large scale problems with a multiplicity of load steps and several iterations in each load step this is not a feasible approach [2]. An alternative to fully 3D computations is a multiscale formulation applying the so-called FE^2 approach. At the integration points of the macro scale representative volume elements (RVEs) are introduced. In case of thin structures the RVEs usually extend through the total thickness of the shell [3]. In comparison to one-scale computations using standard shell elements the computing times prove to be very high.

The discussion shows, that there is a need for further research in this range. Based on above arguments we propose a shell theory and associated finite element formulation which is characterized by the following features.

(i) The underlying nonlinear shell theory is based on Reissner-Mindlin kinematic assumptions. This leads in a basic version to averaged transverse shear strains and vanishing transverse normal strains when exploiting the Green-Lagrange strain tensor. Subsequently the displacement field is enriched by warping displacements and thickness changes using layerwise interpolation functions. Thereby an interface to arbitrary three-dimensional material laws with restriction to small strains is created.

(ii) The weak form of the boundary value problem is derived using the equilibrium equations for the stress resultants and stress couple resultants, the local equilibrium equations in terms of stresses, the geometric field equations, the constitutive equations and a constraint which enforces the correct shape of the displacement fluctuations through the thickness.

(iii) Static condensation is applied to eliminate a set of parameters on element level. The resultant quadrilateral shell element possesses the usual 5 or 6 nodal degrees of freedom. This is an essential

feature since standard geometrical boundary conditions can be applied and the element is applicable also to shell intersection problems. In comparison to fully 3D computations and to FE^2 computations present formulation needs only a fractional amount of computing time.

2. FE formulation for layered shells

Layered shells of thickness h are considered in this contribution. With ξ^iwe denote a convected coordinate system of the body, where for the thickness coordinate $h^- \leq \xi^3 \leq h^+$ holds. Thus, the reference surface Ω can arbitrarily be chosen with respect to the outer surfaces. The coordinate on the boundary $\Gamma = \Gamma_u \cup \Gamma_\sigma$ is denoted by s. The shell is loaded statically by surface loads $\bar{\mathbf{p}}$ in Ω and by boundary forces $\bar{\mathbf{t}}$ on Γ_σ. Inserting the kinematic assumptions according to Reissner and Mindlin into the Green-Lagrange strain tensor one obtains well-known expressions for the shell strains. The membrane strains, curvatures and transverse shear strains are summarized in the vector $\boldsymbol{\varepsilon}_g$.

A displacement field $\tilde{\mathbf{u}}$ is superposed on the displacement shape of the Reissner-Mindlin theory. Its components $\tilde{u}_i$ refer to a constant element basis system, where $\tilde{u}_1, \tilde{u}_2$ denote so called warping displacements and $\tilde{u}_3$ thickness changes. The shape of $\tilde{\mathbf{u}}(\xi^3) = \boldsymbol{\Phi}(\xi^3)\boldsymbol{\alpha}$ through the thickness is chosen as in Ref. [4]. The vector $\boldsymbol{\alpha}$ is element-wise constant and contains displacements at nodes in thickness direction of the laminate. For N layers this leads to $M = 9 \cdot N + 3$ components in $\boldsymbol{\alpha}$. The interpolation matrix $\boldsymbol{\Phi}(\xi^3)$ is formulated with cubic hierarchic functions.

Using admissible variations for the independent mechanical fields the variational equation as basis for the FE formulation is derived.

$$\int_\Omega \delta\boldsymbol{\varepsilon}_g^T \boldsymbol{\sigma} + \delta\boldsymbol{\sigma}^T(\boldsymbol{\varepsilon}_g - \boldsymbol{\varepsilon}) + \delta\boldsymbol{\vartheta}^T\boldsymbol{\psi}\, \mathrm{d}A - \int_\Omega \delta\mathbf{u}^T\bar{\mathbf{p}}\, \mathrm{d}A - \int_{\Gamma\sigma} \delta\mathbf{u}^T\bar{\mathbf{t}}\, \mathrm{d}s = 0.$$

Here, $\boldsymbol{\sigma}$ denotes the vector of independent stress resultants and $\boldsymbol{\varepsilon}$ denote physical shell strains, which enter into the material law. The vector $\boldsymbol{\psi}$ summarizes the material law, the equilibrium of higher order stress resultants and a constraint. The work conjugate vector $\boldsymbol{\vartheta} = [\boldsymbol{\varepsilon}, \boldsymbol{\alpha}, \boldsymbol{\lambda}]^T$ contains besides $\boldsymbol{\varepsilon}$ and $\boldsymbol{\alpha}$ the vector of Lagrange parameters $\boldsymbol{\lambda}$. Integration by parts and using standard arguments of variational calculus yields the associated Euler-Lagrange equations. One obtains the equilibrium of stress resultants, the geometric field equations, the local equilibrium in terms of stresses, a constraint and the static boundary conditions. The interpolation functions for the independent quantities are specified in detail in Ref. [5]. Several linear and nonlinear test examples show the effectiveness of the proposed model.

References

[1] Gruttmann, F., Wagner, W., On the numerical analysis of local effects in composite structures, *Composite Structures*, 29, 1-12, 1994.

[2] Klinkel, S., Gruttmann, F., Wagner, W., A continuum based 3D–shell element for laminated structures, *Computers & Structures*, 71, 43-62, 1999.

[3] Gruttmann, F., Wagner, W., A coupled two-scale shell model with applications to layered structures, *Int. J. Num. Meth.* Eng., 94, 1233-1254, 2013.

[4] Gruttmann, F., Knust, G., Wagner, W., Theory and numerics of layered shells with variationally embedded interlaminar stresses, *Comp. Meth. Appl. Mech. Engrg*., 326, 713-738, 2017.

[5] Gruttmann, F., Wagner, W., An advanced shell model for the analysis of geometrical and material nonlinear shells, *Computational Mechanics*, 66, 1353-1376, 2020.

Stochastic Upscaling Representation of Size & Scale Effects

Adnan Ibrahimbegovic[*1], H.G. Matthies[2], S. Dobrilla[1,2] E. Karavelic[1,3], R.A. Mejia-Nava[1], C.U. Nguyen[1], E. Hajdo[1,3], E. Hadzalic[1,3], I. Imamovic[1,3]

[+]*Institut Univeristaire de France*
[1]*Universite de Technologie Compiegne*
E-mail: adnan.ibrahimbegovic@utc.fr
[2]*Technische Universitat Braunschweig, Germany*
[3]*University of Sarajevo, Bosnia-Herzegovine*

Keywords: fracture mechanics, multi-scale models, stochastic upscaling, size & scale effects

The main goal of this work is to provide a thorough scientific understanding of the interplay between stochastics and mechanics, by classifying what can be achieved by representing mechanical system parameters in terms of deterministic values (homogenization) versus random variables or random fields (stochastic upscaling). The latter is of special interest for novel Bayesian applications capable of successfully handling the phenomena of fracture in both the quasi-static and the dynamic evolution of heterogeneous solids where no scale separation is present, which we refer to as stochastic upscaling. We seek to quantify the sensitivity of these phenomena with respect to the size-effect (changes in characteristic system dimension) and to the scale-effect (changes in characteristic time evolution). The challenge is to provide an answer as to why a system that is big does not break under quasi-static loads in the same way as a small system, even when both are built of the same material, and further extend this to inelasticity and fracture under dynamic loads. We plan to illustrate the crucial role of fine-scale heterogeneities and to develop the groundbreaking concept of stochastic upscaling that can capture their influence on instability and dynamic fracture at the system macro-scale. The stochastic upscaling is the key to size and scale laws in the proposed multi-scale approach, which can reach beyond homogenization to properly account for epistemic uncertainties of system parameters and the stochastic nature of dynamical fracture.

The methodology proposed in this work develops novel concepts in irreversible thermodynamics of nonequilibirum processes (yet referred to as nonequilibrium statistical thermodynamics, where neither space nor time scales are separated. This groundbreaking concept is here referred to as stochastic upscaling, providing a fruitful interaction of Mechanics (multi-scale approach) and Mathematics (uncertainty quantification). The stochastic upscaling truly applies across many scientific and engineering domains, where multiscale structure models are used to replace the testing procedure used to validate structure integrity or structure durability.

The main difficulty pertains to characterizing a number of different failure modes that require the most detailed description and interaction across the scales. Here, we seek to significantly improve the currently dominant experimental approach, because the latter is either not applicable for the sheer size of the structure, or unable to exactly reproduce the extreme loads. We propose to use stochastic upscaling, where extensive small-scale (material) testing is supplemented with large-scale (structure) computations, which allows exploring the real fracture behavior of the system under various load scenarios in optimal design studies, and thus accelerate innovations in this domain. More details are given in refs. [1,2,3, 4].

References

[1] A Ibrahimbegovic, HG Matthies, E Karavelic, Reduced model of macro-scale stochastic plasticity identification by Bayesian inference: Application to quasi-brittle failure of concrete, Comp. Methods Appl. Mech. Eng., 372, 113428, (2020). doi: 10.1016/j.cma.2020.113428

[2] A Ibrahimbegovic, R.A. Mejia Nava, Heterogeneities and material scales providing physically-based damping to replace Rayleigh damping for any structure size, Coupled Systems Mechanics, 10, 201--216, (2021). doi: 10.12989/csm.2021.10.3.201

[3] A Ibrahimbegovic, I Rukavina, S Suljevic, Multiscale model with embedded-discontinuity discrete approximation capable of representing full set of 3D failure modes for heterogeneous materials with no scale separation, Journal for Multiscale Computational Engineering, early view (2022). doi: 10.1615/IntJMultCompEng.2021038378

[4] A. Ibrahimbegovic, H.G. Matthies, S. Dobrilla, E. Karavelic, R.A. Mejia-Nava , C.U. Nguyen, M.S. Sarfaraz, A. Stanic, Jaroslav Vondrejc, Synergy of stochastics and inelasticity at multiple scales, Springer Nature Applied Science (SNAS), in press, 2022

Modeling of heat transfer problems using mixed Meshless Local Petrov-Galerkin collocation method

Boris Jalušić, Tomislav Jarak, Marin Vukovojac, Jurica Sorić, Zdenko Tonković

Faculty of Mechanical Engineering and Naval Architecture,
University of Zagreb, Ivana Lučića 5, 10002 Zagreb, Croatia
E-mails: {boris.jalusic, tomislav.jarak, marin.vukovojac, jurica.soric, zdenko.tonkovic}@fsb.hr

Keywords: Mixed MLPG collocation method, steady state and transient heat transfer

1. Introduction

In recent years, due to its price and time consumption, the fusion welding is the most prevalent joining technique in the production of engineering components, when compared to other joining processes. Thus, the scientific community is trying to increase the efficiency of fusion welding. Therein, the focus is to increase the quality of machined welds without a major degradation of the mechanical properties of the entire structure. Several passes are usually required during the welding of thicker specimens when conventional techniques are used. Thereby, both the preparation of the joining process and the welding procedure itself demand a significant time. Furthermore, these types of techniques directly influence the mechanical properties of the weld, resulting from the coarsening of grains due to a higher cyclic heat input [1]. To avoid some of the mentioned issues, the submerged arc and hybrid laser-arc welding can be used to weld thicker specimens in a single pass. However, they often result in unsatisfactory results in the weld quality and cause the physical distortions of the weld. Recently, the high efficiency modified gas metal active welding (GMAW) has been improved by using the strong electrical current and buried arc technique. In this technology, the electric arc and the molten wire tip are located under the surface level of the molten metal, which enables the welding of thick specimens in a single pass. This welding process often results in smaller values of the obtained residual stresses [2]. However, it must be further improved and potentially tailored to individual engineering materials. Since experimental measurements require expensive equipment, numerical simulations can be considered as a good alternative to cut the financial costs and speed up the calibration of the process.

2. Numerical simulation

The numerical simulation of the fusion welding can be a huge undertaking and is often done using a sequentially coupled thermo-mechanical computation approach [3]. Therein, firstly the thermal, i.e., the heat transfer problem is solved and sequentially utilized in the solution of the elasto-plastic mechanical problem to obtain the corresponding values of residual stresses. This contribution is focused on improving the solution of the heat transfer problem, i.e., the first step of the welding solution procedure, by numerical meshless methods. The motivation for this research stems from the authors previous experiences with the mixed Meshless Local Petrov-Galerkin (MLPG) collocation methods [4]. The steady state thermal problem is described by second-order elliptical partial differential equations, which are analogous to the ones governing the problem of classical elasticity. Hence, as a preliminary test, the potentials of the proposed mixed MLPG formulation and the standard fully displacement (primal) formulation for solving the second-order partial differential equations are demonstrated by considering the problem of homogeneous thick cantilever beam bending with the dimensions of $L \times H = 24\text{m} \times 4\text{m}$, as shown in Figure 1. The presented geometry and the applied boundary conditions, consisting of known displacements $\bar{u}_x$, $\bar{u}_y$ and tractions $\bar{t}_x$, $\bar{t}_y$, have been taken from the well known analytical solution [5]. The material data are Young's modulus and Poisson's ratio . The convergence study of both primal (P) and mixed (M) approaches, employing the relative

error in the L2 norm of nodal displacements, is shown in Figure 2. The nodal distance of the uniform grid is denoted by . The meshless approximation schemes [6] using the first- and second-order basis (IMLS1 and IMLS2) are applied.

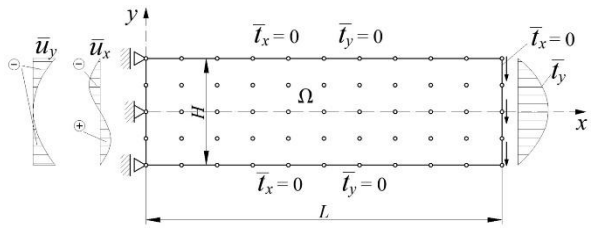

Figure 1: Geometry, discretization and loading of a thick cantilever beam

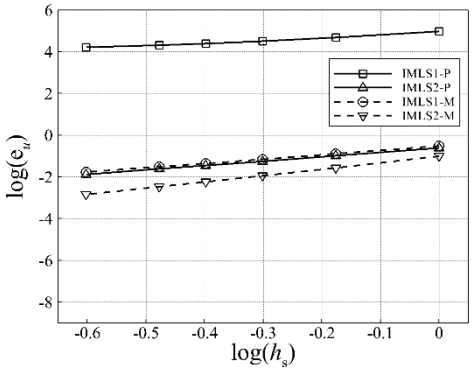

Figure 2: Displacement convergence tests

As evident, the mixed approach is superior to the primal formulation for both approximation functions. Therefore, a more accurate and numerically efficient modeling of steady state heat transfer is also expected when the mixed meshless collocation formulation is used.

3. Conclusions

In the proposed MLPG collocation method [7], the temperature and its first derivatives are approximated separately by using identical trial functions [6]. The compatibility between the approximated variables is then enforced at the discretization nodes, to eliminate the nodal values of first derivatives of temperature from the discretized governing equations. Such approach should lead to a more accurate meshless formulation [4], when compared to the primal approach [3], since only the first-order partial derivatives need to be calculated to assemble the global coefficient matrix. The accuracy and numerical efficiency of the proposed formulation will be demonstrated by a set of suitable numerical examples and compared to the results obtained by the primal meshless approach [3].

Acknowledgement

This work has been supported and co-funded by the European Union through the European Regional Development Fund, Operational Programme "Competitiveness and Cohesion" 2014 – 2020 of the Republic of Croatia, project "Improvement of high-efficiency welding technology" (ImproWE, KK.01.1.1.07.0076).

References

[1] L. Srinivasan, T.D.B. Kannan, P. Sathiya, S. Biju, Effect of heat input, heat treatment on microstructure and mechanical properties of GTA welded aerospace material 15CDV6. *J. Mater. Res.* 32 (2017) 1361–1366.
[2] H. Baba, T. Era, T. Ueyama, M. Tanaka, Single pass full penetration joining for heavy plate steel using high current GMA process. *Weld. World.* 61 (2017) 963–969.
[3] A. Morrefzadeh, S. Shahrooi, M. Azizpour, The application of the meshless local Petrov-Galerkin method for the analysis of heat conduction and residual stress due to welding. *Int. J. Adv. Manuf. Technol.* 104 (2019) 1–20.
[4] B. Jalušić, J. Sorić, T. Jarak, Mixed meshless local Petrov–Galerkin collocation method for modeling of material discontinuity. *Comput. Mech.* 59 (2017) 1–19.
[5] S. Timoshenko, Goodier J N, Theory of elasticity, McGraw-Hill, New York, 1970.
[6] T. Most, C. Bucher, New concepts for moving least squares: An interpolating non-singular weighting function and weighted nodal least squares. *Eng. Anal. Bound. Elem.* 32 (2008) 461–470.
[7] S. Atluri, H. Liu, Z. Han, Meshless Local Petrov-Galerkin(MLPG) Mixed Collocation Method For Elasticity Problems, C. *Comput. Model. Eng. Sci.* 14 (2006).

Strain propagation evaluation based on infrared thermography and digital image correlation

Lovre Krstulović-Opara, Alen Grebo

University of Split, Faculty of Electr. Eng.,Mech. Eng. and Naval Architecture, R. Boškovića 32, 21000 Split, Croatia
E-mails: {Lovre.Krstulovic-Opara, Alen.Grebo}@fesb.hr

Keywords: infrared termography, digital image correlation, machine learning

1. Introduction

Knowledge about material inner behavior during loading has always been of interest in mechanical sciences. Several methods such as strain gauge measuring, photoelasticity, digital image correlation, etc. have been develop trough the years with goal of determining stress and strain distribution of loaded body. Although strain gauges are appropriate approach when acquiring strain of dynamically loaded structure, they are providing just point wise information about the strain distribution. Digital image correlation (DIC) is providing information about dynamically loaded structures up to certain velocities, depending on photographic performances, optics and sensitivity of digital cameras (CMOS or CCD sensor based). In our previous [1] work we have shown similarity of infrared image patterns and effective strain distribution obtained by DIC. When using thermography. It was shown that infrared thermography based on InSb focal point array detector operating on cryogenic temperatures can be used for higher loading velocities where DIC is not providing results. Also infrared thermography cannot be used for lover loading velocities as thermal effect is dissolved due to cooling of unloaded material. Here we present an approach that can be used to relate these two methods and provide system of relating temperature distribution to effective strain.

2. Relating DIC to IR

The relation between stress and thermal distribution is established within method of Thermoelastic stress analysis. The method is based on Lock-in thermography of cyclically loaded structure, where loading frequency is about 10 Hz. The relation in post-elastic (plastic) regime is not jet established as it is influenced by many parameters. In [1] the comparison between DIC and IR showed that IR temperature distribution is similar to effective stress obtained by DIC. Figures 1 and 2 depict an example of aluminum alloy specimen, i.e. a tension test with predefined displacement of 284 mm/s. These images were obtained by Chronos 1.4 digital camera and Flir SC 5000 MW camera, both triggered and acquiring at frequency of 500 Hz. The DIC analysis was performed by open-source software Ncorr [2]. When comparing here presented results with ones reported in [1], the difference is in developing system of trigger based parallel acquisition of DIC and IR images and development of Matlab based image processing procedures, what enabled us integration of both methods for machine learning purpose.

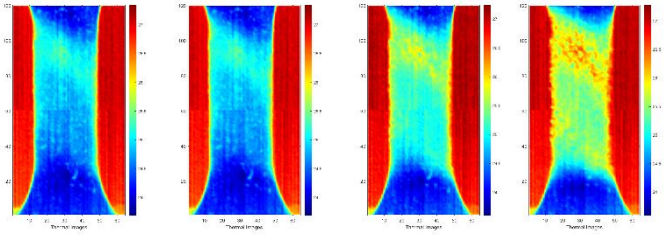

Figure 6 Thermal image

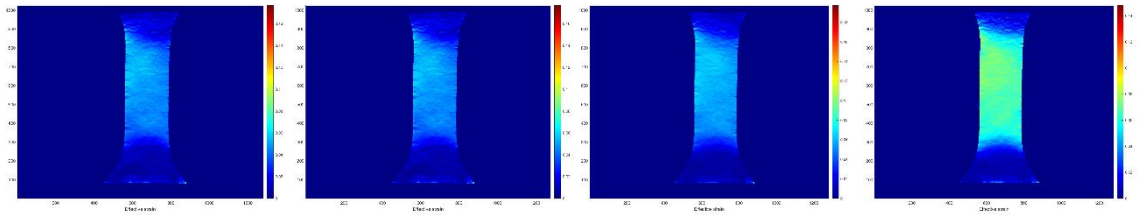

Figure 7 Effective strained obtained by DIC

Effective strain relation used for obtaining DIC imaged in Figure 1, after neglecting strain in z direction is:

$$\varepsilon_{ef} = \sqrt{\frac{3}{2}\varepsilon_{xx}^2 + \frac{3}{2}\varepsilon_{yy}^2 + \frac{3}{4}\varepsilon_{xy}^2}.$$

The approach taken will not focus our effort on finding classical relation between DIC and IR, but on training a deep neural network for finding the relationship between DIC and IR thermography.
As for training of deep neural networks large amounts of data are required, current experimental results obtained by our facilities are not enough. For this purpose, a synthetic dataset (that will complement real data set) is in development. Furthermore, as data for training is high dimensional, dimensionality reduction via REBMIX a finite mixture modeling library [3] using clustering will be implemented. This could potentially speed up the process of training the network.

4. The course

The presented work is still in development phase, and we will need several years to develop robust and general system of analysis. This approach of machine learning based development of physical relations between experimental observations is novel and unpredictable way in mechanics that opens new horizons in research.

References

[1] Krstulovic-Opara, L., Surijak, M., Vesenjak, M., Tonković, Z., Frančeski, J., Kodvanj, J., Domazet, Ž.: Determination of material properties using dynamic tests supported by thermography, digital image correlation and numerical simulation, *8th International Congress of Croatian Society of Mechanics*, eds.: I. Kožar, N. Bićanić, G. Jelinić, M. Čanađija, 29.9.-2.10., Opatija, Croatia, 53, 2015.

[2] Blaber, J., Adair B., and Antoniou A., *Ncorr: Open-Source 2D Digital Image Correlation Matlab Software*. Experimental Mechanics, 2015.

[3] Nagode M (2015). "Finite Mixture Modeling via REBMIX." Journal of Algorithms and Optimization, 3(2), 14-28. doi: 10.5963/JAO0302001, http://paper.academicpub.org/PaperInIssue?IssueId=1677.

Development of Constitutive Modelling for Composite Aeronautical Structures at FMENA

Ivica Smojver, Darko Ivančević, Dominik Brezetić

University of Zagreb, Faculty of Mechanical Engineering and Naval Architecture, I. Lučića 5, 10000 Zagreb, Croatia
E-mails: {Ivica.Smojver, Darko.Ivancevic, Dominik.Brezetic}@fsb.hr

Keywords: composite structures, constitutive modelling, impact damage, HFGMC, self-healing

1. Initial research in the analysis of composite structures

At the beginning of 1990s work at the numerical modelling of composite structures has started with development of 9-noded shell finite element applied in the analysis of layered composites. Using the principle of degeneration of three-dimensional continuum, MATLAB based program has been developed [1]. In addition, research has been performed in the analysis of the behaviour of composite torispherical shells where nonlinearities in the form of large deformations have been analysed [2]. In the next phase of the research, the development of numerical algorithms was performed for the analysis of interlayer delaminations at impact of composite plates with low speed/mass impactors. This leads to barely visible external damage (BVID) and the connection between the appearance of cracks in the matrix and interlayer delaminations was applied in the development of suitable algorithms [3]. Matrix cracks were determined by applying appropriate failure criteria, and the degradation of mechanical properties after the occurrence of damage was modelled. Kinematic connections were used to model the separation of nodes in the occurrence of interlayer delaminations. The numerical procedure developed at the level of the integration point was built into the ABAQUS program.

2. Crash and impact analyses

Crash and impact phenomena in composite structures present a particular concern due to the inherent susceptibility of the rather brittle material to this type of loading. To simulate impact damage and crashworthiness problems, the Abaqus built-in damage initiation and propagation model has been used [4]. This model employs the Hashin failure theory as the damage initiation criterion. Afterwards, damage in the composite was modelled using Continuum Damage Mechanics principles for the four fibre/matrix failure modes. To increase the accuracy of damage initiation modelling and to extend the capabilities of damage modelling in Abaqus/Explicit, various failure criteria have been also implemented in the simulations using the VUMAT user material subroutine. The described Coupled Eulerian Lagrangian numerical methodology has been applied to various foreign object impact damage problems in aeronautical structures (birdstrike, hail impact), ground impact simulations and similar crashworthiness problems, as illustrated in Fig.1. [5]

3. Modelling of damage in composite structures

To further increase the reliability of numerical damage modelling in composite structures, a multiscale approach has been developed within the Aerodamagelab research group. This methodology is established by coupling the computationally efficient semi-analytical High Fidelity Generalized Method of Cells (HFGMC) micromechanical model and the Abaqus/Explicit solver for simulations at the structural level. The HFGMC model has been implemented into the Abaqus/Explicit analysis using the VUMAT software as a separate FORTRAN written subroutine and using the MKL sparse system solver for computational effectiveness [6,7]. The Mixed Mode Continuum Damage Mechanics (MMCDM) model has been employed in this multiscale framework to model the damage processes at the constituent level.

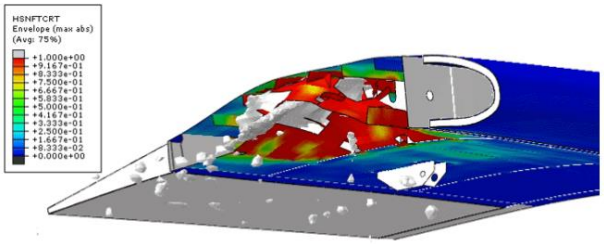

Figure 8: Simulation of a bird strike event – contours of Hashin's fibre tensile initiation criterion at a 1.81 kg bird impact at 100 m/s in the composite flap structure.

4. Self-healing composite structures

Self-healing polymers have proven their applicability in FRP composite structures by being able to mend matrix damage and delamination after LVI, DCB and 3PB tests. The healing phenomenon can be described in a constitutive model as a regain of matrix material's elasticity modulus. Thus, in [8] is presented a multi-scale framework for modelling of self-healing FRP composite structures. Methodology presented in [9] is validated using results of 3PB tests available in the literature. In Fig. 2 a distribution of the effective damage variable in 0- and 90-degree plies, before and after the first healing process is illustrated. Tested specimens had [0/90/0] layup. The effective damage variable is defined to increase during the damaging process and decrease as a result of healing.

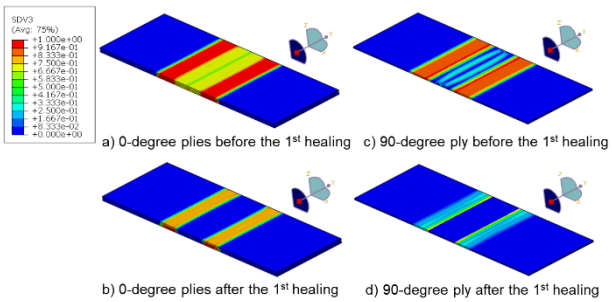

Figure 2: Distribution of the effective damage variable in 0- and 90-degree plies before and after the first healing process.

References

[1] Smojver I., Sorić J., Alfirević I., On nine noded element for analysis of laminated composite shells, *Proceedings of the 1st Congress of Croatian Society of Mechanics*, Pula, 1994, 47 – 54

[2] Sorić J., Smojver I., On the effect of fibre directions in laminated composite torispherical shells, *Engineering Computations* 12, 1995, 85-94

[3] Smojver I., Sorić J., Numerical Modelling of Damage Response of Layered Composite Plates, *CMC: Computers, Materials and Continua*, Vol. 3, No. 1, 13-24, 2006;

[4] Ivančević D., Smojver I., Hybrid Approach in Bird Strike Damage Prediction on Aeronautical Composite Structures, *Composite Structures*, 94, 15 – 23, 2011

[5] Smojver I., Ivančević D., Advanced Modelling of Bird Strike on High Lift Devices Using Hybrid Eulerian-Lagrangian Formulation, *Aerospace Science and Technology*, 23, 224-232, 2012

[6] Ivančević D., Smojver I., Explicit Multiscale Modelling of Impact Damage on Laminated Composites – Part I: Validation of the Micromechanical Model. *Composite Structures*. 145, 248–258, 2016

[7] Ivančević D., Smojver I., Explicit Multiscale Modelling of Impact Damage on Laminated Composites – Part II: Multiscale Analyses. *Composite Structures*. 145, 259–268, 2016

[8] Smojver, I., Ivančević, D., Brezetić, D.: Modelling of micro-damage and intrinsic self-healing in unidirectional CFRP composite structures, *Composite Structures*, 2022; 286: 1-10. doi: 10.1016/j.compstruct.2022.115266

[9] Smojver, I., Ivančević, D., Brezetić, D., Haramina, T.: Constitutive modelling of a self-healing composite matrix polymer material, *International Journal of Damage Mechanics*, 2022; 0(0): 1-18. doi: 10.1177/10567895221095609

Analysis of a Moderate Fire in a Subway Station: FE simulations and Engineering Mechanics Analysis

Maximilian Sorgner*, Rodrigo Díaz Flores*, Hui Wang+, Bernhard L.A. Pichler*

*Institute of Mechanics of Materials and Structures, TU Wien, Karlsplatz 13/202 1040 Vienna
E-mails: {maximilian.sorgner,rodrigo.diaz,bernhard.pichler}@tuwien.ac.at

+School of Naval Architecture, Ocean and Civil Engineering Shanghai Jiao Tong University
E-mail: hui.wang@sjtu.edu.cn

Keywords: engineering-mechanics approach, thermal eigenstresses, moderate fire scenario

Reinforced concrete structures are designed to withstand extreme loading scenarios such as fires. Therefore, structural engineers are interested to analyze the behavior of reinforced concrete structures subjected to a combination of mechanical loads and elevated temperatures. Lu et al. performed a large-scale fire test on a segment of a subway station in Shanghai 0. Díaz et al. used the Finite Element method to analyze the structural behavior of the reinforced concrete structure subjected to regular service loads and a moderate fire, see Fig. 1 and 0. In the present study, an engineering mechanics approach combining (i) fundamental relations of thermo-elasticity of reinforced concrete beams and (ii) software for structural analysis of beam structures is used to describe the structural behavior of the same segment. The results are compared with the Finite Element simulations of Díaz et al., see also [4].

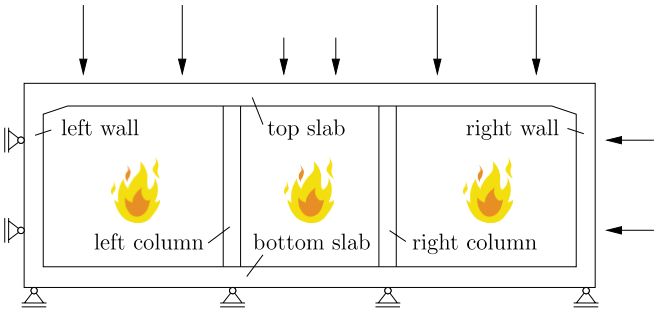

Figure 1. Structure, supports, and loading conditions; after 0.

The three-dimensional reinforced concrete structure is idealized as a frame consisting of straight beams. The prismatic columns with rectangular cross-section are transformed into cylindrical beams with equivalent extensional stiffness. For all structural elements except the columns, solutions for one-dimensional heat conduction in thickness direction are taken from the literature [3]. The ingress of heat into the cylindrical columns is quantified by a series solution for axisymmetric cross-sections based on Bessels functions [4]. The obtained temperature changes of each structural element are translated into thermal eigenstrains by multiplying them with the coefficient of thermal expansion. Thermal eigenstrains (dotted line in Fig. 2a) are decomposed into three parts: a spatially constant contribution representing the eigenstretch of the axis of the structural element (solid line), a spatially linear contribution with vanishing mean value, referring to the eigencurvature of the axis of the structural element (dashed line), and a spatially non-linear contribution representing the eigenwarping of the cross-sections (dash-dotted line). Corresponding decomposition rules are derived for reinforced concrete members. This derivation combines the Bernoulli-Euler hypothesis, geometric and constitutive equations of linear thermo-elasticity, as well as relations between the axial force and the bending moment, on the one hand, and the axial stresses, on the other hand. The eigenstretches and eigencurvatures are constrained at the scale of the statically indeterminate structure. Beam analysis

software is used to study the load carrying behavior of the frame structure subjected to mechanical loads as well as to thermal eigenstretches and eigencurvatures of all structural elements. The obtained axial forces and bending moments result in axial stresses which are linear across the cross-sections, see the dotted line in Fig. 2b. The latter remain plane even under combined mechanical and thermal loading. Because of this planarity, the eigenwarping-part of the thermal eigenstrains is prevented at the scale of the cross-sections. This activates self-equilibrated thermal eigenstresses which are spatially nonlinear across the cross-sections. Total axial stresses are obtained from adding the thermal eigenstresses to the axial stresses quantified based on the axial forces and bending moments. The total stresses agree well with the results of a three-dimensional thermo-elastic Finite Element simulation, compare the solid and the dashed line in Fig. 2b.

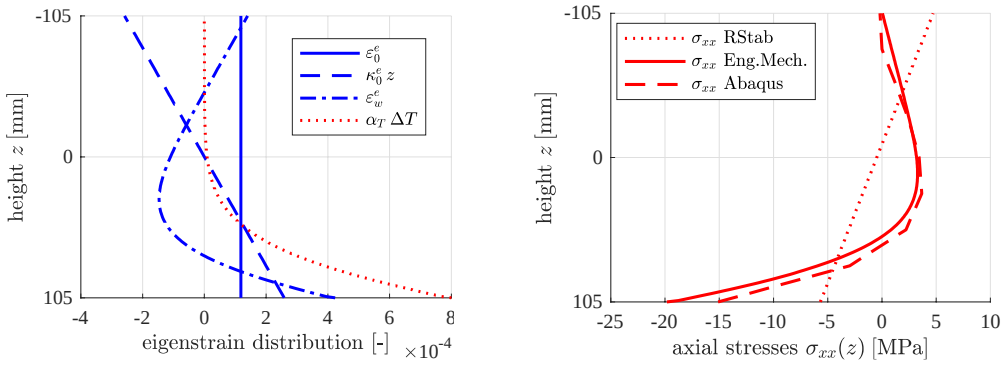

(a) (b)

Figure 2. Results obtained for the Top Slab of the analyzed structure, half an hour after the start of the fire: (a) thermal eigenstrains and (b) axial normal stresses; after [4].

Half an hour after the start of the fire, tensile stresses prevail inside the volume of all structural elements, in the regions around their axes. The computed tensile stresses of the slabs and walls are on the same order of magnitude as the tensile strength of concrete, see Fig. 2b.

It is concluded that spatially non-linear eigenstresses resulting from prevented eigenwarping of the cross-sections represent a significant part of the total stresses. Such eigenstresses must be considered when it comes to the design of reinforced concrete structures subjected to elevated temperatures. The organization of the described engineering mechanics approach in several subproblems allows for relating causes to effects in a more clear and insightful fashion compared to an all-in-one simulation approach such as the Finite Element Method.

References

[1] Díaz, R., Wang, H., Yuan, Y., Pichler, B., Numerical Analysis of a Moderate Fire inside a Segment of a Subway Station. *applied sciences*, 8, 1-34, 2018.

[2] Lu, L., Qiu, J., Yuan, Y., Tao, J., Yu, H., Wang, H., Mang, H., Large-scale test as the basis of investigating the fire-resistance of underground RC substructures. *Engineering Structures*, 178, 12-23, 2018.

[3] Wang, H., Yuan, Y., Mang, H. A., Ai, Q., Huang, X., Pichler, B. L.A., Concrete pavements subjected to hail showers: A semi-analytical thermoelastic multiscale analysis. *Engineering Structures*, 200, 1-19, 2019.

[4] Sorgner, M., Díaz, R., Wang, H., Pichler, B. L.A., Engineering Mechanics Analysis of a Moderate Fire Inside a Segment of a Subway Station. *In: Proceedings of the Conference on Computational Modelling of Concrete and Concrete Structures (EURO-C 2022).* Vienna, Austria. 2022.

On Fracture and Fatigue Failure Modelling of Brittle and Ductile Materials Using Phase-Field Formulation

Zdenko Tonković*, Karlo Seleš+, Zoran Tomić*, Krešimir Jukić*, Tomislav Polančec*, Tomislav Jarak*, Tomislav Lesičar*, Jurica Sorić*

**Faculty of Mechanical Engineering and Naval Architecture, I. Lučića 5, 10000 Zagreb, Croatia*
E-mails: {ztonkov, zoran.tomic, kresimir.jukic, tomislav.polancec, tomislav.jarak, tomislav.lesicar, jurica.soric}@fsb.hr

+Rimac Technology, Savska opatovina 36, 10090, Zagreb, Croatia
E-mail: karlo.seles@rimac-automobili.com

Keywords: brittle/ductile fracture and fatigue, phase-field modelling, Vickers indentation fracture, pitting, welding residual stress

1. Introduction

The phase-field (P-F) approach to fracture modelling has gained much attention in the field of computational fracture mechanics in recent years. In this approach, the sharp crack discontinuity is approximated by a diffusive band whose width is regulated by a user-defined length scale parameter. Its variational based approach has been proven to be thermodynamically consistent and able to solve complex fracture processes. The most important deficiency that prevents the application of the P-F models for fracture in solving practical engineering problems are enormous computational demands in terms of computational time and hardware resources. These computational costs are mainly associated with the necessity to use very dense meshes to obtain small length scale parameter for the representation of sharp crack in the domain [1]. The P-F fracture framework has been very recently extended to the fatigue crack propagation problems. However, the existing models cannot be calibrated to simultaneously reproduce the main features of low- and high-cycle fatigue, and that therefore they are not suitable for engineering application.

This work reviews the main contributions of the authors to the fracture and fatigue failure modelling using P-F formulation. Here, the basic concept and numerical implementation of the proposed generalized P-F framework are presented. To illustrate the applicability and effectiveness of the proposed framework different problems are analysed, such as brittle, ductile, and fatigue fracture on homogeneous and heterogeneous materials, adaptive mesh refinement, Vickers indentation fracture, pitting formation due to rolling-sliding contact as well as crack propagation in welded structure.

2. Brittle, ductile, and fatigue fracture on homogeneous and heterogeneous materials

A general P-F model for fracture and fatigue failure in brittle and ductile materials is described in detail in [2]. This model is based on the P-F staggered scheme with a residual control-based stopping criterion [1]. The implementation of the model is made with the ABAQUS finite element software. The experimental validation of the numerical models is conducted on the homogeneous and heterogeneous materials. It has been demonstrated that with a suitable choice of the length scale parameter, the developed P-F model can provide valid prediction of the brittle and ductile crack initiation and propagation under quasi-static as well as cyclic loading conditions [1-3].

3. Vickers indentation fracture

A 3D P-F model for brittle fracture is applied for analysing the complex fracture patterns appearing during the Vickers indentation of fused silica glass [4]. Herein, an adaptive mesh refinement strategy is utilized for reducing the computational costs [5]. The fracture initiation ring outside the contact

zone is detected by using different energy decompositions, and the dominant cone-crack formation under the Vickers indenter is observed (see Figure 1).

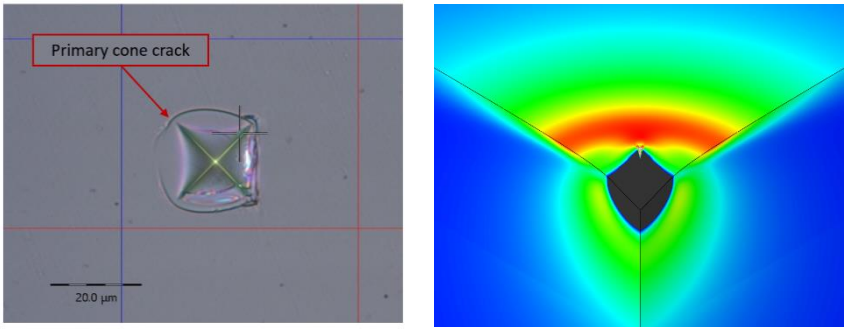

a) b)

Figure 1. Vickers indentation test on fused silica glass: a) experiment, b) numerical simulation

4. Pitting formation due to rolling-sliding contact

A novel computational framework for assessment of a gear lifetime until pitting formation on a gear tooth flank is developed [6]. In this approach, the load distribution as a consequence of a contact pressure distribution is obtained by the elastohydrodynamic lubrication (EHL) theory, while P-F approach is used to model the damage behaviour of sintered material.

5. Crack propagation in welded structure

A P-F procedure has been utilized to model crack propagation in compact tension specimen machined from the pre-welded structure. The influence of the attained welding residual stresses and plastic strains on the crack propagation has been investigated. It has been observed that the proposed P-F approach can properly model crack propagation through the welded structure.

Acknowledgments

This work has been supported by projects "Multiscale Numerical Modelling and Experimental Investigation of Aging Processes in Sintered Structural Components" (PZS-1 2019-02-4177, Croatian Science Foundation), "Protection of Structural Integrity in Energy and Transport" (KK.01.1.1.04.0056, European Regional Development Fund - ERDF) and "Improvement of high-efficiency welding technology" (KK.01.1.1.07.0076, ERDF).

References

[1] Seleš, K., Lesičar, T., Tonković, Z., Sorić, J., A Residual Control Staggered Solution Scheme for the Phase-Field Modeling of Brittle Fracture. *Engineering Fracture Mechanics*, Vol. 205, 370-386, 2018.

[2] Seleš, K., Aldakheel, F.; Tonković, Z., Sorić, J., Wriggers, P., A General Phase-Field Model for Fatigue Failure in Brittle and Ductile Solids. *Computational Mechanics*, Vol 67, 1431-1452, 2021.

[3] Seleš, K., Tomić, Z., Tonković, Z., Microcrack Propagation Under Monotonic and Cyclic Loading Conditions Using Generalised Phase-Field Formulation. *Engineering Fracture Mechanics*, Vol. 255, 107973, 2021.

[4] Tomić, Z., Jukić, K., Jarak, T., Fabijanić, T., Tonković, Z., Phase-Field Modeling of Fused Silica Cone-Crack Vickers Indentation. *Nanomaterials*, Vol. 12, 2356, 2022.

[5] Jukić, K., Jarak, T., Seleš, K., Tonković, Z., Adaptive Phase-Field Modeling of Brittle Fracture. *Proceedings of the 2nd International Conference on Structural Damage Modelling and Assessment (SDMA 2021)*, Ghent, 2021.

[6] Polančec, T,, Lesičar, T., Tonković, Z., Modelling of Pitting Phenomena on Gear Tooth Flank by Phase-Field Method. *11th European Solid Mechanics Conference (ESMC2022)*, Galway, 2022.

[7] Vukovojac, M., Lesičar, T., Perić, M., Skozrit, I., Tonković, Z., Modelling of Crack Propagation in Welded Structure Using a Separated Phase-field Approach. **Proceedings of the** *7th International Conference on Smart and Sustainable Technologies (SpliTech 2022)*, Bol and Split, 2022.

On virtual elements for Kirchhoff-Love plates and shells

Peter Wriggers*, Blaz Hudobivnik+,

*Institute of Continuum Mechanics, Leibniz University Hannover
E-mails: wriggers@ikm.uni-hannover.de

+Institute of Continuum Mechanics, Leibniz University Hannover
E-mail: hudobivnik@ikm.uni-hannover.de

Keywords: Virtual elements, Kirchhoff-Love theory, plate, shell

1. Introduction

The virtual element method was developed in the last 10 years as a new discretization technique for applications in science and engineering. The virtual element method (VEM), see e.g. [1], has some advantageous properties, it allows the use of elements with arbitrary number of nodes and non-convex shapes.

2. Description of the presentation

The virtual element method is based on an ansatz space in which the ansatz is only defined at the boundary. This feature permits to revisit the construction of Kirchhoff-Love (KL) plate elements of arbitrary shape. The C^1-continuity condition is much easier to handle in the VEM framework than in the traditional finite element methodology. We will show various VEM elements suitable for KL plates, see [3] and [5], which are much simpler than the well-known TUBA finite elements in [2]. Based on a geometrically exact thin KL shell models, see [4], we will construct virtual elements for large deflections and compare these with a similar formulation for TUBA elements. The formulation contains new ideas and different approaches for the stabilization needed in a virtual element setting. In the case of C^1-continuous elements it is crucial to use an efficient stabilization, otherwise the rank deficiency of the stiffness matrix associated with the projected part of the test function is more pronounced than for C^0-continuous elements.

In this contribution we demonstrate how to construct simple and efficient virtual plate elements for isotropic and anisotropic materials, an example from [5] is depicted in Fig. 1.

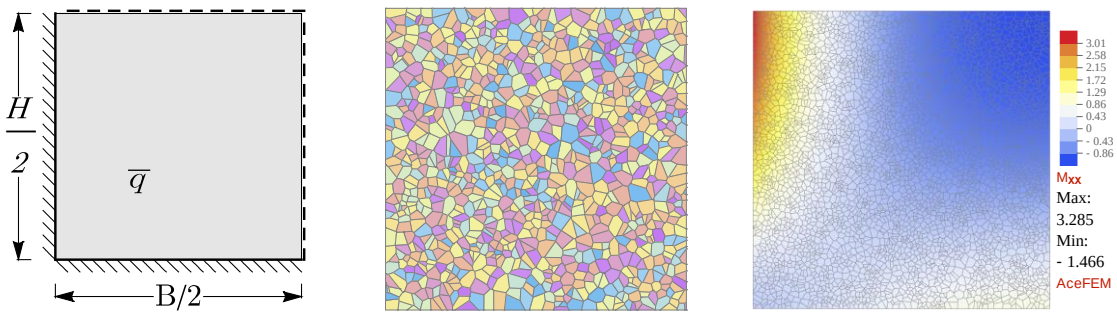

Figure 1. Quarter of a plate under distributed load, problem, Voronoi mesh, moment distribution

The formulation will then be extended to geometrically exact shell elements. Various benchmark examples and convergence studies using isotropic and anisotropic constitutive models demonstrate the accuracy of the resulting VEM elements.

Finally, reduction of virtual plate elements to triangular and quadrilateral elements with 3 and 4 nodes, respectively, yields finite element like plate elements which are much simpler than TUBA elements. It will be shown that these C^1-continuous elements can be easily incorporated in legacy codes and demonstrate an efficiency and accuracy that is much higher than provided by traditional finite elements for thin plates and shells.

References

[1] Beirao da Veiga, L., Brezzi, F., Marini, L. D. & Russo, A. The hitchhiker's guide to the virtual element method. Mathematical Models and Methods in Applied Sciences, 24(08), 1541-1573, 2014.

[2] Argyris, J. H., Fried, I. & Scharpf, D. W., The TUBA family of plate elements for the matrix displacement method, The Aeronautical Journal, 72:701-709, 1968.

[3] Brezzi, F., & Marini, L.D. Virtual element methods for plate bending problems. Computer Methods in Applied Mechanics and Engineering, 253:455-462, 2013.

[4] Ivannikov, V., Tiago, C. & Pimenta, P.M., Generalization of the C^1 TUBA plate finite elements to the geometrically exact Kirchhoff-Love shell model Computer Methods in Applied Mechanics and Engineering, 294:210-244, 2015.

[5] Wriggers, P., Allix O. & Hudobivnik, B., On two simple virtual Kirchhoff-Love plate elements for isotropic and anisotropic materials. Computational Mechanics, Accepted (2021).

Biochemomechanical Fluid-Solid-Growth Model of Aortic Aneurysm

Josip Živić*, Nino Horvat*, Lana Virag*, Igor Karšaj*

* *Faculty of Mechanical Engineering and Naval Architecture, University of Zagreb, Ivana Lučića 5, 10000 Zagreb,*
E-mails: josip.zivic@fsb.hr, nino.horvat@fsb.hr, lana.virag@fsb.hr, igor.karsaj@fsb.hr

Keywords: finite elements, biochemomechanics, intraluminal thrombus

1. Introduction

Abdominal aortic aneurysm (AAA) is asymptomatic disease with high mortality rate. It is, thus, not surprising that more and more effort is being put into understanding its pathology and optimal timing for the treatment of AAAs. Most AAAs harbor intraluminal thrombus (ILT). The role of ILT is controversial: mechanically it shields the wall, but it is also biochemically active. It undoubtably plays a crucial role in the growth and remodeling (G&R) of AAA. We have previously investigated mechanical influence of the ILT on axially symmetric fusiform AAA progress [1]. This work is now extended to include two major changes. Firstly, biochemical influence of ILT is modelled. Additionally, the key factor in ILT deposition and growth is believed to be hemodynamics [2]. It is likely that ILT is formed when regions both favorable to platelet activation (due to high shear stresses in the lumen where platelets activate) and adhesion (due to low wall shear stresses where platelets may aggregate on a vulnerable endothelium) simultaneously exist. Thus, thrombus deposition in this work depends on wall shear stress calculated from computational fluid dynamics (CFD) analyses.

2. Methodology

Mechanical model of the thrombus was described in detail in Horvat et al., 2021 [1]. Briefly, unlike aortic wall, whose mass increases only several fold during aneurysm progression, intraluminal thrombus (ILT) is continuously being deposited, with its mass changing from zero in a healthy artery or small aneurysm to a potentially huge thrombus mass in large AAAs. Therefore, an aortic wall is modelled with a constant number of finite elements with evolving constituent mass, whereas ILT element count increases at each deposition time, but the element mass is considered constant. Mechanical properties of ILT layers were modelled based on the experimental study from [3].

We have loosely coupled long-term growth and remodeling process of aortic wall and ILT (with time step measured in days) with computational fluid dynamics (CFD) analysis (with time scale measured in seconds), thus forming fluid-solid-growth model. ILT deposition time and location is predicted using time-averaged wall shear stress (TAWSS) calculated from CFD simulations [4]. Blood was modelled as a non-Newtonian fluid with implemented Bird-Carreau viscosity model into OpenFOAM – a finite volume software package. Growth and remodeling of aorta and thrombus was previously implemented into finite element program FEAP 8.4. Standard arterial growth and remodeling model based on constrained mixture theory and evolving configurations is used for the aortic wall. The model is extended to describe the biochemical influence of ILT on the wall. This implies that degradation of proteins in the extracellular matrix (collagen and elastin) depends on spatio-temporal distribution of proteolytic enzymes. Proteases are believed to have two sources: luminal layer of ILT adjacent to the fresh blood and continuously increasing vasa vasorum in the wall.

As the initial insult, 15% elastin degradation is locally induced. The irreversible loss of elastin causes slight bulging of the wall. Due to the changed geometry of the aorta, hemodynamics changes and TAWSS decreases. After condition for the thrombus deposition is met, the first layer of ILT finite elements is added. Because ILT introduces proteases, extracellular matrix is increasingly degraded, which triggers further AAA growth. CFD analyses are run after every third growth and remodeling analysis.

4. Results and conclusions

Wall constituent mass evolution at the several locations can be seen in Figure 1. At the healthy part (section C), all wall constituent masses are nearly constant to insure homeostasis. There is no ILT beneath the wall that could induce matrix degradation. At the aneurysm apex (section A) elastin was initially degraded 15%. After that, its mass was kept constant until first ILT layer was deposited (approximately at G&R time 1000 days). After ILT deposition, elastin was degraded again, based on amount of elastases. Because anoikis is modeled (i.e., apoptosis of smooth muscle cells with loss of elastin), SMC mass also initially decreased 15%. However, unlike elastin, SMC is allowed to turnover continuously and before ILT is deposited, its mass was produced due to increased wall stress. When elastin started to further degrade, mass of SMC decreased despite increased production. Collagen mass was always increasing.

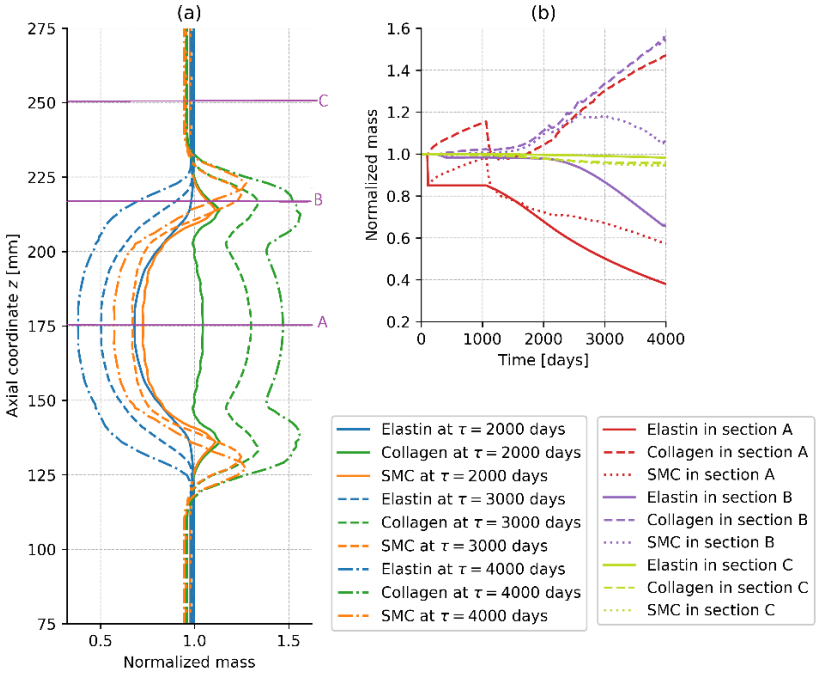

Figure 1. Spatial distribution on wall constituent masses (a) and their evolution at different locations in the aorta (b)

At initially healthy the section B, elastin mass was constant until elastase diffused to the location. At that point, elastin started to degrade. Consequently, at the end of the analysis, more functional elastin remains at that location.

References

[1] N. Horvat, L. Virag, and I. Karšaj, "Mechanical role of intraluminal thrombus in aneurysm growth: A computational study," Biomech. Model. Mechanobiol., no. 0123456789, 2021

[2] J. Biasetti, F. Hussain, and T. C. Gasser, "Blood flow and coherent vortices in the normal and aneurysmatic aortas: a fluid dynamical approach to intra-luminal thrombus formation," J. R. Soc. Interface, vol. 8, pp. 1449–1461, 2011

[3] J. Tong, T. Cohnert, P. Regitnig, and G. A. Holzapfel, "Effects of age on the elastic properties of the intraluminal thrombus and the thrombus-covered wall in abdominal aortic aneurysms: Biaxial extension behaviour and material modelling," Eur. J. Vasc. Endovasc. Surg., vol. 42, no. 2, pp. 207–219, 2011

[4] P. Di Achille, G. Tellides, C. A. Figueroa, and J. D. Humphrey, "A haemodynamic predictor of intraluminal thrombus formation in abdominal aortic aneurysms," Proc. R. Soc. A Math. Phys. Eng. Sci., vol. 470, no. 2172, pp. 20140163–20140163, 2014

10th ICCSM, Pula, 2022

Contributed lectures

Comparison of the conventional loading case on femur with Pauwels type III fracture with force reduction loading: A finite element study

Petra Adamović*, Nina Bočkaj*, Tanja Jurčević Lulić*, Janoš Kodvanj*

*University of Zagreb, Faculty of Mechanical Engineering and Naval Architecture, Department of Applied Mechanics, Ivana Lučića 5, Zagreb, 10000, Croatia
E-mails: {petra.adamovic,tanja.jurcevic.lulic,janos.kodvanj}@fsb.hr, ninabockaj@gmail.com

Keywords: Pauwels type III, finite element method, force reduction, inverted triangle configuration

1. Introduction

The application of finite element method in interdisciplinary sciences such as biomedical engineering has been quite common in the last few decades [1]. Treatment of intracapsular hip fractures such as femoral neck fracture of Pauwels type III still remains a challenging matter, given the fact that this disease nowadays involves more than 50% of all proximal femoral fractures [2]. While creating an internal fixation device for that matter, it is necessary to conduct experimental tests. The goal of simulations is to select the crucial device test loads and setups, i.e., to reduce the cost and time consumption of the tests. While most authors use a very primitive form of model loading in their simulations [3-5], this study uses two types of femur's loading cases (climbing stair and walking) and compares two mechanically equivalent force loadings with their amounts.

2. Materials and methods

A left, 4th generation composite femur (Sawbones®, USA) was scanned using computed tomography and its geometry was obtained using Mimics software (17.0, Materialise NV, Belgium). A 3D model of the femur with three screws in an inverted triangle configuration was created in SolidWorks software (2020, Dassault Systèmes, USA). The screws' material was set to be titanium with a radius of 5 mm. All materials were defined as linearly elastic, homogeneous and isotropic, while their properties and interactions are listed in Table 1.

Table 1. Model properties and boundary conditions in Abaqus

Material	Elastic modulus [GPa]	Poisson's ratio [-]	Boundary condition
Screws (titanium)	110	0.3	With all other models: Tie
Cortical bone	17		On fracture site: surface-to-surface (friction coefficient: 0.2)
Trabecular bone	1.1		

One loading case imitated stair climbing and the other one walking. Both loading cases [6] were divided into a four-point (P1, P2, P3, P4) loading case and in a reduction of those forces in one point (A) on the femur. These were further divided into models with all three force components and the ones with resulting forces and moments only. That resulted in eight simulations made in Abaqus software (6.14-5, Dassault Systèmes, France), schematically shown in Fig. 1.

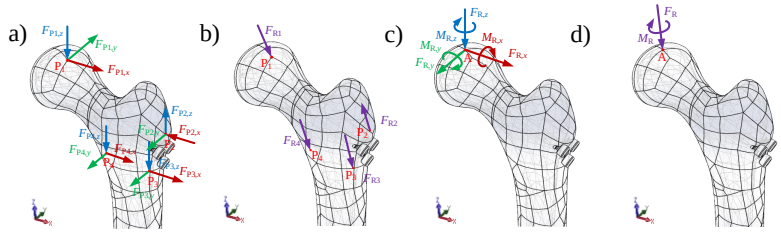

Figure 1. Mechanically equivalent loading forces for both stair climbing and walking

3. Results

Fig. 2 shows the distribution of maximum von Mises stress on elements and displacements of nodes on femur, while Fig. 3 displays the relative fracture displacement (displacements of node pairs) distribution along the upper side of the fracture for stair climbing and walking.

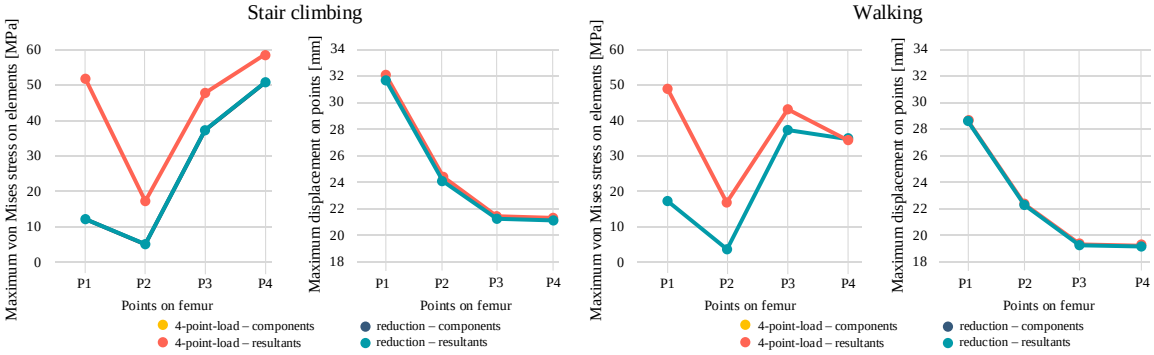

Figure 2. Maximum von Mises stress distribution and displacements for the two load cases

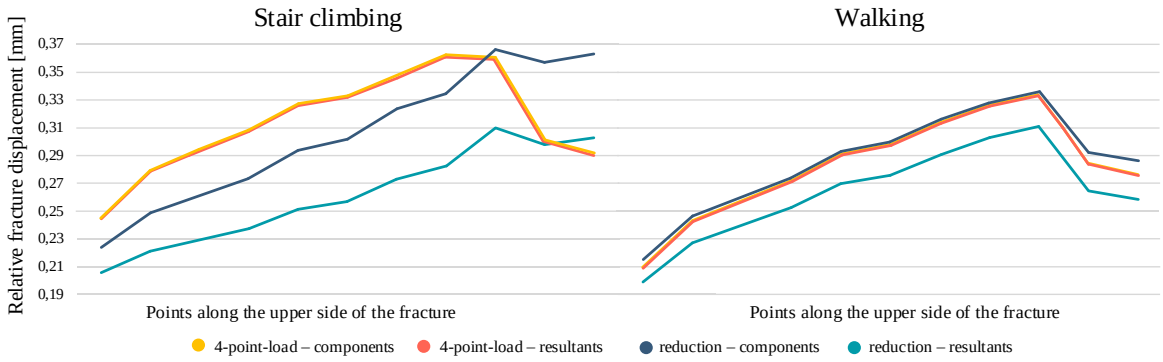

Figure 3. Relative fracture displacement for the two load cases

4. Conclusions

While designing implant devices, multiple loads with various points on femur should be used to determine the maximum von Mises stress values and its distribution. The results further show that almost equal displacements (max. error of 0,52%) are present in all loading cases, thus indicating that this approach of force reduction can be used in the examination of fracture displacements.

References

[1] Taylor, M., Prendergast, P.J. Four decades of finite element analysis of orthopaedic devices: Where are we now and what are the opportunities? *J biomech*, 18;48(5):767-78, 2015.

[2] Ridzwan M.I.Z., Sukjamsri C., Pal B., van Arkel R.J., Bell A., Khanna M., Baskaradas A., Abel R., Boughton R Cobb J Hansen U. Femoral fracture type can be predicted from femoral structure: a finite element study validated by digital volume correlation experiments. *J Orthop Res*, 36(3);993-1001, 2018.

[3] Li, J. Zhao, Z., Yin, P., Zhang, L., Tang, P. Comparison of three different internal fixation implants in treatment of femoral neck fracture – a finite element analysis. *J Orthop Surg Res*, 14:76, 2019.

[4] Corderio, M., Caskey, S., Frank, C., Martin, S., Srivastava, A., Atkinson, T. Hybrid triad provides fracture plane stability in a computational model of a Pauwels Type III hip fracture. *Comput Methods Biomech Biomed Engin*, 476-483, 2019.

[5] Huang, H., Feng, Z., Wang, W., Yang, C., Liao J., Ouyang, J., Finite Element Analysis of Femoral Neck Fracture Treated with Bidirectional Compression-Limited Sliding Screw. *Med Sci Monit*, 30;27:e929163, 2021.

[6] Zeng, W., Liu, Y., Hou, X. Biomechanical evaluation of internal fixation implants for femoral neck fractures: A comparative finite element analysis. *Comput Meth Prog Bio*, 196:105714, 2020.

Linear and nonlinear fracture mechanics vs cohesive-zone models in the failure analysis of structural interfaces

Giulio Alfano*, Leo Škec+, Gordan Jelenić+

*Brunel University London, Department of Mechanical and Aerospace Engineering
Kingston Lane, Uxbridge UB8 3PH, UK
E-mail: giulio.alfano@brunel.ac.uk

+University of Rijeka, Faculty of Civil Engineering
Radmile Matejčić 3, 51000 Rijeka, Croatia
E-mails: {leo.skec, gordan.jelenic}@ uniri.hr

Keywords: Fracture resistance, J integral, energy release rate, work of separation.

1. Introduction

The ranges of validity of different fracture mechanics theories have been extensively studied over the last few decades. Linear elastic fracture mechanics (LEFM) is essentially based on Griffith's energy balance and the concept of critical energy release rate, G_c. It is theoretically valid only for an infinitely brittle material, but it can still be applied with good accuracy when the inelastic zone around the crack tip is sufficiently small [1]. When this condition is not met, the J-integral theory can be used as an alternative approach, within the framework of so-called nonlinear fracture mechanics (NLFM). In its simplest version, NLFM is still based on the idea of characterising the fracture resistance with one single parameter, the critical value J_c of the J integral, but can be used when material behaviour is nonlinear. Although the theory is strictly valid only for nonlinear elastic behaviour, it is still widely applied also when behaviour is not only nonlinear but also inelastic.

In the failure of adhesive joints of structural components, where damage is localised in a thin interface of adhesive, if the bonded components are relatively stiff the size of the inelastic zone is often considered too large for LEFM to be valid and therefore the use of the J integral has been considered necessary to characterise the fracture resistance of the joint [2, 3]. In fact, in some cases any one-parameter theory has been deemed not accurate enough, and therefore the use of a models based on more parameters, such as a cohesive-zone model (CZM), has been considered necessary [4]. CZMs introduce a nonlinear relationship between the components of the relative displacements and those of the interface stresses, which for each component (or 'mode') is also called the traction-separation law (TSL). In the vast majority of cases the parameter of the CZM that has the biggest influence on the model predictions is the area under the TSL, which represents the work of separation per unit of cracked area and will be here denoted by Ω. Interestingly, different researchers assume either that $\Omega = G_c$ or that $\Omega = J_c$ but although the latter can be rigorously justified in some cases (as discussed below), the former is generally an approximation, which is normally overlooked.

On the other hand, despite the widely discussed limitations of the use of LEFM to characterise the fracture resistance of adhesive joints, all the currently approved industrial standards are based on the use of LEFM and therefore provide methods to experimentally evaluate G_c.

Motivated by the aforementioned observations, in this contribution we will present the results of a study [5] that clarified the difference between G_c, J_c and Ω for the case of mode-I failure along adhesive joints, and we will discuss more recent developments.

2. Some key results

It is not difficult to show that the widely accepted interpretation of J as the energy release rate for a nonlinear elastic material leads to the equality $\Omega = J_c$. However, it was noted in [5] that this is true only if the material is homogenous. On the other hand, in many cases the fracture resistance on

adhesive joints has not been found to be constant, so that an R-curve can be determined and the fracture resistance therefore becomes a function of the crack length. In these cases, $\Omega \neq J_c$, in general.

In all cases, during mode-I crack propagation along a thin interface, it was theoretically shown in [5] that the following relationship holds:

$$\Omega = G_c - \frac{\partial \Pi_D}{\partial a} \tag{1}$$

where a is the crack length and Π_D represents the energy dissipated ahead of the crack tip.

For a flat R-curve, as noted above it also results $\Omega = J_c$, and therefore one has:

$$J_c = G_c - \frac{\partial \Pi_D}{\partial a} \tag{2}$$

Equation (2) shows that, unlike what is normally stated in the literature, the difference between G_c and J_c is not due to the size of the cohesive zone but is related to how much Π_D changes during crack propagation. In other words, if the 'damage profile' translates in a steady-state fashion with the crack tip, then $\Omega = G_c$ and, if G_c is constant, then $J_c = G_c$, regardless of the size of the cohesive zone. An example of such case is a double cantilever beam (DCB) with prescribed rotations, also known as moment-loaded DCB [4]. For the more conventional DCB with prescribed displacements, Π_D is not constant but, for most cases of interest, its variation is actually extremely small during crack propagation. An example is reported in Figure 1, which shows the difference between J_c and G_c obtained in numerical simulations of a DCB made of aluminium arms, which are bonded with an adhesive modelled via a bilinear CZM with constant properties along the interface, including constant Ω, so that $J_c = \Omega$. Different cases have been simulated with different strength, σ_{max}, of the adhesive. The smaller σ_{max}, the more ductile the adhesive, but for the most ductile case the difference between J_c and G_c is less than 2% and rapidly decreasing during crack propagation.

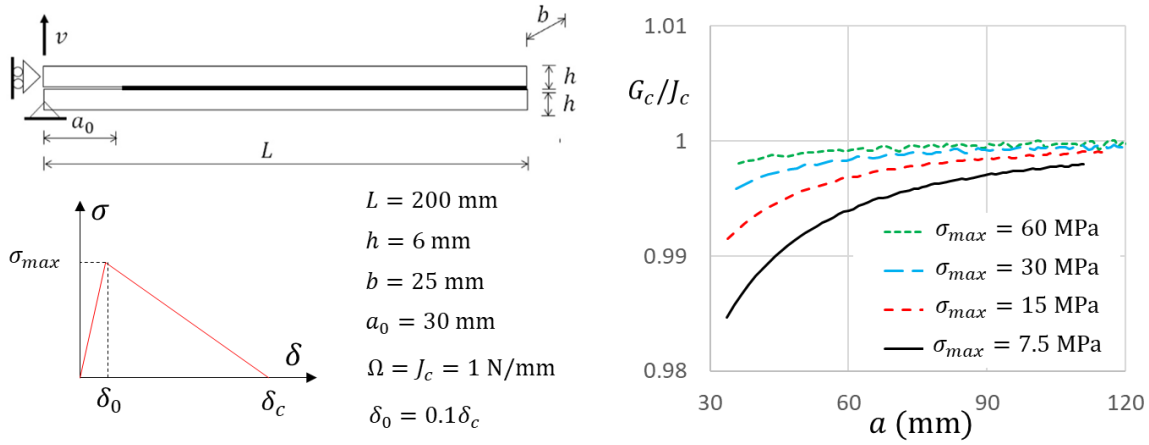

Figure 1. Relation between $J_c = \Omega$ and G_c for numerical simulations of a DCB.

References

[1] Anderson, T.L. Fracture mechanics: fundamentals and applications. CRC Press, Boca Raton, 2017.

[2] Sarrado, C., Turon, A., Costa, J., Renart, J., On the validity of linear elastic fracture mechanics methods to measure the fracture toughness of adhesive joints, *International Journal of Solids and Structures* 81, 110–116, 2016.

[3] Moura, D., Banea, M., da Silva, L., Adhesive thickness effects of a ductile adhesive by optical measurement techniques, *International Journal of Adhesion and Adhesives*, 57, 125–132, 2015.

[4] Sørensen, B.F., Jacobsen, T.K., Determination of cohesive laws by the J integral approach. *Engineering Fracture Mechanics* 70, 1841–1858, 2003.

[5] Škec, L., Alfano, G., Jelenić, G., On G_c , J_c and the characterisation of the mode-I fracture resistance in delamination or adhesive debonding, *Journal of Solids and Structures* 81, 144–145, 100-122, 2018.

An Experimental Study on the Impact of the Core-Coating Inclusions on the Damping Ratio

Meisam Ansari*, Christin Zacharias*, Carsten Koenke*

Institute of Structural Mechanics, Bauhaus-University Weimar, Marienstr. 15, 99423 Weimar Germany, E-mail: meisam.ansari@uni-weimar.de

Keywords: metaconcrete, vibration absorber, damping ratio, mesoscale model

Introduction

S.J. Mitchell in [1] replaced the standard aggregate of regular concrete with engineered inclusions and introduced a new composite material named metaconcrete. The spherical inclusions were composed of a heavy core coated with a thin layer of a soft material. The uniformly distributed inclusions could be tuned such that their natural frequencies would be close to the frequency of the applied dynamic load. This would result in the resonance of the inclusions and consequently the attenuation of the applied wave motion. Similar engineered inclusions had been used in the past under other names such as Locally Resonant Sonic Material (LRSM), Phononic Crystals (PnCs), etc. For example, [2] presented the finite element model of a unit cell composed of a coated inclusion embedded in an epoxy matrix to study the resonance modes and the wave attenuation. [3] proposed the model of a metaconcrete thin plate composed of steel inclusions coated by rubber embedded in a concrete matrix. The thin plate model showed great potential for vibration reduction in low frequencies. Briccola in [4] verified the attenuation-property of metaconcrete in laboratory experiments with the cubic specimens of metaconcrete. The inclusions were composed of a spherical steel core coated with polydimetilsyloxhane (PDMS). They were arranged inside the specimens in several symmetrical patterns.

In the above works, the attenuative character of the engineered inclusions was thoroughly studied. In this work, the impact of the engineered inclusions on the damping ratio is studied. The goal is to investigate, whether the core-coating elements can improve the vibration energy dissipation of an oscillating body and exhibit a larger damping ratio. Numerical models are employed to study the cubic specimens of metaconcrete. Laboratory experiments with steel bars are carried out to investigate the core-coating elements individually.

Estimation of the damping ratio

The half-power bandwidth method is a common way to estimate the damping ratio. However, the method becomes challenging for structures with closely spaced natural frequencies [6]. The specimen of metaconcrete exhibits such natural frequencies. Alternatively, the damping ratio can be estimated by the logarithmic decrement [7]. Therefore, Eq. (1) is used in this work to compute the damping ratio.

$$\Lambda = \ln\frac{x_i}{x_{i+n}} = \frac{2n\pi\zeta}{\sqrt{1-\zeta^2}} \tag{1}$$

The Den Hartog criteria as means of optimization

By considering the core-coating element as a vibration absorber, the Den Hartog criteria [5] are used to optimize the required mass of the inclusion m_D. The natural frequencies of the inclusion ω_D and the main mass ω_m are determined numerically, which are necessary for estimation of m_D with Eq. (2).

$$\kappa_{opt} = \frac{\omega_D}{\omega_m} \quad \Rightarrow \quad m_D = \left(\frac{1}{\kappa_{opt}} - 1\right) m_m \tag{2}$$

Numerical and experimental study

The finite element model of a unit cell containing one core-coating element at its center was successfully employed by [1] and [2] to estimate the natural frequencies of the inclusion. The unit cell is also used in this work for the same purpose. The targeted mode shape is the translational vibration of the core along either of the Cartesian axis.

For the numerical study, the cubic specimen of metaconcrete is created at the mesoscale composed of three phases: mortar matrix, aggregate, and the rigid ITZ. The normal aggregate is partially replaced with the core-coating inclusions, which are uniformly distributed. (Figure 9.a)

For the experimental study, steel bars with rectangular cross-sections are used. The first vibratory mode of the bar is activated by point-supporting the bar at the locations with zero displacement. Those points are determined by the first mode shape of the bar without boundary conditions. The core-coating element is fixed at the middle of the bar. (Figure 9.b)

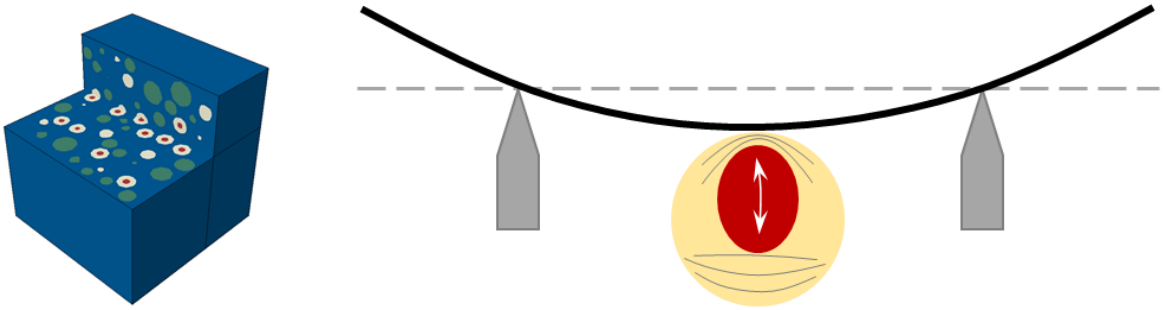

(a) metaconcrete (b) the point-supported bar and the core-coating element at the mid-span

Figure 9. Mesomodel of metaconcrete (a); Illustration of the experimental test setup (b)

Conclusive findings

The numerical study showed only a minor improvement in the damping ratio of metaconcrete. However, the oscillation amplitudes of the specimen reduced, which signifies the energy dissipative character of the core-coating elements.

The laboratory tests could exhibit that the free oscillation of the bar decayed much faster when the core-coating element was fixed to the mid-span. Consequently, a larger damping ratio was measured, which is again evidence of the dissipated energy through the engineered inclusions.

References

[1] S. J. Mitchell, *Metaconcrete: Engineered aggregates for enhanced dynamic performance*, California Institut of Technology, 2016.

[2] M. Hirsekorn, P. P. Delsanto, A. C. Leung and P. Matic, "Elastic wave propagation in locally resonant sonic material: Comparison between local interaction simulation approach and modal analysis," *Journal of Applied Physics*, vol. 99, p. 124912, 2006.

[3] E. J. P. M. Jr., A. F. Angelin, F. M. Silva and J. M. C. D. Santos, "Passive vibration control using a metaconcrete thin plate," *Cerâmica,* vol. 65, pp. 27-33, 2019.

[4] D. Briccola, M. Tomasin, T. Netti and A. Pandolfi, "The Influence of a Lattice-Like Pattern of Inclusions on the Attenuation Properties of Metaconcrete," *frontiers in Materials*, vol. 6, 2019.

[5] J. P. Den Hartog, "Mechanical Vibration," *Dover Publications, INC. New York*, 1985.

[6] G. A. Papagiannopoulos and G. D. Hatzigeorgiou, "On the use of the half-power bandwidth method to estimate damping in building structures," *Soil Dynamics and Earthquake Engineering*, vol. 31, pp. 1075-1079, 2011.

[7] L. Gaul and A. Schmidt, "Experimental Determination and Modeling of Material Damping," *VDI-Berichte*, 2007.

Application of infrared thermography as a non-destructive testing method: feature extraction

Petra Bagavac*, Lovre Krstulović-Opara*, Željko Domazet*

*FESB, University of Split, Croatia
E-mails: {petra.bagavac,opara,domazet}@fesb.hr

Keywords: infrared thermography, non-destructive testing, edge detection, feature extraction, delamination.

1. Introduction

The term post-processing of thermal images mainly refers to the search for non-uniformity of the structure, reduction of noise, maximizing of thermal contrast or segmentation of the object of interest [1]. Edge detection algorithms can effectively highlight edges: edges between damaged and undamaged areas, the edges between object and environment, or the edges between inhomogeneous areas. Solving these problems is crucial for conducting quantitative damage detection and for process automation.

2. Feature extraction

Characteristic information in the image can be highlighted by finding the edge. The edge in the image is actually a set of pixels that represent a sudden change in the intensity of the image, and is found by describing the intensity of the image (I) with a gray level [2-4]. The largest change in intensity is the local minimum or maximum of the first derivative of a two-dimensional function, $f(x, y)= I$. In Fig. 1. thermal image is shown on the far left, and in the other figures represent the most commonly used operators for edge detection: Prewit filter; Roberts filter; Sobel filter; Log filter and Canny filter, respectively.

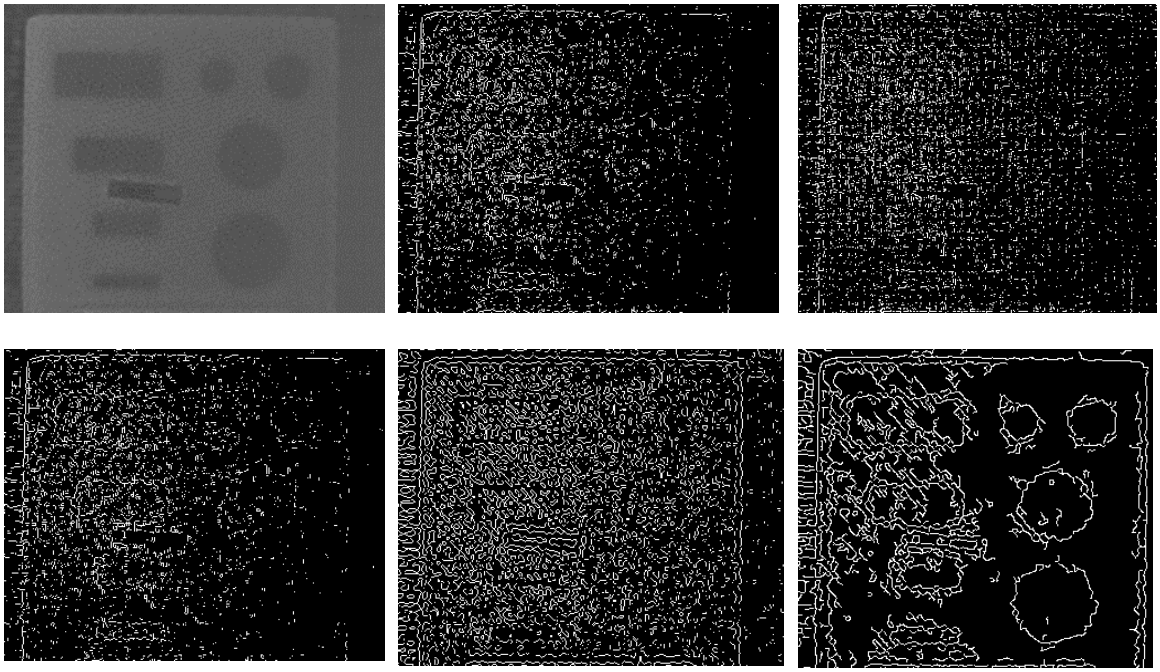

Fig. 1. a) Image; b) Prewit filter; c) Roberts filter; d) Sobel filter; e) Log filter; f) Canny filter

The operators Prewit, Roberts and Sobel are not precise enough, detected edges are very short and discontinuous which can lead to inaccurate, incomplete and even incorrectly determined edges. Edges of damaged areas are fairly detected by the LOG operator. However, using this operator, a lot of

useless information was found. Weak edges can cause interference with finding the actual edge of the damage. The best result was obtained using Canny algorithm, so the next steps will be performed on the last image, Fig. 2.

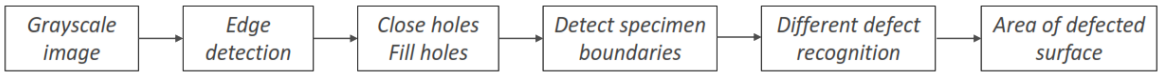

Fig. 2. Proposed algorithm for feature extraction

Proposed algorithm separated the environment from the sample, and isolated the damaged areas on the sample, Fig.3. In addition, algorithm effectively recognizes different defected areas, so here, for a better display, they are painted in different colors, Fig. 3.c. All damaged areas have been successfully detected.

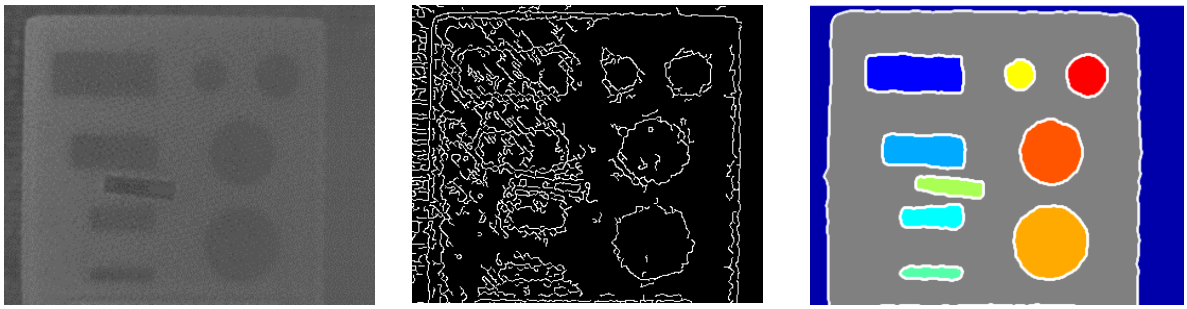

Fig. 3. a) Thermal image; b) Canny operator Edge detection; c) Segregation

3. Conclusions

These classically used algorithms require a gradient on the gray level image, and are quite sensitive to noise. In the case of a lower SN ratio, it can easily happen that the edges will become parts of the image with high noise intensity, and it is possible that they will not recognize the actual edges due to insufficient signal contrast to noise contrast. This can lead to the loss of important information, or to the reading of false edges.

With proposed method, characteristic information for non-destructive testing can be obtained:

- Feature extraction: sample/object (region of interest), environment (background) and damaged surfaces (object of interest) on a thermal image.
- Automation of non-destructive testing, diminution of operator subjectivity and faster non-destructive testing process.
- Autonomous identification of damaged areas on the inspected object.

References

[1] X. P. V. Maldague. Theory and Practice of Infrared Technology for NonDestructive Testing. John Wiley – Interscience. 684 p., 2001

[2] Tse, Peter W.; Wang, Gaochao (2017). Sub-surface defects detection of by using active thermography and advanced image edge detection. Journal of Physics: Conference Series, 842(), 012029–. doi:10.1088/1742-6596/842/1/012029

[3] Yuanlin, Liu; Qingju, Tang; Chiwu, Bu; Chen, Mei; Pingshan, Wang; Jiansuo, Zang (2015). Pulsed infrared thermography processing and defects edge detection using FCA and ACA. Infrared Physics & Technology, 72(), 90–94. doi:10.1016/j.infrared.2015.07.010

[4] Bagavac, Petra; Krstulović-Opara, Lovre; Domazet, Željko (2021). Enhancing IR Thermographic Inspection of Subsurface Defects by Using the Technique of Edge Detection. Russian Journal of Nondestructive Testing 57(7):609-618. DOI: 10.1134/S1061830921070020

Stability analysis of composite beam-type structures including shear deformation effects

Damjan Banić*, Goran Turkalj*, Domagoj Lanc*, Sandra Kvaternik Simonetti*

*University of Rijeka, Faculty of Engineering, Vukovarska 58 Rijeka Croatia
E-mails: {damjan.banic,goran.turkalj,domagoj.lanc,sandra.kvaternik}@riteh.hr

Keywords: thin-walled, composite cross-section, shear deformable beam model, stability analysis

1. Introduction

As load-bearing composite structures generally contain slender beam structural elements of thin-walled cross-section, the response of such optimized structures to the effect of external loading is much more complex and their increased tendency to lose the stability of the deformation form and the appearance of buckling is particularly pronounced [1,2]. In the structure design, special attention should be paid to exact determination of the limit state of stability of deformation forms. Analytical solutions are only available for simpler cases [1,2], and therefore the development and application of numerical solutions is imposed as a necessity [3-5].

The purpose of this work is large displacement nonlinear analysis of thin-walled beam type structures considering shear deformation effects and material inhomogeneity in the form of a composite cross-section. The analysis will be completely based on the numerical model developed by the authors, where the results will be compared to the results obtained by the other relevant sources.

2. Methods

To include the shear deformation effects in the formulation, Timoshenko's theory for non-uniform bending and modified Vlasov's theory for non-uniform or warping torsion are applied. Furthermore, in this work, an improved shear-deformable beam formulation is presented by taking into account the bending-bending and bending-warping torsion coupling shear deformation effects [3-5] occurring for the asymmetric cross-section where the principal bending and principal shear axes do not coincide [6]. The beam member is assumed to be prismatic and straight while external loads are supposed as conservative and static. The element geometric stiffness is derived using the updated Lagrangian (UL) incremental formulation [7] and the non-linear displacement field of a cross-section, which includes the second-order displacement terms due to large rotation effects. In such a way, the incremental geometric potential of the semitangential moment is obtained for the internal bending and torsion moments respectively, thereby ensuring the moment equilibrium conditions to be preserved at the frame joint to which beam members of different space orientations are connected [8]. After adopting a cubic interpolation for the deflections and twist rotation, and an interdependent quadratic interpolation for the slopes and warping parameter that includes shear-deformable effects, a locking-free beam element is obtained. Such an element is also known as a super convergent element, and the reduced integration technique is not needed to avoid the shear-locking effect [9].

To account for material inhomogeneity in the form of the composite cross-section, separate numerical model is used for the calculation of cross-sectional properties. Cross-sectional properties are weighted by the reference modulus and whole procedure can be seen as replacement of the inhomogeneous cross-section with equivalent homogenous cross-section [6]. Since the model does not include the coupling between normal and shear, it is only applicable for the analysis of cross-ply laminates, functionally graded materials and similar materials in which there is not coupling between normal and shear.

3. Results

A computer program called THINWALL v.17 was developed on the basis of the procedures mentioned in the previous section. To analyse the influence of the shear effect on the stability

behaviour of the analysed structural members, two model comparisons are performed. First one neglects the shear deformability (denoted as "SR"), and second one includes shear deformation effects on the basis of the procedure mentioned in this paper (denoted as "SD"). The analysed material is graphite-epoxy (AS4/3501) whose properties are E_1 = 144 GPa, E_2 = 9.65 GPa, G_{12} = 4.14 GPa, ν_{12} = 0.3. Figure 1 shows load-deflection curves for the mid-span of the presented simply supported beam. The obtained results match with the analytical solutions found in Ref [2].

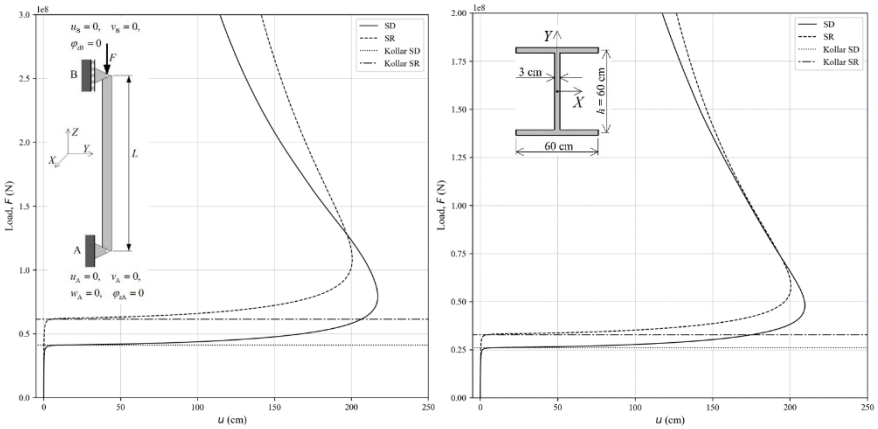

Figure 1. Simply supported I-profile column, L = 500 cm: [0°/0°]$_S$ (left), [0°/90°]$_S$ (right), buckling load vs mid-span displacement in the direction of X axis

4. Conclusions

A refined shear-deformable beam formulation for geometrically nonlinear stability analysis of composite semi-rigid frames has been introduced. The shear deformation effects have been taken into account due to the non-uniform bending and torsion of thin-walled beams with the asymmetric cross-section. Benchmark example has been presented to verify the model. The importance of introducing the shear deformations into the formulation is apparent from the significant reduction of the stability strength. Different material configurations have been analysed and their influence on the critical load has been presented and verified by selected example.

References

[1] Cortínez, V.H., Piovan, M.T. Vibration and buckling of composite thin-walled beams with shear deformability. *Journal of Sounds and Vibrations*, Vol. 258, Issue 4, 2002.

[2] Kollár, L.P, Springer, G.S., *Mechanics of Composite Structures*. New York: Cambridge University Press; 2003.

[3] Turkalj, G., Lanc, D., Banić, D., Brnić, J., Vo, T.P., A shear-deformable beam model for stability analysis of orthotropic composite semi-rigid frames. *Composite Structures*, Vol. 189, 2018.

[4] Kim, N.I., Kim, M.Y., Exact dynamic/static stiffness matrices of non-symetric thin-walled beams considering coupled shear deformation effects. *Thin-Walled Structures*, Vol. 43, 2005.

[5] Minghini, F., Tullini, N., Laudiero, F., Locking-free finite elements for shear deformable orthotropic thin-walled beams. *Int. J. Numer. Meth. Engng*, Vol 72, 2007.

[6] Pilkey, W.D., Analysis and Design of Elastic Beams: Computational Methods. John Wiley & Sons, INC., 2002.

[7] Lanc, D., Vo, T.P., Turkalj, G., Lee, J., Buckling analysis of thin-walled functionally graded sandwich box beams. *Thin-Walled Struct*, Vol. 86, 2015.

[8] Lanc, D., Turkalj, G., Vo, T.P., Brnic, J., Nonlinear buckling behaviours of thin-walled functionally graded open section beams. *Compos Struct*, Vol. 152, 2016.

[9] Reddy, J.N., Energy principles and variational methods in applied mechanics. Hoboken: Wiley, 2002.

Calibration and Validation of a Damage Model for 6005-T6 Aluminum

Roman Baranja[1], Matej Stanić[2], Dr.-Ing. Martin Schwab[3], Dr.-Ing. Richard Tichy[4]

[1]*AVL-AST d.o.o., Strojarska cesta 22, Zagreb, Croatia*
E-mail: roman.baranja@avl.com

[2] *Faculty of Mechanical Engineering and Naval Architecture, Ivana Lučića 5, Zagreb, Croatia*
E-mail: matej.stanic@fsb.hr

[3]*4a engineering Gmbh, Industriepark 1, Traboch, Austria*
E-mail: martin.schwab@4a.at

[4]*AVL List GmbH, Hans-List-Platz 1, Graz, Austria*
E-mail: richard.tichy@avl.com

Keywords: combined Swift-Voce hardening, ductile damage, elastoplastic behavior, triaxiality

1. Introduction and motivation

Ductile fracture occurs after the significant development of permanent plastic deformation, due to the imperfections in the material structure. One of the materials characterized by ductile fracture is aluminum. In addition to relatively low density, aluminum alloys have sufficient strength and ductility to ensure energy absorption on impact. Today, numerical simulations are increasingly used to evaluate structural integrity and predict possible design failures. Therefore, it is necessary to calibrate and validate the actual material behavior to correctly perform numerical simulations. Hence, 6005-T6 aluminum alloy plastic and fracture response are investigated in detail.

2. Material and plasticity model

In order to correctly predict the plastic behavior and damage of components and structures made of the 6005-T6 aluminum alloy, it is necessary to develop a material model which can represent the real physical behavior. Plastic behavior and material hardening are described by the flow (hardening) laws, analytical expressions used to fit the plastic region of an experimental true stress-strain curve. According to Papasidero *et al.* [1] combined Swift-Voce hardening law is the most suitable for numerical modeling of aluminum alloys. This isotropic hardening law in combination with von Mises yield surface is used in this paper.
Swift-Voce hardening law is linear combination of Swift (power) and Voce (exponential) law:

$$\sigma\left[\bar{\varepsilon}_p\right] = \alpha \cdot \sigma_s + \left(1-\alpha\right) \cdot \sigma_v \,. \tag{1}$$

The Swift and Voce parameters are usually gained from approximation of experimental true stress-plastic strain curve up to point of necking onset. Afterwards, the weighting factor α is determined through inverse iterative analysis using finite element simulations and experimental results. The identification of α is posed as a minimization problem, as the difference between experimental and simulated force-displacement curve needs to be minimized.

3. Experimental procedure

Experimental measurements are conducted on 2 and 3 mm thick specimens of 6005-T6 aluminum alloy using a tensile machine and GOM Aramis. All specimens are cut in the extrusion direction, which greatly affects material properties. These flat sheet metal specimens are made in several geometries to cover as many stress states as possible [2]. Four tensile specimens cover triaxiality area from 0.33 to 0.56 and three different shear specimens are selected to describe zero triaxiality area [3].

Due to similar results, only one shear specimen is selected for plasticity and fracture calibration. Specimen geometries are shown in Figure 1.

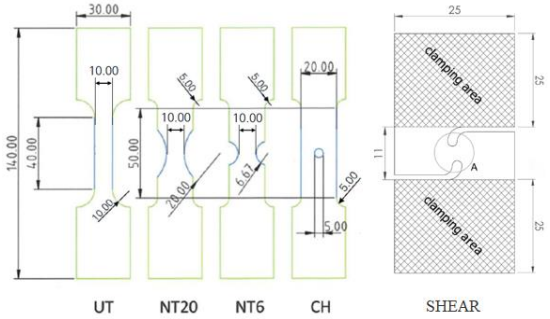

Figure 10. Tensile and shear specimen geometries

4. Swift-Voce calibration

Due to predetermined location of the necking and fracture, the NT20 specimen and its experimental results are chosen to identify parameters. The finite element software Abaqus/Explicit is used to perform the numerical simulations. The final simulation material input is obtained using an inverse iterative analysis. The comparison of experimental and simulated force-displacement curves shows that proposed Swift-Voce model accurately predicts plastic behavior for both thicknesses. The UT, CH and NT20 results are matched with accuracy of 3%. However, the NT6 and shear specimen exhibit greater deviation due to the different mechanical properties in non-extrusion directions. The simulated force level is 10% higher than the experimental for NT6, while the force response of shear specimen is underestimated for 25%. Moreover, the major principal strain comparison shows that simulated strain response is within 1.5% accuracy for every specimen.

5. Ductile damage model validation

The Abaqus ductile damage model is used for simulation and prediction of ductile damage and fracture in this paper. Using a previously gained plasticity model, ductile fracture limit curves are obtained. These curves show the plastic strain-triaxiality dependence. The proposed Abaqus ductile damage model describes damage as function of equivalent plastic strain ε_D^{pl} and stress triaxiality η. Plastic strain at the onset of fracture is determined from experimental results. The force-displacement responses with implemented damage model show great compatibility with experimental results. The prediction of damage initiation of UT and CH specimen is within 1% accuracy. Due to significant deviation of force response in plastic area, damage initiation of NT6 and shear specimen is not adequately described.

6. Conclusion

The proposed Swift-Voce hardening model satisfactorily describes elastoplastic behavior of 6005-T6 aluminum alloy, especially for uniaxial stress state (triaxiality 0.33). However, it is necessary to make further improvements to the material model to accurately describe damage initiation for lower and higher stress triaxialities. The use of Hill or Barlat (2000.) orthotropic yield functions in combination with Swift-Voce hardening law is proposed for future work and better hardening prediction.

References

[1] Papasidero, J., Doquet, V., Mohr, D., Ductile fracture of aluminum 2024-T351 under proportional and non-proportional multi-axial loading: Bao-Wierzbicki results revisited, *International Journal of Solids and Structures*, Volumes 69-70, Pages 459-474, 2015.

[2] Mohr, D., Roth, C., Ductile fracture experiments with locally proportional loading histories, *International Journal of Plasticity*, Volume 79, Pages 328-354, 2016.

[3] Roth, C., Mohr, D., Determining the Strain to Fracture for Simple Shear for a Wide Range of Sheet Metals. *International Journal of Mechanical Sciences*, Volume 149, Pages 224-240, 2018.

Optimization of Chebyshev's Lambda Mechanism stride length by combining Genetic algorithm and numerical simulation

D. Birt*, M. Hoić*, D. Miler*

*University of Zagreb, Faculty of Mechanical Engineering and Naval Architecture
Ivana Lučića 5, HR-10002 Zagreb, Croatia
E-mails: {dominik.birt, matija.hoic, daniel.miler}@fsb.hr

Keywords: Chebyshev's Lambda Mechanism, walking mechanism, optimization, genetic algorithm

1. Introduction

Walking mechanisms are linkages that imitate the walking motion of a human or animal leg, and are considered when wheeled drives are not applicable, mostly on uneven or stepped surfaces. Depending on the number of linkages and joints, as well as the desired leg trajectory, several types of mechanisms were developed. For each type, the leg trajectory is affected by linkage lengths; therefore, default lengths are provided to ensure stable walking motion. In this paper, Chebyshev's Lambda mechanism was optimized to increase the step length, which was selected as the sole objective function. Linkage lengths were varied, while Grashof's law was used to ensure the functionality of each proposed solution. The sum of linkage lengths was kept constant to allow for a meaningful comparison between the proposed solutions. The optimization process was devised next based on the procedure proposed in [1]; the genetic algorithm (GA) was used to generate, vary, and update populations. To obtain the objective function values, Simscape Multibody (a MATLAB Simulink subroutine) analysis was embedded within the GA to numerically determine the positions of significant points within the mechanism for a full cycle. As a result, a feasible mechanism with the largest stride length was obtained.

2. Method

The default-length Chebyshev mechanism was used as a baseline for comparison; its linkage lengths are $\{L_0, L_1, L_2, L_3, L_4, L_5\} = \{200, 100, 250, 250, 250, 1000\}$ mm (see Figure 1). The initial generation of possible solutions is generated by randomizing the L_0, L_1, L_2, and L_4 in a range of ±10% of their respective default values. Further, L_3 was determined based on Grashof's criteria (see Figure 1, left). Finally, L_5 is chosen to ensure the total linkage length L_{sum} of 2050 mm. Both anchors (L_1 and L_2 anchors) were assumed to always be at the same height.

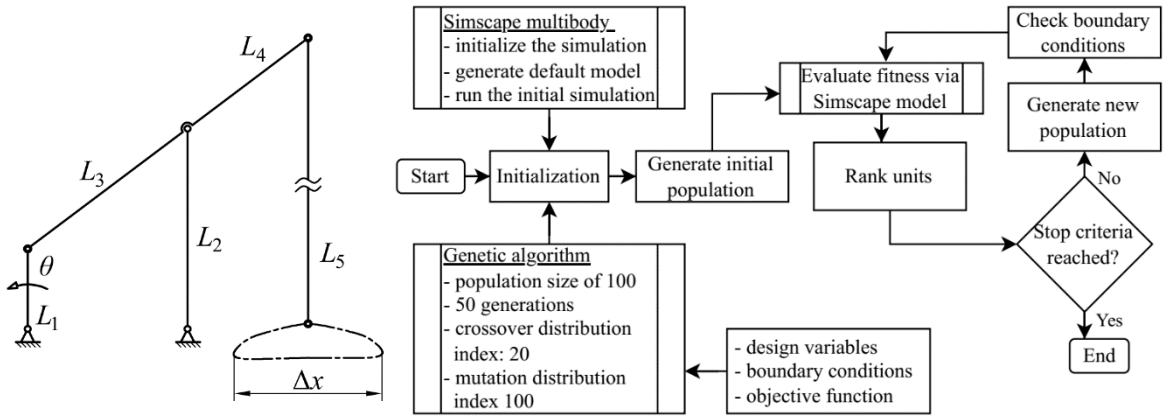

Figure 1. Chebyshev mechanism (left) and the optimization process outline (right)

The optimization process was developed by joining the GA and the Simscape Multibody analysis; see Figure 1, right. The objective function was calculated through Simscape within which the mechanism was assembled for each unit within the population, and the leg tip trajectories and accelerations were calculated for all the points of the cycle. The calculation step was 0.12°, resulting in a total of 3024 points for each unit. The optimized mechanism was obtained using the step length (see Δx in Figure 1) as the objective function. Further, GA was set up as follows: population size was 100, and units were evaluated through 50 generations. Furthermore, the crossover distribution index was set to 20, while the mutation distribution index was 100, selected according to [2].

3. Results and discussion

Aiming to confirm that the proposed optimization process can be used to both accurately and quickly obtain the mechanism parameters, results were obtained for 5000 potential mechanisms. The largest stride length of 603.7 mm was obtained for a mechanism $\{L_0, L_1, L_2, L_3, L_4, L_5\}$ = {186.8, 106, 245.4, 250.5, 268.8, 992,5} mm, which compared to 470 mm for its default counterpart, is an increase of 28%. The calculation time was approx. 2.1 s per unit using the i5-8500 CPU (3 GHz).

It should be noted that the acceleration and stride height should be addressed even though it was not the focus of this study. As shown in Figure 2, acceleration increased along both axes, as well as the variation in stride height. Such behavior could be problematic due to its connection with inertial forces, thus warranting the incorporation of additional objective functions (or boundaries).

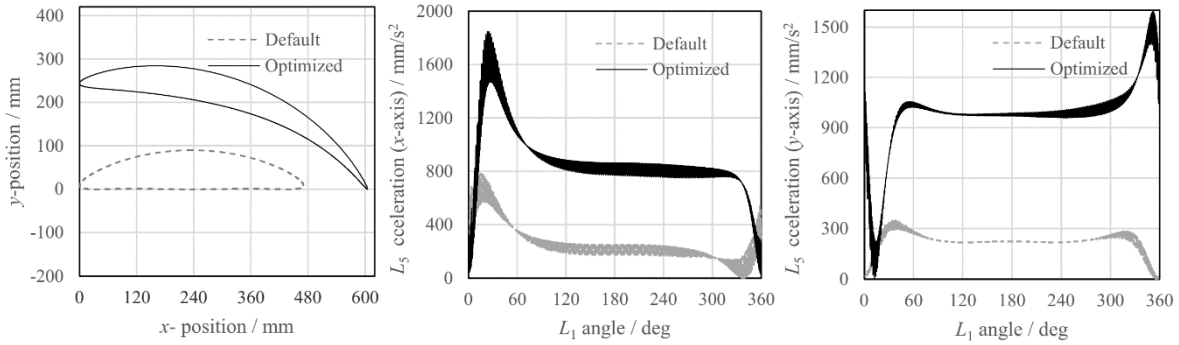

Figure 2. Comparison of the default and stride-optimized mechanism; locus (left), acceleration along the *x*-axis (middle), and acceleration along the *y*-axis (right)

4. Conclusions

The Chebyshev's Lambda mechanism stride length was optimized via a process combining the genetic algorithm and the Simscape Multibody (MATLAB Simulink). The optimization aimed to determine the maximum mechanism stride length for the constant sum of linkage lengths. It should be noted that linkage lengths were only varied within 10% of the default value, with the exception of L_3. Through optimization, stride length was increased by 28% compared to the default mechanism, albeit at the expense of increased acceleration in both the *x* and *y*-axis.

Based on the results, it was concluded that combining the genetic algorithm and numerical tool (Simscape, MATLAB) is advantageous for the design of the walking mechanisms. The latter, Simscape, permits for quick and retailed evaluation of mechanisms without the need for complex analytical tools. Hence, in the future, authors aim to focus on the multi-objective optimization of other types of walking mechanisms while also including additional objectives. Examples of additional objectives include reducing the acceleration and stride height, as well as shaping the leg trajectory for a specific purpose.

References

[1] Arora, J., Introduction to optimum design (4th ed.). Elsevier, Amsterdam, 2017.

[2] Deb, K., Pratap, S., Agarwal, S., Meyarivan, T. A fast and elitist multiobjective genetic algorithm: NSGA-II. *IEEE Trans. Evol. Comput.*, 6(2), 182-197, 2002.

Implementation of the Sliding Wear Analysis into the Finite Element User Interface PrePoMax

Matej Borovinšek*, Zoran Ren*

*Faculty of Mechanical Engineering, University of Maribor, Maribor, Slovenia
E-mails: {matej.borovinsek,zoran.ren}@um.si

Keywords: wear analysis, Archard's model, contact analysis, finite element method, PrePoMax

1. Introduction

Progressing sliding wear between contact surfaces can be estimated by the Archard's model [1]. This linear model predicts the volume of the removed material due to the wear process. Since the model neglects the changes in the geometry of the contacting surfaces during multiple wear cycles, a multistep numerical procedure can be used to determine the wear parameters better.

In this work, the implementation of the multistep numerical procedure to determine the wear parameters integrated into the PrePoMax [2] open-source graphical pre- and post-processor is presented. PrePoMax is being developed by the Faculty of Mechanical Engineering Maribor and uses the open-source code Calculix [3] as a finite element solver. Because CalculiX does not include the wear analysis feature, this capability was implemented into PrePoMax.

2. Methods

Archard's wear model was developed based on the results of the wear experiments between metals in dry conditions. Usually, the model is described as:

$$V = k \cdot \frac{F}{H} \cdot s \tag{1}$$

where V is the wear volume, k is the dimensionless wear coefficient, F is the normal contact load, H is the material hardness of the worn surface, and s is the sliding distance. To use this equation in a multistep numerical procedure where the change of the wear depth must be computed for each wear cycle [4], the equation (1) was rewritten to the following form:

$$h_i = \int \frac{k}{H} \cdot p_i \cdot ds \tag{2}$$

where h_i represents the wear depth accumulated in the i-th wear cycle and p_i stands for the normal contact pressure. The wear depth after multiple wear cycles is then computed by summation of all single cycle wear depths.

The implementation of the sliding wear analysis into the PrePoMax is general in terms of model geometry, boundary conditions and loads and is based on the following assumptions. The continuous wear process between parts can be discretised into several repeating wear cycles, the wear occurs only on a softer surface in the contact pair, the geometry of the contacting surfaces does not change during a single wear cycle, and the dimensionless wear coefficient remains constant during the entire wear process.

Based on these assumptions, a finite element model of a single wear step is first prepared. The model must accurately capture the evolution of the contact conditions through time; thus, a non-linear time-dependent analysis is required. The wear computation starts after the completion of the analysis. All computations of the wear parameters are done in the finite element nodes of the slave surface, which are in contact during the wear cycle. Nodal pressure and slip values are computed from the contact pressure slip fields. The nodal wear depths are then calculated using equation (2) and material properties at contact nodes. The processing of a single wear cycle completes with the computation of the contact surface geometry change due to wear, defined by nodal wear displacements. Single-cycle wear displacements are calculated by multiplying the scalar nodal wear depth value by the nodal

surface normal. Wear displacements of a single cycle are then added to the wear displacements of the previous wear cycles.

The combined wear displacements are then considered during model preparation for the next wear cycle. The initial finite element mesh of the model is updated by the combined nodal wear displacements considering the model boundary conditions. If a zero boundary condition is prescribed on a nodal degree of freedom where the wear displacement component is computed, the wear displacement component is set to zero. The analysis of the symmetric wear models is possible in this way. The procedure repeats until the final number of wear cycles is reached.

3. Results

The implemented procedure was tested on a simple example of oscillating pin contact on a plate, Figure 1. The pin is pressed in contact with the plate with a force of 200 N and oscillates along the plate surface with a frequency of 1 Hz and an amplitude of 10 mm for 10 s. Both parts are made from steel S235 with Young's modulus of 210,000 MPa and Poisson's ratio of 0.3. Material hardness is 100 MPa while the wear coefficient equals 0.001. The contact friction coefficient equals 0.3.

A symmetric model with 2500 linear tetrahedron elements was used for the test. A single wear cycle analysis was divided into 80 time increments to get a smooth transition of contact fields from node to node. The resulting wear depth after 5 and 10 wear cycles is shown in Figure 1. The wear distribution along the pin movement is the smallest at the start and end of the pin path and the largest at the middle. In the transversal direction, the wear depth is the largest in the middle of the plate, where the contact pressure is the largest. A smooth wear depth distribution was achieved even with coarse model discretisation.

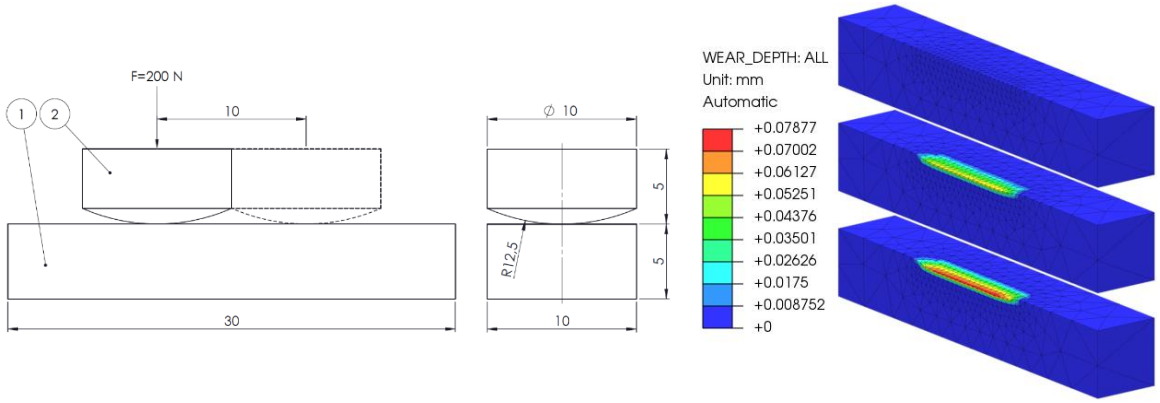

Figure 1. Initial model dimensions (left) and wear displacements after 0, 5 and 10 cycles (right)

3. Conclusions

Using Archard's model, sliding wear was implemented into the PrePoMax open-source graphical pre- and post-processor as a multistep computational procedure. The implementation was successfully tested on a simple example, returning expected results of wear depth distribution.

4. References

[1] J. F. Archard and W. Hirst, "The wear of metals under unlubricated conditions," *Proc. R. Soc. London. Ser. A. Math. Phys. Sci.*, vol. 236, no. 1206, 1956.
[2] M. Borovinšek, "PrePoMax." [Online]. Available: https://prepomax.fs.um.si/.
[3] G. Dhondt, "CalculiX." [Online]. Available: http://www.calculix.de/.
[4] X. Shen, L. Cao, and R. Li, "Numerical simulation of sliding wear based on Archard model," in *2010 International Conference on Mechanic Automation and Control Engineering, MACE2010*, 2010.

Nonlinear static experimental research of steel frames founded on dry sand compared to numerical results

Adriana Brandis*, Ivan Kraus*, Vedran Jagodnik+, Simon Petrovčič~

*Faculty of Civil engineering and Architecture, Vladimira Preloga 3, Osijek, Croatia
E-mails: {acerovecki, ikraus}@gfos.hr

+Faculty of Civil engineering, Radmile Matejčić 3, Rijeka, Croatia
E-mail: vedran.jagodnik@uniri.hr

~ Faculty of Architecture, Zoisova cesta 12, Ljubljana, Slovenia
E-mail: simon.petrovcic@fa.uni-lj.si

Keywords: soil-structure, interaction, experiment, pushover, SAP2000

1. Introduction

Soil-structure interaction is still an open question in the field of seismic design of buildings [1, 2]. Therefore, experimentally tested models are valuable, especially when they are conducted in large scale. Large scale models allow researchers to install larger number of measuring instruments while not influencing overall behaviour of the soil-structure system. In the presented research nonlinear static experimental testing of a steel frame model was conducted for two foundation cases. Firstly, the structure was fixed into the base. Secondly, the model was placed on a shallow strip foundation on dry sand. The description of the experiment with main results is given in following chapters.

2. Experimental setup

The steel frame model comprised of three steel columns 20 x 30 mm, a top beam and a foundations strip. The columns were made weaker, 5 x 30 mm, in the zones of larger stress accumulation to achieve the desired formation of plastic hinges during monotonically increasing horizontal loading. Steel grade used for models was S275. The top beam, weighing 382 kg, was selected in such a way that its behaviour was rigid in comparison with other structural elements. The columns were connected to the top beam with steel rods and were changed after each test. The foundation strip was 131 cm long and 13 cm wide. The foundation mass was measured at approximately 110 kg. The structural model was loaded with monotonically increasing horizontal load induced by hydraulic press at the top beam. The monotonic loading was increased until the model's bearing capacity was lost. For the first analysed case, the columns were fixed into the reaction slab in order to determine the structure's shear capacity. In the next step, the foundation strip was added below the columns and the model was tested as founded on dry local sand deposits from the Drava river. For both cases the natural period of vibration was determined as well as the capacity curves. The model on the soil was tested using dry sand only. The sand was uniformly compacted to the density level of 1550 kg/m^3 resulting with shear wave velocity of 135 m/s.

3. Experimentally and numerically obtained results

The behaviour of the model was recorded using LVDT instruments for displacements and accelerometers for the determination of vibration periods and shear wave velocity in the soil. Further, pressure sensors were placed below the foundation strip to measure pressure changes during tests. Lastly, a force sensor was installed at hydraulic press level to measure force applied at the model. The first period of vibration for the fixed base case was measured around 0,28 s.
Soil was modelled using nonlinear links including soil stiffness determined according to [3], force-displacement curve proposed by [4] and Takeda hysteresis [5] model which corresponded to the shape of sand hysteresis. Numerical models were made using SAP2000 [6] numerical modelling software. The vertical distribution of horizontal load corresponds to the first vibration mode of the model.

Modal distribution for fixed base model applies horizontal force of 100 N at beam, while for the soil-structure system it applies force of 160 N at beam level and 0,5 N at foundation strip level.

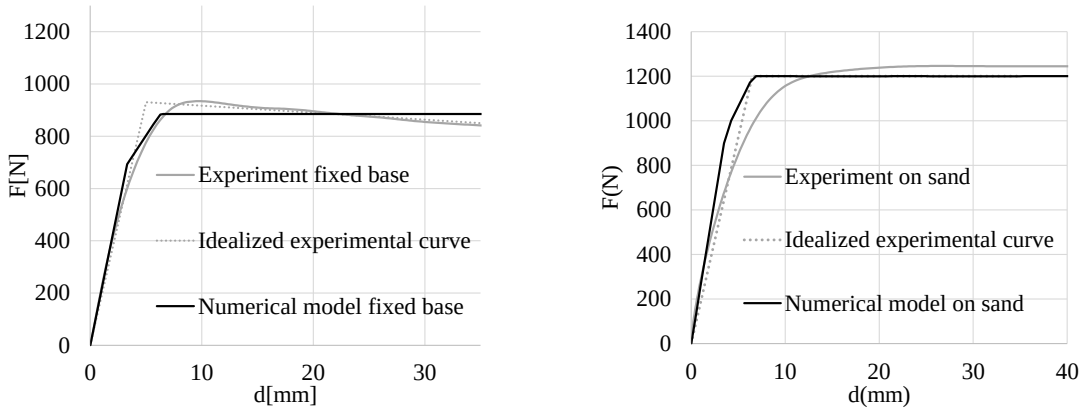

Figure 1. Comparison of numerical experimental results for: a) fixed base and b) soil-structure system

4. Conclusion

Soil-structure systems are observed and numerically modelled. Numerical models give results well matching the experimental models. Soil-structure systems show higher flexibility compared to fixed base model which could possibly lead to lower seismic load.

Acknowledgement

This work has been done in the framework of the Internal project no. 15-04 (Effects of soil-structure interaction in performance based design – PENDULARUM) and it was financially supported by the Faculty of Civil engineering and Architecture Osijek.

References

[1] Anastasopoulos I. *Beyond conventional capacity design: towards a new design philosophy. Soil–foundation–structure interaction* New York: CRC Press, Taylor & Francis Group. 2010:213-20.
[2] Gazetas G. *Soil-foundation-structure systems beyond conventional seismic failure thresholds.* Proc, 18th Int Conf on Soil Mechanics and Geotechnical Engineering: Challenges and Innovations in Geotechnics: French Society for Soil Mechanics and Geotechnical Engineering (CFMS), Rueil; 2013.
[3] NIST. *Soil-structure interaction for building structures*. National Institute of Standards and Technology, US Department of Commerce, Washington DC Project Technical Committee. 2012.
[4] Reese LC, Van Impe WF. *Single piles and pile groups under lateral loading*: CRC press; 2000.
[5] Takeda T, Sozen MA, Nielsen NN. *Reinforced concrete response to simulated earthquakes*. Journal of the structural division. 1970;96:2557-73.
[6] CSI. SAP2000 Integrated Software for Structural Analysis and Design. Computers and Structures Inc. 2013;Berkeley, California.

Evolution of the wrinkling pattern due to growth of elastic films on viscoelastic substrates

Jan Zavodnik, Miha Brojan

Laboratory for Nonlinear Mechanics, University of Ljubljana, Ljubljana, Slovenia
E-mails: jan.zavodnik@fs.uni-lj.si, miha.brojan@fs.uni-lj.si

Keywords: wrinkling, viscoelasticity, growth, substrate, film

1. Introduction

Wrinkling of thin elastic films on compliant viscoelastic substrates under compressive loads is a great toy model for studying interaction between the effects of the kinematic nonlinearity and viscoelastic material properties, because it is simple enough for analytical treatment and at the same time still maintains the effects of the viscoelasticity-nonlinear kinematics interaction. This kind of interaction occurs when the structure transitions from the initial, short time-limit to the final, long time-limit. The transition is essentially governed by the viscoelastic properties of the material. In the regime of the infinitesimal deformations the transition is trivial and therefore unsubstantial, but in the presence of nonlinear kinematic effects the transition becomes highly complex and more strongly dependent on initial conditions, perturbations and boundary conditions.While the purely elastic theory offers discrete wrinkling deformation patterns as the solutions, the viscoelastic theory provides a framework to describe also the transition from the deformation patterns, e.g. from a pattern with a large number of wrinkles to the pattern with a small number of wrinkles. The complexity of this transition is a direct consequence of kinematic nonlinearities, because any rearrangement of wrinkles during the transition causes an energy dissipation while it does not affect the final elastic limit state. However, it can have an influence when the system arrives to the long time-limit state. If the initial energy dissipation during rearrangement of wrinkles is too large the system can become "frozen" in a non-equilibrium deformation state, which can be distinctly different from the purely elastic one. The system can remain there permanently if the system loses more energy than needed to overcome an energy barrier. Alternatively, the system can also transition so slowly that the environmental parameters change during the process and it can therefore remain in the out-of-equilibrium state permanently. Note that in general, these deformation states are unreachable for the elasticity alone [1]. In fact, this deformation patterns are very common in nature, e.g. in microbiology [2-4] and morphogenesis [5].

2. Wrinkling pattern evolution analysis

We analyze the elastic film and the viscoelastic compliant substrate decomposed, as displayed in Fig. 1. The elastic film is modelled with the use of Főppl-von Karman (weakly) nonlinear plate kinematic assumptions. On the other hand, the viscoelastic substrate is modelled as a continuum with infinitesimal deformation theory. Both elements are connected through the continuity of deformations and stresses in the structure.

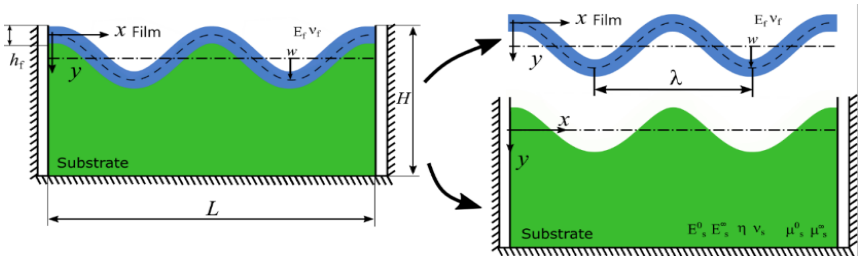

Figure 1. Elastic film and the viscoelastic substrate as separate structural elements.

To solve the obtained system of differential equations we approximate the wrinkles as a harmonic function of the form $w(x,t) = A(t)\cos k\,x$.

The system load in the form of confined growth, external forces etc. can be applied differently in the given time frame. We first analyse a step load. We show that an analytical implicit relation

between the wrinkle amplitude A and time t and the wave number k can be obtained on an infinitely long structure with the use of total strain energy minimization,

$$t = \frac{C_1(\log A - \log A_0) - 12E^*_{s,\mathrm{ee}}(1-\nu_\mathrm{f}^2)\left(\log C_2\,(A) - \log C_2\,(A_0)\right)}{r\left(E_\mathrm{f}h_\mathrm{f}k\left(-h_\mathrm{f}^2k^2 + 12\varepsilon_\mathrm{g}^0\right) - 24E^*_{\mathrm{s,e}}(1-\nu_\mathrm{f}^2)\right)}, \qquad k = 2\sqrt{\frac{\varepsilon_\mathrm{g}^0}{3A^2 + h_\mathrm{f}^2}}.$$

Here the C_1 and C_2 are some auxiliary functions made of material and geometric parameters, A_0 is the initial perturbation amplitude, E is Young's modulus, h is film thickness, ν is Poisson's ratio and r is a viscous relaxation rate. The indices "f" and "s" label the film and substrate properties, respectively. The time at which the wrinkles start to appear depends on the film growth amplitude ε_g^0. We show that if the growth amplitude is subcritical with respect to the long time-limit the wrinkles never appear and alternatively, if it is supercritical with respect to the long time-limit and supercritical with respect to the short time-limit then the wrinkles grow shortly after the growth is applied. Furthermore, if the growth amplitude is supercritical with respect to the short time-limit then wrinkles appear instantly and then continue to grow and transition towards the long time-limit deformation state. If the short time elastic equilibrium deformation pattern is qualitatively different from the long-time time deformation pattern, then the nontrivial transition will occur and the structure may become "frozen" in an out-of-equilibrium state.

In the case where the film growth is a ramp function the ratio between the compliant substrate relaxation rate and the active film growth rate is vitally important. In this case we performed numerical simulation where the growth magnitudes and elastic parameters of the structure were the same, only the ratio between the growth rate and viscoelastic relaxation rate were different. The long-time deformation patterns of two such structures are shown in Fig. 2. We observed that the two simulated structures converged to qualitatively different final deformation pattern.

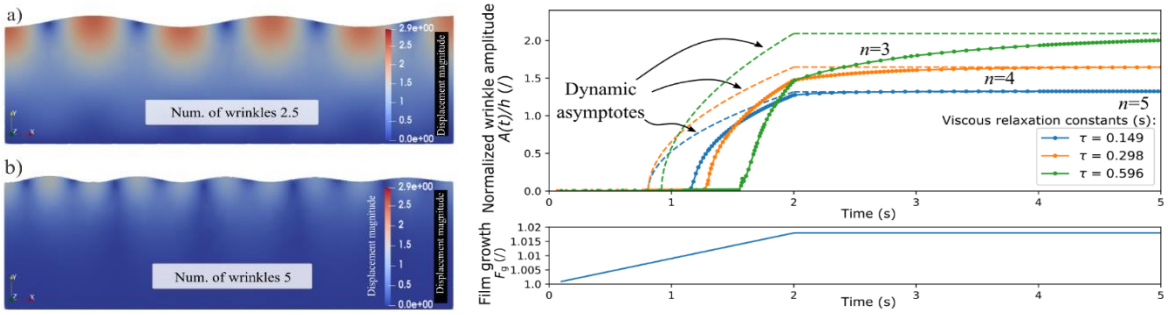

Figure 2. Left: Final deformation states of structures with the same elastic and different viscoelastic properties. Right: Wrinkle amplitude as a function of time for structures with the same elastic and different viscoelastic properties.

3. Conclusions

In this contribution, we show that viscoelastic properties of the material are crucially important for the final development of the pattern even though they seemingly affect only the transition period between the elastic short and long-time equilibrium states of the structure. The interaction between the viscoelastic material properties with the nonlinear kinematics produces interesting deformation patters otherwise unattainable for purely elastic systems. The theory and the principles described are also extremely useful in engineering applications because they allow much simpler fabrication of smart surfaces and coatings that at some point in fabrication behave viscoelasticity.

References

[1] D. A. Matoz-Fernandez, et al.: Wrinkle patterns in active viscoelastic thin sheets. Phys. Rev. Research 2(2020) p. 013165
[2] T. Ruiz-Herrero, et al.: Dynamics of Growth and Form in Prebiotic Vesicles Phys. Rev. Lett. 123(2019) p. 038102
[3] M. Nelson, et al.: Growth-induced buckling of an epithelial layer. Biomech. Model. Mechan. 10(2010) p. 883–900.
[4] D. Espeso, et al.: Differential growth of wrinkled biofilms. Phys. Rev. E, Stat. nonlin. soft matt. Phys. 91(2015) p. 022710
[5] R. de Rooij and E. Kuhl: Constitutive Modeling of Brain Tissue: Current Per-spectives. Appl. Mech. Rev. 68(2016) p. 010801

Development of quick and reliable method for electric terminal crimp design

Ante Bubalo*, Zdenko Tonković+, Dalibor Zorica*

* *Yazaki Europe Limited, Slavonska 26/6, HR-10000 Zagreb, Croatia*
E-mail*: {ante.bubalo,dalibor.zorica}@yazaki-europe.com*

+ *University of Zagreb, Faculty of Mechanical Engineering and Naval Architecture, Ivana Lučića 5, HR-10000 Zagreb, Croatia*
E-mail: *zdenko.tonkovic@fsb.hr*

Keywords: wire crimping, 2D analysis, explicit, compression, wing clearance

1. Introduction

One part of electrical terminal design process is development of terminal crimp wings and appropriate crimping tools for specified wire range. For that purpose, numerical simulations of wire crimping process are widely used in automotive industry, with main goal to predict crimp shape [1,2]. Although computational power is increasing, time demand of three-dimensional simulations can prolong development of new product [3,4]. The current paper presents an attempt to simulate in two dimensions a crimping process using non-linear dynamic analysis, with the aid of commercial FE software ABAQUS/Explicit. For this crimping process, two types of FE models were created and simulated as shown in Figure 1. These different approaches reflect the way of modeling the most important parameters of a real crimping process. The results were compared in order to evaluate matching of simplified 2D method.

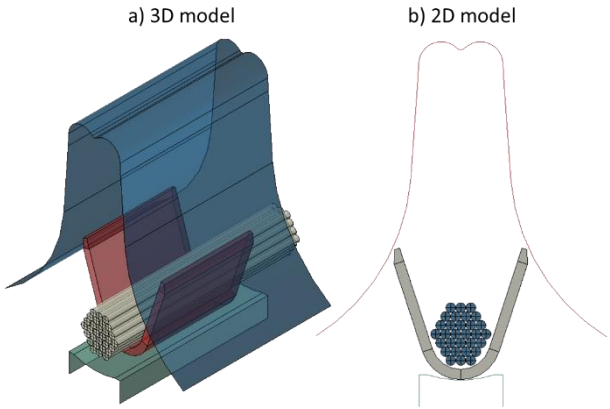

Figure 1. a) 3D and b) 2D model of wire crimping process

2. Numerical simulation

Within the framework of numerical investigations, two methods were considered: three-dimensional and two-dimensional. In which 3D method was used as reference for 2D method validation.

Both methods used same time step of 0.02 seconds with defined coefficient of friction of 0.15 in-between each part. 3D models were discretized with three-dimensional 8-node solid C3D8 elements and 2D models with 4-node bilinear plane stress quadrilateral CPS4R elements. A bilinear constitutive structural model was used, in which both materials shared the same elastic modulus value of 135 MPa with yield strength of 250 MPa for copper and 500 MPa for copper alloy – terminal.

3. Results and discussion

Evaluation of FEA results consists of visual inspection, clearance measurement and material compression calculation for specified crimp height. When visually comparing results of 3D and 2D models it can be determined if we have match in prediction of some unwanted phenomena, like wing rolling. Results of numerical simulations can be seen in Figure 2 including the graph which represents differences in results.

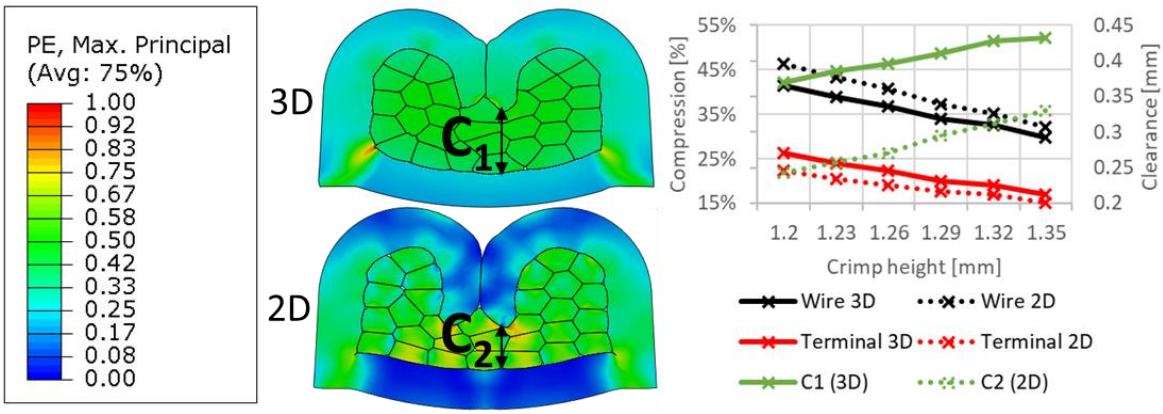

Figure 2. Numerical results of crimping process for 3D and 2D models

According to the presented graph, it can be seen that 2D model have slightly higher wire compression than 3D model for same crimp height. As expected, for terminal compression we would have opposite scenario, due to the constant total area defined by crimping tool shape at specific crimp height. Result differences are below 5% for compression, but difference in clearance is significantly higher up to 35%. By visual comparison of both methods, several differences exist, but are hard to qualify with the numbers.

4. Conclusions

There are several limitations of 2D method, one which is inability to calculate the longitudinal elongation of wire and terminal during crimping process. Additionally, contact between each wire strands individually and terminal or crimping tools must be defined manually. In order to speed up the numerical setup, Python script can be used.

Results obtained shows slight difference in calculated compression ratio, although there is significant difference in wings clearance and visual inspection in general. These results prove that 2D models can be used for initial terminal and crimping tools development, but for final analysis 3D models should be employed.

Acknowledgments. This work has been supported by the company Yazaki Europe LTD. with special thanks to Mr. Thomas Schaller and Mr. Josip Jelak.

References

[1] Bubalo A., Tonković Z., Zorica D., Numerical and experimental investigation of wire crimping process, *Proc. 8th Int. Congress of Croatian Society of Mechanics*, Opatija, 2015.

[2] Mocellin, K., Petitprez, M., Experimental and numerical analysis of electrical contact crimping to predict mechanical strength. *11th International Conference on Technology of Plasticity*, Nagoya, Japan, 2018-2023, 2014.

[3] Zhmurkin, D. V., 3-D Simulation of Open-Barrel Crimping Process. *55th IEEE HOLM 2009 Conference on Electrical Contacts*, Vancouver, Canada, 114–120, 2009.

[4] Kakuta, N., Crimp Analysis Simulation Technology. *SAE Int. J. Passeng. Cars - Electron. Electr. Syst.*, 501-507, 2009.

Newmark Type of Integration Methods with Quasi-Newton Iterations for Flexible Multibody System with Friction

Radek Bulín*, Michal Hajžman+, Pavel Polach*

* *New Technologies for the Information Society, Faculty of Applied Sciences, University of West Bohemia. Technická 8, 301 00 Pilsen, Czech Republic.*
E-mails: {rbulin,ppolach}@ntis.zcu.cz

+ *Department of Mechanics, Faculty of Applied Sciences, University of West Bohemia. Univerzitní 8, 301 00 Pilsen, Czech Republic.*
E-mail: mhajzman@kme.zcu.cz

Keywords: Newmark's method, quasi-Newton's method, absolute nodal coordinate formulation

1. Introduction

In this paper, the usage of Newmark type of integration methods that employ quasi-Newton iterations is studied using a simple cable-weight dynamic system. Newmark's family of methods is commonly used in problems of structural mechanics, but it can be successfully used also in problems of multibody system dynamics which are formulated as index 3 differential-algebraic equations [1]. The most commonly used methods are the Newmark method, Hilber-Hughes-Taylor (HHT) method, and generalized-α method [2]. The predicted solution in a discrete time step needs to be iteratively refined to find the solution satisfying equations of motion and constraint equations. This operation most often relies on the Jacobi matrix of the system equations which leads to the Newton method. The time effectiveness of the iterative procedure can be enhanced using the suitable quasi-Newton method which is studied in this paper.

This work is motivated by the research of the possible use of tensegrity structures in robotics. The main goal is to study efficient numerical algorithms for dynamic simulations of such structures together with their experimental verification.

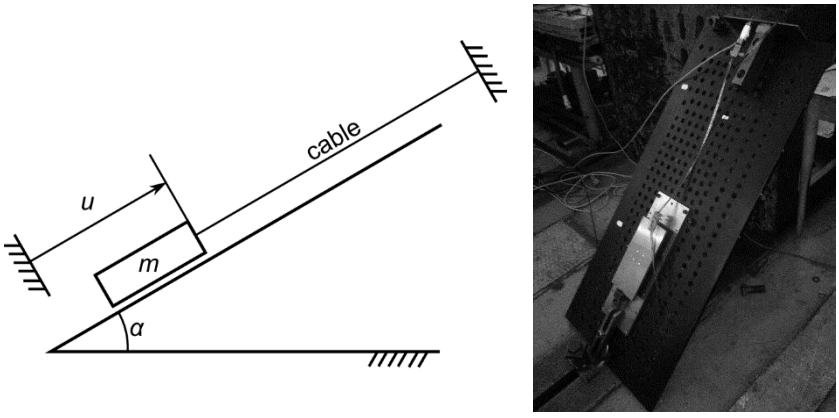

Figure 1. Scheme and experimental setup of the tested system

2. Description of the testing model

The scheme and the experimental setup of the testing system are shown in Figure 1. The system consists of a carbon cable with a silicone coating and a steel weight. The weight is placed on an inclined plane with an angle of $\pi/4$ rad and attached to the cable, which is attached to the base frame on the other end. The cable is 0.599 m long and is modelled using the absolute nodal coordinate formulation (ANCF) of a thin beam [3] which is suitable for flexible bodies performing large deformations. The cable Young's modulus is 6.23 GPa and the density is 272 kg/m^3. The weight of

prism steel weight is 3.096 kg. The friction force between the weight and inclined plane was included based on the Coulomb friction model. The experiment starts with the lifted weight along the inclined line by u_0 = 0.01 m.

3. Results and discussion

In this research, the results of numerical simulations that employ various Newmark type integration methods with different quasi-Newton iteration methods are compared with the experimental results. As can be seen in the left part of Figure 2, a good agreement between the weight position time history obtained from the experiment and simulation was achieved. Then, the effectiveness of the numerical methods was investigated. As an example, the comparison of the effectiveness of the Newmark's method combined with various quasi-Newton methods (i.e. Davidon, Broyden, DPF and BFGS [4]) is shown in the right part of Figure 2. Since the most time-consuming operation of the simulation is the evaluation of elastic forces of the ANCF elements, the number of elastic forces evaluations during the simulation serves as the time efficiency indicator. As can be seen, the Davidon update formula is the most efficient one for all tested numerical damping parameters. All tested quasi-Newtons' formulas are faster than no Jacobian matrix update approach (NoUpdt) which is common in multibody simulations.

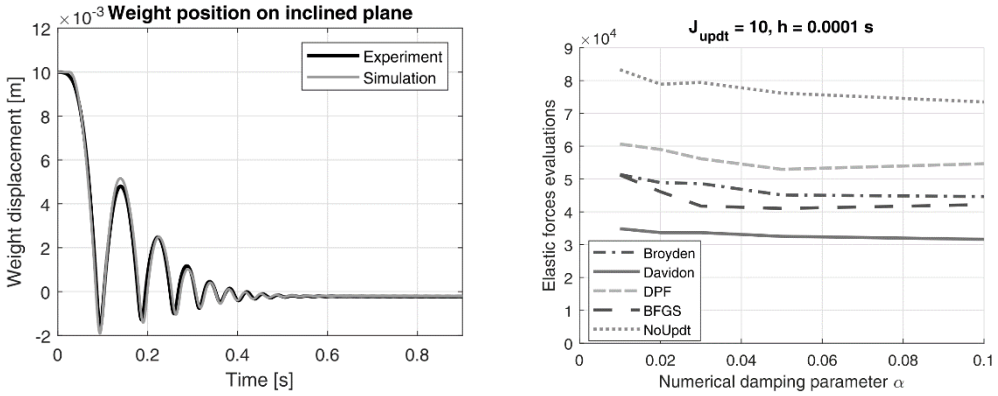

Figure 2. Time history of weight position from experiment and simulation (left) and a number of ANCF elastic forces evaluations for the Newmark method with various quasi-Newton methods (right)

4. Conclusions

Various Newmark type integration methods with different quasi-Newton method formulas were tested on a system composed of the cable and weight on the inclined plane with friction. The cable was modelled by the modern ANCF approach, so its inertia was included in the model and its transverse vibrations can be studied. The results from the model were experimentally verified. The model then serves as a benchmark problem for various integration methods. The goal is to find efficient numerical approaches for simulations of systems containing cables and friction, such as robotic tensegrity structures.

This research work was supported by the Czech Science Foundation project 20-21893S.

References

[1] Negrut, A., Jay, L.O., Khude, N., A discussion of low-order numerical integration formulas for rigid and flexible multibody dynamics. *J. Comput. Nonlinear Dyn.* 4, 021008, 2009.

[2] Arnold, M., Brüls, O., Convergence of the generalized-α scheme for constrained mechanical systems. *Multibody Syst. Dyn.* 18, 185-202, 2007.

[3] Bulín, R., Hajžman, M., Efficient computational approaches for analysis of thin and flexible multibody structures, *Nonlinear Dyn.*, 103, 2475-2492, 2021.

[4] Geradin, H., Idelsohn, S., Hogge, M., Computational strategies for the solution of large nonlinear problems via quasi-Newton methods. *Comput. Struct.*, 13, 73-81, 1981.

Discrete fracture model with improved elastic response

Jadran Čarija*, Mijo Nikolić *, Eduard Marenić+

* *University of Split, Faculty of Civil Engineering, Architecture and Geodesy, Croatia*
E-mails: jcarija@gradst.hr

+ *Institut Clement Ader (ICA), Université de Toulouse, CNRS-INSA-UPS-ISAE-Mines Albi, Toulouse, France*

Keywords: discrete lattice model, fracture, embbed discountinuity, elastic continuum properties

1. Introduction

Discrete lattice model [1] has been successfully used for description and representation of fracture processes that include crack formation and propagation. However, this model is limited in its ability to represent elastic continuum properties. In this work we present the procedure for choosing appropriate parameters that lead to correct elastic continuum response of model.

2. Methodology

Discrete fracture model is based on discretization of the domain by using Voronoi cells and Timoshenko beams as cohesive links between them. Crack formation is result of separation of two adjacent Voronoi cells. In order to represent that phenomenon, embedded strong discontinuity is introduced in the generalized displacement field of each 2D Timoshenko beam [2,3].

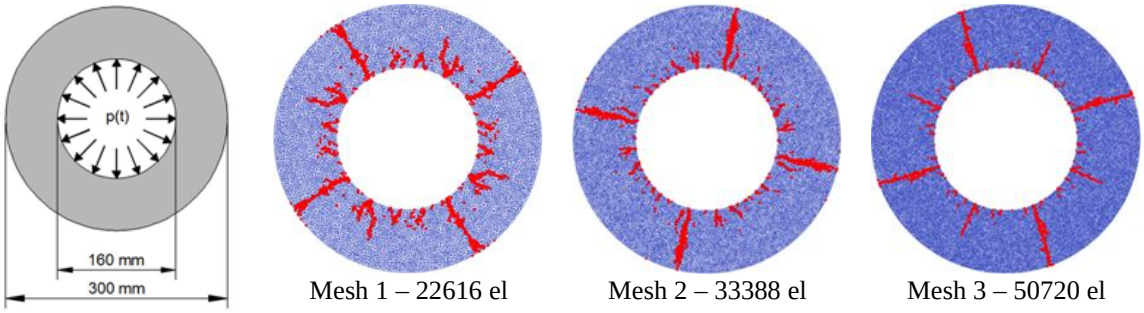

Figure 1. Thick cylinder test

In Figure 1, final crack patterns of thick cylinder subjected to an impulsive internal pressure for three different meshes are presented. We can see, that all three meshes are fragmented into four parts and only difference is that fragamentated parts are rotated with respect to each other. This model provides capturing complex fracture mechanism where both failure modes (mode I and mode II) are simulated.

As previously mentioned discrete lattice models have limitations in their ability to represent elastic continuum properties of material [4,5]. In order to obtain appropriate global representation of continuum properties Young's modulus and Poisson's ratio with the lattice model, local lattice element (beam) axial and shear stiffness and their ratio G_b/E_b need to be adjusted [5,6]. For the purpose of obtaining correct global continuum properties with lattice model, uniaxial compression test was performed (Figure 2 a)) in the linear elastic regime. Figure 2 b) shows relationship between Poisson's ratio and the ratio of the beam stiffness G_b/E_b. G_b represents the beam shear modulus and E_b is elastic modulus which defines axial stiffness of the Timoshenko beam lattice element. Both modulus E_b and G_b can be considered as model parameters. For different Poisson's ratio we got different ratio of the beam stiffness G_b/E_b and from certain stiffness ratio G_b/E_b we obtain proper ratio E_b/E, where E is modulus of elasticity of material (Figure 2 b)). As we can see by properly choosing

E_b and G_b as well as their ratio, lattice model can represent correct global continuum properties of material.

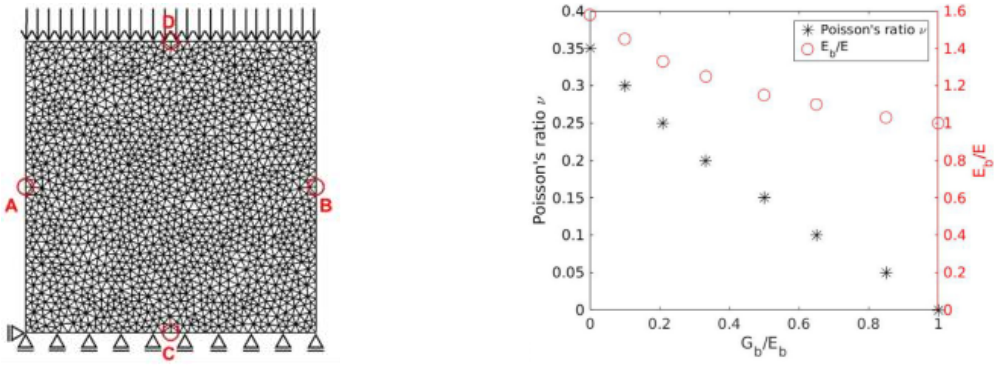

a) b)

Figure 2. Uniaxial compression test - a) Specimen with measuring points, b) Relationship between the beam local stiffness ratio and computed Poisson's ratio, elastic modulus ratio.

3. Conclusions

Discrete lattice models are effective models especially for description and representation of fracture processes with crack formation, development and propagation, however they have some disadvantages like the proper presentation of global continuum properties. In this work we show how to determine appropriate model parameters (E_b and G_b) for lattice model, which will ensure correct global continuum properties of material.

Acknowledgements

This work has been supported through the project 'Parameter estimation framework for fracture propagation problems under extreme mechanical loads' (UIP-2020-02-6693), funded by the Croatian Science Foundation.

References

[1] M. Nikolić, E. Karavelić, A. Ibrahimbegovic, P. Miscević, "Lattice Element Models and Their Peculiarities," *Archives of Computational Methods in Engineering*, vol. 25, no. 3, pp. 753-784, 2018.

[2] M. Nikolić, X. N. Do, A. Ibrahimbegovic, Ž. Nikolić, "Crack propagation in dynamics by embedded strong discontinuity approach: Enhanced solid versus discrete lattice model," *Computer Methods in Applied Mechanics and Engineering*, vol. 340, pp. 480-499, 2018.

[3] J. Čarija, M. Nikolić, A. Ibrahimbegovic, Ž. Nikolić, "Discrete softening-damage model for fracture process representation with embedded strong discontinuities," *Engineering Fracture Mechanics*, vol. 236, pp. 107211, 2020.

[4] J. E. Bolander, S. Saito, "Fracture analyses using spring networks with random geometry," *Engineering Fracture Mechanics*, vol. 61, no. 5-6, pp. 569-591, 1998.

[5] D. Asahina, K. Aoyagi, K. Kim, J. T. Birkholzer, J. E. Bolander, "Elastically-homogeneous lattice models of damage in geomaterials," *Computers and Geotechnics*, vol. 81, pp. 195-206., 2017.

[6] L. L. Rasmussen, A. P. Assis, "Elastically-homogeneous lattice modelling of transversely isotropic rocks," *Computers and Geotechnics*, vol. 104, pp. 96-108, 2018.

Energy-loss mechanism in vertical and horizontal impacts during rocking: experimental investigation and numerical modelling

Nina Čeh[*], Maria Lissner[+°#], Nik Petrinić[#]

[*] *University of Rijeka, Faculty of Civil Engineering, Radmile Matejčić 3, 51000 Rijeka*
[+] *DCIM (Dresden Center for Intelligent Materials), TU Dresden, Dresden 01069*
[°] *ILK (Institute of Lightweight Engineering and Polymer Technology), TU Dresden, Dresden 01307*
[#] *Department of Engineering Science, University of Oxford, Parks Road, Oxford OX1 3PJ*
E-mails: nina.ceh@uniri.hr, maria.lissner@eng.ox.ac.uk, nik.petrinic@eng.ox.ac.uk

Keywords: rocking, energy loss, coefficient of restitution, vertical impact, horizontal impact

1. Introduction

Rocking is an important mode of motion in complex dynamic response of multiple real-life structures, such as dry-stone walls and structures, historical monuments, graphite blocks inside AGR nuclear power plants, and masonry structural components, subject to seismic base excitation. In simple rocking models based on Housner's [1] approach energy dissipation is usually accounted for by introducing a restitution coefficient [2]–[4] which causes an instant drop in the angular velocity of the block at each contact (collision of the block with the base).

Here we aim to analyse the energy dissipation during rocking by relating system parameters describing contacts used in the discrete-element method (such as stiffness and damping at each contact point in the penalty approach) to the experimentally observed behaviour at impacts during rocking. This work focuses on experimental tests of aluminium block specimens rocking freely or when subject to base excitation monitored by high-speed cameras, followed by writing numerical procedures with embedded various contact models to be compared against the experimentally obtained results for rocking.

2. Experimental setup

In order to precisely quantify the energy loss at each impact of the block with the base (the so-called vertical impact) during rocking and relate it to the pre-impact velocity and parameters such as size and slenderness of the block, a series of experiments is designed and carried out. Aluminium block specimens of three different sizes with slenderness ratios between 2.25 and 6.75 which are standing freely on an aluminium base are examined (Figure 1, left). Experiments are aimed at measuring block's rotation histories using high-speed contactless optical measuring system during free and forced rocking. Block's points' velocities are easily obtained by time differentiation of the measured displacements, which enables calculation of coefficient of restitution quantifying the energy loss at each impact and each contact point.

Another experimental program including two adjacent blocks rocking will be designed and conducted, with the aim to describe and quantify the energy loss during contacts between them (the so-called horizontal impact).

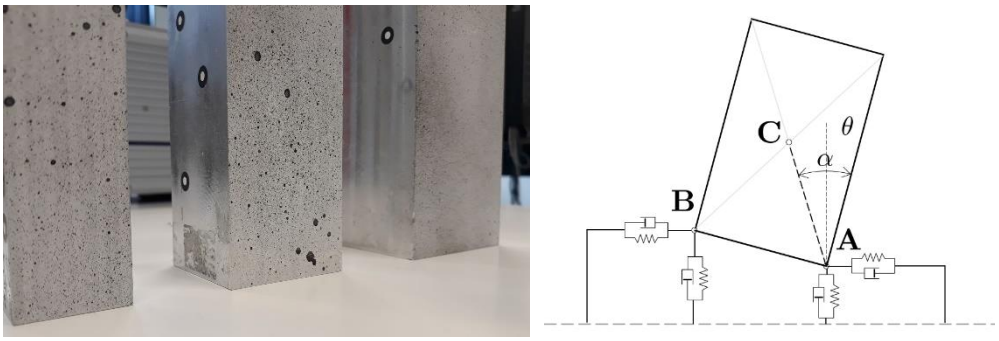

Figure 1. Aluminium specimens of rectangular blocks used in the experiments with surface pre-treated for optical measuring procedure (left), numerical model for simulating contacts between the block and the base (right)

3. Numerical model

Rectangular block and the base beneath it are modelled as rigid bodies, while damped spring and damped Hertzian contact models are used to simulate the normal and tangential contact between (one or both of) block's bottom corners and the base (Figure 1, right). Time integration of differential equations of motion is performed via Newmark's integration method. The stiffness and damping parameters in these two contact models are investigated and compared against the experimental data.

The numerical model will be extended to a system of two adjacent rocking blocks in order to properly model the horizontal contact between them.

4. Conclusions

Restitution coefficients that describe the drop in angular velocity of the block as well as restitution coefficients that describe the energy loss related to a drop in normal and tangential relative velocities at each specific contact point during rocking are obtained experimentally for the described block specimens in case of vertical contacts. The same parameters will be obtained for the system of two adjacent block that experience also horizontal contacts. Furthermore, an attempt will be made in relating the parameters used to numerically model vertical and horizontal contacts with the blocks' size and slenderness by fitting the numerically obtained rotations to the experimentally measured ones.

Acknowledgements

This research is financially supported by University of Rijeka via project 20-41 2645 "Horizontal collisions between adjacent structures due to dynamic base excitation", while the experiments were partially conducted at Impact Engineering Laboratory at the University of Oxford within the project "Collisions in rocking multi-body systems – experimental and numerical investigation" funded by Unity Through Knowledge fund.

References

[1] Housner, G. W., The behavior of inverted pendulum structures during earthquakes. *Bull. Seismol. Soc. Am.*, vol. 53, no. 2, pp. 403–417, 1963.

[2] Chatzis, M. N., Garcia Espinosa, M., Smyth, A. W., Examining the Energy Loss in the Inverted Pendulum Model for Rocking Bodies. *J. Eng. Mech.*, vol. 143, no. 5, 2017.

[3] Kalliontzis, D., Sritharan, S., Schultz, A., Improved Coefficient of Restitution Estimation for Free Rocking Members. *J. Struct. Eng.*, vol. 142, no. 12, 2016.

[4] Čeh, N., Jelenić, G., Bićanić, N., Analysis of restitution in rocking of single rigid blocks. *Acta Mech.*, vol. 229, no. 11, pp. 4623–4642, Nov. 2018, doi: 10.1007/s00707-018-2246-8.

Anisotropic plasticity models with shear constraint

Vedrana Cvitanić*, Ivan Čorić*, Maja Džoja*

*Faculty of Electrical Engineering, Mechanical Engineering and Naval Architecture, University of Split, Ruđera Boškovića 32, 21000 Split, Croatia
E-mails: {vcvit, ivan.coric.00, majkovac}@fesb.hr

Keywords: anisotropic material, constitutive modelling, model calibration, shear constraint, non-associated flow rule

1. Introduction

Sheet metals exhibit initial plastic anisotropy mainly due to the crystallographic texture caused by production rolling steps. Computer simulation codes that are utilized for design and analysis of sheet metal forming processes require accurate and numerically efficient anisotropic elasto-plastic constitutive models. In this study, phenomenological anisotropic plasticity models based on associated or non-associated flow rule approach and isotropic hardening concept are considered. The considered formulations utilize simple four parametric orthotropic stress functions, quadratic Hill48 [1] or non-quadratic Karafillis-Boyce [2], as yield function/plastic potential. The study concerns the calibration procedures for these constitutive models. By conventional approach, anisotropy parameters of Hill48/Karafillis-Boyce yield function/plastic potential are calculated analytically or iteratively from yield stresses/Lankford coefficients obtained in uniaxial tensile tests of sheet specimens with alignment of 0°, 45° and 90° to the rolling direction. Also, the equal-biaxial tensile yield stress is utilized in the calibration procedure for the considered yield functions. By this approach, all together seven experimental data are utilized in the model calibration and only one experimental data corresponds to the biaxial stress state. Furthermore, equal-biaxial tensile yield stress corresponds to the stress region with normal stresses having equal sign. Therefore, in the model calibration, no restrictions related to biaxial stress states with normal stresses having opposite sign are applied.

The shear loading satisfies plane stress conditions and requires zero hydrostatic stress. The individual normal stress components may be non-zero, but their sum must be zero. Several experimental studies, for different materials with different degrees of anisotropy, confirm theoretical observations that in the shear loading, principal strains are also equal and opposite [3]. For the shear loading states, conventional calibration procedures for the considered anisotropic plastic potential functions result in principal strains that have opposite but unequal values and consequently thought-thickness strains are generated.

2. Orthotropic elasto-plastic constitutive models with shear constraint

In this study, anisotropic plasticity models based on associated or non-associated flow rule and Hill48 or Karafillis-Boyce stress function with numerically determined parameters are considered. Parameters of the yield function/plastic potential are calculated by optimization procedure using genetic algorithm based on the experimental yield stresses/Lankford coefficients obtained in uniaxial tensile tests of seven sheet specimens with different alignment to the rolling direction and the yield stress/plastic strain ratio related to the equal-biaxial tensile stress state. By the adopted approach, all together 16 experimental data are utilized in the model calibration. Furthermore, in the calibration procedure for the plastic potential, the constraint is applied to enforce equal and opposite principal strains for the shear loading state, with zero shear stress, that satisfies yield condition. By this constraint, shape of the plastic potential in the shear region is modified. In the calibration procedure, experimental data for aluminium alloy sheet AA2090-T3 with 1.6 mm thickness [4] are utilized.

For the obtained yield functions/plastic potentials, contours and predictions of orientational dependences of yield stresses/Lankford coefficients are analysed. The implications of the applied shear constraint are also considered by calculating the principal strains ratio for all shear loading states obeying yield condition. Also, the stress triaxiality (ratio of hydrostatic stress to equivalent

stress) with respect to the principal strains ratio is considered for all stress states, with zero shear stress, on the yield surface. For illustration, Figure 1. presents contour of Hill48 yield function with numerically determined parameters and contours of differently calibrated Hill48 plastic potentials. Hill48 plastic potential with analytically determined parameters and Hill48 plastic potentials with numerically determined parameters without or with the imposed shear constraint are presented. Considerable difference in the presented contours can be observed. Figure 2. presents predicted principal strains ratio with respect to normal stress obtained by differently calibrated Hill48 plastic potentials. It can be observed that the application of shear constraint results in principal strains ratio values close to -1 for all shear loading states.

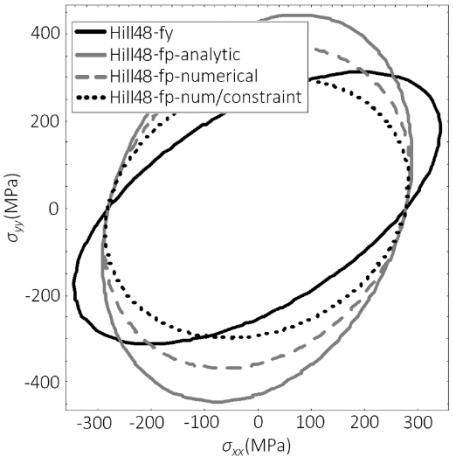

Figure 1. Contours of Hill48 yield function and Hill48 plastic potentials corresponding to zero shear stress for AA2090-T3

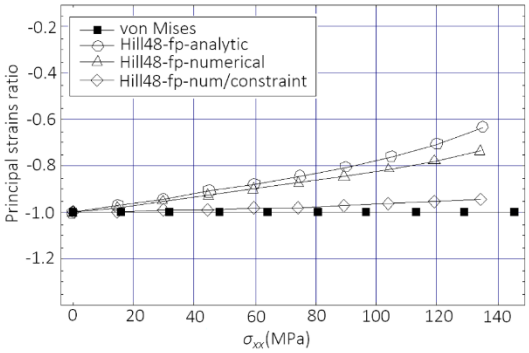

Figure 2. Predictions of principal strains ratio for shear loading states obtained by Hill48 plastic potentials for AA2090-T3

3. Conclusions

In the present study, anisotropic plasticity constitutive models based on associated or non-associated flow rule that utilize Hill48 or Karafillis-Boyce stress function with numerically determined parameters are considered. The constraint is imposed on the plastic potential function to ensure equal and opposite principal strains for shear loading states. For the selected AA2090-T3 sheet, contours of yield function/plastic potential and predictions of orientational dependences of yield stresses/Lankford coefficients are analysed. Also, principal strains ratio and stress triaxiality are considered for stress states satisfying yield condition. The developed formulations result in improved predictions of uniaxial tensile tests data and physically acceptable shear loading states.

References

[1] Hill, R., Theory of yielding and plastic flow of anisotropic metals. *Proc. Roy. Soc. A*, 193, 281-297, 1948.

[2] Karafillis, A.P., Boyce, M., A general anisotropic yield criterion using bounds and a transformation weighting tensor. *Journal of the Mechanics and Physics of Solids*, 41, 1859-1886, 1993.

[3] Abedini, A., Butcher, C., Rahmaan, T., Worswick, M. J., Evaluation and calibration of anisotropic yield criteria in shear loading: constraints to eliminate numerical artefacts. *International Journal of Solids and Structures*, 151, 118-134, 2018.

[4] Barlat, F., Brem, J. C., Yoon, J. W., Chung, K., Dick, R. E., Lege, D. J., Pourboghrat, F., Choi, S. H., Chu, E., Plane stress yield function for aluminum alloy sheets – part I: theory. *International Journal of Plasticity*, 19, 1297-1319, 2003.

Laboratory investigations of horizontal structures with pervious concrete

Kajo Ferić[+], Hrvoje Gotovac[*], Ana Romić[*], Sathish Kumar Veerappan[*], Krste Živković[*]

[+]*Cemex d.o.o., Franje Tuđmana 45, 21000 Split, Kaštel-Sućurac*
E-mail: kajo.feric@cemex.hr

[*]*University of Split, Faculty of Civil Engineering, Architecture and Geodesy, Matice hrvatske 15, 21000 Split, Croatia*
E-mails: {hrvoje.gotovac,aromic,skumarv,kzivkovic}@gradst.hr

Keywords: pervious concrete, laboratory testing, hydrological and mechanical properties of pervious concrete, drainage system

1. Introduction

Urban areas including drainage systems are currently facing the complex effects of climate change, and their respond to the increasingly stringent requirements in rainwater management is important [1], especially for critical public areas like low permeable surfaces: concretes and asphalts. Permeable concrete is one of the environmentally friendly material that can be effectively used to overcome these challenges [2]. The main objective of this research is to develop horizontal systems with pervious concrete that can eliminate or significantly decrease runoff [3]. The mechanical and hydrological properties of the pervious concrete were studied under laboratory conditions to utilize it in a large scale physical model built in the Laboratory for Water Resources and Environmental Engineering in Split. Numerical model was used to verify the test results of the physical model, and the technological concept of future service was generated for a better usage of this material.

2. Methodology and results

2.1. Laboratory investigation

The main variables considered in this present work includes the size of the aggregates and the effect of compaction on the properties of pervious concrete. The concrete samples were compacted using a drop hammer technique developed in the laboratory, and tamping rod in accordance with Eurocode standards. Properties of pervious concrete like compressive strength (cubes), split tensile strength (cylinders), abrasion test with modified LA method (cylinders), and permeability (cylinders) were determined. Table 1 shows the measurements of hydraulic (permeability) and mechanical properties for different pervious concrete mixtures.

Table 1. Results of pervious concrete properties for designed mixtures

Mix ID	Voids (%)	Hardened density (kg/m^3)	Compressive strength, f_c (MPa)	Tensile strength, f_{ct} (MPa)	Abrasion test (Cantabro test) (loss in % of initial mass)	Permeability Coefficient, K (mm/s)
PC1	25.75	1897.63	13.03	1.70	46.7	17.95
PC2	27.9	1812.69	8.92	1.63	100	22.78
PC3	20.6	1946.67	17.02	2.05	29.5	12.71
PC4	22.6	1901.93	12.14	2.03	47.1	16.54
PC5	18.55	2030.07	21.37	2.35	23.1	9.99
PC6	19.1	1921.28	14.12	2.85	91.1	11.24
PC7	27.5	1970.07	14.63	1.40	51.9	23.29
PC8	26.8	1862.42	9.66	1.98	82.5	26.01

Slabs of 1×1x0.2 m were also cast to study the effect of permeability in large scale samples. Those specimens were used as in-situ based, pre-tested samples for larger physical models 4x2x1 m.

2.2. Physical models

Representing the overall system within a controlled urban environment, physical models were built to define the hydrological-hydraulic properties with respect to required mechanical properties. Two selected physical models, named "FM1" and "FM2", are shown in Figure 1. Subgrade (d=40 cm) and subbase (d=25 cm) were the compacted overburden and buffer layer, respectively. The pervious concrete, PC5 (d=20 cm) was chosen based on the preliminary test results, placed and compacted over the subbase. Different approaches were used for drainage system in each model. For FM1 the flow was controlled in the bottom of middle layer (Fig.1 a – yellow pipe) and with blue discharge pipes in reservoir. FM2 model without reservoir in the system, is shown in Figure 1(b). Water drainage and outlet flow was measured through the drainage pipes in every abovementioned layer. The behavior of the system was verified and calibrated by the numerical model to prove the technological concept of the project.

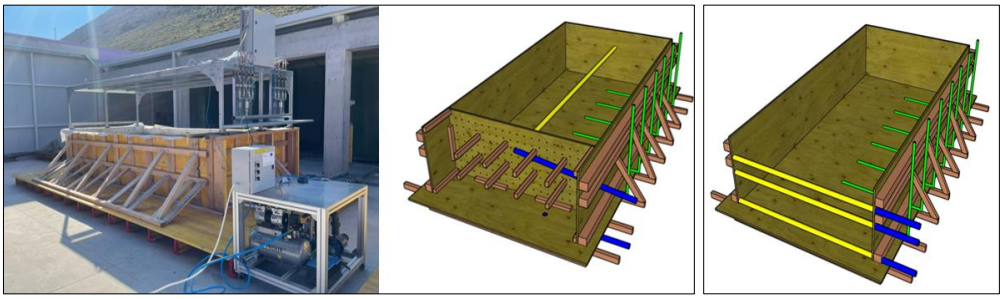

(a) **(b)**

Figure 1. (a) FM1 model with precipitation device and scheme (b) Scheme of FM2 model

2.3. Results and conclusions

In the defined mixtures of pervious concrete, result show that the size of aggregates and the effect of compaction greatly affects the properties of the pervious concrete. Results of physical models showed that pervious concrete possess large discharge capacity for different rainfall values and level of water (related to the groundwater level in reality) in each test set-up. Also, it has been noted that the subbase and subgrade layers affect and contribute to the system capacity and the permeability of the observed concrete surface. These experimental results are calibrated and verified with numerical model (karst flow model by [4]). Finally, the flow model with calibrated unsaturated Van Genunchten and other parameters can serve as technological tool for designing of horizontal pervious concrete pavement systems.

References

[1] Z. Yazdanfar i A. Sharma, Urban drainage system planning and design – challenges with climate change and urbanization: a review, *Water Science & Technology*, pp. 165-179, 2015.

[2] Hung, V.V., Seo, S.-Y., Kim, H.-W., Lee, G.-C., Permeability and Strength of Pervious Concrete According to Aggregate Size and Blocking Material, *Sustainability*, 13, 426, 2021.

[3] P. D. Tennis, M. L. Leming i D. J. Akers, Pervious Concrete Pavements, Portland Cement Association,Skokie, Illinois, and National Ready Mixed Concrete Association, SAD, 2004.

[4] Malenica, L., Gotovac, H., Kamber, G., Simunovic, S., Allu, S., Divic, V., Groundwater Flow Modeling in Karst Aquifers: Coupling 3D Matrix and 1D Conduit Flow via Control Volume Isogeometric Analysis-Experimental Verification with a 3D Physical Model, *Water,* 10, 1787, 2018.

Frequency-Domain Optimization of large Floating Offshore Wind Turbines

Giulio Ferri*, Claudio Borri*, Enzo Marino*

*Department of Civil and Environmental Engineering-University of Florence, Via di Santa Marta 3, Florence, Italy
E-mails: {giulio.ferri,claudio.borri,enzo.marino}@unifi.it

Keywords: Floating Offshore Wind Turbines, Frequency domain model, Platform optimization

1. Introduction

Floating Offshore Wind Turbines (FOWTs) are complex structures composed by slender flexible elements, such as tower, blades and mooring lines, and bluff rigid elements, such as nacelle and floating platform. Due to the multiple fluid-structure interactions, coupled nonlinear, aero-hydro-servo-elastic time-domain tools are fundamental to properly estimate the structural response of such systems. However, optimization-based preliminary designs are fundamental to achieve cost-effective solutions with enhanced structural performances. To this aim, it is crucial to use computationally efficient and sufficiently accurate Frequency-Domain (FD) solvers for coupled aero-hydro-elastic simulations of FOWT. This contribution summarizes the results of an optimization procedure for a 10MW FOWT supported by a semisubmersible platform and moored by catenary cables [1]. An in-house developed FD model is adopted to estimate the response of the FOWT. It is characterized by 6 DoFs, related to the rigid-body platform motions. ANSYS AQWA [2] is adopted to solve the potential flow problems of radiation and diffraction, while FAST v7 [3] is used to estimate rotor blades, tower, and mooring lines contributions to the equation of motion of the system. By solving the linear system for a unit-wave amplitude load, the Response Amplitude Operators (RAOs) of selected DoFs are calculated. The detailed description and the validation of the adopted FD model can be found in [1].The optimizations aim at minimizing the RAO peaks at the eigenfrequency of the platform. Constraints on the maximum admissible displacement of the system, cables and anchors loads are imposed to drive the procedure towards a feasible solution. Results show that optimized configurations can be found with better performances and reduced platform dimensions with respect to the configuration obtained by scaling up the platform geometry designed for a 5MW FOWT.

2. Genetic Algorithm Optimization

The optimization procedures are performed adopting the Genetic Algorithm implemented in MATLAB [4]. At each step, a group of individuals is generated. Then, based on the fitness value, i.e., the objective function, GA repeatedly modifies the population until it evolves towards an optimal solution. The investigated floater concept is a 3-column semisubmersible type with a central column that is an extension of the wind turbine (see Figure 1a), based on the 5MW OC4 DeepCwind FOWT [5]. The geometry is modified to support a reference 10MW WT [6]. Some key geometric parameters of the platform (columns diameter, *d*, platform radius, *r*, and draft, *drf*) are chosen as design variables (see Figure 1b) together with some mooring system-related parameters (cable length, *L*, and anchoring distance, $x_{anch,}$ (see Figure 1c)).

The peaks of the Surge and Pitch FOWT RAOs are considered as objective functions. This means that the optimizations are focused on the minimization of the dynamic amplification of the system response in the proximity of the platform eigenfrequencies. The turbine is considered in parked condition with no wind. This allows to isolate the effects of the substructure (platform and moorings) layout on the response of the FOWT. However, constraints related to the maximum displacements of the system under rated wind speed condition are considered [1] to ensure the correct functioning of the FOWT and to prevent failure of the electric cables connecting the wind farm to land. Also, constraints on the geometry of the catenary cable are imposed.

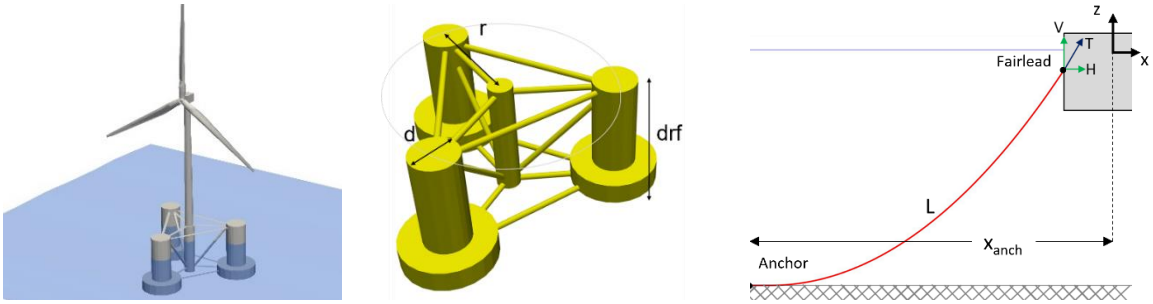

(a) (b) (c)

Figure 1. 5MW OC4 DeepCwind FOWT [5] (a); design variables related to the geometry of the floater (column diameter, *d*, platform radius, *r*, and draft, *drf*) [1]; moorings design variables (x_{anch} and *L*).

4. Results and conclusions

Results of the optimizations are compared with the values scored by an upscaled system (see Figure 2), proving that these the optimized solutions achieve better performances with reduced platform dimensions and mass. Moreover, considering the direct relationship between costs and mass, these results prove the great improvements which can be obtained in the early-stage design phases of FOWTs by adopting efficient optimization procedures.

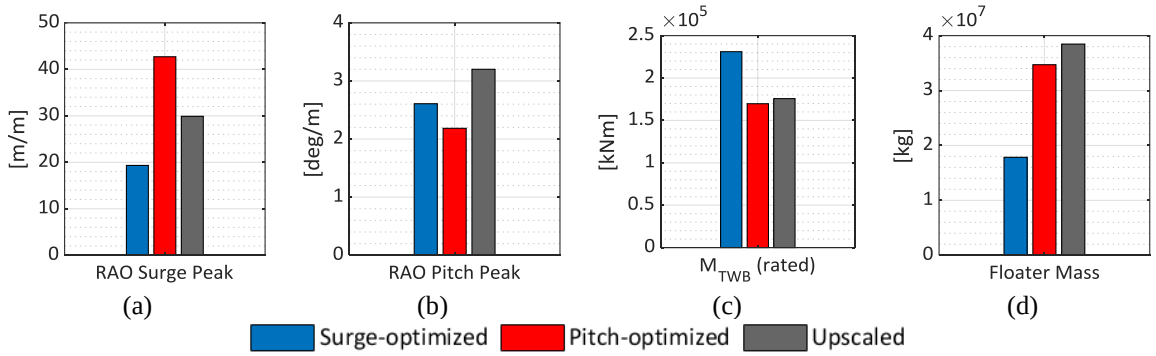

Figure 2. Comparison between the Surge-optimized (blue), the Pitch-optimized (red) and the upscaled (grey) systems: Peak of Surge (a) and Pitch (b) DoFs, Tower-base Bending moment (c) and Floater Mass (d).

References

[1] G. Ferri, E. Marino, N. Bruschi, and C. Borri, "Platform and mooring system optimization of a 10 MW semisubmersible offshore wind turbine," *Renew. Energy*, vol. 182, 2022.

[2] "AQWA User Manual," vol. 15317, no. October, 2012.

[3] J. Jonkman and M. L. Buhl, "FAST User's Guide," vol. 123, no. 6, 2007.

[4] MATLAB, "Optimization Toolbox ™ User ' s Guide R 2014 b," 2014.

[5] A. Robertson and J. Jonkman, "Definition of the Semisubmersible Floating System for Phase II of OC4," no. September, 2014.

[6] M. Borg, M. Mirzaei, and H. Bredmose, "LIFES50+ Deliverable D1.2: Wind Turbine Models for the Design", 2015.

Numerical analyses of laminated glass behaviour in bending under temperature variations

Mirela Galić*, Gabrijela Grozdanić*, Vladimir Divić*, Marko Galić*, Pavao Marović*

**University of Split, Faculty of Civil Engineering, Architecture and Geodesy, Matice hrvatske 15, HR-21000 Split, Croatia*
E-mails: {mirela.galic, gabrijela.grozdanic, vladimir.divic, pavao.marovic}@gradst.hr

Keywords: laminated glass, temperature, numerical analyses, PVB interlayer

1. Introduction

Laminated glass is relatively new structural eco-friendly and recyclable material. Its use like structural element is increasing since it is able to guarantee robustness requirements by improving post-breaking characteristics. Namely, glass is no more only architectural and/or secondary structural element but also bearing structural element. Unfortunately, its brittle nature brings a lot of limits in its use, regarding safety design, limited deformations, and coupling with other building materials. As laminated glass is combination of two different materials, i.e. a minimum of two glass panels which are connected with a thin and soft interlayer, its mechanical properties depend not only on glass but also on the type of interlayer and their coupled behaviour. Generally, as interlayer five different materials can be used: (a) Polyvinil Butyral (PVB); (b) Ethylen Vinil Acetate (EVA); (c) Polyethylene terephthalate + Ethylene Vinyl Acetate (XLAB); (d) Ionoplast, [1] and [2]. Furthermore, the influence of temperature variations on interlayer material and coupled behaviour must not be neglected.

In this paper, we will present some performed numerical analyses of laminated glass behaviour in bending under temperature variations with ANSYS, commercially available finite element software package [3] within two graduation theses [4] and [5] continuing previous research on glass structures exposed to soft body impact [6].

2. Performed numerical analyses

Numerical analyses were performed for two groups of research. In the first performed research [4] the dimensions of laminated glass samples were 900 mm in length and 330 mm in width, with variable cross-sections (6+6 mm, 8+8 mm, 10+10 mm, 10+6 mm and 6+10 mm), and PVB interlayer. The temperatures were 20° C, 40° C and 60° C. In the second performed research [5] the dimensions of laminated glass samples were 470 mm in length and 100 mm in width, with constant cross-sections of 5+5 mm, with variable types and thicknesses of interlayer (EVA 0,38 mm, EVA 0,76 mm, PVB Trosifol BG 15, PVB Saflex DG41, PVB Saflex RB47 Vanceva 9, PVB Saflex RB 71 and Sentry®Glass Ionoplast). The temperatures were 30° C, 40° C and 50° C. All analyses were performed on simple supported beams. Material characteristics of laminated glass panels were taken as: yield tension stress 120 MPa; density 2.500 kg/m^3; Poisson ratio 0,22; and modulus of elasticity 70 GPa. Material characteristics of different types of interlayer depend on temperature level and its variations were taken from literature [7] and [8].

3. Obtained results

The results of the first performed research comprises of distribution of the maximum tensile stresses in the lower glass panel, distribution of the maximum compressive stresses in the upper glass panel, distribution of the maximum tensile and compressive stresses in the interlayer, displacements of the laminated glass panels, slippage between glass and interlayer (no slippage at 20° C, and slippage at 40° C and 60° C), load-displacement curves for different temperatures, and load-stress (tensile and compressive) curves for different temperatures.

The results of the second performed research comprises of distribution of the maximum tensile and compressive stresses in glass panels, shear stresses in different intelayers, displacements of the

laminated glass panels, load-displacement curves for different interlayers, load-displacement curves for different temperatures and load-stress (tensile and compressive) curves for different temperatures.

4. Conclusions

General conclusion can be that the temperature has very important influence on the behaviour of laminated glass panels, primarily on behaviour of the interlayer. Namely, the rise of temperature drastically change material characteristics of interlayer what influence the state of stresses, both tensile and compressive, and displacements. It was interested to note that at different thicknesses of laminated glass panels (i.e. 10+6 mm or 6+10 mm) the increase in stress is always in the thicker panel despite of inside stresses, but the displacements are the same in both situations. According to numerical calculations, comparing three different types of interlayer with the similar thickness (regarding production size) it can be seen that, for constant temperature, laminated glass with Sentry®Glass Ionoplast (0,89 mm) interlayer provides the highest stiffness resulting with lower vertical displacement compared with PVB Saflex DG41 (0,76 mm), PVB Saflex RB47 Vanceva 9 (0,76 mm) and EVA (0,76 mm) interlayers. With increasing interlayer thickness for the Sentry®Glass Ionoplast at lower temperature (up to 20° C) we can notice increasing panel stiffness. But, if the temperature rises over 35° C this effect disappears and increase in thickness brings a slightly higher deflection of the panel. A different trend is observed in the panel with PVB interlayer where it can be seen that at lower temperatures increased thickness of interlayer does not provide any influence on the deflection. For higher temperatures, increase in interlayer thickness shows greater deflection. Higher temperatures bring an increase in deflection and consequently in stress at the bottom panel. This trend is more evident in panels with PVB interlayer.

Acknowledgement

This research is partially supported through project KK.01.1.1.02.0027, a project co-financed by the Croatian Government and the European Union through the European Regional Development Fund - the Competitiveness and Cohesion Operational Programme.

References

[1] Sable, L., Kinsella, D., Kozlowski, M., Influence of EVA, PVB and Ionoplast Interlayers on the Structural Behaviour and Fracture Pattern of Laminated Glass, *International Journal of Structural Glass and Advanced Materials Research*, Issue 3, pp. 62-78, 2019.

[2] Castori, G., Speranzini, E., Structural Analysis of Failure Behaviour of Laminated Glass. *Composites Part B*, Issue 127, pp. 89-99, 2017.

[3] ANSYS ver. 16.2 User Manual, ANSYS Inc. AUTODYN, 2015.

[4] Galić, M., *Numerical analysis of laminated glass element exposed to bending*. University of Split, Faculty of Civil Engineering, Architecture and Geodesy, Split, 2020. (in Croatian)

[5] Šupe, K., Analysis of the influence of the interlayer on the behaviour of laminated glass beams exposed to bending. University of Split, Faculty of Civil Engineering, Architecture and Geodesy, Split, 2021. (in Croatian)

[6] Grozdanić, G., Galić, M., Marović, P., Some Aspects of the Analyses of Glass Structures Exposed to Impact Load, *Coupled Systems Mechanics*, Issue 10, No. 6, pp. 475-490, 2021.

[7] Hana, T., Eliášova, M., Machalická, K., Vokáč, M., Determination of PVB interlayer's shear modulus and its effect on normal stress distribution in laminated glass panels. In: *3rd Int. Conf. on Innovative Materials, Structures and Technologies – IMST 2017*, IOP Conference Series: Materials Science and Engineering, Vol. 251, paper 012076, 8 pages, Riga, 2017.

[8] Bennison, St.J., Qin, M.X.N., Davies, Ph.S., High-performance laminated glass for structurally efficient glazing. In: *Innovative Light-weight Structures and Sustainable Facades*, 12 pages. Hong Kong, 2008.

A Localized Version of the Method of Fundamental Solutions in a Multi-level Context

Csaba Gáspár*

*Széchenyi István University, Egyetem tér 1, H-9026 Győr, Hungary
E-mail: gasparcs@math.sze.hu

Keywords: meshless methods, method of fundamental solutions, localization, multi-level techniques, quadtrees

1. The Method of Fundamental Solutions

Meshless methods have become quite popular because of their simplicity and the unique property that they need neither domain nor boundary mesh or grid structure. Instead, a scattered point set is required on the boundary and/or in the domain of the partial differential equation to be solved.

The Method of Fundamental Solution (MFS) is a special meshless method, which can be applied to a lot of engineering problems, e.g. potential problems or some simple transport problems, Stokes flow problems, Helmholtz problems etc. It produces the approximate solution of the original problem in the following form:

$$u(x) = \sum_{j=1}^{N} \alpha_j \cdot \Phi(x - s_j) \,, \tag{1}$$

where Φ is the fundamental solution of the original differential operator, $\alpha_1, \dots, \alpha_N$ are a priori unknown coefficients, $s_1, \dots, s_N$ are predefined external points (*source points*). The coefficients $\alpha_1, \dots, \alpha_N$ are calculated by enforcing the boundary conditions at some $x_1, \dots, x_M$ *boundary collocation points*. This results in a linear system of equations with *N* unknowns and *M* equations. If the simplest Dirichlet boundary condition is prescribed, this linear system has the form:

$$\sum_{j=1}^{N} \alpha_j \cdot \Phi(x_k - s_j) = u(x_k) =: u_k \qquad (k = 1,2, \dots, M) \,, \tag{2}$$

The numbers *N* and *M* need not be equal. If they differ, a least squares technique or the Singular Value Decomposition can be used.

Though the MFS is a simple and easy-to-program method, it has several disadvantages. First, the fundamental solution must be explicitly known. Some additional problems:

- The location of the source points is not trivial; no optimal arrangement is known;
- The matrix of the system (2) is fully populated;
- Even if the numbers of source and collocation points are equal, the system (2) may be severely ill-conditioned, especially when the sources are located too far from the boundary;
- On the other hand, if they are too close to the boundary, numerical singularities may occur, which increases the error of the approximation, etc.

To overcome these difficulties, a number of special techniques have been developed. A wide class of these methods is based on allowing the source points and boundary collocation points to coincide. This approach has to handle the appearing singular terms in a proper way (regularization, desingularization, see e.g. [1]); moreover, the resulting system remains dense and ill-conditioned. It is also possible to use *several* groups of sources at the same time, the spatial densities of which are decreasing far from the boundary. This idea can be embedded in a multi-level context, which significantly reduces the necessary computational cost. For details, see [2].

2. Techniques based on localization

More recently, a different approach based on some localization techniques has been developed (see [3] for details). It can be considered as a combination of the MFS with classical finite difference schemes. These techniques require a finite point set in the domain and along the boundary as well.

The idea behind the technique is to express a value of the approximate solution at an inner point by the values at the *nearest neighbors* only, using MFS-formulation based on some fictitious source points. This results in a *sparse* system of linear equations, which makes it possible to significantly reduce the computational complexity preserving the good accuracy of the MFS. The idea has been applied to various problems, such as transient convection-diffusion-reaction equations see e.g. [4].

3. Localization in quadtree context

In this talk, a modified localization approach is proposed. In contrast to the localization method of [2], where the inner nodes was defined in a more or less random way, here a quadtree (octtree in 3D) algorithm is used to define inner nodes, similarly to the technique detailed in [5]. The quadtree grid generation is controlled by the boundary of the original domain and produces a non-equidistant, non-uniform cell system, the spatial resolution of which becomes fine in the vicinity of the boundary and remains coarse in the middle of the domain, as can be seen in Figure 1. This technique makes it possible to significantly reduce the number of inner nodes, thus, to reduce the number of the introduced unknowns; besides, it results in a sparse linear system. The localization technique is slightly different from that of [3], but is still based mainly on the MFS.

This quadtree-based localization technique can be embedded in a multi-level context in a natural way. The coarse and fine levels can be defined by the quadtree subdivision algorithm. The multi-level character can speed up the whole algorithm, and makes it possible to use efficient iterative solvers. Moreover, the solutions of large and ill-conditioned linear systems are completely avoided.

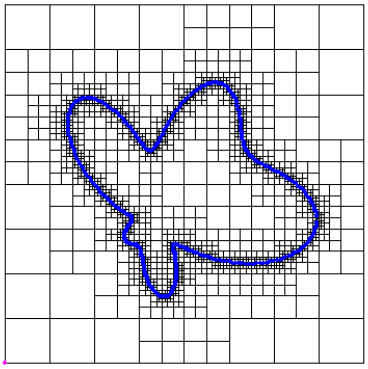

Figure 1. Quadtree cell system generated by the boundary of an amoeba-shaped domain

References

[1] Šarler, B., Solution of potential flow problems by the modified method of fundamental solutions: formulations with the single layer and the double layer fundamental solutions, *Engineering Analysis with Boundary Elements* 33, pp. 1374-1382, 2009.

[2] Gáspár, C., A multi-level technique for the method of fundamental solutions without regularization and desingularization. *Engineering Analysis with Boundary Elements* 103, pp. 145-159, 2019.

[3] Fan, C.M., Huang, Y.K., Chen, C.S., Kuo, S.R., Localized method of fundamental solutions for solving two-dimensional Laplace and biharmonic equations. *Engineering Analysis with Boundary Elements* 101, pp. 188–197, 2019.

[4] Liu, S., Li, P.W., Fan, C.M., Gu, Y., Localized method of fundamental solutions for two- and three-dimensional transient convection-diffusion-reaction equations. *Engineering Analysis with Boundary Elements* 124, pp. 237–244, 2021.

[5] Gáspár, C., Application of quadtrees in the method of fundamental solutions using multi-level tools. In: Alves C., Karageorghis A., Leitão V., Valtchev S., eds., *Advances in Trefftz Methods and Their Applications*, pp. 41-57. SEMA SIMAI Springer Series, vol. 23. Springer, Cham. 2020.

Analytical solutions of internal moments in helical girders and comparison to numerical solutions

Josip Gavran*, Darko Damjanović+, Dražan Kozak+, Pejo Konjatić+

*ĐĐ Specijalna vozila d.d., The Design and Development Department
Ul. Dr. Mile Budaka 1, HR-35000 Sl. Brod, Croatia
E-mail: jogavran@ddsv.hr

+University of Slavonski Brod, Mechanical Engineering Faculty in Slavonski Brod
Trg Ivane Brlić-Mažuranić 2, HR-35000, Slavonski Brod, Croatia
E-mail: ddamjanovic@unisb.hr, dkozak@unisb.hr, pkonjatic@unisb.hr

Keywords: helical girder, spiral beam, morgan method, finite element method

1. Introduction

Helical girders being a 3D structure presents a problem when analytical solutions are concerned. Some researches such as A. Engle (1955.) and V. R. Bergman (1956.) offered a solution by idealizing the structure as a 2D problem, but the results were highly conservative and inaccurate. A. Holmes (1957.), V. A. Morgan and A. C. Scordelis (1960.) presented a solution to internal moments by observing the structure as a 3D model [1-2]. Morgan's method was shown to gain most reliable results when talking about steel girders and although his approach seems most sensible compared to others, it is computationally demanding.

2. Analytical solution

Figure 1 shows the helical girder from top view. At mid-span, due to symmetry all but two redundants cancel out: vertical moment M and horizontal shear force H. Morgan [3] derived the expressions for internal reactions in terms of angle distance θ counting from the mid-span, but the redundant reactions M and H were left as unknowns.

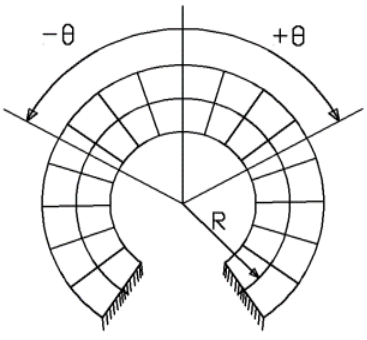

Figure 1. Helical girder [4]

These redundant reactions were computed using Castigliano's second theorem. Because of the symmetry at mid-span, angular displacement around horizontal axis in the section and horizontal deflection are 0. This is important since the reactions M and H act in these directions respectively.

$$\frac{\partial U}{\partial H}=\int_0^{\beta}\frac{M_{\mathrm{v}}}{2EI_{\mathrm{r}}}\frac{\partial M_{\mathrm{v}}}{\partial H}ds+\int_0^{\beta}\frac{M_{\mathrm{h}}}{2EI_{\mathrm{s}}}\frac{\partial M_{\mathrm{h}}}{\partial H}ds+\int_0^{\beta}\frac{T}{2GI_{\mathrm{p}}}\frac{\partial T}{\partial H}ds=0 \qquad (1)$$

$$\frac{\partial U}{\partial M}=\int_0^{\beta}\frac{M_{\mathrm{v}}}{2EI_{\mathrm{r}}}\frac{\partial M_{\mathrm{v}}}{\partial M}ds+\int_0^{\beta}\frac{M_{\mathrm{h}}}{2EI_{\mathrm{s}}}\frac{\partial M_{\mathrm{h}}}{\partial M}ds+\int_0^{\beta}\frac{T}{2GI_{\mathrm{p}}}\frac{\partial T}{\partial M}ds=0 \qquad (2)$$

Conditions above (1) and (2) were further simplified but the solving process was still long and tiresome.

An example was carried out using the realistic model of the helix with I-beam section. Following parameters were used: radius of the girder R = 1,5m, the total span angle of the girder 2β = 270°, height h = 2,8m and distributed load q = 6,5 kN/m. Complex expressions for M and H were solved and substituted into Morgan's expressions for internal reactions.

3. Numerical solution

Obtained analytical results are compared with numerical solution using Finite Element Method, with the same parameters as in analytical approach using beam elements. Slight problem occurred with the mesh as the beam elements wouldn't follow the helical path perfectly in two directions, causing the small spikes in results, but the solution is satisfactory for comparison with analytical one.

Figure 2 shows the distribution of moments with the respect to span angle θ. It is interesting to note that the horizontal moments are in general much larger than vertical moments. It is also a strong indication that the 2D mathematical models which are commonly used to solve these types of problems simply don't work with helical girders as they only consider vertical moment and the torsion.

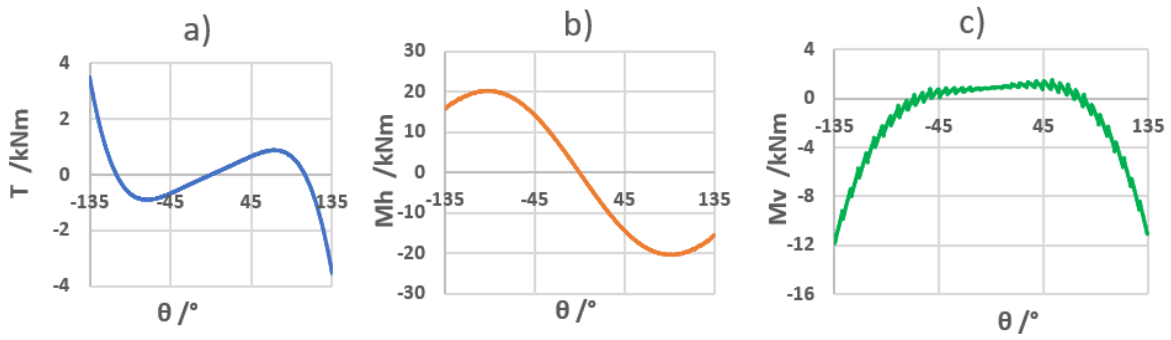

Figure 2. Distribution of internal moments
(a) Torsion, b) Horizontal moment, c) Vertical moment)

4. Conclusions

Vertical moment M_v compared very well with the analytical solution with only 2% margin of error, torsion moment T within the 10% error and horizontal moment M_h in analytical solution was almost 20% higher at the fixed end of the girder and gradually equalized towards the mid-span. Error that big was most likely the result of the simplifying Castigliano's conditions where the influence of the horizontal displacement was ignored.

It can be also concluded that the 2D mathematical models found in literature which are commonly used to solve these types of problems simply don't work well with helical girders as they only consider vertical moment and the torsion.

References

[1] Wadud, Z., *A simple design approach for helicoidal stair slabs*. Dhaka, University of Engineering and Technology, 2002.

[2] Modak, S., *A design rationale for helicoidal stair slabs*. Dhaka, University of Engineering and Technology, 1991.

[3] Morgan, V. A., *Comparison of Analysis of Helical Staircases*, London, Concrete and Construction Engineering, Vol. 55, No. 3, 1960., pp 127-132

[4] Gizaw, Y., Analysis Aid Preparation for Self Supporting Fixed Ended Helical Stairs. Addis Ababa, Addis Ababa University, 2015.

[5] Bangash, M.Y.H., Bangash T., *Staircases – Structural analysis and design*. Rotterdam, A. A. Balkema, 1999.

A Pure Bending Capable Three-Node Membrane Finite Element with True Rotations

Marin Grbac*, Dragan Ribarić*

*University of Rijeka, Faculty of Civil Engineering, Radmile Matejčić 3, 51000, Rijeka, Republic of Croatia
E-mails: {marin.grbac,dragan.ribaric}@uniri.hr

Keywords: finite element method, membrane finite elements, rotational degrees of freedom, true rotations, pure bending

1. Introduction

For finite element analyses of plane elasticity problems, Turner *et al.* [1] formulated the first isoparametric three-node finite element known today as the CST (Constant Strain Triangle) element. Due to its simplicity and reliability, the CST element is still widely employed today, even though its performance is generally not on a desirable level. In order to improve its performance, many researches resorted to introducing (drilling) rotations as additional unknown parameters. Although that is not consistent with the theory since rotations are dependent on displacements, it is not actually against the finite element concept. Anyhow, difficulties were encountered in the early attempts of such an approach. One of the main difficulties is linking nodal rotations to the element side displacements, which is very well explained in Ref. [2].

First successful realisation of introducing rotations as additional unknown parameters was presented independently by Allman [3] for plane elasticity problems, and by Carpenter *et al.* [4] for general shell problems. The authors introduced rotations with the quadratic interpolations of the displacement fields in a way known today as the linked interpolation. However, these finite elements possess the so-called spurious zero-energy mode, and generally, the rotational parameters are not representing true rotations at the nodes.

In finite element analyses, it is convenient to employ a membrane element with true rotations since the analyses would yield real nodal rotations and because such an element has an inherent ability to carry in-plane moments correctly. Additionally, if such an element is the in-plane part of the shell finite element formulation, it would secure the non-singularity of the global stiffness matrix in all cases and provide a full compatible connection with other finite elements.

Although many effective three-node membrane finite elements with drilling rotations have been developed so far, no element has been found capable of achieving the exact response for an arbitrary pure bending problem. This would be of a major importance in the finite element analyses (see Ref. [5]). In contrast, lowest-order linked interpolation beam and plate finite elements have such a capacity. Motivated by that, formulation for such a membrane element has been sought, and ultimately, one has been found which turns to be exact for specific cases only.

2. New finite element

The finite element formulation is given in a standard displacement form. The displacement fields are quadratic polynomials written in the area coordinate system in which the linear coefficients are nodal displacements, and the quadratic coefficients are nonconforming and include both nodal displacements and nodal rotations, in addition to the geometric parameters and Poisson's ratio. The displacement fields satisfy classical theory of plane elasticity definition of rotation in every point inside the element domain, which makes the finite element analysis yield true nodal rotations. Furthermore, the finite element always has a correct rank, *i.e.*, it has no spurious zero-energy mode.

The finite element is also capable of achieving the exact response for a pure bending problem of a simple beam described in Fig. 1., regardless of the Poisson's ratio and the mesh regularity. However, this is only the case if the beam is directed in x or y global axis, *i.e.*, if the beam is rotated by multiples of $\pi/2$. For the Timoshenko beam problem, the new element performs exceptionally well, on regular

(R) or distorted (D) mesh, while its performance is somewhat lower for the Cook's membrane problem, as shown in Table 1.

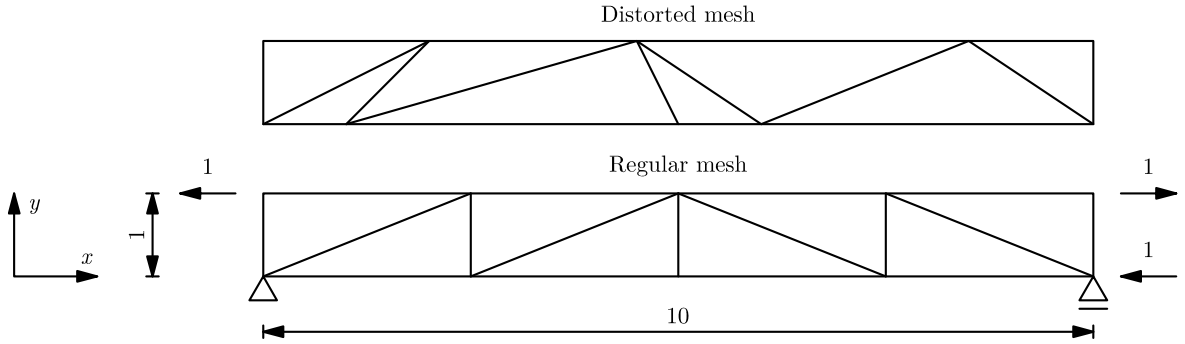

Figure 1. Pure bending of a simple beam

Table 1. Vertical tip displacement for Timoshenko beam (TB) and Cook's membrane (CM) problems

TB	Allman [3]		New FE		**CM**	Allman [3]		New FE	
Mesh	$\nu = 0.25$	$\nu = 0.499$	$\nu = 0.25$	$\nu = 0.499$	Mesh	$\nu = 1/3$	$\nu = 0.499$	$\nu = 1/3$	$\nu = 0.499$
4x1 (D)	0.24312	0.23260	0.34847	0.35228	2x2	20.084	19.884	14.826	14.230
8x2 (D)	0.31884	0.30639	0.35803	0.35620	4x4	22.708	22.630	19.538	18.791
4x1 (R)	0.27282	0.25061	0.35133	0.35399	8x8	23.611	23.694	22.331	22.005
8x2 (R)	0.34007	0.32215	0.36349	0.35095	16x16	23.872	24.044	23.460	23.488
16x4 (R)	0.35466	0.34726	0.35741	0.35239	32x32	23.941	24.154	23.816	23.986
32x8 (R)	0.35608	0.35421	0.35579	0.35454	64x64	23.959	24.191	23.922	24.141
Exact	0.35533	0.35865	0.35533	0.35865	128x128	23.965	24.205	23.953	24.190

3. Conclusions

A new three-node membrane finite element with true rotations is developed. It is capable of achieving exact response for specific cases of pure bending problems regardless of the Poisson's ratio and the mesh regularity. The element exhibits great resistance to mesh distortions and handles (nearly) incompressible materials with no issues. Additionally, it has no spurious zero-energy mode. However, there is a discrepancy in performance between some numerical examples which requires further numerical investigation.

4. Acknowledgements

Financial support of the Croatian Science Foundation, project IP-06-2016-4775: "Assumed strain method in finite elements for layered plates and shells with application on layer delamination problem - ASDEL", is acknowledged.

References

[1] Turner, M. J., Clough, R. W., Martin, H. C., Topp, L. J., Stiffness and deflection analysis of complex structures. *Journal of the Aeronautical Sciences*, 23:9, 805-823, 1956.

[2] Bergan, P. G., Felippa, C. A., A triangular membrane element with rotational degrees of freedom. *Computer Methods in Applied Mechanics and Engineering*, 50:1, 25-69, 1985.

[3] Allman, D. J., A compatible triangular element including vertex rotations for plane elasticity analysis. *Computers & Structures*, 19:1-2, 1-8, 1984.

[4] Carpenter, N., Stolarski, H., Belytschko, T., A flat triangular shell element with improved membrane interpolation. *Communications in Applied Numerical Methods*, 1:4, 161-168, 1985.

[5] Felippa, C. A., A study of optimal membrane triangles with drilling freedoms. *Computer Methods in Applied Mechanics and Engineering*, 192:16-18, 2125-2168, 2003.

Finite element analysis of the pure bending problem in non-linear micropolar elasticity

Sara Grbčić Erdelj*, Gordan Jelenić*

*University of Rijeka, Faculty of Civil Engineering, Croatia
E-mails: {sara.grbcic,gordan.jelenic}@uniri.hr

Keywords: micropolar theory, pure bending, geometrical nonlinearity

1. Introduction

In the micropolar continuum theory, in addition to the displacement field of the classical continuum theory, there exists an independent *microrotation field*, representing the orientation of a materialpoint. This alternative continuum theory is able to capture the so-called *size-effect* phenomenon, manifested in the often-observed increased stiffness of smaller specimens. Since the linear micropolar model is not always appropriate for a realistic description of a structural response, there exists a need for the development of nonlinear micropolar models. In the geometrically nonlinear elasticity, the pure bending state of a beam represents a well-known benchmark problem and in this work a numerical analysis of this problem is presented and compared against the analytical solutions in micropolar elasticity.

2. Nonlinear micropolar analytical model

2.1. Equilibrium equations in material description

Strong form of the equilibrium equations in the material description is given as

$$\mathrm{DIV}(\mathbf{QB}) + \mathbf{P}\mathrm{v} = \mathbf{0} \quad \text{and} \quad \mathrm{DIV}(\mathbf{QG}) + \mathrm{ax}\left(\mathbf{QBF^T} - \mathbf{FB^TQ^T}\right) + \mathbf{M}\mathrm{v} = \mathbf{0}, \tag{1}$$

with the corresponding boundary conditions

$$(\mathbf{QB})\mathbf{N} = \mathbf{P}\mathrm{s} \text{ i } (\mathbf{QG})\mathbf{N} = \mathbf{M}\mathrm{s}, \tag{2}$$

where $\mathbf{Q}$ represents the microrotation tensor belonging to the so-called special orthogonal SO(3) Lie group (i.e. $\mathbf{Q^{-1}} = \mathbf{Q^T}, \det\mathbf{Q} = +1$ i $\mathbf{Q} = \exp\widehat{\boldsymbol{\varphi}}$,) where $\widehat{\boldsymbol{\varphi}}$ is a skew-symmetric tensor belonging to the so(3) Lie algebra. Tensor $\mathbf{F}$ is the deformation gradient tensor, while tensors $\mathbf{B}$ and $\mathbf{G}$ represent the Biot-like stress and couple-stress tensor, respectively. Vectors $\mathbf{P}_\mathrm{v}$, $\mathbf{M}_\mathrm{v}$, $\mathbf{P}_\mathrm{s}$, $\mathbf{M}_\mathrm{s}$ represent body and surface loadings per unit of undeformed volume/area.

2.2. Nonlinear kinematic equations

The nonlinear kinematic equations are

$$\mathbf{E} = \mathbf{Q^T F} - \mathbf{I}, \ \mathbf{K} = -\frac{\mathbf{1}}{\mathbf{2}}\boldsymbol{\varepsilon}\colon\left(\mathbf{Q^T}\mathrm{GRAD}\mathbf{Q}\right), \tag{3}$$

where tensor $\mathbf{E}$ represents the Biot-like strain tensor, owing to its resemblance to the standard Biot strain tensor in classical elasticity. Correspondingly, $\mathbf{K}$ represents the Biot-like curvature tensor, while $\boldsymbol{\varepsilon}$ is Ricci's alternation tensor.

2.3. Constitutive equations

In this work we focus on the geometrically non-linear effects and keep the constitutive equations linear, which, in the tensor form read

$$\mathbf{B} = \lambda(\mathrm{tr}\mathbf{E})\mathbf{I} + (\mu+\nu)\mathbf{E} + (\mu-\nu)\mathbf{E^T} \quad \text{and} \quad \mathbf{G} = \alpha(\mathrm{tr}\mathbf{K})\mathbf{I} + (\beta+\gamma)\mathbf{K} + (\beta-\gamma)\mathbf{K^T}, \tag{4}$$

with λ and μ as the Lame constants and ν, α, β and γ as the additional material parameters taking place in micropolar elasticity. More detail considering these parameters and the geometrically non-linear micropolar model in general may be found in [2].

3. Non-linear cantilever pure bending problem in micropolar elasticity

The pure-bending state of a beam is a state in which an applied bending moment produces only normal cross-sectional stresses providing a vanishing stress resultant and the axis of the beam is bent into a circular curve. The linear micropolar analytical solution for a pure bending problem is given in [1], where it is observed that the bending stiffness is increased by a certain factor with respect to the classical-elasticity solution. In order to describe a deformed state of the beam exhibiting large displacements and large rotations, in [2] a nonlinear generalisation of the linear micropolar pure-bending solution has been presented, which is applicable to thin specimens, where the through-the-thickness normal stresses cannot significantly develop. A closed-form solution of the pure bending problem in a non-linear micropolar elastic continuum applicable to specimens of finite thickness has been derived in [3].

In this work a numerical analysis of both thin and thick cantilever beams subject to pure bending will be presented and compared to the analytical solutions derived in [2] and [3] (see Fig. 1).

Figure 1. Undeformed and deformed configuration of a thin cantilever beam subject to pure bending

4. Conclusions and future work

The finite elements derived in [2] are shown to converge to the nonlinear generalization of the linear micropolar pure-bending solution, valid for thin beams. In order to capture the softening effect present in thick beams [3] further numerical analysis using the derived finite elements will be performed and compared against the analytical solution given in [3].

Acknowledgements

This work has been financially supported by the Croatian Science Foundation research project "Fixed-Pole Concept in Numerical Modelling of Cosserat Continuum" (HRZZ-IP-2018-01-1732) and the University of Rijeka research grant "Computational and Experimental Procedures for Assessment of Material Parameters in Cosserat's Continuum" (uniri-tehnic-18-248 1415).

References

[1] Gauthier, R.D., Jahsman, W.E., A quest for micropolar elastic constants. *Journal of Applied Mechanics* 42(2), 369–374, 1975.

[2] Grbčić Erdelj, S.; Jelenić, G., Ibrahimbegović, A., Geometrically non-linear 3D finite-element analysis of micropolar continuum, *International Journal of Solids and Structures*, 202, 745-764, 2020.

[3] Jelenić, G., Pure bending in non-linear micropolar elasticity, *International Journal of Mechanics and Materials in Design*, 18, 243–265 (2022)

Computational modelling of various journal bearings and related software implementation

Michal Hajžman*, Jan Rendl+, Luboš Smolík+, Pavel Polach+, Štěpán Dyk+, Miroslav Byrtus*

* *Department of Mechanics, Faculty of Applied Sciences, University of West Bohemia. Univerzitní 8, 301 00 Pilsen, Czech Republic.*
E-mail: {mhajzman,mbyrtus}@kme.zcu.cz

+ *New Technologies for the Information Society, Faculty of Applied Sciences, University of West Bohemia. Univerzitní 8, 301 00 Pilsen, Czech Republic.*
E-mails: {rendlj,carlist,ppolach,sdyk}@ntis.zcu.cz

Keywords: dynamics, rotor, journal bearing, Reynolds equation, numerical solution

1. Introduction

Radial journal bearings are widely used in rotating machinery to support high-speed rotating parts with high radial loads and can be found in many applications, from large rotating systems such as turbomachinery to small turbochargers in combustion engines. Fluid film bearings are generally characterized by low friction behaviour, low wear and mainly efficient vibration-damping capabilities. However, the fluid film journal bearings are also known for fluid-induced instability, which causes undamped self-excited vibrations of a supported rotating machine. For this reason, the process of journal bearings design has to be supplemented by suitable computational approaches and dedicated software tools.

This paper deals with the modelling approaches intended to journal bearing dynamic behaviour. First, the general mathematical model for several types of journal bearings [1] (see Figure 1) is presented. Further, the solution methodology and successive software implementation will be described together with possible applications.

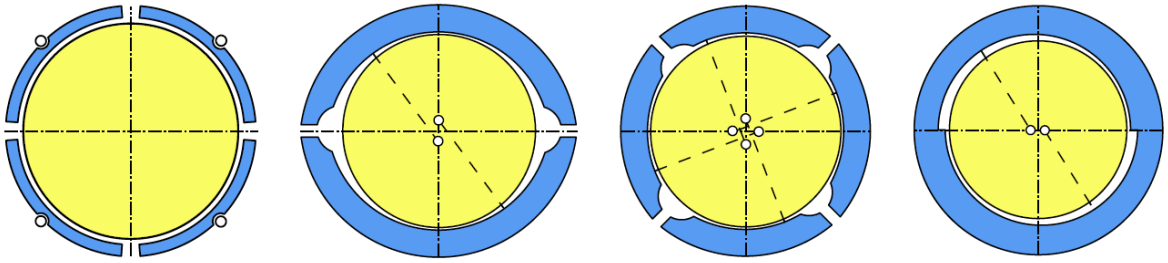

Figure 1. Various types of journal bearings

2. Mathematical model of a general journal bearing

A symmetric flexible rotor generally supported on the tilting pad journal bearings can be decomposed into mutually interacting subsystems – a rotor and movable pads. Equations of motion of such a system can be expressed in the block matrix form as follows

$$\begin{bmatrix}\mathbf{M}_\mathrm{r} & \mathbf{0}\\ \mathbf{0} & \mathbf{M}_\mathrm{p}\end{bmatrix}\begin{bmatrix}\ddot{\mathbf{q}}_\mathrm{r}\\ \ddot{\mathbf{q}}_\mathrm{p}\end{bmatrix}+\begin{bmatrix}\mathbf{B}_\mathrm{r}+\omega\mathbf{G}_\mathrm{r} & \mathbf{0}\\ \mathbf{0} & \mathbf{0}\end{bmatrix}\begin{bmatrix}\dot{\mathbf{q}}_\mathrm{r}\\ \dot{\mathbf{q}}_\mathrm{p}\end{bmatrix}+\begin{bmatrix}\mathbf{K}_\mathrm{r}+\omega\mathbf{C}_\mathrm{r} & \mathbf{0}\\ \mathbf{0} & \mathbf{0}\end{bmatrix}\begin{bmatrix}\mathbf{q}_\mathrm{r}\\ \mathbf{q}_\mathrm{p}\end{bmatrix}=\begin{bmatrix}\mathbf{f}_{\mathrm{g,r}}\\ \mathbf{f}_{\mathrm{g,p}}\end{bmatrix}+\begin{bmatrix}\mathbf{f}_\mathrm{un}\\ \mathbf{0}\end{bmatrix}+\begin{bmatrix}\mathbf{f}_{\mathrm{c,r}}\\ \mathbf{f}_{\mathrm{c,p}}\end{bmatrix}, \tag{1}$$

where subscripts *r* and *p* correspond to rotor and pads subsystems. Vectors $\mathbf{q}_\mathrm{r}$ and $\mathbf{q}_\mathrm{p}$ are vectors of generalized coordinates. Matrices $\mathbf{M}_\mathrm{r}$, $\mathbf{B}_\mathrm{r}$, $\mathbf{G}_\mathrm{r}$, $\mathbf{K}_\mathrm{r}$, $\mathbf{C}_\mathrm{r}$ are constant mass, damping, gyroscopic effects,

stiffness and circulation matrices of the rotor. Matrix $\mathbf{M}_p$ incorporates the mass properties of the pads. Each subsystem is subjected to a gravitational load $\mathbf{f}_g$. The rotor can be excited by out-of-balance forces respected in vector $\mathbf{f}_{un}$. Mutual interaction of the subsystems is described by coupling forces $\mathbf{f}_{c,r}$ and $\mathbf{f}_{c,p}$ dependent on generalized coordinates and generalized velocities. The coupling forces involve hydrodynamic forces generated in oil films, coupling forces between the pads and the ground and elastic forces due to contacts between the subsystems.

The hydrodynamic forces are the most complex forces in the model arising from the solution of the Reynolds equation [2]. It is a partial differential equation introduced on a particular domain for unknown pressure. The equation is derived under assumptions that are fulfilled for various journal bearings in common modes of operation. The pressure solution, which could be obtained numerically or analytically, determines the forces in the equations of motion. These forces are highly nonlinear. However, they can be linearized for fundamental analysis of journal bearing dynamic characteristics.

The presented mathematical model of the journal bearing is general and models of particular bearings (from Figure 1) can be obtained by simply omitting pad subsystems that are not present in the investigated system. Another modification is in the gap definition respecting real bearing shell geometry (i.e. cylindrical, lemon, multi-lobe etc.) for the Reynolds equation solution.

3. Software implementation and application

The whole modelling methodology was implemented in the MATLAB environment into several modules [3]. The Reynolds equation is numerically solved using the finite difference method [2]. The equations of motion could also be solved numerically by MATLAB solvers for sets of ordinary differential equations. The hydrodynamic forces are solved in each time step of the numerical integration.

The software can perform the static analysis, system stability assessment and simulations in the time domain of the rotor response to the harmonic excitation due to out-of-balance force and transient simulations for run-up and coast-down operations. Simulated responses are analyzed using the following tools: threshold speed detection, bifurcation diagrams, fast Fourier transform, phase portraits and Poincaré maps [3].

The software was successfully applied to several types of bearings. Obtained software results were validated for fixed-profile journal bearings and tilting pad journal bearings with reference data in research publications. The cylindrical bearing and textured bearing models were validated with experimental measurements [3].

4. Conclusions

The computational modelling approach for the dynamical analysis of journal bearings with hydrodynamic lubrication is presented in this paper. It is based on rigid body dynamics coupled with the solution of the Reynolds equation by the finite difference method. In-house software based on the presented approach was implemented in the MATLAB environment. It is helpful for various analyses evaluating journal bearing performance, including comprehensive studies on nonlinear dynamics of tilting pad journal bearings [4].

This research work was supported by the Czech Science Foundation project 22-29874S.

References

[1] Someya T., *Journal-Bearing Databook*, Springer-Verlag, Berlin, 1989.

[2] Stachowiak, G.W., Batchelor A.W., *Engineering Tribology*, Butterworth-Heinemann, Boston, 2014.

[3] Rendl J., *Nonlinear Dynamics of Rotating Systems with Journal Bearings*. PhD Thesis, University of West Bohemia, Pilsen, 2021.

[4] Rendl J., Dyk Š., Smolík L., Nonlinear dynamic analysis of a tilting pad journal bearing subjected to pad fluttering. *Nonlinear Dynamics*, 105, 2133-2156, 2021.

Modelling of E-clutch axial dynamics based on experimentally characterized clutch component stress-strain characteristics

K. Haramina*, N. Kranjčević*, M. Hoić*, J. Deur*, A. Tissot+

*University of Zagreb, Faculty of Mechanical Engineering and Naval Architecture
Ivana Lučića 5, HR-10002 Zagreb, Croatia
E-mails: {krunoslav.haramina, nenad.kranjcevic,matija.hoic,josko.deur}@fsb.hr

+Ford-Werke GmbH, Cologne, North Rhine-Westphalia, Germany
E-mail: atissot1@ford.com

Keywords: E-clutch, experimental identification, modelling, validation

1. Introduction

Lumped-parameter E-clutch axial dynamics model was proposed in [1] and parameterized based on experimental identification of input-output characteristics. In this paper, stress-strain characteristics of individual components of disassembled clutch are characterized by using a manually powered spindle-based test rig. The obtained characteristics are firstly used to parameterize the initial, simplified model. While the experimental validation results show satisfactory prediction of the clutch torque static curve, prediction of normal force static curve is worse, thus indicating a potential for further model improvements. Therefore, new, more detailed versions of model containing individual component stress-strain characteristics are gradually proposed and experimentally validated. The validation results indicate considerable improvements in normal force static curve prediction accuracy.

2. Description of E-clutch system

The considered E-clutch system comprises two distinctive (and mechanically separable) subsystems: a hydrostatic-type actuator driven by an electric servomotor and a traditional single-friction plate, normally closed dry clutch assembly. The clutch actuator model has been proposed and experimentally validated in [1], while the focus of this paper is on precise, lumped-parameter clutch axial dynamics modeling.

3. Test rig

The clutch test rig [1] used for parametrization of the actuator and clutch dynamics includes a driving servomotor which transmits the power via a telemetric torque sensor to the DMF and the clutch mounted in the original bell housing. The friction plate is mounted on the fixed transmission input shaft (i.e. friction plate does not rotate). The hydrostatic actuator and release bearing are mounted in the same way as on the real transmission. Following the completion of clutch characterization experiments on the full clutch test rig, the clutch was disassembled, and the individual clutch components were experimentally characterized by using the equipment and procedure described in [1]. The obtained stress-strain characteristics have been used to parameterize different versions of clutch axial dynamics models proposed.

4. Proposed models

The experimental validation results shown in Fig. 1 indicate that the initial, low-order model [1] (Model 0), when properly parameterized, can predict the clutch torque static curve.

However, the accuracy of normal force static curve is relatively low. When introducing more degrees of freedom, related to individual component stress-strain curves, the overall modeling accuracy increases. The best accuracy is obtained for the most-complex model shown in Fig. 2 (Model 4), which precisely predict both static curves.

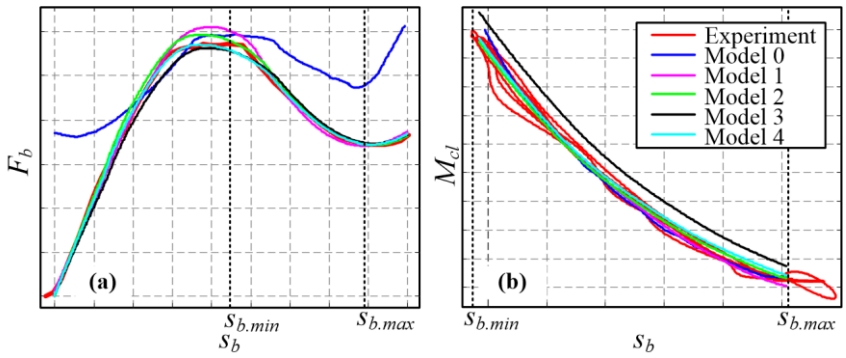

Fig. 1. Results of experimental validation of proposed clutch axial dynamics models: a) Force on release bearing vs. release bearing position, b) Clutch torque vs. release bearing position.

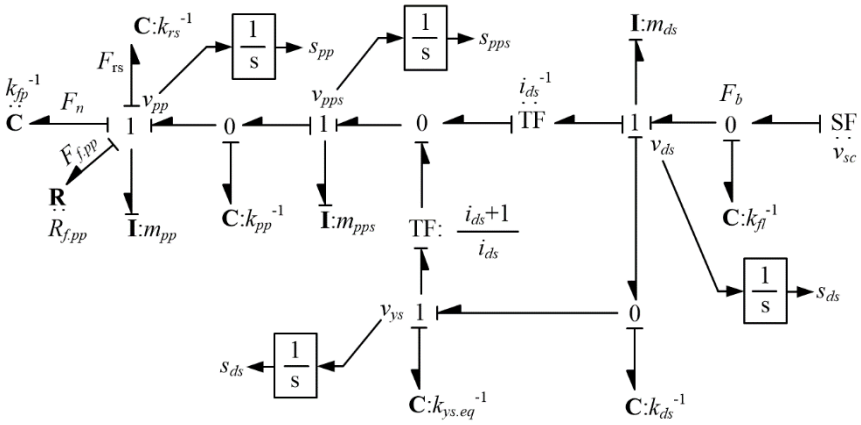

Fig. 2. Bond graph of final clutch axial dynamics subsystem model (Model 4).

5. Conclusion

The previously proposed simplified clutch axial dynamics model has been gradually extended in four steps, thus resulting in four newly proposed lumped-parameter models. All newly proposed models show improvements in prediction of force at the clutch release bearing. The fourth, most detailed model shows the best prediction of both release bearing force and clutch torque compared to other models presented and is thus considered as a basis for future work.

References

[1] Hoić M, Hrgetić, M, Deur J, Tissot, A. Design of a test rig in support of E-clutch dynamics characterization, modelling, and control, Powertrain Modelling and Control Conference PMC 2018, Loughborough, UK, 2018.

Modelling of synchronizer dynamics for dual clutch automatic transmission

K. Haramina*, M. Hoić*, J. Deur*, N. Kranjčević*

*University of Zagreb, Faculty of Mechanical Engineering and Naval Architecture
Ivana Lučića 5, HR-10002 Zagreb, Croatia
E-mails: {krunoslav.haramina, matija.hoic, josko.deur, nenad.kranjcevic}@fsb.hr

Keywords: synchronizer, modelling, dual-clutch transmission

1. Introduction

Paper proposes a model of axial and rotational dynamics of a synchronizer. The proposed model would be useful for transmission design and control strategy development. It may be especially beneficial for dual-clutch based transmissions where engagement duration of a synchronizer can be crucial for successful shifting process [1]. The engagement of synchronizer occurs in five phases, each with different dynamics effects. Therefore, detailed synchronizer dynamics model is needed for engagement process prediction purposes.

2. Description of synchronizer structure and engagement process

Borg-Warner system single-taper synchronizer is used herein. The synchronizer consists of: (i) idler gear with selector teeth and friction taper running on bearings; (ii) synchronizer ring with counter taper and locking teeth; (iii) synchronizer body with external toothing; (iv) synchronizer sleeve with internal toothing, and (v) preload system [2].

Synchronizer engagement can be divided into five phases. In phase 1 initial actuating force results in contact of friction surfaces of the synchronizer ring and idler gear which causes the rotation of the ring into locking position. In phase 2, the synchronizer sleeve contacts the locking teeth of the ring which are angled in axial direction. The angle ensures that the ring remains in locking position during synchronization phase (this way the sleeve teeth cannot reach the selector gear teeth until the speed is synchronized to avoid damage under the torque of the main motor). The axial force is now transferred to the synchronizer ring which results in the contact of the conical friction clutch. The generated friction torque results in almost full synchronization of speeds of the idler gear and the sleeve. In phase 3 synchronizer ring rotates to unlocked position due to diminishing synchronization torque. The sleeve now passes over the synchronizer ring toward the selector teeth on idler gear. In phase 4 the indexing between synchronizer sleeve and selector teeth occurs which results in torque which conduct the synchronization of the remaining difference in speed between the idler gear and the sleeve. Finally, in phase 5, the idler gear is connected to synchronizer hub and torque from the engine can be transferred through the gearbox.

3. Mathematical model

The forces acting on synchronizer sleeve include actuation forces, forces on sleeve teeth and friction. All teeth contacts are modelled with elastic and damping characteristics in a direction normal to the teeth contact surface which supports modelling both the axial and rotational effects. The friction is described by Karnopp friction model. In phases 2 to 4, the sleeves teeth forces acting upon the synchronizer ring generate forces in tangential direction. The resulting torque in combination with friction torque generated on friction surface cause rotational dynamics.

The block diagram of sleeve axial dynamics is shown in Fig. 1a. Torque generation dynamics model is dependent on engagement phases which are switched with respect to sleeve axial position. In Fig. 1b the torque generation dynamics is shown for phases two and three while structure for other phases are submodels of this more complex model.

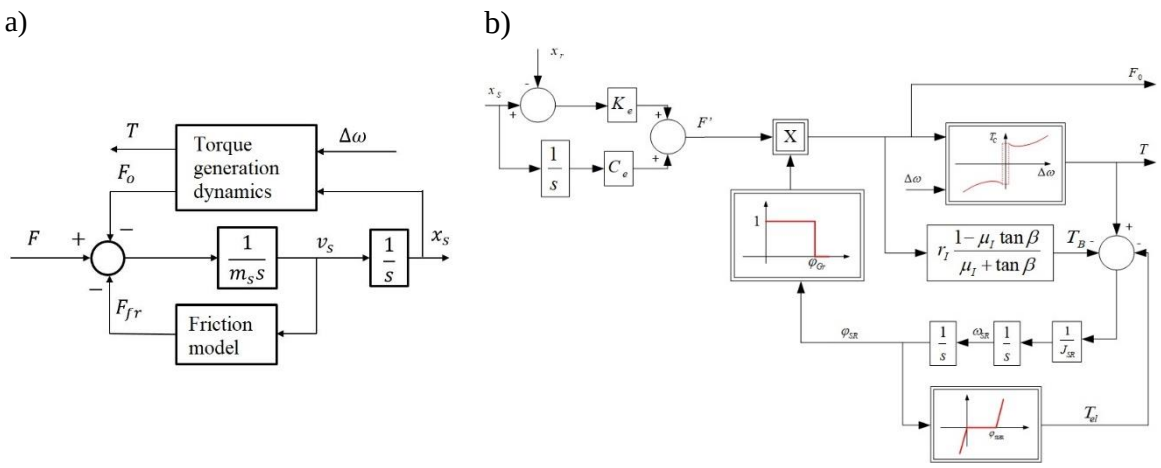

Figure 1. Block diagram of sleeve axial dynamics (a) and torque generation dynamics for second and third phase (b)

4. Proposed simplified model

Due to high rigidity of the tooth contact, the simulations with full model described above take too much time to execute to be of practical use. Separate model is thus proposed where the impact of sleeve axial dynamics on torque generation is calculated separately. Impact force on the teeth is calculated on predefined half period of sinus function so that force impulse is the same as the momentum of synchronizer sleeve before the impact. Fig. 2 shows the simulation results for synchronizer engagement conducted in AVL Cruise environment which includes the axial dynamics of an entire vehicle. The mentioned impact can be observed at 0.17 s including the expected distinguishable drop of slip speed.

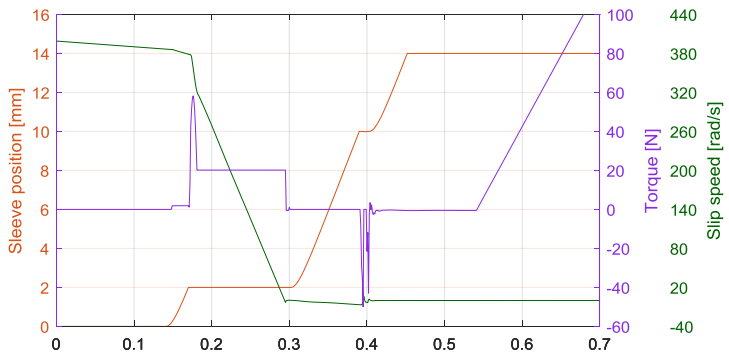

Figure 2. Simulation results for simplified model

4. Conclusion

The dynamic model of synchronizer engagement has been developed. The model includes axial dynamics of synchronizer sleeve and rotational dynamics of synchronizer ring. Model structure is dependent on current sleeve position which defines five phases of synchronizer engagement. The simplified model derived from the full synchronizer model allows for much faster simulation execution time while maintaining all significant effects of synchronizer engagement.

References

[1] Walker, P. D., Zhang, N.,Zhan, W., Zhu, B., Modelling and simulation of gear synchronization and shifting in dual-clutch transmission equipped powertrains, *ARCHIVE Proceedings of the Institution of Mechanical Engineers Part C Journal of Mechanical Engineering Science*, 227(2),276-287, 2012.

[2] Naunheimer, H., Bertsche, B., Ryborz, J., Novak, W., *Automotive Transmissions*, Springer, 2011.

Effect of loading system on double cantilever beam test

Ivan Hlača*, Leo Škec*, Dragan Ribarić*

*Faculty of Civil Engineering, Radmile Matejčić 3, Rijeka
E-mails: {ivan.hlaca,leo.skec,dragan.ribaric}@uniri.hr

Keywords: fracture mechanics, double cantilever beam, digital image correlation, loading system, direct identification

1. Introduction

Double cantilever beam (DCB) is the standard test for determination of the fracture toughness in mode I. Specimens are manufactured by gluing together two equal substrates along the interface, with the exception of the initial notch *a*, as shown in Figure 1. Application of the opening load *P* will cause the crack to propagate and, consequently, the length of the crack *a* to increase. Fracture toughness along the interface length is calculated from measured data, i.e. load-line displacement δ, applied force *P* and crack length *a*.

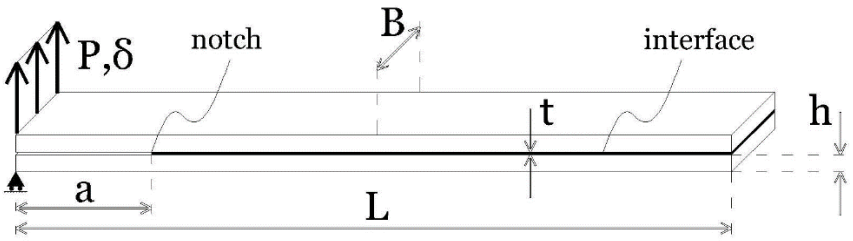

Figure 1. Geometry of a DCB specimen

British standard BS ISO 25217:2009 [1] is one of the standards typically used to determine the mode-I fracture toughness of bonded joints. Three methods, all based on linear elastic fracture mechanics and beam theory, are used to compute the fracture resistance of an adhesive expressed as the critical energy release rate (G_c). The results are usually presented graphically by means of the so-called *R*-curve, in which the change of the fracture toughness along the interface is shown. In an ideal case, the measured fracture toughness should be roughly constant along the interface, but usually the initial values monotonically change before reaching the plateau.

According to standards [1], DCB test has some limiting conditions that ensure that the methods used are valid, e.g. adhesive thickness and loading rate. On the other hand, three different techniques for attaching the DCB specimens on the tensile testing machines are suggested, namely load-blocks, piano hinges and loading holes drilled through the arms of the specimens. The aim of this work is to investigate whether different loading systems have an influence on the computed values of the fracture resistance and the shape of the *R*-curve.

2. Experiments

In experiments performed in this work, the DCB substrates are made from aluminum, while the adhesive used is SikaPower 4720. Dimensions of the specimens, according to Figure 1, are L = 250 mm, h = 8 mm, B = 30 mm and t = 0.6 mm. Four equal specimens were produced and tested in equal conditions using the tensile testing machine.

Load-line displacement and applied load can be measured directly from the tensile-testing machine (TTM). Instead of measuring the load-line displacement at the position of TTM grips, we also measure it on the specimen by utilizing the digital image correlation (DIC) technique. In particular, we use stereo DIC hardware and GOM Aramis V8 software [2]. Full-field displacement data was recorded, which was additionally used to determine the crack length and the cross-sectional rotations of the arms.

3. *R*-curve analysis

In this work we compare the results of the computed fracture toughness for three aforementioned loading systems. Besides the three methods from the standard [1], we use the J-integral [3] and the recently proposed ESBT method [4]. The methods from standards all require the measurement of the crack length, while for computing the *J*-integral only the cross-sectional rotations of the arms need to be measured. For the ESBT method, only load-line displacement and applied load measured from the TTM are needed.

Our *R*-curve results show an excellent agreement between the CBT method from the standard [1], *J*-integral and ESBT method. The remaining two methods from standards (SBT and ECM) show substantial differences in computed fracture toughness, which has been already reported in a numerical analysis presented in [4].

We additionally show that fracture toughness is significantly changed if instead of measuring load-line displacement at the position of TTM grips, we measure it directly on the specimen by utilizing the DIC. The British standard [1] suggests a correction procedure that accounts for system compliance, but this is not sufficient to account for the difference in the fracture toughness results between the two approaches. Corrections for load application system exists only for the stiffening effect of loading blocks, but this effect is found to have negligible influence on the results.

It was found that using the DIC measurement of load-line displacement, unlike the one from the TTM, will lead to plateau-shaped *R*-curve. Moreover, it was shown that using the DIC data, there is essentially no influence of the loading system on the measured fracture resistance. Besides, CBT, J-integral and ESBT show an excellent agreement in that case.

4. Conclusions

This work investigates the effect of loading system on fracture toughness. It was found that the values of the load line displacement measured from the TTM can significantly differ from those obtained from the DIC measurements. As shown, this can have a significant influence on the fracture toughness results, i.e. *R*-curves. The identified values of *J*-integral will be used for the direct identification of the traction-separation law, which is needed for numerical simulations.

References

[1] British Standards Institution BS ISO 25217, Adhesives - Determination of the mode 1 adhesive joints using double cantilever beam and tapered double cantilever beam specimen, *British Standard*, 2009.

[2] Aramis V8 SR1 Manual Basic, GOM mbH Aramis, 2015.

[3] Rice, J., A Path Independent Integral and the Approximate Analysis of Strain Concentration by Notches and Cracks, *Journal of Applied Mechanics*, 35(2): 379-386, 1968.

[4] Škec, L., Alfano, G., Jelenić, G., Enhanced simple beam theory for characterising mode-I fracture resistance via a double cantilever beam test, *Composites Part B*, 167, 250–262, 2019.

Fluid-structure interaction analysis of thoracic aorta blood flow

Anja Horvat*, Željko Tuković*

*University of Zagreb, Faculty of Mechanical Engineering and Naval Architecture, Zagreb, Croatia
E-mails: {anja.horvat, zeljko.tukovic}@fsb.hr

Keywords: Fluid – structure interaction, aorta, computational fluid dynamics, finite volume method

1. Introduction

Aortic dissection is a serious cardiovascular disease, where the inner layer of the aorta is injured enabling blood flow in between layers. Complications can lead to death, however, the preferred method of treatment isn't yet defined. In order to assist clinical decision – making, patient – specific computational modelling has lately been used. In this study, a partitioned FSI solver based on finite volume discretisation is used to calculate the interaction between blood flow through idealised thoracic aorta and flexible vessel wall, as a first step toward the application of a solver on more complex geometries involving aortic dissection. A comparative analysis of the blood flow through the rigid and flexible vessel wall has been performed in order to show the importance of applying FSI analysis for realistic predict thoracic aorta haemodynamics.

2. Methods

A partitioned FSI solver based on finite volume discretisation is used to calculate the interaction between blood flow through idealised thoracic aorta with flexible vessel wall. The laminar flow of incompressible, Newtonian fluid is described by Navier Stokes equations in arbitrary Lagrangian – Eulerian form. The deformation of incompressible, neo-Hookean hyper-elastic material is described by momentum equation in total Lagrangian form. Solid properties are assumed to be homogeneous and isotropic. Fluid and solid properties are given in Table 1.

Table 1. Fluid and solid properties

Property	Value	Unit
Fluid properties		
Fluid density	1000	kg/m^3
Kinematic viscosity	$3\ 10^{-6}$	m^2/s
Solid properties		
Solid density	1200	kg/m^3
Young's modulus	$8\ 10^5$	N/m^2
Poisson	0.5	-

The second-order accurate finite volume method is used for the spatial discretisation of both fluid and solid models and the first-order accurate implicit Euler method is used for temporal discretisation. The solid domain is discretised by the 4-layered prismatic mesh. On the other hand, mostly polyhedral unstructured mesh is used to discretise the fluid domain. The total number of control volumes employed for the solid and the fluid domain is 74088 and 112002, respectively. Solid domain boundary is divided into inlet, outlets, interface, and outer wall. The radial slip boundary condition is imposed on outlets and inlets which enables radial displacements and prevents displacements in the axial direction. The outer wall is defined as traction free. The fluid domain boundary is divided into inlet, outlets, and interface. Time-varying flow rate is imposed on the inlet and three-element Windkessel is imposed on outlets. The Windkessel parameters were set ensuring 10% outflow at smaller branches, and 70% outflow at the main outlet. Coupling between fluid and solid is performed using Robin-Neumann partitioned procedure [1], where the fluid pressure at the interface is bounded by solid inertia which ensures stability. Simulations were performed using open-source toolbox solids4foam [2].

3. Results

CFD and FSI simulations of blood flow are compared for idealised geometry of the aorta in Figure 1. FSI simulations were performed on stress-free geometry. CFD simulations were performed on mean volume geometry obtained from FSI simulation. CFD simulation predicted higher velocity magnitudes at the moment of maximal flow rate compared to FSI simulations. On the contrary, CFD predicted lower velocity magnitudes at the moment of minimal flow rate. The realistic state of stress in the vessel wall can be predicted only with FSI simulations.

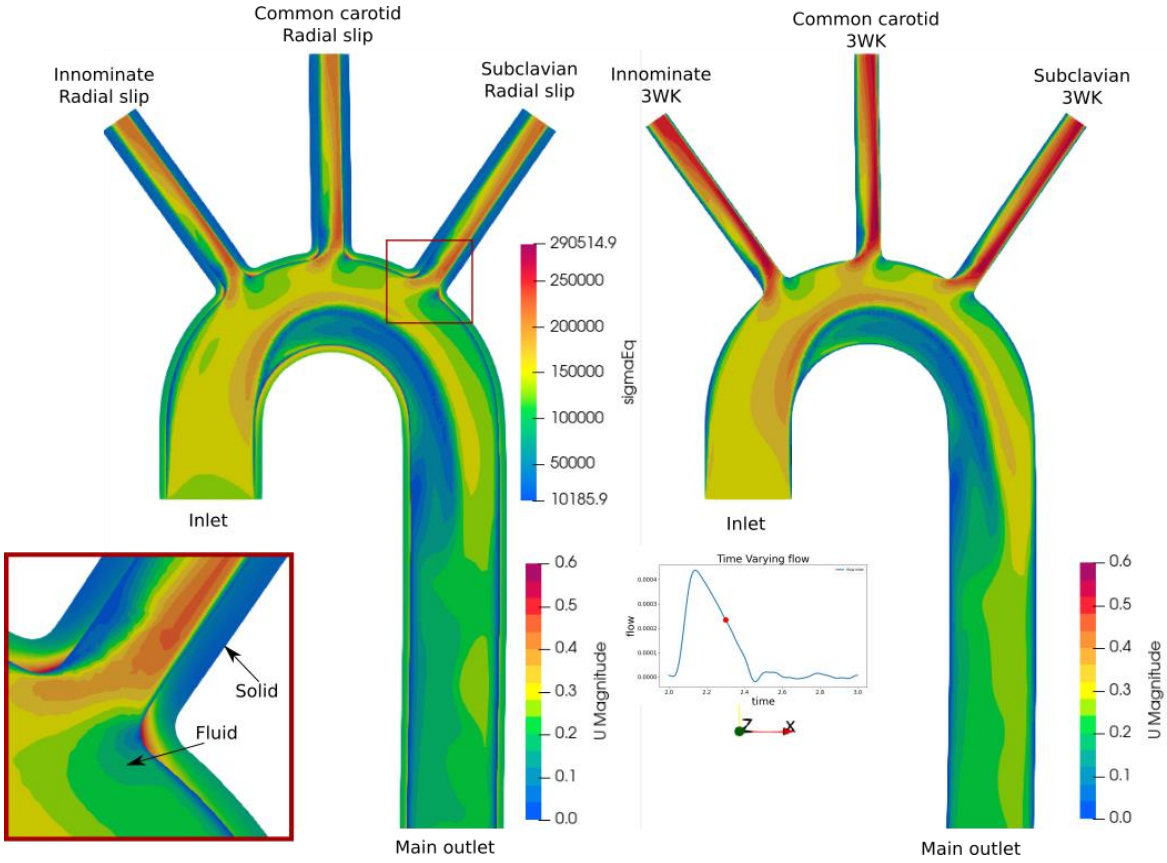

Figure 1. Comparison between velocity fields obtained with FSI (left) and CFD (right) simulation

4. Conclusions

The comparison between FSI and CFD simulations and insight into differences in velocity fields has been presented. Due to the substantial differences, the use of more computationally demanding FSI simulations is required in the future of the work involving aortic dissection.

5. Acknowledgments

This work was supported by grants from the Croatian Science Foundation (project IP-2020-02-4016 and DOK-2021-02-3071).

References

[1] Ž. Tuković, M. Bukač, P. Cardiff, H. Jasak, and A. Ivanković, *Added mass partitioned fluid–structure interaction solver based on a robin boundary condition for pressure*, in Selected Papers of the 11th Workshop, pp. 1–22., Springer International Publishing, 2019.

[2] P., Cardiff, A., Karač, P. D., Jaeger, H., Jasak, J., Nagy, A., Ivanković, and Ž., Tuković, *An open-source finite volume toolbox for solid mechanics and fluid-solid interaction simulations*, 2018.

Design of active tensegrity structures using computational approaches

Martin Hrabačka*, Radek Bulín+, Michal Hajžman*

* *Department of Mechanics, Faculty of Applied Sciences, University of West Bohemia. Univerzitní 8, 301 00 Pilsen, Czech Republic.*
E-mails: hrabackm@students.zcu.cz, mhajzman@kme.zcu.cz

+ *New Technologies for the Information Society, Faculty of Applied Sciences, University of West Bohemia. Univerzitní 8, 301 00 Pilsen, Czech Republic.*
E-mail: rbulin@ntis.zcu.cz

Keywords: form-finding, H_2 control, path-planning, tensegrity

1. Introduction

Tensegrity is a general structural concept that contains a discontinuous set of components in compression (e.g. struts) inside a network of components in tension (e.g. cables) and which integrity relies on pre-stress forces [3]. There are several ways how to actuate tensegrities. In this work, the structure can change its shape by adjusting the cables' rest lengths. The resulting structures can be easily dismantled, they often reach a very good strength to weight ratio and they can perform a wide range of motions. Hence, they can be advantageously utilized in many applications including robotics. This paper focuses on the creation of the methodology of active tensegrity structure design. The main problems solved during the design process are form-finding, path-planning, and active vibration suppression.

2. Path-planning and form-finding

An active tensegrity is naturally derived from its passive version (rest lengths of cables are not variable). All properties of this base tensegrity, including structural topology, spatial configuration (nodal positions), properties of all struts and cables, etc., are assumed to be defined a priori in this work. The principal aim is to design the actuation that leads the structure to follow the desired trajectory in form of trajectories of selected structure nodes.

2.1. Path-planning as an optimization process

It can be done via sampling the desired trajectory leading to N discrete desired configurations $\mathbf{X}_{des,i}$ ($i = 1,2,\ldots,N$). Thus, a specific set of cables' rest lengths is searched for each desired configuration. This is called the path-planning problem which can be approached differently, for instance, as an optimization problem. The objective function $F(\mathbf{X})$ quantifies the error of current configuration $\mathbf{X}$ from desired configuration $\mathbf{X}_{des,i}$ and takes its minimum at $\mathbf{X} = \mathbf{X}_{des,i}$ for the i-th iteration of the path-planning process. The cables' rest lengths $\mathbf{l}$ represent optimization variables and every configuration $\mathbf{X}(\mathbf{l})$ used during optimization must satisfy the static equilibrium condition.

Using this approach, particular sets of rest lengths $\mathbf{l}^*_i$ can be found causing the structure to take desired configurations $\mathbf{X}_{des,i}$. If these discrete sets are linearly interpolated in time, it is possible for the structure to follow the desired continuous trajectory.

2.2. The dynamic relaxation method

Searching for a static equilibrium configuration with specified rest lengths is the basis of the introduced optimization process and it is called the form-finding problem. It can be solved by various numerical methods based on geometric, force, or energetic approaches [5].

For this purpose, the dynamic relaxation method is used in this work. The basic idea of the method is to trace step-by-step the motion of the structure until the structure reaches a static equilibrium due to introduced damping [2]. Because a static solution rather than the real dynamic behaviour is searched for, both artificial damping and fictitious mass are added to the system to assure rapid

convergence [1, 2]. In this paper, artificial damping is used in the form of so-called kinetic damping. According to [2], kinetic damping represents a procedure when movements of an undamped structure are traced until a local maximum of kinetic energy is reached. At this point, all nodal velocities are set to zero and the process is restarted from the current position. These steps are repeated until the energy is completely dissipated and static equilibrium configuration is found.

3. Dynamics of active structure and vibration suppression

Modelling the dynamics of tensegrity structures is done using Simscape software (an extension package of MATLAB-Simulink). It allows quite intuitive creation of structural components (struts, cables) and connecting them together in the block environment. It also provides visualization of simulation without any additional effort. In order to make the generation of dynamic models of tensegrities fast and smooth, a software automatically generating the Simscape model has been developed in the MATLAB scripting environment as an alternative to manual model creation.

If the motion of the structure following the desired trajectory is relatively slow, it can be considered quasi-static, and the proposed process of actuation design is sufficient. But in many applications, motion can be quite fast, and thus, undesirable vibrations can occur. Because the presented path-planning process is based on static analysis only, it cannot suppress them. Therefore, an H_2 controller inspired by [4] is designed to reduce vibrations.

Several steps must be done while designing an efficient H_2 controller. First, the model of the structure has to be linearized in the stable equilibrium around which the structure operates. Then, controller inputs, control objectives, disturbances, and weighting filters need to be specified. In this paper, errors of nodal positions from the desired trajectory are considered as controller inputs, and minimization of both position errors and the actuation effort represents control objectives. Time functions of cables' rest lengths calculated by the process proposed in the previous section represent disturbances. Weighting filters are applied to both external inputs (to approximate their spectrum) and control objectives (to approximate their spectrum and relative importance). After that, the augmented plant corresponding to the topics discussed in this paragraph is designed. Based on the augmented plant, the H_2 controller can be finally produced.

4. Conclusions

The presented methodology allows designing and modelling active tensegrity structures. During the design procedure, various problems are solved: path-planning problem by optimization process, form-finding by the dynamic relaxation method, vibrations suppression by H_2 controller, and automatic computational model generation. The whole methodology was implemented in the in-house software developed in the MATLAB environment. A great advantage of the methodology is the fact that it can be applied to various structures (even on different tensegrity types).

This research work was supported by the project SGS-2022-008 of the Czech Ministry of Education, Youth and Sport, and by the Czech Science Foundation project 20-21893S.

References

[1] Ali N.B.H., Rhode-Barbarigos L., Smith I.F.C., Analysis of clustered tensegrity structures using a modified dynamic relaxation method. *International Journal of Solid and Structures*,48, 637-647, 2011.

[2] Barnes M.R., Form finding and analysis of tension structures by dynamic relaxation. *International Journal of Space Structures*, 14, 89-104, 1999.

[3] Fest E., Shea K., Domer B., Smith I.F.C., Adjustable tensegrity structures. *Journal of Structural Engineering*, 129, 515-526, 2003.

[4] van de Wijdeven, J., de Jager, B., Shape change of tensegrity structures: Design and control. *American Control Conference*, 2522-2527, 2005.

[5] Zhang S.H., Ohsaki M., Tensegrity structures: Form, stability, and symmetry. Springer, Japan, 2015.

Local gradient theory for dielectrics with non-classical heat conduction law

Olha Hrytsyna[*,+], Yuriy Tokovyy[+], Maryan Hrytsyna[*]

[*] *Institute of Construction and Architecture Slovak Academy of Sciences, Dúbravská cesta 9, 84503 Bratislava 45, Slovakia*
E-mails: olha.hrytsyna@savba.sk, maryan.hrytsyna@savba.sk

[+] *Pidstryhach Institute for Applied Problems of Mechanics and Mathematics, National Academy of Sciences of Ukraine, 3B Naukova Str., 79060 Lviv, Ukraine*
E-mail: tokovyy@iapmm.lviv.ua

Keywords: non-equilibrium thermodynamics, non-classical theory, coupled fields, nonlocal heat conduction, surface and size effects

1. Introduction

Evidently, the classical continuum mechanics largely fails in covering the situations when the size of a considered body is comparable to the material micro-structural lengths. Instead, non-classical theories have to be employed engaging the surface and size effects. This talk addresses the advancement in a local gradient theory (LGT) of polarized thermoelastic media, implying a nonlocal heat conduction law with an application of this theory to the analysis of coupled electro-elastic fields induced by thermal inclusions in small-scale dielectric solids.

2. Continuum LGT for elastic solids under nonlocal heat conduction law

Let us consider an elastic polarized solid with the mechanical displacement $\mathbf{u}$, stress tensor $\boldsymbol{\sigma}$ and strain tensor $\boldsymbol{\varepsilon}$. To describe the conduction of heat, we introduce the temperature field T, the entropy s, and the heat and entropy fluxes $\mathbf{J}_q$ and $\mathbf{J}_s$. The electric field vector $\mathbf{E}$ and polarization vector $\boldsymbol{\pi}_e$ characterize the electromagnetic properties of the dielectric body. The LGT for dielectrics is formulated by implying the contribution of the mass flux caused by changes in the material microstructure [1]. The mass flux is associated with the process of a local mass displacement (LMD). In [1], the vector $\boldsymbol{\pi}_m$ of LMD, the specific density of the induced mass ρ_m, and the potential μ_π are introduced to describe the process of LMD. The potential μ_π is the energy measure of the effect of LMD on the internal energy. The balance-type equation subordinating the vector $\boldsymbol{\pi}_m$ and the density of induced mass ρ_m is obtained in [1].

Herein, the generalized relation between the heat $\mathbf{J}_q$ and entropy $\mathbf{J}_s$ fluxes is adopted as [2]: $\mathbf{J}_s = T^{-1}\mathbf{J}_q + \mathbf{J}_q \cdot \mathbf{Q}$, where the second order tensor $\mathbf{Q}$ is the higher-grade flux (i.e., flux of heat flux).

Within the frameworks of the non-equilibrium thermodynamics, continuum mechanics, and electrodynamics, a complete system of equations for the local gradient electro-thermo-mechanics of non-ferromagnetic polarized medium is formulated. The equations of balance of linear momentum and the conservation of mass are derived by requiring the energy balance equation to be invariant under the Galilean transformation. Basing on the total energy balance equation, the electromagnetic energy equation and the entropy balance equations, a generalized Gibbs equation is derived: $df = \rho^{-1}\boldsymbol{\sigma} : d\boldsymbol{\varepsilon} - sdT - \boldsymbol{\pi}_e \cdot d\mathbf{E} - \rho_m d\mu'_\pi + \boldsymbol{\pi}_m \cdot d\nabla\mu'_\pi$ [1]. Here, $f(\boldsymbol{\varepsilon}, T, \mathbf{E}, \mu'_\pi, \nabla\mu'_\pi)$ is the generalized free energy function, ρ is the mass density, $\mu'_\pi = \mu_\pi - \mu$, μ is the chemical potential. Based on the Gibbs relation, the gradient-type constitutive equations can be written as follows:

$$\boldsymbol{\sigma} = \rho\frac{\partial f}{\partial \boldsymbol{\varepsilon}}, \quad s = -\frac{\partial f}{\partial T}, \quad \boldsymbol{\pi}_e = -\frac{\partial f}{\partial \mathbf{E}} \quad \rho_m = -\frac{\partial f}{\partial \mu'_\pi}, \quad \boldsymbol{\pi}_m = \frac{\partial f}{\partial(\nabla\mu'_\pi)}. \tag{1}$$

It follows from (1) that within the framework of LGT, the set of conjugate variables is complemented by two supplementary couples of variables: (ρ_m, μ'_π) and ($\boldsymbol{\pi}_m$, $\nabla\mu'_\pi$) related to the LMD. These variables make the theory to be spatially nonlocal.

In view of the first and second principle of thermodynamics, the dissipation inequality can be obtained as follows: $\sigma_s = \mathbf{J}_q \cdot [\nabla(T^{-1}) + \nabla \cdot \mathbf{Q}] + (\nabla \otimes \mathbf{J}_q) : \mathbf{Q} \geq 0$ (σ_s is the entropy production). To satisfy this inequality, we assume that $\mathbf{J}_q = m_1[\nabla(T^{-1}) + \nabla \cdot \mathbf{Q}]$ and $\mathbf{Q} = m_2 \nabla \otimes \mathbf{J}_q$, where m_1, m_2 are positive constants. The above relations yield the following nonlocal heat conduction law:

$$\mathbf{J}_q - \zeta^2 \nabla^2 \mathbf{J}_q = -\lambda \nabla T \,, \tag{2}$$

where $\lambda = m_1 / T_0^2$ is the coefficient of heat conductivity and $\zeta = \sqrt{m_1 m_2} \geq 0$ is the length scale parameter. In Eq. (2), the term $\zeta^2 \nabla^2 \mathbf{J}_q$ complies with the nonlocal heat conduction model [2].

The governing equations of the linear LGT can be obtained by substituting strain-displacement equation $\boldsymbol{\varepsilon} = [\nabla \otimes \mathbf{u} + (\nabla \otimes \mathbf{u})^{\mathrm{T}}]/2$, the electric field vector $\mathbf{E} = -\nabla \varphi_e$, the electric displacement $\mathbf{D} = \varepsilon_0 \mathbf{E} + \rho_0 \boldsymbol{\pi}_e$, constitutive equations (1) and nonlocal heat conduction law (2) into the field equations

$$\nabla \cdot \boldsymbol{\sigma} + \rho_0 \mathbf{F} = \rho_0 \ddot{\mathbf{u}} \,, \quad \rho_0 T_0 \dot{s} = -\nabla \cdot \mathbf{J}_q + \rho_0 \mathfrak{R} \,, \quad \nabla \cdot \mathbf{D} = \rho_e \,, \quad \nabla \cdot \boldsymbol{\pi}_m + \rho_m = 0 \,. \tag{3}$$

Here, $\mathbf{F}$ is the mechanical force vector, ρ_e is the specific density of the induced charge, φ_e is the electric potential, ε_0 is the permittivity of vacuum, $\mathfrak{R}$ is the distributed thermal source. Note that the use of constitutive equations (1) and nonlocal heat conduction law (2) implies the governing system of partial differential equations, whose order is higher than in classical case. We validated these equations in a simple boundary value problem to investigate the coupled electro-elastic fields induced by the prescribed temperature distributions (i.e., the thermal inclusions) in elastic dielectric plates with mechanically free or clamped periphery. The effect of the temperature on the induced electric fields (electric potential, polarization) in the surfaces vicinity is analyzed. It is shown that in contrast to the classical theory, LGT is able to cover the surface and size effects, as well as the interaction of mechanical, electric and thermal fields in dielectrics including the crystals having a center of inversion.

3. Conclusions

Using the fundamental principles of non-equilibrium thermodynamics, continuum mechanics, and electrodynamics, the new non-classical theory of thermoelastic crystalline dielectrics is proposed. The theory is based on the generalized relation between the heat and entropy fluxes and takes into consideration LMD, caused by the changes in the material microstructure of a body. For the considered continuum, the gradient-type constitutive equations and the nonlocal heat conduction law (the generalized Fourier law) are formulated. The relations of LGT are verified on boundary value problems. It is shown that the theory enables one to capture the size-depending behavior of the piezoelectric solids at the nano-scale. The general results of this study can be used for modeling new devices with account for the size, surface, and thermopolarization effects.

Funding

This research was supported by the Slovak Research and Development Agency and Ministry of Education and Science of the Ukraine (bilateral grant number SK-UA-21-0010).

References

[1] Hrytsyna, O., Kondrat, V., *Local Gradient Theory for Dielectrics: Fundamentals and Applications.* 1st ed. Jenny Stanford Publishing Pte. Ltd., Singapore, 2020.

[2] Yu, Y. J., Tian, X.-G., Xiong, Q.-L., Nonlocal thermoelasticity based on nonlocal heat conduction and nonlocal elasticity. *European Journal of Mechanics A/Solids*, 60, 238-253, 2016.

Experimental and numerical analysis of stress concentration in a plate with a circular hole

Magdy Ismail*, Laura Žiković*, Nina Čeh*, Gordan Jelenić*

*Faculty of Civil Engineering, University of Rijeka
E-mails:{mismail, laura.zikovic, nina.ceh, gordan.jelenic}@uniri.hr

Keywords: stress-concentration factor, classical elastic theory, experimental solution, digital image correlation, circular inclusion.

1. Introduction

The paper presents an analysis of stresses and strains in both finite and infinite rectangular homogeneous, isotropic elastic plates with a circular hole in the middle loaded by a uniform tensile traction. According to Timoshenko and Goodier [1] the ratio between the axial stress in the fibre tangent to the hole and the applied axial traction (the stress-concentration factor) for a plate of infinite width does not depend on the hole size and is equal to $k = \frac{\sigma_{max}}{\sigma_{\text{nom}}} = 3$.

For a plate of finite width, the stress-concentration factor differs somewhat [2], but the difference between the two results is substantial only for relatively narrow plates. A number of experiments in the literature, however, indicate that these analytical results overestimate the stress-concentration factor [3,4].

To investigate this discrepancy further and propose a possible explanation of this phenomenon, a set of experimental and numerical tests is conducted.

2. Numerical analysis

Three specimens of equal length (400 mm) and thickness (4 mm), but of different width (480, 240 and 120 mm) are analysed numerically. The results for the stress-concentration factor obtained using very fine finite-element meshes are shown in Table 1. It is obvious that for the widest specimen the stress-concentration approaches the theoretical result of [1].

Table 1. Stress-concentration factor for different hole diameter to plate width ratio

Specimens	Hole diameter to plate width ratio	Numerical stress concentration factor *k*
1st sample (width 120 mm)	0.08	2.615
2nd sample (width 240 mm)	0.04	2.728
3rd sample (width 480 mm)	0.02	2.774

3. Experimental analysis

3.1 Direct strain measurement

The material is an aluminium alloy with Young's modulus and Poisson's ratio obtained from an earlier experiment [5], as E = 67050.5 MPa and n = 0.3. A number of narrow strain gauges (measurement area 3 x 0.4 mm) will be attached at specific characteristic points. The samples will be subjected to uniaxial tension using the universal pressure-tensile testing machine Zwick-Roell Z600. The load will be applied in the displacement-control mode and the maximum applied displacement is conditioned by the fact that the specimen needs to stay in the liner-elastic region during the whole experiment. The force will be acting on the upper grip while the lower grip will be fixed as shown in Figure 1. For each specimen, three samples will be analysed in detail.

3.2 Optical measurement

While the strains will be monitored at characteristic points using strain gauges, the total displacement field will be monitored by non-contact measurement using GOM Aramis 3D optical system with 12M cameras. The recorded experiment will then be post-processed by a digital image correlation (DIC) method. For this purpose, it is necessary to adequately prepare the surface of the specimens before the experiment. First, the samples should be carefully cleaned and then sprayed with white mat paint in order to provide anti-reflective background. Then, small black paint-drops will be sprayed evenly to form a random black and white pattern.

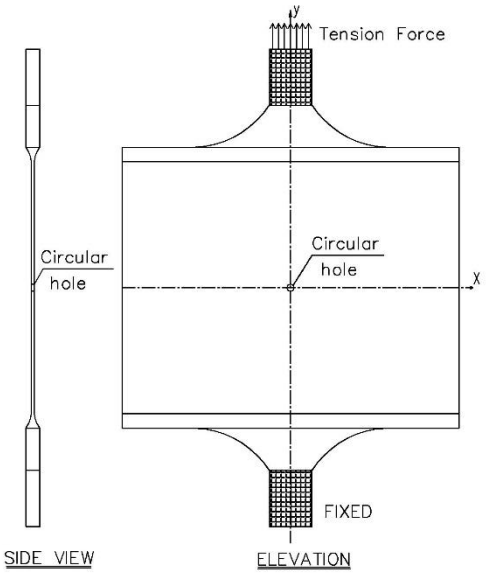

Fig 1. Uniaxially loaded plate with a central circular opening

4. Conclusions

The objective is to perform the lab tests to see if the reduced experimental value for the stress-concentration with respect to numerical simulation reported in the literature may be confirmed for the three samples varying from finite to an infinite plate under uniaxial tension. An attempt will be made to explain any discrepancy between the experimental results and the numerical results that may be encountered by an alternative non-classical theory of elasticity.

Acknowledgements

This work has been financially supported by the Croatian Science Foundation research project "Fixed-Pole Concept in Numerical Modelling of Cosserat Continuum" (HRZZ-IP-2018-01-1732) and the University of Rijeka research grant "Computational and Experimental Procedures for Assessment of Material Parameters in Cosserat's Continuum" (uniri-tehnic-18-248 1415).

References

[1] Timoshenko S., Goodier J.N., *Theory of Elasticity*, McGraw-Hill, New York, pp.78-80,1951.

[2] Howland R. C. J., On the stresses in the neighborhood of a circular hole in a strip under tension, *Proc. Roy. Soc.* London A, 229, pp.49-88,1930.

[3] Wahl, A. M., and Beeuwkes, R., Stress concentration produced by holes and notches, East Pittsburgh, PA, " Trans, ASME, Appl. Mech, Section, pp.617-625,1934.

[4] Griffith, G. E., Experimental Investigation of the Effects of Plastic Flow in a Tension Panel with a Circular Hole, *NACA TN*, 1705, pp1-16,1948.

[5] Žiković, L., and Jelenić, G.; Analysis of stress concentration factor in a homogeneous plate with a circular hole, Report, Faculty of Civil Engineering, Rijeka, 2022

Thermodynamics and Computational Modeling of Strain Induced Crystallization in Rubbers

Mikhail Itskov*, Khiêm Ngoc Vu*, Jean-Benoît Le Cam+

*Department of Continuum Mechanics, RWTH Aachen University, Eilfschornsteinstr. 18, 52062 Aachen, Germany
E-mails: {itskov,vu}@km.rwth-aachen.de

+Institut de Physique UMR 6251 CNRS/Université de Rennes 1, Rennes, France
E-mail: jean-benoit.lecam@univ-rennes1.fr

Keywords: strain-induced crystallization, calorimetric effects, physically-based modeling

1. Introduction

Crystallization is the generation of regular molecular structures (crystallites) from amorphous polymer chains. The high regularity of the side group orientations in polymer chains allows natural rubbers to crystallize when undergoing deformation. This phenomenon is referred to as strain-induced crystallization. The strain-induced crystallization is supposed to play an important role in the elastomer reinforcement and enhances the resistance to crack growth in natural rubbers. So far, it has been mostly investigated by using X-ray diffraction which cannot measure calorimetric effects accompanying the strain induced crystallization. These effects result from the phase transition during crystallite nucleation, growth and melting.

2. Thermodynamics of strain induced crystallization

Recently, infrared thermography has been combined with mechanical measurements to detect the heat production and absorption as well as crystallization degree during cyclic loading of natural rubbers [3]. To this end, the intrinsic dissipation due to viscosity and stress softening is evaluated under cyclic loading by the energy balance. Energy contributions to the hysteresis loop converted into heat and stored in the material are separated. Accordingly, the hysteresis loop in the strain-stress relationship does not systematically correspond to intrinsic dissipation and can be partly due to the stored energy. The percentage of the stored energy has been quantified as a function of the maximum stretch applied. The strain-induced crystallinity and the crystallization onset have also been evaluated from the heat power density response. According to results of biaxial tests strain induced crystallization also takes place in filled rubbers although at higher stretch ratios.

3. Kinetics and computational modeling of strain induced crystallization

In the present contribution (see also [4-5]), a physically-based constitutive model for filled natural rubbers [1-2] is coupled with infrared thermography based calorimetry to study strain-induced crystallization. The kinetics of phase transition outside thermodynamic equilibrium is discussed and underlying mechanisms of nonequilibrium strain-induced crystallization are interpreted. In Fig. 1 a formation of crystal nucleus in polymer chains under stretch is illustrated for example. The crystallization nucleation begins when the nucleus size reaches the critical dimension so that a crystallite forms in the strand. Then, with increasing stretch the nucleation occurs in a neighboring chain in the strand. Further stretching leads to the formation of more and more crystallites in the network strand. Once all chains in the strand become semi-crystalline, the saturation of crystallization nucleation takes place. The so formed crystallites can spontaneously melt. Under unloading the melting rate even exceeds the crystallization rate, which finally leads to the amorphous state.

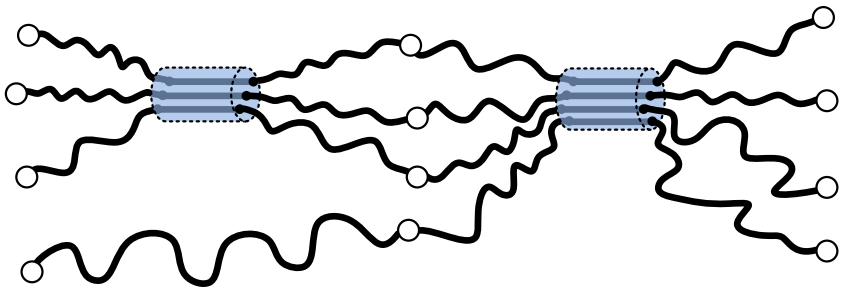

Figure 1. Formation of crystal nucleus in polymer chains under stretch

The constitutive model of strain induced crystallization is based on the free energy formulated for the semi-crystalline network separately for the equilibrium and nonequilibrium state. A special attention is focused on thermic and deformation dependent parts of the entropy of a single polymer chain.

To capture multiaxiality of strain-induced crystallinity, the analytical network-averaging is applied. In order to describe the Mullins and rate-dependent effects in filled natural rubbers, we also consider the filler-interaction. To this end, the rate-independent and dependent damage is captured by an equilibrium and nonequilibrium filler-polymer network, respectively. The total free energy is composed by entropic and energetic contributions of the semi-crystalline chains and of the filler-polymer interaction. Finally, we prove the thermodynamic consistency of the proposed model.

The model was validated by comparison to experimental data both from uniaxial and biaxial cyclic tests. In all these tests, model predictions demonstrated good agreement with the corresponding experimental data not only with respect to stress-strain curves but also to the crystallization degree and the heat source.

4. Conclusions

The proposed model is able to describe many important effects accompanying stress-induced crystallization as for example zero intrinsic dissipation in a loading cycle or the influence of the biaxiality ratio. Another important finding is that not only equilibrium but also nonequilibrium thermodynamics should be involved when studying and modeling strain induced crystallization in rubbers.

References

[1] Khiêm, V. N., Itskov, M., Analytical network-averaging of the tube model: Rubber elasticity, *Journal of the Mechanics and Physics of Solids*, 95, 254-269, 2016.

[2] Khiêm, V. N., Itskov, M., Analytical network-averaging of the tube model: Strain-induced crystallization in natural rubber, *Journal of the Mechanics and Physics of Solids*, 116, 350-369,2018.

[3] Le Cam, J.-B., Albouy, P., Charlès, S., Comparison between X-ray diffraction and quantitative surface calorimetry based on infrared thermography to evaluate strain-induced crystallinity in natural rubber, *Review of Scientific Instruments*, 91(4), 044902, 2020.

[4] Khiêm, V. N., J.-B. Le Cam, S. Charlès, Itskov, M., Thermodynamics of strain-induced crystallization in filled natural rubber under uni- and biaxial loadings, Part I: Complete energetic characterization and crystallinity evaluation, *Journal of the Mechanics and Physics of Solids*, 159, 104701, 2022.

[5] Khiêm, V. N., J.-B. Le Cam, S. Charlès, Itskov, M., Thermodynamics of strain-induced crystallization in filled natural rubber under uni- and biaxial loadings, Part II: Physically-based constitutive theory, *Journal of the Mechanics and Physics of Solids*, 159, 104712, 2022.

Comparison of Lagrangian and Eulerian approach for modeling dynamics of the probability distribution driven by sea surface flow field

Karlo Jakac*, Ante Sikirica*, Luka Lanča*, Stefan Ivić*

*University of Rijeka, Faculty of engineering, Vukovarska 58,51000,Rijeka
E-mails: {kjakac,asikirica,llanca,sivic}@riteh.hr

Keywords: Euler, Lagrange, probability distribution, flow field, search and rescue

1. Introduction

The problem of the target probability distribution assessment is a significant part of maritime operations, specifically search and rescue (SAR) operations. New research into maritime SAR decision-making is urgently needed in order to improve its capabilities [1]. Algorithms that are based on Lagrangian and Eulerian flow field specifications have been widely used to solve this problem[2]. In this study, the precision and computing efficiency of the Lagrangian and Eulerian approaches for the modeling of the dynamics of the probability distribution driven by the sea surface flow will be assessed. The Lagrangian method is based on modeling advection of passive particles with a system of first-order differential equations. The Eulerian approach is based on solving a non-steady two-dimensional partial differential equation which describes the motion of a passive scalar field.

2. Simulations of probability distribution using Lagrangian and Eulerian approach

The Eulerian test model is based on data gathered from the ROMS (Regional Ocean Modeling System) database which is an ocean numerical model that uses primitive equations to describe the behavior of the ocean in a particular area [3]. Simulation of the probability distribution with the Eulerian approach has been conducted using open-source CFD framework OpenFOAM [4]. This approach requires a numerical mesh in order to solve specific equations for reaching the solution. Figure 2 shows probability distribution obtained using the Eulerian approach, where probability (i.e. scalar concentration) is in the range from 0-1 (0-100%).

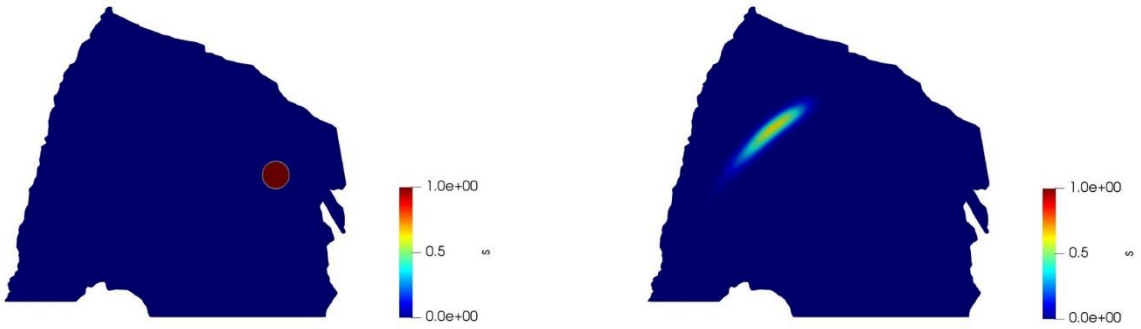

Figure 2. The exact location of the missing person (left) at the beginning of the search, and the drifted probability distribution after 3 days (right). ROMS data is nested to simulate realistic behavior.

In this case, the probability distribution corresponds to a passive scalar in a reference frame that is fixed in space. Scalar concentration is governed by the advection-diffusion equation (1):

$$\frac{\partial c}{\partial t} = D\nabla^2 c - v \cdot \nabla c \qquad (1)$$

where c is a dimensionless passive scalar concentration, D is diffusion coefficient *[m^2/s]*, *t* is time *[s]* and v is velocity field *[m/s]*

The Lagrangian approach is based on a description of the fluid in a reference frame that is moving with an infinitesimal fluid particle [5]. The considered surface flow velocity field for the Lagrangian approach is generated from real data. Surface velocity data of the test model is computed using HYCOM [6]. The data consists of 3-hourly longitudinal and latitudinal velocity components, while the spatial resolution is 1/25 degrees in each direction. The main idea is to induce a high number of tracers within the pre-resolved flow field and model the tracer drift using before mentioned approaches. By computing the local density of tracers, a probability distribution can be assembled at future times (Figure 1). This method does not require a numerical mesh and eliminates the artificial diffusion associated with Eulerian schemes.

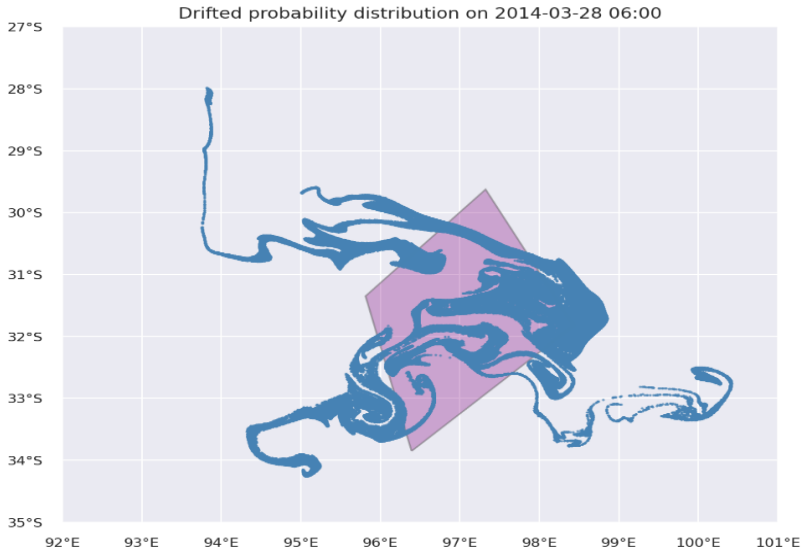

Figure 1. The estimated splash area A (purple diamond) and the drifted probability distribution of search targets on the first day of actual search for plane debris (March 28) [6].

3. Conclusions

We studied computational efficiency and accuracy of Lagrangian and Eulerian approaches for modeling the dynamics of the probability distribution in SAR operations. The appropriate approach in these situations can be a key factor for effective response to tragic accidents. With that in mind, this study addresses and outlines key differences between methods, their precision, total computation time and evaluation of their applicability in real-world SAR operations.

References

[1] China MSA. Maritime Safety, Investigation Report into the Collision between TianYu2 and LiaoSuiYu66528, [Online] Available: https://www.msa.gov.cn/public/documents/mdkz/mtm1/~edisp/20190428093135683.pdf (2018)

[2] Ai B, Li B, Gao S, Xu J, Shang H. An Intelligent Decision Algorithm for the Generation of Maritime Search and Rescue Emergency Response Plans. IEEE Access 2019;7:155835–50. https://doi.org/10.1109/ACCESS.2019.2949366.

[3] CT-ROMS - Model , [Online] Available: https://www.cgd.ucar.edu/projects/ctroms/ct-roms.html (2021).

[4] Fontanini AD, Vaidya U, Passalacqua A, Ganapathysubramanian B. Contaminant transport at large Courant numbers using Markov matrices. Building and Environment 2017;112:1–16. https://doi.org/10.1016/J.BUILDENV.2016.11.007.

[5] van Sebille E, Griffies SM, Abernathey R, Adams TP, Berloff P, Biastoch A, et al. Lagrangian ocean analysis: Fundamentals and practices. Ocean Modelling 2018;121:49–75. https://doi.org/10.1016/j.ocemod.2017.11.008.

[6] Ivić S, Crnković B, Arbabi H, Loire S, Clary P, Mezić I. Search strategy in a complex and dynamic environment: the MH370 case 2020. https://doi.org/10.1038/s41598-020-76274-0.

Stability and Performance Analysis of a Reciprocity Defying Active Acoustic Metamaterial Cell

Marin Jalšić*, Neven Alujević+, Srećko Arandia-Krešić+, Ivan Ćatipović+

*AVL-AST d.o.o, Strojarska cesta 22, Zagreb
E-mails: marin.jalsic@gmail.com

+University of Zagreb, Faculty of Mechanical Engineering and Naval Architecture, Ulica Ivana Lučića 5, Zagreb
E-mail: {neven.alujevic, srecko.arandia-kresic, ivan.catipovic}@fsb.hr

Keywords: active metamaterials, Finite element method (FEM), active vibroacoustic control

1. Introduction

This paper deals with stability and performance analyses of an active acoustic metamaterial cell. The cell can be used to propagate vibrations in a non-reciprocal manner. A fully coupled structural-acoustic FEM model of the system is used to derive mobility functions necessary to analyse its dynamic behaviour. Idealised velocity sensors and force actuators are assumed.

2. Active acoustic metamaterial cell modelling, stability and performance analysis

The scheme of the active acoustic metamaterial barrier and a cross-section of its single cell are shown in **Figure 11**. The barrier is a repeating pattern of identical cells stacked in the *x*- and *y*-directions, transmitting vibrations in the *z*-direction. Each cell consists of four rectangular panels and three rectangular air cavities between them. The two actuators are driven by velocity signals obtained by sensors collocated with one mechanical terminal of each actuator. The other terminal is not equipped with a sensor so that the transducer pairs are in a non-collocated configuration. The two feedback loops are utilised in a decentralized configuration implementing the same feedback gain *g*.

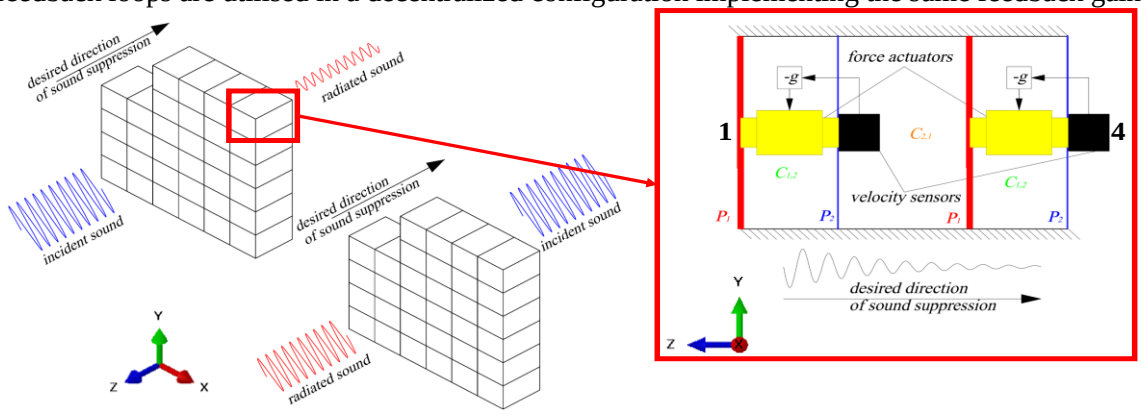

Figure 11 Active metamaterial barrier (left) and single cell concept (right)

Mobility functions, considering point forces at centres of the panels as inputs and velocities at the same points as outputs, are obtained using the modal decomposition method, 0.The modal decomposition is performed by a fully coupled structural-acoustic finite element model.

The derived mobility functions are used to obtain the sensor-actuator open-loop frequency response function (OL-FRF) matrix in order to assess the closed-loop system stability properties using the generalized Nyquist stability criterion, 0. **Figure 12** shows the two eigenvalues of the sensor-actuator OL-FRF matrix indicating a nearly unconditional control system stability.

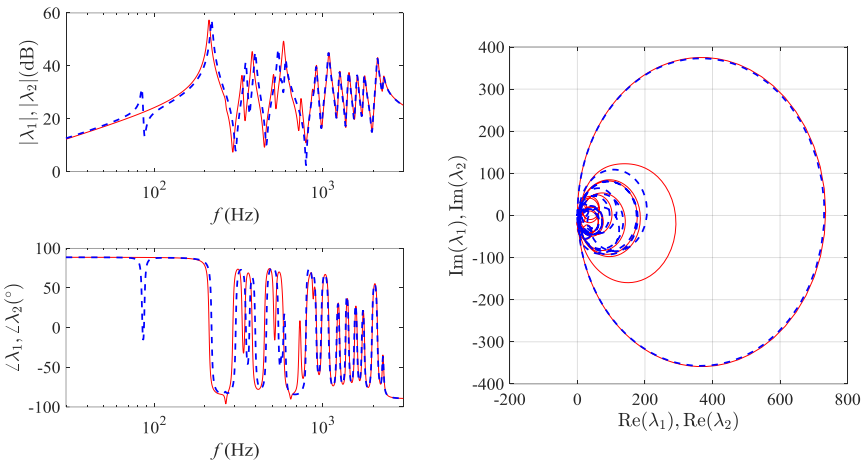

Figure 12 Amplitude and phase plots (left) and Nyquist contour (right) of the two eigenvalues of the sensor-actuator open-loop frequency response matrix: faint red line - λ_1, dashed blue line - λ_2

Additionally, the mobility matrix of the closed-loop system is derived, in order to evaluate the cell performance using an approach similar to that of reference [2]. Figure 3 shows the characteristic mobility functions of the system, $\mathcal{Q}_{41}$ and $\mathcal{Q}_{14}$, for active (red and blue lines) and passive (two overlapping black lines) systems. $\mathcal{Q}_{41}$ determines the velocity of point 4 when the system is excited by a force at point 1, whereas $\mathcal{Q}_{14}$ determines the velocity of point 1 when the system is excited by a force at point 4, (see Figure 1, right plot).

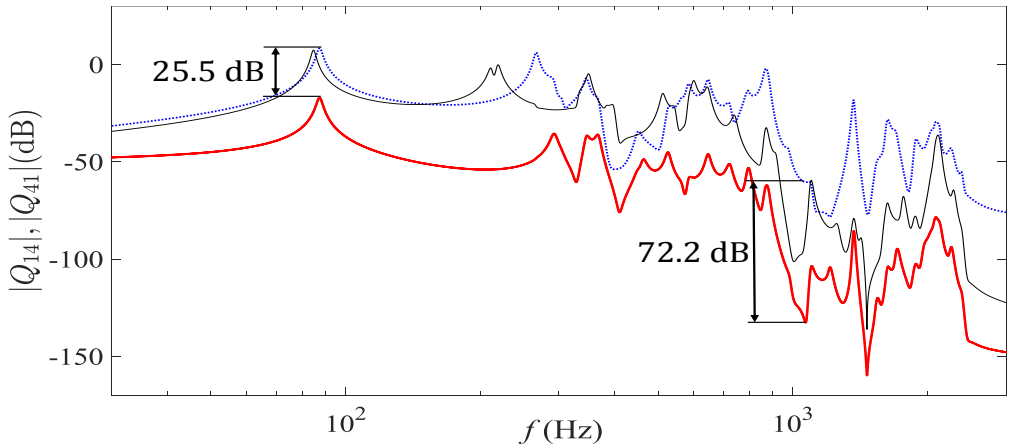

Figure 13 Amplitudes of the characteristic frequency response functions of the activated system $\mathcal{Q}_{14}$ and $\mathcal{Q}_{41}$: faint black line – passive system (reference), dotted blue line – $\mathcal{Q}_{14}$, solid red line – $\mathcal{Q}_{41}$

3. Conclusions

A decentralized control scheme, utilizing sensors and actuators in a non-collocated configuration, is used to develop an active acoustic metamaterial. Such an active waveguide is able to propagate vibrations in a non-reciprocal manner over a broad frequency band, suppressing them in one direction, while amplifying them in the opposite direction. The active system can also be designed to have desirable stability properties, at least under the assumption of ideal sensors and actuators.

References

[1] Fahy, F., Walker, J., Advanced Applications in Acoustics, Noise and Vibration, CRC Press, London, 2017.

[2] Caiazzo, A., Alujević, N. Pluymers, B., Desmet, W., Active control of turbulent boundary layer-induced sound transmission through the cavity-backed double panels, *Journal of Sound and Vibration*, 422, 161-188, 2018.

[3] Skogestad, S., Postlethwaite, I., *Multivariable Feedback Control: Analysis and Design*, Chichester, 2005.

Experimental approach for optimal design of a TMD in a lightweight footbridge

Tomislav Jarak*+, Alvaro Iglesias-Pordomingo+, Alvaro Magdaleno+, Antolin Lorenzana+

* *Faculty of Mechanical Engineering and Naval Architecture, Ivana Lučića 5 10002 Zagreb*
E-mails: tomislav.jarak@fsb.hr

+ *ITAP, School of Industrial Engineering, EII. Paseo del Cauce 59 Valladolid*
E-mail: tomislav.jarak@uva.es, alvaro.iglesias@uva.es, alvaro.magdaleno@uva.es, antolin.lorenzana@uva.es

Keywords: structural control, vibrations

1. Introduction

Serviceability limit state is a key issue in the assessment of slender structures under pedestrian loads. Guidelines and standards [1,2] require that accelerations do not exceed certain limit values. When not meeting this requirement, an increase of the structural damping is usually prescribed. The simplest way to do this is by means of inertial devices such as Tuned Mass Dampers (TMD).
The present work is based on the Experimental Modal Analysis (EMA) [3] to estimate the modal properties of a structure using a set of Frequency Response Functions (FRF) and the subsequent assembly of the TMD (as a Single Degree of Freedom (SDOF) system) and its optimisation for minimizing the dynamic response of the structure. Entire procedure is made using modal coordinates.

2. Experimental layout

The structure under study is a walkable timber footbridge 13.5 metres long and weighing 855 kg (Figure 1). Although it is mainly simply supported at its ends, it also has a central elastic support. Also shown in Figure 1 is a commercial shaker and a homemade TMD. The TMD consists of a frame attached to the side of the timber structure. The frame supports a certain moving mass cantilevered by flexible frictionless elements so that the movement is vertically confined without the need for additional mechanical elements such as linear guides. The damping is achieved through eddy currents in such a way that it does not induce friction. Consequently, the whole device can be perfectly modelled as a linear SDOF system. More details can be found in [4].

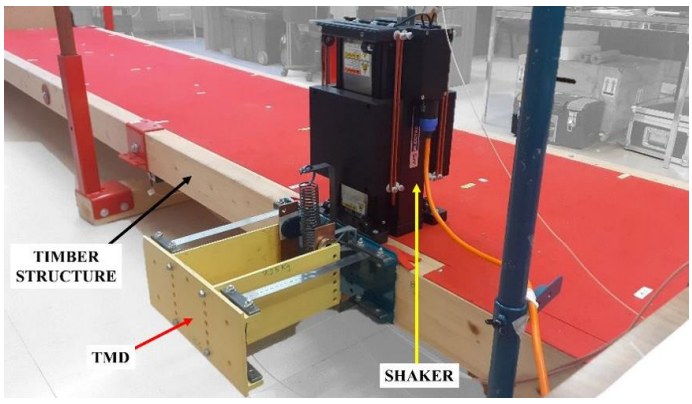

Figure 1. Timber structure, shaker, accelerometers and TMD

3. Developed methodology

A control technology approach, which models physical systems as MIMO (multi-input, multi-output) systems through a state space, has been used to address the problem. The methodology developed has two steps:

The first step consists of the modal identification of the system. To do this, design curves are created, relating the physical properties of the actual TMD to its identified on-board properties. Once the EMA of the footbridge is performed (without any TMD), experimental FRF are obtained for a certain parameter of the SDOF assembled. Specifically, in all scenarios the stiffness and damping are invariant and just the moving mass varies in a narrow range. Then, the modal properties of the generic TMD that, coupled to the model of the structure, best fit each of the experimental FRFs are found, and the design curve for the effective mass of the TMD in the structure is constructed. The obtained curve has the slope close to 1, as expected, so that the increase in the physical moving mass coincides with the increase in the effective moving mass.

The second step consists of tuning the TMD and testing its on-board performance. To do this, another computational optimisation process is employed where, fixing stiffness and damping, the mass that minimises the largest amplitude of the accelerance may be found. Using the design curve, the actual mass corresponding to the optimal effective mass is found and installed in the real TMD. Finally, it is checked that the computational FRF set matches the experimental FRF with the new moving mass attached.

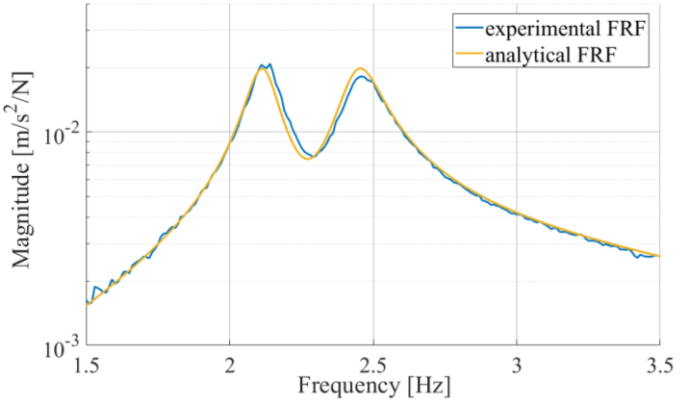

Figure 2. Comparison between experimental and computational results

4. Conclusions

Figure 2 shows the comparison between the computational FRF, in yellow, and the experimental FRF, in blue, with the objective moving mass installed, according to the proposed methodology. The similarity of the results validates the presented approach, so that it is possible to prescribe and to install, in a single attempt, the best TMD, according to the defined criteria, to be fit to any structure under study.

Acknowledgments

The authors wish to acknowledge Ministerio de Economía y Competitividad, Spanish Government, for the partial support through the RTI2018-098425 Research Project.

References

[1] International Standard ISO 10137: 2007(E), Bases of for design of structures - Service-ability of buildings and walkways against vibrations. ISO 10137:2007, International Organization for Standardization, 2007.

[2] SETRA. Technical guide - footbridges - Assessment of vibrational behavior of footbridges under pedestrian loading, Service d'Etudes Techniques des Routes et Autoroutes, 2006.

[3] Ewins, D.J., *Modal testing : theory, practice, and application*. Research Studies Press, Place of Publication, Baldock, England, 2000.

[4] Magdaleno, A., Lorenzana, A., A transmissibility-based procedure to estimate the modal properties of an on-board tuned mass damper. *Mechanical Systems and Signal Processing Title*, 135, 106378, 2020.

How to Model a 3D Battery Module in 5 Simple Steps?

Mario Jelović, Mate Šimundić, Filip Kozlik, Matej Poletar

AVL-AST d.o.o. Strojarska cesta 22, HR-10000 Zagreb, Croatia
E-mails: mario.jelovic@avl.com, mate.simundic@avl.com,
filip.kozlik @avl.com, matej.poletar@avl.com

Keywords: BEV, Battery Module, Electric, Thermal, Mechanic

1. Introduction

Questions on 3D phenomena in battery thermal management systems are no longer exclusively answered by 3D-CFD. Modeling engineers target to resolve 3D problems already on the system level (Figure 1a). CRUISE™ M's [1] answer to this is new "Battery Module" component (Figure 1b). It describes the electrical, thermal, and mechanical interaction of pouch and prismatic cells on module level.

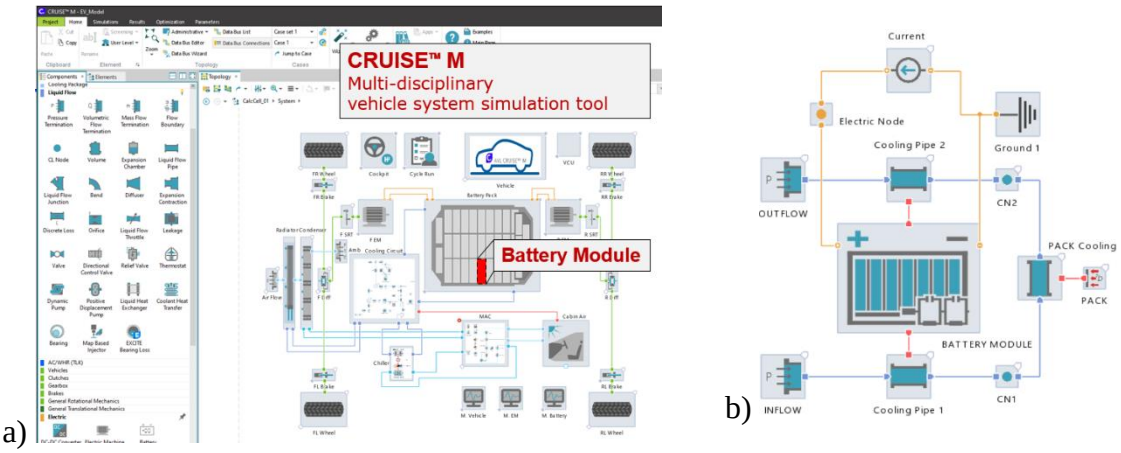

Figure 1. BEV system level model featuring multiple physical domains (a) and simplified model with single battery module (b)

2. Battery Module component

The Battery Module component features various stack assemblies, thermoregulation concepts and operating conditions. The component facilitates modeling of battery modules with a maximum flexibility through a tailored input workflow.

A simulation engineer can easily configure (Figure 2) the assembly of battery cells, compression pads, cooling plates and housing, their geometries and materials (1st step), define the electrical connection pattern of the battery cells (2nd step), specifies the thermal contact resistances between stack elements and the housing plates and configures arbitrary thermal connections to any kind of thermoregulation network (3rd step). Additionally, he/she can opt for different kinds of battery cell models: AVL model, Batemo models [2] or even a custom cell model (4th step).

To get first insights into mechanical aspects you can opt for mechanical model [3]. You need to provide information on the cell swell as a function of state-of-charge, state of health and temperature and you can tick a few boxes to turn on a bending model or the consideration of bolds added to the housing (5th step).

What is innovative? Battery Modul offers right sizing the model complexity (away from full blown CFD) to a nearly RT capable approach.

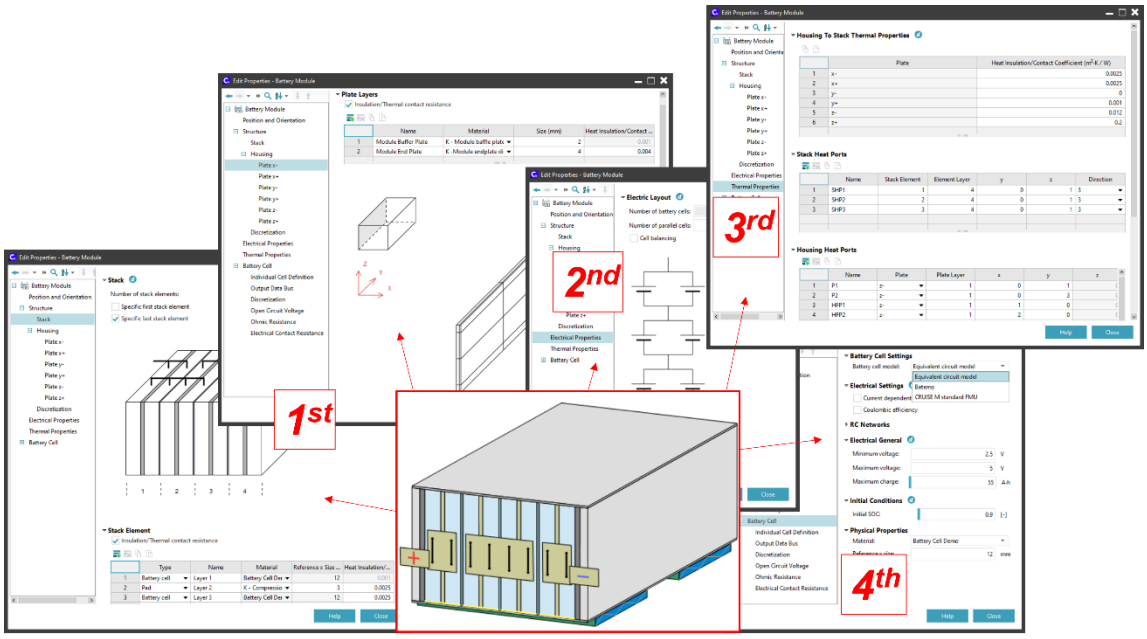

Figure 2. Let us have a look at the 4 steps we need to take to get a Battery Module ready for the electrothermal simulation.

3. Results

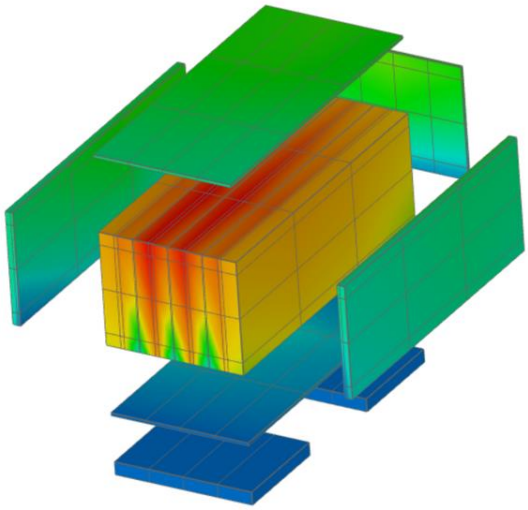

Figure 3. 3D Results – Temperature distribution in Battery Module

The Battery Module component features the potential to pull classical 3D-CFD simulation activities to the level of system simulation.

- The time to setup comprehensive thermal models is drastically reduced
- The model size and number of components in a model is melted down
- The maintenance of thermal models significantly simplified
- The computational performance is raised
- Simulation of entire battery packs is made possible with reasonable effort

References

[1] AVL CRUISE™ M User Manual, Version 2022 R1

[2] Batemo GmbH, Batemo Cell Library (https://www.batemo.de/products/batemo-cell-library/)

[3] R. Rebba, J.H. Seo, A.M. Sastry, M. Fortier, Design Parameter Trade-off for Packaging of Stacked Prismatic Batteries, SAE Technical Paper 2011-01-0667

Length-scale insensitive phase-field model and dual-mesh FEM discretization for phase-field problems for reduced mesh requirements

Krešimir Jukić*, Tomislav Jarak+*, Zdenko Tonković*

*Faculty of Mechanical Engineering and Naval Architecture, Ivana Lučića 5 10002 Zagreb
E-mails: kresimir.jukic@fsb.hr, tomislav.jarak@fsb.hr, zdenko.tonkovic@fsb.hr

+ ITAP, School of Industrial Engineering, EII. Paseo del Cauce 59 Valladolid
E-mail: tomislav.jarak@uva.es

Keywords: phase-field, fracture, lenght-scale sensitivity, dual mesh

1. Introduction

The phase-field (P-F) method is the most promising diffusive approach for modelling fracture phenomena, but it is sensitive on the value of the length-scale parameter [1], and requires the use of high-density mesh as well as high computation costs.

This paper presents a length-scale insensitive P-F model. In contrast to the model in [2], where the derivatives of a degradation function and the local part of a crack surface density function with respect to the phase-field at the undamaged state are utilized, we employ the scaling factor of the crack surface density function to obtain length-scale insensitivity. Following ideas from [3], a new family of crack surface density functions and a new softening law concept are introduced, which enable independent calibration of the P-F profile, the stress-strain response and the critical stress. In the conventional Finite Element Method (FEM) framework, a fully broken specimen contains one layer of fully broken elements. To develop this layer, additional spurious fracture energy needs to be dissipated, and the critical energy release rate and the critical force are seemingly increased. To reduce this additional parasitic fracture energy and reduce the mesh density requirements, a discretization by finite elements and finite volumes was utilized in [4]. In this work, a new dual-mesh discretization scheme is proposed, with the primary triangular mesh and the secondary polygonal or triangular mesh.

2. Methodology

Length-scale insensitivity is obtained defining the considered softening law in the form

$$\alpha = \alpha(g) = \alpha\big(g(\phi, a)\big), \tag{1}$$

and by using the new crack surface density function defined by

$$\gamma = \frac{1}{c}\left(\frac{1}{l}\phi^a + l^{b-1}k|\nabla\phi|^b\right), c = c(a,b), k = k(b), \tag{2}$$

where ϕ, g and l are the phase field, the energy degradation function, and the length-scale parameter, respectively. a and b are tunable scalar parameters. The considered softening law can always be written as $\bar{\sigma} = \bar{\sigma}(\bar{\varepsilon})$, with $\bar{\sigma}$ and $\bar{\varepsilon}$ as scaled (dimensionless) stress and strain. We additionally obtain:

$$\phi_{opt} = \left(1 - \frac{|x|}{pl}\right)^p, p = p(a,b), \sigma_{crit} \sim \sqrt{\frac{G_c E}{cl}}, \tag{3}$$

where ϕ_{opt} is the optimal 1-D phase-field profile with $\phi_{opt}(0) = 1$ and $\phi_{opt}(\pm\infty) = 0$. It is clear now that by choosing a, b, l and α, one can control the stress-strain response, the critical stress and the phase-field profile independently.

A new dual-mesh discretization approach is proposed, with the primary triangle mesh used for the deformation energy and the secondary polygonal mesh for the fracture energy. The nodes of the secondary mesh are placed at the centers of mass of triangle elements of the primary mesh. The nodes of the primary mesh contain only displacements, while the nodes of the secondary mesh carry the phase-field information. Two methods for generating the secondary mesh are proposed. Firstly, the

polygonal mesh is formed by connecting the centers of mass of primary mesh elements. The second option is a further triangulation of thus obtained polygons.

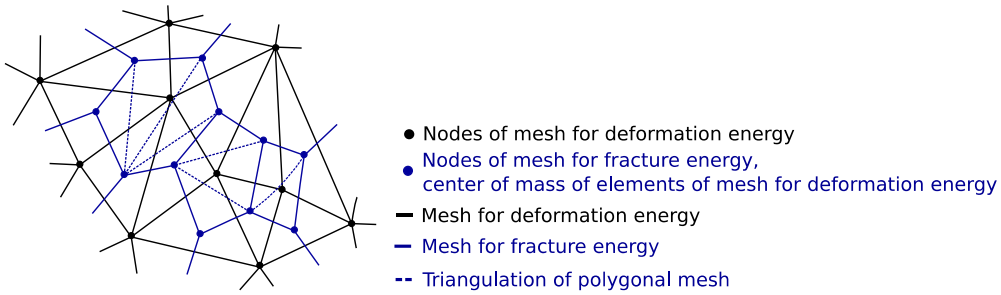

Figure 1. Generation of secondary mesh (blue lines and dots) from primary mesh (black lines and dots)

3. Preliminary results

A rectangular plate with a horizontal predefined crack is considered. The crack length is equal to the plate half-width. The length and width of the plate are 6mm and 1mm, respectively. Material parameters are $G_c = 0.1\text{MPa} \cdot \text{mm}$, $E = 10000\text{MPa}$, $\nu = 0.3$, and $l = 0.1\text{mm}$. Uniform tensile stress is applied of both the top and the bottom surface of the plate. The convergence of the critical force with respect to the size of the primary mesh is observed. The mesh size is normed to the length-scale. In Fig. 2, we observe a superior convergence of the dual-mesh approach in comparison to the standard FEM approach and the FEM-Finite Volume (FV) approach [4]. In case of the secondary polygonal mesh, the critical force is somewhat underestimated. Preliminary results have shown that in all discretization schemes mesh requirements might dominantly be set by the critical stress, rather than by the length-scale.

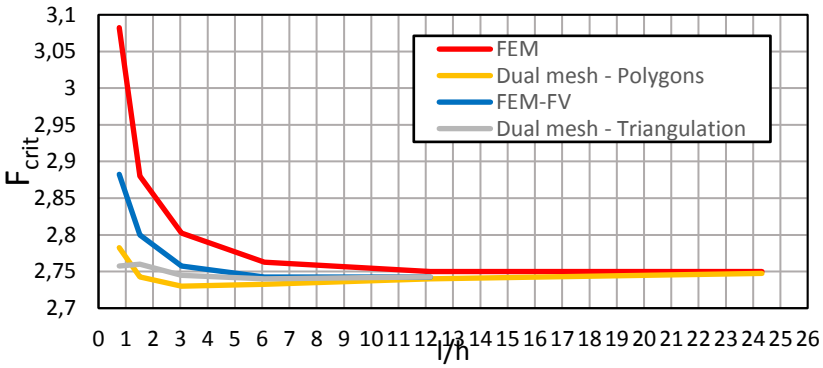

Figure 2. Critical force with respect to length-scale

Acknowledgements

This work has been supported and co-funded by the European Union through the European Regional Development Fund, Operational Programme "Competitiveness and Cohesion" 2014 – 2020 of the Republic of Croatia, project "Protection of Structural Integrity in Energy and Transport" (Zacjel, KK.01.1.1.04.0056). The second author wishes to acknowledge Ministerio de Economía y Competitividad, Spanish Government, for the partial support through the RTI2018-098425 Research Project.

References

[1] P. Kristensen, C. Niordson, E. Martínez-Pañeda, An assessment of phase field fracture: crack initiation and growth, 2021.
[2] J.-Y. Wu, V.P. Nguyen, A length scale insensitive phase-field damage model for brittle fracture, Journal of the Mechanics and Physics of Solids 119 (2018) 20-42.
[3] T. Gerasimov, L. De Lorenzis, Second-order phase-field formulations for anisotropic brittle fracture, Computer Methods in Applied Mechanics and Engineering 389 (2022) 114403.
[4] J. Sargado, E. Keilegavlen, I. Berre, J. Nordbotten, A combined finite element–finite volume framework for phase-field fracture, Computer Methods in Applied Mechanics and Engineering 373 (2021) 113474.

Multiscale submodeling technique for ductile heterogeneous materials

Ante Jurčević*, Tomislav Lesičar*, Zdenko Tonković*, Jurica Sorić*

*Faculty of Mechanical Engineering and Naval Architecture, I. Lučića 5, 10000 Zagreb
E-mails: {ante.jurcevic,tomislav.lesicar,zdenko.tonkovic,jurica.soric}@fsb.hr

Keywords: multiscale analysis, macroscale, microscale, Self-consistent clustering analysis, submodeling

1. Introduction

The mechanical behaviour of materials is largely influenced by their microstructure, which consists of several constituents of different properties and shares. To consider the impact of the structural phenomena at the microscale of materials, the last few decades have been characterized by the intense development of multiscale methods, which are able to analyse material behaviour at multiple levels, i.e., scales. Concurrent multiscale methods [1, 2] are based on the realization of a direct link between the lower and higher level, i.e., the microstructure's behaviour and the response of the material at the macroscale. After solving the boundary value problem at the microscale, which is defined through the Representative Volume Element (RVE), the results of the analysis need to be homogenized, i.e., averaged. The averaged results are then used as input for solving the macroscale boundary value problem. Since both micro- and macro-level are discretized by finite elements, the whole process, which includes analysis at both scales leads to long computational time and high costs of computational resources.

Intensive development of the computational resources and novel multiscale algorithms have lowered the computational time needed to complete the analysis and brought the multiscale procedures closer to commercial use. Significant progress in computational resources savings and computational time shortening of a concurrent multiscale approach has been achieved by using a data-driven, self-consistent clustering algorithm [3]. Based on the data compression and k-means clustering, the algorithm is characterized by a significant reduction in the number of degrees of freedom at the microscale, which is decomposed into a relatively small number of sub-domains, i.e., clusters – Figure 1.

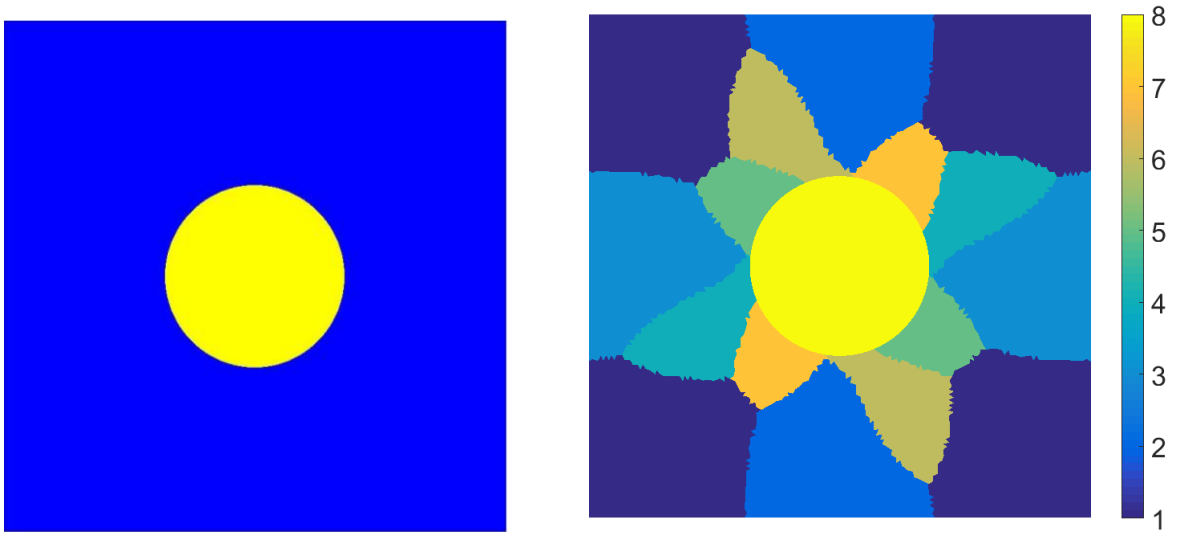

a) b)

Figure 1. a) Unit cell, b) Unit cell decomposed into eight clusters

Although the number of degrees of freedom at the micro-level is significantly reduced, the homogenized values do not deviate significantly from the homogenized values obtained via the Finite Element Method. Because of this, the time needed to perform a concurrent multiscale procedure is reduced by several orders of magnitude, while the accuracy of the final result is satisfactory.

However, complex problems involving a significant number of degrees of freedom at the macroscale, the occurrence of large strains [4], and localized effects such as plasticity and damage [5] still require a long computational time. Conducting microscale analysis for each integration point inside each increment greatly contributes to the overall computational time, while the use of homogenized values in finite element analysis reduces the convergence rate of a global system of equations.

2. Submodeling approach

To further increase computational time efficiency, this study will examine the influence of the choice of the multiscale submodel size on the test specimens. The aim is to determine to what extent is possible to omit the multiscale procedure from macroscale finite elements, without significantly altering the accuracy. It is not unknown that geometric discontinuities, notches, and various constrictions create areas with high concentrations of stress and strain, for which fine mesh density with a low level of distortion is needed. Following the same principle, it can be assumed that the multiscale analysis is crucial at points of high concentrations of stress and strain since the occurrence of plastic deformations and damage will start there. Therefore, the multiscale procedures will be performed exclusively on elements that fall into the defined submodel, while for the second group of other elements a standard analysis of homogeneous material, according to the laws of local continuum mechanics, will be utilized.

Examples will include 2D and 3D samples with geometric discontinuities and notches which will be analysed with different sizes of multiscale submodels. By varying the size of the submodel, it will be possible to determine the true benefits of this approach and conclude the optimal size of a submodel for a given problem.

Acknowledgment

This work has been supported by Croatian Science Foundation under the project “Multiscale Numerical Modelling and Experimental Investigation of Aging Processes in Sintered Structural Components” (MultiSintAge, PZS-1 2019-02-4177).

References

[1] Lesičar, T., Tonković, Z., Sorić, J., A second-order two-scale homogenization procedure using C^1 macrolevel discretization. Computational Mechanics, 54, 425-441, 2014.

[2] Lesičar, T., Sorić, J., Tonković, Z., Large strain, two-scale computational approach using C^1 continuity finite element employing a second gradient theory. Computer Methods in Applied Mechanics and Engineering, 298, 303-324, 2016.

[3] Liu, Z., Bessa, M. A., Liu, W. K., Self-consistent clustering analysis: An efficient multi-scale scheme for inelastic heterogeneous materials. Computer Methods in Applied Mechanics and Engineering, 319-341, 2016.

[4] Yu, C., Kafka, O. L., Liu., W. K., Self-consistent clustering analysis for multiscale modeling at finite strains. Computer Methods in Applied Mechanics and Engineering, 339-359, 2019.

[5] Fleming, M., Liu, W. K., Microstructural material database for self-consistent clustering analysis of elastoplastic strain softening materials. Computer Methods in Applied Mechanics and Engineering, 547-577, 2017.

Adaptive modeling with hierarchical Fup basis functions and control volume within isogeometric analysis

Grgo Kamber*, Hrvoje Gotovac*, Vedrana Kozulić*

*University of Split, Faculty of Civil Engineering, Architecture and Geodesy
Split, Matice hrvatske 15
E-mails: {grgo.kamber, hrvoje.gotovac, vedrana.kozulic}@gradst.hr

Keywords: Hierarchical Fup basis functions, IsoGeometric Analysis, Local refinement

1. Introduction

In this work, adaptive procedure using hierarchical Fup [1] basis functions and control volume, is presented. Fup basis functions belong to the class of atomic basis functions and can be regarded as infinitely differentiable splines [2]. Hierarchical Fup (HF) basis functions and hierarchical B-splines (HB and truncated version THB) are closely related. However, HF have the option of local *hp*-refinement such that they can replace certain basis functions at one resolution level with new basis functions at higher resolution level that have a smaller length of the compact support (*h*-refinement) and higher order (*p*-refinement). Using adaptive hierarchical procedure with Fup basis functions provides spectral convergence rate [3] which presents a substantial improvement in comparison to the HB or THB that enables polynomial convergence. Conservation is an interesting feature of the control volume formulation. The conservation is exactly satisfied over any CV (local conservation), as well as over the whole computational domain (global conservation.)

2. Methodology

2.1. Basis functions

Fup basis functions belong to the class of atomic functions (see [1,2]) and span vector space of algebraic polynomials. Furthermore, their properties are closely related to the more known B-splines. For 1-D Fup basis functions, Fup_n^l defined on Ξ^l (resolution level l) can be represented as linear combination of $(n+2)$ Fup_{n+1}^{l+1} defined on Ξ^{l+1} (higher resolution level). However, since 2-D Fup basis functions are made as tensor product of the 1-D Fup basis functions, $Fup_n^l(x,y)$ defined on level l can be represented as a linear combination of $(n+2)x(n+2)$ i.e., $(n+2)^d$ Fup_{n+1}^{l+1} defined on the level $l+1$,

$$Fup_n^l(x,y) = \sum_{i=0}^{n+1}\sum_{j=0}^{n+1} C_{n+1}^i C_{n+1}^j Fup_{n+1}^{l+1}\left(x - \frac{i}{2^{n+1}} + \frac{n+1}{2^{n+2}}\right) Fup_{n+1}^{l+1}\left(y - \frac{j}{2^{n+1}} + \frac{n+1}{2^{n+2}}\right) \quad (1)$$

where C_{n+1}^i and C_{n+1}^j are refinement coefficients and d represents dimensional (in this case $d=2$).

2.1. Control volume isogeometric analysis (CV-IGA)

To derive CV-IGA, the 2-D parameter space defined by uniform knot vector is shown in Figure 1. Domain is subdivided into a set of control volumes (CVs) such that each CV surrounds one corresponding vertex (Figure 1- black dots) of basis functions and CVs boundary is defined at half distance between neighboring vertices.

In Figure 1, the focus is on the grid point $V_{i,j}$ (represents basis function vertex), which has the surrounding grid points V_u , V_d , V_l and V_r as its neighbors. Moreover, $CV_{i,j}$ boundaries (Figure 1 – red line) are marked as $\Gamma_{i,j,u}, \Gamma_{i,j,d}, \Gamma_{i,j,l}$, and $\Gamma_{i,j,r}$.

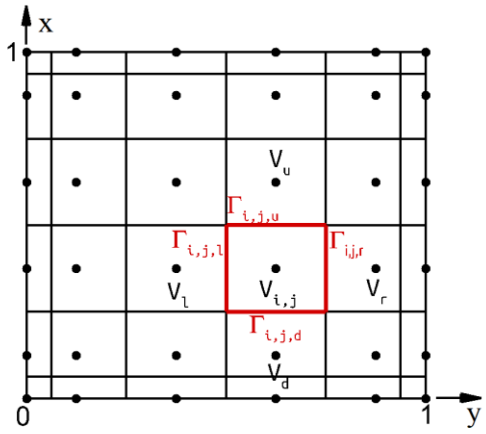

Figure 1. Control volume scheme for 2-D case.

In Figure 1, the focus is on the grid point $V_{i,j}$ (represents basis function vertex), which has the surrounding grid points V_u , V_d , V_l and V_r as its neighbors. Moreover, $CV_{i,j}$ boundaries (Figure 1 – red line) are marked as $\Gamma_{i,j,u}, \Gamma_{i,j,d}, \Gamma_{i,j,l}$, and $\Gamma_{i,j,r}$.

Figure 2 shows a nested sequence of CVs domain, together with the corresponding vertices for each resolution level l, where each CV is linked with only one vertex (basis function). This means that the number of basis functions corresponds to the number of CVs.

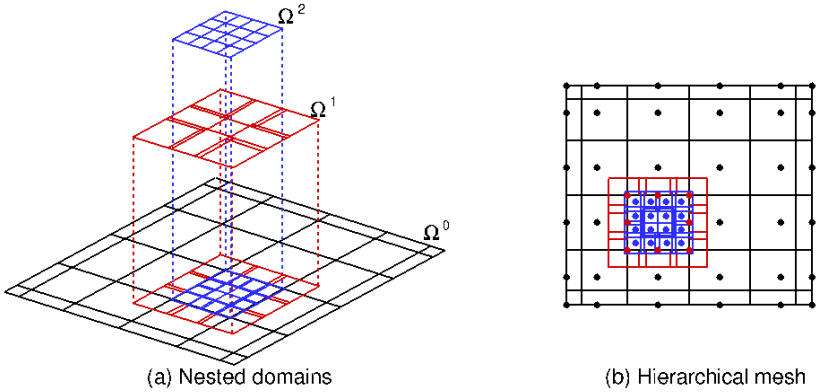

Figure 2. A nested sequence of CV domains for the construction of the Fup hierarchy according to relation $\Omega^l \supseteq \Omega^{l+1}$ for $l = 0,1,2$ for 2-D case.

4. Conclusions

Adaptive procedure based on hierarchical Fup (HF) basis functions and the control volume IGA formulation is presented. Fup basis functions belong to the class of atomic functions and have the option of local *hp*-refinement. The application of hierarchical Fup basis functions enables higher continuity and smoothness of the solution while providing spectral convergence. Furthermore, control volume formulation retains the conservation property of governing equations.

References

[1] Rvachev, V.L., Rvachev, V.A., On a finite function. *Dokl. Akad. Nauk Ukrainian SSR*, ser A, (6): 705-707, 1971.

[2] Gotovac, B., Kozulic, V., On a selection of basis functions in numerical analyses of engineering problems. *International Journal for Engineering Modelling, 12(1-4):24-41*, 1999.

[3] Kamber, G., Gotovac, H., Kozulic, V., Malenica, L., Gotovac, B., Adaptive numerical modeling using hierarchical fup basis functions and control volume isogeometric analysis. *International Journal for Numerical Methods in Fluids*, 92(10): 1437-1461, 2020.

A Multiscale Phase-field Analysis of the Dynamic Fracture Behavior of Fiber-Reinforced Concrete

Hannah Knobloch*, Stefan Loehnert *

*Institute of Mechanics and Shell Structures, Technische Universität Dresden,
August-Bebel-Str. 30, 01219 Dresden, Germany
E-mails: hannah.knobloch@tu-dresden.de,stefan.loehnert@tu-dresden.de

Keywords: multiscale methods, fracture behavior, phase-field, dynamics

1. Introduction

In the past years the development and investigation of composite materials with improved mechanical properties has been an important area of interest, both in practical applications and in research. One example is fiber-reinforced concrete, which consists of a fine-grained concrete matrix, into which short fibers are embedded to enhance its tensile strength and ductility. The interaction of the different components and microstructural effects, such as micro cracks, influence the macroscopic properties. The resulting complexity of the material behavior makes accurate predictions and the safe application of such new materials rather difficult. Therefore, detailed simulative investigations of these materials are an essential contribution to understanding their material properties and failure mechanisms.

Inertia effects due to dynamic loads complicate predictions of the material response even further. Phenomena like crack branching and coalescence lead to complicated fracture networks, making accurate and efficient simulations challenging. Fully macroscopic models oversimplify the problem, leaving potentially important fine scale effects disregarded, while micro- and mesoscale models lead to an immense computational effort. That is why in this contribution a multiscale approach is employed that combines the accuracy advantages of a detailed micro model with the efficiency of a macro model.

2. Numerical methods

2.1. Multiscale approach

Many common multiscale methods show difficulties regarding localization effects, such as fracture. Moreover, modeling dynamic phenomena and wave propagation can be problematic due to the occurrence of spurious wave reflections within the fine scale and along the interface between fine and coarse scale. That is why special care must be taken when choosing an appropriate multiscale method. The multiscale approach employed here, is based on the Multiscale Projection Method (MPM) 0 and the Generalized Finite Element Method with global-local enrichment ($GFEM^{gl}$) 0. They share the basic idea that in certain areas of interest, a more detailed analysis is conducted, in order to include fine scale effects in the coarse scale simulation. The two approaches are concurrent, meaning that the scales are coupled both ways. In both cases, the solution from the coarse scale problem is used as boundary condition for the fine scale simulation. While the MPM transfers information from fine to coarse scale by projecting certain values, in the $GFEM^{gl}$ the coarse scale displacement field is enriched with information from the fine scale. For the extension to dynamics, inertia terms are added to the governing equation on both scales.

2.2. Fine scale

On the fine scale, a phase-field approach is employed, in order to capture the behavior of evolving crack surfaces efficiently and accurately. The phase-field method originates in the variational formulation of brittle fracture by Francfort and Marigo 0, which permits the development of almost arbitrary fracture networks. It is related to Griffith's energy-based theory of fracture and states that

the energy, consisting of internal elastic, external and dissipation energy from the formation of new surfaces, must be minimized. Later, Bourdin et al 0 proposed a way to numerically treat the problem, by introducing an additional scalar field, the phase-field ϕ, which distinguishes between an undamaged and a broken phase of the material. Consequently, fractures are no longer considered discrete, but are smeared over an area regulated by a length parameter l_c. Since complex loading scenarios are considered, including both tensile and compressive parts, it is important to apply a split of the elastic strain energy. That way, only tensile contributions lead to fracture propagation, while compressive parts have no influence.

2.3. Coarse scale

On the coarse scale, only a basic elasticity problem is solved, where the displacement field within the multiscale domain is enriched. In contrast to other common enrichment strategies for cracks, which consist of a jump and crack tip enrichment, here, a numerical enrichment is applied. It is automatically obtained from the displacements calculated on the fine scale. In order to avoid near linear dependencies and conditioning issues, a Babuška 0 stabilization is used. This enrichment strategy is similar to the one by Geelen et al 0, who developed an enriched multiscale method for quasi-static fracture simulations. In addition, the material degradation, resulting from the smeared crack approach on the fine scale, is projected to the coarse scale, modifying the elastic stiffness of the material.

3. Conclusion

Overall, an accurate, but efficient way to simulate dynamic fracture propagation in fiber-reinforced concretes is presented. By combining the two multiscale methods, even detailed microscopic features can be resolved in the vicinity of cracks, while the overall structural analysis is kept simple and efficient. The extension to dynamics allows for the simulation of impact loads and wave propagation in the specimen. Additionally, the phase-field approach is convenient, since crack nucleation, coalescence and branching are possible without the need for additional propagation criteria or geometry information. Since in 3D simulations fractures take up only a small fraction of the full volume, single scale phase-field simulations are cumbersome, due to the necessary local mesh refinements. The resulting differences in element size are especially unfavorable for transient analyses, which is why keeping fine and coarse scale problems separate is particularly suitable in this case. Moreover, the simulations of independent fine scale problems allow for an efficient parallelization.

References

[1] Loehnert, S., Belytschko, T., A multiscale projection method for macro/microcrack simulations. *International Journal for Numerical Methods in Engineering*, Vol 71, pp. 1466-1482, 2007.

[2] Duarte, C.A., Kim, D.-J., Babuška, I., A global-local approach for the construction of enrichment functions for the generalized FEM and its application to three-dimensional cracks. In: *Advances in Meshfree Techniques. Computational Methods in Applied Sciences.* Leitão, V.M.A., Alves, C.J.S., Armando Duarte, C. (eds), Dordrecht, pp. 1-26, 2007.

[3] Francfort, G. A., Marigo, J.-J., Revisiting brittle fracture as an energy minimization problem. *Journal of the Mechanics and Physics of Solids*, Vol 46(8), pp.1319-1342, 1998.

[4] Bourdin, B., Francfort, G. A., Marigo, J.-J., Numerical experiments in revisited brittle fracture. *Journal of the Mechanics and Physics of Solids*, Vol 48, pp. 797-826, 2000.

[5] Babuška, I., Banerjee U., Stable generalized finite element method (SGFEM). *Computer Methods in Applied Mechanics and Engineering*, Vol 201-204, pp. 91-111, 2012.

[6] Geelen, R., Plews, J., Tupek, M., Dolbow, J., An extended/generalized phase-field finite element method for crack growth with global-local enrichment. *International Journal for Numerical Methods in Engineering*, Vol 121, pp. 2534-2557, 2020.

Neural network approach for predicting stress-strain behavior of carbon nanotubes

Valentina Košmerl*, Ivan Štajduhar+, Marko Čanađija*

*University of Rijeka, Faculty of Engineering, Department of Engineering Mechanics, Vukovarska 58, 51000 Rijeka, Croatia
+University of Rijeka, Faculty of Engineering, Department of Computer Engineering, Vukovarska 58, 51000 Rijeka, Croatia
E-mails: {vkosmerl,ivan.stajduhar,marko.canadija}@riteh.hr

Keywords: artificial neural networks, molecular dynamics, single-walled carbon nanotubes, constitutive behavior

1. Introduction

Carbon nanotube (CNT) properties research has been one of the most active research fields in nanomechanics and nanotechnology for more than two decades, as CNTs enable exciting new design ideas and advances. Computational modeling has improved our understanding of the properties and structural behavior of CNTs. Due to time-consuming simulations, available molecular dynamics (MD) models are usually assessed on a limited set of single-walled carbon nanotube (SWCNT) configurations. Therefore, a thorough research of the stress-strain relationship of CNTs is still missing. As many MD simulations are required to generate a large and reliable dataset, machine learning approaches can effectively reduce these computational costs,

In this study, a novel neural network approach for modeling uniaxial stress-strain curves of SWCNTs with diameters less than 4 nm is proposed. Multilayer perceptron (MLP), an architecture most commonly used in materials science, was compared to 1D convolutional neural network (CNN), a state-of-the-art DL algorithm, and residual neural network (ResNet) - a popular image classification model architecture. Data extracted directly from atomic-scale simulations in [1] was used to train the above model architectures. The three trained models were validated by comparing the estimated uniaxial stress-strain curves with those obtained from MD simulations. The impact of various input feature combinations on the prediction of thermal fluctuations is studied.

2. Methods

2.1 Molecular dynamics model

The tensile stress-strain curve dataset was created through a series of molecular dynamics calculations in LAMMPS. The system was first energy-minimized, then equilibrated at 300 K for 25 ps, which inevitably introduced thermal noise into the results. The uniaxial tensile test was the final step, which involved applying loading to one end of the SWCNT by prescribing the velocity. The SWCNT's length and diameter as geometric properties were constantly monitored and recorded. With the current diameter, which is significantly affected by thermal vibrations, and current length at hand, the volume of the SWCNT was then approximated by a hollow cylinder. The volume is used to obtain the axial stress in a SWCNT by averaging the virial stresses in the SWCNT. The true stresses were accompanied by the true strains to obtain the uniaxial stress-strain curve.

2.2 Machine learning model

Each of the 818 configurations was tested for three different equilibrated configurations due to the stochastic nature of the atoms' thermal fluctuations. The obtained results were then averaged over three sets of simulations. The total number of points is 1,592,272 with an average of 1,946 points per curve. The dataset was randomly split into the training, validation, and test sets in a 60:20:20 ratio. The input data was comprised of the chiral indices n and m, the current diameter D, the true strains ε_t,

and the current temperatures T. The output data was the uniaxial true stress σ_t. For the MLP and CNN model architectures, a sequential model was constructed, whereas the ResNet model architecture was implemented from [2]. The mean square error loss function was used for optimization, with smaller loss values indicating better model fit. The most successful network architectures were chosen based on the lowest error.

3. Results and discussion

The best MLP is 2-Dense50 model with RMSE = 0.0045, the CNN is 1-Conv64-Dense50 model with RMSE = 0.0043, and for the ResNet architecture this is 10-ResNet16 model with RMSE = 0.0065. The near-ideal predictions of the three models for the CNT (11, 2), which has rather strong thermal fluctuations, are shown in Fig. 1.

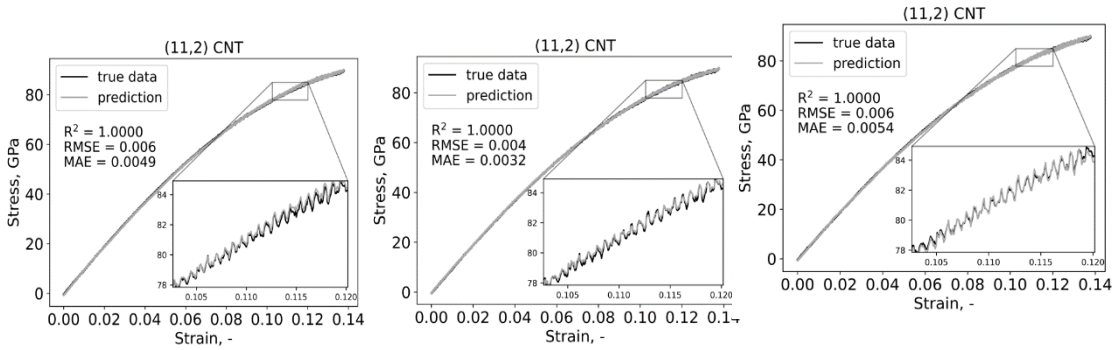

(a) **(b)** **(c)**

Figure 1. Stress-strain curves for CNT (11, 2) predicted by: (a) 2-Dense50, (b) 1-Conv64-Dense50, (c) 10-ResNet16

The NN does not begin to predict thermal fluctuations with great precision until the current diameter D is added to the initial list of input features n, m, ε_t, and T. In terms of metrics, CNN performs somewhat better than MLP and ResNet in predicting stress-strain curves with included thermal fluctuations, regardless of whether the prediction is for small or large nanotubes. Both MLP and CNN model architectures perform similarly when thermal fluctuations are completely smoothed out, whereas ResNet is incapable of smoothing out the stress-strain curve.

4. Conclusions

The uniaxial stress-strain curves estimated by the trained artificial neural networks correlate highly with the curves calculated using atomistic simulations. MLP, 1D CNN and ResNet precision was primarily compared using RMSE, MAE, and R2, indicating that the 1D CNN model architecture is slightly more accurate than both MLP and ResNet. It was found that only the diameter together with the chiral indices and the true strain in the input features leads to a completely accurate prediction of atomistic thermal fluctuations.

Acknowledgments

This work has been fully supported by the Croatian Science Foundation under the project IP-2019-04-4703. This support is gratefully acknowledged.

References

[1] Čanađija, M., Deep learning framework for carbon nanotubes: Mechanical properties and modeling strategies. *Carbon*, 184, 891-901, 2021.

[2] Chen, D., Hu, F., Nian, G., Yang, T., Deep residual learning for nonlinear regression. *Entropy*, 22(2), 193, 2020.

Nonlinear model for analysis of asphalt mixtures

Ivica Kožar*, Ivana Pranjić*

*University of Rijeka, Faculty of Civil Engineering
E-mails: {ivica.kozar, ivana.pranjic}@gradri.uniri.hr

Keywords: asphalt mixtures, indirect tension test, Burger's rheological model, parameter analysis

1. Introduction

The behavior of asphalt mixtures is described by linear or nonlinear viscous material models, usually with temperature-dependent properties 0. One of the simplest rheological models suitable for the analysis of asphalt mixtures is Burger's model. It consists of a Kelvin and a Maxwell element connected in series. In this work, we introduced nonlinearity into the classical Burger model since the springs are described by an exponential force-displacement law 0. The laboratory experiments used for testing asphalt specimens are based on indirect tensile tests. In these tests, a cylindrical specimen is loaded along the edge to failure while force and displacement are recorded. Viscous materials are sensitive to the rate of loading 0, so the load is applied very slowly.

2. Mathematical model

Burger's rheological model is shown in Figure 1 and is mathematically formulated with equation (1), which is a system of algebraic differential equations.

$$\begin{aligned} F_{11}(\varepsilon_{e1}(t)) &= \mu_M \frac{d\varepsilon_{v1}(t)}{dt} \\ F_{21}(\varepsilon_K(t)) + \mu_K \frac{d\varepsilon_K(t)}{dt} &= \mu_M \frac{d\varepsilon_{v1}(t)}{dt} \\ \varepsilon_{e1}(t) + \varepsilon_{v1}(t) + \varepsilon_K(t) &= \varepsilon_a(t) \end{aligned} \tag{1}$$

The unknown variables are ε_{e1}, ε_{v1} and ε_K and are all functions of the pseudo time t. Further, $F_{11}(\varepsilon_{e1}) = \varepsilon_{e1}\, E_M exp\left(-\frac{\varepsilon_{e1}}{a_M}\right)$ and $F_{21}(\varepsilon_K) = \varepsilon_K\, E_K exp\left(-\frac{\varepsilon_K}{a_K}\right)$. In total, our model has six parameters: viscosities μ_M and μ_K, moduli E_M and E_K, and non-physical parameters a_M and a_K.

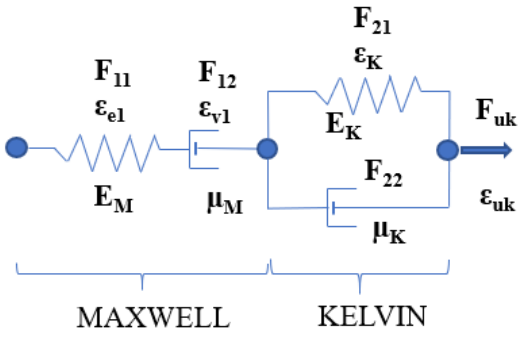

Figure 1. Scheme of Burger's rheological model, with notation

2.1. Experimental procedure

The experiments were performed in two phases according to the standard HRN EN 12697-23:2003. In the first phase, the specimens were tested to determine the effect of temperature and bitumen-to-sand ratio on the peak force at failure. In the second phase, the specimens with extreme results were further tested. The tests were performed in the laboratory of the Faculty of Civil

Engineering in Rijeka. The resulting force-displacement curve was plotted until the failure of the specimen and presented in Figure 1. The force-displacement curve resulting from equation (1) is also shown in Figure 1 for comparison. No specific procedure was used to estimate the model parameters, so there is clearly room for improvement.

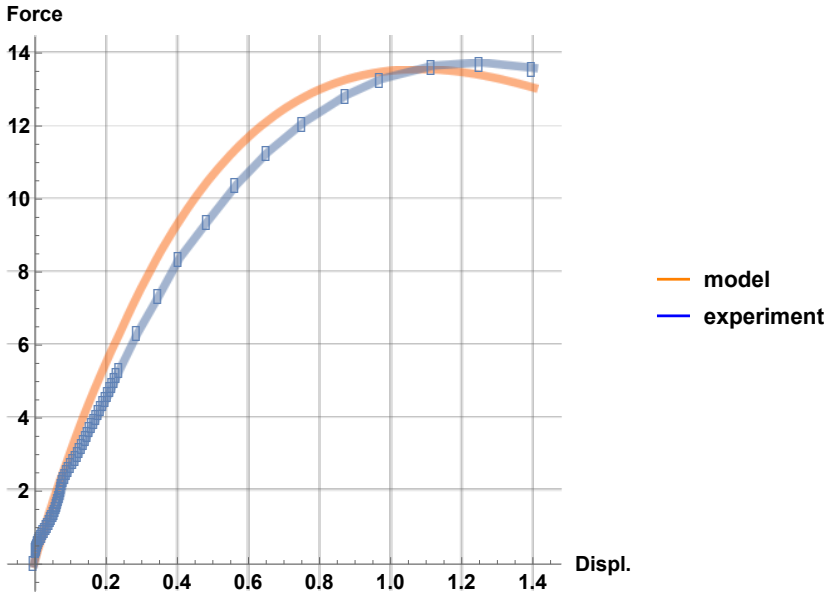

Figure 2. Experimental results, displacement - force diagram

4. Conclusions

We are developing a model to estimate parameters from indirect tension tests for asphalt. At this stage, no specific method has been used to estimate the model parameters. Further work will include appropriate inverse methods for estimating the relevant parameters.

Acknowledgments

This work was supported by project HRZZ 7926 "Separation of parameter influence in engineering modeling and parameter identification" and project KK.01.1.1.04.0056 "Structure integrity in energy and transportation", for which we gratefully acknowledge.

References

[1] Pranjić, I., Torić Malić N., Kožar, I., Eksperimentalna analiza i numeričko modeliranje ponašanja asfaltnih mješavina. In: Brčić, M., Skoblar, A., Ribarić, D., ed., *Zbornik radova jedanaestog susreta Hrvatskog društva za mehaniku*, 227-233. Hrvatsko društvo za mehaniku, Rijeka, 2021.

[2] Kožar, I., Ožbolt, J., Pecak, T., Load-rate sensitivity in 1D non-linear viscoelastic model. *Key Eng. Mater.*, 488-489, 731-734, 2012.

[3] Kožar, I., Ibrahimbegovic, A., Rukavina, T., Material model for load rate sensitivity. *Coupled Systems Mechanics*, **7(2)**, 141-162, 2018.

Estimation of glass plate boundary conditions using laser Doppler vibrometer

Ivica Kožar*, Marina Plovanić*, Tea Sulovsky*

*University of Rijeka Faculty of Civil Engineering
E-mails: {ivica.kozar,marina.plovanic,tea.sulovsky}@gradri.uniri.hr

Keywords: parameter estimation, boundary conditions, laser Doppler vibrometer, glass plate

1. Introduction

Many sensors and data acquisition devices provide us with a large amount of data, and estimating properties and parameters from measurements is becoming increasingly important. Some material properties can be measured directly, but most can only be estimated indirectly. Structural parameters can almost always only be estimated indirectly.

Due to the mounting technique with an elastic resin, the boundary conditions of a glass plate are between simply supported and clamped. However, comparing the results of computer models and experiments requires a fairly accurate knowledge of the extent to which the supports are clamped.
In this paper, we present a method for estimating the boundary conditions of glass plates based on measurements of the vibration velocity at some points on the plate.

2. Model

The mathematical model is based on the theory of thin plates discretized with spectral elements 0. Among other possibilities, Chebyshev polynomials are chosen for spatial interpolation of the domain of the differential equation. The application of the spectral method is to solve the strong formulation of a structural problem. The method can be formulated using matrix differentiation operators

$$\boldsymbol{p}_x = \boldsymbol{D}_N \cdot \boldsymbol{p} \ . \tag{1}$$

where $\boldsymbol{p}$ is a vector of discrete data of size N, $\boldsymbol{p}_x$ is its derivative, and $\boldsymbol{D}_N$ is a matrix differential operator, a square matrix of size [NxN]. The boundary conditions must be included in $\boldsymbol{D}_N$. The plate is modelled with the Kirchhoff equation for thin plates discretized with N and M points in each direction. After discretization, the thin plate equation has the form

$$\Delta\Delta\boldsymbol{w} = (\boldsymbol{I}_M \oplus \boldsymbol{D}_N^4) + 2(\boldsymbol{D}_M^2 \oplus \boldsymbol{I}_N)(\boldsymbol{I}_M \oplus \boldsymbol{D}_N^2) + (\boldsymbol{D}_M^4 \oplus \boldsymbol{I}_N) \ . \tag{2}$$

Here $\oplus$ is the Kronecker product and $\boldsymbol{D}_N$ and $\boldsymbol{D}_M$ are the derivative matrices for the respective directions. The corresponding boundary conditions are substituted into equation (2) with Lagrange multipliers. The load must be discretized in a form compatible with equation (2).

3. Experimental procedure

Our experimental setup consists of a laser Doppler vibrometer, an excitation device with frequency generator, and accelerometers with loggers. The glass plate is excited and the vibration velocities are measured with the laser Doppler and the accelerations with the accelerometers. The spectrum of the excitation is as close as possible to the white noise spectrum. Fig.1 shows some of the experimental equipment and some measurement results. The recorded data are then compared with the vibration results from the numerical model.

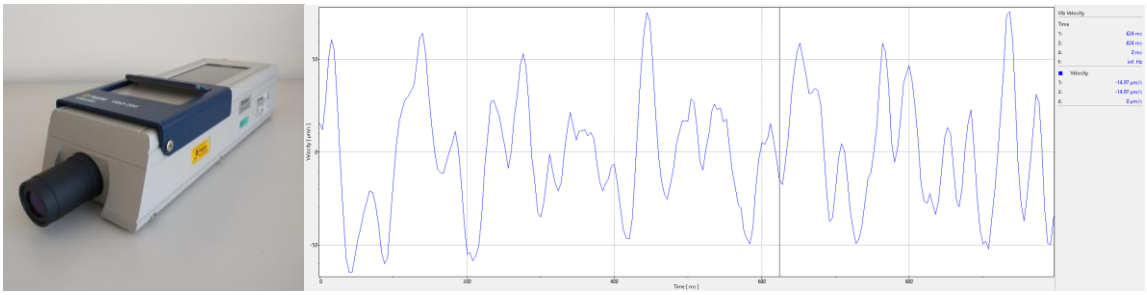

Figure 1. Laser Doppler vibrometer and recorded vibration velocities

4. Parameter estimation

Unknown boundary conditions are parameterized with the parameter 'k', which describes the extent of the constraint on the supports and has a value in the interval (0..1). The parameter 'k' is visible only after the boundary conditions are introduced using Lagrange multipliers. The procedure is similar to [1], [2] and [3], but at this stage of development only experimental and calculated vibration results are compared.

5. Conclusions

We propose to estimate the constraint on thin plates using experimental measurements and numerical simulations. The unknown extent of the constraint on the supports is determined from different types of data sets, such as displacements, velocities, and accelerations at different sampling frequencies. The extraction of the unknown parameter 'k' is done using inverse analysis techniques.

Acknowledgments

This work was supported by project HRZZ 7926 "Separation of parameter influence in engineering modeling and parameter identification" and project KK.01.1.1.04.0056 "Protection of structural integrity in energy and transportation", for which we gratefully acknowledge.

References

[1] Kožar, I., Torić Malić, N., Spectral method in realistic modelling of bridges under moving vehicles. *Engineering Structures*, 50, 149-157, 2013.

[2] Kožar, I., Torić Malić, N., Rukavina, T., Inverse model for pullout determination of steel fibers. *Coupled Systems Mechanics* , 7, 197-209, 2018.

[3] Kožar, I., Relating structure and model. In: Ibrahimbegović, A., ed., *Computational Methods for Solids and Fluids*, 161-183. Springer, Heidelberg, 2016.

Analysis of a simple model for inverse estimation of material parameters from three-point bending of beams

Ivica Kožar*, Tea Sulovsky*, Marina Plovanić*

*University of Rijeka Faculty of Civil Engineering
E-mails: {ivica.kozar, tea.sulovsky, marina.plovanic}@gradri.uniri.hr

Keywords: three-point beam bending, fiber reinforced concrete, mathematical model, parameter estimation,

1. Introduction

Laboratory experiments provide us with a large amount of data, and estimation of properties and parameters from measurements is becoming increasingly important. Usually, the data are linked to a mathematical model that must establish the appropriate connections between the parameters.

2. Mathematical model

The mathematical model is based on simple beam theory and a fractured cross section discretized into layers 0. The material behavior is different in tension and compression; equation (1) describes the concrete and equation (2) the force-displacement law of the steel fibers.

$$f(x, a_t, b_t, a_c, b_c) = \begin{cases} a_c x E exp(-b_c x) & if x < 0 \\ a_t x E exp(-b_t x) & if x \geq 0 \end{cases} \tag{1}$$

$$f(x, F_t, E_u, E_d) = \begin{cases} xE_b exp(-b_c x) & if x < 0 \\ xE_u & if x > 0 \wedge x < x_{elast} \\ (x - x_{elast})E_d & if x \geq x_{elast} \wedge x < x_{limit} \\ 0 & if x > x_{limit} \end{cases} \tag{2}$$

Here a_t, b_t are the concrete parameters in tension and a_c, b_c in compression. The parameters for steel fibers are: F_t is the threshold force, E_u and E_d are the elastic moduli at loading and unloading. Equations (1) and (2) are shown graphically in Figure 1.

The material behavior of concrete and steel is related in the equilibrium equations

$$\begin{aligned} F(\epsilon, \kappa) &= \Delta h \sum_{i=1}^{layers} f_c[(h_i - \epsilon h)tan(\kappa)] + \Delta a \, f_a(h_a - \varepsilon \, h) = 0 \\ M(\epsilon, \kappa) &= \Delta h \sum_{i=1}^{layers} (h_i - \epsilon h) f_c[(h_i - \epsilon h)tan(\kappa)] + \Delta a \, (h_a - \varepsilon \, h) \, f_a(h_a - \varepsilon \, h) = 0 \end{aligned}. \tag{3}$$

In equations (3) the first one stands for the force balance and the second one for the moment balance. Equation (3) is shown graphically in Figure 2.

Unknown parameters are defined in equation (1) and (2). At this stage of development, we perform only a parametric analysis; the optimal parameters are determined by testing from a set of solutions. Further work would involve an inverse procedure for parameter estimation, similar to 0 and 0.

2.1. Experimental procedure

Three beams of each type were tested; dimensions were 70 x 70 x 280 mm with 210 mm span between supports, without and with steel fibers. For the beams with fibers, several steel fibers were placed in a row in the notch. The bending tests were performed with a servo-controlled hydraulic machine in the laboratory of the Faculty of Civil Engineering in Rijeka. The resulting force-displacement curve was recorded until the failure of the beam, i.e. until a deflection of at least 3 mm, in order to determine the post-peak behavior. During the experiments, we recorded three parameters in the middle cross section of the tested beam: Deflection, Crack Opening Deflection (CMOD) and the loading force. All data are recorded together with the magnitude of the time step.

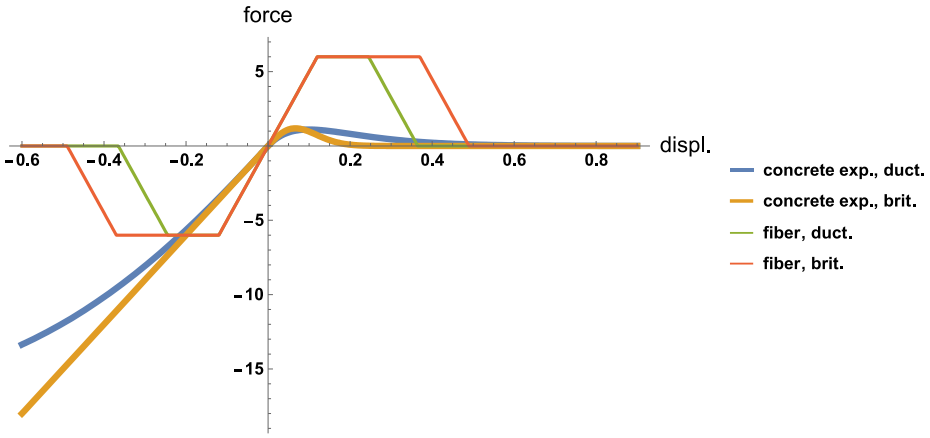

Figure 1. Force displacement diagram for concrete and fiber, ductile and brittle

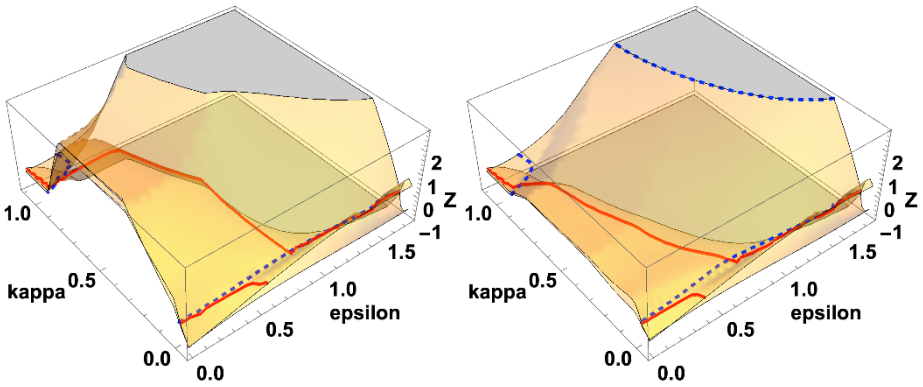

Figure 2. Equilibrium equation for many and for few fibers in the cross section

4. Conclusions

We perform a verification of the model using a parametric analysis. At this stage, it is important that we obtain numerical results that are mathematically similar to the experimental data. Further work will include appropriate inverse methods to estimate the relevant parameters.

Acknowledgments: This work was supported by project HRZZ 7926 "Separation of parameter influence in engineering modeling and parameter identification" and project KK.01.1.1.04.0056 "Structure integrity in energy and transportation", for which we gratefully acknowledge.

References

[1] Kožar, I., Bede, N., Mrakovčić, S., Božić, Ž., Layered model of crack growth in concrete beams in bending. Procedia Structural Integrity, **31**, 134-139, 2021.

[2] Cukor, I., Galić, I., Tonković, Z., Sorić, J., Kožar I., Inverse method for load identification of components containing crack-like defects. Božić, Ž., ed., *ICSID 2020, 4th International Conference on Structural Integrity and Durability*, 18. Fakultet strojarstva i brodogradnje, Dubrovnik, 2020.

[3] Kožar, I., MODEL FOR PARAMETER ESTIMATION FROM CRACK GROWTH IN CONCRETE. In: Božić, Ž., ed., *ICSID 2020, 4th International Conference on Structural Integrity and Durability*, 18. Fakultet strojarstva i brodogradnje, Dubrovnik, 2020.

The effect of turbulence on surface pressure underlying conical vortices

Hrvoje Kozmar

Faculty of Mechanical Engineering and Naval Architecture, University of Zagreb, Ivana Lučića 5, 10000 Zagreb, Croatia
E-mail: hrvoje.kozmar@fsb.hr

Keywords: Cubic building, turbulent boundary layer, conical vortices, surface pressure, wind-tunnel experiments

1. Introduction

Conical vortices develop on the top surface of cubic buildings subjected to oblique wind flow. Extreme suction occurs on the body surface underlying such vortices. These aerodynamic loads may cause severe structural damage and failure. Conical vortices are highly relevant for a wide range of aerospace, civil, mechanical, and wind engineering applications. Many studies have comprehensively tackled this complex issue, while there are still some open questions including further aspects of the boundary layer turbulence effects on pressure distribution and particularly fluctuations on a flat top body surface in the oblique fluid flow.

2. Methodology

Experiments were performed in a boundary layer wind tunnel at the Technical University of Munich, Germany. Three turbulent boundary layers (TBLs) were created using the Counihan [1] approach, i.e. the castellated barrier wall, vortex generators and surface roughness elements. The fundamental difference between these three TBLs was in their turbulence levels, i.e. they were either low-turbulent (LT), mid-turbulent (MT), or high-turbulent (HT). Instantaneous velocities were first measured in the empty wind-tunnel test section, i.e. without the cube. This was performed simultaneously in three coordinate directions using a triple hot-wire probe DANTEC 55P91. The sampling rate was 1.25 kHz and the total record length was 150 s. One cube with 0.2 m long edges was the experimental model. It created the test section blockage of 0.84% that is considerably smaller than the critical blockage of 6%, West and Apelt [2], so the results were not corrected. The pressure measurements were simultaneously performed on all cube surfaces except the bottom surface. The flow incidence angle was at 40° in all experiments. On each of the vertical cube surfaces there were 35 pressure taps and on the top surface there were 49 pressure taps used for performing steady pressure measurements. The sampling rate in steady pressure measurements was 100 Hz during 15 s. The unsteady surface pressure was measured at 15 points on the top cube surface The sampling rate in unsteady pressure measurements and the recording time were 2 kHz and 20 s, respectively. The steady pressure coefficient c_p and the unsteady pressure coefficient $c_{p,\mathrm{rms}}$ on the cube were calculated using the mean flow velocity at the height that corresponds to the height of the top cube surface. More details are available in Kozmar [3].

3. Results

The conical vortices develop above the top surface of the wall-mounted cube as the flow separates from the leading edges of the top cube surface. These flow characteristics are exhibited in the c_p distribution on the top cube surface, Figure 1. Two zones immediately downstream of the leading edges of the top cube surface characterized by strong suctions can be clearly observed. These two suction zones are underlying the cores of the two conical vortices. The larger mean suction acts on the top body surface in less turbulent flows (e.g. the LT boundary layer compared to the MT boundary layer and more so to the HT boundary layer), thus indicating that the conical vortices are generally stronger in the smooth flow than in the turbulent flow.

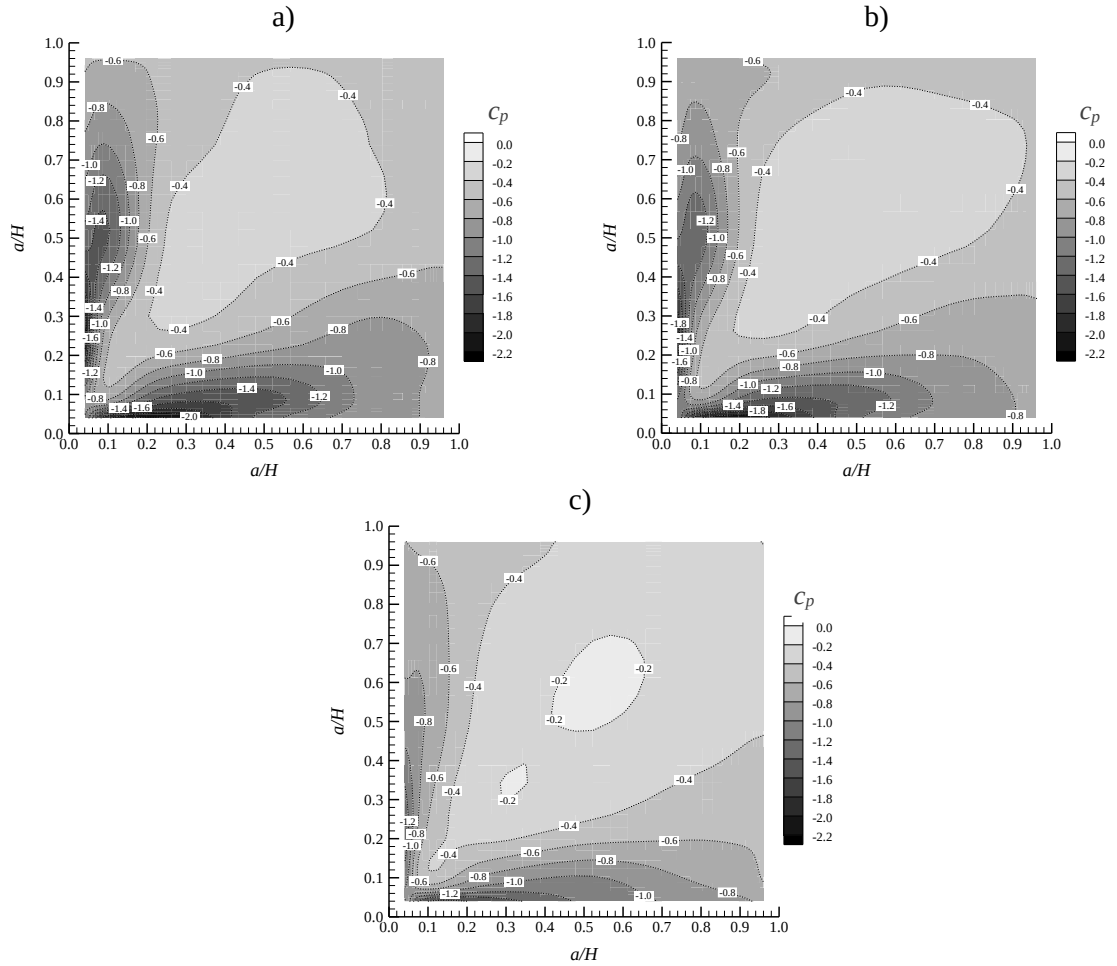

Figure 14. Distribution of c_p coefficients on the top surface of the wall-mounted cube subjected to a) low-turbulent, b) mid-turbulent, c) high-turbulent boundary layers, adopted from [3]

4. Conclusion

The conical vortices developed above the top surface of the wall-mounted cube are clearly observed as two zones characterized by strong suction. With an increase in the turbulence in the incoming flow, the strong suction zones decrease in size with a simultaneous increase in the size of the weak suction zone on the central area of the top cube surface. This indicates that the conical vortices are generally larger in less turbulent (smoother) flows than in more turbulent flows.

Acknowledgments

The study was funded by the Croatian Ministry of Science and Education, German Academic Exchange Service and the Croatian Academy of Sciences and Arts. Professor Boris Laschka is gratefully acknowledged for his kind support and advice.

References

[1] Counihan, J., An improved method of simulating an atmospheric boundary layer in a wind tunnel. *Atmospheric Environment*, 3, 197-214, 1969.

[2] West, G.S., Apelt, C.J., The effects of tunnel blockage and aspect ratio on the mean flow past a circular cylinder with Reynolds numbers between 10^4 and 10^5. *Journal of Fluid Mechanics*, 114, 361-377, 1982.

[3] Kozmar, H., Surface pressure on a cubic building exerted by conical vortices. *Journal of Fluids and Structures*, 92, 1-18, 2020.

A new approach to solving boundary value problems in arbitrarily bounded domains

Vedrana Kozulić*, Blaž Gotovac*, Nives Brajčić Kurbaša*

*Faculty of Civil Engineering, Architecture and Geodesy, University of Split, Matice hrvatske 15, Split, Croatia
E-mails: {vedrana.kozulic, blaz.gotovac, nbrajcic}@gradst.hr

Keywords: collocation method, atomic basis functions, Dirichlet boundary condition, Neumann boundary condition

1. Introduction

Widely used mesh-based methods, such as the finite element, finite difference, and finite volume methods, use spatial grids to approximate the geometric shape of a model and introduce a finite number of nodes to specify boundary conditions and perform numerical computations. In addition to standard techniques, collocation method is particularly easy to implement because no mesh generation and numerical integration is required, regardless of the geometric shape of the domain. We only need to ensure that the functional basis is smooth enough to be inserted into the resulting differential equation at the collocation points. There is a well-developed WEB-spline method for arbitrary bounded multidimensional domains based on a collocation method and B-splines as basis functions [1]. However, the problem of how to incorporate mixed boundary conditions into the collocation space for boundary value problems on general domains in two or more dimensions still remains. One possibility is a numerical method that enables exact treatment of all prescribed boundary conditions at all boundary points that combines the solution structure method and a collocation technique [2]. In this paper, a new algorithm is presented to solve the boundary value problems on general domains.

2. Methodology

The approach combines the collocation method and atomic basis functions of algebraic type called Fup functions [3]. This choice of basis functions provides smooth approximation on regular grids. The marked dots in Fig. 1 show the centers of the supports of internal and external basis functions. The internal basis functions have a large portion or all of their support in the domain. The external basis functions are close to the boundary with a support that is partly in the domain and partly outside the domain. In order for the Fup functions approximation to be complete, we need to keep all external functions in the base and write a conditional equation for each of them.

The centers of the supports of internal Fup basis functions can be used as collocation points. All conditional equations related to the boundary of the domain are written at the collocation points on a stepped polygon inscribed in the given domain. The known value of the boundary condition at a point on the boundary of the domain is satisfied from the collocation point inside the domain in such a way that the Dirichlet or Neumann boundary condition develops into the Taylor series. The mismatch between the number of basis functions and interpolation conditions is solved by writing additional equations from the known conditions at the boundary of the domain also in the form of development into the Taylor series.

The method is particularly successful in combination with Rvachev's theory of R-functions [4] that provide a powerful tool for accurate geometry description. The domain is represented in implicit form by means of some smooth function ω that takes on zero values on the boundary of the domain and is positive in the interior of the domain. Rvachev's R-function method combines ω functions for elementary domains according to Boolean operations.

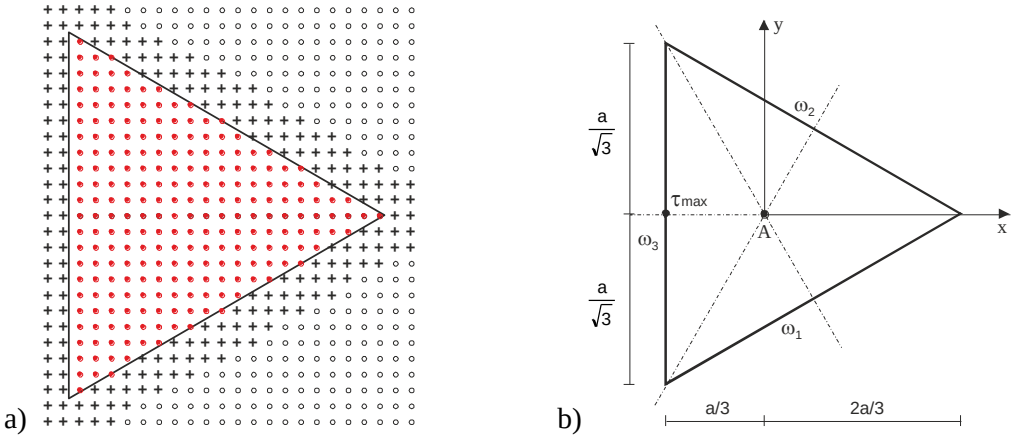

Figure 1. a) Internal (full circles) and external (crosses) Fup basis functions. White circles mark the irrelevant Fup functions having no support inside of the domain. b) Triangular cross section

3. Numerical results

Numerical properties of the proposed approach are demonstrated by solving boundary value problem for Poisson equation with homogeneous Dirichlet boundary conditions. We analyzed a benchmark torsion problem for a bar with the cross section shown in Fig. 1b) with known exact solution. Numerical results for shear stresses and the torsional rigidity of cross section are obtained using $Fup_2(x,y)$ basis functions. Fig. 2 presents convergence diagram of torsion rigidity value. It can be seen that the expected convergence rate p = 2 is achieved.

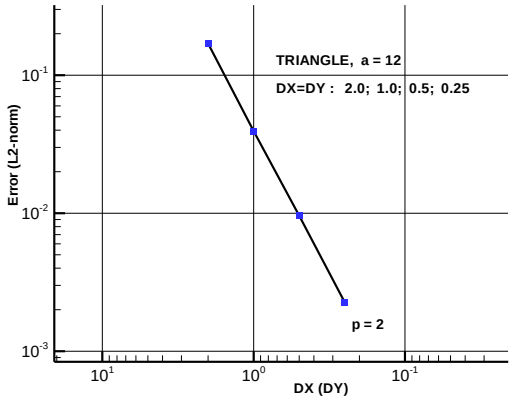

Figure 2. Convergence diagram of torsion rigidity value for triangular cross section

4. Conclusions

The high efficiency of the proposed method is achieved by using a collocation technique that allows easy application, as well as by using atomic Fup basis functions that ensure the accuracy of the approximation and the smoothness of the solution. The use of R-functions enables the accurate description of the geometry of the domain and the writing of equations that satisfy the boundary conditions at the points of the boundary of the domain.

References

[1] Höllig, K., Reif, U., Wipper, J., Weighted extended B–spline approximation of Dirichlet problems. *SIAM J. Numer. Anal.*, 39(2), 442–462, 2001.

[2] Kozulić, V., Gotovac, B., Application of the Solution Structure Method in Numerically Solving Poisson's Equation on the Basis of Atomic Functions. *Int.J. Comput. Methods,* 15(5), 2018.

[3] Gotovac, B., Kozulić, V., On a selection of basis functions in numerical analyses of engineering problems. *Int. J. Eng. Model.*, 12(1–4), 25–41, 1999.

[4] Rvachev, V.L., Theory of R-functions and Some Applications, Naukova Dumka, Kiev, 1982.

An Enriched Phase-Field Method for the Simulation of Fracture Processes

Christian Krüger*, Verena Klempt*, Stefan Loehnert*

*Institute of Mechanics and Shell Structures, Technische Universität Dresden, Germany
E-mails: christian.krueger@tu-dresden.de, verena.klempt@tu-dresden.de, stefan.loehnert@tu-dresden.de

Keywords: Fracture Mechanics, Phase-Field Method, Extended Finite Element Method (XFEM)

1. Introduction

Within the last decade, the phase-field method (PFM) gained increasing popularity in the context of computational fracture mechanics because of its beneficial behaviour regarding fracture phenomena like crack initiation, propagation, branching and merging, even though extremely fine meshes around discontinuities are necessary. In this contribution, a Finite Element Method (FEM) is presented that uses a transformed phase-field ansatz and an enriched displacement field ansatz in order to be able to reduce the computational effort without loss in accuracy, compared to standard PFM simulations.

2. Transformation and Enrichment of the Phase-Field Approach

In contrast to the eXtended Finite Element Method (XFEM) [1], where the geometry of a discontinuity is represented in an explicit manner by e.g. level-set functions, the PFM describes a discontinuity in a regularized manner. In the context of fracture mechanics, a phase-field variable ϕ interpolates between unbroken ($\phi=0$) and fully fractured material ($\phi=1$). Formulating GRIFFITH-theory as an energy minimization problem [2], the energy E_s dissipated for creating a new crack surface Γ reads

$$E_s = G_c \Gamma \quad \text{with} \quad \Gamma \approx \Gamma_l = \int_{\mathscr{B}} \gamma_l \, \mathrm{d}v = \frac{1}{2l} \int_{\mathscr{B}} \phi^2 + l^2 \|\nabla \phi\|^2 \, \mathrm{d}v \tag{1}$$

where G_c is the material depended fracture energy and γ_l the regularized crack surface density function [3]. The parameter l defines the width of the transition zone between the broken and unbroken material. Depending on ϕ, the elastic energy E_e is degraded by a degradation function $g(\phi)$. Within a one-dimensional setup, the solution $\phi(x) = \exp(-|x|/l)$ can be identified for a fully developed crack if the crack is located at $x = 0$ and $\phi(x=-\infty) = \phi(x=+\infty) = 0$ holds. In this case, the displacements u must follow the slope of a jump function (e.g. HEAVISIDE step function as used in the XFEM). In order for the regularized crack surface Γ_l to converge to the correct crack surface Γ, the length parameter l must be small compared to the dimension of the considered body. As a consequence, high gradients $\nabla\phi$ and strains ε occur. These gradients can only be approximated precisely within the FEM, if the element size h goes to zero (using linear or quadratic standard shape functions).

To overcome this deficiency, a transformation of the phase-field ansatz and an enrichment of the displacement field ansatz is introduced. A possible transformation for the approximation of the phase-field ϕ^h can be defined as

$$\phi^h := f\left(\bar{\phi}^h\right) \quad \text{with} \quad \bar{\phi}^h = N_I \phi_I \tag{2}$$

where N_I are quadratic standard shape functions and ϕ_I are the nodal degrees of freedom. The choice for the function f should somehow match to the desired solution, e.g.

$$f(\bar{\phi}^h) = \exp(-\sqrt{\bar{\phi}^h}) \, . \tag{3}$$

FINEL et. al. first introduced such a transformation of a phase-field ansatz in the context of the Finite Difference Method and a weak discontinuity [4]. For the approximation of the displacement field, the XFEM [1] is applied. Thereby, the crack geometry is directly extracted from the phase-field ϕ rather than described by level-set functions. A possible choice for the approximation $\boldsymbol{u}^h$ of the displacement field reads

$$\boldsymbol{u}^h = \sum N_I \boldsymbol{u}_I + \sum N_I \boldsymbol{a}_I u^{\phi}_{enri} \quad \text{with} \quad u^{\phi}_{enri} = \frac{D_{\boldsymbol{r}} \bar{\phi}^h}{\sqrt{\bar{\phi}^h}} \tag{4}$$

where $\boldsymbol{u}_I$ are the standard degrees of freedom and $\boldsymbol{a}_I$ the enriched degrees of freedom. The enrichment function u^{ϕ}_{enri} directly depends on the phase-field degrees of freedom. The directional derivative $D_{\boldsymbol{r}}$ is defined in direction $\boldsymbol{r}$ perpendicular to the crack surface.

3. Numerical results

To demonstrate the method, a square plate with an initial crack exposed to a tensional load is considered. The element size h of the quadratic triangular elements is chosen equal to the internal length l. Fig. 1 shows the results for the phase-field and the displacement field in vertical direction. The detailed views demonstrate the insensitivity against coarse meshes.

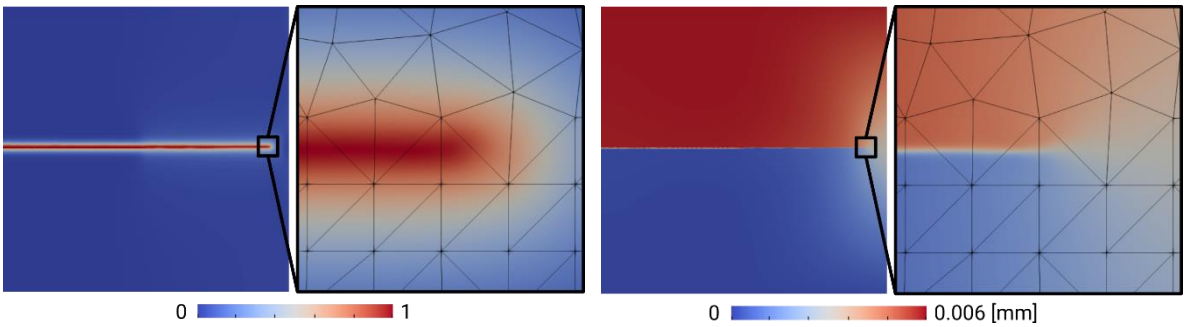

(a) Phase-Field (b) Displacement-Field (vertical direction)

Figure 1: Phase- and displacement field of a mode I tension test directly before total failure

References

[1] Moës, N., Dolbow, J., Belytschko, T., A finite element method for crack growth without remeshing. *International Journal for Numerical Methods in Engineering*, 46(1), 131–150, 1999.

[2] Francfort, G.A., Marigo, J.-J., Revisiting brittle fracture as an energy minimization problem. *Journal of the Mechanics and Physics of Solids*, 46(8), 1319–1342, 1998.

[3] Miehe, C., Hofacker, M., Welschinger, F., A phase field model for rate-independent crack propagation: Robust algorithmic implementation based on operator splits. *Computer Methods in Applied Mechanics and Engineering*, 199(45-48), 2765–2778, 2010.

[4] Finel, A., Le Bouar, Y., Dabas, B., Appolaire, B., Yamada, Y., Mohri, T., Sharp phase field method. *Physical Review Letters*, 121(2), 025501, 2018.

3D thermal FE analysis of a railway disc brake at coefficient of friction dependent on temperature, velocity and contact pressure

Michal Kuciej*, Aleksander Yevtushenko*, Piotr Grzes*, Piotr Wasilewski+

*Faculty of Mechanical Engineering, Bialystok University of Technology (BUT)
45C Wiejska Street, 15-351, Bialystok, Poland
E-mails: {m.kuciej,a.yevtushenko,p.grzes}@pb.edu.pl

+Frimatrail Frenoplast S.A.
15 Watykańska Street, 05-200, Majdan, Poland
E-mails: pwasilewski@frimatrail-frenoplast.pl

Keywords: variable coefficient of friction, temperature, ventilated brake disc, friction

1. Introduction

The coefficient of friction during braking changes. Its value is the result of a number of physical processes occurring on the contact surfaces of the contacting bodies. The most important measurable parameters are the velocity, temperature and contact pressure. In order to take into account the variable value of the coefficient during braking in modeling temperature, it is necessary to solve the system of equations of heat dynamics of friction and wear [1,2]. Calculations of the axisymmetric temperature fields with velocity, temperature and pressure dependent coefficient of friction were performed in the article [3].

2. Measurement of the thermophysical properties and coupled calculations of temperature of the brake using the finite element method

In this work, a computational model of a railway vehicle disc brake was proposed to simulate changes in temperature fields. The purpose of calculations was to estimate an effect of material properties on the basis of five different formulations of the organic composite linings on the friction characteristics of the brake at the coefficient of friction dependent on velocity, temperature and contact pressure. The prototype brake pads were manufactured from friction mixtures by molding to comply with standard UIC200 shape of railway brake pads. In order to compare different mixtures, the basic composition was created. It consisted of a rubber, phenol-formaldehyde resin, vulcanizers and curing agents, mineral fibers, graphite, antimony sulfide and calcite. Then five mixtures were made according to the following recipes. First included only calcite, second – calcite and steel fiber, third – steel fiber, forth – calcite and copper fiber and the last one – copper fiber only. After preparing the material samples, the temperature-dependent thermophysical properties were determined. It was specific heat capacity, thermal conductivity, and thermal diffusivity.

Having the brake pads prepared, the measurements of brake disc temperature 1 mm under the friction surface in six points were carried out at the Railway Research Institute in Warsaw. The process of braking for each material lasted more than one hour, however in this study, only the beginning of that period was taken into account.

The main goal was to include in the computational model dependence of the coefficient of friction on velocity, temperature and contact pressure. Therefore the data measured at the test stand in the Railway Research Institute in Warsaw were adapted. Five initial braking applications at one nominal contact pressure $p = p_0$ were taken into account. In order to obtain two parameter function of the coefficient of friction $f(V,T)$ data in the tabular form consisted of three columns was created. This table was imported to the software for creating 3D plots (Surfer). Next the developed graphical representation of the function $f(V,T)$ in a grey scale was imported to the finite element based software COMSOL Multiphysics® and transformed into analytical function (Fig. 1a). That process

was repeated for five different material of the brake pad. Similar approach was proposed in the article [4].

After preparing five dependences of the coefficient of friction, the calculations of temperature of the pads and the disc were carried out for the first braking application. The simulation was coupled which means that the only parameter defined was the initial velocity, mass per one braking system, function of exponential increasing contact pressure and the developed two-parameter function for the coefficient of friction $f(V,T)$. In order to verify the model, mechanical energy converted into hear was calculated and shown in Fig. 1b. The calculated temperature was verified by experimental data.

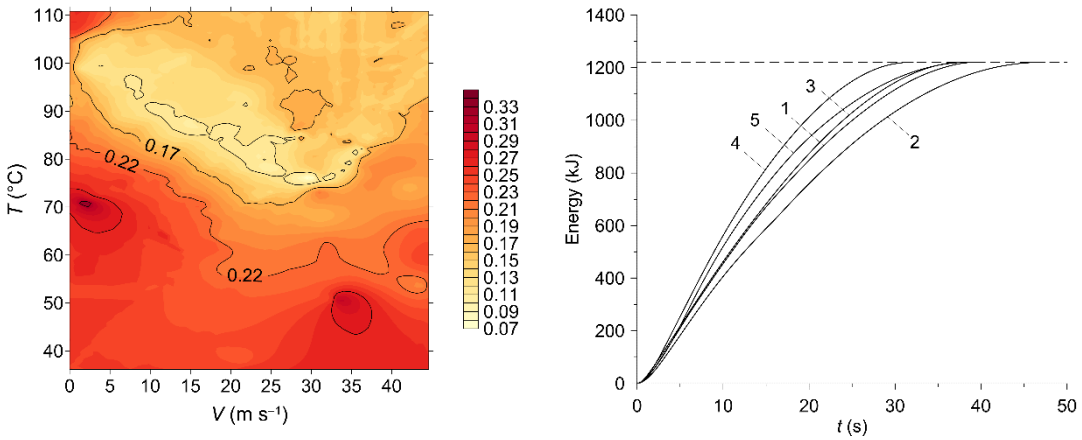

(a) **(b)**

Figure 1. Approximated dependence of the coefficient of friction on velocity and temperature (a); changes in energy converted into heat during braking for five brake pad materials 1–5 (b)

3. Conclusions

Based on the carried out research it was found that the calculations of changes in the brake disc temperature using the 3D finite element coupled model and the corresponding values of temperature measured agreed well. Better coincidence was found for the change in the velocity of the vehicle. The main difficulty in obtaining agreement in temperature stems from the measurement. The thermocouples used in the experiment introduce additional heat generation due to friction. Therefore further studies will focus on searching for other method the better copy the changes in contact temperature on the friction surface of the disc.

Acknowledgement

This study was supported by the National Science Centre of Poland (Research project No. 2017/27/B/ST8/01249).

References

[1] Chichinadze, A.V., Processes in Heat Dynamics and Modelling of Friction and Wear (Dry and Boundary Friction). *Tribology International*, 28, 55–58, 1995.

[2] Grzes, P., Determination of the Maximum Temperature at Single Braking from the FE Solution of Heat Dynamics of Friction and Wear System of Equations. *Numerical Heat Transfer Part A Applications*, 71, 737–753, 2017.

[3] Yevtushenko, A.A., Grzes, P., Adamowicz, A., The Temperature Mode of the Carbon-Carbon Multi-Disc Brake in the View of the Interrelations of Its Operating Characteristics. *Materials (Basel)*, 13, 1–16, 2020.

[4] Riva, G., Varriale, F., Wahlström, J., A Finite Element Analysis (FEA) Approach to Simulate the Coefficient of Friction of a Brake System Starting from Material Friction Characterization. *Friction*, 9, 191–200, 2021.

Strain softening in spatial frame like structures using velocity-based formulation for a geometrically exact beam

Sudhanva Kusuma Chandrashekhara*, Dejan Zupan *

*Faculty of Civil and Geodetic Engineering, Jamova 2, University of Ljubljana, Ljubljana 1000, Slovenia.
E-mails: {skusuma, dzupan}@ fgg.uni-lj.si

Keywords: Strain softening, localization, embedded discontinuities, three-dimensional rotations

1. Introduction

Modelling instabilities in structures undergoing complex deformation is usually reflected in sensitive behaviour of numerical solution methods and thus represents a significant challenge in the numerical modelling. In the present work, we address the problem of strain softening which is often observed in brittle heterogeneous materials in combination with non-linear response of spatial frames. When a stress dependent critical condition is reached at a material point of a body, discontinuities in strain field occur due to the loss of uniqueness of strain measures when evaluated from known stresses in the localized region. In our analysis we will focus on beam-like structural elements with proper consideration of nonlinear geometry and material nonlinearity including the softening regime. Such model requires accurate detection of critical conditions corresponding to the singularity at the cross-sectional level and efficient treatment of discontinuities in the strain field as well as the efficient and robust evaluation of stress resultants and cross-sectional tangent modulus [1]. The proposed approach is based on velocity-based beam formulation with energy preservation by Zupan and Zupan [2] where the tangent space of the non-linear configuration space of the beam is spanned using only additive quantities and thus avoiding typical problems with rotational degrees of freedom. The computational advantages of the formulation are preserved after the efficient detection of cross-sectional singularity and post-critical treatment of localized strains are implemented into the formulation.

2. Methodology

The present formulation is based on a second order approximation in time using the implicit energy-preserving midpoint time integration. Among the various possibilities of describing the rotations, the quaternion algebra is employed. The primary unknowns in the present work are chosen to be velocities and angular velocities as it provides convenient representation of tangent space with distinct numerical advantages of additive type update procedure and consistency of standard additive type interpolations when expressed in suitable reference frame. Standard Galerkin finite element method is employed for the spatial discretization [2]. The final discretized governing equations of the three-dimensional beam reads

$$\int_0^L \left[\frac{\rho A}{h}\left(\boldsymbol{v}^{[n+1]}-\boldsymbol{v}^{[n]}\right)P_i+\ \boldsymbol{n}^{[n+1/2]}P_i'-\tilde{\boldsymbol{n}}^{[n+1/2]}P_i\right]dx-\delta_p\boldsymbol{f}_e^{[n+1/2]}=\boldsymbol{0}, \tag{1}$$

$$\int_0^L \left[\frac{\boldsymbol{J}_\rho}{h}\left(\boldsymbol{\Omega}^{[n+1]}-\boldsymbol{\Omega}^{[n]}\right)P_i+\ \boldsymbol{\Omega}^{[n+1/2]}\times\boldsymbol{J}_\rho\boldsymbol{\Omega}^{[n+1/2]}P_i+\boldsymbol{M}^{[n+1/2]}P_i'\right.$$
$$\left.-\left(\boldsymbol{\Gamma}^{[n+1/2]}-\boldsymbol{\Gamma}_0\right)\times\boldsymbol{N}^{[n+1/2]}P_i-\boldsymbol{K}^{[n+1/2]}\times\boldsymbol{M}^{[n+1/2]}P_i\right. \tag{2}$$

$$-\left(\hat{\boldsymbol{q}}^{*[n+1/2]} \circ \hat{\boldsymbol{m}}^{[n+1/2]} \circ \hat{\boldsymbol{q}}^{[n+1/2]}\right) P_i \big] \, dx - \delta_p \boldsymbol{M}_e^{[n+1/2]} = \boldsymbol{0}.$$

The description of the notation used can be found in [2]. Furthermore, the formulation has been upgraded to enable for the detection of critical load level and critical cross-section. The stress-strain relations of the material fibre and the stress-resultants over the cross-section are evaluated by numerical integration of stresses over the cross-section [1]. The post-critical treatment for the singular cross-sections is implemented at the level of primary unknowns by introducing additional degrees of freedom that account for peak-like discontinuities in strain measures. The robustness and accuracy of the proposed methodology will be demonstrated using the following numerical example.

3. Numerical Example

A spatial cantilever beam with softening hyper-elastic constitutive law is considered here. The geometric and material properties of the beam are: length $L = 100$, width $t = 2$, height $h = 5$, shear modulus $G = 7692$, torsional moment of inertia $J_1 = 20.8333$, shear areas $A_2 = A_3 = 8.3333$, yield stress $\sigma_y = 50$, yield strain $\epsilon_y = 0.0025$ and ultimate strain $\epsilon_u = 0.0075$.

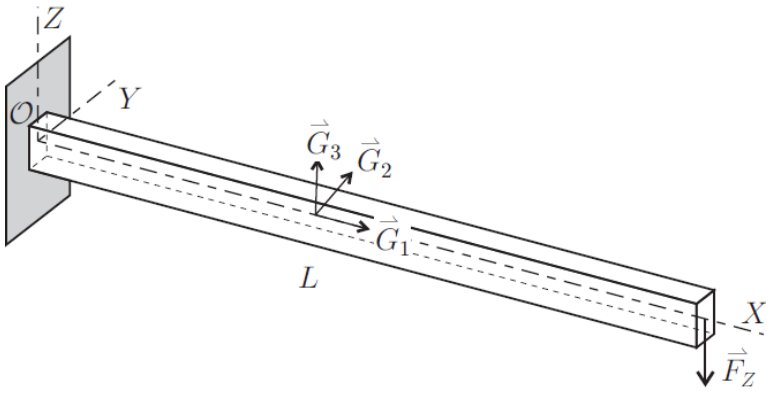

Figure 1. Spatial bending of hyper-elastic cantilever beam

We assume the following stress-strain law for the material:

$$\sigma(\epsilon) = \begin{cases} \dfrac{\sigma_y}{\epsilon_y}\epsilon & 0 \le |\epsilon| \le \epsilon_y, \\ \dfrac{\sigma_y}{\epsilon_u - \epsilon_y}(\epsilon_u - \epsilon) sign(\epsilon) & \epsilon_y < |\epsilon| < \epsilon_u, \\ 0 & |\epsilon| \ge \epsilon_u, \end{cases}$$

where $\epsilon(y,z) = \Gamma_x - yK_z + zK_y$ is the normal strain of an arbitrary fiber (y,z).

References

[1] D. Zupan and M. Saje, Analytical integration of stress field and tangent material moduli over concrete cross-sections. Computers and Structures., Vol. 83, pp. 2368-2380, 2005.

[2] E. Zupan and D. Zupan, On conservation of energy and kinematic compatibility in dynamics of nonlinear velocity-based three-dimensional beams, Nonlinear Dynamics, Vol. 95, pp. 1379–1394, 2019.

Thermal buckling analysis of thin-walled FG closed sections beams

Sandra Kvaternik Simonetti*, Domagoj Lanc*, Goran Turkalj, Martin Zlatić*

*University of Rijeka, Fauculty of Engineering
E-mails: {skvaternik1, dlanc, gturkalj, mzlatic}@riteh.hr

Keywords: thermal buckling, thin-walled, FGM, FEM

1. Introduction

Functionally graded thin-walled beams and structures are used in many engineering applications due to their very good strength-to-weight ratio, improved thermal resistance and high fracture toughness. Many papers have addressed the behaviour of FGM box-beams subjected to a variety of loading and placed in a high-temperature environment, but only some of them are cited here [1-6].

In this paper, a beam model for thermal buckling analysis of FG thin-walled closed sections beams is discussed. The model is based on Euler-Bernoulli-Navier bending theory and Vlasov torsion theory, assuming large displacement and small strains. The equilibrium equations of the finite elements are developed by an updated Lagrangian formulation. Material properties are assumed to be graded across the wall thickness and temperature-dependent. Three cases of the temperature rise over wall thickness are considered, which are uniform, linear and nonlinear. Numerical results are obtained for closed sectoins beams with different boundary conditions and temperature distributions to investigate the effects of the power-law index on the critical buckling temperature and post-buckling response.

2. Numerical model

Assume that the beam is made of a functionally graded material. The material properties are assumed to vary continuously through the wall thickness from a metal-rich outer surface to a ceramic-rich innerr surface according to power-law as defined in [7]:

$$P(n,T)=[P_o(T)-P_i(T)]\cdot V_c(n)+P_i(T), \tag{1}$$

where P represents the effective material property such as Young's modulus E, shear modulus G, coefficient of thermal expansion α, and thermal conductivity κ, respectively. The subscripts i and o represent the inner and outer surface constituents while Vc is the volume fraction of the ceramic phase. In this work, the material properties are assumed to be temperature-dependent.

$$V_c = (0{,}5+n/t)^p. \tag{2}$$

The stress-strain relation in terms of generalized Hooke's law form can be written as follows:

$$\begin{aligned} \sigma_z &= E\,(n,T)\cdot[\varepsilon_z-\alpha\,(n,T)\cdot\Delta T], \\ \tau_s &= G\,(n,T)\cdot\gamma_{zs}, \end{aligned} \tag{3}$$

where σ_z and τ_{zs} are stress components, ε_z and γ_{zs} are strain components; n, s denote the flange normal and transverse direction while z is parallel to the beam axis; ΔT is a temperature change, T_0 is the reference temperature.

The beam is subjected to a uniform, linear and nonlinear temperature distribution over the beam wall thickness.

2.1. Examples

The thermal buckling of the beam was analyzed for three different boundary conditions (double-sided clamping, double-sided joint supports and, combination) and different values of the power-law index p. The results of the author's beam model were verified with a numerical model based on

solid and shell finite elements. FG material was simulated through homogeneous layers. Table 1 shows a comparison of the critical temperatures obtained by the beam, solid and shell model for the simply supported beam and the different potency values *p*.

In the following examle, thin-walled FG box beam with the length l = 8 m, height h = 0.2 m, width b = 0.1 m and wall thickness t = 0.005 m is carried out. The FG material properties are assumed as follows: Alumina (E_c = 380 GPa, $\alpha_c = 7.2 \cdot 10^{-6}$ 1/C^0) and Aluminium (E_m = 70 GPa, $\alpha_m = 2.3 \cdot 10^{-5}$ 1/C^0). The Poisson's ratio is assumed to be constant v = 0.3. Table 1 shows a comparison of the critical temperatures obtained with the beam, shell and solid model for the double clamped box beam and the different power-law values p subjected to uniform temperature rise. Table 1 shows critical temperatures obtained with the beam and solid model for the double clamped box beam and the different power-law values p subjected to linear temperature rise.

Table 1 Critical temperatures for simply supported box beam; uniform temperature distribution

p	**0**	**0,2**	**0,5**	**1**	**5**	**10**
Beam model	41,683	31,665	26,893	23,033	17,3099	15,713
Shell model	41,578	31,568	26,395	23,004	17,792	16,511
Solid model	41,329	31,769	26,678	23,373	18,12	16,749

Table 2 Critical temperatures for clamped box beam; linear temperature distribution

p	**0**	**0,2**	**0,5**	**1**	**5**	**10**
Beam model	333,67	245,97	212,09	196,71	165,08	144,79
Solid model	337,53	256,00	219,60	204,50	175,72	156,74

4. Conclusions

A beam model for thermal buckling analysis of FG thin-walled beams has been developed and verified on the example of thermal buckling of a beam with different boundary conditions and functions of changing the material through to the wall thickness, and the results were compared with a numerical model.

In future work, it is planned to analyze the geometrically nonlinear behavior of FG composite beams and frames exposed to the environment with variable temperatures.

References

[1] Librescu L., Oh S.-Y. and Song O., "Thin-walled beams made of functionally graded materials and operating in a high temperature environment: Vibration and stability", *Journal of Thermal Stresses*, 28 (6-7), 649–712, 2005.

[2] Vo T.P. and Lee J., "Flexural-torsional behavior of thin-walled closed-section composite box beams", *Engineering Structures*, 29, 1774–1782, 2007.

[3] Nguyen T.-T., Kim N.-II. and Lee J., "Analysis of thin-walled open-section beams with functionally graded materials", *Composite Structures*, 138, 75-83, 2016.

[4] Vo T.P., Thai H.-T., Nguyen T.-K., Maheri A. and Lee J., "Finite element model for vibration and buckling of functionally graded sandwich beams based on a refined shear deformation theory", *Engineering Structures*, 64, 12- 22, 2014.

[5] Lanc D., Turkalj G. and Pesic I., "Global buckling analysis model for thin-walled composite laminated beam type structures", *Composite Structures*, 111, 371-380, 2014.

[6] Lanc D., Vo T.P., Turkalj G. and Lee J., "Buckling analysis of thin-walled functionally graded sandwich box beams", *Thin-Walled Structures*, 86, 148-156, 2015.

[7] Lanc D., Turkalj G., Vo T.P and Brnić J., "Nonlinear buckling behaviours of thin-walled functionally graded open section beams", *Composite Structures*, 152, 829-839, 2016.

Deformation Analysis of Advanced Pore Morphology Foam Elements using 4D X-ray Computed Micro-tomography

Daniel Kytyr[1], Petr Zlamal[1], Michal Vopalensky[1],
Matej Borovinsek[2], Matej Vesenjak[2], Zvonimir Tomicevic[3]

[1]*Czech Academy of Sciences, Institute of Theoretical and Applied Mechanics,*
Prosecka 76, 190 00 Prague 9, Czechia
E-mails: {kytyr;zlamal;vopalensky}@itam.cas.cz

[2]*University of Maribor, Faculty of Mechanical Engineering,*
Smetanova ulica 17, 2000 Maribor, Slovenia
E-mail: {matej.borovinsek;matej.vesenjak}@um.si

[3]*University of Zagreb, Faculty of Mechanical Engineering and Naval Architecture*
Ivana Lucica 5, 10002 Zagreb, Croatia
E-mail: zvonimir.tomicevic@fsb.hr

Keywords: advanced pore morphology foam; x-ray computed micro-tomography; in-situ mechanical testing; digital volume correlation

1. Introduction

This study applied in-situ 4D X-ray Computed Micro-tomography (XCT) experiments, where the advanced pore morphology (APM) foam elements were 3D scanned and compressed simultaneously for the first time [1,2]. Such an approach enables a direct comparison between the mechanical response and the internal structure of the closed-cell foam and gives results on how the deformation of the internal structure affects the mechanical response of the aluminum alloy foam.

2. Materials and Methods

To determine how the deformation of the internal structure and its changes during compression are related to its mechanical response, in-situ time-resolved XCT experiments were performed (Fig. 1), where the APM foam elements were 3D scanned during a compressive loading procedure.

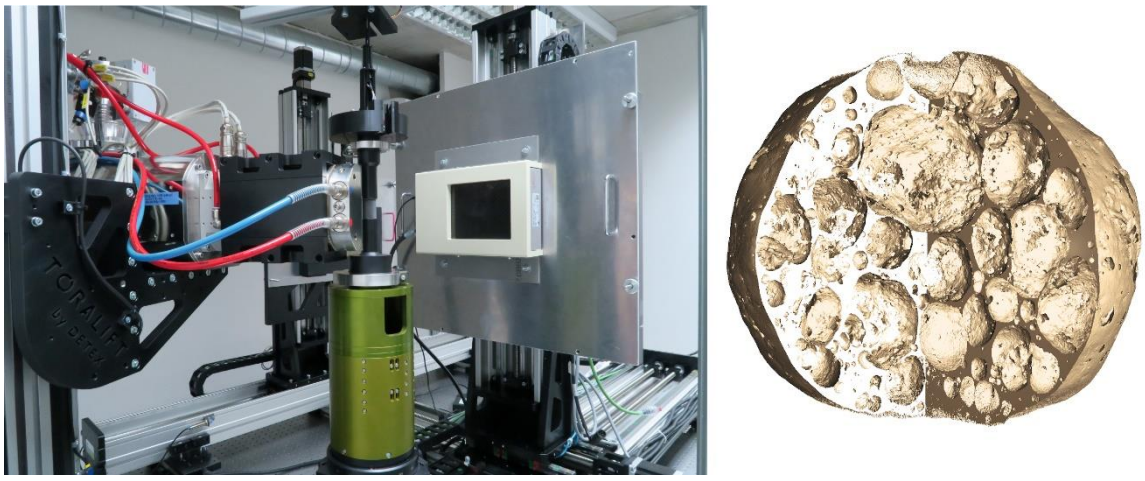

Figure 1. Experimental setup (left), visualization of APM foam element microstructure (right)

Simultaneously applying mechanical loading and radiographical imaging enabled new insights into the deformation behaviour of the APM foam samples when the mechanical response was correlated with the internal deformation of the samples. The experimental procedure consists of 25 loading steps using in-house developed loading and imaging devices (Fig. 2).

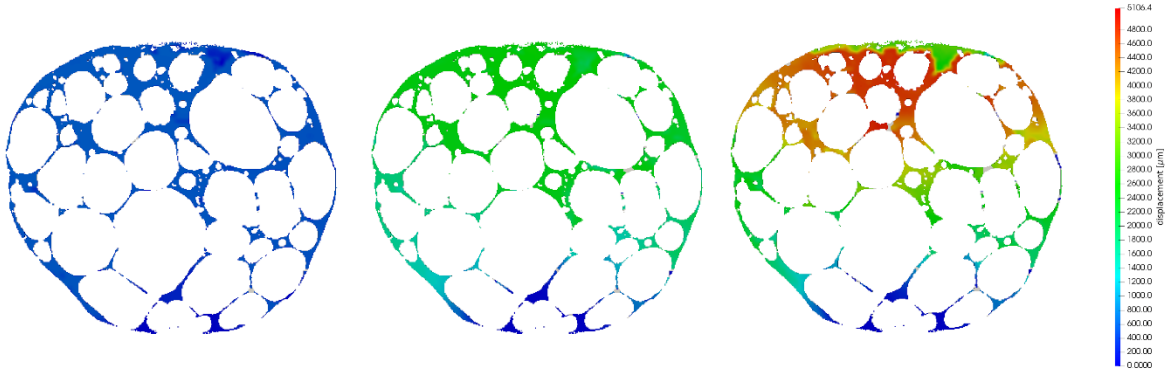

Figure 2. Displacement field presented on frontal section in 5th, 15th and 25th loading step

The data from the tomographic reconstruction has been processed by an in-house two-step digital volume correlation (DVC) procedure. The algorithm uses a two-step procedure to estimate the correlation coefficients, initially at the pixel level and then at the sub-pixel level to reach higher accuracy.

4. Conclusions

Combination of 4D XCT is highly effective method for full field assessment of the deformation characteristics of the objects with complex microstructure. Using DVC algorithm, the 25 displacement fields up to 50% macroscopic engineering deformation was calculated. This result could be used for validation of the numerical simulation.

Acknowledgements

Financial support from the Operational Programme Research, Development and Education in the project INAFYM (CZ.02.1.01/0.0/0.0/16_019/0000766) and the Slovenian Research Agency (research core funding No. P2-0063) are greatly acknowledged.

References

[1] Borovinsek M., Koudelka P., Sleichrt J., Vopalensky M., Kumpova I., Vesenjak M., Kytyr D. Analysis of advanced pore morphology (APM) foam elements using compressive testing and time-lapse computed microtomography (2021) Materials, 14 (19), art. no. 5897 DOI: 10.3390/ma14195897

[2] Vopalensky M., Koudelka P., Sleichrt J., Kumpova I., Borovinsek M., Vesenjak M., Kytyr D. Fast 4D on-the-fly tomography for observation of advanced pore morphology (APM) foam elements subjected to compressive loading (2021), 14 (23), art. no. 7256 DOI: 10.3390/ma14237256

Two-dimensional flow reconstruction from scattered measurements using CFD model fitting

Luka Lanča*, Luka Grbčić*, Karlo Jakac*, Stefan Ivić*

* University of Rijeka, Faculty of Engineering, Vukovarska 58, 51000, Rijeka
E-mails: {llanca,lgrbcic,kjakac, sivic}@riteh.hr

Keywords: fitting, optimization, bounary condition, velocity field, scattered measurments

1. Introduction

The main goal of this research is to reconstruct detailed flow field based on sea surface velocity measurements collected at scattered points (e.g., velocity values obtained by floating drifters). Accurate velocity field reconstruction on various scales is a common problem in oceanography [1–3]. We propose a simulation-optimization approach where the resulting flow filed is obtained by fitting boundary conditions of two-dimensional fluid flow numerical simulation in order to determine the flow field by minimizing the difference between the measured and simulated velocities. We designed three steady-state test cases which were simulated within the OpenFOAM CFD framework. The proposed velocity field reconstruction is thoroughly tested using several heuristic optimization algorithms. We investigate efficiency and accuracy of implemented framework for different number of optimization parameters and number of scattered measurements locations.

2. Simulation-optimization approach for velocity field reconstruction

Numerical flow field simulations are computed using simpleFoam solver incorporated inside OpenFOAM [4]. SimpleFoam employs semi-implicit method for pressure linked equations [5] in order to solve the continuity equation:

$$\nabla \cdot \boldsymbol{u} = 0 \tag{1}$$

and momentum equation:

$$\nabla \cdot (\boldsymbol{u} \otimes \boldsymbol{u}) - \nabla \cdot \boldsymbol{R} = -\nabla p + \boldsymbol{S}_u \tag{2}$$

where $\boldsymbol{u}$ is velocity, $\boldsymbol{R}$ is stress tensor, p is kinematic pressure and $\boldsymbol{S}_u$ is momentum source.

We developed three synthetic test cases with increasing complexity and number of boundary conditions. The optimization vector consisted of values which define the inlet velocity profile. Figure 1 displays the second test case with five optimization variables used to describe every inlet. Each optimization variable represents fluid velocity component normal to the inlet surface and they are uniformly spaced across the inlet area starting from the edges. The optimization goal is to find the velocity at inlets which lead to the minimal discrepancy between measured velocities and simulated flow velocities at certain points.

Numerous simulation-optimization runs were executed to determine the optimal size of the optimization vector. The aim of varying the number of optimization variables is to balance computing time and flow filed accuracy. Every unnecessary variable vastly increases computing time and provides negligible changes in accuracy, so it is essential to assign an optimal number of variables.

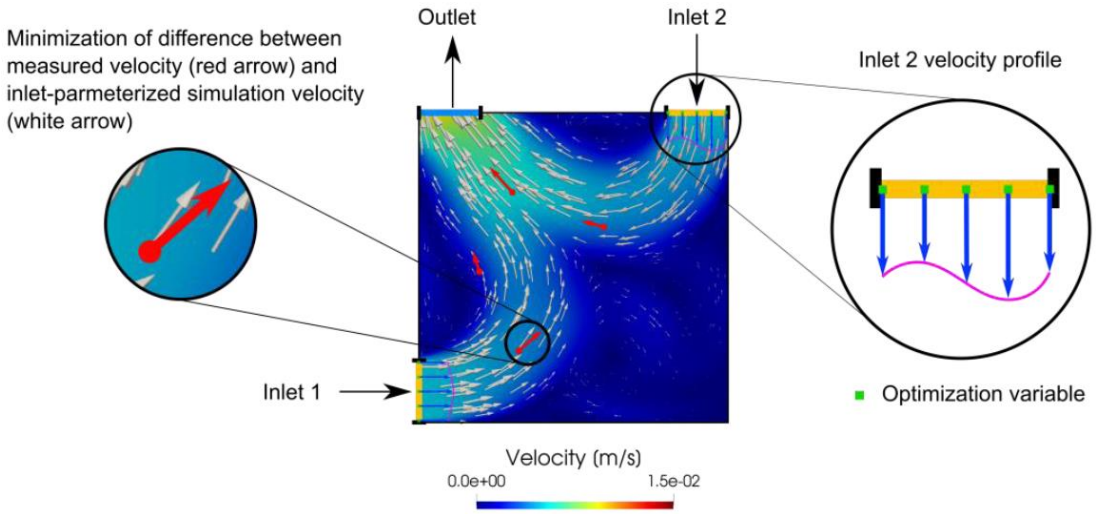

Figure 15. Synthetic test case consisting of two inlets and an outlet with simulated flow field. White arrows represent simulated fluid velocity vectors which are scaled by velocity magnitude. Red arrows depict measured velocity vectors and the optimization goal is to minimize the difference between red and white arrows (velocity vectors). Inlet velocity values are represented with blue arrows and specified by optimization variables which describe the velocity profile as shown in detail on inlet 2.

Optimization was conducted using Indago numerical optimization module for Python 3 [6,7]. It was developed at the Department for Fluid Mechanics and Computational Engineering of the University of Rijeka, Faculty of Engineering and contains several swarm-based optimization algorithms for real fitness function optimization over a real parameter domain. Particle Swarm Optimization (PSO) and Fireworks algorithm (FWA) were used, both of which are heuristic optimization methods.

3. Conclusions

Investigation of required boundary conditions degrees of freedom was conducted to make the flow field simulation of the given problem satisfactory. Number of needed drifters (scattered measurements) for precise flow field reconstruction was analyzed. Different heuristic optimization methods were compared in terms of efficiency.

References

[1] Gonçalves RC, Iskandarani M, Özgökmen T, Thacker WC. Reconstruction of Submesoscale Velocity Field from Surface Drifters. Journal of Physical Oceanography 2019;49:941–58. https://doi.org/10.1175/JPO-D-18-0025.1.

[2] Toner M, Poje AC, Kirwan AD, Jones CKRT, Lipphardt BL, Grosch CE. Reconstructing Basin-Scale Eulerian Velocity Fields from Simulated Drifter Data. 2001.

[3] Chang Y, Hammond D, Haza AC, Hogan P, Huntley HS, Kirwan AD, et al. Enhanced estimation of sonobuoy trajectories by velocity reconstruction with near-surface drifters. Ocean Modelling 2011;36:179–97. https://doi.org/10.1016/j.ocemod.2010.11.002.

[4] Weller HG, Tabor G, Jasak H, Fureby C. A tensorial approach to computational continuum mechanics using object-oriented techniques. Computers in Physics 1998;12:620. https://doi.org/10.1063/1.168744.

[5] Caretto LS, Gosman AD, Patankar S v., Spalding DB. Two calculation procedures for steady, three-dimensional flows with recirculation. Proceedings of the Third International Conference on Numerical Methods in Fluid Mechanics 1973:60–8. https://doi.org/10.1007/BFB0112677.

[6] Družeta S, Ivić S. Examination of benefits of personal fitness improvement dependent inertia for Particle Swarm Optimization. Soft Computing 2017;21:3387–400. https://doi.org/10.1007/S00500-015-2016-7.

[7] Družeta S, Ivić S, Grbčić L, Lučin I. Introducing languid particle dynamics to a selection of PSO variants. Egyptian Informatics Journal 2020;21:119–29. https://doi.org/10.1016/J.EIJ.2019.11.005.

A posteriori estimates by the hypercircle method

Philip L. Lederer*, Rolf Stenberg+, Third Author*

* Department of Mathematics and Systems Analysis
Aalto University, Espoo, Finland
E-mail: philip.lederer@aalto.fi

+ Department of Mathematics and Systems Analysis
Aalto University, Espoo, Finland
E-mail: rolf.stenberg@aalto.fi

Keywords: mixed finite elements, postprocessing, a posteriori error estimates, hypercircle method

1. Introduction

The classical Prager-Synge hypercircle theorem [4] for linear elasticity can be stated as follows. Let σ be the exact stress field and let Σ be a statically admissible approximation to it. Further, let U be a kinematically admissible approximation to the displacement and let $A\varepsilon(U)$ be the corresponding stress approximation with A being the constitutive equation. Then it holds

$$\|\sigma - \tfrac{1}{2}(\Sigma + A\varepsilon(U))\| = \tfrac{1}{2}\|\Sigma - A\varepsilon(U)\|,$$

where $\|\cdot\|$ is the energy norm. In other words, with $\frac{1}{2}(\Sigma + A\varepsilon(U))$ as the approximation, we know the error exactly.

2. The approximation by mixed finite element methods

This theorem we use in the following manner [2, 3]. By a mixed method we obtain a statically admissible stress field. The kinematically admissible displacement we get by a two-step postprocessing of the displacement of the mixed method. By a local, element-by-element, computation [1, 5], we get a new displacement field with an increased accuracy. From this we compute a new continuous displacement by averaging the degrees of freedom along edges and nodes. For the approach we perform a complete numerical analysis and present supporting numerical results.

References

[1] Arnold, D. N., Brezzi, F. Mixed and nonconforming finite element methods: implementation, postprocessing and error estimates. *RAIRO Modél. Math. Anal. Numér. 19*, 1 (1985), 7–32.
[2] Lederer, P., Stenberg, R. Analysis of mixed finite elements for elasticity. I. Exact stress symmetry. *https://arxiv.org/abs/2111.13513*.
[3] Lederer, P., Stenberg, R Analysis of mixed finite elements for elasticity. II. Weak stress symmetry. *In preparation*.
[4] Prager, W., Synge, J. L. Approximations in elasticity based on the concept of function space. *Quart. Appl. Math. 5* (1947), 241–269.
[5] Stenberg, R. Postprocessing schemes for some mixed finite elements. *RAIRO Modél. Math. Anal. Numér. 25*, 1 (1991), 151–167.

Phase field modelling of material fatigue

Tomislav Lesičar*, Zdenko Tonković, Srečko Glodež+

*University of Zagreb, Faculty of Mechanical Engineering and Naval Architecture,
Ivana Lučića 5, 10 000 Zagreb, Croatia
E-mails: {tomislav.lesicar, zdenko.tonkovic}@fsb.hr

+University of Maribor, Faculty of Mechanical Engineering,
Smetanova 17, 2000 Maribor, Slovenia
E-mail: srecko.glodez@um.si

Keywords: phase field, fatigue, damage, staggered solution, Abaqus

1. Introduction

The modern engineering seeks for the design of structures with an increased complexity, which leads to the necessity for new materials with enhanced properties to meet the demands put on efficiency, costs, and environmental impact. To meet this increasing standard on structural design as structural health, material failure is one of the most important factors which govern the design life of the structures and structural components. A significant number of components and constructions is subjected to the repeated loading cycles, causing material fatigue [1]. Material fatigue can be classified as low- and high-cyclic fatigue regime [6]. In high-cyclic regime (over 100 000 cycles), material behaviour is elastic, leading to a brittle fracture. The numerical methods for modelling of the material fatigue are mostly based on the principles of the classical fracture mechanics, relying on Paris' law [2]. Alternative methods are based on the extension of the constitutive material models by fatigue effects [3,4].

The phase-field approach to fracture modelling recently attracted many researchers due to its abilities to encompass crack initiation and propagation without introducing any ad hoc criteria. Crack topology is approximated by a continuous variable differentiating broken and unbroken material state. In solid mechanics, phase-field models are derived as the energy minimization problem, and furthermore reformulated into a system of partial differential equations [5]. The phase field methodology has been recognized as a very popular approach with application in brittle [6], as well as ductile fracture [7]. In the latest publications phase-field framework has been adopted for the fatigue problems [8,9]. An approach to phase field modelling of high-cyclic fatigue is also discussed in the presented research.

2. Separated phase field algorithm for modelling of high-cyclic fatigue

In the phase field methodology, the governing set of equations is

$$\begin{aligned} \nabla \cdot \boldsymbol{\sigma} + \mathbf{b} &= \mathbf{0}, \\ -l^2 \Delta \phi + (1 + \mathcal{H})\phi &= \mathcal{H}. \end{aligned} \tag{1}$$

In Eqs. (1), $\boldsymbol{\sigma}$ is the Cauchy stress, while $\mathbf{b}$ represents the vector of the volume forces. ϕ is a damage parameter, and l represents the crack width. To enforce damage irreversibility, a history parameter $\mathcal{H}(t)$ is introduced. For more details about derivation of the Eqs. (1), see [5,6,9]. Unfortunately, in numerical approaches, solution of the governing equations (1) cannot be efficiently obtained by monolithic solution scheme due to non-convexity of the energy functional. It has been demonstrated that the staggered strategy, in an iterative manner [10] is one of the best methodologies to resolve this problem.

In this research, a separated approach of solving equation system (1) is proposed and applied to the problems of high-cyclic fatigue. The scheme of the algorithm is displayed in Fig. 1. To remedy

the usual difficulty of standard single iteration staggered algorithm, a criterion for determination of the global minimum in both equations is introduced

$$\frac{\|\phi\|_i - \|\phi\|_{i-1}}{\|\phi\|_{i-1}} \leq \text{tol}, \tag{2}$$

allowing imposition of arbitrarily large loading increments in the simulations. To account for the fatigue phenomena, a fatigue degradation function has been utilized in the framework, which degrades the critical fracture energy density G_c, as a consequence of the repeated loading [9]. To speed up to the computations, cyclic skipping technique is embedded. The framework is embedded into FE software Abaqus via user subroutines and tested on the standard examples.

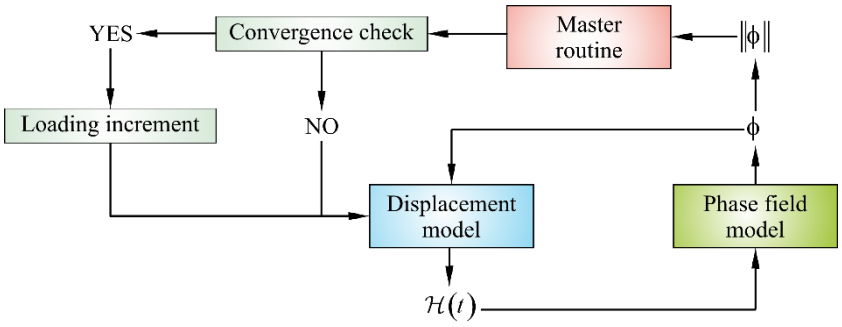

Figure 1. The scheme of separated phase field algorithm

Acknowledgments

This work has been fully supported by Croatian Science Foundation under the project "Multiscale Numerical Modelling and Experimental Investigation of Aging Processes in Sintered Structural Components" (MultiSintAge, PZS-1 2019-02-4177).

References

[1] Stephens RI, Fatemi A, Stephens RR, Fuchs HH. Metal Fatigue in Engineering. New York: Wiley; 2000.

[2] Maierhofer J, Pippan R, Gänser HP. Modified NASGRO equation for physically short cracks. Int J Fatigue. 2014;59:200–7.

[3] Xu K, Qiao GY, Pan XY, Chen XW, Liao B, Xiao FR. Simulation of fatigue properties for the weld joint of the X80 weld pipe before and after removing the weld reinforcement. Int J Press Vessel Pip. 2020;187:104164.

[4] Borges MF, Neto DM, Antunes F V. Numerical simulation of fatigue crack growth based on accumulated plastic strain. Theor Appl Fract Mech. 2020;108:102676.

[5] Bourdin B, Francfort GA, Marigo J-J. The Variational Approach to Fracture. J Elast. 2008;91(1):5–148.

[6] Miehe C, Hofacker M, Welschinger F. A phase field model for rate-independent crack propagation: Robust algorithmic implementation based on operator splits. Comput Methods Appl Mech Eng. 2010;199(45–48):2765–78.

[7] Dittmann M, Aldakheel F, Schulte J, Wriggers P, Hesch C. Variational phase-field formulation of non-linear ductile fracture. Comput Methods Appl Mech Eng. 2018;342:71–94.

[8] Schreiber C, Kuhn C, Müller R, Zohdi T. A phase field modeling approach of cyclic fatigue crack growth. Int J Fract. 2020;225(1):89–100.

[9] Seleš K, Aldakheel F, Tonković Z, Sorić J, Wriggers P. A general phase-field model for fatigue failure in brittle and ductile solids. Comput Mech. 2021;67(5):1431–52.

[10] Molnár G, Gravouil A. 2D and 3D Abaqus implementation of a robust staggered phase-field solution for modeling brittle fracture. Finite Elem Anal Des. 2017;130:27–38.

Numerical Growth and Remodeling Study of the Abdominal Aortic Aneurysm tortuosity

Ana Lisac*, Lana Virag*, Igor Karšaj*

*Faculty of Mechanical Engineering and Naval Architecture, University of Zagreb, Ivana Lučića 5, 10000 Zagreb, Croatia
E-mails: ana.lisac@fsb.hr, lana.virag@fsb.hr, igor.karsaj@fsb.hr

Keywords: growth & remodeling , abdominal aortic aneurysms, finite element method, boundary conditions

1. Introduction

Abdominal aortic aneurysms (AAA) represent a significant medical problem, and therefore, numerical models describing changes during aneurysm growth and rupture, have been developed to help with disease progression and optimal medical treatment [1], [2]. The growth and remodeling (G&R) model is a 3D constrained mixture model based on [3], that, in this case, describes the aorta as a mixture of different constituents (elastin, four families of collagen fibers, and smooth muscle cells) that possess different mechanical and structural properties. The model has been proven to successfully describe the changes in mass and remodeling of complex structures, such as blood vessels, and their response to different mechanical and chemical stimuli.

In a previous study, the AAA has been modeled with the G&R model as a three-layer composite (where the layers in the computational model represented the layers of an artery – intima, media, and adventitia) [2]. The growth of AAA was stimulated by the non-uniform irreversible loss of elastin. The study showed that the wall thickness of an aneurysm decreased, while stresses increased. However, the model did not allow aortic tortuosity or bending commonly seen in AAAs [4], [5].

Since the previously mentioned work did not achieve appropriate arterial curvature, in this study, we investigate the influence of various boundary conditions and mesh changes to determine the model that describes the changes in an aneurysm more accurately.

2. Methods

The G&R model used in this study has been presented in [2]. The aortic wall was modeled as a one-layered structure with different ratios of structurally important constituents (elastin, collagen, and smooth muscle cells).

The healthy aorta was modeled as a cylindrical model. Because axially-symmetric fusiform aneurysms cannot achieve tortuosity due to the boundary condition, in this work we focused on asymmetric AAAs. Still, only a portion of a cylinder, with a central angle of 180°, can be modeled with imposed axisymmetric boundary conditions. The model was then discretized with hexahedral Q1P0 elements, with 3 and 16 elements in the radial and circumferential direction, respectively.

To model the growth and changes of an aneurysm at the apex, elastin was gradually degraded with a time-depended degradation function. To examine the relationship between arterial curvature and the aneurysm placement, different meshes were created where the aneurysm apex was placed at different heights (in the middle and on 1/3 of the modeled aorta). Also, different boundary conditions were examined.

3. Results and conclusions

Figure 1. (a) shows the growth of an AAA inner diameter for an aneurysm with the apex at $z = 100$ mm and $z = 66$ mm, respectively. It can be noted that the growth of an AAA with the apex positioned at the $z = 66$ mm is slower than the growth of an AAA with the apex in the middle. Figure 1. (b) shows a 200 mm long segment of an aorta with an aneurysm with the apex in the middle of the model, i. e. z = 100 mm, and (c) shows an aorta with an aneurysm with the apex on z = 66 mm at the same G&R time at 1810 days. It can be noticed that the aortic tortuosity increases with the lowering of the apex position, i. e. with the apex approaching the boundary. Also, the dimensions of an apex are greater for case (c), which is in accordance with the medical observations [4], [5]. Here, it can be concluded that the position of an aneurysmatic apex in a computational model has a significant impact on the growth of an aneurysm and the aortic tortuosity.

This simplified model provided satisfying results, and further examinations are needed to investigate the optimal combination of boundary conditions, length of modeled aorta and position of the apex which will ensure the most realistic results.

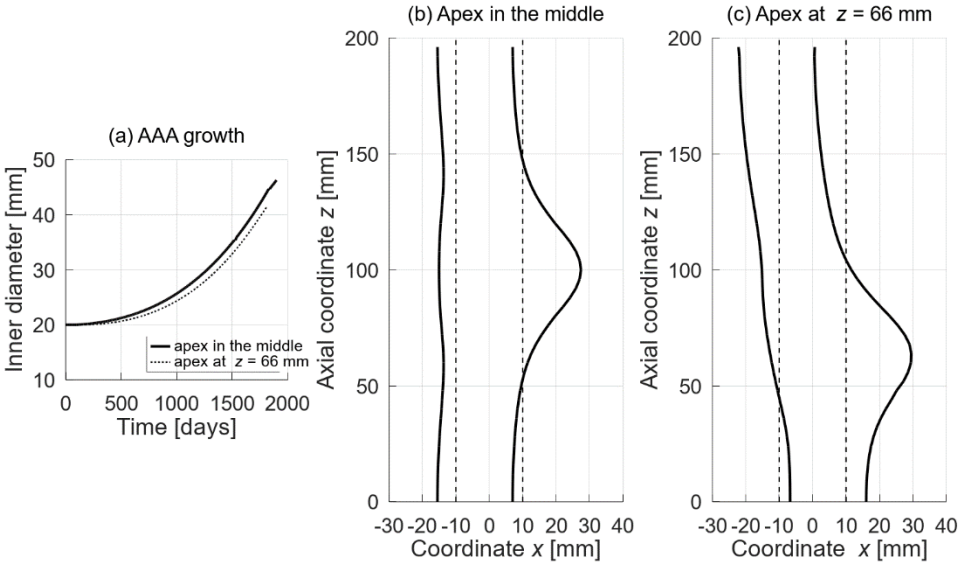

Figure 1. (a) Growth of inner diameter of an AAA, (b) Aorta with an aneurysm with the apex on z = 100 mm, (c) aorta with an aneurysm with the apex on z = 66 mm; dotted lines represent the diameter of a healthy aorta

References

[1] T. Canchi, S. D. Kumar, E. Y. K. Ng, and S. Narayanan, "A Review of Computational Methods to Predict the Risk of Rupture of Abdominal Aortic Aneurysms," *Biomed Res. Int.*, vol. 2015, 2015, doi: 10.1155/2015/861627.

[2] N. Horvat, L. Virag, G. A. Holzapfel, J. Sorić, and I. Karšaj, "A finite element implementation of a growth and remodeling model for soft biological tissues : Verification and application to abdominal aortic aneurysms," *Comput. Methods Appl. Mech. Eng.*, vol. 352, pp. 586–605, 2019, doi: 10.1016/j.cma.2019.04.041.

[3] J. D. Humphrey and K. R. Rajagopal, "A constrained mixture model for growth and remodeling of soft tissues," *Math. Model. Methods Appl. Sci.*, vol. 12, no. 03, pp. 407–430, Mar. 2002, doi: 10.1142/S0218202502001714.

[4] B. A. Zambrano *et al.*, "Association of Intraluminal Thrombus, Hemodynamic Forces, and Abdominal Aortic Aneurysm Expansion Using Longitudinal CT Images," *Ann. Biomed. Eng.*, vol. 44, no. 5, pp. 1502–1514, 2016, doi: 10.1007/s10439-015-1461-x.

[5] E. Metaxa, N. Kontopodis, K. Tzirakis, C. V Ioannou, and Y. Papaharilaou, "Effect of intraluminal thrombus asymmetrical deposition on abdominal aortic aneurysm growth rate," *J. Endovasc. Ther.*, vol. 22, no. 3, pp. 406–412, 2015, doi: 10.1177/1526602815584018.

Computational aspect of a reconstruction of heritage structure built as ribbed masonry vaults

B. A. Lógó*, M. Bruggi+, J. Lógó[1]

*Department of Engineering Geology and Geotechnics, Budapest University of Technology and Economics, Budapest, Hungary
E-mails: logo.benedek@emk.bme.hu

+Department of Civil and Environmental Engineering, Politecnico di Milano, Milano, Italy
E-mail: matteo.bruggi@polimi.it

[1]Department of Structural Mechanics, Budapest University of Technology and Economics, Budapest, Hungary
E-mail: logo@ep-mech.me.bme.hu

Keywords: funicular analysis, masonry vaults, ribbed vaults, stellar vaults, historical constructions

1. Introduction

The study deals with the renovation of the vault of the Church of the Assumption in Tereke, presenting the history of the church, the surroundings of the settlement from a geological point of view and the calculation. During the church's nearly 800-year history, several alterations have taken place, the study showing the most recent, which ended in 2020. As it is a listed building, during the renovation they sought to use the same building materials as the original structure to be restored. This was also an important consideration in the calculation, as it was possible to determine the material properties. Since the original building materials were preferred during the construction of the original structure, it is essential to describe the geology of the area in order to get to know the material that makes up the structure. A numerical method is implemented to cope with the funicular analysis of ribbed masonry vaults under self-weight. A two-layer spatial network with given plan geometry is adopted to account for the load path in the overlying vault and in the supporting ribs. The minimization of the horizontal thrusts is formulated in terms of an independent set of force densities, and in the vertical coordinates of the restrained nodes. Constraints are enforced on the height of the nodes and on the sign of the force densities, to seek anti-funicular networks in equilibrium with the loading that lie within the envelope of the ribbed vault.

2. A brief historical overview and geology

Tereske is an Árpádian settlement in northern Hungary, in Nógrád county. The village is first mentioned in a document from 1219 as Triskai, although it may have been inhabited earlier based on archaeological monuments. It can be read there is a monastery belonging to an unnamed order in the settlement. The time of the founding of the monastery itself and the person of the founder are unknown, no sources have survived. The church belonging to the monastery was first mentioned in 1485 due to a fire. The development of history had a significant impact on both the area of the settlement and the church itself. It functioned as a mosque during the Ottoman occupation for nearly a hundred years, after which the church regained its original function. [1] Sandstone was used during the construction of the church building, as well at the restored vault.

Like most of Hungary, Tereske was built on sedimentary soil, its immediate surroundings being mainly loess. There are three sandstone formations with different properties near the settlement, i.e. the Miocene part of the Pétervásár sandstone formation, the Törökbálint sandstone formation and the Hárshegy one. The Miocene part of the Pétervásár sandstone formation (fine, medium and coarse-grained sandstone, often glauconite, clayey, mica fine sandstone, with siltstone settlements) and the Törökbálint sandstone formation (coarse-fine-grained sandstone, fine sandstone clay at the bottom; with calcareous fine-sand siltstone settlements at the top) are not suitable to obtain building stones.

Indeed, both the walls and ribs of the vault were built using the sandstone of Hárshegy formation. The sandstone of Hárshegy formation was formed in the early Oligocene, about 30 million years ago, in a shallow marine environment (littoral and shallow sublittoral, with reduced saltwater and lagoon in the lower part). The yellow, reddish-brown, or grayish-colored rock is composed almost entirely of quartz grains of sand or fine gravel, but in some places contains deposits of refractory clay and coal. The gravel material of the rock is of metamorphic and igneous origin. Its binder is mostly siliceous, making Hárshegy sandstone a relatively hard and durable rock which was an appreciated building material across the time, see Vattai and Rozgonyi-Boissinot[2].

3. Methods, results

Funicular analyses are applied to investigate the equilibrium of the stellar vault under self-weight, using two different assumptions in the modelling of the ribs. At first all the members of the funicular network are assumed to belong to a one-layer grid and later a two-layer grid is applied with the aim of modelling the ribs separately. In the latter case, vertical members are introduced to allow the load pass from the upper layer (masonry webbing) to the lower one (stone ribs). To avoid the arising of vertical members with zero length (it means infinite force densities) the bounds assigned to the nodes of the lower layer are shifted downwards by a given amount, with no effect on the equilibrium in the case of vertical loads. Alternatively, a minimum gap could be enforced by selecting a suitable set of lower and upper bounds for the coordinates of the extremal nodes of these elements. For the numerical calculation a computational procedure elaborated by Bruggi [3] is used. The result can be seen briefly in Fig.1.

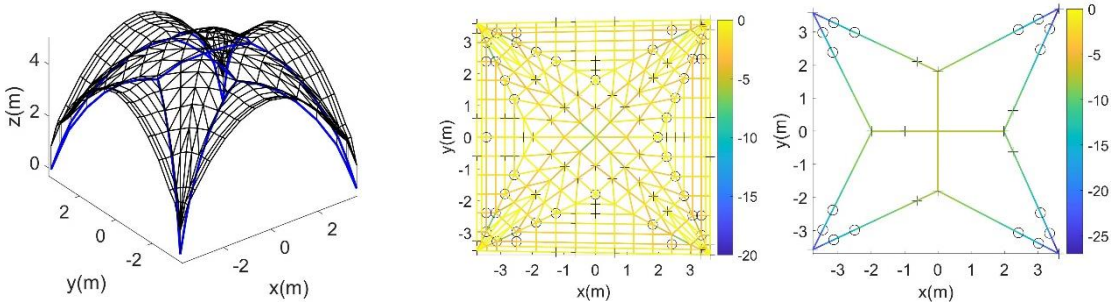

(a) (b) (c)

Figure 16 - Two-layer funicular network (with 221 parameters): overall view (a); overlying layer - webbing (b); underlying layer - ribs (element forces are in kN).

4. Conclusions

A computational procedure is presented for the calculation of ribbed masonry vaults. The results are in good agreement with the results from control analysis obtained at the reconstruction and restoration works of Church of the Assumption in Tereke.

References

[1] Mag H., *Tereske temploma a késő középkorban.* - Church of Tereske in the late Middle Ages- Archeologia - Altum Castrum Online Magazin. Last retrieved on 12/06/2020 at www.archeologia.hu (in Hungarian). 2014

[2] Vattai A., Rozgonyi-Boissinot N., The effect of grain size, surface roughness, and joint compressive strength on shear strength along discontinuities of Hungarian sandstones. Central European Geology, 61(1), 34-49.

[3] Bruggi, M. A constrained force density method for the funicular analysis and design of arches, domes and vaults. International Journal of Solids and Structures, 193-194, 251-269.

New type of optimal topologies of elastoplastic structures based on different reliability methods

János Lógó*, Piotr Tauzowski+, Bartlomiej Blachowski+

* *Budapest University of Technology and Economics, Műegyetem rkp. 3, Budapest, Hungary*
E-mails: logo@ep-mech.me.bme.hu

+ *Institute of Fundamental Technological Research, Polish Academy of Sciences, Pawińskiego St. 5B, Warsaw, Poland*
E-mail: ptauzow@ippt.pan.pl , bblach@ippt.pan.pl

Keywords: *Topology optimization, Stochastic load, Elastoplastic FE analysis, Plasticity*

1. Introduction

The paper [1] presents a new topological optimization algorithm for elastoplastic structures. In this algorithm, material is removed in places with little stress intensity, until the optimal structure is obtained. However, such action causes a loss of structural reliability. Therefore, it is necessary to control the reliability by supplementing the formulation of topological optimization with reliability constraints. Since the failure probabilities of the structure should be low, we can use relatively fast First Order Reliability Method (FORM) [2]. There are many variations of linear approximation methods such as: Reliability Index Approach (RIA) or the family of Performance Measure Approach (PMA) algorithms. In the presented work, the above methods will be used for safety control in the process of topological optimization of elastic-plastic structures.
To carry out these tasks, it was necessary to design and implement these algorithms. The system architecture for FEM analysis and topological optimization toolkit built by the authors will also be presented.

2. Methods

The proposed methodology consists of two parts: a return mapping-based algorithm for topology optimization and a first order reliability method (FORM) for reliability assessment. Both methods operate in nested loop where at each iteration step update in the topology of the structure is performed and then reliability constraint is checked if required level of safety is assured.

Below we present briefly the basics of the formulation of the elastic-plastic problem as well as the iterative formula for estimating the reliability index. The proposed approach utilizes elastoplastic finite element analysis together with optimality criteria based on sequential removal of the least stressed elements. The problem is similar in spirit to the stress constrained one. Major difference is that in our formulation the stress constraint is automatically satisfied by the use of an elastoplastic material. One should only be careful that the load of the structure is not greater than the collapse load. The topology optimization works with an objective function representing the volume of the material required to safely carry the applied loading. The density of the material at a given point in three dimensional space is described by an indicator function $\chi(\mathbf{x})$, taking values 0 or 1. We are looking for a solution to the above problem within a set of kinematically admissible displacement fields V. Additionally, constraints are imposed on stresses $\sigma(\mathbf{x})$ at any the given point of the design domain Ω.

$$\begin{aligned} &\min_{\chi,u\in V} \int_{\Omega} \chi(\mathbf{x}) d\Omega \\ \text{s.t.} \quad &\int_{\Omega} \chi \varepsilon(\mathbf{u}) : \mathbf{D} : \varepsilon(\mathbf{v}) d\Omega - \int_{\Gamma n} \bar{t}.\mathbf{v} d\Gamma = 0, \ \mathbf{v} \in \mathrm{V}, \\ &\frac{|\sigma(\mathbf{x})|}{\sigma_0} - 1 \le 0, \qquad \mathbf{x} \in \Omega_{mat}, \end{aligned} \tag{1}$$

$$\chi(x) = \begin{cases} 1, & \mathbf{x} \in \Omega_{mat} \\ 0, & \mathbf{x} \in \Omega_{mat} \setminus \Omega_{mat} \end{cases}.$$

here $\mathbf{u}(x)$, $\mathbf{v}(x)$, $\varepsilon(\mathbf{u})$ represent displacement, virtual displacement and strain fields, respectively. $\mathbf{D}$ is the elasto-plastic material matrix, $\bar{t}$ is the traction on the boundary, σ_0 is the stress limit and finally Ω_{mat} represents the material domain defined as $\Omega_{mat} := \{ \mathbf{x} \in \Omega \mid \chi(\mathbf{x}) = 1 \}$.

Probabilistic task is transformed to standard normal space $\mathbf{w}$. The most probable point is the closest point to the centre of the coordinate system of this space, which lies on the limit state surface. Therefore determination of this point is optimization problem formulated as follow:

$$\begin{aligned} &\min \|\mathbf{w}\|_2 = \mathbf{w} \cdot \mathbf{w}^T \\ &\text{s.t.} \quad G(\mathbf{w}) = 0. \end{aligned} \tag{2}$$

To tackle this problem Rackwitz and Fiesler [2] proposed the following gradient-based iterative scheme:

$$\mathbf{w}^{(n+1)} = \frac{1}{\|\nabla G(\mathbf{w}^{(n)})\|^2} \left(\nabla G(\mathbf{w}^{(n)})^T \mathbf{w}^{(n)} - G(\mathbf{w}^{(n)}) \right) \nabla G(\mathbf{w}^{(n)}). \tag{3}$$

By the use of the formula above and applying the theory of the Reliability Index Approach (RIA) and the Performance Measure Approach (PMA), respectively, topology optimization algorithms were elaborated and applied. Comparison of deterministic and reliability-based optimal topologies are presented.

4. Conclusions

This work presents a new iterative, nested (double loop) algorithm for topological optimization with regard to reliability constraints. The external topological optimization loop implements a heuristic algorithm of material removal in the least stressed areas. The internal loop controls whether the failure probability is not exceeded. The applied first-order approach (FORM) to the safety control in the topological optimization process is not a high time overhead. Both Reliability Index Approach (RIA) and Performance Measure Approach (PMA) algorithms estimate the reliability index in a relatively short time especially when the algorithm is implemented using parallel computing. The effectiveness of the presented method has been confirmed by a numerical example, known from the literature as L-shape benchmark. Topologies taking into account reliability conditions have not only higher volume fraction but also their different shape is more resistant to random load conditions. The calculated optimal topologies in case of deterministic and probabilistic cases are almost the same ones, however the stress distributions are significantly different.

Acknowledgements

The present study was supported by the NKFI (grant K 119440) – and Joint grant of the Hungarian and the Polish Academy of Sciences.

References

[1] Blachowski, B., Tauzowski, P., Lógó, J. Yield Limited Optimal Topology Design of Elasto-Plastic Structures, *Structural and Multidisciplinary Optimization*, 61, 1953–1976 (2020).

[2] Rackwitz, R., Flessler, B., Structural reliability under combined random load sequences, *Computers & Structures*, 9, 5, 489–494, 1978.

Simulation of High-Strength Concrete under Cyclic Compressive Loads

Stefan Löhnert*, Nadja Oneschkow+

*Technische Universität Dresden, Institute of Mechanics and Shell Structures,
01062 Dresden, Germany
E-mails: stefan.loehnert@tu-dresden.de

+Leibniz Universität Hannover, Institute of Building Materials Science,
Appelstr. 9a, 30167 Hannover, Germany
E-mail: n.oneschkow@baustoff.uni-hannover.de

Keywords: compressive fatigue, gradient-enhanced damage, high-strength concrete

1. Introduction

The accurate prediction of the fatigue behaviour of high-strength concrete under compressive fatigue loads is still a challenging task. In recent years the efforts to develop material models capable of predicting the fatigue behaviour and life time of concrete have increased. However, the complexity of the material behaviour of concrete on different scales leads to significant challenges for the development of an appropriate material model. Currently, there is no material model available that has been proven to accurately predict the fatigue behaviour of concrete under arbitrary cyclic loads.
In this contribution, we present a novel framework for the simulation of the fatigue behaviour of high strength concrete based on a gradient-enhanced damage model in combination with a fatigue model similar to the approach presented in [1]. Simulations indicate that all three phases of fatigue can be captured. The presented approach can be enhanced by more advanced material models suitable for concrete simulations such as microplane models [2].

2. The gradient-enhanced fatigue damage model

To simulate the fatigue behaviour of high strength concrete under compressive cyclic loads the weak form of equilibrium

$$\int_\Omega \boldsymbol{\sigma} : \delta\boldsymbol{\varepsilon}\,\mathrm{d}\Omega - \int_{\partial\Omega} \boldsymbol{t}\cdot\delta\boldsymbol{u}\,\mathrm{d}\partial\Omega = 0 \tag{1}$$

needs to be solved. Assuming linear elastic material behaviour including gradient-enhanced damage, the stresses become

$$\boldsymbol{\sigma} = (1-d)\boldsymbol{\sigma}_0 \quad \text{with} \quad \boldsymbol{\sigma}_0 = 2\mu\boldsymbol{\varepsilon} + \Lambda\,\mathrm{tr}(\boldsymbol{\varepsilon})\mathbf{1} \tag{2}$$

Here, μ and Λ are the Lamé parameters. We assume the damage model of Mazars and Pijaudier-Cabot [3] leading to the damage function

$$d(\kappa) = 1 - \frac{\kappa_0}{\kappa}(1-\alpha) - \alpha\, e^{-\beta(\kappa-\kappa_0)} \tag{3}$$

Here, α and β are parameters influencing the shape of the damage function and κ_0 is the initial threshold value for the history variable κ beyond which damage proceeds. The quantity κ depends on a gradient-enhanced equivalent strain $\bar{\varepsilon}$ which is determined according to the model of Peerlings [4] by solving the weak form of the inhomogeneous Helmholtz equation

$$\int_\Omega \left(\bar{\varepsilon} - \tilde{\varepsilon}(\boldsymbol{\varepsilon})\right)\cdot\eta\,\mathrm{d}\Omega + c\int_\Omega \mathrm{grad}(\bar{\varepsilon})\cdot\mathrm{grad}(\eta)\,\mathrm{d}\Omega = 0 \tag{4}$$

For the simulation of concrete, it is necessary that the scalar valued function $\tilde{\varepsilon}$ allows for a differentiation between damage under tension and damage under compression. We employ the modified von Mises function

$$\tilde{\varepsilon}(\boldsymbol{\varepsilon}) = \frac{(k-1)I_1}{2k(1-2\nu)} + \sqrt{\left(\frac{(k-1)I_1}{2k(1-2\nu)}\right)^2 + \frac{3J_2}{k(1+\nu)^2}} \tag{5}$$

Here ν is Poisson's ratio, I_1 is the first invariant of $\boldsymbol{\varepsilon}$ and J_2 is the second invariant of the deviator of $\boldsymbol{\varepsilon}$. For a classical damage model which does not contain fatigue the condition to determine progressing damage is

$$f(\bar{\varepsilon}, \kappa) = \bar{\varepsilon} - \kappa \leq 0 \tag{6}$$

The approach presented in [1] assumes that for fatigue crack propagation the critical energy release rate reduces in each load cycle depending on some monotonically increasing accumulated equivalent strain measure. This principle can be extended to the gradient-enhanced damage formulation presented in this contribution as well. One possible reduction function for the material strength is

$$\phi(\gamma) = \begin{cases} 1 & : \quad \gamma < \gamma_t \\ (1 - a \log(\gamma/\gamma_t))^2 & : \quad \gamma_t \leq \gamma \leq 10^{1/a}\gamma_t \\ 0 & : \quad \gamma > 10^{1/a}\gamma_t \end{cases} \tag{7}$$

where a is a parameter to set the rate of the reduction of the material strength and γ_t is a threshold value for γ beyond which the material strength is reduced. The function γ is a monotonically growing accumulated equivalent strain function that can be defined by

$$\gamma = \int_0^t H(\bar{\varepsilon}\dot{\bar{\varepsilon}})|\dot{\bar{\varepsilon}}| \, \mathrm{d}\tau \tag{8}$$

with H being the Heaviside function. Including the reduction function in the yield condition (6) leads to

$$f(\bar{\varepsilon}, \kappa) = \bar{\varepsilon} - \phi(\gamma)\kappa \leq 0 \tag{9}$$

Simulating the mesostructure of high-strength concrete under cyclic compressive loading and comparing the results to experimental data reveals the applicability of the model, see Fig 1.

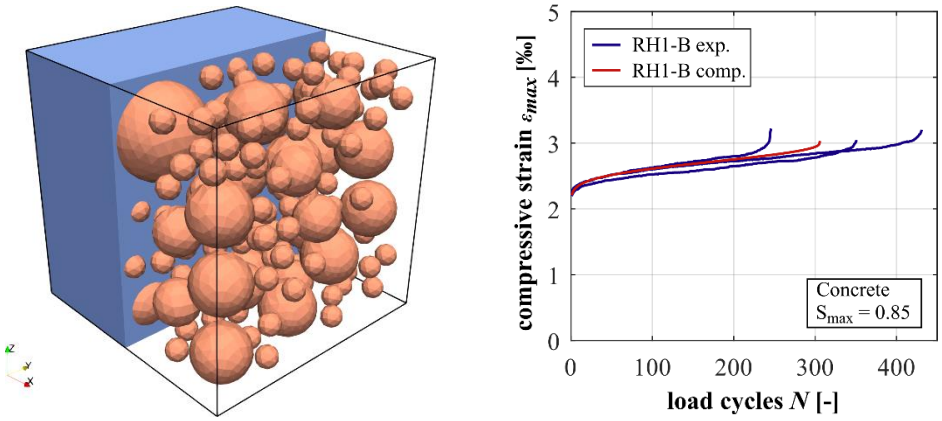

Figure 1: left: meshed mesostructure model of HPC, right: maximum compressive strain – experimental and computational results [5]

References

[1] Carrara, P., Ambati, M., Alessi, R, de Lorenzis, L: A novel framework to model the fatigue behavior of brittle materials based on a variational phase-field approach. *Comput. Methods Appl. Mech. Eng.*, 361, 112731, 2020

[2] Caner, F.C., Bažant, Z.P.: Microplane model M7 for plain concrete. I: Formulation, *J. Eng. Mech.*, 139, 1714–1723, 2013

[3] Mazars, J., Pijaudier-Cabot, G.: From damage to fracture mechanics and conversely: A combined approach, *Int. J. Solids Struct.*, 33, 3327–3342, 1996

[4] Peerlings, R.H.J., de Borst, R., Brekelmans, W.A.M., de Vree, J.H.P.: Gradient enhanced damage for quasi-brittle materials, *Int. J. Numer. Methods Eng.* 39, 1996, 3391–3403

[5] Oneschkow, N., Timmermann, T., Löhnert, S.: Compressive fatigue behaviour of high-strength concrete and mortar: Experimental investigations and computational modelling, *Materials* 15, 319, 2022

Torsional vibration induced with the position dependent impacts

Željan Lozina, Damir Sedlar, Anđela Bartulović

University of Split, FESB, R. Boškovića 32, 21000 Split, Croatia
E-mails: {zeljan.lozina, damir.sedlar, abartulo}@fesb.hr

Key words: modal analysis, nonclassical damping, nonlinearity, impact load, torsional vibration

1. Introduction

The important issue of the torsional vibration induced with impacts which depend on position is investigated in terms of nonlinearities that can still be handled with modal superposition. The considered models involve non-classical damping and rigid body modes. It is proved that it is possible to establish efficient algorithms based on modal superposition.

2. Nonclassically damped system driven with the load dependent on position

The governing equation of the common linear dynamic system reads, [1]:

$$\mathbf{M}\ddot{\mathbf{q}} + \mathbf{D}\dot{\mathbf{q}} + \mathbf{K}\mathbf{q} = \mathbf{Q}(t) \tag{1}$$

The classical damping is of the form $\mathbf{D} = \alpha\mathbf{M} + \beta\mathbf{K}$ and using $\mathbf{M}$ normed eigenvectors of the eigenproblem $(\mathbf{K} - \lambda\mathbf{M})\phi = 0$, we reach the uncoupled system (2):

$$\ddot{r}_i + (\alpha + \beta\omega_i^2)\dot{r}_i + \omega_i^2 r_i = f_i(t) \tag{2}$$

where modal displacements and modal loads (in matrix form) are defined as:

$$\mathbf{r} = \mathbf{\Phi}^{-1}\mathbf{q}$$

$$\mathbf{f} = \mathbf{\Phi}^{T}\mathbf{Q}$$

However, when the damping is not classical, transformation $\mathbf{\Phi}^T\mathbf{D}\mathbf{\Phi} \neq \alpha\mathbf{I} + \beta\mathbf{\Lambda}$ and therefor system cannot be decoupled. When additionally, load depends on position, e.g. [2], we have an extra source of the nonlinearity, and the governing equation now reads as follow, (3):

$$\mathbf{M}\ddot{\mathbf{q}} + \mathbf{D}\dot{\mathbf{q}} + \mathbf{K}\mathbf{q} = \mathbf{Q}(\mathbf{q}, t) \tag{3}$$

As far as the model typically involves rigid body modes it would be very convenient to filter out their contribution to solution in order to deal with elastic behavior only as often required in structural analysis. Such filtering is possible in the state space, e.g. [3], however, that approach blurry physical meaning.

The important implementation of the non-classically damped structures is a power propulsion system. These mechanisms typically consist of engines, couplings, reduction gears, shafts, and propelling gear. The most common propulsion model is lumped mass with simple discrete damping elements. When analyzed from vibration aspect, the propulsion systems besides elastic modes involve rigid body modes, too.

3. Theoretical Example

The simple theoretical example of such propulsion system can be seen in Figure 1.

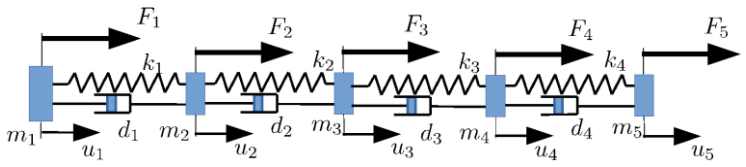

Figure 1. The simple theoretical example with non-classical damping and position firing forces

The system properties and initial conditions are given in Table 1 as well as the force dependence on position/displacement.

Table 1. Theoretical model properties

masses	damping	stiffness	force	initial conditions

$m_i = 2$ i=1,2,3,4	$d_i = 0.02$, i=1,2,4 $d_3 = 2$	$k_i = 10$ i=1,2,3,4	`Ft = zeros(N,1);`
			`if(X(1)>X1 && X(1)<X2)`
			`  Ft(1,1) =  F0;`
			`  Ft(N,1) = -F0;`
				`t0  = 0;`
				`q0  = zeros(Ndof,1);`
				`qt0 = 0.01*ones(Ndof,1);`

The result of calculation is presented in Figure 2.

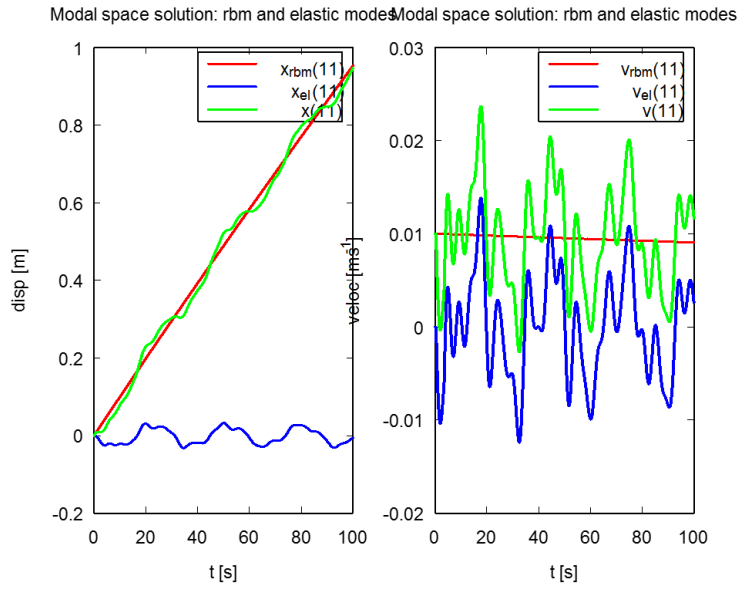

Figure 2. Result of numerical integration in modal space

It is obvious that filtering of rigid body modes dramatically improves insight in elastic behavior of a model, what can be of paramount importance in control of smart structures.

3. Conclusions

It is proved that nonclassically damped system loaded with the position dependent impact forces can be efficiently solved using modal superposition that involves nonlinear tightening iterations. The time step convergence depends on time step size, tolerance threshold and character of non-classical damping. In the illustrative example provided in this text, it is required at most two tightening iteration per time step.

References

[1] Bathe, k.J.: Finite element procedures. Prentice-Hall, NJ (1996)

[2] DNV-GL: Rules for classification - Ships, Part 6, Ch 6: Cold climate, 2020.

[3] Ma, F., Imam, A., Morzfeld, M.: The decoupling of damped linear systems in oscillatory free vibration. Journal of Sound and Vibration 324 (1--2), 408--428 (2009)

Experimental Investigation of Face-to-Core Bond Strength between Gypsum Fibreboard and PU Rigid Foam

Lazar Lukačević*, Paulina Krolo*, Antonio Bakran*

*Faculty of Civil Engineering University of Rijeka, Radmile Matejčić 3, 51000 Rijeka, Croatia
E-mails: {llukacevic,paulina.krolo,abakran}@gradri.uniri.hr

Keywords: sandwich structure, bond strength, tensile test, foam core, gypsum fibreboard

1. Introduction

The bond strength between the foam core and faces usually has two evaluation criteria: shear and tensile strength. Typical tests used to determine bond strength are tensile tests [1] and three or four-point bending tests [2,3]. It is known that debonding of the face and the core is the critical failure mode that can lead to catastrophic events, so careful investigation is recommended. The bond strength between rigid polyurethane (PU) foam core and gypsum fiberboard faces was experimentally investigated by conducting a tensile test according to ASTM C 297 standard [4]. The bonding of the sandwich panel components is performed without adhesive in such a way as to ensure the bonding of the face and the core during the expansion of the foam. The research aims to obtain the failure modes of the composite panel exposed to tensile load and determine the face-to-core bond strength.

2. Experimental research

In this study, four different sandwich composite panels were manufactured. The core material of sandwich composites was made of PU foam with two nominal densities of 40 and 45 kg/m^3, while the faces were made of fermacell® Gypsum fiberboards (Gp2) and fermacell® Firepanel fiberboard (Fp2) with the same thicknesses of 15 mm (Table 1). A total of 20 test specimens were cut, 5 specimens from each sandwich composite panel. The faces of the test specimens are bonded to steel T-blocks with Araldite 2012 two-component epoxy glue. The dimension and shapes of the specimens are shown in Figure 1a. Tensile tests of the composite specimens were performed on the universal tension-compression test machine Zwick/Roell Z600, using mechanical jaws with capacities up to 10 kN, and load cell capacity of 50 kN (Figure 1b). The test speed is equal to 1.5 mm/min.

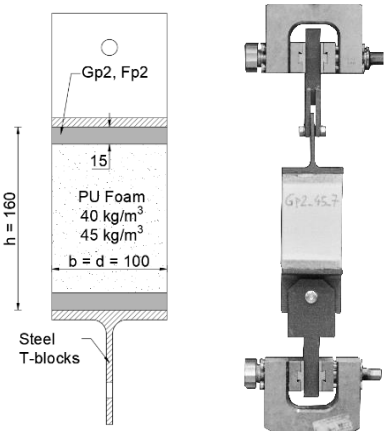

(a) (b)

Figure 1. (a) Test specimen geometry; (b) Test set-up for tensile test

Table 1. Specification of the sandwich composite specimens

Specimen	PU foam density [kg/m^3]	Type of fiberboard
Gp2-40-x (x=1to5)	40	Gp2 - fermacell® Gypsum fiberboards, 15 mm
Gp2-45-x (x=3to7)	45	
Fp2-40-x (x=1to5)	40	Fp2 - fermacell® Firepanel A1 fiberboards, 15 mm
Fp2-45-x (x=3to7)	45	
Test specimens are marked as Gp2-40-x/Fp2-40-x, where the first mark defines the type of fiberboard, the second mark defines the nominal density of PU foam, and the last mark defines the number of specimens.		

3. Results

The tension behaviour of the sandwich composite specimens is represented by force-displacement curves, which are shown in Figures 2a and 2b. The curves show the test results of 20 specimens with

two nominal densities and two types of fiberboards, while the greyscale represents the failure modes. Since the specimens were made without glue between the sandwich panel components, the adhesive failure modes according to ASTM C297 do not apply to these specimens. Therefore, failure at the contact between the face and core is defined with bond failure and mixed failure represent combinations of the main failure modes. The influence of foam densities on failure modes is visible from the results. The specimens with 40 kg/m^3 foam density generally have core and mixed failure modes, while specimens with 45 kg/m^3 foam density show all failure modes. The bond strength of the specimens with 40 kg/m^3 foam density was calculated based on the maximum force measured at the core and mixed failure modes. The average bond strength is equal to 0.146 MPa. Average bond strength for specimens with 45 kg/m^3 foam density foam was calculated as an average of strengths for bond failure mode and is equal to 0.183 MPa. The stiffnesses were calculated in the elastic range of force-displacement curves for all specimens. The stiffness values are in the range from 150 and 385 N/mm for 40 kg/m^3 density foam, while for 45 kg/m^3 density foam are in the range from 350 to 520 N/mm.

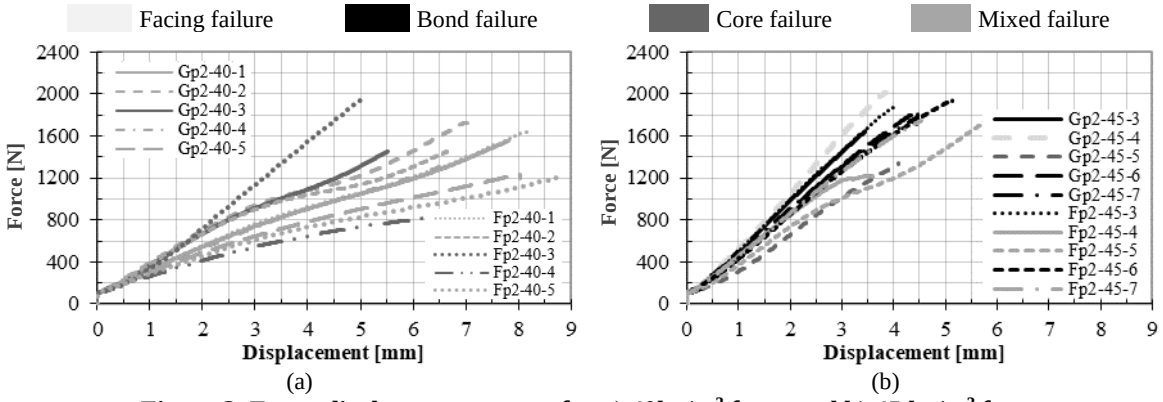

Figure 2. Force-displacement curves for a) 40kg/m^3 foam and b) 45 kg/m^3 foam

4. Conclusions

This study focused on determining the bond strength between two types of gypsum fibreboards and PU rigid foam with two nominal densities. Based on the conducted laboratory tests on sandwich specimens, the following conclusions are made: (i) To determine the correct type of the tensile bond failure mode, except for the data on the maximum tensile force, it is necessary to know the stiffness of the specimen; (ii) Due to lower stiffness and strengths of the 40 kg/m^3 density PU foam, face and bond failures have not occurred. It can be concluded that the bond strength is at least equal to or higher than the core strength; (iii) The 45 kg/m^3 density PU foam has greater stiffness and strengths but have all failure modes; (iv) The application of different types of fiberboards do not affect bond strength or failure mode and (v) In the production of composite sandwich panels, the expansion of foam is unpredictable and the density can vary within the core. It is recommended to consider a larger number of samples to obtain more reliable strengths and failure modes.

Acknowledgements

The research presented in this work was done within the scientific project ZIP-UNIRI-1500-2-20 and IRI 2 industrial project KK.01.2.1.02.0046.

References

[1] Yalkin, E.H., Icten, M.B., Tensile and compressive performances of foam core sandwich composites with various core modifications. Journal of Sandwich Structures and Materials, 2016

[2] Bragagnolo, G., Crocombe, A.D., Investigation of skin-core debonding in sandwich structures with foam cores. Materials and design, 108312, 2020

[3] Lukačević, L., Testing of Composite Panel on Bending to Determine Adhesive Properties of Panel Cover and Core. Master thesis, University of Rijeka, Faculty of Civil Engineering, 2021

[4] *ASTM C297/C297M-16;* Standard Test Method for Flatwise Tensile Strength Of Sandwich Constructions, ASTM International: West Conshohocken, PA, USA, 2016

Smart polygonal structures based on 2D tensegrity modules

Kamila Martyniuk-Sienkiewicz*, Wojciech Gilewski*

*Warsaw University of Technology, Faculty of Civil Engineering, Institute of Building Engineering, Al. Armii Ludowej 16, 00-637 Warsaw, Poland
E-mails: {kamila.martyniuk-sienkiewicz.dokt,wojciech.gilewski}@pw.edu.pl

Keywords: tensegrity, smart structures, polygonal structures

1. Introduction

Smart systems are a contemporary engineering general challenge. One of the possible applications are smart structures [1], which should be characterized, among others, by the possibility of active control of mechanical properties, including self-diagnosis and self-repair. This class also includes deployable structures. A specific structure that allows the creation of smart objects are tensegrities [2]. For the purpose of this study, we define tensegrities as a truss in which there is an infinitesimal mechanism stabilized by a system of self-equilibrated forces. 2D tensegrities [3] is a special class, in which modules based on hexa- and octagonal cells can be distinguished. The main objective of the paper is to describe different shapes that form plane truss polygonal structures [4] based on selected 2D tensegrity modules. The proposed modular tensegrity polygons allow to take full advantage of the smart features and describe the control of possible stiffening and weaknesses of the structure or diagnose potential failures. The additional aim of the paper is to discuss how polygon shapes are used and analyzed in the engineering area.

2. 2D tensegrity modules

2D trusses can be described mathematically in a purely algebraic way [5,6] or by the formalism of the finite element method [7]. In both formulations, formally exact stiffness and geometric stiffness matrices can be obtained. In the literature, tensegrity trusses are often identified as structures with an only self-equilibrated system of normal forces (eg. "X" truss). These myths were verified mathematically in [3]. For the purpose of this study, hexagonal and octagonal tensegrity modules were used, presented in Fig. 1. Hexagonal modules have one infinitesimal mechanism stabilized by one self-stress. Octagonal modules have two infinitesimal mechanisms stabilized by one self-stress.

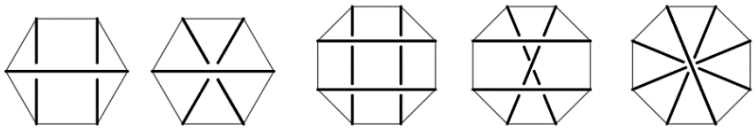

Figure 1. Selected 2D hexagonal and octagonal tensegrity modules

Figure 2. Possible geometries of hexagonal and octagonal tensegrity modules

The analysed structures do not have to be composed on geometrically regular modules and they do not lose their tensegrity features in terms of geometries presented in Fig. 2. This allows for a significant extension of the class of polygonal structures, from flat to slender structures. The features of the tensegrity modules were verified based on the algebraic formulation [5,6], using the *Mathematica* program. The modules can be used to build a wide class of polygonal structures.

3. Modeling of smart polygonal structures

Plane polygonal structures are commonly found as computational schemes in civil, aerospace and mechanical engineering [5]. A few selected structures are shown in Fig. 3.

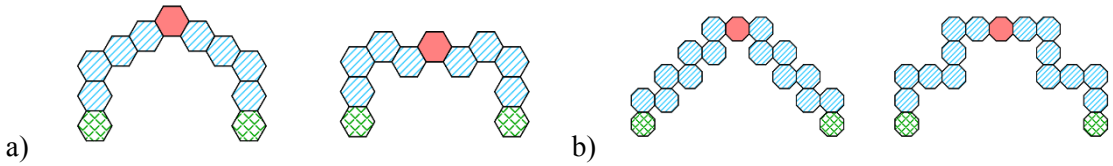

Figure 3. Selected regular polygonal structures: a) hexagonal, b) octagonal

In principle, each of the polygon modules may have different mechanical properties. Let us assume, however, that the material and geometric properties are the same (distinguishing between the tendon (c) and the strut (s) - $E_cA_c/E_sA_s=k$) where: E - Young's modulus, A - cross-sectional area). The control of stiffening or weakening the mechanical properties of the modules will be done internally by changing the sets of self-equilibrated normal forces. This practically means the need to install appropriate sensors/actuators in selected modules. It may apply to e.g. modules marked in red in Fig. 3, which will allow to model internal pin joints, or bottom modules, in order to model soft properties of supports. Global matrices of linear and geometric stiffness can be composed of the matrices of modules, using the formalism of the allocation similarly to the FEM. The exemplary results of modelling a pin joint in the middle of the structure are shown in Fig. 4. The coefficient α is a measure of weakening by reducing self-equilibrated normal forces of the central module.

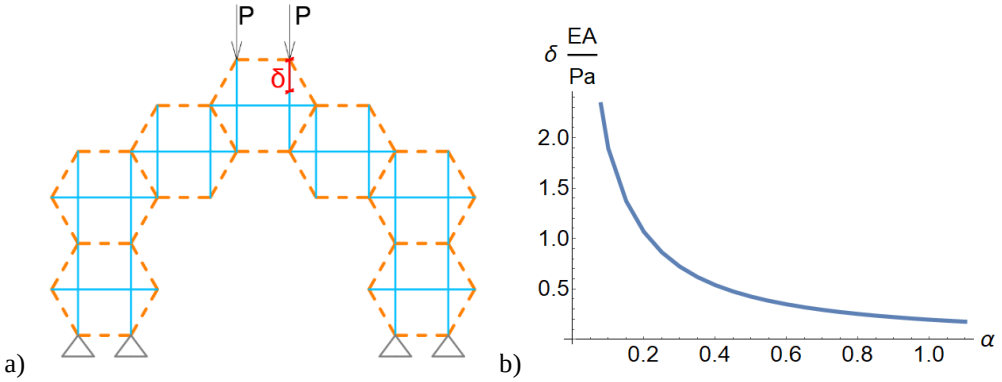

Figure 4. Hexa-polygonal structure: a) geometry, boundary conditions, b) modeling middle pin-joint

4. Conclusions

The paper discusses the possibility of creation smart truss polygonal tensegrity structures. It is presented that the mechanical properties of a structure can be changed by self-equilibrated normal forces in individual modules. The concept is promising in view of smartness of the structure.

References

[1] Gilewski, W., Al Sabouni, A., On possible applications of smart structures controlled by self-stress, *Archives of Civil and Mechanical Engineering*, 15, 469-478, 2015.

[2] Motro, R., *Tensegrity: structural systems for the future*. Kogan Page Science, London, 2003.

[3] Obara, P., Kłosowska, J., Gilewski, W., Truth and myths about 2D tensegrity trusses. *Applied Sciences*, 9, 179, 2019,.

[4] Usman, K.M., The new formulation for application of polygons in engineering design and practice. World Academy of Science, Wngineering and Technology, 70, 2010.

[5] Pełczyński, J., Gilewski, W., Algebraic formulation for moderately thick elastic frames, beams, trusses and grillages with Timoshenko theory. *Mathematical Problems in Engineering*, 7545473, 2019.

[6] Pełczyński, J., Gilewski, W., An extension of algebraic equations of elastic trusses with self-equilibrated systems of forces. European Congress on Computational Mechanics VI, Glasgow, UK, 2018.

[7] Bathe, K.J., *Finite element procedures in engineering analysis*. Prentice Hall, New York, USA, 1996.

Rocking of a rigid block on an elastic beam – a non-smooth contact dynamics approach

Teo Mudrić [*], Nina Čeh [*], Gordan Jelenić [*], Emina Smlatić [*], Stefan Hante [+], Martin Arnold [+],

[*]*Faculty of Civil Engineering, University of Rijeka*
E-mails: {teo.mudric2,nina.ceh,gordan.jelenic}@gradri.uniri.hr, esmlatic@student.uniri.hr

[+]*Institute of Mathematics, Martin Luther University, Halle-Wittenberg*
E-mails: {stefan.hante,martin.arnold,manuela.paschkowski}@mathematik.uni-halle.de

Keywords: non-smooth contact dynamics, rocking, contact, block, beam

1. Introduction

In this work the Moreau-Jean θ-scheme [1] is applied in the simulation of a problem involving a rigid block rocking on an elastic beam. Due to contact occurrence between the beam and the block such a system represents a non-smooth mechanical problem, namely, the velocity functions will exhibit jumps at impact instants which will result in non-smoothness of the position function. The applied numerical scheme falls within the category of the so-called event-capturing time integration schemes, in which the time step is kept constant during the simulation. Within each time step a check is performed to determine if a contact between the bodies has occurred. If the contact is detected, appropriate constraints on position or velocity functions are imposed in order to evaluate the impulse forces at the end of the time step. If there is no contact within a time step, the simulation proceeds to the next time step in an ordinary manner. Furthermore, several experiments have been performed on a shake table in which spedific data regarding the block motion subjected to given excitation have been measured.

2. Experimental set-up and problem description

A sketch of the experimental setup is shown in Figure 1 (a). The beam is fixed to a rigid base via one pinned and one sliding support. The block is freely placed on the beam and the two are interacting only through contact forces. The rigid base is subjected to a horizontal harmonic displacement that varies with time $x(t)$ and causes the beam and block to move. The problem is considered as two dimensional. In Figure 1 (b) the physical model of the addressed problem is photographed.

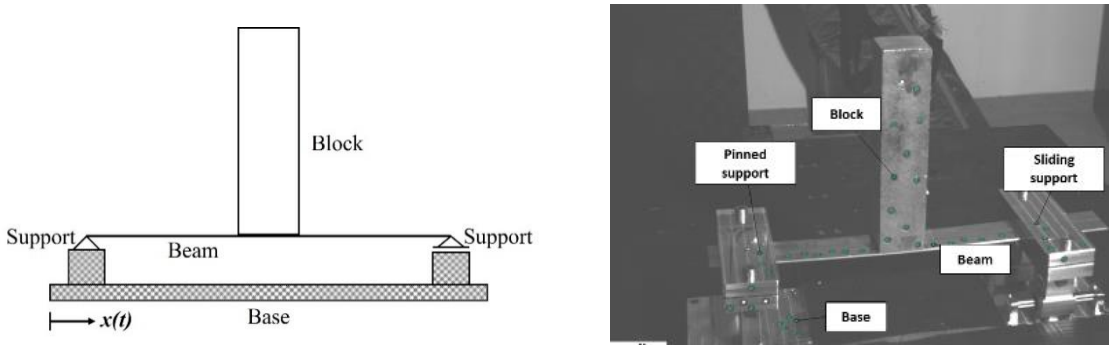

a) b)

Figure 1. Beam-block experiment sketch (a) and laboratory set-up (b)

The base of the supports is fixed to the Quanser STI-III biaxial seismic platform. The measurements are obtained by filming the model through the experiment using GOM Aramis 4M 3D optical measurement system of two high-speed cameras and post-processing software. The dots on the block in the photograph are markers tracked by the Aramis system.

3. Mathematical modelling

The beam is modelled using the finite element method, while the block is considered a rigid body, with the position of its center of gravity and its rotation as its degrees of freedom. Denoting as $\boldsymbol{q}$ the position vector, motion of the system is described by the following equation and conditions:

$$\dot{\boldsymbol{q}}(t) = \boldsymbol{v}(t) \tag{1}$$

$$\mathbf{M}\dot{\boldsymbol{q}}(t) = \boldsymbol{F}\big(t, \boldsymbol{q}(t), \dot{\boldsymbol{q}}(t)\big) + \boldsymbol{r} \tag{2}$$

with $\boldsymbol{q}(t_0)$ and $\boldsymbol{v}(t_0)$ as the initial position and velocity vectors. Here, $\mathbf{M}$ is the mass matrix of the system, $\boldsymbol{F}\big(t, \boldsymbol{q}(t), \dot{\boldsymbol{q}}(t)\big)$ is the vector of internal and external forces and $\boldsymbol{r}$ is the vector of contact forces, while the superimposed dot denotes the time differentiation. Furthermore, at each moment the following unilateral constraint, known as the Signorini velocity condition, must be satisfied:

$$U_n^+(t) \geq 0, \qquad R_n(t) \geq 0, \qquad U_n^+(t)R_n(t) = 0. \tag{3}$$

In (3) U_n^+ and R_n are respectively the normal relative velocity after contact and the normal contact force in some local reference frame at the contact point. Furthermore, sliding between bodies is also considered through the Coulomb friction model.

4. Results

A comparison of the preliminary simulation results with experimental measurements for the rotation angle of the block is given in Figure 2. A discrepancy in the block rotation amplitude can be observed, while the overall shape of the numerical curve seems to resemble the experimental one.

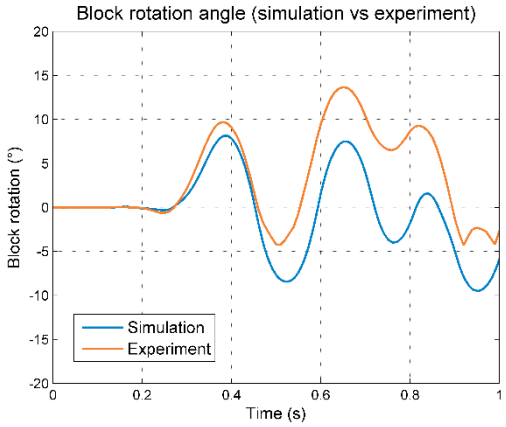

Figure 2. Comparison between numerical and experimental results for the block rotation angle

5. Conclusions

The amplitude of the block rotation angle obtained numerically differs from the experimentally measured values, therefore further investigation has to be devoted to the identification of the main causes for the observed discrepancy. To this end, four possible causes will be considered: eccentric initial position of the block in the experiment, value of the friction coefficient, value of the coefficient of restitution and damping of the beam model (which has not been implemented in the present model). The influence of the listed causes on the numerical results will be investigated and analyzed into more detail in future work.

References

[1] Jean, M., The non-smooth contact dynamics method. *Comput. Mehods Appl. Mech. Engrg.*, 177, 235-257, 199.

Influence of angular deviation of rollers on the performance and results of the cross roll straightening of bars

Tomáš Návrat, Bořek Ščerba, Jindřich Petruška

Brno University of Technology, Technicka 2, 616 69 Brno, Czech Republic
E-mails: {navrat, scerba, petruska}@fme.vutbr.cz

Keywords: bar straightening, residual stress, plastic deformation, optimization, FE analysis

1. Introduction

Optimal setting of parameters of straightening machines is still a complicated problem, as it is influenced by many input variables. It is the diameter of the straightened bar, its initial curvature and residual stress as the result of previous technological operations and its material parameters like yield stress and hardening. Some of them are even variable along the length of the bar. Different intermeshing of rollers is necessary to reach an optimal straightening performance in different situations. Still more complicated is the situation in the case of cross roll straightening, where the intermeshing is coupled with the angular deviation β between the axes of rollers and bar as in Fig.1

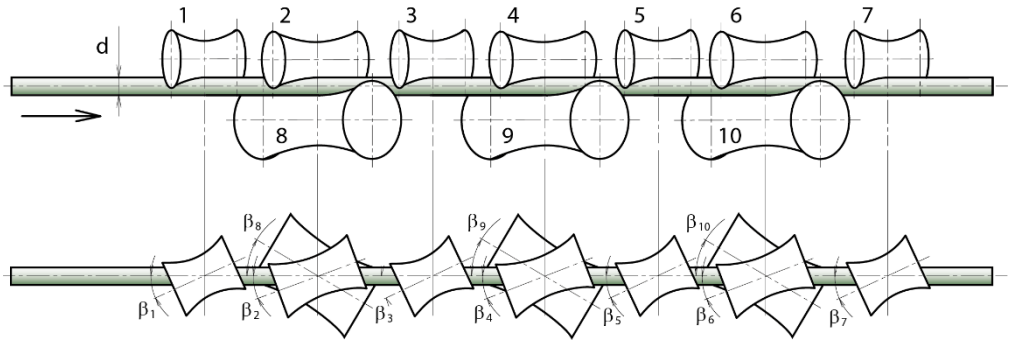

Figure 1. Ten rollers straightening machine

All operators and producers of the straightening machines use sophisticated strategy to keep the performance near the optimal point. It is often difficult due to conflicting intentions to minimize both final curvature with residual stress and rollers loading and wear. Many theoretical studies of the problems have already been published with various initial simplifications, starting from simple elastic-plastic theory of beam bending [1]-[3] up to full 3D FE analysis [4].

In [5] we published a fast FE algorithm based on the Eulerian flow of material through the straightening machine, using 1D beam elements. It proved to be an effective tool for setting the rollers intermeshing. In this contribution, we concentrate especially on the influence of the angular deviation of the rollers.

2. Analysis of the problem

The influence of angular deviation of rollers on final straightness of bar is less important than their intermeshing. Nevertheless, it has an impact on the contact area between the hyperbolic roller surface and bar, which affects the rollers wear and lifespan. It is illustrated in Fig.2. Our analysis was focused on the extremely loaded bending and supporting rollers no. 3, 5, 8, 9 and 10 on Fig.1. A 3D FE computational model of the straightening process was prepared, based on the parameters taken from analyses in [5], [6]. The only parameters subjected to change were the angular deviation

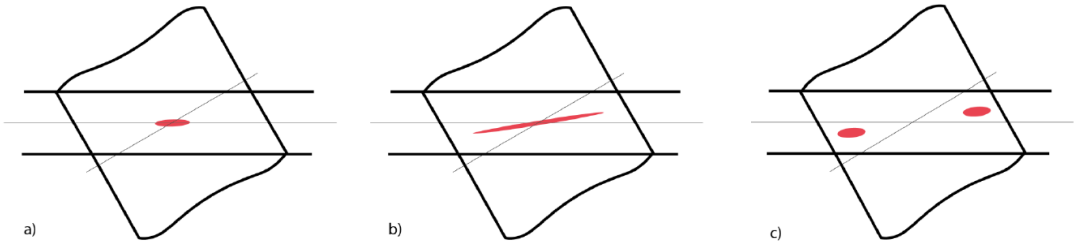

Figure 2. Contact area roller-bar with decreasing angle between roller and bar axes

between the rollers no. 3, 5, 8, 9, 10 and straightened bar. Their starting deviation 27.4° was individually changed by ±0.5° and ±0.75° in subsequent computational simulations, realized by explicit FE analyses of the straightening process in Abaqus. Results of final curvature, residual stress in bar, rollers loading and their contact areas were monitored and their sensitivity to angular deviations was evaluated. The sensitivity of each variable is first represented by a discrete set of FE results, which is subsequently expressed in the form of a continuous polynomial response surface, obtained from regression analysis. This representation makes possible the final multi-objective optimization, providing the best combination of angular deviations to reach the demanded level of residual stress and curvature together with low level of rollers loading and wear.

3. Conclusions

This contribution is an extension of the previous works of authors in the area of cross roll leveling theory and computations. The previous works dealt with the problem of fast and reliable optimal setting of the intermeshing rollers under different input parameters of the straightened bar and the leveling machine. Here we deal with the subtle problem of angular deviations between the rollers and straightened bar axis. Its importance is in the minimization of rollers loading, wear and subsequent prolongation of their service life. The algorithm is based on repeated computational experiments, simulating the straightening process, and final multi-objective optimization. Obtained results will be in detail presented at the conference.

References

[1] Tokunaga, H., On the Roller Straightener. *Bul. JSME 15*, 605-611, 1961.

[2] Das Talukder, N.K., Singh, A.N., Mechanics of Bar straightening, part 2: straightening in cross roll straighteners. *J. Manuf. Sci. Eng*. *113*, 228–232, 1991.

[3] Wu, B.J., Chan, L.C., Lee, T.C., Ao, L.W., Study on the precision modeling of the bars produced in two cross roll straightening. *J. Mater. Process. Technol. 99*, 202–206, 2000.

[4] Mutrux, A., Berisha, B., Hochholdinger, B., Hora. P., Numerical Modelling of Cross Roll Straightening. *In: LS-DYNA Anwenderforum*, Bamberg, 33–40, 2008.

[5] Petruška, J., Návrat, T., Šebek, F., Novel approach to computational simulation of cross roll straightening of bars. *Journal of Materials Processing Technology 233,* 53-67, 2016.

[6] Ščerba, B., Influence of setting and configuration of straightening machine on results of simulation of cross roll straightening (in Czech). *Master´s Thesis*, TU Brno, 2019.

Computational modelling of fatigue behaviour by using the inelastic energy approach

Branko Nečemer*, Zdenko Tonković+, Tomaž Vuherer*, Srečko Glodež*

* *University of Maribor, Faculty of Mechanical Engineering, Smetanova 17, 2000 Maribor, Slovenia*
E-mails: {branko.necemer,tomaz.vuherer, srecko.glodez}@um.si

+ *University of Zagreb, Faculty of Mechanical Engineering and Naval Architecture, Ulica Ivana Lučića 5, 10000 Zagreb, Croatia*
E-mail: zdenko.tonkovic@fsb.hr

Keywords: low cycle fatigue, energy approach, aluminium alloys, computational analysis, experimental testing

1. Introduction

In the presented study the experimental and computational investigation of fatigue crack growth behaviour of the ductile aluminium alloy AA 5083-H111 was investigated. The Compact Tensile (CT) specimen was selected for experimental testing and computational analysis. In the computational analysis, the material damage approach, based on the accumulated inelastic hysteresis strain energy density was used to analyse the fatigue behaviour of the analysed CT-specimen [1].

2. Numerical and experimental methods

In the computational model the nonlinear isotropic/kinematic material model developed by Lemaitre and Chaboche [2] was used. The constitutive material parameters of the analysed material were determined from the experimental data performed on the flat tensile specimen in a Low Cycle Fatigue (LCF) regime. More about the mechanical properties and microstructure of the analysed aluminium alloy AA 5083-H111 is presented in Ref. [3]. The proposed computational model is based on the inelastic energy approach, including the damage initiation and damage evolution criteria. In the proposed approach, the damage initiation period, N_0, can be mathematically expressed as [3]:

$$N_0 = c_1 \Delta w_{sta}{}^{c_2} \tag{1}$$

where Δw_{sta} is the inelastic strain energy density of the stabilised cycle, and c_1 and c_2 are the material parameters. Once the damage initiation phase is finished, the material stiffness decreases progressively in each loading cycle, based on the accumulated stabilised inelastic hysteresis strain energy. The obtained computational results at each discrete point are then used to predict the stiffness degradation and evolution of the material's properties, which are then considered in the following calculation step. In the proposed computational model, the damage evolution phase (damage rate $\Delta D/\Delta N$) is expressed mathematically as [3]:

$$\frac{\Delta D}{\Delta N} = \frac{c_3 \Delta w_{avg}{}^{c_4}}{L} \tag{2}$$

where ΔD is the range of the damage variable, which specifies the material stiffness degradation, ΔN is the number of loading cycles for damage evolution, Δw_{avg} is the average inelastic strain energy density, c_3 and c_4 are material constants, and L is the characteristic element length which is based on the element geometry and formulation. In the computational analyses, the direct cyclic algorithm implemented in the Abaqus software [4] is used as a solver. The direct cyclic algorithm is based on the continuum damage mechanics approach and provides a computationally effective modelling technique to obtain the stabilised response of the analysed geometry subjected to periodic cyclic loading. For the validation of the computational model the Fatigue Crack Growth (FCG) experimental

test was performed. The FCG test was carried out on the pulsating testing machine Smith weld 1405. The tests were performed at an ambient temperature (≈ 22 °C) in a load control regime, with the load ratio $R = 0.1$ and the constant loading frequency of 0.1 Hz. During the FCG test, the fatigue crack growth was monitored by a camera. From the obtained images, the crack growth diagram was generated, using the GOM Correlate software package. The crack growth diagram was then used for the subsequent validation of the proposed computational model. The comparison between the experimentally and computationally determined damage (crack) path in the analysed CT specimen is shown in Figure 1.

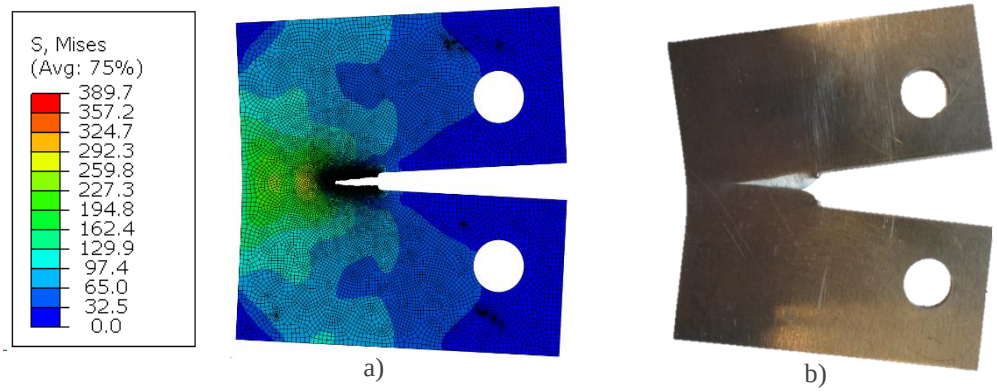

Figure 1. Damage (crack) path in the analysed CT specimen: a) Computational, b) Experimental

3. Conclusions

In the proposed research work, the fatigue behaviour of the ductile aluminium alloy 5083-H111 was analysed using an experimental and computational approaches. The proposed computational model was based on the inelastic energy approach including the damage initiation and damage evolution criteria and was used initially in some of the author's previous work. However, the damage evolution criterion was not validated. For that reason, an additional novel aspect was proposed in this study to validate the maximum damage variable D_{max}, which defines the stage of the accumulated damage where the finite elements lose their stiffness. In the computational model, four different values of the maximum damage variable $D_{\max}$ were taken into consideration. The computational results showed a significant influence of the maximum damage variable $D_{\max}$ on the damage propagation rate. To validate the computational model, a comparison between computational and experimental results has been made, where the diagrams were compared of damage (crack) length versus the number of loading cycles. The best fit was obtained in the case when the maximum damage variable was set to $D_{\max} = 0.22$. The comparison between the experimentally and computationally determined damage (crack) path in the analysed CT specimen showed a reasonable agreement. Based on these finding it can be concluded that the proposed computational model was validated and could be used for the further low cycle fatigue analyses of structural components made of the aluminium alloy AA 5083-H111.

References

[1] P. Čanžar, Z. Tonković, and J. Kodvanj, 'Microstructure influence on fatigue behaviour of nodular cast iron', *Mater. Sci. Eng. A*, vol. 556, pp. 88–99, 2012, doi: 10.1016/j.msea.2012.06.062.
[2] J. Lemaitre and J.-L. Chaboche, *Mechanics of Solid Materials*. Cambridge University Press, 1990.
[3] B. Nečemer, F. Zupanič, D. Gabriel, E. A. Tarquino, M. Šraml, and S. Glodež, 'Low cycle fatigue behaviour of ductile aluminium alloys using the inelastic energy approach', *Mater. Sci. Eng. A*, vol. 800, no. October 2020, 2021, doi: 10.1016/j.msea.2020.140385.
[4] Dassault Systèmes, 'Abaqus 6.14 Online Documentation'. Providence, Rhode Island, USA, 2014.

Fracture parameter identification with Bayesian framework and discrete embedded strong discontinuity model

Mijo Nikolić[1], Andjelka Stanić[2], Noemi Friedman[3], Hermann G. Matthies[4]

[1] *University of Split, Faculty of Civil Engineering, Architecture and Geodesy, Croatia, E-mail: mijo.nikolic@gradst.hr*

[2] *University of Twente, Faculty of Engineering Technology, The Netherlands*

[3] *Institute for Computer Science and Control (SZTAKI), Hungary*

[4] *Technische Universität Braunschweig, Institute of Scientific Computing, Germany*

Keywords: parameter identification, Bayesian framework, embedded strong discontinuity

1. Introduction

Identification of fracture parameters represents a challenging task since these parameters are strongly influenced with the microstructural defects and heterogeneities. Moreover, sophisticated fracture models cannot provide reliable responses with unreliable choice of parameters.
In this work, we present the identification of parameters by solving an inverse problem using Bayesian statistical inference [1].

2. Methodology

2.1. Fracture model

The fracture model is based on discrete lattice representation of the domain, where Timoshenko beams are used as cohesive links and Voronoi cells are used as grains of the material [2]. Embedded strong discontinuities [3,4] are positioned in the middle of beam elements where failure naturally occurs.

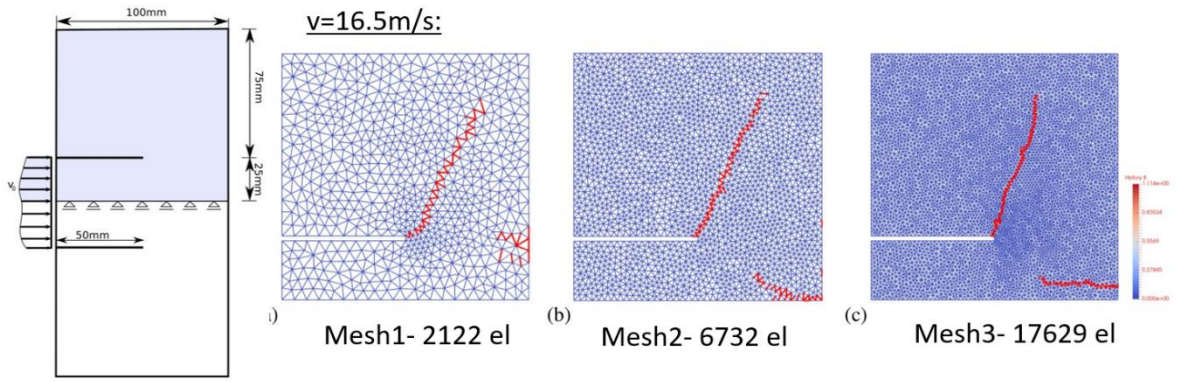

Figure 1. Kalthoff test simulation

Total failure is happening by progressive failure of adjacent beam elements, like shown in Kalthoff test example (Figure 1). In this test, the dynamic impact on the pre-notched plate is causing the initiation and propagation of the inclined crack from the tip of the notch.

The model has two failure modes, where mode I represents tensile crack opening, and mode II is for shear failure. Fracture parameters for the chosen model are maximal stress and fracture energy for both failure modes.

2.1. Stochastic parameter identification

We use the Bayesian inverse method to identify the unknown input parameters. In the case when parameters cannot be measured directly from the experimental test, or the testing procedure is unavailable, indirect measurements can be used for identification of such parameters. This is often the case with fracture energy, as unreliable and unavailable input parameter. The proposed methodology allows us to measure certain response of the sample or structure and by using Bayesian stochastics and the FEM model we can identify the desired parameters (Figure 2).

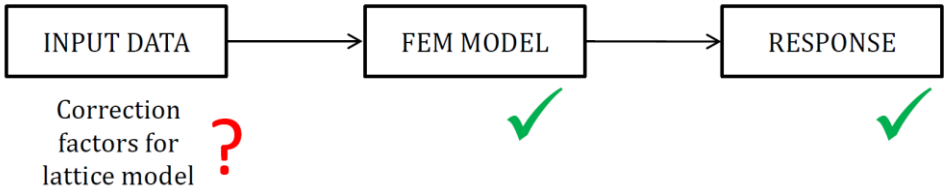

Figure 2. Identification procedure

The stochastic Markov Chain Monte Carlo method is employed for the identification of fracture parameters. Moreover, we use polynomial chaos expansion model for reducing the computational cost of Monte Carlo procedure.

3. Conclusions

Unavailable and unreliable parameters represent a difficulty in solving engineering problems where unreliable response due to lack of knowledge of parameters can be expected. In this work, we show the procedure for indirect identification of parameters which uses Bayesian stochastics, numerical model and measurements and can provide us with more reliable responses.

Acknowledgements
This work has been supported through the project 'Parameter estimation framework for fracture propagation problems under extreme mechanical loads' (UIP-2020-02-6693), funded by the Croatian Science Foundation.

References

[1] Matthies, H. G., Zander, E., Rosic, B. V., Litvinenko, A., Pajonk, O. Inverse Problems in a Bayesian Setting. In: Ibrahimbegovic A. (eds) *Computational Methods for Solids and Fluids. Computational Methods in Applied Sciences*, vol 41. Springer: 245-286 (2016)
[2] Nikolić, M., Karavelić, E., Ibrahimbegovic, A., Miščević, P., "Lattice element models and their peculiarities", *Archives of Computational Methods in Engineering*, 25, 753-784 (2018)
[3] Stanic, A., Brank, B., Ibrahimbegovic, A., Matthies, H. G., "Crack propagation simulation without crack tracking algorithm: Embedded discontinuity formulation with incompatible modes", *Computer Methods in Applied Mechanics and Engineering*, 386, 114090, (2021)
[4] Ibrahimbegovic, A., Nonlinear solid mechanics: theoretical formulations and finite element solution methods, *Springer Science & Business Media* (2009).

Fully coupled hydro-mechanical model for failure of unsaturated soils and desiccation cracking

Mijo Nikolić[1]

[1] *University of Split, Faculty of Civil Engineering, Architecture and Geodesy, Croatia,*
E-mail: mijo.nikolic@gradst.hr

Keywords: unsaturated soils, failure mechanisms, embedded discontinuity

1. Introduction

Fully coupled hydro-mechanical model for the failure analysis of unsaturated soils is presented [1]. The model can simulate tensile cracks and shear bands in soils subjected to matric suction effects. Such failure mechanisms are captured with discrete lattice model with embedded strong discontinuities [2,3]. Unsaturated fluid flow is governed with Richards equation and van Genuchten model.

2. Methodology

2.1. Fully coupled hydro-mechanical model

The failure model is based on discrete lattice representation of the domain, where Timoshenko beams are used as cohesive links and Voronoi cells are used as grains of the material [2]. Embedded strong discontinuities are positioned in the middle of modified beam elements where failure naturally occurs (Figure 1.a.).

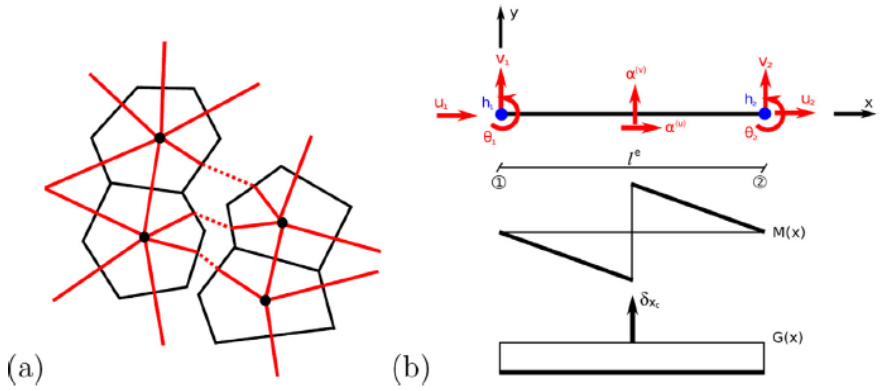

Figure 1. (a) crack growth is modelled as progressive failure of neighbouring cohesive links (b) Timoshenko beam element with mechanical degrees of freedom and fluid flow degree of freedom.

The proposed coupled model uses the same lattice domain discretization for mechanical part and for the fluid part. Additional pore pressure degree of freedom is added along with mechanical ones (Figure 1.b.). Matric suction effects are considered in this model through the van Genuchten model which relates saturation state and suction. The coupled processes between the mechanical strain and fluid flow are considered through the generalized Biot porous media theory. Bishop effective stress concept is used for stress computation. The model can simulate two failure modes, where mode I represents tensile crack opening, and mode II is for shear failure.

2.1. Shear band and desiccation cracking example

The dilatant shear band example is given in Figure 2. Namely, mechanical load in terms of imposed displacement is applied on the top boundary of the unsaturated sand specimen.

The shear band propagated through the sample, modified the pore pressure field and saturation state. Fluid flux is increased in the failure zone.

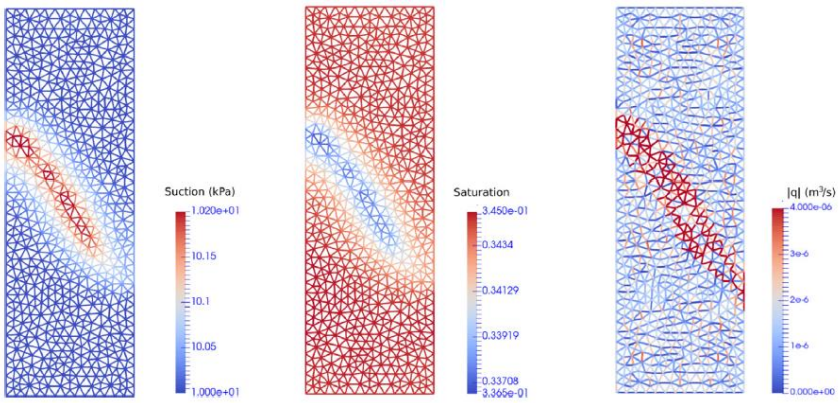

Figure 2. Shear band example, unsaturated sand specimen

The desiccation cracking of clay specimen is considered in Figure 3. Namely, the drying flux is imposed on the top boundary, causing the tensile cracks which propagate from the top of the specimen towards its interior.

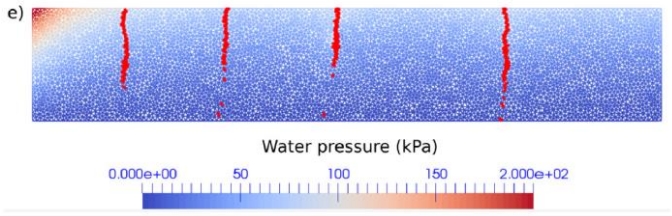

Figure 3. Desiccation cracking of clay specimen

3. Conclusions

The presented fully coupled hydro-mechanical model can simulate tensile cracks and shear bands in unsaturated soils.

Acknowledgements

This work has been supported through the project 'Experimental and numerical investigations of mechanisms in unsaturated geomaterials' (UIP-2017-05-3429), funded by the Croatian Science Foundation.

References

[1] Nikolić, M. "Discrete element model for failure analysis of partially saturated porous media with propagating cracks represented with embedded strong discontinuities", *Computer Methods in Applied Mechanics and Engineering*, 390, 114482 (2022)

[2] Nikolić, M., Karavelić, E., Ibrahimbegovic, A., Miščević, P., "Lattice element models and their peculiarities", *Archives of Computational Methods in Engineering*, 25, 753-784 (2018)

[3] M. Nikolic, A. Ibrahimbegovic, P. Miscevic, "Discrete element model for the analysis of fluid-saturated fractured poro-plastic medium based on sharp crack representation with embedded strong discontinuities", *Computer Methods in Applied Mechanics and Engineering*, 298, 407–427 (2016).

70 years old concrete bridge - is it still safe for the today´s heavy traffic?

Drahomír Novák * and Radomír Pukl +

*Brno University of Technology, Faculty of Civil Engineering, Institute of Structural Mechanics, Veveří 95, 60200 Brno, Czech Republic
E-mail: novak.d@fce.vutbr.cz

+Červenka Consulting s.r.o., Na Hřebenkách 55, 150 00 Praha 5, Czech Republic
E-mail: radomir.pukl@cervenka.cz

Keywords: bridge assessment, nonlinear simulation, degradation, reliability, structural safety

1. Introduction

Numerous failures of bridges are recently registered - Troja footbridge in Prague, Czech Republic, 2017, Ponte Morandi motorway bridge collapse in Genoa, Italy, 2018, and many others *(https://en.wikipedia.org/wiki/List_of_bridge_failures).* Many countries worldwide are currently experiencing a problem of aging and deterioration of reinforced concrete bridges and their remaining reliability for the actual traffic - the question of structural safety is becoming more and more important. Several current standards advocate probabilistic approaches, utilization of mathematical models and design of structures for durability, i.e. time-dependent limit state approach (LS) with service life consideration: ISO 13823 and the fib-Model Code. In such advanced reliability assessment, material nonlinearities, material deterioration, traffic load as well as several types of uncertainties are considered.

2. Methodology for advanced complex assessment of the service life safety of bridges

In this respect it is an important task to develop relevant advanced assessment method, evaluation procedures and service life prognoses for concrete structures. This contribution describes keystones of a complex methodology for statistical, reliability and risk analyses of concrete structures including advanced nonlinear finite element analysis, uncertainties simulation and degradation modeling. It presents virtual simulation used on the way from assessment of experimental results to reliability analysis of a bridge structure, based on randomization of nonlinear fracture mechanics finite element analysis.

Local material damages causing nonlinear response of the structure to the acting load are modeled by means of the nonlinear finite element software ATENA [1, 2] developed by Červenka Consulting s.r.o. This software includes elite material models for the basic materials - concrete and reinforcing steel. It is able to reflect in a realistic way material damage such as concrete tensile cracks, compressive crushing, reinforcement yielding and reinforcement debonding. The material properties and parameters of the nonlinear models are reduced in time due to material aging and consequent degradation. Selected basic degradation models are embedded directly in the ATENA software. Common feature of all these models (both nonlinear and degradation) is that the input data are random and often very uncertain.

For the global structural modeling advanced computational models are needed, where aspects of nonlinear behavior of concrete and reliability modeling are combined. The problem involves uncertainties in material, geometry, loading and degradation phenomena and therefore the concept of reliability theory has to be applied. The combination of structural analysis and reliability assessment has been developed and is presented together as the SARA software [3, 4] – a software shell which controls the communication and automatized data exchange between two individual programs: ATENA – FEM nonlinear analysis of concrete structures, and FReET [5, 6] – the probabilistic engine based on stratified Monte Carlo type Latin Hypercube Sampling. In contradiction to the deterministic nonlinear analysis, which result to a single limit load value, the stochastic nonlinear simulation has an additional effect. Beside the possibility for randomization of input parameters in order to reflect

their randomness and uncertainty, the result of the stochastic nonlinear analysis provides probability of structural failure, and consequently, in combination with the prescribed loading (in deterministic or probabilistic way) the structural safety index. Considering material degradation and realistic prediction of growing traffic load it can offer development of the structural safety over time.

For the advanced modeling of material deterioration there is also another software implementation where all relatively well-known degradation models are summarized within the framework of unified software environment called FReET-D [6]: a combination of analytical models and stochastic simulation techniques has been amalgamated to form of specialized software for assessing the potential degradation of newly designed as well as existing concrete structures. Models implemented for carbonation, chloride ingress, corrosion of reinforcement and others may serve directly in the durability assessment of concrete structures.

There are already several practical applications of the tools described above during last decades worldwide. Let us mention only two selected publications with examples solved by the software developer´s team: analysis of Kristienberg bridge, Stockholm - statistical analysis of crack width [7], and an advanced stochastic analysis of 10 existing reinforced and prestressed concrete bridges in the Austria-Czech Republic region (within the international Interreg project) [8].

3. Conclusions

The advanced methods for nonlinear, reliability and degradation analyses are integrated in a software package for reliability assessment of concrete structures, which allows to predict structural safety under the actual or expected traffic load. The tools have been already used in several practical applications, and they are continuously improved by implementation of new state of art methods (in particular within the research project mentioned below).

Acknowledgement

This research was funded by Czech Science Foundation under project No. 22-00774S MAPAB (Metamodel-assisted probabilistic assessment in bridge structural engineering).

References

[1] Červenka, V., Červenka, J., Pukl, R., ATENA – A tool for engineering analysis of fracture in concrete, *Sadhana* 27(4), 485-492, 2002.

[2] Červenka, V., Jendele, L., Červenka, J., *ATENA Program Documentation – Part 1: Theory*. Červenka Consultin s.r.o., Prague, Czech Republic, 2022.

[3] Bergmeister, K., Novák, D., Pukl, R., An advanced tool for reliability assessment of concrete structures. In: Zingoni, ed., *Progress in Structural Engineering, Mechanics and Computation*, Proc. of 2nd int. conf., Cape Town, South Africa, Taylor & Francis Group, 899-904, 2004.

[4] Strauss, A., Novák, D., Lehký, D., Vořechovský, M., Teplý, B., Pukl, R., Červenka, V., Eichinger-Vill, E. M., Santa, U., Safety analysis and reliability assessment of engineering structures – The success story of SARA. *ce/papers*, 3(2), 38–47, 2019.

[5] Novák, D., Vořechovský, M., Rusina, R., *FReET v.1.5 – program documentation*. *User´s and Theory Guides*. Červenka Consulting s.r.o., Brno, Czech Republic, http://www.freet.cz, 2015.

[6] Novák, D., Vořechovský, M., Teplý, B., FReET: Software for the statistical and reliability analysis of engineering problems and FReET-D: Degradation module. *Advances in Engineering Software*, Vol. 72, 179-192, 2014.

[7] Pukl, R., Sajdlová, T., Řoutil, L., Novák, D., Šeda, P., Case study - Nonlinear reliability analysis of a concrete bridge. In: *Maintenance, Monitoring, Safety, Risk and Resilience of Bridges and Bridge Networks*, Foz do Iguaçu, Taylor & Francis Group, 2503-2507, 2016.

[8] Apostolidi, E., Šomodíková, M., Strauss, A., Pukl, R., Lehký, D., Novák, D., The Interreg „ATCZ190 Safebridge“ project… In: *The 10th International Conference on Bridges in Danube Basin (Danube Bridges 2019)*, Vienna, Austria, 228–231, 2019.

Piezoelectric beam element with embedded discontinuity

Matija Novak[1], Eduard Marenić[3], Tomislav Jarak[1,2], Mijo Nikolić[4]

[1] *Faculty of Mechanical Engineering and Naval Architecture, University of Zagreb*
Ivana Lučića 5, 10 002 Zagreb, Croatia
E-mails: {matija.novak,tomislav.jarak}@fsb.hr

[2] *ITAP, School of Industrial Engineering, EII. Paseo del Cauce 59 Valladolid*
E-mail: tomislav.jarak@uva.es

[3] *Institut Clément Ader, CNRS UMR 5312, Université Fédérale Toulouse Midi-Pyrénées, INSA/UPS/Mines Albi/ISAE, France*
E-mail: marenic@insa-toulouse.fr

[4] *Faculty of Civil Engineering, Architecture and Geodesy, University of Split*
Matice hrvatske 15, 21 000 Split, Croatia
E-mails: mnikolic@gradst.hr

Keywords: piezoelectric materials, beam finite element, embedded discontinuity, polarization

1. Introduction

In modern times, many devices can be called "smart". They are equipped with sensors and actuators so they can sense external stimuli and react to them in a predetermined way. Because of their ability to transform mechanical energy into electrical and vice versa, piezoelectric materials are often used as active parts of "smart" devices.

Most of the piezoelectric materials are quasi-brittle and subjected to mechanical and electrical loading, which can lead to mechanical damage or dielectric breakdown. If mechanical damage or dielectric breakdown occurs in an active part of a "smart" device, it can lead to the malfunction of the entire device. A reliable numerical model for predicting the damage behavior of piezoelectric materials can facilitate the prediction and extension of the service periods and the work life of "smart" devices.

One type of numerical models for the description of damage in brittle materials are lattice models [1], where continuum is represented by solid particles interacting by cohesive forces, represented in the model by one-dimensional finite elements. The softening of the lattice elements will cause the damage propagation through the material. This can be described objectively by introducing the displacement discontinuity at the integration points of the elements. In this work a piezoelectric beam finite element with embedded discontinuity is presented, which could be suitable for the use in lattice models for the description of damage in piezoelectric materials.

2. Piezoelectric beam finite element

A piezoelectric beam finite element, based on the Timoshenko theory, is a one-dimensional finite element with two nodes and four degrees of freedom in each node, two translational, one rotational and electric potential, as shown in Fig. 1. The polarization of a material can in general be in an arbitrary direction with respect to the element axial direction. Motivated by [2], the displacement and electrical discontinuities are added at the Gauss point of the element, enabling the description of the crack propagation in the material. Consequently, the displacement and potential fields contain regular and singular parts, where the singular parts are products of the Heaviside function and the displacement and potential jumps, respectively, as written in equation (1):

$$\mathbf{d}(x)=\begin{bmatrix}\bar{u}(x)\\ \bar{v}(x)\\ \bar{\vartheta}(x)\\ \bar{\varphi}(x)\end{bmatrix}+\begin{bmatrix}\alpha_u\\ \alpha_v\\ 0\\ \alpha_\varphi\end{bmatrix}H_{x_C}, \tag{1}$$

where $\bar{u}(x),\bar{v}(x),\bar{\vartheta}(x)$ and $\bar{\varphi}(x)$ are the regular parts of the displacement and electric potential fields, α_u,α_v and α_φ are the displacement and electric potential jumps and H_{x_C} is the Heaviside function defined by $H_{x_C}(x)=0$ for $x\le x_C$ and $H_{x_C}(x)=1$ for $x>x_C$, where x_C is the Gauss point of the element. From equation (1) it can be seen that the jumps occur in the longitudinal and transversal displacements as well as in the electric potential, while the rotation remains continuous along the element.

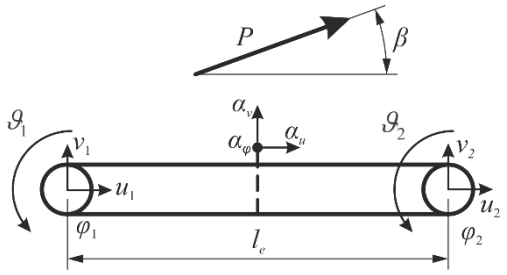

Figure 1. Piezoelectric beam element

The discontinuity in the longitudinal displacement field represents the mode I or tensile failure mode, while the discontinuity in the transversal displacement field represents the mode II or shear failure mode [1]. The discontinuity in electric potential field reflects the altered distribution of electrical fields due to the mechanical particles separation and is used to describe the electrical permittivity reduction in the material [2]. In our model, this electrical discontinuity is always triggered by the mechanical damage and can occur only at the places where the displacement jump arises due to mechanical damage.

Material behavior is linear elastic until the stress reaches a critical value and then the discontinuities are activated. After satisfying the damage criterion, the material softening begins, described here by employing the exponential softening laws for both the longitudinal and transversal directions [1], as well as for the axial electrical displacements. The constitutive model is analogous to those in classical elastoplasticity, where the total strain contains the elastic component and a contribution from the singular part related to the crack opening. Again analogous to elastoplasticity solution procedures, at the local level, a standard return mapping algorithm is used, where internal variables related to the discontinuity are computed. With the internal variables computed locally, the global step of the solution procedure for the forces equilibrium is then performed, where the final stiffness matrix is formed through the static condensation of the local variables.

References

[1] Nikolić, M., Karavelić, E., Ibrahimbegovic, A., Miščević, P., Lattice Element Models and Their Peculiarities. *Archives of Computational Methods in Engineering*, 25, 753-784, 2018.

[2] Linder, C., Rosato, D., Miehe, C., New finite elements with embedded strong discontinuities for the modeling of failure in electromechanical coupled solids. *Computer Methods in Applied Mechanics and Engineering*, 200, 141-161, 2011.

Short thin-walled columns of open section subjected to partially distributed axial loads

Radoslav Pavazza*, Frane Vlak*, Marko Vukasović*, Branka Bužančić Primorac*

*University of Split, FESB, Rudjera Boskovica 32, Split, Croatia
E-mails: {rpavazza,fvlak,mvukasov,branka}@fesb.hr

Keywords: columns, thin-walled, shear deformations, distributed loads

1. Introduction

An analytic solution for thin-walled columns of open section subjected to eccentric partially distributed loads is considered. Neglecting shear deformations (Vlasov theory) leads to inaccurate results for short thin-walled beams. The stresses and displacements for short and particularly extremely short thin-walled beams can be successfully analyzed by the theory of bending and torsion with influence of shear.

2. Partially distributed column loads

The stresses and displacements of short steel (E = 210 GPa, ν = 0.3) thin-walled columns with bisymmetrical cross-sections with wide flanges ($b = h$ = 600 mm, $t_0 = t_1$ = 20 mm, l = 1800 mm), shown in Fig. 1, are examined by Vlasov analytical method [1], finite element method (FEM) and the theory of bending with influence of shear (TBTS) [1, 2, 5] and the theory of torsion with influence of shear (TTTS)[3-5]. For short thin-walled beams, the St.Venant torsion component can be neglected with respect to warping component of torsion that leads to the analogy between bending and torsion [4].

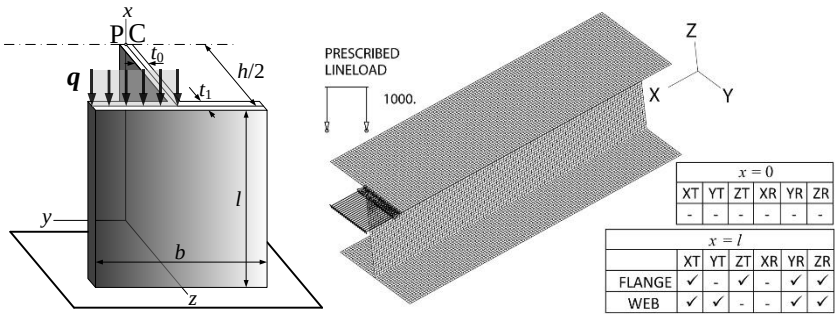

x = 0						
XT	YT	ZT	XR	YR	ZR
-	-	-	-	-	-

x = l						
	XT	YT	ZT	XR	YR	ZR
FLANGE	✓	-	✓	-	✓	✓
WEB	✓	✓	-	-	✓	✓

Figure 1. Column loading, half of cross-section (left); FEM model (right)

The thin-walled beam loaded by line loads, q = 1000 N/mm, acting along a part of the cross-section middle line (Fig. 1), will be subjected to compression, bending and torsion [6, 7]. The analytical solutions are obtained by using the method of initial parameters [5-7], where the internal force components for the beam end ($x = l$) are $N(l) = -qb/2$, $M_y(l) = -qbh/4$, $M_z(l) = qb^2/8$ and $B(l) = qb^2h/16$. For the clamped end ($x = 0$) and the simply supported end ($x = l$) the non-zero initial parameters are

$$Q_{z0,y0} = \frac{3M_{y,z}(l)}{2l(1+3k_a^{w,v})}, \quad M_{y0,z0} = -\frac{3(1-6k_a^{w,v})M_{y,z}(l)}{2l(1+3k_a^{w,v})}$$
$$M_{\omega 0} = \frac{3B(l)}{2l(1+3k_a^{\alpha})}, \quad B_0 = -\frac{3(1-6k_a^{\alpha})B(l)}{2l(1+3k_a^{\alpha})}, \quad N_0 = N(l) \tag{1}$$

where shear coefficients

$$k_a^w = \frac{\kappa_z EI_y}{GAl^2}, \quad k_a^v = \frac{\kappa_y EI_z}{GAl^2}, \quad k_a^\alpha = \frac{\kappa_\omega EI_\omega}{GI_p l^2}, \quad . \tag{2}$$

are defined in [6, 7]. The stress distribution along the cross section contour at $x = l/6$ is shown in Fig. 2 (left). The well agreement between FEM and TBTS and TTTS solutions is obtained. Due to the different definition of the clamped end by the analytical methods and FEM, certain noticeable discrepancies occur at $x = 0$ and are decreasing while approaching to $x = l$.

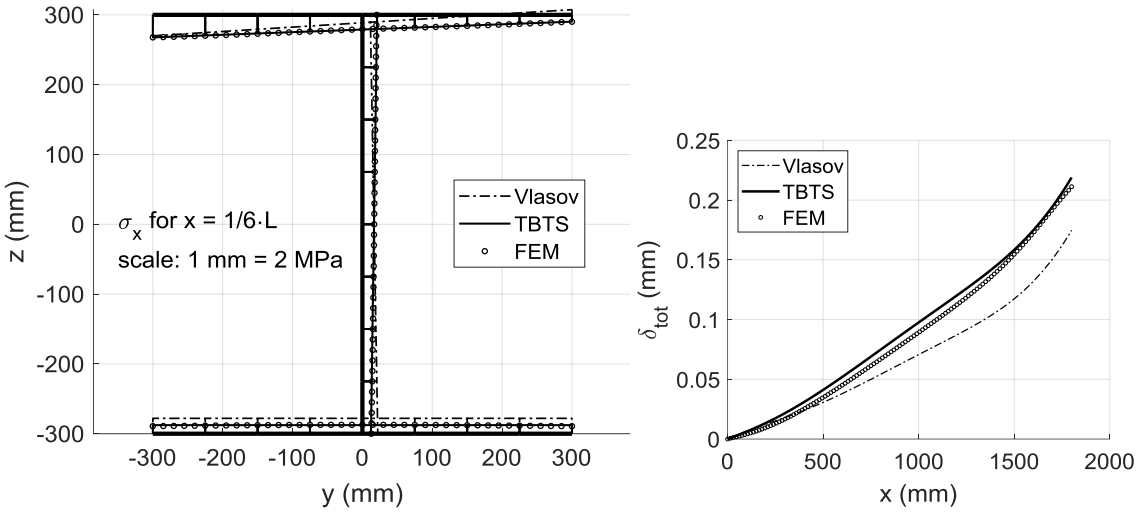

Figure 2. Stress distribution at $x = l/6$ (left); Displacement distribution along beam length (right)

Displacement magnitude distributions δ_{tot}, as square root of the sum of the squares of the displacement components, along the beam length for $y = b/2$ and $z = h/2$ are presented in Fig. 2 (right).

3. Conclusions

The comparison of the Vlasov analytical solution with FEA proves that analysis of the short thin-walled columns subjected to tip loads partially distributed along the column flanges must take into account shear deformations. For that reason, the solution obtained by using the theory of bending and torsion with influence of shear is given, which shows a well agreement with FEA. The presented approach provides the simple expressions in closed analytical form both for the normal stresses and displacements.

References

[1] Vlasov, V. Z., *Thin-walled elastic beams*. Israel Program for Scientific Translation Ltd., Jerusalem, 1961.

[2] Pavazza, R., Matoković, A., Bending of thin-walled beams of open section with influence of shear, part I: Theory. *Thin-walled Structures*, 116, 357-368, 2017.

[3] Pavazza, R., Matoković, A., Vukasović, M., A theory of torsion of thin-walled beams of arbitrary open sections with influence of shear. *Mechanics Based Design of Structures and Machines*, 0, 1-36, 2020.

[4] Pavazza, R., Torsion of thin-walled beams of open cross-section with influence of shear. *International Journal of Mechanical Sciences*, 47, 1009-1122, 2005.

[5] Pavazza, R., *Introduction to the analysis of thin-walled beams (in Croatian)*. Kigen d.o.o., Zagreb, 2007.

[6] Pavazza, R., Vlak, F., Vukasović, M., Short Steel Thin-walled Columns Subjected to Eccentric Axial Loads. *Procedia Engineering*, 161, 349–355, 2016.

[7] Pavazza, R., Vlak, F., Vukasović, M., Kustura, D., Stresses and Displacements of Short Orthotropic Thin-walled Columns under Eccentric Axial Force. In: P. Marović, L. Krstulović-Opara, M. Galić, eds., *Proceedings of the 9th International Congress of CSM*, 9. Redak d.o.o., Split, 2018.

Bootstrap technique for Coulomb friction estimation

Stipe Perišić*, Jani Barle*, Predrag Đukić+

*FESB, University of Split, R. Boškovića 32, 21000 Split, Croatia
E-mails: {sperisic,jbarle}@fesb.hr

+ Department of Professional Studies, University of Split, Kopilica 5, 21000 Split, Croatia
E-mail: pdukic@oss.unist.hr

Keywords: Bootstrap, Coulomb friction, signal processing

1. Introduction

The bootstrap (BT) is a technique that resamples a small dataset to estimate statistical value of interest [1]. In this paper, the BT is used to estimate the Coulomb friction force from the free decay response. Since noise and interference always exist in real data, the BT is used to capture the uncertainty of the estimated value by calculating confidence intervals. The proposed procedure is tested numerically and experimentally on testbed. As shown, it is possible to efficiently estimate the friction force on real data set.

2. Numerical example

To verify the presented procedure, numerical example is analysed first since the exact parameters are known. The model is nonlinear with Coulomb dry friction, Eq.(1), [2].

$$m\ddot{x} + r\ sign(\dot{x})\ + kx = f(t) \tag{1}$$

In Eq.(1), m is the mass, k is the spring stiffness and r is Coulomb friction force. Although an analytical solution for the initial condition of Eq.(1) can be found in [3], the Simulink model is used here, Figure (1), due to robustness regarding input force. The model parameters are set to m= 2 kg, k = 1000 N/m, and r = 0.12 N. To simulate realistic conditions, the noise is added to the response (μ=0, σ=0.2·10^{-4}).

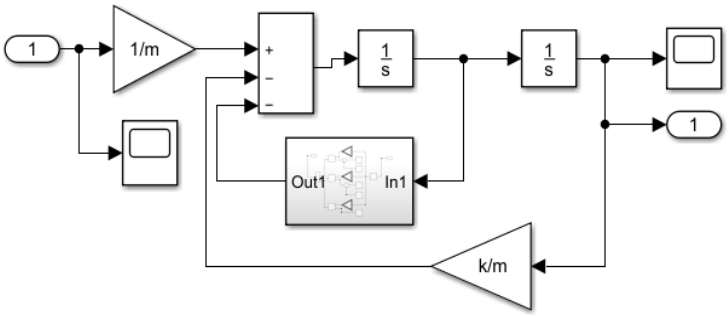

Fig. 1. Simulink SDOF model with Coulomb friction

To calculate friction force by BT, the amplitudes i.e. slope of amplitudes are used. Eq. 2, relates the slope y, friction force r, natural frequency ω and stiffens k [4]. Since BT is resampling technique, the result is in form of histogram.

$$y=2r\omega/\pi k \tag{2}$$

Figure 2. (left) represents friction estimation. The mean value is the average slope which is then related to friction force via Eq.(2). In this example, the estimated value is r=0.1209 N while the exact value is r=0.12 N.

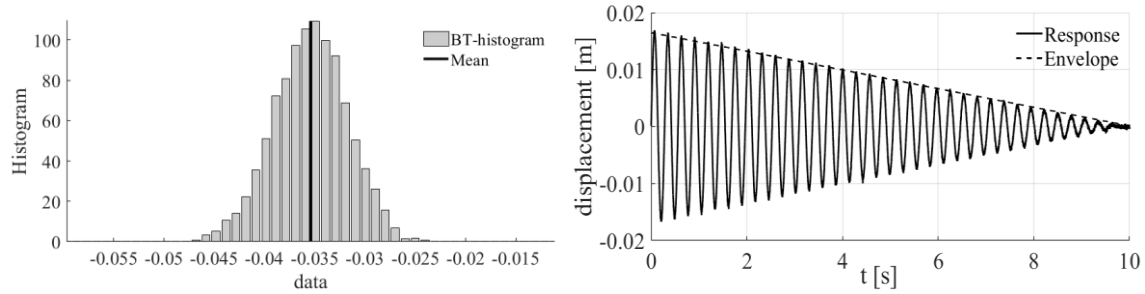

Fig. 2. Friction force estimation via BT (left) and analysed response (right) on numerical example

According to the estimation and fitted envelope shown in figure 2 (right), BT can be efficiently used for friction estimation.

3. Experimental analysis

The proposed friction estimation procedure is tested experimentally on an air-bearing testbed where all parameters are easily controlled. More information on the testbed can be found in [5]. To determine the reference friction value the binocular load cell was used. Here two catachrestical cases were analysed, the first one with a lower (r=0.1834 N) and the second with a higher friction value (r=0.2933 N).

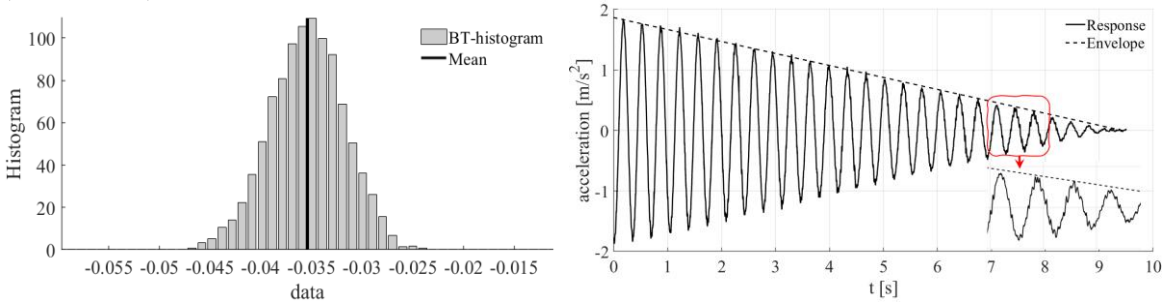

Fig. 3. Friction force estimation for the first case and recorded response

Figure 3. (left) represents friction estimation for the first case and the estimated value is r=0.1846 N. Graphical representation for the second case is left out due to briefness, but estimation is, r=0.2899 N. Comparing estimated values with the reference ones it is evident that the estimation is more than satisfactory.

4. Conclusions

Considering the above results, both numerical and experimental, it is more than clear that BT can be used for friction estimation. Besides friction estimation, the BT can be used in the same manner to calculate confidence intervals and thus capture uncertainty. Since it is relatively simple yet efficient it is applicable to technical diagnostic.

References

[1] Zoubir AM, Boashash B. The bootstrap and its application in signal processing. IEEE Signal Process Mag 1998;15:56–76.

[2] Hoffmann R, Liebich R. Experimental and numerical analysis of the dynamic behaviour of a foil bearing structure affected by metal shims. Tribol Int 2017;115:378–88.

[3] Marino L, Cicirello A. Experimental investigation of a single-degree-of-freedom system with Coulomb friction. Nonlinear Dyn 2020;99:1781–99.

[4] Perišić S, Barle J, Đukić P, Wolf H. A Bayesian Conjugate Model for the Estimation of Friction Intensity. Trans FAMENA 2021;45.

[5] Perišić S. Okvir za praćenje i prihvaćanje dijagnostičkih signala mehaničkog sustava pomoću Bayesove analize. Split, 2021.

Novel numerical approach for modelling of subsurface pitting phenomena by phase–field method

Tomislav Polančec*, Tomislav Lesičar+, Zdenko Tonković*

*Faculty of Mechanical Engineering and Naval Architecture, Ivana Lučića 5, 10000 Zagreb
E-mails: tomislav.polancec@fsb.hr , tomislav.lesicar@fsb.hr, kresimir.vuckovic@fsb.hr, zdenko.tonkovic@fsb.hr

Keywords: gears, pitting, EHL, phase–field

1. Introduction

Commonly used power transmission machine elements are gears. Gears in operation are subjected to rolling-sliding contact fatigue under elastohydrodynamic lubrication (EHL) [1]. Common gear fatigue damage mechanisms are divided on pitting and bending in tooth root fatigue. Pitting can be initiated on the surface of the tooth flank and in the subsurface. Surface initiated pitting appears as a consequence of the surface roughness, residual stress, material treatment, etc., while a subsurface pitting appears as a result of a shear stress as a main driving force. In this research, subsurface pitting is considered. The latter mentioned fatigue mechanism is initiated at the location of maximum shear stress in the subsurface and propagates toward the free surface [2]. After reaching the free surface, lubrication fluid enters the crack and accelerates the crack growth toward subsequent free surface. Through years, several investigations in literature have been developed numerical models for predicting subsurface rolling-sliding contact fatigue failure [1-4]. This research presents a novel approach for numerical modelling the subsurface pitting phenomenon by the phase–field method established by Seleš at al [5] and implemented into the software ABAQUS.

2. Modelling of the subsurface pitting phenomena

Novel numerical model for description subsurface fatigue phenomena has been developed. As a fatigue mechanism, pitting formation is described by the phase–field method. Above mentioned method can very smoothly describe deterioration of material stiffness by the phase–field parameter ϕ [0,1]. One denotes fully damaged material, while zero denotes undamaged material. Method is based on minimization of the free energy functional [6]:

$$\Psi = \Psi^b + \Psi^s = \int_{\Omega/\Gamma} \psi_e(\varepsilon)\mathrm{d}\Omega + \int_{\Gamma} G_c \mathrm{d}\Gamma. \tag{3}$$

Ψ^b represents the elastic deformation energy, while Ψ^s denotes the dissipated fracture surface energy, ε is the strain tensor and G_c is the fracture toughness.

In the literature is established that two coupled gears in rolling–sliding contact (Fig. 1.a and 1.b) can be replaced by the equivalent problem of the flat plate loaded by EHL pressure profile [1-4]. EHL pressure profile is computed from six coupled equations: Reynold's equation, film thickness equation, deformation equation, viscosity–pressure relationship, density–pressure relationship and force balance. Distribution of friction profile is computed by the Coulomb friction law [1]. Contact between two tooth flanks at various locations is simulated by the moving load [1], simulating the influence of close contact points meshing gear teeth on crack initiation and propagation (Fig. 1.c). Figure 2 represents qualitative example of subsurface initiated pitting formation. Influence of the hydrostatic pressure within the crack is neglected. As a material, ductile cast nodular iron EN-GJS-400-18-LT is used, with material parameters of nonlinear isotropic and kinematic hardening taken from [7].

In the research, constitutive material behaviour is embedded into Abaqus by user subroutine UMAT. Pressure profile is calculated and imposed via the user subroutine DLOAD, while the

influence of the friction is programmed into the user subroutine UTRACLOAD. Phase–field parameter is included in user element in user subroutine UEL as an additional degree of freedom.

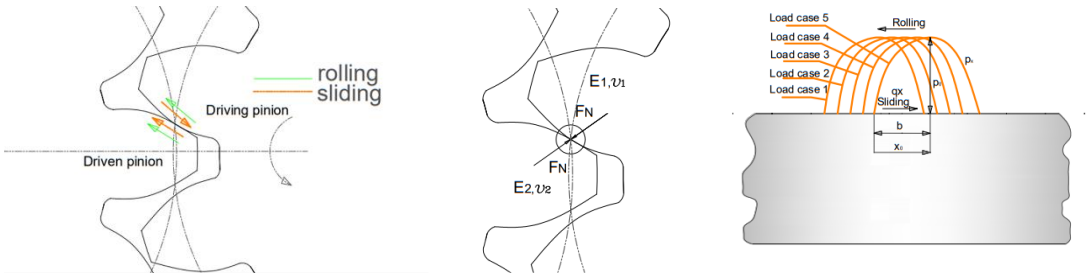

Figure 17. a) rolling – sliding contact, b) two gear teeth in operation, c) moving load

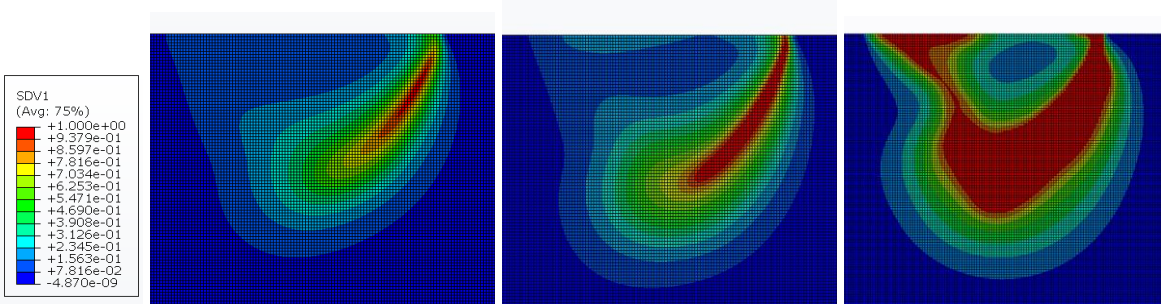

Figure 2. Subsurface pitting formation

References

[1] Fajdiga, G., Glodež, S., Kramar, J., Pitting formation due to surface and subsurface initiated fatigue crack growth in contacting mechanical elements. *Engineering Fracture Mechanics*, vol. 262, pp. 1217–1224, 2007.

[2] Weibring, M., Gondecki, L., Tenberge, P., Simulation of fatigue failure on tooth flanks in consideration of pitting initiation and growth. *Tribology International*, vol. 131, no. October 2018, pp. 299–307, 2019.

[3] Savolainen, M., Lehtovaara, A., An approach to investigating subsurface fatigue in a rolling\sliding contact. *International Journal of Fatigue*, vol. 117, no. August, pp. 180–188, 2018.

[4] Heirani, H., Farhangdoost, K., Predicting depth and path of subsurface crack propagation at gear tooth flank under cyclic contact loading."*Journal of Solid Mechanics*, vol. 9, no. 3, pp. 587–598, 2017.

[5] Seleš, K., Lesičar, T., Tonković, Z., Sorić, J., A residual control staggered solution scheme for the phase – field modelling of brittle fracture. *Engineering Fracture Mechanics*, vol. 205, pp. 370-386, 2019.

[6] Francfort, G.A., Marigo, J.J., Revisiting brittle fracture as an energy minimization problem. *J Mech Phys Solids*, vol 46., pp. 1319-42, 1998.

[7] Čanžar P., Eksperimentalno i numeričko modeliranje zamornog ponašanja nodularnog lijeva [Doctoral thesis]. Zagreb: University of Zagreb, Faculty of Mechanical Engineering and Naval Architecture; 2012.

[8] Hannes, D., Alfredsson, B., Numerical investigation of the spall opening angle of surface initiated rolling contact fatigue. *Engineering Fracture Mechanics*, vol. 131, pp. 538-556, 2014.

Modeling of concrete during early age hydration

Silvio Prskalo[1], Martin Schanz[1], Michael Gfrerer[1]

[1]*Institute of Applied Mechanics, Graz University of Technology, Graz, Austria*
E-mails: prskalo@tugraz.at

Keywords: multiphase porous material, early age hydration, hygro-thermo-chemo-mechanical modeling

1. Introduction

Prediction of behavior of concrete is of great practical importance and as such, it has been researched throughout the years 000. During the initial period of concrete maturing complex physicochemical phenomena cause considerable non-uniform deformations of material. Most models consider only thermo-mechanical phenomena 0 assuming the hygral phenomena of less importance due to high liquid saturation. In order to clasp all the mentioned effects the proposed model is based on Gawin's research paper 0. Contrary to his model, here, beside the effect of hydration-dehydration, the effect of the evaporation-condensation will be taken into account. It is the goal to use the proposed model to investigate the relation between waves propagation speed and the strength of concrete.

2. Model

Concrete is considered as a multiphase porous material with the solid, liquid and gas constituents. The governing equations of this model are written by considering concrete to be in thermal-, hygral- and mechanical equilibrium state locally, even if chemical reactions (hydration process) are progressing with a certain rate. Characteristic times of their local progresses are much smaller than of hydration reaction, hence, for these processes the equilibrium relations are used (with the actual value of hydration degree being "frozen"). For the early stages of hardening the hydration process plays a crucial role in changes of concrete properties, i.e., porosity, density, permeability and strength properties.

The macroscopic balance equations used in this model are obtained by averaging the balance equations for phases and inter-phases at micro-scale level, (see Table 1., with π standing for each phase $\pi = s, l, g$). The model takes into account full coupling between each phenomena, where all changes of material properties are expressed through hydration dependent parameters.0

Table 1. Balance equations of the constituents in multi-phase material [5]

Mass balance equation	$\frac{D^\pi \rho_\pi}{Dt} + \rho_\pi \mathrm{div}\boldsymbol{v}^{\boldsymbol{\pi}} = \rho_\pi e^\pi(\rho)$
Linear momentum equation	$\mathrm{div}\boldsymbol{t}^{\boldsymbol{\pi}} + \rho_\pi \boldsymbol{g} + \rho_\pi[\boldsymbol{e}^{\boldsymbol{\pi}}(\rho\dot{\boldsymbol{r}}) + \hat{\boldsymbol{t}}^{\boldsymbol{\pi}}] = 0$
Enthalpy equation	$\rho_\pi C_p^\pi \frac{D^\pi T^\pi}{Dt} = \rho_\pi h^\pi - \mathrm{div}\tilde{\boldsymbol{q}}^{\boldsymbol{\pi}} + \rho_\pi R_H^\pi - \rho_\pi e^\pi(\rho) H^\pi$

The solid skeleton voids are filled partly by liquid water and partly by a gas phase, which is a mixture of dry air and water vapor (condensible gas constituent). It is assumed to behave as an ideal gas. This model equations are obtained by means of the hybrid mixture theory (HTM) originally proposed by Hassanizadeh and Gray 0, and then applied for geomaterials 0. The full development of the model equations are presented in References.00

2.1. Choice of state variables

A proper choice of state variables for hygro-thermo-chemo-mechanical modelling of concrete, in particular, at early stages of hydration plays a important role. From a practical point of view the physical quantities should be easily measurable during experimental tests, and from a theoretical point of view, must uniquely describe the state of the material. The computer code need to have a good numerical performance, based on the mathematical equations. The number of the state variables is reduced due to assumption of local thermodynamic equilibrium at each point of the medium. Hence, it is assumed that all constituents of the porous medium have the same temperature, it is a isothermal problem.

Having in mind all from the above, the solid skeleton displacement vector, gas pressure and temperature are the obvious choices. For the description of the hygrometric state or advancement of cement hydration the capillary pressure is taken before the relative humidity and the vapor pressure. For its applicability in wide hygroscopic moisture range, good numerical performance and a clear relation between pressures and stresses for the analysis of concrete's stress state is chosen as model's state variable.

2.2. Modeling of cement hydration

From the macroscopic point of view, hydration of cement is a complex interactive system of competing chemical reactions of various kinetics and amplitudes. This physical and chemical phenomena at the micro-level of material structure results in considerable changes of concrete's properties. Kinetics of cement hydration (hydration rate), proposed by Ulm and Coussy 0, are described using the chemical affinity, as a driving force of chemical reactions.
The evolution equation, considering additionally the effect of relative humidity may be written in terms of the hydration degree rate as,

$$\frac{d\Gamma_{hydr}}{dt} = A_{\Gamma hydr}(\Gamma_{hydr})\beta_{\varphi}(\varphi)exp\left(\frac{-E_a}{RT}\right) \tag{3}$$

where $A_{\Gamma hydr}$ is the hydration degree-related, normalized affinity, which is determined from adiabatic calorimetric experiments.0

3. Numerical simulation

The presented model is solved with the research code PANDAS. PANDAS is a multi-field finite-element solver using the variational method for solving the system of strongly coupled differential equations. Some results will be presented at the conference.

References

[1] Bazant, ZP. (ed.), Mathematical Modeling of Creep and Shrinkage of Concrete. Wiley: Chichester, 1988.

[2] Ulm, F-J., Coussy, O., Modeling of thermo-chemo-mechanical couplings of concrete at early ages. *Journal of Engineering Mechanics*, (ASCE), 121(7):785-794, 1995.

[3] Cervera, M., Faria, R., Olivier, J., Prato, T., Numerical modeling of concrete curing, regarding hydration and temperature phenomena. *Computers and Structures*, 80:1511-1521, 2002.

[4] Gawin, D., Pesavento, F., Schrefler, B., Hygro-thermo-chemo-mechanical modelling of concrete at early ages and beyond. Part I: Hydration and hygro-thermal phenomena. *International Journal for numerical methods in engineering*, Wiley, 2006.

[5] Schrefler, BA., Mechanics and thermodynamics of saturated-unsaturated porous materials and quantitative solutions. *Applied Mechanics Reviews*, (ASME), 2002.

[6] Hassanizadeh, SM., Gray, WG., General conservation equations for multi-phase systems: 1. Averaging procedure. *Advances in Water Resources*, 2:131-144, 1979.

Steady-State Creep of the Gas Turbine Disk-an Analytical Approach

Dragan Pustaić*

University of Zagreb, Faculty of Mechanical Engineering and Naval Architecture,
Institute of Applied Mechanics, Ivana Lučića 5, 10 000 Zagreb, Croatia
E-mail: dragan.pustaic@fsb.hr

Keywords: gas turbine disk, stationary temperature field, steady-state creep, mechanical and thermal load of the disk, stresses and the displacements in the disk in the steady-state creep conditions, analytical methods

1. Introduction

The disk of the gas turbine rotor is usually performed as a disk of variable thickness. At the *stationary* operation the disk is exposed to great mechanical and thermal loads. This primarily refers to the centrifugal forces of the disk´s own mass and the centrifugal forces of the blades, all at the speed of, for example, n = 7200 rpm. Regarding thermal loads, the disk is exposed to the *stationary* temperature field at the temperature of T = 600 ^{0}C. The *creep* of the disk will be especially expressed at so high temperatures and long duration of continuous operation, [1-2, 5]. The creep of the disk will particularly influence disk´s displacements. In order to endure this high loads, the disk material has to be high strength alloyed steel as, for example, 45Cr14Ni14W2Mo, which in addition has a great elongation, [2, 5]. The analysis of the stresses and displacements at the *stationary* state of a disk was performed by analytical methods in the combination with contemporary mathematical tools as, for example, the software *Wolfram Mathematica.*

2. Differential equation of equilibrium

The disk on the rotor of gas turbine is considered as the thin disk on which the *axial stresses* are $\sigma_z \approx 0$. Plane stress is present in the disk. As an answer to mechanical and thermal loading, the *radial,* σ_r, and the *circumferential stresses,* σ_φ, are appeared in the disk. The differential equation of the equilibrium of the element of rotating disk will be, according to [3]

$$\mathrm{d}\left(\sigma_r hr\right)/\mathrm{d}r - \sigma_\varphi \cdot h + \rho\omega^2 \cdot hr^2 = 0. \tag{1}$$

The general solution of that equation could be written in a form of the *integral equation,* as

$$\sigma_r hr - \sigma_r\left(r_1\right)\cdot h_1 \cdot r_1 - \int_{r_1}^{r} \sigma_\varphi h \cdot \mathrm{d}r + \rho\omega^2 \cdot \int_{r_1}^{r} hr^2 \cdot \mathrm{d}r = 0. \tag{2}$$

3. Circumferential and radial stress at the disk

The analytical expressions for the circumferential and radial stress in the disk, will be, [2]

$$\sigma_\varphi = \left(p_2 r_2 h_2 + p_1 r_1 h_1 + \Phi_2\right)\cdot\eta \Big/ \int_{r_1}^{r_2} h\cdot\eta\cdot\mathrm{d}r. \tag{3}$$

$$\sigma_r = \frac{1}{rh}\cdot\left[-p_1 r_1 h_1 + \left(p_2 r_2 h_2 + p_1 r_1 h_1 + \Phi_2\right)\cdot\int_{r_1}^{r} h\cdot\eta\cdot\mathrm{d}r \Big/ \int_{r_1}^{r_2} h\cdot\eta\cdot\mathrm{d}r - \Phi\right]. \tag{4}$$

4. Radial displacements of the disk at the steady-state creep conditions

The analytical expression for determining the disk radial displacements at the steady-state creep conditions, u_c, can be written, after arranging, in the following form, [1-2]

* *Professor in the retirement*

$$u_{\mathrm{c}} = \left(\sigma_{\varphi}^{2} - \sigma_{\varphi} \cdot \sigma_{r} + \sigma_{r}^{2}\right)^{\frac{n-1}{2}} \cdot \left(2\sigma_{\varphi} - \sigma_{r}\right) \cdot \Omega(t,T) \cdot r \Big/ 2. \tag{5}$$

It is particularly of interest to investigate the dependence of the *radial displacements due to creeping*, on the disk´s external boundary on *time.* The whole radial displacement of any arbitrary point of the disk and also the point lying on the external boundary of the disk, is composed of *three* components, which are: a) the radial displacement which appears at the initial moment due to the rotation of the disk. It appears instantaneously, i.e. as soon as the number of the rotor revolutions *n* has achieved the nominal value, b) the radial displacement due to heating of the disk. It appears instantaneously as well, i.e., as soon as, the temperature of the disk assumes the value of the stationary temperature field, and, c) the radial displacement which appears due to *creeping* of the disk. As it was already pointed out, those displacements *are dependent on time*, i.e. they *increase with time.* All the components of the displacements are diagrammatically presented on the Fig. 1.

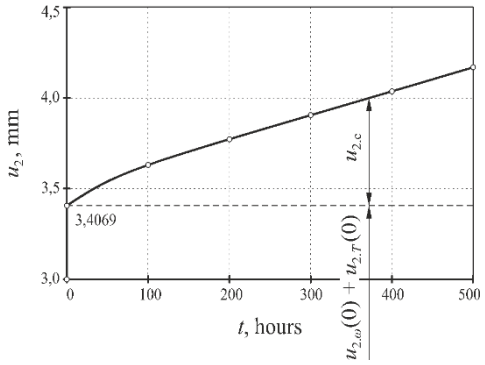

Figure 1. The dependence of the radial displacement, u_2, of the external boundary of the gas turbine disk on time t

5. Retrospect to the results

The stresses and the displacements at the gas turbine disk, in the *stationary* operations state, were analyzed in the paper. At that state, the disk is exposed to the great mechanical and thermal loads. The uniformly heating of the disk and the long duration of operating in such regimen lead to the phenomenon of *creeping* of the disk material. The creep of the disk will not considerably influence the change of the stresses at the disk. The heating especially influences the displacements on those which occurred instantaneously, as well as on the delayed displacements which appear as a consequence of the *creeping* of the disk material. Those displacements *are depended on time* and for the considered disk the maximum displacement amounts about 22% of the initial displacement.

The mathematical algorithm, derived and applied in the analysis is an exact analytical approach, based on solving of the system of the differential equations, which can be found at the books [2, 3] and at the papers [1, 4]. All the numerical computations were performed by using the contemporary mathematical tools as, the software *Wolfram Mathematica.*

References

[1] Pustaić, D., Steady-State Creep Analysis of Thick-Walled Pressure Vessels and Piping. In: Z. Virag, H. Kozmar, I. Smojver, eds., Proceedings of the 7th International Congress of Croatian Society of Mechanics, Book of Abstracts, 197–198, and CD-ROM, Croatian Society of Mechanics, Zagreb, 2012.

[2] Malinin, N. N., Applied Theory of Plasticity and Viscoelasticity, Mashinostroenie, Moscow, 1975.

[3] Pustaić, D., Tonković, Z., Wolf, H., Mechanics of Solid Bodies, 2nd part–Strength of the Elements of Structures, Uni. Zagreb, Faculty of Mech. Engineering and Naval Arch., Zagreb, 2014 (in Croatian).

[4] Kobelev, V., Some basic Solutions for Nonlinear Creep, *International Journal of Solids and Structures,* Vol. 51, 19-20, 3372-3381, 2014.

[5] Lubhan, J. D., Felgar, R. P., *Plasticity and Creep of Metals,* John Wiley & Sons, N. Y. / London, 1961.

Using Timoshenko beams with Quadratic Linked Interpolation for Modelling Mixed-mode Delamination

Maedeh Ranjbar, Leo Škec, Gordan Jelenić, Dragan Ribarić

University of Rijeka, Faculty of Civil Engineering, Radmile Matejčić 3, 51000 Rijeka, Croatia.
E-mails: {maedeh.ranjbar,leo.skec,gordan.jelenic,dragan.ribaric}@uniri.hr

Keywords: Delamination, Linked interpolation, Cohesive element, cohesive zone model

1. Introduction

The use of beam finite elements instead of 2D-solid finite elements to model the layers in delamination problems has recently been proposed as a useful method to reduce simulation costs and total number of degrees of freedom in the model [1]. This approach has already been applied to both Euler-Bernoulli [2] and Timoshenko beam finite elements [1]. For the latter, it is common to use Lagrangian polynomials as interpolation functions. To scope of this work is to investigate whether the use of alternative interpolation functions can further improve the performance of Timoshenko-beam finite-element model (FEM) for mixed-mode delamination.

In so-called linked interpolation, the displacement field is interpolated using not only the contribution of nodal displacements, but also nodal cross-sectional rotations. Such interpolation functions are derived from the closed-form solution of the Timoshenko beam problem [3]. Therefore, they converge to the reference solutions faster (with coarser meshes) than those with standard Lagrangian interpolations [4]. In this work we apply the quadratic linked interpolation functions of two-node Timoshenko beam elements to corresponding 4-node interface elements. These interpolation functions are enhanced by introducing a second-order interpolation function in the field of transverse displacements, which, in addition to nodal transverse displacements, takes into account also the nodal cross-sectional rotations. At the same time, the fields of axial displacement and cross-sectional rotation are interpolated using the linear Lagrange polynomials.

2. Formulation and Simulation

A sample 4-node cohesive element (BINT4) attached to the nodes of two adjacent two-node beam finite elements and the corresponding degrees of freedom in each node is shown in Figure 1(a). A bi-linear cohesive zone model in both mode I and II (Figure 1(b)) is embedded in BINT4 elements.

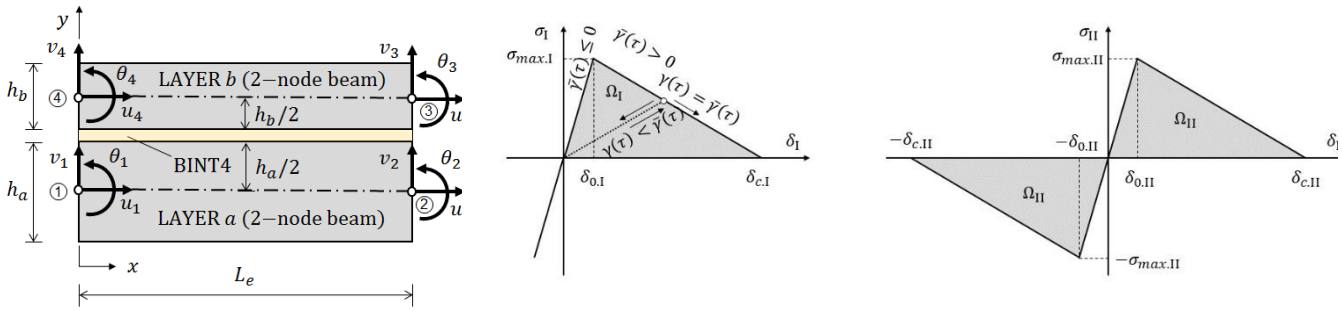

(a) (b)

Figure 18. a) BINT4 cohesive element attached to nodes of two-node beam finite elements, b) Bi-linear cohesive-zone model embedded in BINT4 element

The second-order linked interpolation for two-node Timoshenko beam element of length L_e reads:

$$v = \frac{1-\xi}{2} v_1 + \frac{1+\xi}{2} v_2 + \frac{1-\xi^2}{4} L_e(\theta_1 - \theta_2) \tag{1}$$

where $-1 < \xi < 1$ is the natural coordinate of each integration point. Note that by cancelling the last term in Equation (1), it becomes the standard linear Lagrangian interpolation function.

The presented FEM based on two-node Timoshenko beam elements and corresponding beam-linked interface elements is implemented in FEAP [5] and used to solve several delamination problems in mode I, II and mixed-mode. A comparison between the linear and quadratic linked interpolation on a DCB example from [6] is given in Figure 2. It can be seen that for the same number of elements, the linked interpolation elements give a smoother solution. This implies that to obtain a satisfactory level of accuracy, the mesh size, and therefore the computational time, can be significantly reduced when linked interpolation is employed for solving delamination problems.

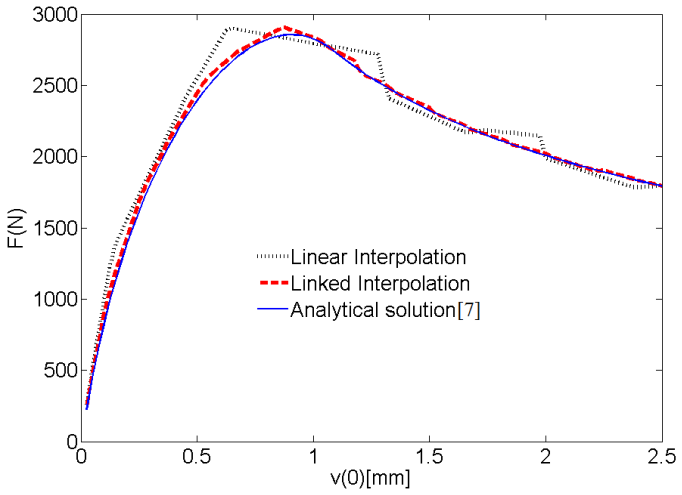

Figure 2. Comparing the performance of linear and linked interpolation for Le=20mm

4. Conclusions

We present a novel FEM for efficient and accurate modelling of mixed-mode delamination. It is based on two-node Timoshenko beam finite elements with quadratic linked interpolation and the corresponding beam-linked interface elements. It is shown that quadratic linked interpolation for the same mesh size can provide a more accurate solution compared to the linear Lagrangian interpolation, which is very relevant for simulation of delamination problems. However, more investigation is necessary to assess the performance of the new model on as many as possible different combinations of geometrical and material parameters of specimens.

References

[1] Škec, L., Jelenić, G., Lustig, L., Mixed-mode delamination in 2D layered beam finite elements. Int. J. Numer. Meth. Engng, 104(8), 767-788, 2015.

[2] Russo, R., Chen. B., Overcoming the cohesive zone limit in composites delamination: modeling with slender structural elements and higher-order adaptive integration. Int. J. Numer. Meth. Engng, 121(24), 5511-5545 2020.

[3] Jelenić, G., Papa, E., Exact solution of 3D Timoshenko beam problem using linked interpolation of arbitrary order. Archive of Applied Mechanics, 81(2), 171-183, 2011.

[4] Ribarić, D., Jelenić, G., Higher-order linked interpolation in quadrilateral thick plate finite elements. Finite Elements in Analysis and Design, 51, 67-80, 2012.

[5] Talyor, R. L., FEAP - Finite Element Analysis Program, 2020, http://www.ce.berkeley/feap.

[6] Škec, L., Alfano, G., Jelenić, G., Enhanced simple beam theory for characterising mode-I fracture resistance via a double cantilever beam test. Composites Part B, 167, 250–262, 2019.

[7] Škec, L., Alfano, G., Jelenić, G., Complete analytical solutions for double cantilever beam specimens with bi-linear quasi-brittle and brittle interfaces. International Journal of Fracture, 215, 1-37, 2019.

A comparison of finite element schemes for micromagnetic simulations

Maximilian Reichel*, Jörg Schröder +

*Institute of Mechanics, University of Duisburg-Essen, Universitätsstr. 14, 45141 Essen, Germany
E-mails: {maximilian.reichel , j.schroeder}@uni-due.de

Keywords: Micromagnetic Simulation, Finite Elements, Numerical Methods

1. Introduction

Continuous development and improvement of technical devices lead to an increasing demand for high-performance magnets. Here, micromagnetic simulations can be used to determine the distribution of magnetization vectors on fine scales and predict material properties. However, a central and challenging requirement in micromagnetism is to constrain the length of the magnetization vectors to the Euclidean norm. In this contribution, different methods to preserve this norm are compared and evaluated.

2. Magneto-elastic micromagnetic setup

The governing equations in micromagnetic simulations are the magnetic Gauss law div $\boldsymbol{B} = 0$ and the balance of linear momentum div $\boldsymbol{\sigma} = \boldsymbol{0}$, where $\boldsymbol{B}$ defines the magnetic induction and $\boldsymbol{\sigma}$ the linear Cauchy stress tensor. The magnetic induction is defined as $\boldsymbol{B} = \mu_0(\boldsymbol{H} + \boldsymbol{M})$, where μ_0 is the magnetic vacuum permeability, $\boldsymbol{H}$ the magnetic field and $\boldsymbol{M}$ the magnetization. The magnetic field is derived via a magnetic scalar potential $\boldsymbol{H} = -\nabla\varphi$ and the magnetization $\boldsymbol{M} = M_s\boldsymbol{m}$ is a composition of the magnetic saturation magnetization M_s and the unit director $\boldsymbol{m}$. The stress tensor follows the definition as $\boldsymbol{\sigma} = \mathbb{C} : \boldsymbol{\varepsilon}$, where $\mathbb{C}$ defines the material elastic tensor and $\boldsymbol{\varepsilon} = \frac{1}{2}(\nabla^{\mathrm{T}}\boldsymbol{u} + \boldsymbol{\nabla u})$ the linear elastic strain tensor. The energy functional $\mathcal{H}$ of the magnetic solid contains different competing energy parts, such as contributions to magnetostatics $\mathcal{H}^{\mathrm{mag}}$ ($\boldsymbol{H}$, $\boldsymbol{m}$), to the magnetic exchange $\mathcal{H}^{\mathrm{exc}}$ ($\nabla\boldsymbol{m}$), to the magneto crystalline anisotropy $\mathcal{H}^{\mathrm{ani}}$ ($\boldsymbol{m}$) and to elastic properties $\mathcal{H}^{\mathrm{ela}}$ ($\boldsymbol{\varepsilon}$, $\boldsymbol{m}$). Depending on this energy functional, the constitutive relations for the magnetic induction and the mechanical stresses can be represented as $\boldsymbol{B} = -\partial\mathcal{H}/\partial\boldsymbol{H}$ and $\boldsymbol{\sigma} = \partial\mathcal{H}/\partial\boldsymbol{\varepsilon}$. The evolution of the magnetization vectors is described by the well-known Landau-Lifshitz-Gilbert (LLG) equation, that yields the following representation

$$\dot{\boldsymbol{m}} = -\gamma_0\mu_0\,\boldsymbol{m} \times \boldsymbol{H}^{\boldsymbol{eff}} + \alpha\,\boldsymbol{m} \times \dot{\boldsymbol{m}}, \tag{1}$$

where γ_0 is the gyromagnetic ratio, α the Gilbert damping parameter and $\boldsymbol{H}^{\mathbf{eff}} = \frac{-\mathbf{1}}{\mu_0 \mathrm{Ms}}\delta\mathcal{H}/\delta\boldsymbol{m}$ is the effective field. A crucial aspect in micromagnetic simulations is the conservation of the length of the magnetization vector $\|\boldsymbol{m}\|=1$. Within this contribution the constraint is enforced in three different ways. First, a penalty term $\mathcal{H}^{\mathrm{pen}}$ $(\boldsymbol{m})=\kappa(||\boldsymbol{m}|| - 1)^{\mathbf{2}}$ is added to the total energy functional, that penalizes the deviations of $\boldsymbol{m}$ from the Euclidean norm in dependency of the penalty parameter κ, compare [1]. Second, the set of equations to be solved is extended by a perturbed Lagrange multiplier

$$\Pi = \int_{\mathbf{B}} \lambda\left(||\boldsymbol{m}||^2 - 1\right)\mathrm{dv} - \int_{\boldsymbol{B}} \frac{\lambda^2}{2\,k}\,\mathrm{dv} \tag{2}$$

that constraints the magnetization vectors as introduced in [2]. The difference between the penalty method and the perturbed Lagrange multiplier is the determination of the penalization intensity.

While the penalty must be set initially, the Lagrange multiplier is adjusted in each iteration. This leads to a more precise preservation of the norm and thus to better results, but also implies longer

computation times due to the additional degree of freedom. Third, a method that satisfies the constraint a priori is the use of spherical coordinates. Here, the magnetization vectors are parameterized as $\boldsymbol{m} = [\sin\theta_1 \cos\theta_2, \sin\theta_1 \sin\theta_2, \cos\theta_1]^T$ and the angles are the interpolated quantities, compare [3].

3. Numerical examples

A permalloy nano disk with a radius of 150nm and a thickness of 32nm is initialized with a random magnetization and subsequently relaxed to its self-equilibrium vortex state. Afterwards, an external magnetic field $\mu_0 H_2$ is applied to the nano structure and cycled between 200mT and -200mT to gain the characteristic hysteresis loops, presented in Figure 1c. The material parameters are taken from [4] and a Gilbert parameter $\alpha = 0.5$ was used. To stress the differences in the introduced restrictions, all methods are applied to simulate the loops.

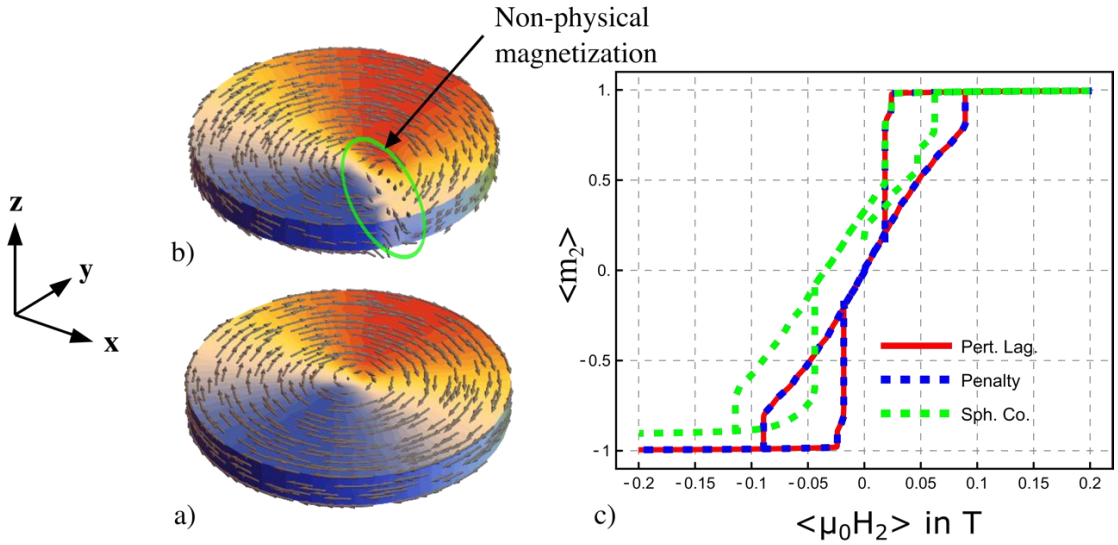

Figure 1. The vortex gained by a) the penalty method and b) the spherical coordinates. The hysteresis in c) show good agreement for the penalty and the Lagrange method, but not for the sph. coordinates.

4. Conclusion

In this contribution, different methods to preserve the length of the magnetization vectors are compared. While the results of the penalty method and the Lagrange multiplier agree well, the results of the spherical coordinates show non-physical behavior, which is also reflected in the hysteresis.

Acknowledgement We gratefully acknowledge the financial support of the German Research Foundation (DFG) in the framework of the CRC/TRR 270, project A07 "Scale-bridging of magneto-mechanical mesostructures of additive manufactured and severe plastically deformed materials", project number 405553726.

References

[1] Prohl, A, *Computational Micromagnetism*, BG Teubner, Wiesbaden, 2001.

[2] Ohmer, D., Yi, M., Gutfleisch, O., Xu, B.-X., Phase-field modeling of paramagnetic austenite-ferromagnetic martensite transformation coupled with mechanics and micromagnetics. International Journal of Solids and Structures, 238, 111365, 2022.

[3] Yi, M., Xu, B.-X., A constraint-free phase field model for ferromagnetic domain evolution. *Proceedings of the Royal Society A: Mathematical, Physical and Engineering Science*, 470, 20140517, 2014.

[4] Miehe, C., Sridhar, A., A geometrically consistent incremental variational formulation for phase field models in micromagnetics. *Comput. Methods Applied Mech. Engrg.*, 245-246, 331-347, 2012.

Stress-induced martensitic transformation in shape memory alloys during nano-indentation: insights from phase-field simulations

Mohsen Rezaee-Hajidehi*, Karel Tůma+, Stanisław Stupkiewicz*

*Institute of Fundamental Technological Research (IPPT), Polish Academy of Sciences, Pawińskiego 5B, 02-106 Warsaw, Poland
E-mails: {mrezaee,sstupkie}@ippt.pan.pl

+Faculty of Mathematics and Physics, Charles University, Sokolovská 83, 186 75, Prague, Czech Republic
E-mail: ktuma@karlin.mff.cuni.cz

Keywords: SMA, Pseudoelasticity, Nano-indentation, Martensitic microstructure, Phase-field method

1. Introduction

Instrumented micro- and nano-indentation is a powerful and widely used experimental technique for the characterization of the material behavior at small scales. This concerns also the shape memory alloys (SMAs), which have gained considerable attention in science and industry thanks to their spectacular features of pseudoelasticity and shape memory effect, originating from the crystallographically reversible martensitic phase transformation [1]. In general, when the SMA material is in the pseudoelastic state, the indentation-induced martensitic microstructure disappears during unloading, as a result of the reversible transformation, and thereby, the load–indentation depth response is the only available data from the experiment that is used for material characterization, see e.g. [2]. It thus appears that modeling is the primary means to examine the martensitic microstructure and can be exploited to supplement the experiment.

Modeling the indentation in SMAs has been the subject of numerous studies. The majority of the modeling studies available in the literature are limited to macro and meso scales, where either macroscopic phenomenological models or micromechanical crystal plasticity-like models are used. These models are relevant for scales higher than the spatial arrangement of individual martensite variants and phase boundaries. On the other hand, atomistic simulations that employ the molecular dynamics (MD) are limited to very small spatial and temporal scales. It seems that continuum modeling of spatially-resolved martensitic microstructure at an intermediate scale between atomistic and micromechanical modeling is desired. Phase-field method is a suitable computational tool applicable at this scale, and has thus been employed in this work to analyze the microstructure evolution in pseudoelastic SMA during nano-indentation.

2. Finite-strain phase-field model

A recently-developed phase-field model for multivariant martensitic transformation has been used in this work [3,4]. The model possesses a number of important features that enables it to provide a physically relevant description of martensitic transformation under nano-indentation. More specifically, the model is formulated in the finite-deformation framework, admits an arbitrary crystallography of phase transformation, and an arbitrary elastic anisotropy of phases (consistent with crystallographic symmetry of phases). Computer implementation is done based on the finite-element method, and thus allows a natural treatment of the indentation contact problem.

In view of the high mesh density needed to capture the detailed microstructures, the computational problems addressed are quite expensive. The computational model has proved to be robust and

exhibited a good parallel scaling performance, and as a result, is able to handle large-scale 3D simulations, reaching 150 million degrees of freedom [3].

3. Simulation of the microstructure evolution in CuAlNi during nano-indentation

Having this advanced model at hand, the goal in this work is to thoroughly investigate the martensitic microstructure evolution in CuAlNi SMA (where most of the material parameters are known from the experiments reported in the literature) during nano-indentation. In particular, the impact of the crystallographic orientation on the load–indentation depth response and the microstructure is studied, see Fig. 1. In addition, we show that the characteristic features of our model, namely the finite-deformation formulation and elastic anisotropy, are crucial elements to correctly predict the microstructure. To our knowledge, such a comprehensive high-resolution microstructure-based modeling study has not been reported so far.

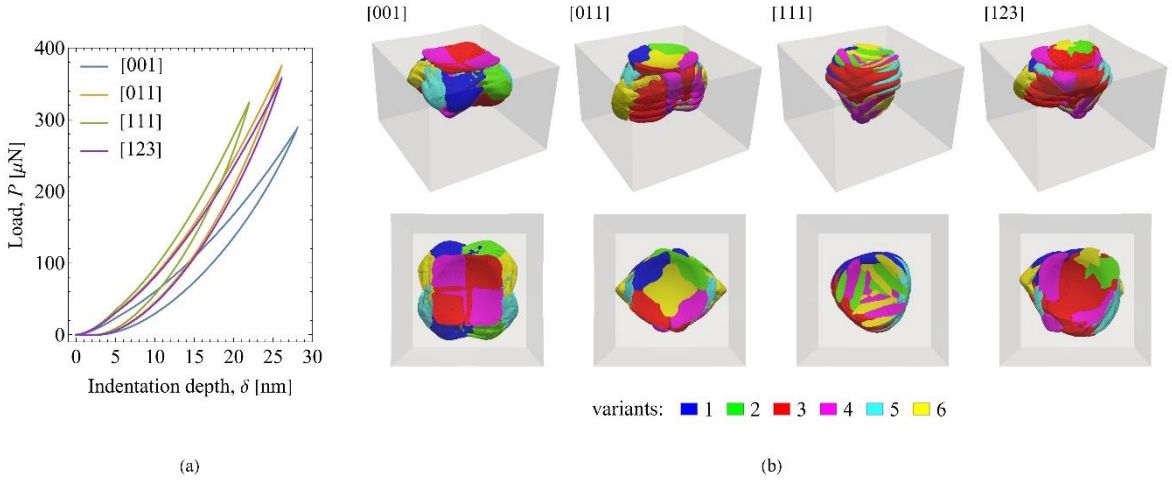

Figure 1. The effect of crystallographic orientation on (a) the load-indentation depth response, and (b) the martensitic microstructure.

References

[1] Bhattacharya, K., Microstructure of martensite: why it forms and how it gives rise to the shape-memory effect. Oxford University Press, Oxford, 2003.

[2] Pfetzing-Micklich, J., Wieczorek, N., Simon, T., Maaβ, B., Eggeler G., Direct microstructural evidence for the stress induced formation of martensite during nanoindentation of NiTi. *Materials Science & Engineering A*, 591, 33–37, 2014.

[3] Rezaee-Hajidehi, M., Stupkiewicz, S., Phase-field modeling of multivariant martensitic microstructures and size effects in nano-indentation. *Mechanics of Materials*, 141, 103267, 2020.

[4] Tůma, K., Rezaee-Hajidehi, M., Hron, J., Farrell, P.E., Stupkiewicz, S., Phase-field modeling of multivariant martensitic transformation at finite-strain: Computational aspects and large-scale finite-element simulations. *Computer Methods in Applied Mechanics and Engineering*, 377, 113705, 2021.

Space Interface Element with Exponential Cohesive Zone Law in Delamination of Layered Sructures

Dragan Ribarić*, Ivan Hlača*

*Faculty of Civil Engineering in Rijeka
E-mails: {dragan.ribaric,ivan.hlaca}@uniri.hr

Keywords: interface element, cohesive zone model (CZM), delamination, linked interpolation, plate layer elements

1. Introduction

A cohesive interface element for layered shell analysis is presented. The element can be used to simulate the initiation and growth of delamination between stacked noncoincident layers of facet shell elements. Cohesive zone law is expressed with continuous exponential expressions relating tractions to the separations in mode I and mode II interactively.

2. Facet shell elements used for layers

Layers are modelled with four-node facet shell elements that are derived for the Mindlin plate theory accounting for the plate shear deformations and with the membrane in-plane deformations. So-called problem-dependent linked interpolations of cubic order are used for lateral displacement and in plane rotation fields (w, θ_x, θ_y) of the plate part of the element stiffness matrix [1], that is capable to model one-dimensional problems exactly even in the thin limit conditions (Kirchhoff plate theory). Interpolations for the in plane displacements (u, v) are also enriched with higher order terms dependent on the nodal drilling rotations (θ_z). The element passes the constant bending patch test for arbitrary node positions and the in plane patch test for regular meshes.

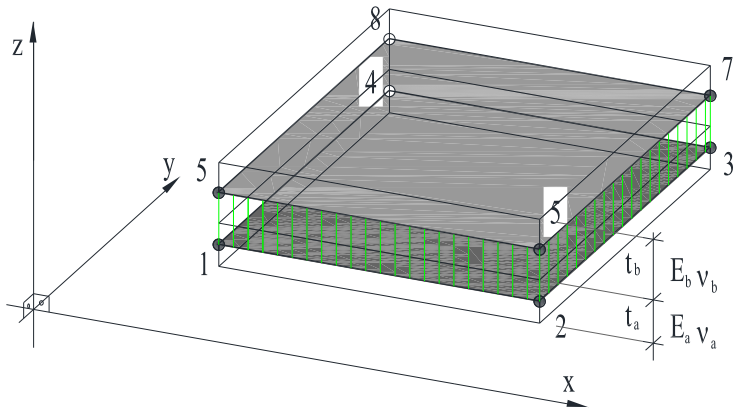

Figure 1. 8-node cohesive element between two layer facet shell elements: 1-2-3-4 and 5-6-7-8

3. Cohesive interface element

8-node cohesive interface element connects two adjacent plate elements (Fig. 1) in the aligned mesh of the modelled problem. The procedure to construct the interface element accounts for the thickness offset by applying the kinematic relations of shell displacement and shell in plane section rotations to transform the stiffness and internal force of a zero-thickness cohesive element such that interfacial continuity between the layers is enforced at the contact surface until delamination.

Interpolation functions for the displacement fields over the interface element are compatible to the interpolations of the adjacent shell elements, involving in plane rotations in lateral displacement expressions (linked interpolations).

3.1. Cohesive zone law

We prefer to use continuous functions for the cohesive zone law to avoid sudden jumps in the stiffness matrix during the force increment process. For that reason we have chosen the exponential functions for the cohesive zone law (eCZM) which in our interface element will have the following expressions [2]:

$$\sigma^{I}(\delta_I, \delta_{II}) = \frac{G_{IC}}{\delta_{0,I}^2}\delta_I \cdot e^{-\frac{\delta_I}{\delta_{0,I}}} \cdot e^{-\frac{\delta_{II}}{\delta_{0,II}}}, \tag{1}$$

$$\sigma^{II}(\delta_{II}, \delta_I) = \frac{G_{IIC}}{\delta_{0,II}^2}\delta_{II} \cdot e^{-\frac{\delta_{II}^2}{2\delta_{0,II}^2}} \cdot \left(1 + \frac{\delta_I}{\delta_{0,I}}\right) e^{-\frac{\delta_I}{\delta_{0,I}}}, \tag{2}$$

σ in (1) and (2) represents traction and δ separation in the cohesive zone law, while G_C is a critical energy release rate and δ_0 separation at maximum traction. eCZM is actually determined by only two parameters representing cohesive connecting material between the layers. Indices *I* and *II* in (1) and (2) are relating the mode of delamination and the blue parts are expressions of interactivity of the other mode to the actual mode.

The relation between the exponential cohesive zone law and the most used bilinear cohesive lew is depicted in Fig. 2. Both have the same traction maximum at the same separation value δ_0 and have the same G_C represented by the area under CZM curve.

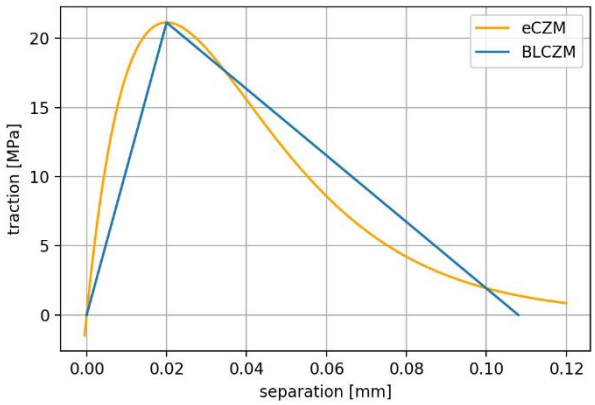

Figure 2. Exponential (eCZM) vs. bi-linear (BLCZM) traction-separation law with equal maximum traction

4. Conclusions

The results indicate that simple facet shell models and displacement compatible cohesive interface models can retain many of the necessary predictive attributes of much more complex three-dimensional models while providing accuracy and the computational efficiency that is necessary for the design of the layered structures.

References

[1] Ribarić, D., Problem-dependent cubic linked interpolation for Mindlin plate four-node quadrilateral finite elements. *Structural engineering and mechanics: An international journal* 59.6: 1071-1094, 2016.

[2] Van den Bosch, M. J., Schreurs, P. J. G., Geers, M. G. D., An improved description of the exponential Xu and Needleman cohesive zone law for mixed-mode decohesion. *Engineering Fracture Mechanics* 73.9: 1220-1234, 2006.

Grouping sensors into preset clusters with a mixed L_2/L_0 norm

Jurica ROŽIĆ*, Marko JOKIĆ*

*University of Zagreb, Faculty of Mechanical Engineering and Naval Architecture, Ivana Lučića 5, HR-10000 Zagreb, Croatia
E-mails: {jurica.rozic,marko.jokic}@fsb.hr

Keywords: Sensor placement optimization, Convex optimization, Mixed L_0/L_2 norm, L_0 norm relaxation, Observer error

1. Introduction

Sensor Placement Optimization (SPO) has been a topic of interest for over four decades now, as it is crucial in many technical fields. While computational power continually evolves, demands evolve as well because SHM is being applied to more complex structures. There is a lot of room for improvement of SPO within SHM alone, including specialized cost functions [1], as encompassing all the relevant data of a real-world problem is often way out of reach, financially and numerically.

We present an algorithm with the ability to force grouping of possible sensor positions from individual physical locations into sensor clusters, and then optimize the number and position of clusters using a series of convex optimizations through an iterative process. This is mostly applicable to SHM systems but can be adapted for use elsewhere. Examples of when might such clustering be beneficial include: to avoid separating axes for multi-axis values like vibration, or limit the number of physical locations with sensor mounts and cabling.

2. Method

Developed algorithm transforms the stiffness, damping and mass matrices from a 2D mass-spring grid into a continuous time state space system and minimizes the observer error to find observer gain values that best approximate it. So far, this is a standard procedure for unrestricted observer design that isn't applicable to restricted designs in general (like this one), but it was proven in [2] that it can be used for SPO in this manner.

The method introduced in this paper is an addition to the cost function that minimizes the observer error: grouping of sensors together into clusters in a way that makes it possible to optimize sensor placement while using either none or all the sensors from each cluster, while still remaining in convex optimization space. This is achieved by grouping columns of the observer gain matrix for desired sensor clusters with an L_2 norm and then inducing sparsity within those clusters. Inducing sparsity with an L_0 norm would be ideal, but that is not a convex problem, so instead an iterative technique (based on [3]) for relaxing an L_0 norm within SPO is modified to work with pre-defined clusters of sensors. Each cluster's value is weighted with its near inverse value from the previous iteration, effectively making each cluster worth either a one or a zero after the iteration process, thus approximating the L_0 norm. The simplified form of the final cost function is:

$$\min \quad \underbrace{\gamma^2}_{\substack{Observer\ error \\ substitute}} + \alpha \sum_{g \in G} \left(\beta_g^{it} \underbrace{\sqrt{\sum_{j \in g} \left(\left(\sum_i \left| L_{ij}^* \right| \right)^2 \right)}}_{Single\ cluster\ L2\ norm} \right), \tag{1}$$

where α is a weight factor that can be used to regulate the number of used possible clusters, β_g^{it} is the weight factor of group (cluster) g on iteration it. L_{ij} is the value of *i-th* column and *j-th* row of the

observer gain matrix **L**. G is the set of all clusters g, and γ^2 is the substitute for the observer system error. Additional constraints for the optimization process are present but not shown here.

3. Results and conclusion

Clustering algorithm was tested and compared to unrestricted, free SPO. Figure 1 compares the results of a grid with springs in 3 directions and two clamped corners:

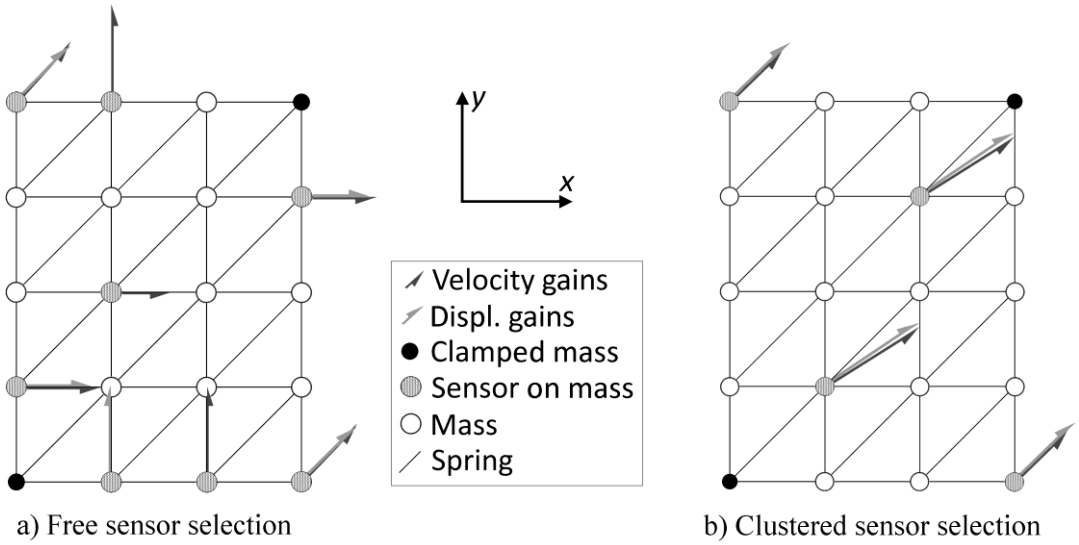

Figure 1. Sensor locations for a 4 x 5 mass-spring grid with two clamped corners

Arrows are a visual representation of the sum of observer gains for each sensor location. They are all in their first quadrant because they are drawn from positive values, but each arrow really consists of the positive value of observer gains for the *x* axis and the analogous part for the *y* axis. Left-head arrow is for displacement, and right-head arrow is for velocity data. All dots are masses, black dots are clamped in space, and thin lines visualize the positions of springs. SPO result for no clustering (free SPO, control) is shown on the left of Figure 1: some masses have utilized all four available sensors (two unclamped corners), but others use either one or two sensors. The result for clustered sensor selection is on the right side of Figure 1: masses with sensors have both *x* and *y* components on both velocity and distance data. Therefore, set goal is achieved: the clustering algorithm forces each utilized sensor location to take advantage of all the possible data and in turn reduce the number of locations containing sensors. Free SPO uses 16 sensors on 8 masses, and clustered SPO uses 16 sensors on 4 masses.

4. Acknowledgements

This work has been supported and co-funded by the European Union through the European Regional Development Fund, Operational Programme "Competitiveness and Cohesion" 2014 – 2020 of the Republic of Croatia, project "Protection of Structural Integrity in Energy and Transport" (Zacjel, KK.01.1.1.04.0056).

References

[1] Barthorpe, R.J., Worden, K., Emerging Trends in Optimal Structural Health Monitoring System Design: From Sensor Placement to System Evaluation. *Journal of Sensor and Actuator Networks*, 3, 31, 2020.

[2] Münz, U., Pfister, M., Wolfrum, P., Sensor and Actuator Placement for Linear Systems Based on H_2 and H_∞ Optimization. *IEEE Transactions on Automatic Control*, 11, 2984-2989, 2014.

[3] Candès, E., Wakin, M. B., Boyd, S. P., Enhancing Sparsity by Reweighted l_1 Minimization. *Journal of Fourier Analysis and Applications*, 5-6, 877-905, 2008.

Predictive modelling of the indentation size effect: gradient-enhanced hardening law combined with Cosserat crystal plasticity model

Maciej Ryś*, Stanisław Stupkiewicz*, Henryk Petryk*

*Institute of Fundamental Technological Research, Polish Academy of Sciences
E-mails: {mrys,sstupkie,hpetryk}@ippt.pan.pl

Keywords: gradient plasticity, crystal plasticity, Cosserat continuum, length scale, 3D model

1. Introduction

Significant research interest is currently focused on size effects in metal plasticity. As a prominent example, the size-dependent behaviour in indentation testing, the indentation size effect (ISE), is observed experimentally and also modelled theoretically [1,2]. However, predictive modelling of the ISE still constitutes a challenge, even if a great variety of gradient plasticity and gradient crystal plasticity models exist in the literature.

In this work, a gradient crystal plasticity model is developed [3] by combining the small-strain Cosserat crystal plasticity model [4] with the concept of the natural length scale that results from the minimal gradient enhancement of crystal plasticity proposed in [5,6]. Our finite-element simulations of spherical indentation in a Cu single crystal show that the model delivers quantitative predictions of the effect of indenter radius on hardness without introducing any adjustable parameters.

2. Gradient-enhanced hardening law and Cosserat crystal plasticity

The Cosserat crystal plasticity framework [4] provides the description of lattice rotation which allows one to determine Nye's dislocation density tensor. Nye's tensor is often used as a measure of geometrically necessary dislocations (GNDs) that are known to be responsible for the size effects in crystals deformed by plastic slip. Following [5,6], the GND-type hardening is here modelled by introducing a single internal length scale. This natural length scale is an explicit function of the flow stress defined as the isotropic part of critical resolved shear stresses. Accordingly, size effects are modelled without introducing any additional material parameters.

In the resulting model, the incompatibility of plastic deformation field is simultaneously included in two different ways. The first one is well known and incorporates the gradient effect of accumulated rotation of the crystallographic lattice on the kinematic hardening in the Cosserat crystal plasticity model. The second way incorporates the effect of the current incompatibility of lattice spin on the total dislocation density rate, resulting in an additional isotropic hardening term in the gradient-enhanced hardening law [5,6].

The model has been implemented in the finite element method. In practical terms, the Cosserat framework is computationally beneficial because it requires only three additional global unknowns in a general 3D problem, as opposed to 9 up to 12 additional unknowns in the micromorphic framework [7] and in the original implementation of the minimal gradient enhancement [6]. Note that two additional parameters that appear in the elastic strain energy of the Cosserat continuum are calibrated such that they do not significantly influence the material response within the range of scales of interest.

3. Size effect in spherical indentation of a Cu single crystal

Finite-element simulations of spherical indentation of a Cu single crystal have been performed in 3D showing that the model is capable of predicting the indentation size effect. The predicted increase of the indentation hardness with decreasing indenter radius shows a good agreement with experimental observations. For instance, Figure 1 shows the dependence of the nominal hardness on the nominal contact radius for the indenter radius R varied between 250 μm and 1.75 μm. Experimental data has been taken from [8]. It is recalled that the gradient-enhanced hardening law does not involve any adjustable parameter, hence the indentation size effect is here predicted rather than fitted.

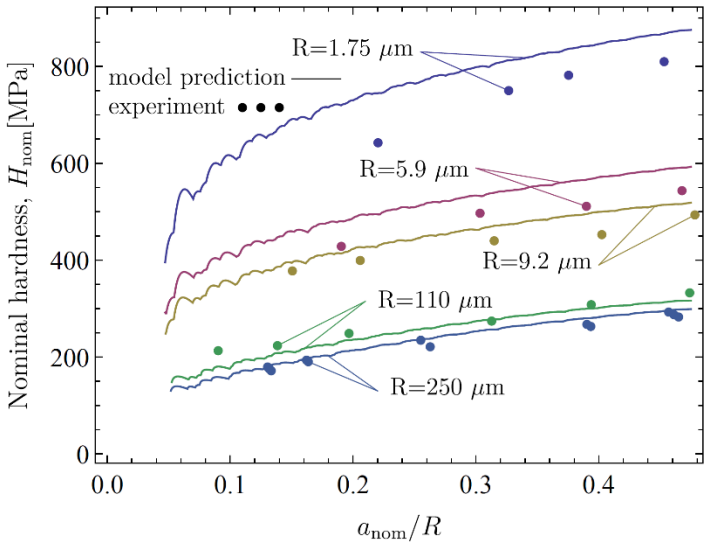

Figure 1. Size effect in spherical indentation: dependence of the nominal hardness on the normalized nominal contact radius.

References

[1] Pharr, G.M., Herbert, E.G., Gao, Y., The indentation size effect: a critical examination of experimental observations and mechanistic interpretations. *Annual Review of Materials Research*, 40, 271-292, 2010.

[2] Nix, W.D., Gao, H., Indentation size effects in crystalline materials: A law for strain gradient plasticity. *Journal of the Mechanics and Physics of Solids*, 46, 411-425, 1998.

[3] Ryś, M., Stupkiewicz, S., Petryk, H., Micropolar regularization of crystal plasticity with the gradient-enhanced incremental hardening law, 2022 (submitted).

[4] Forest, S., Sedlacek, R., Plastic slip distribution in two-phase laminate microstructures: dislocation-based versus generalized continuum approaches, *Philosophical Magazine*, 83, 245-276, 2003.

[5] Petryk, H., Stupkiewicz, S., A minimal gradient-enhancement of the classical continuum theory of crystal plasticity. Part I: The hardening law. *Archives of Mechanics*, 68, 459-485, 2016.

[6] Stupkiewicz, S., Petryk, H., A minimal gradient-enhancement of the classical continuum theory of crystal plasticity. Part II: Size effects. *Archives of Mechanics*, 68, 487-513, 2016.

[7] Ryś, M., Forest, S., Petryk, H., A micromorphic crystal plasticity model with the gradient-enhanced incremental hardening law, *International Journal of Plasticity*, 128, 102655, 2020.

[8] Kucharski, S., Woźniacka, S., Size effect in single crystal copper examined with spherical indenters. *Metallurgical and Materials Transactions A*, 50, 2139-2154, 2019.

Recent advances in experiments and numerical modelling of microfluidic sample delivery systems for femtosecond crystallography

Božidar Šarler[1,2], Saša Bajt[3,4], Grega Belšak[1], Henry Chapman[3,4,5], Jurij Gregorc[1], Krištof Kovačič[1], Ajda Kunavar[1], Khush Bakhat Rana[1], Zlatko Rek[1], Gal Savšek[1], Rizwan Zahoor[1], Bor Zupan[1]

[1] *Laboratory for Fluid Dynamics and Thermodynamics, Faculty of Mechanical Engineering, University of Ljubljana, 1000 Ljubljana, Slovenia*
[2]*Laboratory for Simulation of Materials and Processes, Institute of Metals and Technology, 1000 Ljubljana, Slovenia*
E-mail: {bozidar.sarler,jurij.gregorc,ajda.kunavar,khush.bakhat.rana,zlatko.rek, rizwan.zahoor}@fs.uni-lj.si

[3]*Center for Free-Electron Laser Science CFEL, Deutsches Elektronen-Synchrotron DESY, 22607 Hamburg, Germany*
[4]*The Hamburg Centre for Ultrafast Imaging, 22761 Hamburg, Germany*
[5]*Department of Physics, Universität Hamburg, 22761 Hamburg, Germany*
E-mail: {sasa.bajt,henry.chapman}@desy.de

Keywords: femtosecond crystallography, sample delivery system, microfluidics, numerical modelling, experiments

1. Introduction

X-ray Free-Electron Lasers (XFELs) emit intense femtosecond X-ray pulses and are increasingly being used to obtain diffraction data from hard to crystallize protein crystals. To reconstruct the structure of a protein macromolecule it is necessary to record and process a very large amount of diffraction images [1]. Since protein crystals hit by this intense X-ray beam are destroyed during this process, data collection requires a continuous supply of fresh samples. The microcrystals dispersed in a buffer liquid are typically delivered into an X-ray beam with a gas-focused micro-jet. However, these samples are hard to prepare and usually available in very small quantities. Therefore, one of the goals is to obtain high-quality measurements with the least sample consumption. To detect weak signal from individual protein crystals the signal coming from the surrounding buffer liquid should be minimized. This means the liquid in the jet should be as thin as possible. To avoid any interference from the nozzle the interaction with the X-ray should happen away from the nozzle meaning the jet has to be reasonably long and stable, pointing in the same direction. High repetition rate XFELs also require fast jets so that the interaction region is constantly replenished with fresh samples.

2. Overview of Developments

Our developments based on computer simulations [2] and experimental validation [3] of such micro-fluidic systems for sample delivery as well as sensitivity studies of process parameters [4,5] and material properties [6,7] on their behavior will be presented. The simulation is performed with the finite volume OpenFOAM® code using volume of fluid approach as well as own meshless phase-field formulated one-domain approaches [8,9] and front-tracking boundary meshless technique [10,11]. We will elaborate research and development of some of the new sample delivery systems, including the deposition of the samples on the tape, gas and liquid focusing nozzles [12,13], nozzles producing thin liquid micro-sheets [14], as well

as the design of newly developed convergent-divergent nozzles [15] and nozzles with liquid acceleration in an electric field that create even thinner micro-jets.

3. Acknowledgement

This research was funded by DESY (Hamburg, Germany), a member of the Helmholtz Association HGF, by the Centre of Free Electron Laser (CFEL) under the project: Innovative methods for imaging with the use of x-ray free-electron laser (XFEL) and synchrotron sources: simulation of gas-focused micro-jets, Slovenian Grant Agency (ARRS) within Program Group P2-0162 Multiphase Systems and Project J2-1718 Advanced Meshless Methods, and by the Cluster of Excellence "CUI: Advanced Imaging of Mater" of DFG - EXC 2056 - project ID 390715994. The computations were performed on high-performance computational resources at the Faculty of Mechanical Engineering, University of Ljubljana.

References

[1] Chapman, H. N., Fromme, P., et al., Femtosecond X-Ray Protein Nanocrystallography. *Nature*, 470, 73–77, 2011.

[2] Zahoor, R., Belšak, G., Bajt, S., Šarler, B., Simulation of Liquid Micro-Jet in Free Expanding High Speed Co-Flowing Gas Streams. *Microfluidics and Nanofluidics*, 22, 87, 2018.

[3] Zahoor, R., Knoška, J., Bajt, S., Šarler, B., Experimental and Numerical Investigation of Gas-Focused Liquid Micro-Jet Velocity. *International Journal of Multiphase Flow*, 135, 103530, 2020.

[4] Zahoor, R., Bajt, S., Šarler, B., Influence of Gas Dynamic Virtual Nozzle Geometry on Micro-Jet Characteristics. *International Journal of Multiphase Flow*, 104, 152–165, 2018.

[5] Zahoor, R., Bajt, S., Šarler, B., A Numerical Investigation of Micro-Jet Characteristics in Different Pressure Environments. *International Journal of Hydromechatronics*, 4, 368–383, 2021.

[6] Zahoor, R., Regvar, R., Bajt, S., Šarler, B., A Numerical Study on the Influence of Liquid Properties on Gas-Focused Micro-Jets. *Progress in Computational Fluid Dynamics: International Journal*, 20, 71–83, 2020.

[7] Zahoor, R., Bajt, S., Šarler, B., Numerical Investigation on Influence of Focusing Gas Type on Liquid Micro-Jet Characteristics. *International Journal of Hydromechatronics*, 1, 222–237, 2018.

[8] Talat, N., Mavrič, B., Hatić, V., Bajt, S., Šarler, B., Phase Field Simulation of Rayleigh–Taylor Instability with a Meshless Method. *Engineering Analysis with Boundary Elements*, 87, 78–89, 2018.

[9] Talat, N., Mavrič, B., Belšak, G., Hatić, V., Bajt, S., Šarler, B., Development of Meshless Phase Field Method for Two-Phase Flow. *International Journal of Multiphase Flow*, 108, 169–180, 2018.

[10] Wang, K., Weng, S., Zahoor, R., Li, M., Šarler, B., Method of Regularized Sources for Axisymmetric Stokes Flow Problems, *International Journal of Numerical Methods in Heat & Fluid Flow*, 26, 1226-1239, 2016.

[11] Rek, Z., Šarler, B., The Method of Fundamental Solutions for the Stokes Flow with the Subdomain Technique. *Engineering Analysis with Boundary Elements*, 128, 80–89, 2021.

[12] Oberthuer, D., Knoška, J., et al., Double-Flow Focused Liquid Injector for Efficient Serial Femtosecond Crystallography. *Scientific Reports*, 7, 44628, 2017.

[13] Belšak, G., Bajt, S., Šarler, B., Numerical Study of the Micro-Jet Formation in Double Flow Focusing Nozzle Geometry Using Different Water-Alcohol Solutions. *Materials*, 14, 3614, 2021.

[14] Belšak, G., Bajt, S., Šarler, B., Computational Modeling and Simulation of Gas Focused Liquid Micro-Sheets. *International Journal of Multiphase Flow*, 140, 103666, 2021.

[15] Šarler, B., Zahoor, R., Bajt, S., Alternative Geometric Arrangements of the Nozzle Outlet Orifice for Liquid Micro-Jet Focusing in Gas Dynamic Virtual Nozzles. *Materials*, 14, 1572, 2021.

How to improve the numerical integration in peridynamic models

Francesco Scabbia*, Mirco Zaccariotto+, Ugo Galvanetto+

*Center of Studies and Activities for Space "G. Colombo", University of Padova, Padova, Italy
E-mail: francesco.scabbia@phd.unipd.it

+Department of Industrial Engineering, University of Padova, Padova, Italy
E-mails: {mirco.zaccariotto,ugo.galvanetto}@unipd.it

Keywords: Peridynamics, numerical integration, cube-sphere intersection, quadrature weights, accurate results

1. Introduction

Peridynamics is a non-local continuum theory of mechanics which was proposed to model spontaneous crack initiation and propagation in solid bodies [1]. The peridynamic formulation is based on integral equations, such that the interactions between material points, the so-called "bonds", exist only within a finite cut-off distance δ. The peridynamic equation of motion is given as:

$$\rho(\boldsymbol{x})\ddot{\boldsymbol{u}}(\boldsymbol{x},t) = \int_{H_{\boldsymbol{x}}} \mathbf{f}(\boldsymbol{x},\boldsymbol{x}',t)\,\mathrm{d}V_{\boldsymbol{x}'} + \boldsymbol{b}(\boldsymbol{x},t)\,, \tag{1}$$

where ρ is the density, $\ddot{\boldsymbol{u}}$ is the acceleration, $\mathbf{f}$ is the force of the bond between the interacting points $\boldsymbol{x}$ and $\boldsymbol{x}'$, $H_{\boldsymbol{x}}$ is the neighborhood of point $\boldsymbol{x}$, $dV_{\boldsymbol{x}'}$ is the differential volume associated to point $\boldsymbol{x}'$ and $\boldsymbol{b}$ is the external force density. Note that the neighborhood $H_{\boldsymbol{x}}$ is the set of points with which point $\boldsymbol{x}$ interacts, namely the sphere centered in $\boldsymbol{x}$ with a radius δ. However, the neighborhoods of the points closest to the boundary of the body are incomplete, thus there is an undesired stiffness fluctuation in those regions. This issue can be solved by using the fictitious node method which completes the partial neighborhoods near the boundary of the body [2,3].

Peridynamic equations are solved by means of numerical integration: the body is discretized with a meshfree method in a regular grid of nodes, each representative of a cubic cell with edges of length h, where h is the uniform grid spacing. Therefore, the discretized equation of motion of a node i is given as:

$$\rho(\boldsymbol{x}_i)\ddot{\boldsymbol{u}}(\boldsymbol{x}_i,t) = \sum_{j\in H_i} \mathbf{f}(\boldsymbol{x}_i,\boldsymbol{x}_j,t)\beta_{ij}\Delta V + \boldsymbol{b}(\boldsymbol{x}_i,t)\,, \tag{2}$$

where $\Delta V = h^3$ is the volume of the cells and β is the quadrature weight of the bond connecting nodes i and j. The value of β is determined as the fraction of cell volume lying within the neighborhood, as shown in Figure 1. The more correctly β is computed, the more accurate the numerical results are [4,5].

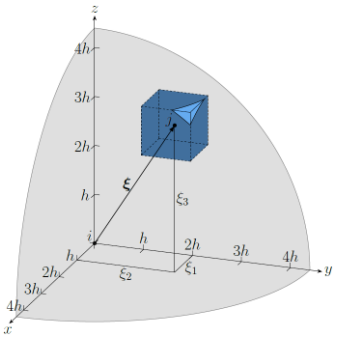

Figure 1. A bond in which node j has a quadrature weight $\beta \approx 0.97$.

2. Exact computation of the quadrature weights

A bond between nodes i and j is identified by the vector

$$\boldsymbol{\xi} = \boldsymbol{x}_j - \boldsymbol{x}_i \,. \tag{3}$$

For the computation of β, we can consider only bonds with $\xi_3 \geq \xi_2 \geq \xi_1 \geq 0$, where ξ_1, ξ_2 and ξ_3 are the 3 components of $\boldsymbol{\xi}$, since for instance bonds (ξ_1, ξ_2, ξ_3) and $(\xi_1, \xi_2, -\xi_3)$ have the same quadrature weight for symmetry reasons. The integral to compute the quadrature weights is given as:

$$\beta = \frac{1}{h^3} \int_{x_1}^{\min\left(x_2, \sqrt{\delta^2 - {y_1}^2 - {z_1}^2}\right)} \int_{y_1}^{\min\left(y_2, \sqrt{\delta^2 - x^2 - {z_1}^2}\right)} \int_{z_1}^{\min\left(z_2, \sqrt{\delta^2 - x^2 - y^2}\right)} \mathrm{d}z \, \mathrm{d}y \, \mathrm{d}x \,, \tag{4}$$

where $x_1 = \xi_1 - h/2$, $x_2 = \xi_1 + h/2$, $y_1 = \xi_2 - h/2$, $y_2 = \xi_2 + h/2$, $z_1 = \xi_3 - h/2$, $z_2 = \xi_3 + h/2$ are the coordinates of the cell faces.

The integral in Equation 4 should be split into a sum of integrals over domains in which the minimum functions have the same values. This procedure leads to 10 different cases of cube-sphere intersections, as shown in Figure 2. Then, the split integrals can be solved exactly: some of the integrals have their analytical solutions, whereas some others do not have an explicit solution. In the latter case, a Taylor series expansion of the integrand is performed, and the resulting polynomial can be integrated. If the truncation order of the Taylor series is high enough, the errors arising from this approximation can be kept under machine precision.

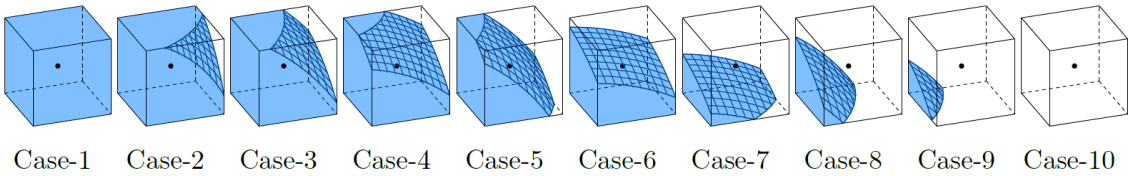

Figure 2. Possible cases of cell-neighborhood intersections. The symmetric intersections are not shown here because they can be reduced to one of the above cases by considering only one half or one fourth of the integration domain and multiplying the result by 2 or 4. For instance, the spherical cap can be reduced to Case-9 by considering only one-fourth of the cube-sphere intersection.

3. Conclusions

The accurate numerical integration in peridynamic meshfree uniform grids has been an issue for years because it ensues the complex computation of several cube-sphere intersection volumes. We proposed an innovative method to exactly compute the cube sphere intersections for any radius δ of the neighborhood, any grid spacing h and any position of the cell within the neighborhood.

Acknowledgements
The authors would like to acknowledge the support they received from the Italian Ministry of University and Research under the PRIN 2017 research project "DEVISU" (2017ZX9X4K) and from University of Padova under the research projects BIRD2018 NR.183703/18 and BIRD2020 NR.202824/20.

References

[1] Silling, S.A., Epton, M., Weckner, O., Xu, J., Askari, E., Peridynamic states and constitutive modeling. *Journal of Elasticity*, 88(2), 151-184, 2007.

[2] Scabbia, F., Zaccariotto, M., Galvanetto, U., A novel and effective way to impose boundary conditions and to mitigate the surface effect in state-based Peridynamics. *International Journal of Numerical Methods in Engineering*, 2021.

[3] Scabbia, F., Zaccariotto, M., Galvanetto, U., A new method based on Taylor expansion and nearest-node strategy to impose Dirichlet and Neumann boundary conditions in ordinary state-based Peridynamics. *Computational mechanics*, 2022.

[4] Seleson, P., Improved one-point quadrature algorithms for two-dimensional peridynamic models based on analytical computations. *Computer Methods in Applied Mechanics and Engineering*, 282, 184-217, 2014.

[5] Scabbia, F., Zaccariotto, M., Galvanetto, U., Exact computation of the quadrature weights in 3D peridynamics. *Submitted*.

Multiple-support excitation of slender long-span structures: numerical investigation and experimental validation

Bepo Schira*, Paolo Fabijan*, Gordan Jelenić+, Nina Čeh+

University of Rijeka, Faculty of Civil Engineering, Radmile Matejčić 3, 51000 Rijeka
*E-mails: *{bschira, pfabijan}@student.uniri.hr +{gordan.jelenic,nina.ceh}@uniri.hr*

Keywords: finite element method, structural dynamics, earthquake, beam, support excitation

1. Introduction

Earthquake loading might represent the worst loading condition the structure will experience in its design life. If not accounted for it properly, the loading might be devastating for the structure and people using it, as recently witnessed during the devastating earthquakes in north-western Croatia. However, overestimating the loading might lead to very redundant structures, an unnecessary waste of resources, with negative implications to sustainability. As demonstrated in previous research, if a long-span structure's supports are excited with the same function, but with a time delay, the resulting structure loading will be less severe than if the same excitation is applied simultaneously at all supports. This is particularly interesting when it comes to long-span bridges, where accounting for the phase shift could noticeably reduce the demand on the structure.

This work presents results obtained by a numerical procedure as well as an experimental program on a simply supported beam model (as shown in Figure 1). In the numerical procedure 3D beam Euler-Bernoulli and Timoshenko finite elements are used for determining the stiffness matrix, while both lumped and consistent mass matrices were implemented. The damping matrix is based on the Rayleigh damping theory, while Newmark's method was used for direct integration. The experimental program is conducted on a simply supported beam model attached to two seismic platforms used to simulate synchronous and asynchronous multiple-support excitation. Support excitation in the transversal horizontal direction is considered, while the vertical and longitudinal horizontal excitation are neglected for this purpose. Excitation function and response of the model are monitored by a contactless optical measuring system based on digital image correlation procedure.

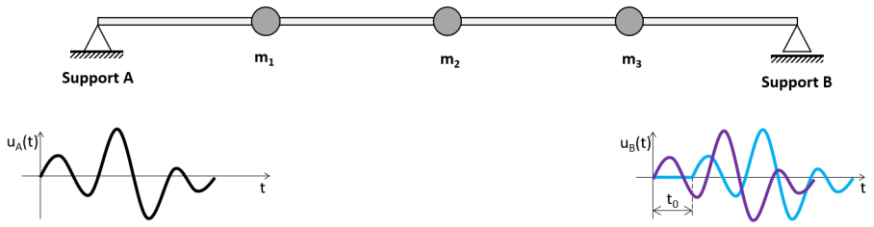

Figure 1. Scheme of the model with 3 added masses

3. Numerical algorithm

A numerical algorithm has been developed to solve the following equation of motion governing the linear dynamic response of finite elements [1]:

$$\boldsymbol{M\ddot{U} + C\dot{U} + KU = P}_{eff} \qquad (1)$$

where $\boldsymbol{M}$, $\boldsymbol{C}$ and $\boldsymbol{K}$ are the mass, damping and stiffness matrices, $\ddot{\boldsymbol{U}}$, $\dot{\boldsymbol{U}}$ and $\boldsymbol{U}$ are the acceleration, velocity and displacement vectors, while $\boldsymbol{P}_{eff}$ is the vector of externally applied loads for the finite element model of the structure, defined as $\boldsymbol{P}_{eff} = -\boldsymbol{M\iota\ddot{u}_g}(t)$ for multiple-support excitation system, where $\boldsymbol{\iota}$ is the influence matrix, as given in [2]. The numerical algorithm has been implemented in the programming language Python.

The finite element formulation of 3D beam elements is used, where Both Euler-Bernoulli and Timoshenko beam elements are implemented to assemble the structure stiffness matrix $\boldsymbol{K}$. Both lumped and continuous mass matrices have been implemented. Reyleigh damping has been assumed [1, 2]. The code has been validated against a commercial finite-element in static analyses.

Equation (1) has been solved using Newmark's direct time-integration method as described in [1]. Numerical results have been compared with the experimental results presented in [3].

4. Experimental programme

An experimental programme has been carried out in order to get a better insight into dynamic response of simply supported beam models subject to synchronous and asynchronous multiple-support excitation. The setup consists of an aluminium beam with 3 added weights, attached to two seismic platforms via aluminium supports and an optical system for measurement of 3D displacements. Two Quanser ST-III seismic platforms are used. The specimen has been prepared for the measurement by sticking round markers at positions of interest and photographed throughout the experiment via a set of high-speed cameras from GOM Aramis 4M optical measuring system. The series of photographs obtained has been post-processed using digital image correlation approach, which enabled calculation of the displacements of markers (from which velocities and acceleration are computed via time differentiation).

Thirty-three experiments have been conducted, with sinusoidal excitation as well as excitation from historic earthquake data (Northridge 1994, El Centro 1940 and Kobe 1995). The beam model has been subjected to each excitation function both synchronously (the excitation started at the same time at both platforms) and with a delay of 0.5 and 1 second for support B.

5. Conclusions

The described numerical approach and experimental programme provide a useful insight into the dynamic response of long structures to seismic base excitation without and with a given delay between excitation of the supports. The contribution of governing modes of oscillation changes with respect to the delay between the excitation of the supports. The experimentally obtained results show that some delay conditions result in a significant decrease of the 1st (symmetric) mode of oscillation, while other conditions can amplify the 2nd (asymmetric) mode. The described numerical procedure, once properly validated against experimentally obtained data, will enable running multiple simulations with variations in static system and material and geometry parameters of the model, as well as variation in initial conditions, and excitation functions of the supports. Furthermore, such model can be used to simulate the behaviour of longer real-life structures with more than two supports.

Acknowledgements

This research is a part of bilateral project "Experimental study of bridge structures considering the asymmetric effect under multiple support excitation" between Faculty of Civil Engineering in Rijeka (Croatia) and Dalian University of Technology (China). Experimental model has been partially financed through University of Rijeka student scientific fund Sizif within the project N-SZF 2/2021.

References

[1] Bathe, K.-J., *Finite Element Procedures*. Prentice Hall, New Jersey (USA), 1996.

[2] Chopra, A. K.; Dynamics of structures: Theory and applications to earthquake engineering, 2nd edition; 1995.

[3] Fabijan, P., Guy de Chamisso, Q., Ceh, N., Eksperimentalno ispitivanje dinamickog odziva dugacke gredne konstrukcije na visestruku pobudu oslonaca. 11. Susret Hrvatskog drustva za mehaniku, 16-17 rujna 2021, Rijeka.

Acoustic signal analysis using cross-correlation method in experiments with different sound source

Damir Sedlar*, Željan Lozina*, Andela Bartulovic*

* *University of Split, Faculty of Electrical Engineering, Mechanical Engineering and Naval Architecture, Rudjera Boskovica 32, 21000 Split, Croatia*
E-mails: { dsedlar, lozina, abartulo }@fesb.hr

Keywords: cross-correlation, MLS, signal detection, long pipe

1. Introduction

Acoustic signal detection and analysis is problem of special interest for many years. The reason for this interest is its usefulness and applicability in different field such as leak detection, underwater communication, medical examinations, architectural acoustics, etc. [1][2]. The analytical solutions for problem of the propagation of sound waves are based on basic governing equation or approximations of the Kirchhoff solution [3]. Numerical solutions are commonly based on some type of finite element methods. This paper concentrates on a practical example in experimental acoustic signal detection, using cross-correlation method.

2. Application of cross-correlation

Cross-correlation is a measure of similarity between two waveforms. It is obtained as a shifted dot product between two signals *x* and *y*

$$(x * y)[n] = \sum_{m=1}^{N} x[m]y[m+n] \, . \tag{1}$$

The auto-correlation is the cross-correlation of a signal with itself.

In this paper, the propagation of an acoustic signal through a long pipe was measured. The excitation signal is generated in two ways, the first is a clap and the second is Maximum Length Sequence (MLS). MLS is a pseudo random signal consisting of the values 1 and -1. The use of a MLS signal in acoustics is well established, e.g. for measuring impulse responses [4]. The pipe used is 24 meters long, with inside diameter 28 millimeters and wall thickness of 3 millimeters. An obstacle in the form of rockwool 10 centimeters thick was placed in the middle of the pipe. One microphone is placed at the beginning of the tube (at the end where excitation signal is generated).

The intent of this work is to observe the feedback, reflected, wave from the obstacle in measured signal. Knowing the exact location of the microphone and the obstacle in the tube, it is possible to predict where the reflected wave is expected in the measured signal. Figure 1 shows the measured signal: a) when the MLS excitation was applied, and b) when the clamp excitation was applied. On the figure 1b) with a red vertical line is marked the place of the expected reflected wave. As can be noticed at this point the measured signal has oscillations. Naturally, nothing can be noticed on the measured signal when the MLS excitation is applied., figure 1a).

Further, auto-correlation was applied to the measured signal. Since the signal contains the initial wave as well as the reflected wave, by applying correlation, it is possible to find, spotlight, the moment when the reflected wave passes by the sensor, figure 2. The expected moment of the reflected wave is marked with a red and green vertical line, and it coincides very well with the experimental measurement using auto-correlation.

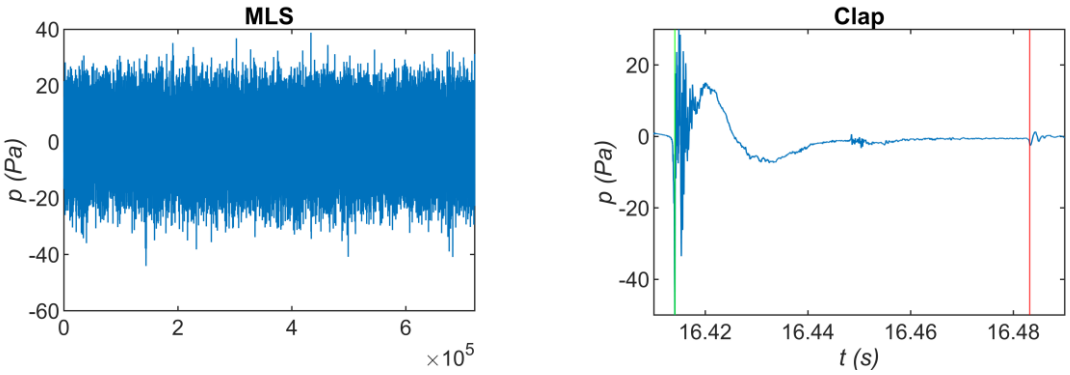

a) b)

Figure 1. Response to different types of source

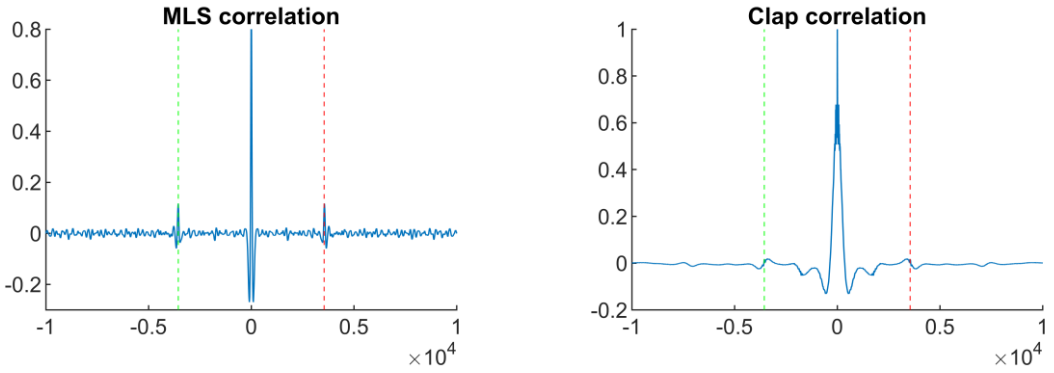

a) b)

Figure 2. Cross-correlation for different types of source

After applying auto-correlation, the MLS excitation perceptible shows the lag of the reflected wave relative to the initial wave.

3. Conclusions

It has been shown that by applying auto-correlation one can easily point out, find, the point of passage of a reflected wave relative to the initial wave. The reflected wave is detected at a large distance after rebound off a highly absorbent obstacle. It has been experimentally confirmed that the application of MLS excitation gives clearer results than excitation by clap.

References

[1] Hafezi, M.M, Mirhosseini, M, Application of Cross-Correlation in Pipe Condition Assessment and Leak Detection; Using Transient Pressure and Acoustic Waves, Resources and Environment, 5(5), 159-166, 2015.

[2] Adrian-Martinez, S., Bou-Cabo, M., Felis, I., Llorens, C.D., Martinez-Mora, J.A., Saldana, M., Ardid, M., Acoustic Signal Detection Through the Cross-Correlation Method in Experiments with Different Signal to Noise Ratio and Reverberation Conditions. In: Garcia Pineda, M., Lloret, J., Papavassiliou, S., Ruehrup, S., Westphall, C. (eds) Ad-hoc Networks and Wireless, 2015.

[3] Tijdeman, H., On the propagation of sound waves in cylindrical tubes. Journal of Sound and Vibration, 39, 1-33, 1975.

[4] Rife, D.D., Vanderkooy J., Transfer-function measurement with maximum length sequences. Journal of the Audio Engineering Society, 37(6), 419-444, 1989.

Experimental validation of a novel numerical model for rate-dependent mode-I delamination of adhesive joints

Leo Škec*, Giulio Alfano+

*University of Rijeka, Faculty of Civil Engineering
Radmile Matejčić 3, 51000 Rijeka, Croatia
E-mail: leo.skec@uniri.hr

+Brunel University London, Department of Mechanical and Aerospace Engineering
Kingston Lane, Uxbridge UB8 3PH, UK
E-mail: giulio.alfano@brunel.ac.uk

Keywords: delamination, cohesive-zone model, finite-element analysis, rate-dependent behaviour, DCB experiment

1. Introduction

Adhesive joints are nowadays used in a very wide ranging variety of structural engineering applications, because of the associated reduction of stress concentrations and their suitability for joining lightweight components. Although a number of procedures are available to characterise the interface fracture resistance in such structures for quasi-static problems, the increasing use of adhesive bonding in the automotive and aerospace sectors makes it particularly important to evaluate the rate dependence of the fracture resistance, because of the importance of modelling these structures under dynamic loading, and in particular during impact loading.

In this paper we present a numerical and experimental study of the rate dependence of the failure of adhesive joints based on DCB tests. For the experimental part, we tested 24 adhesive joints made of aluminium Al 2082-T6 bonded with the epoxy adhesive Araldite® 2015, in a DCB configuration with a prescribed cross-head displacement rate ranging between 0.1 to 5000 mm/min.

2. Experimental results

The average load-displacement curves for each speed shown in Figure 1 clearly show that the adhesive has shown a considerable amount of rate dependence, because the fracture resistance of the adhesive (and therefore the overall bearing capacity of the adhesive joint) obviously increases with the load-line displacement speed. However, it can be noticed that the two lowest speeds (namely 0.1 and 1 mm/min) essentially overlap, which suggests that the slow limit (i.e. the limit below which the rate dependence of the adhesive is negligible) has been reached. In order to characterise the behaviour when the fast limit is approached more tests would be needed, which could not be conducted in this project because the maximum speed of the testing machine available was 5000 mm/min.

3. Numerical model

The numerical simulations use a previously proposed cohesive-zone model (CZM) based on fractional viscoelasticity [1] and a novel finite element combining a Timoshenko beam and an interface element. The advantages of using beam finite elements for modelling DCB specimens have been reported in [2,3]. The model has 7 parameters in total and a simple procedure for their identification is proposed. The parameters defining the slow and fast limit can be easily identified using the previously proposed algorithm [4] implemented in software *DCB PAR*. A simple procedure for identifying the two remaining rate-dependent parameters is also proposed.

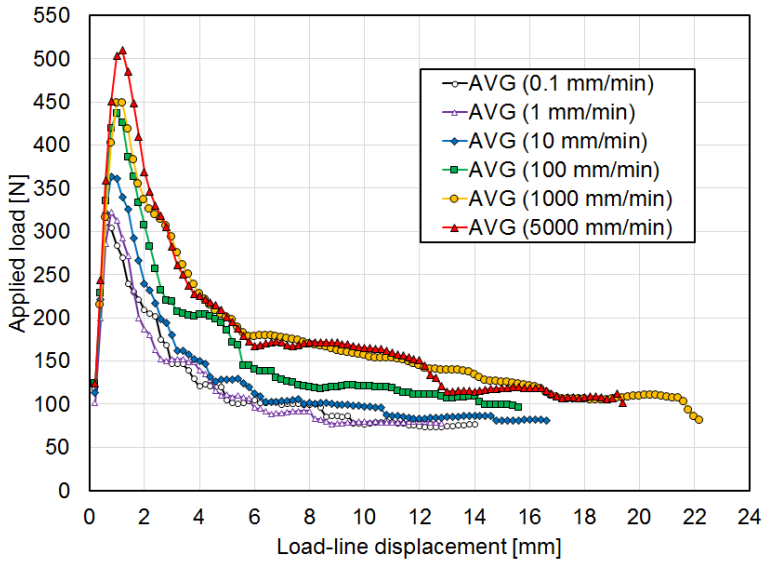

Figure 1. Average experimental load-displacement curves for DCB tests performed at different speeds

4. Results and conclusions

The comparison between experimental and numerical results confirms the capability of the CZM of capturing the experimental response, also for a glassy polymer, over a wide range of speeds with the same set of 7 parameters, only two of which are related to the model rate dependence. This is unlike models based on experimental kernels, which require a much larger number of parameters.

We also present an effective procedure to determine the `fracture resistance-crack growth' curve without the need for measuring the crack length and the crack speed, but only by closed-form post-processing of the measurements of the load and the displacement, immediately available at the end of the tests.

Although the curve found is sigmoidal, we do not think we have sufficient evidence to exclude that at higher speeds than those tested in this work the motonicity could be lost and the fracture resistance could decrease. This would in turn result in some sort of `bell shape' of the curve, such as the results theoretically obtained in [5] when damage is assumed to be driven by the entire free energy. This final observation suggests that more tests should be done to fully characterise the behaviour of the adhesive, which will be the objective of future work.

References

[1] Musto, M., Alfano, G., A fractional rate-dependent cohesive-zone model, *International Journal for Numerical Methods in Engineering*, 103, 313–341, 2015.

[2] Škec, L., Jelenić, G., Lustig, N., Mixed-mode delamination in 2D layered beam finite elements, *International Journal for Numerical Methods in Engineering*, 104(8), 767-788, 2015.

[3] Škec, L., Alfano, G., Jelenić, G., Enhanced simple beam theory for characterising mode-I fracture resistance via a double cantilever beam test, *Composites Part B*, 167, 250–262, 2019.

[4] Škec, L., Identification of parameters of a bi-linear cohesive-zone model using analytical solutions for mode-I delamination, *Engineering Fracture Mechanics*, 214, 558–577, 2019.

[5] Alfano, G., Musto, M., Thermodynamic Derivation and Damage Evolution for a Fractional Cohesive Zone Model, *Journal of Engineering Mechanics*, 143(7), D4017001, 2017.

Applicability of Michell Wave Resistance Theory During Preliminary Design of Marine Vehicles

Renato Skejic

Dept. of Ships and Ocean Structures, SINTEF Ocean, Trondheim, Norway
E-mails: Renato.Skejic@sintef.no

Keywords: Design of marine vehicles, Michell wave resistance theory with viscous effects, Calm water, Deep water, Shallow/Finite water depth

1. Introduction

One of the main parameters during the design of the marine vehicles in the preliminary stages requires knowledge of the vehicle resistance in calm water at the interval of the design forward speeds. In situations when the vessel operational profiles take place in the coastal and inland areas often restricted by the water depth, the variable water depth effect (variable bathymetry of the sea bottom) has an important role upon the estimation of wave making resistance.

In this study an investigation of the wave making resistance in both; deep and shallow/finite water depth scenarios is carried out within the framework of the Michell thin ship theory. The theory has been applied on several marine vehicles designs where it has been demonstrated that the successful estimation of the wave making resistance parameter can be obtained in comparison to more complex theoretical methods such are for instance BEM or CFD.

2. Applicability of wave making resistance models

The estimation of the wave resistance R_W in calm water within the framework of the potential fluid flow theory is carried out based on the foundation of ordinary and modified Michell thin-ship theory with inclusion of the viscous effects by adopting the approach given by [1] and [2], and [3] and [4], respectively. In particular, the deep water, i.e., infinite water depth and shallow/finite water depth effects are investigated by considering different type of the floating type of bodies (mono- and multihulls) and the submarine like, type of bodies operating in a vicinity of calm free surface.

Figure 1 shows predicted nondimensional wave making resistance C_W $|R_W|/(0.5\rho U^2 S)$ in deep and shallow/finite water depth for the interval of water depth to ship length ratios $|h|/L \in [0.1, 0.6]$. The calculated results for $|h|/L = 0.1$ are compared with [5] results (black dots) showing that excellent agreement is obtained. As can be normally expected the increase of C_W in the shallow/finite water depth scenario is a direct consequence of the ship generated wave system (for more details see also [6]).

Second example given in Figure 2, shows estimation of the nondimensional wave making resistance C_W for two different submarine like bodies designs, namely the DARPA SUBOFF and Joubert BB2 submarine. As can be seen from the figure, for both parts a) and b), the Michell model although in qualitative agreement with the more complex, and sophisticated methods [7] and [8] it significantly underestimates the wave resistance in the interval of higher Froude numbers Fn (around and above 0.2). The viscosity effects in the ordinary Michel wave making resistance model are investigated on Joubert BB2 bare hull submarine including deck, see part b) of Figure 2.

As can be observed from the figure the ordinary Michell wave resistance curve (solid black line) is significantly damped due to presence of the viscosity effects in the range of Froude numbers $Fn > 0.2$. For the lower Froude numbers, the situation concerning the behavior of the wave making resistance curve is inversed, i.e., the wave making resistance is increasing and the obtained results for both submarines are more in agreement with the steady CFD VoF method (and experimentally) obtained results.

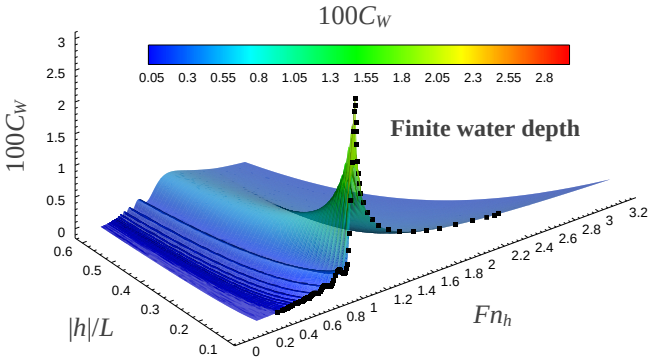

Figure 1. Nondimensional wave making resistance $C_W = |R_W|/(0.5\rho U^2 S)$ for Wigley hull in deep water and shallow/finite water depths.

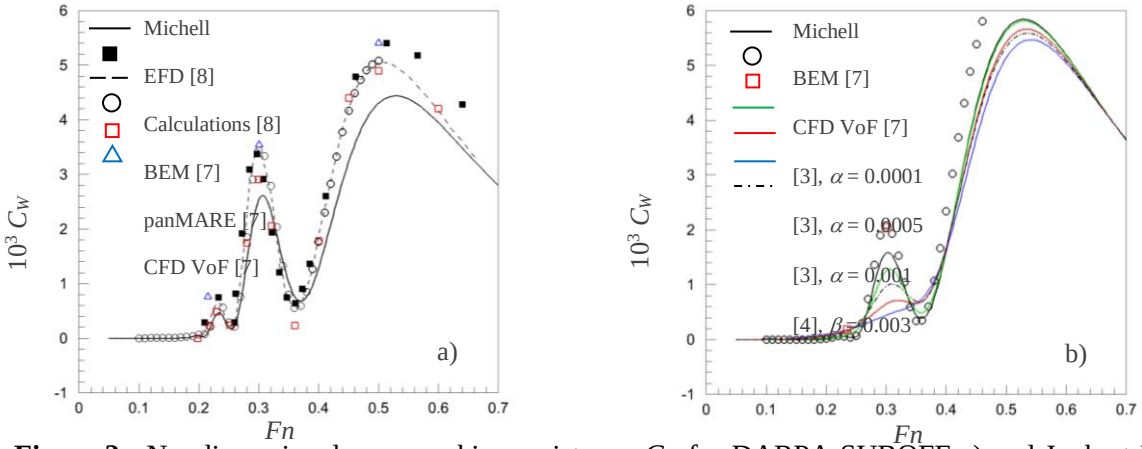

Figure 2. Nondimensional wave making resistance C_W for DARPA SUBOFF a) and Joubert BB2 submarine b) at the submergence to maximum height (of submarine) ratio $d/H_h = 1.1$.

3. Concluding remarks

Present work investigates application feasibility of the ordinary and modified (viscosity effects included) Michell thin ship wave making resistance theory. By doing so, the wave making resistance has been studied on a preselected different marine vehicles design (the ships and the submarine like bodies) by considering the deep water and the shallow/finite depth water effects.

Based on the satisfactory agreement with the publicly available results, the presented theory can be utilized in the optimization process of the hull form designs of marine vehicles as seen from the perspective of minimized wave making resistance in calm water.

References

[1] Yeung, R. W. and Wan, H., Multi-Hull and Surface-Effect Ship Configuration Design: A Framework for Powering Minimization. *Journal of Offshore Mechanics and Arctic Engineering*, 130(3), 2008.

[2] Zhu, Y., Wu, H., Ma, C., He, J., Li, W., Wan, D. and Noblesse, F., Michell and Hogner models of far-field ship waves. *Applied Ocean Research*, 68 (2017) 194–203, 2017.

[3] Tuck, E. O., The effect of a surface layer of viscous fluid on the wave resistance of a thin ship. *Journal of Ship Research*, Vol. 18, No. 4, pp. 265–271, 1974.

[4] Lazauskas, L., Resistance, Wave-Making and Wave-Decay of Thin Ships, with Emphasis on the Effects of Viscosity. PhD Thesis, University of Adelaide, Adelaide, Australia, 2009.

[5] Yang, Q., Faltinsen, O. M., Zhao, R., Green Function of Steady Motion in Finite Water Depth. *Journal of Ship Research*, Vol. 50, No. 2, pp. 120–137, 2006.

[6] Faltinsen, O. M., *Hydrodynamics of High–Speed Marine Vehicles.* Cambridge University Press, 2005.

[7] Skejic, R., Daum, S. and Greve, M., On the Added Resistance of Underwater Vehicles in Close Proximity to Regular Waves. *WARSHIP 2017: Naval submarines and UUV's*, Bath, UK. June 2017.

[8] Gourlay, T. and Dawson, E., A Havelock Source Panel Method for Near-Surface Submarines., *Journal of Marine Science and Application*, Volume 14, issue 3, September 2015.

Aerodynamic Interference of Tall Buildings subjected to the Atmospheric Boundary Layer Flow

Petar Škvorc*, Petar Melnjak*, Hrvoje Kozmar*, Andrea Giachetti+, Gianni Bartoli+

*Faculty of Mechanical Engineering and Naval Architecture, University of Zagreb, Ivana Lučića 5, 10000 Zagreb, Croatia
E-mails: petar.skvorc@fsb.hr, petar.melnjak@stud.fsb.hr, hrvoje.kozmar@fsb.hr
+Department of Civil and Environmental Engineering, University of Florence, Via di Santa Marta 3, 50139 Florence, Italy
E-mails: andrea.giachetti@unifi.it, gianni.bartoli@unifi.it

Keywords: Tall buildings, aerodynamic interference, wind loads, wind-tunnel experiments

1. Introduction

Tall buildings are particularly sensitive to wind loads which can result in excessive building motion. In densely populated areas, the assessment of wind loads on buildings can be an issue because of the interference effects between neighboring buildings. Complex airflows in urban areas can result in strong local pressures on engineering infrastructure. This can have an adverse effect on building façades, potentially causing cladding failure. In this work, the interference effect of two high-rise buildings was investigated regarding integral wind loads and pressure distribution on the building situated at various distances in the wake of another building of equal dimensions.

2. Experimental setup

Experiments were performed in the CRIACIV (Inter-University Research Centre on Building Aerodynamics and Wind Engineering) boundary layer wind tunnel at the University of Florence, Italy. A model of a suburban-type atmospheric boundary layer (ABL) was generated in the wind tunnel. The ABL model corresponds to the international standard EN1991-1-4:2005 [1] category III regarding the mean wind velocity, turbulence intensity and integral turbulence length scale profiles. The simulation length scale of the model ABL was 1:400. The 500 mm high building model has a square base with the edge length D = 100 mm, thus the geometric aspect ratio is 1:1:5, with more details provided in [2]. The dummy building model of the same dimensions was placed upstream of the studied building model to create aerodynamic interference. Four experimental configurations were analyzed, where the dummy building model was situated at 2D, 3D, 4D and 5D upstream of the studied building model; these distances refer to the spacing between the leeward surface of the upstream building model and the windward surface of the downstream building model. Integral aerodynamic loads were measured using a high-frequency force balance (time record length 100 s, sampling rate 2000 Hz), while pressure sensors were used for surface pressure measurements (time record length 100 s, sampling rate 500 Hz) on the building model. The mean freestream flow velocity and dynamic pressure at the building model height were used for normalization purposes.

3. Results and discussion

The studied building model experiences substantial sheltering effects caused by the dummy building model situated upstream in all experiments. The integral mean along-wind moment coefficient C_{MD}, calculated using the integral mean along-wind moment, freestream velocity at the model height, dynamic pressure and windward surface area of the building model, in the 2D configuration is halved compared to the 5D experiment. The mean C_{MD} is lower at smaller spacing of building models and approaches the C_{MD} experienced by the unsheltered building model, Figure 1.

The pressure distributions on the windward façade of the sheltered building model are crucial in the interpretation of the results obtained with the force measurements. For instance, as shown in Figure 2, the mean pressure coefficients (C_p) on the studied building model in the 2D configuration

are nearly zero for the most of its surface area, while the upper portion experiences a slightly positive pressure, indicating the dominant role of the interaction with the wake of the dummy building model placed upstream.

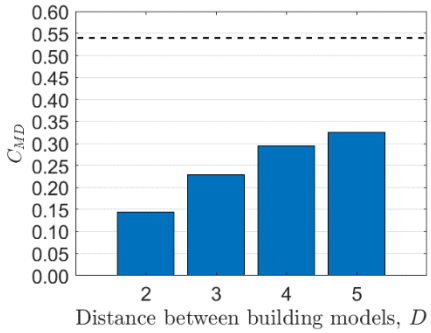

Figure 19. Mean integral along-wind moment coefficient C_{MD} at various distances between building models; horizontal dashed line refers to the mean C_{MD} of the stand-alone building model

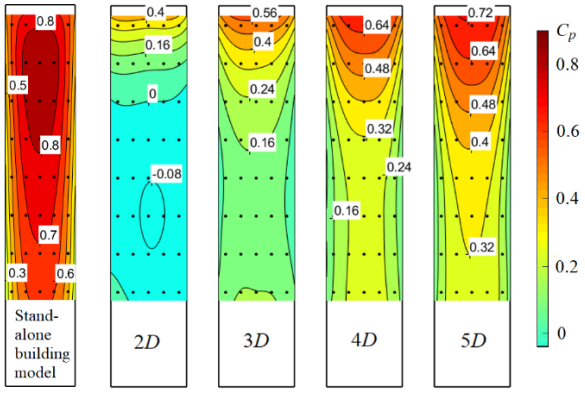

Figure 20. Mean surface pressure coefficient C_p distribution on the windward surface of the studied building model

4. Conclusions

This experimental study provides insight into the effect of sheltering of two equally sized tall building models subjected to turbulent flow. It was performed by measuring integral aerodynamic loads on the tall building model placed downstream of the dummy building model by using high-frequency force balance and pressure sensors. The along-wind moment and respective pressure coefficients on the windward surface of the sheltered building model substantially decrease when the distance between the two building models decreases.

Acknowledgements

The work of doctoral student Petar Škvorc has been fully supported by the "Young researchers' career development project – training of doctoral students" of the Croatian Science Foundation.

References

[1] EN1991-1-4:2005, (2005), Eurocode 1: Actions on structures – General actions, Part 1-4: Wind actions. CEN.

[2] Giachetti, A., Bartoli, G., Mannini, C., Wind Effects on Permeable Tall Building Envelopes: Issues and Potentialities, *CTBUH Journal,* 3, 2019.

Enhanced and embedded strong discontinuity model for fracture in solids with quadrilateral elements

Matej Šodan*, Mijo Nikolić*, Andjelka Stanić+

*University of Split, Faculty of Civil Engineering, Architecture and Geodesy, Croatia
E-mails: matej.sodan@gradst.hr

+2University of Twente, Faculty of Engineering Technology, The Netherlands

Keywords: Quadrilateral finite element, Incompatible mode method, Embedded strong discontinuity, Plasticity softening

1. Introduction

We present here enhanced quadrilateral finite element with implemented embedded strong discontinuity for crack propagation analysis of quasi brittle solids. Apart embedded discontinuity, this model also contains incompatible modes for solving bending dominating and locking phenomena problems while achieving distortion insensitivity [1].

2. Methodology

2.1. Enhanced strain

In order to obtain excellent solution accuracy for bending dominating and locking phenomena problems, even for chosen coarse mesh, we use Hu-Washizu variational principle with enriched strain field based on the method of incompatible modes. Improved properties of that element are presented in bending test (Figure 1), selected from paper [2], for which a comparison was made between standard (Q4) and enhanced (Q6) quadrilateral element. The test results (Table 1) of the Q6 element show significant accuracy compared to the ordinary Q4 element for both LC1 and LC2 load cases.

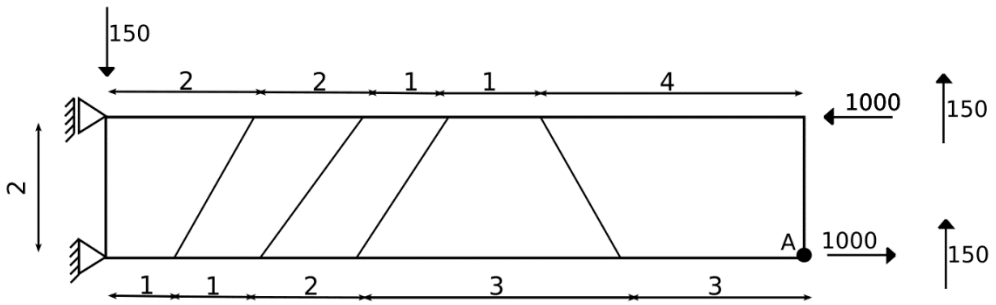

Figure 1. Finite element mesh for Beam bending test

Table 1. Displacement (point A) results comparison of elements for beam bending test: LC1 (horizontal) and LC2 (vertical)

	LC1	LC2
Element	v_A	v_A
Q4	45.7	50.7
Q6	96.1	98.1
Exact	100	102.6

2.2. Embedded discontinuity

In order to simulate discrete crack in mode I and mode II, embedded discontinuity formulation is implemented into the element. In this presented model bulk area is described by elasticity continuum model and crack surface with plasticity softening model. Crack formation criterion follows the state of the principal stresses in each element in a such way that no crack tracking algorithm is used to obtain the results [1,3,4]. The overall work of enhanced embedded element is presented in tension test (Figure 2), chosen from paper [3], for which a result comparison was made for three different structured meshes. The test results in Figure 3 show an almost perfect overlap of results for all three selected meshes.

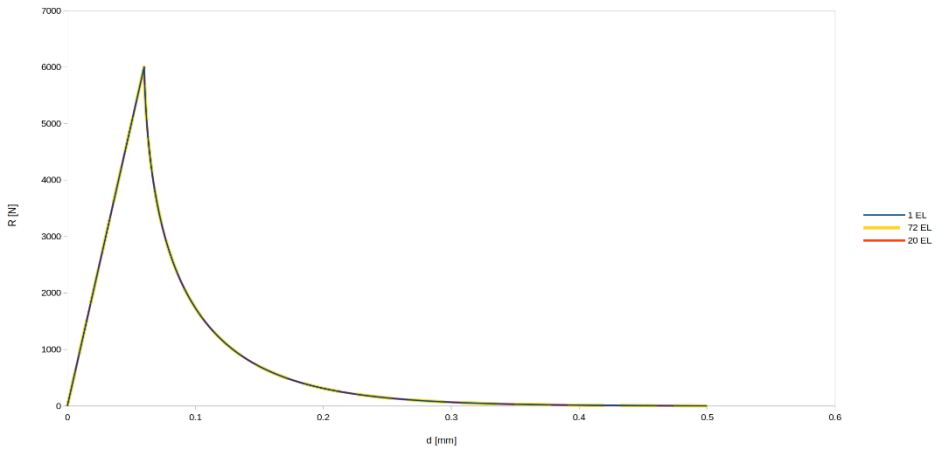

Figure 1. Please write your figure caption here

4. Conclusions

In this paper we have shown a model of enhanced embedded quadrilateral element that is able to accurately simulate the fragmentation process for 2D quasi brittle solids, without using a crack tracking algorithm while maintaining the same dimensions of the stiffness matrix as for the initial element.

Acknowledgements

This work has been supported through the project ’Parameter estimation framework for fracture propagation problems under extreme mechanical loads’ (UIP-2020-02-6693), funded by the Croatian Science Foundation.

References

[1] Ibrahimbegovic A., Nonlinear solid mechanics. In Solid Mechanics and its Applications (Vol. 160).(2009.

[2] Ibrahimbegovic A., Wilson E. L. Modified method of incompatible modes. Communications in Applied Numerical Methods, 7(3), 187–194. (1991).

[3] Stanic, A., Brank, B., Ibrahimbegovic, A., Matthies, H. G., “Crack propagation simulation without crack tracking algorithm: Embedded discontinuity formulation with incompatible modes”, Computer Methods in Applied Mechanics and Engineering, 386, 114090, (2021).

[4] Nikolić, M., Karavelić, E., Ibrahimbegovic, A., Miščević, P., “Lattice element models and their peculiarities”, Archives of Computational Methods in Engineering, 25, 753-784 (2018).

Modelling the elastoplastic behaviour of heterogeneous materials using neural networks

Matej Stanić*, Tomislav Lesičar*, Ante Jurčević*, Zdenko Tonković*

*Faculty of Mechanical Engineering and Naval Architecture, I. Lučića 5, 10000 Zagreb
E-mails: {matej.stanic,tomislav.lesicar,ante.jurcevic,zdenko.tonkovic}@fsb.hr

Keywords: neural networks, heterogeneous materials, machine learning, elastoplastic behaviour, nodular cast iron

1. Introduction

For centuries, constitutive material behaviour is described by long-established analytical expressions. Such constitutive material models have been obtained using many experimental trials conducted over many years throughout history. Traditionally, these expressions have been sufficient to describe classical engineering problems. However, due to increasing exploitation of known materials and usage of new materials with heterogeneous microstructure, there is need for more accurate and better description of the material constitutive behaviour.

Most of the existing phenomenological constitutive models do not consider the influence of the microstructural effects. Furthermore, experimental measurements are expensive and often not feasible on actual constructions. Hence, they are increasingly being replaced by validated numerical simulations based on the finite element method. Several different approaches have been proposed to describe the constitutive behaviour of heterogeneous materials over past few decades, among which the most popular is the *multiscale* method. According to this method, the constitutive material behaviour is determined by a direct link between the two scales, the microstructure and the macrolevel. After solving the boundary value problem at the microlevel, which is represented by a representative volume element (RVE), the results are averaged (homogenized) and then the boundary value problem is solved at the macrolevel [1]. Although the results of multiscale numerical simulations are satisfactory accurate, the two-scale calculation is time-consuming and computationally expensive process. For this reason, many homogenization methods (reduced homogenization methods) have been developed that seek to find the optimum between the accuracy of the results and the complexity of the calculation. A robust and efficient method of homogenization with a reduced number of degrees of freedom, based on machine learning, has led to significant acceleration of multiscale modelling. In discretization of RVE by applying machine learning, material points that have similar mechanical behaviour are grouped into the so-called clusters [2]. The use of self-consistent clustering to solve multiscale problems has proven to be extremely useful for obtaining a large database that will be used to create neural network-based material models. Large databases, obtained by validated finite element numerical simulations under different loading conditions, replace classical experimental measurements. The present work shows the use of the mentioned methods for numerical modelling of deformation processes of nodular cast iron. The microstructure of this material consists of three constituents: graphite nodules, ferrite, and perlite. A higher proportion of ferrite phase increases the ductility of the material and lowers the tensile strength while an increased proportion of perlite has the opposite effect. Graphite nodules have the greatest influence on fracture toughness, and depending on their shape, size and distribution, fatigue resistance can be increased [3]. Therefore, calculations are performed on the simplified microstructural geometry of nodular cast iron RVE using the clustering, and a large database is obtained for different cases of monotonic loading. This database is used to train the neural network. The entire analysis is performed assuming small strains and plane strain conditions.

2. Neural networks

The main advantage of neural network material models is that the mechanical behaviour can be described without the need for classical constitutive law and does not require *a priori* assumptions

about constitutive model and microstructure effects. This advantage is even more pronounced when it comes to new materials with complex microstructure. Successful prediction of the constitutive behaviour of materials by neural networks requires only a sufficient amount of data obtained by numerical simulations of experiments. Also, once a neural network-based material model is developed, it can be improved if more numerical simulations or experimental results are available.

Each neural network consists of neurons arranged in layers. The first layer consists of input values, the last layer represents output values, while all layers in between are called hidden layers. Mathematical operations and training process depends on the network architecture, two of which are most common. The first is the *feedforward* neural network in which all neurons are interconnected and in which data move only in one forward direction. On the other hand, in *recurrent* neural networks connections between nodes form a cycle, i.e., information about previous history of inputs is transferred from neuron to neuron. This type of network architecture is suitable for time-dependent data, like path-dependent plasticity [4,5]. Both architecture types are shown in Figure 1.

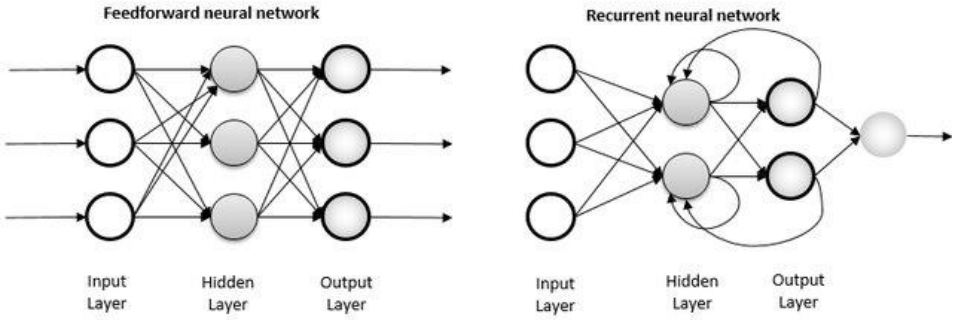

Figure 1. Feedforward and recurrent neural network architecture [6]

Training of neural networks is performed using *backpropagation* algorithm. This algorithm is used in combination with one of the optimization methods such as stochastic gradient descent, on a set of known input and output data. The goal is to minimize the difference between known and predicted output values [7].

In this paper, strains and strain energy are used as input data for neural networks, while the goal is to accurately predict homogenized stress and homogenized stiffness matrix of nodular cast iron RVE. A feedforward network architecture and *long short-term memory* (LSTM), type of recurrent neural network, is used predict constitutive behaviour of nodular cast iron. Efficiency of both network architectures is compared to experimental measurements and validated numerical results. Neural networks are built using open-source software *TensorFlow* and *Keras* API based on the *Python* programming language. The material model obtained by neural networks is implemented into *Abaqus* software through UMAT routine.

References

[1] Matouš, K., Geers, M.G.D., Kouznetsova V.G., Gillman, A., A review of predictive nonlinear theories for multiscale modelling of heterogeneous materials, *Journal of Computational Physics*, 330, 192-220, 2017.

[2] Yu, C., Kafka, O. L., Liu, W. K., Self-consistent clustering analysis for multiscale modelling at finite strains, *Computer Methods in Applied Mechanics and Engineering*, 349, 339-359, 2019.

[3] Čanžar, P., Tonković, Z., Kodvanj, J., Microstructure influence on fatigue behaviour of nodular cast iron, *Materials Science & Engineering A*, 556, 88-99, 2012.

[4] Mozaffar, M., Bostanabad, R., Chen, W., Ehmann, K., Cao, J., Bessa, M. A., Deep learning predicts path-dependent plasticity, *Proceedings of the National Academy of Sciences, USA*, 116(52):201911815, 2019.

[5] Logarzo, H. J., Capuano, G., Rimoli, J. J., Smart constitutive laws: Inelastic homogenization through machine learning, *Computer Methods in Applied Mechanics and Engineering*, 373, art. no. 113482, 2021

[6] Pekel, E., Kara, S., A comprehensive review for artificial neural network application to public transportation, *Sigma J Eng & Nat Sci*, 35, 157-179, 2017.

[7] Hagan, M. T., Demuth, H. B., Beale, M. H., De Jesus, O., Neural network design 2nd edition, 2014.

A numerical modeling method to predict failure in polymer sandwich structures with inhomogeneous core

Laszlo Takacs[1,2], Laszlo Kovacs[1,2], Anna Nagy[2], Milena Babic[2]

[1]*Budapest University of Technology, Department of Polymer Engineering, Budapest, Hungary*
E-mails: takacsl@pt.bme.hu, kovacsl@pt.bme.hu

[2]*ECON Engineering Kft., Budapest, Hungary*
E-mails: anna.nagy@econengineering.com, milena.babic@econengineering.com

Keywords: polymer sandwich, failure, numerical modeling

1. Introduction

Polymer sandwich structures have an increasing importance in the transportation industry due to their excellent stiffness to weight ratio. The different core structures however can have a significant effect on the stiffness and strength behavior of the material [1]. Many researches have been conducted to investigate the mechanical behavior of special types of core materials [2]. One of the typical failure modes of a sandwich structure is the delamination of the face-sheet and the core [3] but when a grooved foam is applied as core material for better formability, the failure process becomes more complex due to the existence of resin walls in the foam core.

This paper aims to introduce a finite element modeling method to simulate the stiffness and strength behavior of sandwich structures effectively and with high accuracy even in full-vehicle scale by using layered shell elements. The method is validated with standard bending tests.

2. Materials and experimental tests

The investigated material has glass-fiber reinforced vinyl-ester matrix composite face-sheets with a closed-cell PET foam core, which is typically used in the transportation industry. The fiber reinforcement is a multidirectional fabric with a stacking sequence of 0°/45°/90°/-45°. The face-sheet of the sandwich structure has 3 layers of this fabric with the same orientation and with a symmetric lay-up. The core is a FlexiCut type, 25 mm thick PET foam, that has 1.2 mm cuts in every 30 mm. Both sides have cuts, on one side the 85 % of the thickness is cut, on the other side the 20 % of the thickness. These cuts help the manufacturing, they transfer the resin and this structure allows the full impregnability of the sandwich as well as the formability to a complex 3D shape.

The stiffness constants of the face-sheets were determined by standard tensile- and shear-tests and with the sandwich beams, 3- and 4-point bending were performed. The core structure and the bending test set-up is shown in Figure 1.

(a) (b)

Figure 1. Structure of the foam (a) 4-point bending of the sandwich (b)

3. FE analysis

As a first step we built a detailed finite element model of the sandwich specimen with solid elements in the core and with an explicit FE analysis in Ls-Dyna environment. We have also managed to predict the crack propagation process as a function of deflection. This provided input about the failure mode of the structure that agreed with the experiments. In the second step we performed the bending analysis on the detailed FE model with the Ansys implicit solver to investigate the 3D stress state at the critical deflection. After that we built the simplified model with layered shells and compared its stress-state to the results of the detailed model and determined a strength-factor. This strength-factor is defined as the shear strength of the homogeneous foam and the shear strength of the inhomogeneous foam including resin walls. By knowing this factor, one can model a complete structure in a simplified way with layered shells and evaluate load bearing capacity of this kind of complex material with high accuracy.

As an example, the typical failure mode and the stress-state of the detailed FE model is shown in Figure 2.

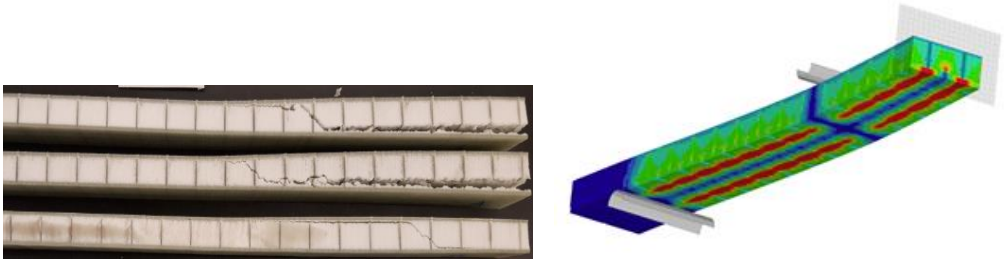

(a) (b)

Figure 2. Failure of the sandwich specimen (a) a stress result of the detailed FE model (b)

4. Conclusions

We have developed a modeling method with which one can model the stiffness and strength of polymer sandwich panels with a heterogeneous core structure with layered shell elements, taking into account the stiffening effect of the resin walls in the core. We proved that by modeling the heterogeneous core structure with orthotropic material model, a high accuracy can be achieved compared to the detailed finite element model, while requiring two orders of magnitude less computational time. The stiffness constants of the core-layer can be determined by either extending the rules of mixture or performing virtual tension- and shear-tests on detailed 3D finite element models. To characterize the failure, we introduced a strength-factor that modifies the initial strength of the homogeneous core material for the core structure containing the resin walls. By extending the introduced factor, a master curve can be determined as a function of the resin wall thicknesses. The method can be effectively used in the conceptual design phase of polymer sandwich vehicle chassis as the whole body can be modeled in full-scale this way.

References

[1] Tuswan Tuswan, Kharis Abdullah, Achmad Zubaydi, Agung Budipriyanto, Finite-element Analysis for Structural Strength Assessment of Marine Sandwich Material on Ship Side-shell Structure. *Materials Today: Proceedings.* 13, 1, 109-114, 2019.

[2] Xu Gao, Miaomiao Zhang, Yaodong Huang, Lin Sang, Wenbin Hou, Experimental and numerical investigation of thermoplastic honeycomb sandwich structures under bending loading. *Thin-Walled Structures*. 155, 106961, 2020.

[3] Gholami V, Taheri-Behrooz F, Memar Maher B., Fracture toughness and crack growth resistance of sandwich panels with grooved cores. *Journal of Sandwich Structures & Materials*. 24, 3, 1746-1767, 2022.

The Fast Boundary-Domain Integral Method: An overview and application on fluid flow simulation

Jan Tibaut*, Jure Ravnik+, Martin Schanz*

*Institute of Applied Mechanics, Technikerstraße 4 Graz, Austria
E-mails: {jan.tibaut, m.schanz}@tugraz.at

+Faculty of Mechanical Engineering, Smetanova ulica 17 Maribor, Slovenia
E-mail: jure.ravnik@um.si

Keywords: Boundary-Domain Integral Method, Adaptive Cross Approximation, $\mathcal{H}$-structure, $\mathcal{H}^2$-structure

1. Introduction

In most applications in engineering, the underlying partial differential equations are inhomogeneous. Applying the boundary element method to such problems is not straightforward. However, the boundary-domain integral method can be used, which accounts for the inhomogeneity by means of a domain integral. As with all boundary element methods, the complexity is quadratic, i.e., in terms of the domain integral, the method scales with $\mathcal{O}(m^2)$, where *m* is the number of nodes in the domain. This prevents the boundary domain integral method from being applied to large real-world problems.

It is known that there are methods that speed up this method and reduce the complexity to $\mathcal{O}(m \log m)$ or even $\mathcal{O}(m)$. Most methods are based on a hierarchical decomposition of the domain, i.e., the $\mathcal{H}$-structure and the use of an approximation technique. After the $\mathcal{H}$-matrix is formed an approximation method is employed, e.g., the Adaptive Cross Approximation (ACA). A kind of generalization are $\mathcal{H}^2$-matrices based on kernel interpolation [1]. The integral kernel is approximated with the Lagrange interpolation function. The theoretical complexity of the method is reduced to $\mathcal{O}(m)$ in terms of memory. To further reduce the memory, the parts of the $\mathcal{H}^2$-matrices are further compressed, e.g., with ACA or another approximation technique. Further, another domain decomposition method is the sub-domain boundary-domain integral method [2]. The method employs the Green's second identity to each element in the domain. The numerical complexity is comparable to the finite element method.

2. Governing problem

In the proposed talk, we give an overview of fast methods that can be used to solve fluid flows with the boundary domain integral method. Two conservation equations were employed to solve the fluid flow. The kinematic equation and the vorticity transport equation. To reduce the complexity of the boundary domain integral method we employed the Modified Helmholtz approach [3]. For example, the Modified Helmholtz form of the kinematic equation is:

$$\vec{\nabla} \times \vec{\omega} = (\mu^2 - \nabla^2)\vec{v} + \mu^2 \vec{v}_{n-1}, \tag{1}$$

where $\vec{v}$ is the velocity, $\vec{v}_{n-1}$ velocity of previous time step, $\vec{\omega}$ the vorticity and μ^2 the underrelaxation parameter. With the Green's second identity we derive the integral form for equation (1):

$$c\vec{v} + \int_\Gamma \vec{v}\vec{\nabla}u^* \, d\Gamma = \int_\Gamma \vec{v} \times \left(\vec{n} \times \vec{\nabla}\right) u^* d\Gamma + \int_\Omega \left(\vec{\omega} \times \vec{\nabla}u^*\right) d\Omega + \mu^2 \int_\Omega u^* \vec{v}_{n-1}, \tag{2}$$

where *c* is the integral free term and the integral equation is solved with the collocation method. To discretize the integral formulation. The domain Ω is divided into cells and surface elements. Implementing this on equation (3) the discrete form is:

$$[H]\{v_i\} = [H_k^t]\{v_j\} - [H_j^t]\{v_k\} + [D_k]\{\omega_j\} - [D_j]\{\omega_k\} + [B]\{v_i^{F-1}\},\ i,j,k = 1,2,3 \quad (4)$$

where the indices i, j, k are directions for the Cartesian coordinate system. Overall, we store eight full matrices in memory. The size of $[H]$, $[H_1^t]$, $[H_2^t]$, $[H_3^t]$ are $n \times n$ and the size of $[B]$, $[D_1]$, $[D_2]$ and $[D_3]$ are $n \times m$, where n is the number of collocation points. To give an example, to store all matrices for a large mesh (approx. 750.000 nodes) a memory storing space of approximately 1TB would be necessary. To reduce the computational cost, we employ fast methods.

3. Results and Conclusions

In Figure 1, we present the memory storing space depending on the parameter μ. The discretised integral formulation from (4) was approximated with the $\mathcal{H}^2$-matrix technique. Red and orange lines display the storage requirement of the developed algorithm.

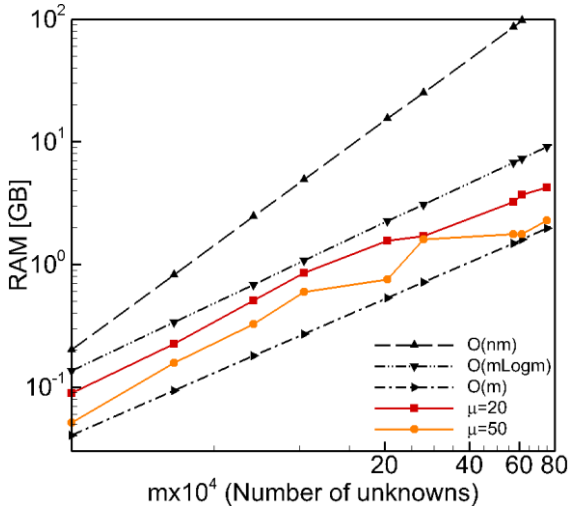

***Figure 21 Storage of the matrix [B] using the $\mathcal{H}^2$-matrix and ACA for different μ and mesh densities* [4].**

Fast methods reduce the memory storing space and CPU-time for computing the numerical simulation. However, one must take care that the error introduced by adding additional approximations is at the same order of magnitude as the discretization error and/or due to the solver of the system of linear equations.

References

[1] S. Börm, "Approximation of integral operators by H2-matrices with adaptive bases," *Computing*, vol. 74, no. 3, pp. 249–271, 2005.

[2] J. Ravnik, L. Škerget, and Z. Žunič, "Combined single domain and subdomain BEM for 3D laminar viscous flow," *Eng. Anal. Bound. Elem.*, vol. 33, no. 3, pp. 420–424, 2009.

[3] J. Tibaut and J. Ravnik, "Fast boundary-domain integral method for heat transfer simulations," *Eng. Anal. Bound. Elem.*, vol. 99, 2019.

[4] J. Tibaut, M. Schanz, and J. Ravnik, "Fast Boundary-Domain Integral Method with the H2-matrix formulation for large scale numerical investigations," *Eng. Anal. Bound. Elem.*, vol. 138, pp. 1–12, 2022.

Objective Formulation for Beam-to-Beam Contacts

Jan Tomec*, Gordan Jelenić*

*University of Rijeka, Faculty of Civil Engineering, R. Matejčić 3, Rijeka
E-mails: {jan.tomec, gordan.jelenic}@uniri.hr

Keywords: Beam-to-beam contact, Finite element method, Mortar method, Line-to-line contact

1. Introduction

The use of beam theories in the finite element method is usually motivated by clear application of model-reduction techniques and computational efficiency. Advanced mathematical theories on groups are often employed [1,2,3] to provide a detailed description of dynamics of such structures as a single-dimensional function of an arc-length coordinate. The current treatment of contacts between beams is somewhat less mathematically rigorous. A simplified contact geometry and integration is mostly used resulting in non-objective, though numerically efficient formulations [4,5]. In a physical world, interactions between beam-like structures emerge in many different practical applications e.g., robotics [5], textile [6], or hair [7] modelling. Usually, these involve very slender structures i.e., the beams used to model them are very long and thin. Modelling contacts thus exhibits robustness issues manifesting in slow convergence or even divergence when larger changes in configuration need to be modelled. We are proposing a new description of contact geometry based on an equidistance curve between the two beams with the aim of improving the numerical stability of the method and possibly its convergence rate. Although applicable to most contact formulations, we present it here in conjunction with the mortar method developed in [4], following our previous research.

2. Beam-to-beam contact

2.1. Beam theory

A beam is described by a single arc-length coordinate spanning along its entire length, which makes a basis for parametrisation of the centerline position and cross-section orientation. In this paper we use geometrically exact beam finite element [1]. The contact formulation presented here does not exploit the full geometric description of the beam but only its centerline position $\boldsymbol{x}(s) \in \mathbb{R}^3$. This neglects any shear deformation of the beam in contact detection and is a common assumption in beam-to-beam contact formulations [4,5,6]. As this is the only value that we use from the beam element, any specific kind of a beam element is equally applicable within the formulation.

2.1. Contact

Generally, all types of contact between beams are regarded as beam-to-beam contacts. This includes point-to-point contacts, where a contact occurs at a discrete point, and line-to-line contacts, where the contact is distributed along a line. Because lateral compression and tension are not included in the conventional beam theory the point- or line-like contact region is conforming to either a point or a line in space. A frictionless contact can be represented through a set of constraints designed to prevent penetration by introducing additional forces at the position of the contact. These are mathematically analogous to the Karush–Kuhn–Tucker conditions

$$g \geq 0, \tag{1}$$

$$F_N \leq 0 \quad \text{and} \tag{2}$$

$$gF_N = 0, \tag{3}$$

where g is a gap between the beams and F_N is a normal contact force. These conditions are written in a strong form and as such hold for any point on the beam. Their weak form leads to the mortar method where we impose the constraints in an integral sense.

Next, a proper gap function must be defined to enable measurement of the distance between the beams in interaction. Its mathematical description is usually related to the distance of an orthogonal projection of the centreline of a selected beam to the other beam's centreline, reduced by the combined thickness of the two beams [4,5]. This allows a unique and simple definition which provides consistently the shortest distance between the two beams. It is, however, affected by the choice for the primary beam and is thus not objective. It also features a geometrical error in the gap since the projection vector is not perpendicular on the primary beam centerline and therefore simply subtracting that beam's thickness results in an apparent gap which is larger than the real gap.

Taking a step back allows to re-evaluate the contact geometry resulting in an objective gap function. Instead of looking at the distance between the two beams directly, we construct a middle curve to which the distance from each beam is measured. Defining an appropriate middle curve allows an objective definition of the distance between the two centerlines. It might seem counterintuitive to prefer a formulation as this one, which evidently does not provide the shortest distance between the beams, but we should not forget that the main task of the gap function is nevertheless to prevent penetration. As long as its differentiation between the positive and the negative gap conforms to its physical meaning, the gap function is valid. Indeed, the magnitude of the penetration deviates from the one provided by orthogonal projection; however, the penetration is correctly predicted because the middle curve is designed to be always between the two centerlines.

For the middle curve we select an equidistance curve specifically defined to be objective. First, one needs to solve a projection problem defined as

$$(\boldsymbol{t}_1 \pm \boldsymbol{t}_2)^T(\boldsymbol{x}_1 - \boldsymbol{x}_2) = 0. \tag{4}$$

Afterwards, the equidistance point $\boldsymbol{x}_m$ can be computed. Finally, the gap function is defined as

$$g = 2\|\boldsymbol{x}_1 - \boldsymbol{x}_m\| - r_1 - r_2, \tag{5}$$

for the case of beams of circular cross-sections with r_1 and r_2 as the cross-section radii. This gap is simply inserted into the formulation defined in [4] and the rest of developments follow automatically.

3. Conclusions

A new contact formulation is proposed based on the objective contact geometry. It has been implemented in combination with the mortar method. An improvement in the algorithm's stability is expected while the computational cost should slightly increase. Since the contact formulation is objective, switching between the beams as the carriers of the contact variables does not affect the solution.

References

[1] Simo, J. C., Vu-Quoc, L., A three-dimensional finite-strain rod model. part II: Computational aspects. Computer Methods in Applied Mechanics and Engineering, 58:1, 79-116, 1986.

[2] Crisfield, M.A., Jelenić, G., Objectivity of strain measures in geometrically exact 3D beam theory and its finite element implementation. Proceedings of the Royal Society of London Series A - Mathematical Physical & Engineering Sciences, 455:1983, 1125-1147, 1999.

[3] Sonneville, V., Cardona A., Brüls, O., Geometrically exact beam finite element formulated on the special Euclidean group SE(3). Computer Methods in Applied Mechanics and Engineering, 268, 451-474, 2014.

[4] Tomec, J., Jelenić, G., Analysis of static frictionless beam-to-beam contact using mortar method. Multibody System Dynamics (2022), under review.

[5] Bosten, A., Cosimo, A., Linn, J., et al, A mortar formulation for frictionless line-to-line beam contact. Multibody System Dynamics, 54, 31-52, 2022.

[6] Durville, D., Simulation of the mechanical behaviour of woven fabrics at the scale of fibers. International journal of material forming, 3:2, 1241-1251, 2010.

[7] Audoly, B., Cani, M.P., et al, Super-helices for predicting the dynamics of natural hair. Transactions on Graphics, 25:3, 1180-1187, 2006.

Mechanical Properties of Hardox 450 Steel After Heat Treatment

Damir Tomerlin*, Marija Magić Kukulj*, Dražan Kozak+, Darko Damjanović+

*DOK-ING, Slavonska avenija 22 G,HR-10000 Zagreb, Croatia
E-mails: {damir.tomerlin, marija.kukulj}@dok-ing.hr
+University of Slavonski Brod, Mechanical Engineering Faculty in Slavonski Brod, Trg Ivane Brlić Mažuranić 2, HR-35000 Slavonski Brod, Croatia
E-mails: {dkozak, ddamjanovic}@unisb.hr

Keywords: Hardox 450, heat treatment, mechanical properties, wear-resistant steel

1. Introduction

Stress-relief Heat Treatment (HT) is an important procedure used to reduce the residual material stresses that occurred during various manufacturing processes. During the HT procedure, a metallic material is subjected to controlled time-temperature cycle. This cycle typically consists of several phases: heating the structure to required temperature below the transformation temperature A_1, holding it at stress relieving temperature until the structure is homogeneously heated, and finally cooling it down slowly to environmental temperature, [1].

In multi-material structures that require HT, the thermal influence on all materials must be determined and considered. Wear-resistant steel for structural purposes, with high strength and hardness in delivered condition, is sensitive to subsequent heating in excess of 250 °C, and therefore generally not intended for HT. This paper aims to experimentally investigate influence of HT on general mechanical properties of Hardox 450. This is necessary to gain further insight into HT and residual stresses correlation, and to create valid material model for numerical simulations.

2. Material and methods

Test plate sample dimensions are 10x200x500 mm is made from Hardox 450 steel. It is characterized as low-alloy abrasive-wear resistant martensitic steel, with high hardness, coupled with high mechanical properties. Such properties are achieved through controlled chemical composition and special heat treatment quenching and tempering processes during the steel manufacture. Due to good weldability and overall suitability for fabrication, it is a steel choice for various structural applications, [2].

HT cycle parameters used in this investigation relate to preheating at 55-75 °C/h rate, holding at 550 °C stress relieving temperature for 4 h, and finally cooling at 55-80 °C/h rate, Figure 1. For the thermal process, industrial furnace with air convection system, is used. Temperature control is maintained through thermocouples connected to the test plate surface.

Experimental investigation of general monotonic mechanical properties includes tensile testing, impact testing, and hardness examination. Tensile testing is done transversal to plate rolling direction on the basis of three specimens. Specimens conform to ASTM E8 standard for tensile testing of metallic materials. Round tension small-size specimen proportional geometry with dimensions L = 50 mm, A = 20 mm, D = 4 mm, R = 4 mm. M8 threaded ends are used for specimen holding. Testing is done at environmental temperature of 22 °C.

Impact Charpy V-notch testing is done at environmental temperature of 20 °C. Three transverse oriented standard 55x10x7,5 mm specimens are used, conforming to EN ISO 148-1.

Hardness testing is done on a special sample, with an area of hardness measurement along the cross section of the plate. 5 indentations are made on the vertical line over 10 mm plate thickness. Hardness is tested according to EN ISO 6507-1 with HV10 test force setup.

3. Results

After exposing the Hardox 450 steel material to HT cycle conditions, significant changes of general monotonic mechanical properties, in contrast to properties of material in delivered condition,

were observed, see Table 1. Tensile values of HT specimens experience significant drop in $R_{p0.2}$ proof strength to approximately 700 MPa, and R_m tensile strength to 800 MPa. Material becomes more ductile, giving rise of A value from 10 % to average 19 %. Impact toughness tested is high with average of 155 J (20 °C). Hardness which is the flagship characteristic of this steel grade, is lowered to average of 255 HV10 (243 HBW), thereby losing wear resistance.

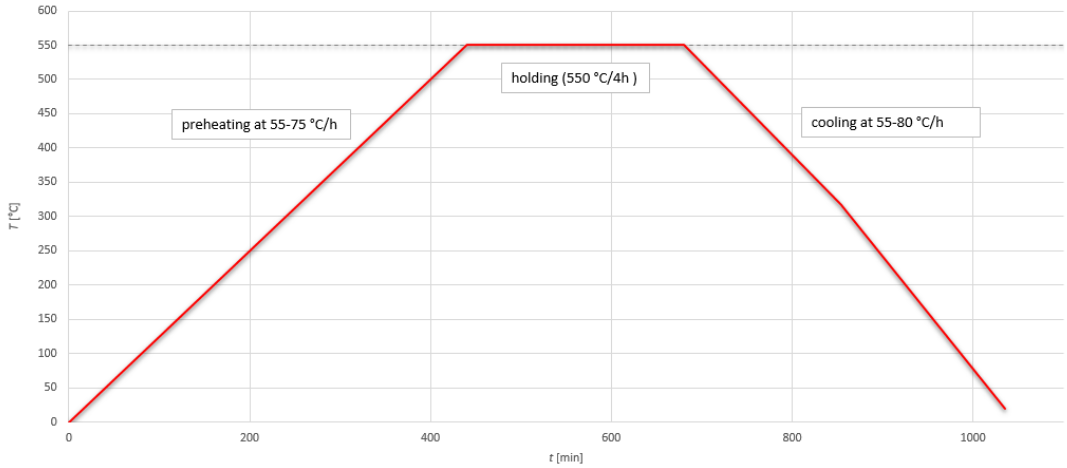

Figure 1. Heat treatment cycle

Table 1. Mechanical properties of Hardox 450 steel

Tensile					
Specimen Designation	Condition	$R_{p0.2}$ [MPa]	R_m [MPa]	A [%]	
Declared	U	1200	1400	10	
TT-1	HT	704.3	792.7	17.6	
TT-2	HT	708.9	796.1	19.1	
TT-3	HT	708.2	798.0	21.4	
Impact Charpy V-notch					
Declared	U	min. 27 J (-20 °C)			
IT-1	HT	161 J (20 °C)			
IT-2	HT	150 J (20 °C)			
IT-3	HT	158 J (20 °C)			
Hardness [HV10/HBW]					
U	HT				
	Indent 1	Indent 2	Indent 3	Indent 4	Indent 5
425–475 HBW	254.0/242	257.1/245	254.6/242	253.2/241	257.6/245

4. Conclusions

Significant changes of Hardox 450 steel mechanical properties, subjected to heat treatment procedure, have been experimentally determined. Exposure to high temperatures over 250 °C undoubtedly cause hardness and strength degradation in the range up to 50% of declared values, due to materials structural changes. This is in accordance to manufacturer recommendation against any further heat treatment. Removal of residual stresses from the material needs to be carried out using some alternative methods that are not based on thermal inputs.

References

[1] ASM Handbook. Volume 4. Heat Treating. ASM International, 2002.

[2] Konat, Ł., Białobrzeska, B., Białek, P., Effect of Welding Process on Microstructural and Mechanical Characteristics of Hardox 600 Steel. *MDPI metals*, 7, 349, 2017. doi:10.3390/met7090349

Effect of different porosity of sintered steel on fatigue S-N curves

Zoran Tomić [a*], Nenad Gubeljak [b], Tomislav Jarak [c], Luka Ferlič [b], Zdenko Tonković [a]

[a] *University of Zagreb, Faculty of Mechanical Engineering and Naval Architecture, Croatia*
E-mails: zoran.tomic@fsb.hr, zdenko.tonkovic@fsb.hr

[b] *University of Maribor, Faculty of Mechanical Engineering, Slovenia*
E-mails: *nenad.gubeljak@um.si, luka.ferlic@um.si*
c ITAP, School of Industrial Engineering, University of Valladolid, Spain

E-mail: tomislav.jarak@uva.es

Keywords: sintered steel, porosity, fatigue

1. Introduction

The use of sintered materials for various purposes has several technological advantages. With sintered material is possible to achieve a fairly precise shape of the element with minimal material waste. The problem is that the sintered material is porous, which caused a lower density and leads to a decrease in mechanical strength as well as dynamic strength. The paper analyzed the effects of different porosity on the dynamic strength of the sintered material.

2. Material and methods

In this study, sample batches of three different densities were compacted and sintered from identical metallic powder, the low-prealloyed steel powder Astaloy™ Mo+0,2C produced by Höganäs AB, Sweden [1]. The uniaxial samples are manufactured in three densities compacted with corresponding pressures: 7.1 g/cm^3 under the pressure of 600 MPa, 6.8 g/cm^3 at the pressure of 440 MPa, and 6.5 g/cm^3 under the pressure of 360 MPa. After compacting, sintering is conducted at 1120°C for half an hour. Finally, the samples are cooled first to 70°C and then to room temperature (25°C) in duration of approximately 40 min. The theoretical density of the Astaloy metallic powder is [1]. Porosity volume is determined as ratio between the volume of pores Vp to the volume of material without pores V0, as was explain in paper [2].

3. Results

Macroscopic quasistatic tensile tests are conducted on the Instron servo-hydraulic machine. All specimens are tested in the strain-controlled loop with the strain rate of 1 mm/min and the DIC GOM® Aramis™ 12M system. The elastic modulus at the macrolevel is determined as a slope of the linear part of the stress-strain curve for a material under tension. Experimentally obtained tensile mechanical properties are listed in Table 1.

Table 1. Macromechanical properties obtained by uniaxial tests and metallographic analysis

Sintered density, g/cm^3	Porosity (V_p/V_0), %	Macroproperties		
		Modulus of elasticity, GPa	Yield stress, MPa	Tensile strength, MPa
6.5	20	98.2 ± 4.1	218.9 ± 8.7	269.8 ± 9.4
6.8	14.7	115.1 ± 12.1	242.5 ± 11.6	326.7 ± 12.2
7.1	9,9	131 ± 12.3	369.0 ± 26.9	471.7 ± 16.5

Table 1 shows a significant degressive characteristic in macromechanical properties with the increase of porosity, as is also noticed by other authors [3,4]. Table 1 shows a significant degressive characteristic in macromechanical properties with the increase of porosity, as is also noticed by other authors [3,4]. Uniaxial fatigue testing was performed on Instron servo-hydraulic machine and RUMUL resonant pulsator by loading ratio $R=F_{min}/F_{max}=0.05$ in order to determine points on S-N curves, as is shown in Fig.1.

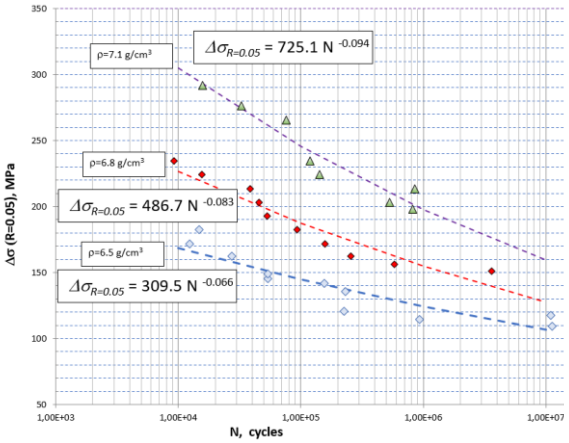

Figure 1. S-N curves obtained by loading ratio R=0.05 at room temperature

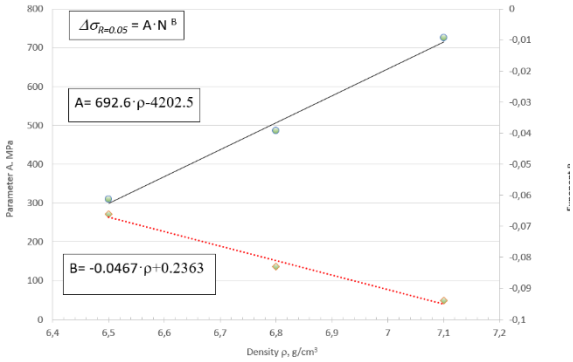

Figure 2. Parameters of power low eq. A and B vs. density of sintered material

4. Conclusion

Figure 1 shows S-N curves for all three different densities of samples with equations for determination fatigue strength of material with different density. It was shown that with the same dynamic load ratio R=0.05, there is a significant difference in the dynamic strength of the material in the area of lower density, i.e. increased porosity of the material. The results show that at the same working load, material with a higher density has significantly higher dynamic strength. It was used power low equation with parameters A and exponent B. In order to determine fatigue strength vs. material density for loading ratio R=0.5, it is possible to determine the parameters of A and B by linear interpolation, as is shown in Fig. 2. Based on the experimental results, the dependences between density and dynamic strength parameters were determined.

Acknowledgment

This work has been fully supported by Croatian Science Foundation under the project "Multiscale Numerical Modelling and Experimental Investigation of Aging Processes in Sintered Structural Components" (MultiSintAge, PZS-1 2019-02-4177) and Slovenian research agency ARRS for part of the research supported by Program P2-0137 "Numerical and Experimental Analysis of Nonlinear Mechanical Systems".

References

[1] Höganäs, Iron and steel powders for sintered components: Handbook for Sintered Components, 2017.
[2] Z. Tomić, N. Gubeljak, T. Jarak, T. Polančec, Z. Tonković, Scripta Materialia 217 (2022)
[3] A. Falkowska, A. Seweryn, Int. J. Fatigue. 117 (2018) 496–510.
[4] N. Chawla, J. Williams, X. Deng, C. McClimon, Int J Powder Met. 45 (2009) 19–27.

DVC analysis of mat glass fiber reinforced polymer applying heterogeneous mechanical regularization at the mesoscale

Zvonimir Tomičević*, Dalibor Leljak*, Ana Vrgoč*, François Hild+

*Faculty of mechanical engineering and naval architecture, Ivana Lučića 5, 10 000 Zagreb
E-mails: {zvonimir.tomicevic,ana.vrgoc}@fsb.hr, dalibor.leljak97@gmail.com

+Université Paris-Saclay, CentraleSupélec, ENS Paris-Saclay, CNRS, LMPS - Laboratoire de Mécanique Paris-Saclay, 91190 Gif-sur-Yvette, France
E-mail: francois.hild@ens.paris-saclay-fr

Keywords: Fibrous Material, X-Ray Computed Tomography, Digital Volume Correlation, Mechanical Regularization

1. Introduction

The analysis of the behavior of materials with complex and/or heterogeneous microstructures at low scales calls for the enhancement of full-filed measurement techniques. For homogenous materials with complex microstructure (*e.g.*, cellular materials) Architecture-Driven Digital Image Correlation Technique (ADDICT) 0 approaches are considered. The proposed digital image correlation (DIC) framework consists of a weak regularization using an elastic B-spline image-based model. Even more challenging scenarios arise for heterogeneous materials (*e.g.*, fiber reinforced polymers or FRPs) where the presence of different constituents that possess specific material properties result in complex strain localization and damage phenomena. This challenge can be addressed with the application of FE-DIC based upon heterogeneous mechanical regularization 0. The proposed methodology treats differently phases of the heterogeneous material by taking into account the contrast of their elastic properties. The same principle can be adapted to heterogeneous materials in a Digital Volume Correlation (DVC) frameworks 0 0.

The present work is devoted to the assessment of strain localization and damage quantification in a mat glass fiber reinforced polymer (GFRP) via DVC measurements. The fibrous architecture of the monitored region of interest (ROI) was obtained from volumetric images acquired with an X-ray scanner. The application of heterogeneous regularization over the underlying microstructure led to displacement fields consistent with damage mechanisms arising in the bulk of the investigated material.

2. Material and Methods

In this work, a notched dogbone specimen made of polyester resin reinforced with mat glass fiber was subjected to a cyclic tensile loading. The *in situ* test consisted of four loading steps, and tomographic scans were acquired at sustained and constant load with the X-View X50-CT scanner of LMPS (North Star Imaging) with a 14.6 μm/voxel resolution.

The first estimation of the material behavior was performed over the entire ROI (*i.e.*, 401 × 630 × 945 voxels) with the assumption of homogeneous elasticity 0 in the regularization process, even though the elastic properties of the fibers and matrix are different. A subvolume with dimensions 65 × 84 × 61 voxels (Figure 1(a)) was selected for further analysis. It was positioned around the notch root since this zone yielded the highest strain levels. Multiple damage mechanisms were expected to occur in the selected ROI. The FE mesh corresponding to the observed microstructure (Figure 1(b)) was generated from a segmented image of the ROI. It was performed by setting three threshold levels, defining the gray level range of the voids, glass fibers and polyester resin.

DVC measurements based on heterogeneous regularization were initialized with the kinematics obtained over the entire ROI (with homogenous regularization). The displacements of the edge nodes were kept constant and consistent with the measurement over the entire ROI, while the displacements

of the bulk and Neumann nodes (*i.e.*, free edges) were updated in the new DVC analysis. The microstructure-based mesh differentiated matrix and fiber elements. Hence, it was possible to assign different elastic properties in the regularization scheme, and take into account the heterogeneous nature of the composite. Since the investigated GFRP material is a two-phase material, the elastic contrast C is defined as the ratio of Young's moduli of the matrix E_m and the fiber E_f.

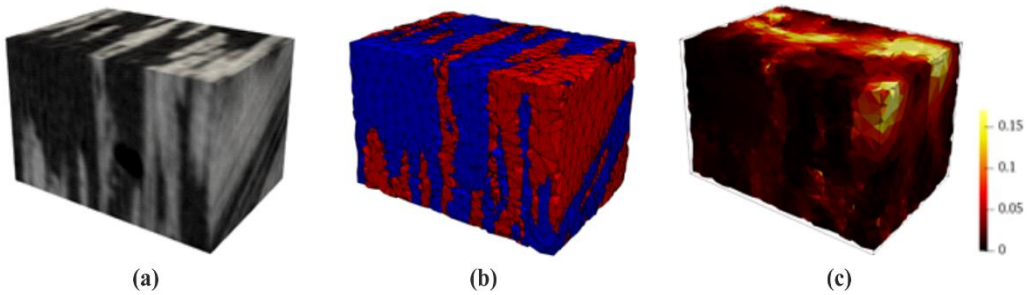

Figure 1. (a) 3D rendering of the analyzed subvolume inside the monitored ROI. (b) Finite element mesh corresponding to the underlying architecture. (c) Measured major principal strain field.

3. Results and Conclusion

The realistic 3D mesh generated with the underlying microstructure of the GFRP and heterogeneous mechanical regularization were used to study displacement fluctuations at the observed mesoscale. In addition, the application of the appropriate elastic contrast between the constituents provided the possibility to better capture displacement gradients at yarn-matrix interfaces. Furthermore, strain heterogeneities (Figure 1(c)) were more pronounced around the damaged areas.

Global DVC and numerical simulation are strongly interconnected by means of finite element meshes. Moreover, the measured kinematics can be prescribed as boundary conditions of mechanical simulations without introducing additional interpolation errors. In addition, the proposed FE-DVC approach improved with heterogeneous mechanical regularization is in line with micro- and meso-mechanical FE modeling of complex materials. Thus, coupling FE-DVC with numerical simulations provides a natural framework for model validation and calibration of material parameters in a more thorough manner.

Acknowledgements

This work was performed within the FULLINSPECT project supported by the Croatian Science Foundation (UIP-2019-04-5460 Grant).

References

[1] Rouwane, A., Bouclier, R., Passieux, J.-C., Périé, J.-N., Architecture-Driven Digital Image Correlation Technique (ADDICT) for the measurement of sub-cellular kinematic fields in speckle-free cellular materials. *International Journal of Solids and Structures*, 234–235, 111223, 2022.

[2] Naylor, R., Hild, F., Fagiano, C., Hirsekorn, M., Renollet, Y., Tranquart, B., Baranger, E., Mechanically Regularized FE DIC for Heterogeneous Materials. *Experimental Mechanics*, 59(8), 1159–1170, 2019.

[3] Hild, F., Bouterf, A., Roux, S., Damage measurements via DIC. *International Journal of Fracture*, 191(1), 77–105, 2015.

[4] Tsitova, A., Bernachy-Barbe, F., Bary, B., Dandachli, S. A., Bourcier, C., Smaniotto, B., Hild, F., Damage Quantification via Digital Volume Correlation with Heterogeneous Mechanical Regularization: Application to an In situ Meso-Flexural Test on Mortar. *Experimental Mechanics*, 62, 333–349, 2022.

[5] Mendoza, A., Neggers, J., Hild, F., Roux, S., Complete mechanical regularization applied to digital image and volume correlation. *Computer Methods in Applied Mechanics and Engineering*, 355, 27–43, 2019.

Multi-parameter Weight and Efficiency Optimization of a Cylindrical Gear Pair without Standard Basic Rack Geometry Limitations

Niko Trumbić*, Ian Strelec*, Ivan Čular+, Krešimir Vučković+

*Rimac Technology d.o.o., Savska Opatovina 36, 10 000 Zagreb
E-mail: niko.trumbic@rimac-technology.com, ian.strelec@rimac-technology.com

+Faculty of Mechanical Engineering and Naval Architecture, Ivana Lučića 5, 10 000 Zagreb
E-mail: kresimir.vuckovic@fsb.hr, ivan.cular@fsb.hr

Keywords: multi-parameter optimization, cylindrical gears, mass, efficiency, genetic algorithm

1. Introduction

In recent years, growing demand for light-weight, efficient and quiet transmissions, fueled by the introduction of electric vehicles is observed. This calls for simultaneous gear optimization regarding efficiency, mass, and NVH (noise vibration harshness). NVH behavior can be assessed in terms of transmission error, which is the main contributor to gear vibrations [1]. Manual optimization is tedious due to a large number of variables and trade-offs, such as the mass/efficiency trade-off reported by Miler et al. [2] and experimentally confirmed by Kahraman et al. [3] or efficiency/transmission error trade-off reported in [4]. Generally, optimization for any two of the above-mentioned parameters independently results in the deterioration of the third one [1]. The aforementioned reasons emphasize the need for optimization algorithms in finding the optimal design. Patil et al. [5] used a modified NSGA-II (Non - dominated Sorting Genetic Algorithm - II) to minimize volume and power loss, while Yao [6] optimized a spur gear design for axis distance, bearing capacity, and efficiency. Fu et al. [7] developed an algorithm combining the Crow Search algorithm with PICEA-w (Preference-Inspired Co-Evolutionary Algorithm using Weights) to optimize a two-stage transmission for volume, surface fatigue life and load capacity. Hammoudi et al. [8] proposed employing the AMDE (Adaptive Mixed Differential Evolution) algorithm to optimize a spur gear pair for balanced bending stresses and minimized wear. Researchers mostly omit pressure angle as an optimization parameter with the exception of Kim et al. [1] and Hammoudi et al [8]. This is also evident in a field of study review by Miler and Hoić who have not identified any additional publications using this parameter [9]. Additionally, studies using pressure angle as a variable tend to allow only discrete values, thus limiting optimization possibilities. Since they are standardized in ISO53 [10], pressure angle and tooth profile parameters are rarely used as optimization variables. This allows for tooling inventory reduction and calculation simplification but restricts optimization possibilities [11].

2. Methods

Herewith gear macro-geometry was optimized for efficiency and mass using pressure and helix angles, gear width, modulus, tooth count, addendum, dedendum and root radius coefficients as variables. Weight objective function was established by approximating a gear as a cylinder with a diameter equal to the gear pitch diameter according to Eq. (1):

$$m = \frac{{m_n}^2 \cdot \rho \cdot b \cdot \pi}{4} \cdot ({z_1}^2 + {z_2}^2) \tag{1}$$

Efficiency was calculated based on the power loss equation proposed by Mauz [12]:

$$P_{loss} = P_A \cdot \mu_{mz} \cdot H_v \tag{2}$$

Profile and axial contact ratios, specific sliding, roll angle to the start of active profile, tip thickness and clearance, pinion and wheel profile shift coefficients were used as design space constraints. Optimization was carried out using NSGA-II.

3. Conclusions

The optimization algorithm results have shown that a clear trade-off between weight and efficiency exists, as previously reported by other authors [2,3]. Since the third axis of solution space, the transmission error, was not implemented yet the algorithm will tend to minimize addendum coefficient values so as to minimize sliding. In-turn, this will worsen the NVH (noise vibration harshness) behavior of the gear pair. Consequently, minimum transverse and axial contact ratio value constraints were implemented to ensure that the algorithm returns a solution with decent NVH behavior. On the other hand, such constraints will prevent the algorithm from finding the actual global optimum of the original objective function. This was implemented to prepare the algorithm for the future introduction of the third objective, which is the transmission error. With the current setup of constraints, the resulting gearing will always fall in the category of high contact ratio gearing.

References

[1] Kim, S., Moon, S., Sohn J., Park Y., Choi C., Lee G., Macro geometry optimization of a helical gear pair for mass, efficiency, and transmission error. *Mechanism and Machine Theory*, 144, 2020.

[2] Miler, D., Žeželj, D., Lončar, A., Vučković, K., Multi-objective spur gear pair optimization focused on volume and efficiency. *Mechanism and Machine Theory*, 125, 185–195, 2018.

[3] Petry-Johnson, T.T., Kahraman, A., Anderson, N.E., Chase, D.R., An Experimental Investigation of Spur Gear Efficiency. *Journal of Mechanical Design*, 130, 2008.

[4] Younes, E., Changenet, C., Bruyère, J., Rigaud, E., Perret-Liaudet, J., Multi-objective optimization of gear unit design to improve efficiency and transmission error. *Mechanism and Machine Theory*, 167, 2022.

[5] Patil, M., Ramkumar, P., Krishnapillai, S., Multi-Objective Optimization of Two Stage Spur Gearbox Using NSGA-II. *SAE Technical Paper*, 2017.

[6] Yao, Q., Multi-objective optimization design of spur gear based on NSGA-II and decision making. *Advances in Mechanical Engineering*, 11, 1-8, 2019.

[7] Fu, G.Z., Huan, H.Z., Li, Y.F., Zheng, B., Jin, T., Multi-objective design optimization for a two-stage transmission system under heavy load condition. *Mechanism and Machine Theory*, 122, 308–325, 2018.

[8] Hammoudi, A., Djeddou, F., Atanasovska, I., Adaptive mixed differential evolution algorithm for bi-objective tooth profile spur gear optimization. *The International Journal of Advanced Manufacturing Technology*, 90, 2063–2073, 2017.

[9] Miler, D., Hoić, M., Optimisation of cylindrical gear pairs: A review. *Mechanism and Machine Theory*, 156, 2021.

[10] ISO Standard 53:1998, *Cylindrical gears for general and heavy engineering – Standard basic rack tooth profile*, International Organization for Standardization, Geneva, Switzerland, 2021.

[11] Kapelevich, A.L., *Direct gear design*. CRC Press, Boca Raton, 2013.

[12] Mauz W., Zahnradschmierung – Leerlaufverluste. *FVA – Forschungsheft Nr. 185*, 1985.

Added-mass partitoned fluid-structure interaction solver for aorta disection blood flow

Željko Tuković*, Anja Horvat*, Lana Virag*, Philipp Milović+, Ivan Batistić*

*University of Zagreb, Faculty of Mechanical Engineering and Naval Architecture
E-mails: {zeljko.tukovic, anja.horvat, lana virag, ivan.batistic}@fsb.hr
+University of Zagreb, School of Medicine
E-mail: philipp.milovic@mef.hr

Keywords: fluid-structure interaction, finite-volume method, Robin boundary condition, incompressibility, hyperelasticity, aorta, disection

1. Introduction

Loosely or strongly coupled Dirichlet-Neumann (DN) partitioned fluid-structure interaction (FSI) algorithms are stable only if the density of the structure is much higher than that of the fluid. This requirement is difficult to achieve in hemodynamics where the density of blood is on the same order of magnitude as the density of arterial walls. The stability issue is even more pronounced when the blood vessel walls are surrounded by the blood flow from both sides, as is the case for an aortic dissection.

2. Methods

The laminar flow of an incompressible Newtonian fluid (blood) is described by Navier Stokes equations in arbitrary Lagrangian-Eulerian form. On the other hand, deformation of incompressible neo-Hookean hyperelastic material (aortic wall) is defined by momentum equation in total Lagrangian form. Both fluid and solid models are spatially discretised using cell-centered finite volume method, whereas temporal discretisation is preformed by first order accurate Euler implicit scheme. FSI problem is solved using added-mass partitioned scheme, meaning the fluid sub-problem is solved with a Dirichlet boundary conditions (BC) for velocity (structure velocity) and Robin BC for pressure at the FSI interface, while the solid sub-problem is solved with a Neumann BC (fluid stress) at the interface. The stability of the scheme is ensured by the Robin BC for pressure, where the normal derivative of the pressure at the interface is defined by the reduced momentum equation, while the value of the pressure is bounded by solid inertia. In the original Robin BC, as defined in [1]:

$$p^k + \frac{\rho_s h_s}{\rho_F}\left(\frac{\partial p}{\partial n}\right)^k = p^{k-1} - \rho_s h_s \left(\frac{\partial v_n}{\partial n}\right)^{k-1}, \tag{1}$$

the virtual thickness h_S is calculated using propagation speed of p-waves in an elastic media. Since p-wave speed is infinite in the case of incompressible solid, virtual thickness is set to local thickness of the structure. Such an approach seams appropriate in the case of shell-like structures such as blood vessel walls. In the case of internal elastic walls surrounded by fluid flow from both sides, we propose a modified Robin BC in a following form:

$$\left(p^k - p_o^k\right) + \frac{\rho_S h_S}{\rho_F}\left(\frac{\partial p}{\partial n}\right)^k = \left(p^{k-1} - p_o^{k-1}\right) - \rho_S h_S \left(\frac{\partial v_n}{\partial n}\right)^{k-1}, \tag{2}$$

where p_o is the fluid pressure at the opposite side of the internal wall. This is taken into account implicitly during the solution of pressure equation.

3. Results

Proposed numerical model is tested on a wave propagation in an elastic tube test case intended to demonstrate the capability of the model to predict blood flow in large arteries. Two geometrical variants of the case are tested: standard *single tube case* [1] and modified *double tube case* which

consists of an additional centrally positioned shorter internal tube. Both tubes are clamped at the inlet and outlet. During the first 0.003 s, a uniform over-pressure is applied at the inlet in both cases. Figures 1 and 2 shows fluid pressure field and solid equivalent stress field at time instance 0.005 s and Figure 3 shows convergence history of the applied FSI coupling algorithm. Double tube test case, which can be considered as a representative test case for the aorta dissection, requires twice as mach FSI coupling iterations, but number of iterations is still acceptable considering complexity of the problem.

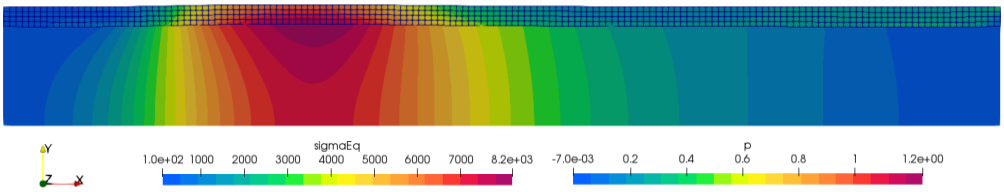

Figure 1. Single tube case; fluid pressure and solid equivalent stress at *t*=0.005 s

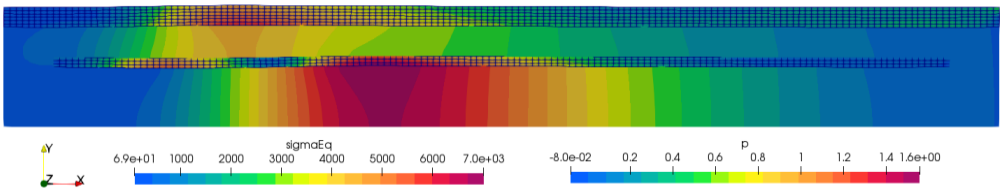

Figure 2. Double tube case; fluid pressure and solid equivalent stress at *t*=0.005 s

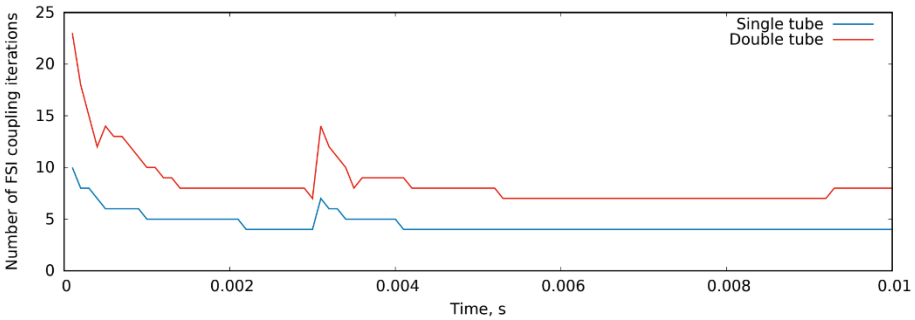

Figure 3. Convergence history; number of FSI coupling iterations as a function of time

4. Conclusions

It is proposed new added-mass partitioned FSI solution procedure based on Robin BC for pressure, which can handle incompressible solid and internal walls. There is no need for any under-relaxation during data transfer between fluid and solid analysis, which ensures good convergence of the solution procedure.

Acknowledgments

This work was supported by grants from the Croatian Science Foundation (projects IP-2020-02-4016 and DOK-2021-02-3071, PI: Ž Tuković).

References

[1] Ž. Tuković, M. Bukač, P. Cardiff, H. Jasak, and A. Ivanković, *Added mass partitioned fluid-structure interaction solver based on a Robin boundary condition for pressure*, in Selected Papers of the 11th OpenFOAM Workshop, pp. 1–22., Springer International Publishing, 2019.

Damage characterization via Digital Volume Correlation: Application to an *in-situ* cyclic test on glass fiber reinforced polymer

Ana Vrgoč*, Zvonimir Tomičević*, Benjamin Smaniotto+, François Hild+

*Faculty of Mechanical Engineering and Naval Architecture, Ivana Lučića 5, 10 000 Zagreb
E-mails: ana.vrgoc@fsb.hr, zvonimir.tomicevic@fsb.hr

+Université Paris-Saclay, CentraleSupélec, ENS Paris-Saclay, CNRS, LMPS - Laboratoire de Mécanique Paris-Saclay, 91190 Gif-sur-Yvette, France
E-mail: benjamin.smaniotto@ens-paris-saclay.fr, francois.hild@ens.paris-saclay-fr

Keywords: Digital Volume Correlation, Damage, Fiber reinforced Polymer, Gray level residuals

1. Introduction

X-Ray Computed Tomography (XCT) coupled with Digital Volume Correlation (DVC) enables for *in-situ* measurements of bulk displacements and calculation of 3D strain maps 0. Capturing the bulk kinematics and microstructural changes is crucial in understanding the complex behavior of fiber reinforced polymers (FRPs) as various damage mechanisms are induced on different scales in such heterogeneous materials 0.

The *in-situ* cyclic tensile test reported herein was performed on a dogbone specimen made of a glass fiber mat reinforced polyester resin. The experiment was imaged via XCT, while the bulk kinematics was measured via global DVC based on finite element (FE) discretizations of the inspected Region of Interest (ROI). Damage mechanisms were identified by laying the correlation residuals (corresponding to the gray level difference between the reference volume and the volume of the deformed material corrected by the measured displacement field) and major eigen strain fields over the corresponding mesostructure sections. They are further compared to the deformed volumes. Last, damage growth was quantified by analyzing major eigen strain and correlation residual histograms.

2. Experimental protocol and DVC measurements

A 5.2 mm thick dogbone specimen containing a rectangular notch (Figure 22(a)) was subjected to four loading cycles corresponding to 25%, 50%, 75% and 90% of its ultimate tensile strength (Figure 22(b)). During the *in-situ* experiment, 12 scans in total were acquired in the loaded/unloaded stages with a lab CT scanner (X-View X50-CT, North Star Imaging) of LMPS. Two scanning parameters were employed (*i.e.*, High Quality (HQ) and Continuous) to reduce the experiment duration and mitigate relaxation phenomena. The size of the ROI (tailored to the thinned ligament of the dogbone specimen) was 401 × 630 × 945 voxels, whose physical size was 14.6 μm. As it resulted in lower noise levels, the HQ scan 0 was considered as the reference for volumetric full-field measurements. The global DVC algorithm implemented within the *Correli 3.0* framework was employed 0. The ROI was discretized with first-order tetrahedral elements. The average element length, computed as the cube root of the mean element volume, was 11 voxels. The quality of the measured kinematics was evaluated from the correlation residual maps, as high values reveal local violations to gray level conservation (being the underlying hypothesis of DVC). Localized phenomena observed in the correlation residual maps indicate damage initiation and growth.

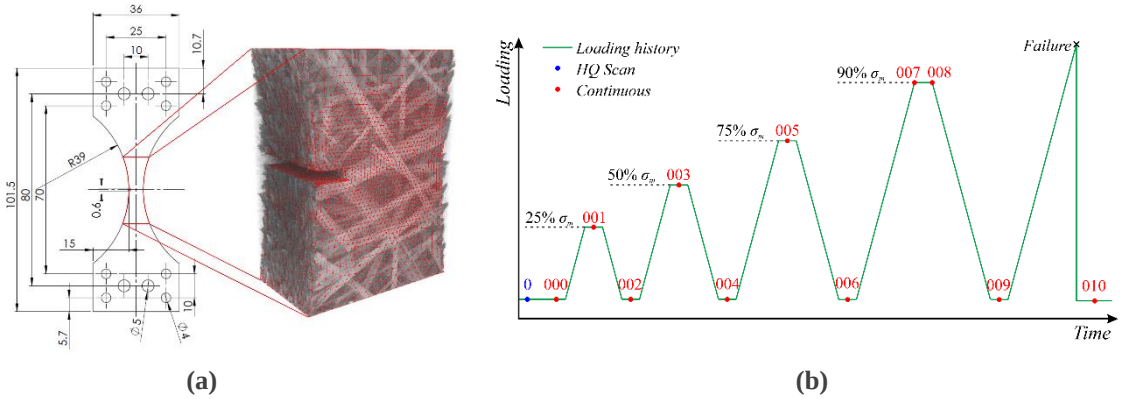

(a) **(b)**

Figure 22. (a) Geometry of the dogbone specimen together with the studied ROI. (b) Schematic representation of the loading and acquisition history of the in-situ *cyclic experiment.*

3. Results and Conclusion

During the prescribed loading history, permanent strains accumulated within the inspected ROI. The correlation residual maps revealed that numerous mesocracks initiated in the material bulk. Damage growth was quantified by analyzing major eigen strain and correlation residual histograms. The spread of the corresponding distributions was observed as the load levels increased. Furthermore, various damage mechanisms were observed (*i.e.*, intra-yarn debonding, fiber breakage, yarn pull-out). They were identified by laying the correlation residuals over the corresponding mesostructure, and the analysis of the corrected volumes enabled for a precise identification of the damage mechanism at the observed mesoscale. The present study exemplifies the ability of FE-based DVC to measure complex kinematics even in the presence of strained band. In addition, the methodology employed herein could efficiently detect multiple damage mechanisms in fiber reinforced polymers.

Acknowledgements

This work was performed within the FULLINSPECT project supported by the Croatian Science Foundation (UIP-2019-04-5460 Grant). This work was also partially supported by the French "Agence Nationale de la Recherche" through the "Investissements d'avenir" program (ANR10-EQPX-37 MATMECA Grant).

References

[1] Buljac, A., Jailin, C., Mendoza, A., Neggers, J., Taillander-Thomas, T., Bouterf, A., Smaniotto, B., Hild, F., Roux, S., Digital Volume Correlation: Review of progress and challenges, *Experimental Mechanics*, 58, 661-708, 2018.

[2] Brunner, A., Identification of damage mechanisms in fiber-reinforced polymer-matrix composites with acoustic emission and the challenge of assessing structural integrity and service-life, *Construction and Building Materials*, 173, 629-637, 2018.

[3] Leclerc, H. et al. Correli 3.0. Agence pour la Protection des Programmes, Paris (France), IDDN.FR.001.520008.000.S.P.2015.000.31500, 2015.

Influence of the cross wire welding parameters on the weld breaking force

Domagoj Vrtovšnik*, Marino Brčić+

* *Faculty of Engineering, University of Rijeka, Vukovarska 58, Rijeka, Croatia*
E-mail: dvrtovsnik@riteh.hr

+ *Faculty of Engineering, University of Rijeka, Vukovarska 58, Rijeka, Croatia*
E-mail: mbrcic@riteh.hr

Keywords: cross wire welding, electric resistance welding, destructive testing, weld strength, breaking force

1. Introduction

Electric resistance welding (ERW) is the welding process that involves passing of an electric current through the components with no filler material being used [1].
In the production of the cross wire welded reinforced meshes corrosion resistance has important role. Every resistance welding causes expulsion of material. Too much expulsion creates welds that can't be adequatly protected against corrosion. If the expulsion amount can be controlled, satisfactory weld appearance can be achiveved. While the weld appearance is an important factor, weld strength can not be ignored. The aim of this reasarch is to find the correlation between welding parameters and the weld strenght in order to obtain the weld with satisfactory appearance and required strength.
In this case, two steel wires of the same radii are joined together to form reinforcing wire mesh. Mesh production, where multiple welds are being produced at the same time has been described by both Bushell [2] and Jordan [3].

2. Testing procedure

Tested samples are made using process called indirect [4] cross-wire welding, with three welds being made simultaneously. From the wire mesh, test samples are cut out, sorted and prepared for the destructive testing on the universal testing machine. Before destructive testing each sample is photographed with the microscope for the purpose of noting the weld appearance prior to applying the anti-corrosion powder coat. Photo of the sample taken with the microscope is shown on Figure 1.

Figure 1 Close up image of the weld taken with the microscope

Because the project requires analyzing and testing steel wires of different radii, modular testing fixture is constructed according to the instructions found in the Resistance Welding Manual [5]. Testing fixture and test setup is shown on Figure 2.

Figure 2 Weld strenght test setup

Breaking force values are recorded using the Bürster 8524 load cell [6] and Bürster DigiVision [7] software. Observed input parameters are welding time and weld current strength.

Acknowledgement

This research is fully funded by the European structural and investment fund (ESIF) under the project number KK.01.2.1.02.0039.

References

[1] Pfeifer, Michael ,Manufacturing Process Considerations, *Materials Enabled Designs*, Elsevier ,p. 115-160, 2009.
[2] Bushell, R., Resistance welding of cross-wire joints, Weld. Metal Fabr. , Vol. 19, No. 5, p. 175-178, 1951.
[3] Jordan, R. H. , Productivity in multiple cross-wire welding., Weld. Metal Fabr., Vol. 32, No. 1, p. 19-26, 1964.
[4] Scotchmer, N. The other resistance process: Cross wire welding, *Welding Journal (Miami, Fla)* Vol. 86, No. 12, p. 36-39, 2007.
[5] Nielsen, C. V. / Zhang, W. / Bay, N. / Martins, P. A. F., Cross-wire welding analyzed by experiments and simulations,., *Journal of Advanced Joining Processes* , Vol. 3., 100039, 2021.
[6] Bürster tension and compression load cell model 8524 operation manual, (https://www.burster.com/fileadmin/user_upload/redaktion/Documents/Products/Manuals/Section_8/BA_8524_EN.pdf) (14.01.2022.)
[7] BürsterBürsteraDigiVision,a(https://www.burster.com/de/sensorelektronik/digitalanzeiger/p/detail/digivision) (14.01.2022.)

Application of transformed area section method in bending analysis of thin-walled laminated composite beams with symmetrical open sections and shear influence

Marko Vukasović*, Radoslav Pavazza*, Frane Vlak*, Karla Delić*

*University of Split, FESB, Rudjera Boskovica 32, Split, Croatia
E-mails: {mvukasov,rpavazza,fvlak, kdelic00}@fesb.hr

Keywords: thin-walled composite beams; transformed area section method; bending; shear.

1. Introduction

In structural analysis of thin-walled laminated composite beams subjected to bending and torsion types of loading, well known expressions for the geometric characteristics used in classical beam theories [1] cannot be applied due to variability of elastic properties. New mechanical properties based on both geometric and material characteristics had to be defined for that reason [2, 3]. With application of transformed area section method, thin walled laminated composite beams with variable elastic properties can be analyzed in the same manner as beams with constant elastic properties [4], i.e. as beams made of conventional isotropic materials [5].

2. Illustrative examples

The displacement analysis of laminated mono-symmetric I-beams (Fig. 1) is presented. The results obtained with respect to the fiber orientation and by application of transformed area section method are compared with the results provided by analytic model developed for laminated beams with variable elastic properties [6], and also with the results obtained by finite element method (FEM). 3D FEM models were made by using ADINA software and four-noded composite shell elements are employed in numerical analysis. The cross-section geometric properties are (Fig. 1a): $b_1 = 4$ cm, $b_2 = 3$ cm, $h = 5$ cm, $t_1 = 0.312$ cm, $t_2 = 0.208$ cm and $t_0 = 0.104$ cm. All the computations were carried out for the glass-epoxy composite material with the elastic properties:

$$E_1 = 53.78\,\text{GPa}, \quad E_2 = 17.93\,\text{GPa}, \quad G_{12} = 8.96\,\text{GPa}, \quad \nu_{12} = 0.25, \tag{1}$$

where the subscripts "1" and "2" correspond to the directions parallel and perpendicular to the fibers. The detailed stacking sequences of the laminates in cross-section are given in Table 1, where α_f is the angle between the fiber direction and the longitudinal x-axis.

Table 3 Stacking sequences of mono-symmetric I-beams

Stacking sequence	top flange	bottom flange	web
CASE 1	$\left[+\alpha_f/-\alpha_f\right]_{6s}$	$\left[+\alpha_f/-\alpha_f\right]_{4s}$	$[0/45/90/-45]_s$
CASE 2	$[0/45/90/-45]_{3s}$	$[0/45/90/-45]_{2s}$	$\left[+\alpha_f/-\alpha_f\right]_{2s}$

The vertical displacement w at the mid-span of the simply-supported thin-walled laminated beams with constant elastic properties over the cross-section can be written as [4]

$$w = w_b \eta_w, \quad w_b = \frac{5 q_z l^4}{384 a_{11}^* I_y}, \quad \eta_w = 1 + \frac{48}{5} \frac{a_{11}^* I_y}{a_{66}^* A_{zz} l^2}, \tag{2}$$

where η_w is the shear correction factor with respect to the displacements w_b obtained by neglecting the shear influence; q_z is the uniformly distributed load in the plane of symmetry; l is the beam length, I_y is the second moment of area; A_{zz} is the reduced shear area; a_{11}^* and a_{66}^* are the elements of reduced extensional stiffness matrix (laminate elastic properties) [4].

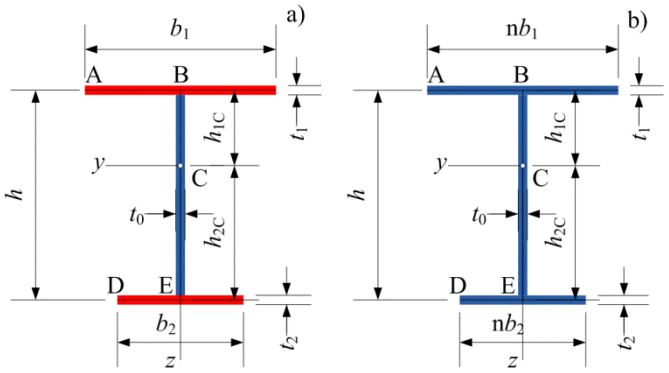

Figure 1. Mono-symmetric I-section: a) original section; b) equivalent section.

In order to keep the cross-section thickness as it is, the original section (Fig 1a) is transformed to equivalent section (Fig 1b) by scaling the top and bottom flange area (top and bottom flange width), to account the stiffness difference, using the scaling factor n as $n = a^*_{11,top\ and\ bottom\ flange} \big/ a^*_{11,web}$. The elastic properties of equivalent section are defined with the stacking sequence of the web.

The displacements of the simply supported I-beams with respect to fiber orientations in top and bottom flange (CASE 1) and in web (CASE 2) are presented on Fig. 2 according to Eq. (2) for q_z = 1N/mm and l/h = 3 aspect ratio.

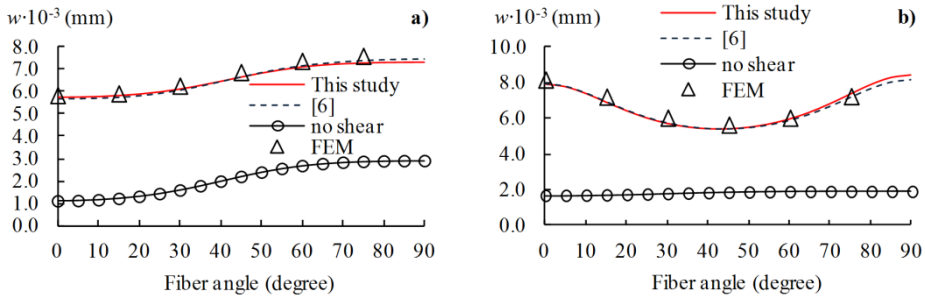

Figure 2. Vertical displacements at the mid-span of the simply supported beams: a) CASE 1; b) CASE 2.

3. Conclusions

Transformed area section method is successfully implemented in bending analysis with shear influence of thin-walled laminated composite beams with symmetrical open sections and variable elastic properties. Comparisons with the FEM calculations and with the results obtained by analytic model developed for beams with variable elastic properties have shown the efficiency of applied method.

References

[1] Vlasov, V. Z., *Thin-walled elastic beams*. Israel Program for Scientific Translation Ltd., Jerusalem, 1961.

[2] Lee, J., Center of gravity and shear center of thin-walled open section composite beams. *Composite Structures*, 52, 255-260, 2001.

[3] Ramaprasad, S., Dattaguru, B. & Singh, G., Exact solutions for thin-walled composite open section beams using a unified state space coupled field formulation. *Mechanics Based Design of Structures and Machine*, DOI: 10.1080/15397734.2021.2024846, (2022).

[4] Vukasović, M. & Pavazza, R., Flexural analysis of thin-walled laminated composite beams with arbitrary open sections and shear influence. *Mechanics of Advanced Materials and Structures*, DOI: 10.1080/15376494.2021.1946222, (2021).

[5] Pavazza, R., Matoković, A. & Vukasović, M., Bending of thin-walled beams of open sections with influence of shear, part II: Application. *Thin-walled Structures*, 116, 369-386, (2017).

[6] Vukasović, M., Pavazza, R. & Vuko, M., Contribution to bending with shear influence of thin-walled laminated composite I-beams with mono-symmetric cross-section and variable elastic properties, article submitted to CIET 2022, Valencia, Spain.

Fatigue analysis of seam welds in lightweight aluminum structures

Mislav Vukić[1], Roman Baranja[1], Richard Tichy[2], Harald Pramberger[2]

[1]*AVL-AST d.o.o., Strojarska cesta 22, Zagreb, Croatia*
E-mails: {roman.baranja,mislav.vukic}@avl.com

[2]*AVL List GmbH, Hans-List-Platz 1, Graz, Austria*
E-mail: {richard.tichy,harald.pramberger}@avl.com

Keywords: fatigue assessment, seam weld, aluminum, FEMFAT Weld, notch stress

1. Introduction and motivation

Due to the overall requirements for general mass reduction that are imposed throughout the modern automotive industry for various reasons, lightweight materials such as aluminum can play a major role in the optimization and development process of powertrain components and vehicles in general. However, regardless of the reduced mass requirements, the selected materials must fulfill the overall strength criteria for the sake of ensuring the structural integrity of the whole system. Extruded aluminum components have shown to be the "go to" choice for keeping the structural integrity of modern vehicles, with welding being used as the main joining technology. With welded joints considered to be the weakest points of any welded structure in terms of long-term application, fatigue assessment of welded joints still remains to be one of the most important procedures in powertrain development. In order to avoid expensive experiments for conducting a successful fatigue assessment, numerical simulations are increasingly used for such purposes. Hence, experimental, and numerical fatigue assessment of welded joints from 6060-T66 extruded aluminum alloy has been conducted and compared in detail.

2. Considered fatigue life assessment methods

In order to assess the fatigue life of welded components, four different fatigue assessment methods have been considered including stress-based approaches such as nominal stress, structural hot-spot stress, and effective notch stress as well as crack propagation analysis. With one of the goals being to investigate the capabilities of *FEMFAT Weld* as a numerical fatigue assessment tool dominantly based on the effective notch stress approach by Radaj et. al [1], naturally the focus was put on this method. According to the fictious notch rounding approach by Radaj [2], value of fictious notch radius ρ_f that can faithfully represent the existing weld geometry in numerical simulations should be equal to 1 mm, while *FEMFAT* recommendation suggests the value of $t/10$, with t being the material thickness. Both assumptions have been investigated throughout this work.

3. Fatigue life assessment using *FEMFAT Weld*

FEMFAT is a universally applicable software program used for the fatigue assessment of statically or dynamically loaded components and one of many modules that the software provides is in fact *FEMFAT Weld* which is designed to simplify the fatigue assessment of welded joints. The main advantage this module has is the database of pre-defined welded joints that can be used for numerical simulations with weld joint definition in said database based on effective notch stress approach. Besides the database itself, the software provides the user with an option of extending the weld database with user-defined welded joints by following a specific procedure provided by *FEMFAT*. The aforementioned procedure was thoroughly investigated and applied to welded joints examined through this work.

4. Experimental procedure

Experimental measurements were conducted on butt joint and T-joint specimens with their respective geometry depicted in Figure 1. For the production of the specimens, extruded aluminum profile of 6060 T66 aluminum alloy with the wall thickness of t=3 mm was used. Welding (MIG) was conducted perpendicular to the extrusion direction with final specimens cut from the welded sections of the said profile by using electrical discharge machining (EDM). Total of 24 specimens of each type were subjected to HCF testing with two different loading setups for each set of specimens, tension and 3-point bending, in order to achieve crack initiation at two different locations in the weld. Some additional specimens were used for microscopical, metallographic and hardness measurements for the purposes of weld database extension in *FEMFAT* and weld geometry assessment.

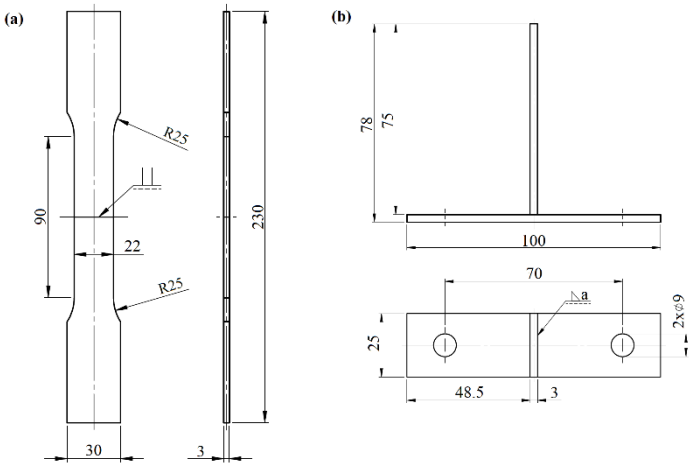

Figure 1. Geometry of a) butt joint specimen, b) T-joint specimen

5. HCF testing and *FEMFAT Weld* results comparison

The HCF testing resulted in a unique set of S-N curves for each of the four different setups used in regard to the specimen type and loading conditions. Data acquired from the HCF testing and additional measurements was also used for the extension of the weld database in *FEMFAT* with newly defined weld joints used for the numerical fatigue assessment of the four different setups in question. In regard to the experimental 50% survival probability curve for both loading setups of the butt joint specimen, the simulation results with the use of ρ_f=0.3 mm show to be far too conservative while the value of ρ_f=1 mm provides more realistic results, much closer to the experiment. As for the T-joint specimen the experimental and numerical results for the 50% survival probability in both setups show much better matching in the case of the fictious notch radius ρ_f=0.3 mm, with ρ_f=1 mm predicting much longer fatigue life than it was shown in the experiment for the same load value.

6. Conclusion

The fictious notch radius value of ρ_f=0.3 mm proposed by *FEMFAT* showed to be a good assumption for successful numerical fatigue assessment when no large variations in real weld radius exist as is the case with the T-joint specimens i.e., with larger radius deviations the results may be too conservative. *FEMFAT Weld* showed to be a reliable tool for fatigue assessment with great weld joint modification possibilities for the user.

References

[1] Radaj, D., Sonsino, C. M., Fricke, W.: *Fatigue assessment of welded joints by local approaches*, Woodhead Publishing, Cambridge, England, 2006

[2] Radaj, D.: *Design and analysis of fatigue resistant welded structures*, Abbington Publishing, Cambridge, England, 1990

Numerical simulation of high-efficiency welding process and subsequent heat treatment for reduction of residual stresses

Marin Vukovojac*, Boris Jalušić*, Tomislav Lesičar*, Mato Perić+, Ivica Skozrit*, Ivica Garašić*, Zdenko Tonković*

*Faculty of Mechanical Engineering and Naval Architecture, University of Zagreb, Ivana Lučića 5, 1000 Zagreb, Croatia
E-mails: {marin.vukovojac, boris.jalusic, tomislav.lesicar, ivica.skozrit, ivica.garasic, zdenko.tonkovic}@fsb.hr

+University North, Trg dr. Žarka Dolinara 1, 48000 Koprivnica, Croatia
E-mail: mato.peric@fsb.hr

Keywords: high-efficiency welding, residual stresses, heat treatment, fracture-mechanics

1. Introduction

Most of the products that are made of steel contain parts which have to be joined together during the production. Welding is used as primary joining technology in various industries like civil engineering, ship-building and heavy-duty machinery building, etc., where machine components of significant thickness need to be welded together. In recent times, many researchers and companies are trying to improve the efficiency of existing welding processes, which is mostly measured in higher deposition rate of molten metal per unit of time. Welding of thick plates is usually done in multiple passes. The positive side of the multi-pass welding procedure is that it reduces the levels of residual stresses by reheating beads which were laid down in previous passes. Fewer passes are usually achieved by ensuring greater heat input in order to achieve better penetration of base metal, which is crucial for welding of thick plates. Baba et al. [1] developed a novel modified GMAW process by employing *buried arc* which enables welding 20-mm-thick plates in single pass. Perić et al. [2, 3] further investigated the buried arc welding. The results show that the tensile residual stresses were exceeding the yield stress of S355J2+N steel, but no further experimental testing was done in terms of evaluation of mechanical properties of the welded joint. This is a relatively new technology which allows higher productivity, but it must be more closely examined to evaluate its applicability for industrial purpose, which is an actual motivation for this work.

The second goal, after improving the efficiency of existing welding processes, is to achieve lower values of tensile residual stresses in the welded joint, or in other words to achieve the highest possible values of mechanical properties of the welded joint. Since lower values of residual stresses are hard to achieve without implementing welding in multiple passes, other procedures should be applied after the welding. The most common technology for reduction of residual stresses is post-weld heat treatment (PWHT). Liu et al. [5] studied experimentally and numerically the influence of PWHT and ultrasonic impact treatment (UIT) on residual stresses in GMAW butt-welded 40-mm-thick plates made of Q390B low-carbon steel. It was found that UIT mainly affects the residual stresses only within the boundaries of the treated region, while the PWHT had much larger effect on the surface stress distribution.

2. Experimental investigation

Since buried arc technology has been developed only recently, there are no prescribed regimes of PWHT for reduction of residual stresses. The goal of the experimental work is to measure the residual stresses after the welding by using the X-Ray diffraction (XRD) method. The welded specimens will be subjected to the heat treatment in relatively compact furnaces for a period of time. The PWHT temperature and duration will be varied during the experimental testing. After the cool down, the residual stresses will be measured again in order to determine the efficiency of the each PWHT

regime. Experimental testing and measuring are the most accurate way of obtaining data, but they require a lot of time and can be very expensive.

3. Numerical model

In order to reduce the costs of the testing, the numerical models of heat treatment will be developed on the basis of obtained experimental data in order to examine each PWHT parameter in detail. PWHT model will be built from numerical model of welding process, which is usually done in two subsequent steps. In the first step, temperature field is being calculated for transient heat transfer by implementing element birth and death (EBD) method and by implementing prescribed welding temperature (PWT), which allows for a reduction in computation time because there is no need to calculate the welding temperature from welding heat flux parameters. Mechanical analysis is done in subsequent step in order to calculate strains and stresses from the previously obtained temperature field. PWHT model will be done in two subsequent steps, just like the welding model. Mechanical analysis will include a creep model in order to calculate the reduction of residual stresses obtained from mechanical analysis of the welding model.

4. Conclusions

The contribution of this work is not only focused on achieving the highest possible levels of mechanical properties of the joint welded by the buried arc technology, but also on achieving the minimal levels of residual stresses and angular distortion of the welded joint. Also, numerical models and experimental data from this work could be used for the future work in topics of fracture mechanics and fatigue.

Acknowledgement

This work has been supported and co-funded by the European Union through the European Regional Development Fund, Operational Programme "Competitiveness and Cohesion" 2014 – 2020 of the Republic of Croatia, project "Improvement of high-efficiency welding technology" (ImproWE, KK.01.1.1.07.0076).

References

[1] H. Baba, T. Era, T. Ueyama, M. Tanaka, Single pass full penetration joining for heavy plate steel using high current GMA process, Weld. World. 61 (2017) 963–969. https://doi.org/10.1007/s40194-017-0464-7.

[2] M. Perić, K. Seleš, Z. Tonković, M. Lovrenić-Jugović, Numerical simulation of welding distortions in large structures with a simplified engineering approach, Open Phys. 17 (2019) 719–730. https://doi.org/10.1515/phys-2019-0076.

[3] M. Perić, S. Nižetić, I. Garašić, N. Gubeljak, T. Vuherer, Z. Tonković, Numerical calculation and experimental measurement of temperatures and welding residual stresses in a thick-walled T-joint structure, J. Therm. Anal. Calorim. 141 (2020) 313–322. https://doi.org/10.1007/s10973-019-09231-3.

[4] C.H. Lee, K.H. Chang, V.N. Van Do, Modeling the high cycle fatigue behavior of T-joint fillet welds considering weld-induced residual stresses based on continuum damage mechanics, Eng. Struct. 125 (2016) 205–216. https://doi.org/10.1016/j.engstruct.2016.07.002.

[5] C. Liu, J.B. Shen, J.L. Yan, Q.L. Chu, J.X. Wang, Y. Zhao, Experimental Investigations on Welding Stress Distribution in Thick Specimens After Postweld Heat Treatment and Ultrasonic Impact Treatment, J. Mater. Eng. Perform. 29 (2020) 1820–1829. https://doi.org/10.1007/s11665-020-04731-y.

Periodic heating in the FE axisymmetric model of the railway brake disc

Aleksander Yevtushenko*, Michal Kuciej*, Piotr Grzes*, Piotr Wasilewski+

*Faculty of Mechanical Engineering, Bialystok University of Technology (BUT)
45C Wiejska Street, 15-351, Bialystok, Poland
E-mails: {a.yevtushenko,m.kuciej,p.grzes}@pb.edu.pl

+Frimatrail Frenoplast S.A.
15 Watykańska Street, 05-200, Majdan, Poland
E-mails: pwasilewski@frimatrail-frenoplast.pl

Keywords: moving heat source, temperature, ventilated brake disc, friction

1. Introduction

Numerical modeling of transient temperature fields of disc brakes sliding components, despite the development of computer technology, often requires the introduction of simplifications such as the shape of the analyzed object, conditions in the contact area (e.g. perfect thermal contact, application of the heat partition coefficient), variability of thermophysical properties of materials and the coefficient of friction, wear, non-uniformity of the temperature field in the circumferential direction of the disc [1,2]. In the case of the latter aspect, it is assumed that the angular velocity of the rotor is so high that, despite the coefficient of covering the brake pads and the disc rubbing path less than one, the temperature field of the disc is uniform.

This work proposes an axisymmetric computational model of the brake disc to determine transient changes in temperature fields during braking. The main objective of the study was to take into account the cyclic temperature course of the disc friction surface resulting from its mutual contact with the brake pads. The searched time course of the function defining the contact (value 1) and the lack of contact (value 0) was determined on the basis of the known velocity change during single braking at a fixed brake pad angle. The temperature evolutions obtained numerically using the finite element method were compared with the known methods of cyclic heating of the disc and with the results of experimental tests by other authors with the same input parameters [3,4].

2. Numerical model of a railway vehicle brake disc

The process of a single braking of a railway vehicle is analyzed. At the initial time moment, the vehicle moves at its velocity V_0. As a result of the pressure of the pads against the opposite working surfaces of the disc, heat is generated due to friction at a constant contact pressure p_0 and a simultaneous linear decrease of the vehicle velocity over time t_s.

Assumptions taken in the finite element simulations:
– deformation of the elements of the considered friction pair was ignored;
– only half of the disc with one pad was analyzed;
– ventilated brake disc was represented by simplified axisymmetric (2D) geometrical object;
– coefficient of friction f_0 was constant;
– thermophysical properties of materials were temperature independent;
– contact pressure p_0 was uniformly distributed on the frictions surfaces;
– partition of heat between the disc and the pads was found using the heat partition coefficient γ (Charron's formula);
– on the free surfaces convection heat transfer with the constant heat partition coefficient was set;
– thermal radiation was neglected.

In order to obtain a cyclical course of the disc temperature during the braking process, it was necessary to determine the change of the function $n(t)$ (Fig. 1d) determining the heating and cooling

states of the disc. The product of the function $n(t)$ and the part of the power density of the frictional force directed to the disc $q_d(r,t) = \gamma f_0 r \omega(t) p_0$ was a boundary condition in the area of the working surface of the axisymmetric model of the brake disc. The temperature calculated was compared with the experimental measurements using thermocouples and the data obtained from other numerical models developed in the article [4] (Fig. 1c).

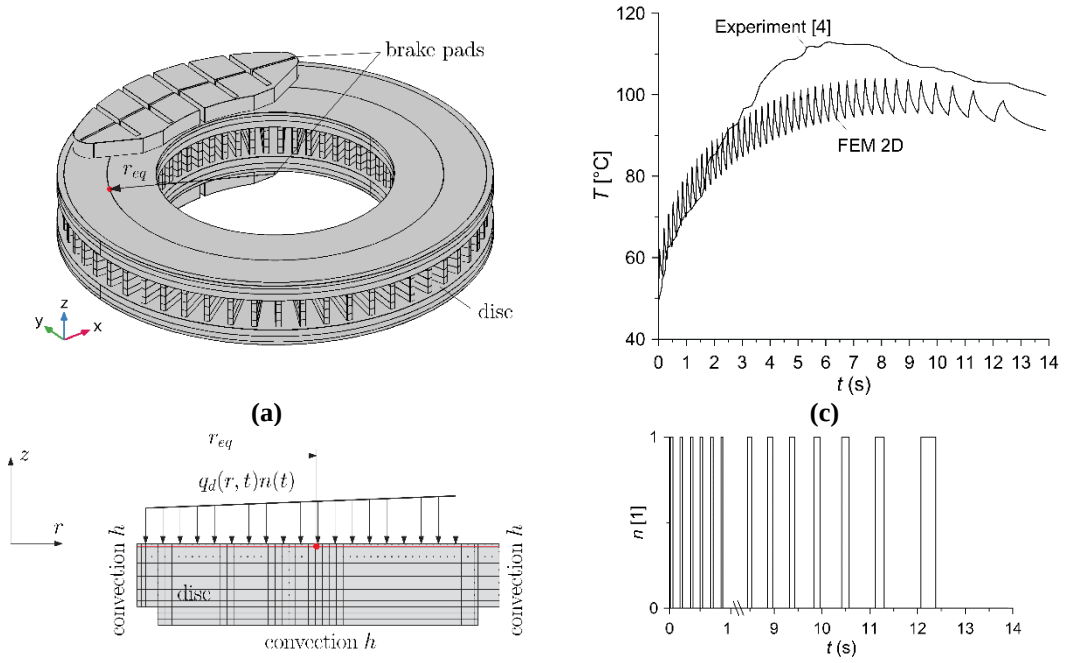

Figure 1. Disc brake CAD model (a); 2D finite element mesh of the brake disc (b); periodic function $n(t)$; calculated temperature changes of the brake disc at $z = -1\text{mm}$, $r = r_{eq} = 247\text{mm}$ (c) and experimental measurements from the article [4]

3. Conclusions

Based on the performed analysis, it was found that the calculated transient temperature obtained from the developed 2D axisymmetric model of the brake disc agree well with the temperature measured using thermocouples [3,4]. Despite the fact that in the numerical model, thickness of the disc was smaller due to simplifying ribs of the ventilated disc the temperature was lower. The difficulty in obtaining better agreement of the results stems mainly from the complex shape of the nominal contact area of the brake pad.

Acknowledgement: This study was supported by the National Science Centre of Poland (Research project No. 2017/27/B/ST8/01249).

References

[1] Adamowicz, A., Grzes, P., Analysis of Disc Brake Temperature Distribution during Single Braking under Non-Axisymmetric Load. *Applied Thermal Engineering*, 31, 1003–1012, 2011.

[2] Yevtushenko, A., Kuciej, M., Grzes, P., Wasilewski, P., Comparative Analysis of Temperature Fields in Railway Solid and Ventilated Brake Discs. *Materials (Basel)*, 14, 1–21, 2021.

[3] Yuan, Z.; Tian, C.; Wu, M.; Wang, G., A Modified Uniformly Distributed Heat Source Method for Predicting Braking Temperature of Railway Brake Disc, *International Journal of Rail Transportation*, 10, 216–229, 2022.

[4] Zewang, Y., Chun, T., Mengling, W., Jiajun, Z., Chao, C., Modeling and Model Validation of Thermal Behavior of Railway Disc During Single Braking. *Journal of Thermal Science and Engineering Applications*, 13, 1–7, 2021.

Some Thermal Problems of Friction of Functionally Graded Materials

Aleksander Yevtushenko, Katarzyna Topczewska, Przemysław Zamojski

Faculty of Mechanical Engineering, Bialystok University of Technology (BUT)
45C Wiejska Street, 15-351, Bialystok, Poland
E-mails: {a.yevtushenko, k.topczewska, p.zamojski}@pb.edu.pl

Keywords: functionally graded materials, temperature, thermal sensitivity, friction, braking

1. Introduction

Most models of frictional heating for braking systems have been developed only for homogeneous materials, while modern friction materials are usually composites with complex internal structure, such as functionally graded materials (FGMs). Since brakes with FGMs are commonly subjected to a wide temperature range, the temperature-dependencies of materials properties should be considered during modeling the frictional heating process in such systems [1]. Severe temperature conditions may cause significant changes of thermal and mechanical properties of friction materials and thermal instability of the friction pair.

2. Development of the model

The mathematical model of frictional heating process was proposed for a braking system with friction pair elements made of two–component functionally graded materials (FGMs) with non-uniform thermal conductivities along the thickness direction. The main part of this model is an exact, analytical solution to the linear thermal problem of friction for a single braking process with constant deceleration. One–dimensional, initial–boundary problem of heat conduction for a system consists of two semi–infinite bodies under sliding with linearly decreasing friction power was formulated. The assumptions of perfect thermal contact conditions on the contact surface and the exponential variations of thermal conductivities in the axial direction, across the volume of the elements, were adopted.

In order to take into account the influence of the thermal sensitivity of friction materials, calculations of temperature distributions were performed involving the thermo–physical properties of FGMs component materials determined at the volume temperature, achieved during braking process. For this purpose, the volume temperature of the friction pair elements were established according to the following steps:

1) approximation of the experimental data of temperature–dependent thermal properties of the functionally graded materials (FGMs) components;
2) finding the FGMs thermal properties: thermal conductivities change exponentially along the thickness, and the effective specific heat and density of elements were found based on mixture law;
3) establishing the volume temperature of FGMs;
4) determining the thermo–physical materials properties corresponding to the volume temperature;
5) correction of the above determined values by repeating the steps 2) – 4) and finding the final values of the volume temperature.

The temperature distributions with consideration of thermal sensitivity of materials were determined based on solution to the thermal problem of friction for the effective thermo–physical properties of FGMs found from approximation formulas at the obtained volume temperatures.

3. Numerical analysis

A comparative analysis was performed based on results obtained for temperature–dependent FGMs and the corresponding data, calculated without consideration of materials thermal sensitivity.

Friction pair elements are made of FGMs with ceramics (Al_2O_3 and ZrO_2) at the friction surfaces to resist wear and severe thermal loading, and their structures gradually change along the thickness of elements approaching metal–based component (Cu and Ti-6Al-4V) in the element core to maintain the structural rigidity [2].

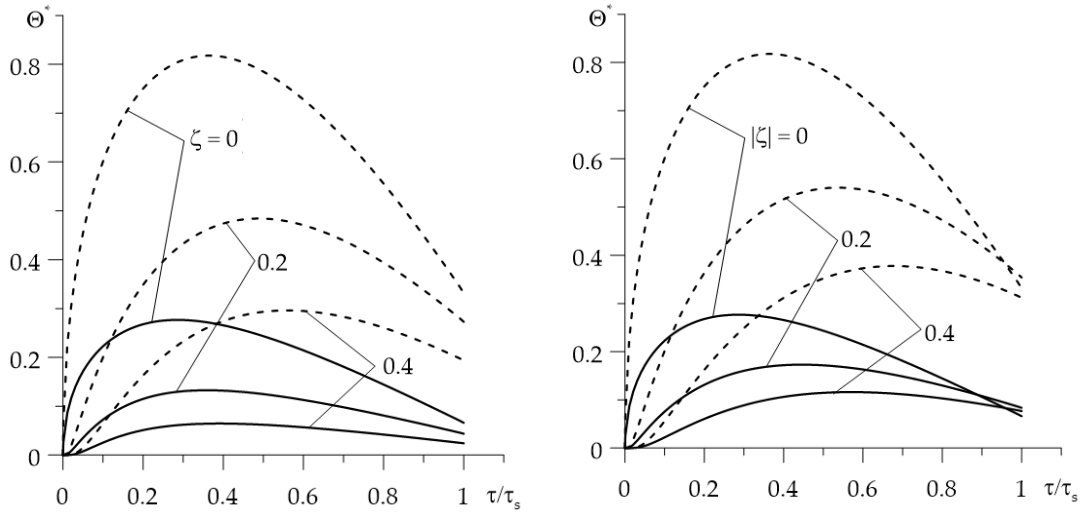

Al_2O_3 – Cu **ZrO_2 – Ti-6Al-4V**

Figure 1. Dimensionless temperature changes during braking at the different distances from the friction surface in both elements of friction pair [3]

Evolutions of dimensionless temperature rise $\Theta^*(\zeta,\tau)$ during braking $0 \le \tau \le \tau_s$, at the few selected distances ζ from the contact surface $\zeta = 0$ are presented in the Figure 1. Levels of the temperature calculated with account of the thermal sensitivity of the materials (solid lines) are significantly lower in both friction elements comparing to the results achieved with temperature–independent properties of FGMs (dashed lines). The greatest differences between these results appear on the contact surfaces. It can be seen that maximum values of temperature are achieved earlier when considering the temperature–dependent materials properties.

4. Conclusions

Based on the performed analysis, it was found that the effect of thermal sensitivity of functionally graded friction materials on the temperature may be significant. The assumption of FGMs thermal stability during single braking process caused the overestimation of temperature achieved in the friction elements.

It should be mentioned that only the case of single braking was analyzed. In the case of other operating modes of the braking system, such as repetitive braking, when the volume temperature may attain greater values, the influence of the temperature–dependent properties of materials on the thermal behavior of brakes may be even higher.

References

[1] Noda, N. Thermal stresses in functionally graded materials. *Journal of Thermal Stresses*, 22, 477–512, 1999.

[2] Hosseini, T.P., Talebi, M. Stress and temperature distribution study in a functionally graded brake disk. *International Journal of Automotive Engineering*. 2, 172–179, 2012.

[3] Yevtushenko, A., Topczewska, K., Zamojski, P., Influence of Thermal Sensitivity of Functionally Graded Materials on Temperature during Braking. *Materials*, 15(3), 963, 2022.

Evolution of the wrinkling pattern due to growth of elastic films on viscoelastic substrates

Jan Zavodnik, Miha Brojan

Laboratory for Nonlinear Mechanics, University of Ljubljana, Ljubljana, Slovenia
E-mails: jan.zavodnik@fs.uni-lj.si, miha.brojan@fs.uni-lj.si

Keywords: wrinkling, viscoelasticity, growth, substrate, film

1. Introduction

Wrinkling of thin elastic films on compliant viscoelastic substrates under compressive loads is a great toy model for studying interaction between the effects of the kinematic nonlinearity and viscoelastic material properties, because it is simple enough for analytical treatment and at the same time still maintains the effects of the viscoelasticity-nonlinear kinematics interaction. This kind of interaction occurs when the structure transitions from the initial, short time-limit to the final, long time-limit. The transition is essentially governed by the viscoelastic properties of the material. In the regime of the infinitesimal deformations the transition is trivial and therefore unsubstantial, but in the presence of nonlinear kinematic effects the transition becomes highly complex and more strongly dependent on initial conditions, perturbations and boundary conditions.While the purely elastic theory offers discrete wrinkling deformation patterns as the solutions, the viscoelastic theory provides a framework to describe also the transition from the deformation patterns, e.g. from a pattern with a large number of wrinkles to the pattern with a small number of wrinkles. The complexity of this transition is a direct consequence of kinematic nonlinearities, because any rearrangement of wrinkles during the transition causes an energy dissipation while it does not affect the final elastic limit state. However, it can have an influence when the system arrives to the long time-limit state. If the initial energy dissipation during rearrangement of wrinkles is too large the system can become "frozen" in a non-equilibrium deformation state, which can be distinctly different from the purely elastic one. The system can remain there permanently if the system loses more energy than needed to overcome an energy barrier. Alternatively, the system can also transition so slowly that the environmental parameters change during the process and it can therefore remain in the out-of-equilibrium state permanently. Note that in general, these deformation states are unreachable for the elasticity alone [1]. In fact, this deformation patterns are very common in nature, e.g. in microbiology [2-4] and morphogenesis [5].

2. Wrinkling pattern evolution analysis

We analyze the elastic film and the viscoelastic compliant substrate decomposed, as displayed in Fig. 1. The elastic film is modelled with the use of Főppl-von Karman (weakly) nonlinear plate kinematic assumptions. On the other hand, the viscoelastic substrate is modelled as a continuum with infinitesimal deformation theory. Both elements are connected through the continuity of deformations and stresses in the structure.

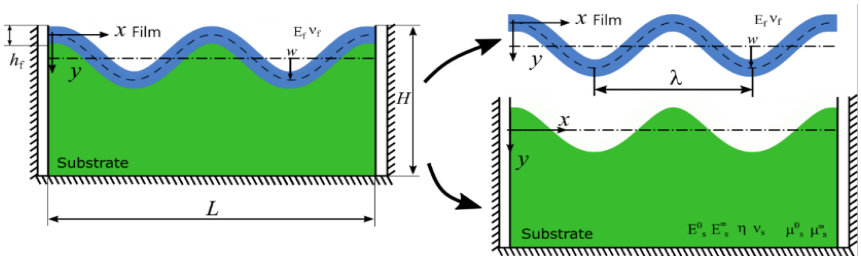

Figure 1. Elastic film and the viscoelastic substrate as separate structural elements.

To solve the obtained system of differential equations we approximate the wrinkles as a harmonic function of the form $w(x,t) = A(t)\cos k\,x$.

The system load in the form of confined growth, external forces etc. can be applied differently in the given time frame. We first analyse a step load. We show that an analytical implicit relation

between the wrinkle amplitude A and time t and the wave number k can be obtained on an infinitely long structure with the use of total strain energy minimization,

$$t = \frac{C_1(\log A - \log A_0) - 12E^*_{s,\mathrm{ee}}(1-\nu_\mathrm{f}^2)\left(\log C_2\,(A) - \log C_2\,(A_0)\right)}{r\left(E_\mathrm{f}h_\mathrm{f}k\left(-h_\mathrm{f}^2k^2 + 12\varepsilon_\mathrm{g}^0\right) - 24E^*_{\mathrm{s,e}}(1-\nu_\mathrm{f}^2)\right)}, \qquad k = 2\sqrt{\frac{\varepsilon_\mathrm{g}^0}{3A^2 + h_\mathrm{f}^2}}.$$

Here the C_1 and C_2 are some auxiliary functions made of material and geometric parameters, A_0 is the initial perturbation amplitude, E is Young's modulus, h is film thickness, ν is Poisson's ratio and r is a viscous relaxation rate. The indices "f" and "s" label the film and substrate properties, respectively. The time at which the wrinkles start to appear depends on the film growth amplitude ε_g^0. We show that if the growth amplitude is subcritical with respect to the long time-limit the wrinkles never appear and alternatively, if it is supercritical with respect to the long time-limit and supercritical with respect to the short time-limit then the wrinkles grow shortly after the growth is applied. Furthermore, if the growth amplitude is supercritical with respect to the short time-limit then wrinkles appear instantly and then continue to grow and transition towards the long time-limit deformation state. If the short time elastic equilibrium deformation pattern is qualitatively different from the long-time time deformation pattern, then the nontrivial transition will occur and the structure may become "frozen" in an out-of-equilibrium state.

In the case where the film growth is a ramp function the ratio between the compliant substrate relaxation rate and the active film growth rate is vitally important. In this case we performed numerical simulation where the growth magnitudes and elastic parameters of the structure were the same, only the ratio between the growth rate and viscoelastic relaxation rate were different. The long-time deformation patterns of two such structures are shown in Fig. 2. We observed that the two simulated structures converged to qualitatively different final deformation pattern.

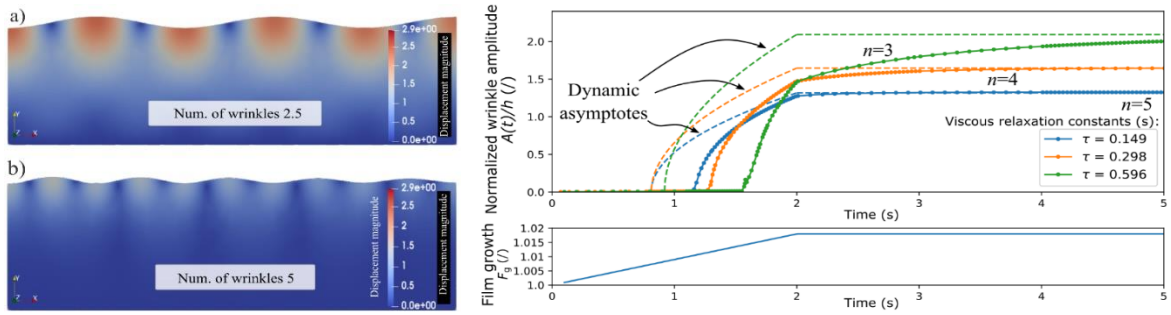

Figure 2. Left: Final deformation states of structures with the same elastic and different viscoelastic properties. Right: Wrinkle amplitude as a function of time for structures with the same elastic and different viscoelastic properties.

3. Conclusions

In this contribution, we show that viscoelastic properties of the material are crucially important for the final development of the pattern even though they seemingly affect only the transition period between the elastic short and long-time equilibrium states of the structure. The interaction between the viscoelastic material properties with the nonlinear kinematics produces interesting deformation patters otherwise unattainable for purely elastic systems. The theory and the principles described are also extremely useful in engineering applications because they allow much simpler fabrication of smart surfaces and coatings that at some point in fabrication behave viscoelasticity.

References

[1] D. A. Matoz-Fernandez, et al.: Wrinkle patterns in active viscoelastic thin sheets. Phys. Rev. Research 2(2020) p. 013165
[2] T. Ruiz-Herrero, et al.: Dynamics of Growth and Form in Prebiotic Vesicles Phys. Rev. Lett. 123(2019) p. 038102
[3] M. Nelson, et al.: Growth-induced buckling of an epithelial layer. Biomech. Model. Mechan. 10(2010) p. 883–900.
[4] D. Espeso, et al.: Differential growth of wrinkled biofilms. Phys. Rev. E, Stat. nonlin. soft matt. Phys. 91(2015) p. 022710
[5] R. de Rooij and E. Kuhl: Constitutive Modeling of Brain Tissue: Current Per-spectives. Appl. Mech. Rev. 68(2016) p. 010801

A neural network model for incompressible rubber thermo-elasticity

Martin Zlatić*, Marko Čanađija*

*Faculty of Engineering, University of Rijeka, Vukovarska 58, Rijeka, Croatia
E-mails: {mzlatic,marko.canadija}@riteh.hr

Keywords: thermo-elasticity, rubber, machine learning, neural network

1. Introduction

Machine learning has become a tool that is used in solid mechanics with the first applications reaching as far back as 1977 (see [1] for a review of work until 1996.). In recent years it is becoming more widely used for a variety of purposes such as a surrogate model for faster computation in medical usage [2] or for a data-driven solver [3]. Of more importance to this work is the possibility to model material behaviour witht he use of neural networks, much work has been done on this topic but for the subject at hand only few dealing with rubber elasticity are mentioned. Shen et al. [4] have used a neural network to model incompressible rubber elasticity by describing the free-energy function with a neural network. Similarly Weber et al. [5] have also used a neural network to model compressible rubber behaviour however instead ofthe free energy they used a neural network to predict stresses from strains and thus obtain the material tangent matrix by partially deriving the networks outputs w.r.t. the inputs. This work draws on the same idea as Weber et al. however applied to thermo-elasticity in incompressible rubber behaviour.

2. Incompressible rubber thermo-elasticity

The data for training the neural network is generated via Ogden's three term model for incompressible hyperelastic materials with the follow form:

$$\psi(\lambda_1,\lambda_2,\lambda_3) = -p(J-1) + \sum_{p=1}^{3} \frac{\mu_p}{\alpha_p}(\lambda_1^{\alpha_p} + \lambda_2^{\alpha_p} + \lambda_3^{\alpha_p} - 3) \tag{1}$$

with stretch $\lambda_3 = \frac{1}{\lambda_1 \cdot \lambda_2}$ which follows from the incompressibility constraint $\lambda_1 \cdot \lambda_2 \cdot \lambda_3 = 1$ for a case of plane stress. Pairs of Cauchy stresses and Green-Lagrange strains for a 2D case were generated to train the neural network. With the use of a feed-forward neural network (FNN) we achieved near identical results when compared to Ogden's model, see Figure 1. The FNN has 2 hidden layers with 15 neurons and a hyperbolic tangent activation function was used. Mean squared error was used as a loss measure during training. The TensorFlow library was used for training.

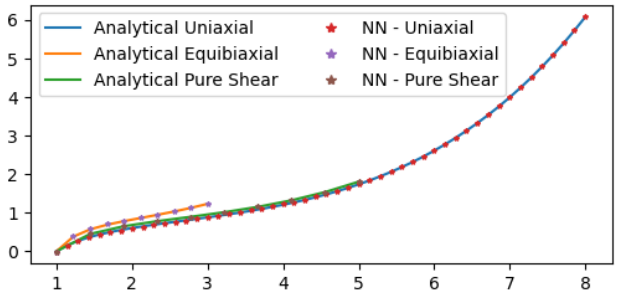

Figure 23. Kirchhoff stress P [MPa] vs. uniaxial stretch λ [-].

An extension is made to Eq. 1 by making the shear moduli linearly dependent on temperature and adding the thermal contribution *T* to the free-energy function.

$$\psi(\lambda_1,\lambda_2,\lambda_3,\Theta) = -p(J-1) + \frac{\Theta}{\Theta_0}\sum_{p=1}^{3} \frac{\mu_p}{\alpha_p}(\lambda_1^{\alpha_p} + \lambda_2^{\alpha_p} + \lambda_3^{\alpha_p} - 3) \; + c_0\left[(\Theta-\Theta_0) - \Theta\ln\frac{\Theta}{\Theta_0}\right] \tag{2}$$

$$P = \frac{\partial \psi(F,\Theta)}{\partial F}, \qquad \eta = -\frac{\partial \psi(F,\Theta)}{\partial \Theta} \tag{3}$$

Deriving the expression given in Eq. (2) w.r.t. temperature Θ we obtain the expression for entropy $\eta(\lambda_1, \lambda_2, \Theta)$. If we consider an adiabatic process of stretch then entropy can be considered constant and thus the temperature change can be computed as we stretch a piece of rubber. The FNN is modified by simply increasing the hidden layers to 3, everything else is kept the same. It should be noted that in both examples a FNN was used to predict each of the stress components individually. The results are presented in Figure 2 for a thermomechanically coupled, an uncoupled purely mechanical, and a thermomechanically coupled FNN result. Stress is calculated as a function of principal stretches, $P^{NN}(\lambda_1, \lambda_2) = FNN(\lambda_1, \lambda_2)$ for both hyper- and thermos-elastic behaviour.

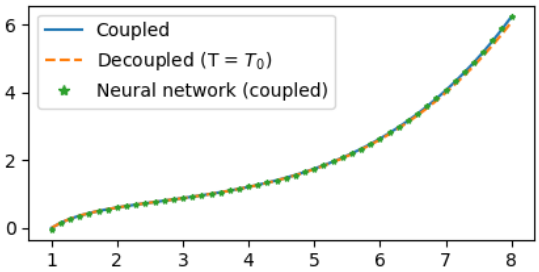

Figure 24. Kirchhoff stress P [MPa] vs stretch λ [-].

The data for training was generated randomly with limits to the principal stretches with 200 samples generated and separated in a 80/20 train/test split. The limits were chosen as $\lambda_1 \in [1,8], \lambda_2 \in [1,8]$. The FNN results are in good accordance with a mean relative error for results in Figure 2 being 2.8%, a mean absolute error of 0.008 MPa, and an R^2 value of 0.999.

3. Conclusions

Drawing from the results in Figures 1 and 2 simple FNNs can be used to model thermos-elasticity in rubber materials and a simplified model can be obtained which simply requires the stretches at any point in time. This is done on a small number of samples even without preprocessing the inputs of the network. Using the built-in auto differentiation function of TensorFlow the tangent moduli can also be obtained and thus the network can be implemented into an FEA software without difficulty.

Acknowledgements

This work was supported in part by the University of Rijeka under project number uniri-tehnic-18-37 and in part by the Croatian Science Foundation under project IP-2019-04-4703.

References

[1] Yagawa G., Okuda H., Neural networks in computational mechanics. *Archives of Computational Methods in Engineering*, 3, 4, 435-512, 1996.

[2] Liang L., Liu M., Martin C., Sun W., A deep learning approach to estimate stress distribution: a fast and accurate surrogate of finite-element analysis. *Journal of The Royal Society Interface*, 15, 2018.

[3] Carrara, P., Lorenzis L. D., Stainier L, Ortiz M., Data-driven fracture mechanics. *Computer Methods in Applied Mechanics and Engineering*, 372, 2020.

[4] Shen Y., Chandrashekhara K., Breig W. F., Oliver L. R., Neural Network Based Constitutive Model for Rubber Material. *Rubber Chemistry and Technology*, 77, 257-277, 2004.

[5] Weber P., Geiger J., Wagner W., Constrained neural network training and its application to hyperelastic material modelling, *Computational Mechanics*, 68, 1179-1204, 2021.

Quadrilateral 2D Finite Elements with Enhanced Fixed-Pole Interpolation in Linear Analysis of Micropolar Continuum

Laura Žiković*, Gordan Jelenić*

*Faculty of Civil Engineering, University of Rijeka
Radmile Matejčić 3, 51000 Rijeka, Croatia
E-mails: {laura.zikovic, gordan.jelenic}@uniri.hr

Keywords: Cosserat continuum, microstructure, fixed-pole concept, finite element method

1. Introduction

The classical (Cauchy) continuum theory faithfully describes the behavior of homogeneous materials such as steel or aluminum. However, discrepancies between theory and experimental results have been observed for inhomogeneous materials, especially those with pronounced microstructure. Moreover, the classical theory cannot describe the so-called size effect, a phenomenon observed in specimens of same material with microstructure in which smaller specimens are usually stiffer than larger ones. In problems where significant stress gradients occur, the analytical solutions obtained using the classical theory do not coincide with experimental results. One such example is an "infinite" homogeneous plate with a circular hole subjected to uniform tension, where the stress concentration near the hole provided by the classical theory is larger than the measured experimentally. In order to realistically describe the behavior of a material with internal structure and capture the phenomena that the classical theory cannot, several alternative theories have been developed by generalizing the classical theory, one of which is the micropolar (Cosserat) continuum theory [1].

In the micropolar continuum theory there is an additional kinematic field (microrotation), which gives an orientation to each material point and is completely independent of the skew-symmetric part of the displacement gradient at the observed point (macrorotation). In order to describe a linear centrosymmetric isotropic micropolar continuum, it is necessary to know six independent material parameters [2]. The theory itself is well known, but reliable experimental methods for determining the material parameters are still not established, which prevents wider application of the theory. Alternatively, in some cases, the additional material parameters may be obtained with the help of numerical analysis in an inversely posed problem. To this end, the development of robust micropolar finite elements is very important.

2. Micropolar 2D finite elements with fixed-pole interpolation

The present so-called "fixed-pole" interpolation is inspired by the fixed-pole concept first introduced in [3] where Bottasso and Borri applied the concept to the geometrically nonlinear 3D beams. The concept has proven to be particularly useful in nonlinear dynamics, but so far, no attempts have been made to apply it in linear analysis, where some advantages of the concept can be also expected. The fixed-pole concept naturally introduces a new kinematic field combining the displacement field and the rotational field, which results in non-standard degrees of freedom in place of displacements. The interpolation is further enhanced by a coefficient derived from observing the relationship with the linked interpolation, which is known to provide exact solution for the Timoshenko beam, thus obviously eliminating the shear-locking effect. Given the fact that the Timoshenko beam actually represents a 1D micropolar continuum, this type of element provides the basis for the further development of 2D and 3D micropolar finite elements with interpolation based on the fixed-pole concept.

Isoparametric quadrilateral finite elements with 4 nodes and 3 degrees of freedom per node have been used here for the simulation of micropolar 2D continuum. The displacement-type weak formulation is obtained by means of the principle of virtual work. The microrotation field is interpolated by standard Lagrangian interpolation, while the displacement field is enhanced by applying the fixed-pole interpolation. It is important to note that an external force vector should be

determined according to the chosen interpolation functions in order to satisfy the finite element equilibrium equation. The elements have been tested through numerical examples consisting of a set of patch tests and in Figure 1. we present convergence of the element on a higher-order patch test – a cantilever beam subjected to pure bending. The analytical solution of the problem for the micropolar continuum was given by Gauthier and Jahsman [4] and this test is very important in the process of experimental determination of material parameters. They have shown that, in the micropolar continuum, the state of pure bending requires a linearly varying normal surface traction and a constant surface moment acting on the cross section at the loaded end. Moreover, both surface loads must be given in a unique proportion that depend on the material parameters. A numerical solution to this problem has been obtained using the elements with Lagrangian, enhanced fixed-pole, and linked interpolation [5], where for the last two we may show that they lead to an identical finite element formulation. Figure 1. shows much faster convergence of the fixed-pole element, in particular for the low values of the characteristic length for bending l_b (which is one of the parameters of the micropolar continuum).

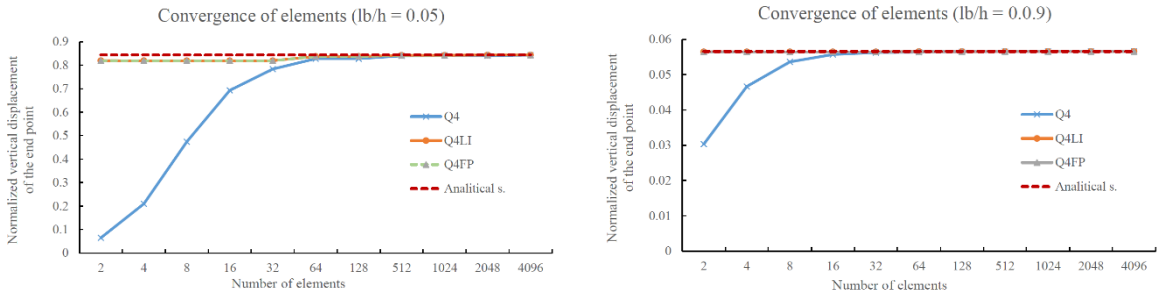

Figure 1. Convergence of the quadrilateral 2D micropolar finite element using the Lagrangian interpolation (Q4) and the fixed-pole interpolation (Q4FP) for normalized vertical displacement

3. Conclusion

We have applied the fixed-pole concept to linear analysis of the micropolar continuum. The enhanced fixed-pole interpolation provides better convergence towards the solution than the Lagrangian interpolation. Development of robust micropolar finite elements is of vital importance for future progress of the micropolar continuum theory. In the future work, the enhanced fixed-pole interpolation will be also applied to the dynamic analysis of the micropolar continuum.

This work has been financially supported by the Croatian Science Foundation research project "Fixed-Pole Concept in Numerical Modelling of Cosserat Continuum" (HRZZ-IP-2018-01-1732) and the University of Rijeka research grant "Computational and Experimental Procedures for Assessment of Material Parameters in Cosserat's Continuum" (uniri-tehnic-18-248 1415).

References

[1] Nowacki, W., *Theory of micropolar elasticity*. Springer-Verlag, Vienna, 1972.

[2] Eringen, A. C., Microcontinuum Field Theories: I. Foundations and Solids. Springer-Verlag; New York, 2012.

[3] Bottasso, C., Borri, M., Integrating Finite Rotations. *Comut. Methods Appl. Mech. Eng*, 164 (3-4), 307-331, 1998.

[4] Gauthier, J., Jahsman, W. E., A Quest for Micropolar Elastic Constants. *Journal of Applied Mechanics*, 42, 369-374, 1975.

[5] Grbčić, S., Jelenić, G., Ribarić, D., Quadrilateral 2D linked-interpolation finite elements for micropolar continuum. *Acta Mechanica Sinica*, Vol. 35, 1001-1020, 2019.

Author index

H

I

J

K

L

M

N

O

P

R

S

Š

T

U

V

W

Y

Z

Ž

Sponsors

Reimagining Motion

AVL-AST d.o.o.
Strojarska cesta 22
10000 Zagreb
Croatia
avl_croatia@avl.com
www.avl.com/avl-ast-d-o-o

AVL Croatia was founded in 1996 with headquarters in Zagreb as **a member of the AVL List GmbH.**
As a strategic partner, we are mainly oriented **to software production, electrification, creating and implementing software solutions for simulation, testing and optimization** of all types of propulsion systems for passenger and commercial vehicles. We are a significant partner to a large number of car manufacturers worldwide who, due to stringent environmental standards and fuel consumption reduction, need to continuously improve their products.

Our Areas of Expertise:
Software Development
Desktop & web simulation products, data analytics, co-simulation, distributed computing and visualization

Simulation Technologies
Multibody Dynamics and NVH, Structural FEA Analysis, System Simulations.

Virtual Testing
Virtual Testbed and HiL setup, MiL&SiL setup and sensor/actuator model development, test case automation for powertrain and Infotainment systems control units.

Autonomous Driving
Ontology engineering, test cases generation, route planning.

Power Electronics
Design of power converters based on wide band-gap transistors (SiC, GaN), battery cell cyclers, dyno inverters & AFE-s.

"At AVL Croatia, we keep pace with the changes in the automotive industry and look forward to working with our customers on improving their products and services, in quality, competitiveness, usability, and availability. We believe that our support to our customers can be valuable, only when given at the right time."
- Goran Mirković, Managing Director

AVL List GmbH (“**AVL**”) with its headquarters in Graz, is one of the world’s leading mobility technology companies for development, simulation and testing in the automotive industry, and in other sectors. Drawing on its pioneering spirit, the company provides concepts, solutions and methodologies for a greener, safer and better world of mobility. AVL constantly expands its portfolio of high-end methodologies and technologies in the areas of vehicle development and testing. With a holistic approach - from ideation phase to serial production – the company covers vehicle architectures and platform solutions including the impact of new propulsion systems and energy carriers. To achieve the vision of climate-neutral mobility, AVL drives innovative and affordable solutions for all applications - from traditional to hybrid to battery and fuel cell electric technologies.

As a global technology provider, AVL’s offerings range from simulation, virtualization and test automation for product development to ADAS/AD and vehicle software. The company combines state-of-the-art and highly scalable IT, software and technology solutions with its application knowhow, thereby offering customers extensive tools in areas such as Big Data, Artificial Intelligence, Cybersecurity or Embedded Systems. Furthermore, AVL is striving towards a safe and comfortable driving experience for everyone and brings a comprehensive understanding of assisted and automated driving functions in different vehicles and environments into play. AVL's passion is innovation. Together with 10,700 employees at more than 90 locations and with 45 Tech and Engineering Centers worldwide, AVL is supporting customers in their mobility ambitions. In 2021, the company generated a turnover of 1.6 billion Euros, of which 12% are invested in R&D activities to ensure continuous innovation.

PROBABILISTIC EVALUATION METHOD OF COMPOSITE FAILURE MODELS

STATE-OF-THE-ART

- **Continuous fibre reinforced composites** are the best candidates for future materials
- FE method is the only reliable tool to assess these structures from strength POV
- Distinction upon stress compliance is based on **1st-ply-failure models**
- These models are available in commercial FE tools with user input parameters
- Getting the **failure model** parameters right is prime to get reliable results
- **Identifying strength** / failure parameters is hard:
  - Multiple strength components affect failure
  - Multiaxial stress state occurs
  - High scatter in experimental data is possible
  - Strength components require proper uncertainty quantification
  - Complex limit stress state equations are necessary

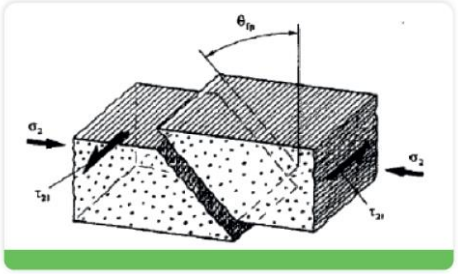

R&D ACTIVITY, INNOVATION

- **High-fidelity** material parameter fitting processes with UQ and probabilistic methods
- Method for direct evaluation of **stiffness** constants and their **variation**
- Method for direct evaluation of **failure model parameters** and the variation of them (Tsai-Wu, Puck, Hashin etc.)
- Possibility to derive **FE material input** corresponding to predefined **probability of survival**
- Opportunity to compute **cost of safety**

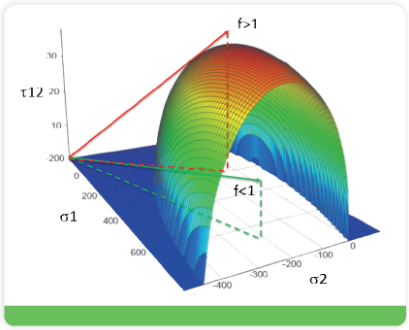

WHY IS ECON YOUR PARTNER?

CAPABILITIES AND ENABLERS FOR R&D ACTIVITIES

- **20 years** expertise in engineering simulation & automation services
- **90+** professional engineers with up-to-date knowledge
- Numerous **international** customer and R&D projects in different industries and areas
- In-house **material testing laboratory**
- **Wide simulation portfolio** covering all important areas as:
  - Structural (finite element analysis)
  - Fluid (computational fluid dynamics analysis)
  - Electromagnetic analysis
  - Multibody simulation (MBS)
  - 1D system simulation
  - Injection moulding simulations
  - Method development
- **Industrial automation** expertise, capability of designing special testing equipment for R&D purposes

SIMULATION REFERENCES

your anastomosis · thyssenkrupp · BYD · HARMAN · HYUNDAI HEAVY INDUSTRIES CO.,LTD. · GE · KNORR-BREMSE · HILITE INTERNATIONAL · BOSCH · ACPS AUTOMOTIVE · SIEMENS · BMW · Continental · YUTONG · CLAAS · SUMITOMO ELECTRIC · BorgWarner

CERTIFICATIONS & AWARDS

MSZT CERT · CERTIFIED IQNet MANAGEMENT SYSTEM · Registration number: ISO 9001:2015: 593/1374-1:283 ISO/IEC 27001:2013: ISMS/044-43 · TISAX® RESULT AVAILABLE · JEC WORLD INNOVATION AWARDS PARTNER 2019

www.econengineering.com

cae@econengineering.com

Center for Vehicles of Croatia (CVH) has been synonymous with benchmark for technical inspections, testing and homologation of vehicles in Croatia. However, apart from being the authority in the broad domain of vehicles, CVH has surpassed its primary business activity over the years.

Investing in technological development, corporate social responsibility, employee training and connecting with leading institutions has enabled us to positively influence the safety of traffic participants, environmental protection, energy saving and human health.

We are proud to point out that we are part of the vehicle inspection system which today has more than 1600 employees at 159 locations across Croatia and that we actively participate within the framework of that system in the development of national, European and international standards of prominent Croatian and world organisations.

Our responsible and professional "drive" in the story of our success has allowed us to grow together with our employees, customers and other citizens, building a place of trust and security for drivers, associates and partners.

It is our greatest success and an additional incentive to continue in the same direction in order to make the whole society an even better and safer place for future generations.

Eco-friendly distribution transformer

- Rated power: 250 kVA (KNAN)
- No-load losses AA0 = 270 W
- Load losses Ak = 2350 W (Ecodesign Tier 2)
- OLTC with vacuum technology “Ecotap VPD”
- Sound pressure level Lp(A) ≤ 32 dB(A)
- Low magnetic field: 1 µT @ H=2.5 m
- Filled with natural ester-based fluid

KONČAR
D&ST

Project UK

- Type designation: TRP60000-145/P
- Rated power: 60 MVA
- Rated voltages: 132(+6,-12)x1.67%/33 kV
- Connection symbol: Ynd1(d11)

ORGANISED BY

CSM

CROATIAN SOCIETY OF MECHANICS

ZAGREB – OSIJEK – RIJEKA – SL. BROD – SPLIT

CO-ORGANIZER

ceacm

Central European Association
for Computational Mechanics

UNDER THE AUSPICES OF

ACADEMIA SCIENTIARUM ET ARTIUM CROATICA

MDCCCLXI

SPONSORS

Golden sponsors

Silver sponsor

Bronze sponsors

Sponsor